CHEMTECH '15
3RD INTERNATIONAL CHEMICAL ENGINEERING AND CHEMICAL TECHNOLOGIES CONFERENCE PROCEEDINGS

Özgür Öztürk DAKAM YAYINLARI
November 2015, İstanbul.

www.dakam.org
Firuzağa Mah. Boğazkesen Cad., Çangar İş Merkezi 36/ 2, 34425, Beyoğlu, İstanbul
CHEMTECH '15 / 3rd International Chemical Engineering and Chemical Technologies Conference Proceedings
November 23-24, 2015, İstanbul
organized by DAKAM (Eastern Mediterranean Academic Research Center)

Edited by: Barış Öztürk
Cover Design: D/GD (DAKAM Graphic Design)
Print: Metin Copy Plus
Mollafenari Mah., Türkocağı Cad. 3/1, Mahmutpaşa/Istanbul, Turkey
ISBN: 978-605-9207-17-1

CHEMTECH '15
3RD INTERNATIONAL CHEMICAL ENGINEERING AND CHEMICAL TECHNOLOGIES CONFERENCE PROCEEDING

DAKAM PUBLISHING

CONTENTS

FERULA GUMMOSA BOISS REVERSE THE ACETAMINOPHEN-INDUCED OXIDATIVE STRESS IN RAT LIVERS 9
ABOLFAZL DADKHAH, FAEZEH FATEMI, SALOME DINI, GHASEM KHALAJ, SABEREH NAIJ

DEVELOPMENT AND CHARACTERIZATION OF IN-SITU POLYMERIZATION OF LACTIC ACID AND NANO CRYSTALLINE CELLULOSE (NCC) BIO-NANO-COMPOSITE 14
RACHEL SI EN CHOK, BAHMAN AMINI HORRI, BABAK SALAMATINI

MODIFICATION OF CU AND CUO NANOPARTICLES WITH OLEIC ACID AND THERMAL CHARACTERIZATION OF PARAFFINS: TOWARDS THE PREPARATION OF A STABLE NANOPCM 22
DIEGO VASCO, MANUEL MUÑOZ, PAULA GALVEZ, PAULA ZAPATA

SYNTHESIS OF CARBON SPHERULES AND PREPARATION OF DISPERSIONS BASED ON GLYCEROL: STABILITY TEST AND THERMAL CONDUCTIVITY MEASUREMENT 32
DIEGO VASCO, CAMILO CASTILLO, RODRIGO PIZARRO, VALDERES DRAGO

EXTRACTION OF LEAD FROM LIQUID WASTES BY EMULSION LIQUID MEMBRANE CONTAINING TRI-OCTYL PHOSPHINE OXIDE 37
ELSAYED FOUAD1, FAROOQ AHMAD, KHALED ABDELRAHMAN

BACTERIA EFFICIENCY ENHANCEMENT FOR URANIUM RECOVERY USING DIETHYL SULFATE 49
FAEZEH FATEMI, MOHAMMAD ALI FIROOZE ZAREH1, SAMANEH JAHANI

EFFECTS OF ULTRAVIOLET IRRADIATION ON BACTERIA AND BIOLEACHING OF LOW-GRADE URANIUM ORE 54
FAEZEH FATEMI, SAMANEH JAHANI, SABA MIRI

DEVELOPMENT OF A THERMAL KINETIC DEGRADATION MODEL FOR LINEAR LOW DENSITY POLYETHYLENE (LLDPE) BLENDS WITH POLYSTARCH-N (PSN) 59
F.A. AL-TURKI, S.M. Al-SALEM, A. BUMAJDAD, A.R. KHAN

SUSTAINABILITY ASSESSMENT OF RICINUS COMMUNIS BIODIESEL USING LCA APPROACH 65
MOHAMMED AMOURI, TOUDERT AHMED ZAID, MAJDA AZIZA

A USE OF ACTIVATED CARBON DEVOLOPPED FROM JUJUBE STONE FOR THE REMOVAL OF A LEAD FROM AQUEOUS SOLUTIONS BY SORPTION 66
NESMA BOUCHELKIA, LOTFI MOUNI, LAZHAR BELKHIRI, ABDELKRIM BOUZAZA

HYDROGEN STORAGE IN A RECYCLABLE ORGANIC HYDRIDE: THE DEHYDROGENATION OF METHYLCYCLOHEXENE 71
MUHAMMAD R USMAN

SYNTHESIS OF AG-TIO2 BIMETALLIC NANOPARTICLES WITHIN PS-B-PAA REVERSE MICELLE CORES 76
NUMAN HODA, BURÇIN ACAR ÇAKIR, ÖNDER TOPEL, LEYLA BUDAMA

COMPREHENSIVE STUDY ON GEOTHERMAL POWER PLANT BY MIXTURE FLUIDS 77
TALIEH RAJABLOO, PAOLO IORA AND COSTANTE MARIO INVERNIZZI

STEEL SLAG AS FERTILIZER 78
PEGAH MOGHADAM, MOHSEN NASR ISFAHANI

EFFECTS OF CURING TIME ON CORROSION RESISTANCE OF HYBRID SILANE COATING FOR LOW CARBON STEEL 79
ALI RAHIMI FERDOSINEZHAD, LOH HWEI LING, POOVARASI BALAN

MEASUREMENTS AND MODELING OF TERNARY SYSTEMS CONTAINING THIOLS (ORGANIC SULFUR SPECIES) IN HYDROCARBON AND WATER AT 303, 335, AND 365 K AND PRESSURE UP TO 9 MPA 87
JAVEED A. AWAN, CHRISTOPHE COQUELET, IOANNIS TSIVINTZELIS, GEORGIOS M. KONTOGEORGIS

SYNTHESIS OF NOVEL N SULFONAMIDOXAZOLIDIN-2-ONES 88
RADIA BOUASLA, MALIKA BERREDJEM AND NOUR-EDDINE AOUF

THE FLUORESCENCE QUENCHING OF DNA-ETHIDIUM BROMIDE BY TETRABUTYLAMMONIUM BROMIDE-BASED DEEP EUTECTIC SOLVENTS 89
RIZANA YUSOF, KHAIRULAZHAR JUMBRI, HASLINA AHMAD, MOHD BASYARUDDIN ABDUL RAHMAN

SUPERHYDROPHOBIC SURFACE DEVELOPMENT BASED ON POLYURETHANE CHEMISTRY FOR COATING MATERIALS 97
SEHER ŞENADA, SENNUR DENIZ

INCORPORATING PROTEIN FLEXIBILITY IN THE IDENTIFICATION OF SMALL MOLECULES AS PROTEIN ARGININE DEIMINASE IV (PAD4) INHIBITORS 103
ZALIKHA IBRAHIM, BIMO A. TEJO, MUHAMMAD ALIF MOHAMMAD LATIF,
MOHD BASYARUDDIN ABDUL RAHMAN

THERMAL AND MECHANICAL PROPERTIES OF COMPRESSION-MOLDED POLY (LACTIC ACID)/GLUTEN/CLAYS BIO (NANO) COMPOSITES 104
ABDELLATIF MOHAMED

PHYTOREMEDIATION OF PETROLEUM RELEASES BY PHRAGMITE AUSTRALIS 105
AMEL NASRI, SEGNI LADJEL, FATIHA DJAFRI, AYADA DJAFRI

X RAYS ANALYSIS OF MICROSTRUCTURE IN AL-LI ALLOYS 106
RACHIDA AMICHI, SMAINE BOURAHLA

SPECTROSCOPIC STUDIES OF INCLUSION COMPLEX OF 2-BENZOTHIAZOLETHIOL AND Β- CYCLODEXTRIN 111
SONIA BADI, ACHOUR SERIDI, MEKKI KADRI

GROWTH OF METAL OXIDE (TIO2/AG) THIN FILMS SPUTTERED BY HIPIMS EFFECTIVE IN BACTERIAL INACTIVATION: PLASMA CHEMISTRY AND ENERGETIC 112
OUALID BAGHRICHE, ABDENOUR ZERTAL, JUAN KIWI

COMPARATIVE STUDY OF CDS/PS AND CDS/PMMA COMPOSITE FILMS 113
HARIECHE, BOUBEKEUR BOUDINE, M SEBAIS

ANTIMICROBIAL ACTIVITY OF MENTHA ROTUNDIFOLIA ESSENTIAL OILS AND METHANOLIC EXTRACTS 114
RACHID BELHATTTAB, SIHAM FERDJIOUI

RELATIONSHIP BETWEEN MICROSTRUCTURE, MICROHARDNESS AND CORROSION RESISTANCE OF ALUMINUM ALLOY TYPE 2017A 115
SOFIA BENAMIROUCHE, ABDEREZAK ABDI, MOHAMED EL AMINE BELOUCHRANI

STEEL CORROSION INHIBITION BY ELAEOSELINUM THAPSIOIDES EXTRACT IN ACID SOLUTION 126
MERZOUG BENAHMED, NOUREDDINE DJEDDI, BRAHIM HARKATI, SALAH AKKAL

SYNTHESIS AND CHARACTERIZATION OF SOME CHLORINATED 3, 5-DIARYL-2-PYRAZOLINES ANALOGUE OF NATURAL PRODUCT AS ANTIMICROBIAL AGENTS **135**
BENMEKHBI LOTFI , BENCHARIF LEILA

ENVIRONMENTAL WASTEWATER IMPACT ON THE WATER RESOURCES OF THE REGION OF KHENCHELA (EASTERN ALGERIA) **136**
BENRABAH SAMIA, ATTOUI BADRA, HANNOUCHE MANI

EFFECTS OF COPPER AND COBALT CO-DOPING ON STRUCTURAL, OPTICAL AND ELECTRICAL PROPERTIES OF TIO2 THIN FILMS PREPARED BY SOL GEL METHOD **137**
BADREDDINE. TOUBAL, RABAH. BENSAHA, FAHRETTIN YAKUPHANOGLU

CHEMICAL COMPOSITION, ANTIMICROBIAL AND ANTIOXIDANT PROPERTIES OF MARGOTIA GUMMIFERA ESSENTIAL OIL **153**
BOUCHEKRIT MOUFIDA, LAOUER HOCINE, HAJJI MOHAMED, NASRI MONCEF, FLAMINI GUIDO

RELIABILITY OF HYDROCARBONS TRANSPORT PIPELINES SUBJECTED TO CONTINUOUS DEGRADATION **164**
BOUZID RACHID, BOUALI ELAHMOUNE, GACEB MOHAMED

MODELING OF DESWELLING BEHAVIORS OF PH AND TEMPERATURE SENSITIVE POLY (N-ISOPROPYL ACRYLAMIDE-ACRYLIC ACID) INTERPENETRATING HYDROGELS BY ARTIFICIAL INTELLIGENCE SYSTEM **168**
CIHANGIR BOZTEPE, MEHMET YÜCEER, ASIM KÜNKÜL

THE SYNTHESIS, CHARACTERIZATION AND INVESTIGATION OF ANTIMICROBIAL INHIBITION KINETICS OF ACRYLAMIDE BASED HYDROGEL-SILVER NANOCOMPOSITE SYSTEM **169**
CIHANGIR BOZTEPE, EMIR TOSUN, TUĞÇA BILENLER, KÜBRA ŞIŞLIOĞLU

HYDROGEL SUPPORTED NHC-PD CATALYST SYSTEMS FOR THE SUZUKI REACTION **170**
CIHANGIR BOZTEPE, ASIM KÜNKÜL, ISMAIL ÖZDEMİR, NEVIN GÜRBÜZ

THE CATALYTIC ACTIVITIES OF SOME NOVEL POLYMERIC NHC-PD HYDROGEL SYSTEMS **171**
CIHANGIR BOZTEPE, ASIM KÜNKÜL, ISMAIL ÖZDEMİR, NEVIN GÜRBÜZ

EFFECT OF TEMPERATURE AND TIME ON VULCANIZING A FABRIC CONVEYOR BELT WITH A COLD VULCANIZING ADHESIVE **172**
DENIZ AKIN SAHBAZ, CAGLAYAN ACIKGOZ, OMER METE KOCKAR

PATH INTEGRAL TREATEMENT OF THE DEFORMED GENERALIZED DENG-FAN POTENTIAL PLUS THE DEFORMED ECKART POTENTIAL IN D-DIMENSIONS **176**
DIAF AHMED, HADJER BAKHTI, HADDA BADANI

VOLUMETRIC THERMODYNAMIC'S PROPERTIES OF DILUTE ANALGESIC SUBSTANCES IN ALCOHOLS AT DIFFERENT TEMPERATURES **177**
SAÉDA DIDAOUI, AHCÈNE DOUAS, AHMED AIT-KACI

ADSORPTION AND CORROSION INHIBITIVE PROPERTIES OF RUTA CHALEPENSIS ON API X52 STEEL IN HYDROCHLORIC ACID MEDIA **178**
MERYEM AMAL BENGHALIA, CHAHINEZ FARES, MOHAMED HADJ MELIANI, ABDELKADER KHADRAOUI

INVESTIGATION OF METHYLENE BLUE ADSORPTION OF AGRICULTURAL WASTES WITH ELOVICH ADSORPTION KINETICS IN FIXED BED **187**
FATIH KILIÇ, ÇIGDEM SARICI OZDEMIR

REMOVAL OF PHARMACEUTICAL COMPOUNDS USING ACTIVATED CARBON CLOTH FROM AQUEOUS SOLUTIONS 188
FIRDEVS MERT, SADIK ÇALIK, LEYLA BUDAMA AKPOLAT, NUMAN HODA

MATHEMATICAL MODELING OF PLATFORMING 189
K. HACHAMA, R. KERFAH

STRUCTURAL AND OPTICAL PROPERTIES OF LEAD OXIDE/POLYSTYRENE NANOCOMPOSITE FILMS 190
B. TROUDI, O. HALIMI, M. SEBAIS, B. BOUDINE, B. HARIECHE, B. KEHAL

PHYTOCHIMICAL STUDY AND ANTIOXIDANTS ACTIVITY OF PLANTAGO ALBICANS L. 198
BRAHIM HARKATI, ALI KALLA, MERZOUG BENAHMED, HOCINE LAOUER, SALAH AKKAL

JUNIPERUS SABINA L. OF ALGERIA: CHEMICAL COMPOSITION AND ANTIBACTERIAL ACTIVITY OF THE AERIAL PARTS ESSENTIAL OILS 201
ABDENOUR ADJOUAD, HOCINE LAOUER, ROBERT P. ADAMS, SALAH AKKAL

MICROPOROUS SYNTHETIC CO-SILICALITE-1 FROM LUDOX SILICA PREPARED BY A HYDROTHERMAL PROCESS AS A CATALYST FOR OXIDATION OF CONGO RED 202
IMÈN BENCHIKH, FATIHA DJAFRI, AYADA DJFRI, FRANCK LAUNAY

EFFECT OF CONSTRUCTION, METEOROLOGICAL AND OPERATIONAL PARAMETERS ON THE FRESH WATER YIELD OF A CONDENSATION CHAMBER OF A MODULAR SOLAR STILL 203
RABAH KERFAH, NOURA BELKHEIR, ZAARAOUI ABDEL KADER, EL GHALIA FILALI

KINETICS OF INHIBITION OF XANTHINE OXIDASE BY LYCIUM ARABICUM AND ITS PROTECTIVE EFFECT AGAINST OXONATE-INDUCED HYPERURICEMIA AND RENAL DYSFUNCTION IN MICE 210
NAOUEL BOUSSOUALIM, HAYAT TRABSA, IMANE KRACHE, ABDERRAHMANE BAGHIANI, SEDDIK KHENNOUF, NOUREDDINE CHAREF, LEKHMICI ARRAR

MODELING OF THE SOLUBILITY OF ANTILIPEMIC AGENTS IN SUPERCRITICAL CARBON DIOXIDE APPLICATION TO CLOFIBRIC ACID 211
ABDESLAM-HASSEN MENIAI, ISMAHENE HALOUI, ABIR BOULEDJOUIDJA, AHMED ZERMANE, OUASSILA LARKECHE, RANIA DJERAFI, ELISABETH BADENS

ANTIOXIDANT ACTIVITY OF ARISTOLOCHIA LONGA L. EXTRACTS 219
MEROUANI N, BELHATTAB R.

SYNTHESIS OF NEW MATERIALS DERIVES OF (Z) 2 - (2 PHENYL-3-THIENYL) ACRYLONITRILE) CARACTERISATIONS: CYCLIC VOLTAMMETRY AND IMPEDANCE SPECTROSCOPY 220
S. MOSBAH, M.BENCHARIF, L.BENCHARIF

FIRST-PRINCIPLES CALCULATIONS OF THE PHASE STABILITY AND SURFACE ENERGY OF TIO2 (100) AND (110) 221
MOURAD AZIBI, NADIA SAOULA

ABSORPTION SPECTROSCOPY OF SINGLE GOLD NANOPARTICLES 227
MUSTAFA YORULMAZ, SARA NIZZERO, ANNELI HOGGARD, LIN-YUNG WANG, YI-YU CAI, WEI-SHUN CHANG, STEPHAN LINK

SYNTHESIS AND CHARACTERIZATION OF MG-AL-CO3-LDHS: A HIGHLY EFFICIENT CATALYST FOR THE SYNTHESIS OF 3,4-DIHYDROPYRIMIDIN-2(1H)-ONES AND THIONES ANALOGS BY BIGINELLI REACTION UNDER SOLVENT-FREE CONDITIONS 228
MUSTAPHA DIB, SOUFIANE AKHRAMEZ, ABDELLATIF ESSOUMHI, HAJIBA OUCHETTO, KHADIJA OUCHETTO, ABDERRAFIA HAFID AND MOSTAFA KHOUILI

STRUCTURAL AND OPTICAL PROPERTIES OF PURE AND SN, IN AND CU DOPED ZNO **229**
OUILI ZEINEDDINE, ALLIOUCHE HAYETTE, BOUDINE BOUBEKEUR, SEBAIS MILOUD AND HALIMI OUAHIBA

THEORETICAL STUDY OF THE DOPAMINE: β CD COMPLEX USING DFT-ONIOM METHODS **230**
RAYENNE DJEMIL, DJAMELEDDINE KHATMI

EVALUATION OF FLOCCULANTS FOR THE RECOVERY OF CHAETOCEROS GRACILIS MICROALGAE **235**
LETICIA PÉREZ, ROCÍO MACEIRAS, J. LUIS SALGUEIRO, ÁNGELES CANCELA, ÁNGEL SÁNCHEZ

DEFECTS EVOLUTION IN CVD ZINC CHALCOGENIDES AT DOPING PROCESS BY TRANSITION METALS **242**
EUGENI GAVRISHUK, VLADIMIR IKONNIKOV, DMITRY SAVIN, ELENA MOZHEVITINA, ROMAN AVETISOV

NEW FLUORESCENT HYBRID MATERIALS BASED ON Eu-COMPLEXES IN OXYFLUORIDE GLASS AND GLASSCERAMIC MATRIX **243**
OLGA PETROVA, ILYA TAYDAKOV, MARİA ANUROVA, ALİNA AKKUZİNA, ROMAN AVETİSOV, ANDREW KHOMYAKOV, IGOR AVETİSSOV

FABRICATION AND CHARACTERIZATION OF NANOCOMPOSITE $Nb2O5$/KBr **249**
S. HALIMI, M. HEMARA, M.SEBAIS, Z. OUILI, O. HALIMI, B. BOUDINE. A. DJEBLI

PHYTOCHEMICAL ANALYSIS, DIURETIC AND FREE RADICAL SCAVENGING ACIVITIES OF ORIGANUM GLANDULOSUM DESF. LEAVES EXTRACTS **250**
AMEL BOUAZIZ, SEDDIK KHENNOUF, SALIHA DJIDEL, MUSSA ABU ZARGA, SHTAYWY ABDALLA, ABDERAHMANE BAGHIANI, SALIHA DAHAMNA, SMAIN AMIRA, LEKHMICI ARRAR

ANTIOXIDANT ACTIVITY AND POLYPHENOLIC CONTENT OF ACETONE EXTRACT OF ALGERIAN PISTACIA LENTISCUS LEAVES **249**
SENATOR ABDERRAHMANE, MORCHEDI WAHIBA AND BOURICHE HAMAMA

CHARGE-TRANSFER COMPLEX OF TETRACYANOETHYLENE WITH SULFAHYDANTOIN IN POLAR SOLVENT **252**
SAIDA SERIDI, SONIA BADI, MALIKA BERREDJEM, MEKKI KADRI

COMPARISON OF HYDROGEN SORPTION PROPERTIES OF ACTIVATED CARBONS PREPARED BY H3PO4 AND K2CO3 ACTIVATION OF CHERRY STONES **254**
TANER ERDOGAN, FATMA OGUZ ERDOGAN

APPLICATIONS AT CLAY CHARACTERIZATION, WHICH SYNTHESIZED BY SUBJECTING WITH ACID, BASE, SALT, NEUTRAL MEDIA **263**
TÜLAY ARASAN, ÇİĞDEM SARICI ÖZDEMİR

DESIGN OF IMPLEMENTATION OF RENEWABLE ENERGIES IN A SPANISH TRAINING SHIP **266**
VÍCTOR ALFONSÍN, ROCÍO MACEIRAS, ANDRÉS SUÁREZ, MARTÍN SANJORGE

CHEMICAL COMPOSITION AND BACTERICIDAL ACTIVITY OF AQUEOUS PROPOLIS EXTRACTS FROM BABOR ALGERIA **273**
SOLTANI EL-KHAMSA, MEZAACHE-AICHOUR SAMIA, CHAREF NOUREDDINE AND ZERROUG MOHAMED MIHOUB

POLYPHENOL CONTENTS AND ANTIOXIDANT ACTIVITY OF AQUEOUS EXTRACT OF PROPOLIS FROM SÉTIF, ALGERIA **274**
EL-KHAMSA SOLTANI, NOUREDDINE CHAREF, SAMIA MEZAACHE, MOHAMED MIHOUB ZERROUG

INVESTIGATING THE APPLICABILITY OF MECHANICAL RECYCLING IN KUWAIT BY STUDYING DEVELOPED STANDARDIZED FILM SAMPLES FROM VIRGIN/WASTE POLYMER RESINS SUBJECTED TO ACCELERATED WEATHERING **278**
S.M. AL-SALEM, G. ABRAHAM, A.M. DASHTI, O.A. AL-QABANDI

FERULA GUMMOSA BOISS REVERSE THE ACETAMINOPHEN-INDUCED OXIDATIVE STRESS IN RAT LIVERS

ABOLFAZL DADKHAH, FAEZEH FATEMI, SALOME DINI, GHASEM KHALAJ, SABEREH NAIJ

[1] Department of Medicine, Faculty of Medicine, Qom Branch, Islamic Azad University, Qom, I.R. Iran, *Corresponding author: dadkhah_bio@yahoo.com
[2]Nuclear Fuel Cycle Research School, Nuclear Science and Technology Research Institute,Tehran, I.R. Iran. ffatemi@aeoi.org.ir
[3]Young Researchers and Elite Club, Karaj Branch, Islamic Azad University, Karaj, Iran, Salomehdini6@gmail.com
[4]Faculty of Science, Qom Branch, Islamic Azad University, Qom, I.R. Iran.
[5]Department of Botany, Payame-e-Noor University, Tehran, Iran. sabere.naij.66@gmail.com

Abstract

The objective of the study is to identify the hepatoprotective efficacy of the Ferula (F.) gummosa Boiss essential oils against acetaminophen induced liver damage. 80 male Wistar rats were divided into four groups (n=10). Group 1 received only DMSO as i.p injection, group 2 received acetaminophen at the dose of 500 mg/k b.w dissolved in 400 DMSO as i.p injection, group 3 received F. gummosa essential oils (100 and 200 mg/kg b.w) diluted in 400 DMSO and injected i.p immediately after acetaminophen administration. Then, the hepatic oxidative/antioxidant parameters such as lipid peroxidation (LP), glutathione (GSH) and ferric reducing ability of plasma (FRAP) were estimated 2, 4, 8, 16 and 24h after the treatments. Additionally, histopathology changes in the liver were considered. The results showed that the treatment rats with the F. gummosa essential oils could considerably reversed the changes in serum biochemical parameters for instance LP, GSH and FRAP as well as histology of liver in the acetaminophen indicating hepatoprotective activity of the essential oils. In conclusion, the data strongly indicate the hepatoprotective properties of the oils against acute liver injury and thereby scientifically support its medical use.

Key words: Frula gummosa, Liver injury, Oxidative stress, Hepatoprotective activity.

1. Introduction

Hepatic disorder is a global metabolic and epidemic disease affecting essential biochemical activities in almost every age group [1]. Excess consumption of some drugs such as chemotherapeutic agents, antibiotics, acetaminophen, and exposure to some chemicals such as peroxidised oils, aflatoxin, CCl4 are the major role in the hepatic disorders that almost causes almost 20000 deaths every year [1, 2].

Acetaminophen (Paracetamol) is commonly prescribed for the relief of headaches and other minor aches and pains and is a major ingredient in numerous cold and flu remedies [3]. Acetaminophen at therapeutic doses is primarily metabolized in the lever by cytochrome P_{450} (CYP$_{450}$) and detoxified by glucuronidation and sulphation and subsequently followed by renal excretion [4]. Otherwise, when the acetaminophen is taken in a toxic dose the compound is converted to a toxic form N-acetyl-p-benzo-quinone imine (NAPQI) [2]. NAPQI can increase the formation of reactive oxygen species (ROS) and reactive nitrogen species (RNS) such as superoxide anion and hydroxyl radical leading to hepatic toxicity [6]. Many bioactive compounds and extracts from plants have thus been investigated for hepatoprotective and antioxidant effects against hepatotoxin-induced liver damage [7, 8].

Ferula gummosa Boiss (Persian name “Baridje”) belonging to Apiaceae family is a perennial plant native to central Asia, growing in the northern and western parts of Iran [9]. Baridje have been traditionally used for treatment of various diseases like anticonvulsant, tonic, anti-hysteric, decongestant, treatment of neurological disorders, and stomachache [10-13]. Recent investigations have led to the discovery of some new biological activities of the plant including antiinflammatory, anticonvulsant, antioxidant, antimycobacterial, and antispasmodic [14, 15].

To best of our knowledge, there is no scientific report on hepatoprotective activity of F. gummosa roots, so the goal of this study was to determine the hepatoprotective effects of essential oil isolated from Baridje against paracetamol overdose induced hepatotoxicity in rats.

2. Material and Methods

2.1. Oil Extraction

The dried roots of Baridje were purchased and the oils were extracted from the roots by a Clevenger-type apparatus. The extraction was carried out for 2 h and the essential oils were stored in dark glass bottles in a freezer until further use (1 month).

2.2. Animal Treatments

Male Wistar rats were used throughout this study. The animals were obtained from the Pasteur Institute of Iran and maintained in the animal house facilities with 20 to 22 C° and light/dark cycles of 12 h. Adult animals were 3–4 months of age, weighing about 100 g. They were maintained on a commercial pellet food and tap water ad libitum. The animals were divided into 4 groups (n=5). In negative control group (Group 1), the DMSO was only i.p injected. In control group (Group 2), the acetaminophen (500 mg/kg b.w) dissolved in 400 µl DMSO was i.p injected. In the treatment groups, the F. gummosa E.O at 100 (F 100) and 200 (F 200) mg/kg b.w doses was diluted in 400 µl DMSO and injected i.p immediately after acetaminophen administration (Group 3 and 4).

2.3. Preparation of Tissue Homogenate and Plasma

The heparinated blood samples were collected at different time intervals (4, 8, 16 and 24 h after APAP administration) by heart puncture from all the animals and centrifuged at 3000g for 10 min to obtain the plasma. Liver samples were immediately transferred to ice-cold containers and homogenized (20%, w/v) in the appropriate buffer using a homogenizer (E.L.M 2500). The homogenates were used to measure the biochemical parameters.

2.4. Biochemical Assays

2.4.1. LP Assay: The concentration of LP was measured spectrophotometrically according to the instruction of the kit purchased from Enzo Life Sciences, Inc, UK.

2.4.2. Ferric Reducing Ability of Plasma (FRAP) Assay: This assay was performed using TPTZ reagent as described by Benzie and Strain (1996).

2.4.3. GSH Estimation: GSH was estimated by Ellmans and according to the methods of Seldak and Lindsay (1986).

2.5. Histophatological Assessment

After 24 hours of acetaminophen injection, the biopsy of liver tissue for histopathological examination is removed. For this purpose, small portion of the tissues (maximum 0.5 cm) were fixed in 10% formalin buffer solution. 48 hours later, the formalin solution was replaced and then the samples were kept at room temperature until the preparation of microscopic sections.

2.6. Statistical Analysis

Data are presented as means±Standard error of mean (SEM). The results were subjected to One-way ANOVA followed by Tukey's HSD using SPSS (version 19.0) software. Significant levels were defined as $P<0.05$.

3. Results

3.1. The Effect of Baridje Oils On The Stress Oxidative Parameters In Rats Intoxicated With Acetaminophen

Acetaminophen intoxication produces significant adverse effect on the redox status of the liver evidenced by the biochemical tests such as LP, GSH and FRAP. Administration of the acetaminophen to experimental rats caused a significantly ($P<0.05$) elevation in LP value compared to the group 1 at 16 and 24 h (Table. 1). Likewise, the toxic dose of acetaminophen remarkably ($P<0.05$) reduced the GSH level of liver tissue at 4 and 8 h after acetaminophen treatment found in Table 1.

Table 1: The effect of F. gummosa Boiss oils on LP and GSH levels at different time intervals after acetaminophen treatments

Groups	LP (pmol/mg protein)					GSH (nmol/mg)			
	4 h	8 h	16 h	24 h		4 h	8 h	16 h	24 h
Group 1	10.825±0.5	10.825±0.5	10.825 ±0.5	10.825±0.5	Group 1	42.17±3.3	42.17 ±3.3	42.17±3.3	42.17±3.3
Group 2	11.3±0.4	12.62±1.07	14.75±1.1*	16.12±0.7*	Group 2	25.2±1.2*	31.55±1.8*	42±0.7	40.25±2.1
Group 3	11.1±0.53	10.82±0.5	12.85±0.7	13.27±0.5**	Group 3	24.75±1.3	30.75±1.7	41.25±2.7	42±2.16
Group 4	10.4±0.2	11.07±0.3	11.1±0.4**	12.92±0.6**	Group 4	34.25 ±2.7**	40.25±3.3**	42 ±4.5	41.25±2.2

*P<0.05 is considered significantly between Negative control group (Group 1) and Control group (Group 2). **P<0.05 is considered significantly between Control group (Group 2) and F. gummosa Boiss essential oils (Groups 3 and 4)

The administration of Baridje oil at 200 mg/kg b.w reduced the elevated levels of LP at 16 and 24 h, while the oil at 100 mg/kg b.w modulated the level of LP just at 24 h after acetaminophen treatment (Table. 1). In addition, the rats treated with Baridje oil at 200 mg/kg b.w dose indicated a significant (P<0.05) increase in the levels of GSH at 4 and 8 h (Table. 1).

As shown in Table 2, in acetaminophen group, the amount of FRAP was significantly (P<0.05) risen due to the injection of toxic dose of acetaminophen (4 & 8 h). However, the level of FRAP was significantly (P<0.05) lowered in the rats pretreated with Baridje oil at the dose of 100 & 200 mg/kg b.w at 4& 8 h, respectively as compared with the acetaminophen-intoxicated animals in group 2 (Table 2).

Table 2: The effect of F. gummosa Boiss oils on FRAP at different time intervals after acetaminophen treatments

Groups	FRAP (Umol/L)			
	4 h	8 h	16 h	24 h
Group 1	366.25± 35. 55	366.25± 35. 55	366.25 ±35. 55	366.25 ±35. 55
Group 2	16662.5± 85.08*	696.25 77.81*	510± 65.57	357.5 ±37.94
Group 3	517.5± 13.14**	477.5 ±11.08	355± 35.23	377.5 ±37.05
Group 4	1600± 7.71	990 ±9255**	507.5± 35.90	395 ±37.74

*P<0.05 is considered significantly between Negative control group (Group 1) and Control group (Group 2). **P<0.05 is considered significantly between Control group (Group 2) and F. gummosa Boiss essential oils (Groups. 3 and 4).

3.2. Histopathological Analysis

Histopathological studies indicated the normal structure of liver tissue without necrosis in negative control group (Fig. 1 A). In the acetaminophen group, sever tissue injuries including sever necrosis, vacuolar degeneration of hepatocytes with increasing in kupffer cells were observed (Fig. 1 B). In the liver of rats treated with acetaminophen together with 100 mg/kg b.w of F. gummosa essential oils, there are the mild necrotic hepatocytes and mild vacuolar degeneration of hepatocytes without any increase in the kupffer cells (Figs. 1 C). But, there are no acute liver injuries in the group 4 treated with 200 mg/kg b.w dose of the essential oils (Fig. 1D).

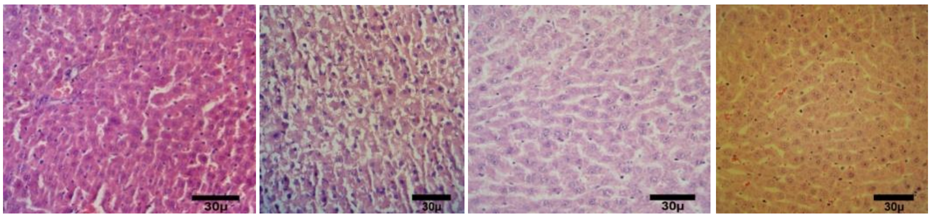

Fig 1: Effect of F. gummosa Boiss oil on histopathological changes after acetaminophen administration.

4. Discussion

The present survey were founded the potential protective effect of F. gummosa Boiss on acetaminophen-induced hepatotoxicity. In our experiments it is observed that the LP and GSH levels in the paracetamol group were changed (Table. 1). We also observed the total antioxidant capacity of plasma (FRAP) was remarkably increase in acetaminophen group (Table. 2). In fact, damage to the liver by acetaminophen is not due to the drug itself, but to a toxic metabolite, N-acetyl-p-benzoquinone imine (NAPQ) produced by CYP_{450} enzymes [16]. Semiquinone radicals, obtained by one electron reduction of NAPQ can covalently binds to macromolecules of cellular membrane and increases the lipid peroxidation resulting in the tissue damage. Indeed, it can alkylate and oxidise intracellular GSH, which results in the depletion of liver GSH pool subsequently leads to increased lipid peroxidation and liver damage [17]. Furthermore, these free radicals mediated oxidative damage to macromolecules such as lipids, proteins and DNA [18, 19]. Also, the histopatology results clearly indicated that there is a significant hepatic damage due to paracetamol (Fig. 1).

Otherwise, treatment rats with 200 mg/kg b.w dose of the essential oils could surprisingly reverse the levels of LP, FRAP and GSH against the liver injuries induced by high dose of acetaminophen. While, the 100 mg/kg b.w of essential oils could modulate the levels of some parameters like FRAP and LP in compared to the group 2 (Table. 2). The above results are completely agreement with our histopatology findings (Fig. 1). Natural products that possess antioxidant properties have been reported to prevent liver damage caused by free radicals by interfering with the oxidation process through radical scavenging [20]. It suggests that this hepatoprotective action of the oil may correlate with its natural antioxidant components made up of phenolics. Previous research was informed the antioxidative potential of F. gummosa essential oil in 2'-diphenyl-1-picrylhydrazyl radical (DPPH) as well as β-carotene/linoleic acid assays [21]. In conclusion, F. gummosa oils were effective in protecting rats against acetaminophen induced hepatotoxicity via modulating the levels of LP, GSH and FRAP.

References

[1] Akhil Bhardwaj, Pankaj Khatri, Soni ML. 2011, Potent Herbal Hepatoprotective Drugs:A Review. Journal of Advanced Scientific Research, 2(2): 15-20.

[2] Nirmala M, Girija K, Lakshman K, Divya T. 2012, Hepatoprotective activity of Musa paradisiaca on experimental animal models. Asian Pacific Journal of Tropical Biomedicine, 10:11-15.

[3] Scottish Intercollegiate Guidelines Network (SIGN), "6.1 and 7.1.1". Guideline 106: Control of pain in adults with cancer (PDF). Scotland: National Health Service (NHS), 2008.

[4] Parmar D, Ahmed G, Kandakumar MA and Katyare SS, Mitochondrial ATP ase: a target for Paracetamol induced hepatotoxicity. Eur. J. Pharmacol., 1995, 293, 225- 229.

[5] Miner DJ, Kissinger PT. 1979, Evidence for the involvement of N acetyl-p-benzoquinone imine in acetaminophen metabolism, Biochemicalpharmacology, 28, 3285-3290.

[6] Michael SL, Pumford NR, Mayeux PR, Niesman MR, and Hinson JA, 1999, Pretreatment of mice with macrophage inactivators decreases acetaminophen hepatotoxicity and the formation of reactive oxygen and nitrogen species. Hepatology, 30: 186–195.

[7] Yousef, M.I.; Omar, S.A.; El-Guendi, M.I.; Abdelmegid, L.A. 2010, Potential protective effects of quercetin and curcumin on paracetamol-induced histological changes, oxidative stress, impaired liver and kidney functions and haematotoxicity in rat. Food Chem. Toxicol. 48, 3246–3261.

[8] Choi, J.H.; Choi, C.Y.; Lee, K.J.; Hwang, Y.P.; Chung, Y.C.; Jeong, H.G. 2009, Hepatoprotective effects of an anthocyanin fraction from purple-fleshed sweet potato against acetaminopheninduced liver damage in mice. J. Med. Food , 12, 320–326.

[9] ZARGARI A. 1991, Medicinal Plants. Vol. 2. Tehran: Tehran University Publication.

[10] Zargari A. 1996, Medicinal Plants (in Persian). Vol. 2. Tehran: Tehran University Publications; 592-602.

[11] Eigner D, Scholz D. 1990, Das zauberbchlein der gyani dolma. Pharm Unserer Zeit. 19:141-52.

[12] Afifi FU, Abu-Irmaileh B. 2000, Herbal medicine in Jordan with special emphasis on less commonly used medicinal herbs. J Ethnopharmacol. 72:101-10.

[13] Plants for a Future [online] Available from http:// www.pfaf.org/index.php [Accessed February 02, 2009]

[14] Asili J, Sahebkar A, Fazly Bazzaz BS, Sharifi S, 2009, Iranshahi M. Identification of essential oil components of Ferula badrakema fruits by GC-MS and13C-NMR methods and evaluation of its antimicrobial activity. J Essent Oil-Bear Plants. 12:7-15.

[15] Maggi F, Cecchini C, Cresci A, Coman MM, Tirillini B, Sagratini G, et al. 2009, Chemical composition and antimicrobial activity of the essential oil from Ferula glauca L . (F. communis L. subsp. glauca) growing in Marche (central Italy). Fitoterapia. 80:68-72.

[16] Wallace JL, 2004, Acetaminophen hepatotoxicity: NO to the rescue. Br J Pharmacol, 143: 1-2.

[17] Diadelis R, Jan NM, Commandeur ED, Groot, Nico PE, Vermeulen. Eur J Pharmacol: Environ Toxicol Pharmacol Sect 1995; 293:301.

[18] Srinivasan, R., Chandrasekar, M.J.N., Nanjan, M.J. and Suresh, B. 2007, Antioxidant Activity of Caesalpiniadigyna Root. Journal of Ethnopharmacology, 113, 284-291.

[19] Gao, M., Li, Y. and Yang, J. 2011, Protective Effect of Pedicularisdecora Franch Root Extracts on Oxidative Stress and Hepatic Injury in Alloxan-Induced Diabetic Mice. Journal of Medicinal Plants Research, 5, 5848-5856.

[20] Olatosin T. M., Akinduko D. S., Uche C. Z., Bardi J. 2014, Effects of Moringa oleifera Seed Oil on Acetaminophen-Induced Oxidative Stress and Liver Damage in Wistar Albino Rats, 9(2), 53-59.

[21] Kartal N, Sokmen M, Tepe B, Daferera D, Polissiou M, Sokmen A. 2007, Investigation of the ntioxidant properties of Ferula orientalis L. using a suitable extraction procedure. Food Chem. 100:584-9.

DEVELOPMENT AND CHARACTERIZATION OF IN-SITU POLYMERIZATION OF LACTIC ACID AND NANO CRYSTALLINE CELLULOSE (NCC) BIO-NANO-COMPOSITE

RACHEL SI EN CHOK, BAHMAN AMINI HORRI, BABAK SALAMATINI

Rachel Si En Chok, Ms., Discipline of Chemical Engineering, School of Engineering, Monash University Malaysia, Jalan Lagoon Selatan, Bandar Sunway, 47500, Subang Jaya, Selangor, Malaysia, Tel: +603-55146000, Fax: +603-55146207, Email: rscho1@student.monash.edu Bahman Amini Horri, Dr., Discipline of Chemical Engineering, School of Engineering, Monash University Malaysia, Jalan Lagoon Selatan, Bandar Sunway, 47500, Subang Jaya, Selangor, Malaysia, Tel: +603-55144420, Fax: +603-55146207, Email: bahman.amini@monash.edu, Babak Salamatinia, Dr., Discipline of Chemical Engineering, School of Engineering, Monash University Malaysia, Jalan Lagoon Selatan, Bandar Sunway, 47500, Subang Jaya, Selangor, Malaysia, Tel: +603-55146249, Fax: +603-55146207, Email: babak.salamatinia@monash.edu

Abstract

In order to address the issue of the non-biodegradable properties of petro-plastic, the usage of polylactic acid (PLA) as a replacement material has received many attentions. However, improving the mechanical properties of PLA based products is a challenge in this area. This study focuses on the effect of addition of NCC to lactic acid prior to polymerization where the temperature for the polymerization of lactic acid with NCC as filler, the effect of dispersing NCC in water before mixing with lactic acid where most studies have focused on adding NCC to PLA. The effect of the variation of NCC content in the composite was determined. From the study carried out, it can be concluded that in order for the polymerization of lactic acid having NCC as filler, a temperature of 110 °C will be required for the first 48 hours and 140°C for the last 24 hours. Lastly, a 10 wt% of NCC added as filler proved to be having the most increment in tensile strength of 5.8 MPa, an improvement of 489%.

Keywords

NCC, Biocomposite, PLA, Polymer, Mechanical properties

Introduction

The lifestyle of a fast-paced world has inspired human beings to come up with inventions that further make life easier, which for this case, disposable utensils. This practice had imposed great impacts on the environment as disposable utensils are mainly made of plastic (van der Harst et al., 2014). According to van der Harst et al. (2014), plastic can be divided into two main categories based on the raw materials used: (i) petro-plastic from fossil fuels and (ii) biobased plastic manufactured using renewable sources such as corn, tapioca, sugar cane and sugar beets (Narayanan et al., 2004). By having great toughness as one of the main reason for their more commonly usage, petro-plastics are strongly discouraged to be sent to landfills or incinerated as they are non-biodegradable and will release toxic gases during combustion. This contributes in shifting researchers' focus in seeking a more environmental friendly way of manufacturing disposable utensils, without compromising the toughness of the material.

Polylactic acid (PLA) is one of the materials that has attracted interests from researchers due to its biodegradability and renewability. PLA is derived from lactic acid, through direct polycondensation (Xiao et al., 2012), azeotropic dehydrative condensation (Auras et al., 2004) or by the ring-opening of lactide (Conn et al., 1995). Lactic acid is an organic acid that exists in nature, which can be obtained through chemical synthesis or fermentation (Madhavan Nampoothiri et al., 2010). Chemical synthesis of lactic acid can be done by hydrolysis of lactonitrile by strong acids, base catalyzed degradation of sugars, oxidation of propylene glycol, reaction of acetaldehyde with carbon monoxide, nitric acid oxidation of propylene etc (Madhavan Nampoothiri et al., 2010). The common industrial applications of lactic acid include: as buffering agent, acidic flavoring agent, acidulant and bacterial inhibitor (Collins et al., 2010, Mani-López et al., 2012) particularly for processing foods such as bread, sour dairy products, fermented fruits, sausages and etc (Kauffman, 1992, Datta et al., 1995). High molecular weight PLA is commonly obtained using the lactide ring-opening method (Madhavan Nampoothiri et al., 2010), with the aid of catalyst. Tin(II) 2-ehtylhexanoate, commonly known as tin octoate, is preferred to be used as compared to lead oxide, antimony octoate and bismuth octoate due to its low toxicity, high catalytic activity and solubility in many lactones (Mazarro et al., 2012). By having a process temperature of 120 - 150°C, conversions of more than 90% and less than 1% racemization could be achieved (Kurcok et al., 1995).

Being biodegradable and renewable is not sufficient for making PLA a suitable choice in replacing petro-plastic for disposable utensils production. Further advantages it offers include its relatively cheaper selling price and easily processing into different configurations using standard plastics equipment (Sin et al., 2013; Auras et al., 2004). With mechanical properties, which are comparable to other commodity thermoplastics, it consumes less energy and resources as compared to petroleum-based synthetic fibers during the manufacturing process (Beslikas et al., 2011). At the end of its life cycle, PLA can be degraded into carbon dioxide, methane, water, inorganic compounds or biomass products by simple hydrolysis, without the use of enzymes (Hartmann, 1998, Schwach and Vert, 1999).

Though having interesting properties and ease of the process, manufacture of disposable utensils from PLA is still far from being commercialized as PLA itself is highly brittle (Auras et al., 2004). Its low gas barrier properties to O_2, CO_2 and H_2O are to be improved in order to prevent the foods that it contains to be damaged (Cabedo et al., 2006, Li and Huneault, 2007). Furthermore, with a high hydrolysis rate and low thermal resistance, reinforcements are required for the improvement of PLA's properties in order to achieve the target of being less dependent on petro-plastic.

High availability and biodegradability contribute in making cellulose to be one of the potential materials for the reinforcements of PLA (Brinchi et al., 2013). It is used in our daily lives, mainly as first generation uses, in the form of wood and plant fibers (Biagiotti et al., 2004). Cellulose can be further divided into three categories according to the dimensions, functions and preparation methods: nanocrystalline cellulose (NCC), microfibrillated cellulose (MFC) and bacterial nanocellulose (BNC) (Klemm et al., 2011).

NCC is formed by fully cellulose and highly crystalline rigid rod-like particles, having widths of 5-70nm and lengths of 100nm to several micrometers, extracted from the crystallites regions of the cellulose fibrils where the particles are having crystallinity of 54-88% (Moon et al., 2011). Due to its containment of small number of defects, it acts as the reinforcement unit that strengthen structures in plants, trees etc (Brinchi et al., 2013). Extraction of NCC can be carried out through hydrolysis (Rosa et al., 2010), mechanical treatment of cellulose (Lee et al., 2009), by cavitation milling (Pinjari and Pandit, 2010), through acid hydrolysis or steam explosion coupled with high shear homogenization (Liu et al., 2011), TEMPO(2,2,6,6-tetramethyl-piperidine-N-oxyl)-mediated oxidation (Iwamoto et al., 2010, Shimizu et al., 2013), using ionic liquids (Deng et al., 2009, Tsioptsias and Panayiotou, 2008) and by the controlled enzymolysis of cellulose (Hayashi et al., 1997, Satyamurthy et al., 2011). Properties such as low density, high aspect ratio, high surface area and modifiable surface properties also make NCC a great candidate for the reinforcement of PLA (Kümmerer et al., 2011).

By far here is no report on in-situ reinforcement of lactic acid and NCC to make a PLA/NCC bio-composite. The objectives of this study were to obtain the optimum conditions for the polymerization of mono lactic acid/NCC composite, to study the effects of the pre-mixing condition of NCC and effects of the variation of NCC content on the mechanical and surface properties of the composite.

Experiment

Materials

DL-lactic acid, with a concentration of 90%, was supplied by Sigma-Aldrich Co. The boiling point (T_{bp}) is 122°C, having a molecular weight (M_w) of 90.08 g/mol and density 1.209 g/mL at 25°C. Tin (II) 2-ethylhexanoate, as the initiator, with concentration of 92.5 – 100%, was supplied by Sigma-Aldrich Co. The molecular weight (M_w) is 405.12 g/mol and density 1.251 g/mL at 25°C. Cellulose nano-crystals (NCC) dry, with sulphur content of 0.94wt%, was supplied by the University of Maine Process Development Center. All the chemicals were of analytical grade and were used directly without further modification.

Processing of cellulose nanocomposites

Preparation of materials prior to polymerization

5 wt% of tin octoate ($Sn(Oct)_2$) was added to the lactic acid and NCC solutions of 3 wt% to 15 wt% were prepared using a ratio of 1g of NCC to 10mL of water. These solutions underwent ultrasonication prior to and after mixing at an amplitude of 30% for 1 minute, using an ultrasound generator (CV 334, Cole-Parmer, Chicago, US). A water bath was used during ultrasonication in order to prevent the adverse effect of high temperature on the composites.

Polymerization of mono lactic acid/NCC composite

The solutions were poured into molds (30 × 20 × 5 mm) and placed in an oven for 3 days. The oven was maintained at 110°C for the first two days with capped samples during the first day and uncapped on the second. Temperature was then increased to 140°C for the last day with the samples being exposed to heat. Table of shows the ratio of the mixing solution in this study

Material Abbreviations	PLA	$Sn(Oct)_2$	NCC
PLA	95	5	-
PLA-3wt% NCC	92	5	3
PLA-5wt% NCC	90	5	5
PLA-10wt% NCC	85	5	10
PLA-15wt% NCC	80	5	15

Table 1. Formulations of prepared materials (wt%)

Characterization Methods

Microscopy

Fractured samples were studied using scanning electron microscope (SEM), Hitachi S-3400N Type II, and field emission scanning electron microscope (FESEM), Hitachi SU8010, at 5.0kV and 8.0kV. Both studies were performed with surface coating of the samples with platinum as the coat.

Tensile testing

Tensile testing of test specimens measuring 30 × 20 × 5 mm was performed using a miniature material tester (TA.XT plus Texture Analyzer, Stable Micro System Ltd., Surrey, UK) with a load cell of 2000g. Initial grip distance was 20mm and tensile modulus, tensile strength and elongation was determined at a crosshead speed of 2mm/min.

Results and discussion

Polymerization

In order to prevent the degradation of NCC, trial-and-error method was used to find the optimum conditions consist of the lowest temperature for the polymerization of lactic acid/NCC. It was determined that the polymerization can only be carried out at a minimum temperature of 110°C with the sample being capped to prevent vaporization.

The use of ultrasonication is to ensure good dispersion of NCC where it helps in making the cellulose particles to be more finely dispersed. This leads to the increment of surface area resulting in a better adhesion of NCC on lactic acid surface (Hal et al., 2013, Li et al., 2012).

Dispersion

Effects of Dispersion of NCC in Water

Figure 1(a) and Figure 1(b)show SEM images of 10 wt% NCC dispersed in water before mixing with lactic acid whereas Figure 1 (c) and Figure 1(d) show SEM images of 10wt% NCC mixed with lactic acid without prior dispersion in water.

Comparing Figure 1(a) with Figure 1(c) and Figure 1(b) with Figure 1(d), a smoother surface can be observed for the sample that had NCC dispersed in water before mixing with lactic acid. This shows a better dispersion of NCC mainly due to its hydrophilicity nature (Peng et al., 2011). The quality of the dispersion can further be confirmed through the FE-SEM images shown in Figure 2.

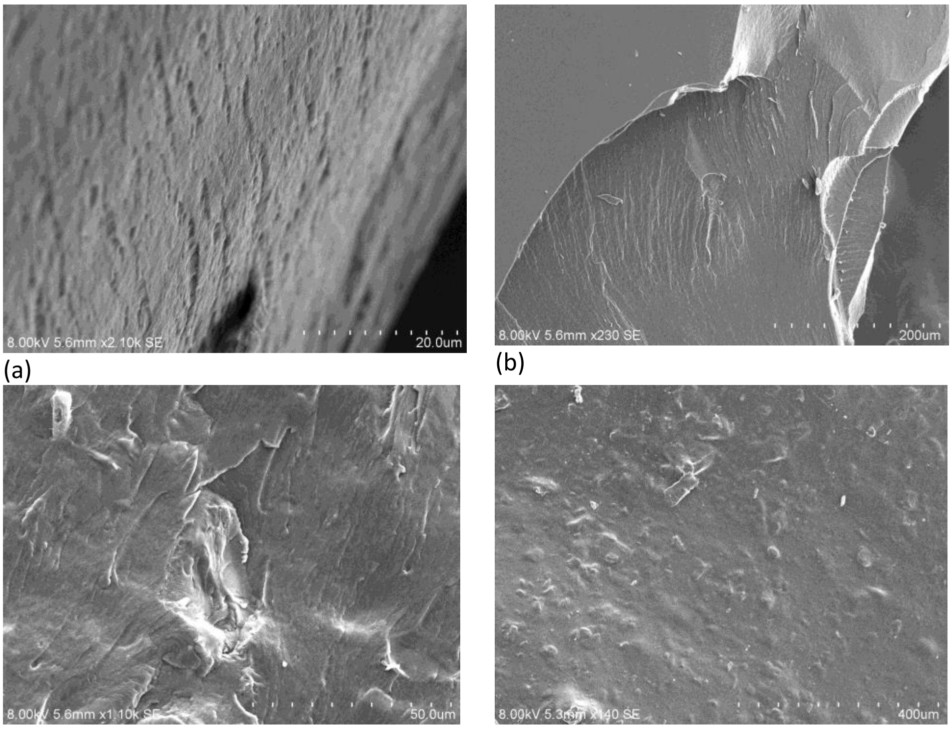

(a) (b) (c) (d)

Figure 1. SEM image of 10wt% NCC (a)(b) dispersed in water before mixing with lactic acid (c) (d) mixed with lactic acid without prior dispersion in water

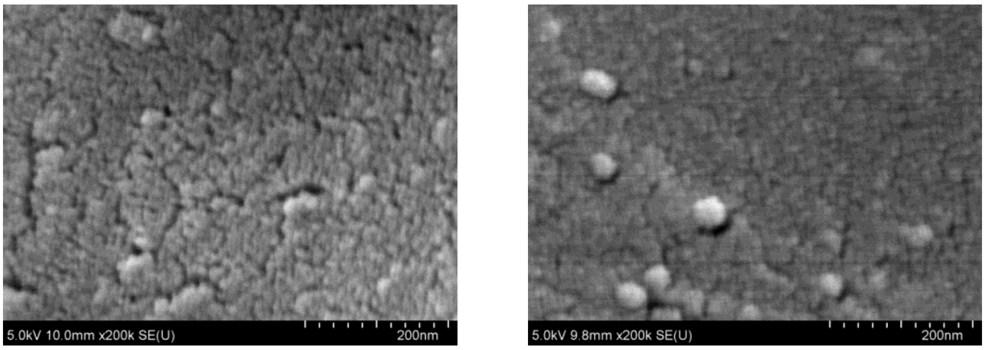

(a) (b)

Figure 2. FE-SEM image of 10wt% NCC (a) dispersed in water before mixing with lactic acid (b) mixed directly with lactic acid without dispersion in water

Mechanical properties

Effects of Dispersion of NCC in Water

The tensile strength, tensile strain and Young's modulus for pure PLA, polymerized composite of 10wt% NCC dispersed in water before mixing with lactic acid and polymerized composite of 10wt% NCC mixed directly with lactic acid are shown in Table 2.

	Tensile Strength (MPa)	Increase in Tensile Strength (%)	Young's Modulus (MPa)
Pure PLA	1.0	-	29.43
10wt% NCC dispersed in water	5.8	489	54.28
10wt% NCC without dispersion in water	5.0	413	117.06

Table 2. Mechanical properties for pure PLA, composite of 10wt% NCC dispersed in water before mixing with lactic acid and composite of 10wt% NCC mixed directly with lactic acid

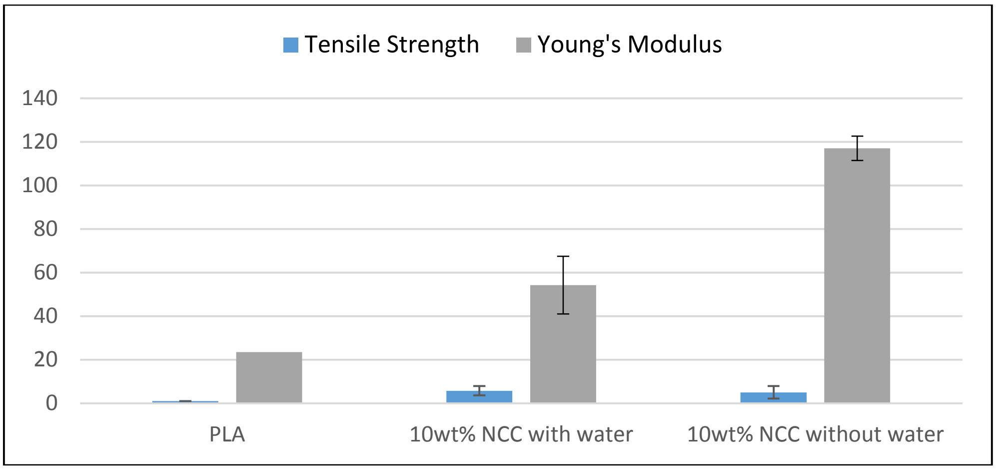

Figure 3: Graph of tensile strength, strain and Young's modulus for PLA, PLA+10wt% NCC dispersed in water and PLA+10wt% NCC without dispersion in water

Based on Table 2 and Figure 3, it can be observed that there is a higher increase of tensile strength for the sample which NCC was first dispersed in water compared to the one where NCC was added directly to lactic acid. This further confirms the conclusion made based on the images of the surface morphology, which is due to the poorer dispersion of NCC in lactic acid compared to in water. The Young's modulus however, shows a different trend by having a higher Young's modulus for the composite which prior dispersion of NCC in water was not carried out compared to the one with NCC first dispersed in water. By having Young's modulus defined as the ratio of the tensile stress and strain in the elastic region (straight line) of the stress-strain curve, the Young's modulus calculated for the composites will be having a certain degree of inaccuracy due to the absence of a distinctive elastic region.

Effects of Variation of NCC Content

The tensile strength, tensile strain and Young's modulus for pure PLA and polymerized composites of lactic acid with NCC content of 3wt%, 5wt%, 10wt% and 15wt%, with NCC first dispersed in water before adding to lactic acid are shown in Table 3.

	Tensile Strength (MPa)	Increase in Tensile Strength (%)	Young's Modulus (MPa)
PLA	1.0	-	29.43
PLA + 3wt% NCC	1.0	-	34.34
PLA + 5wt% NCC	2.5	155.0	96.35
PLA + 10wt% NCC	5.8	489.0	54.28
PLA + 15wt% NCC	1.3	34.7	19.62

Table 3. Mechanical properties of pure PLA and polymerized composites of lactic acid with NCC content of 3wt%, 5wt%, 10wt% and 15wt%

Based on Table 3 and Figure 4, the tensile strength for the composite with the addition of 3wt% of NCC remained the same as pure PLA. This insignificant increase in tensile strength is due to the small amount of NCC added where the reinforcement effect is not obvious. By further adding 5wt% and 10wt% of NCC, there will be an increase in tensile strength of 155% and 489% respectively. The trend however experiences a decline for the addition of 15wt% of NCC. Iwatake et al. (2008) suggested that the increment of flocculated nanofibers might be due to the formation of hydrogen bonds (Li et al., 2012) where this effect dominates the mechanical properties of the composite, making it to be more brittle and having a lesser strength.

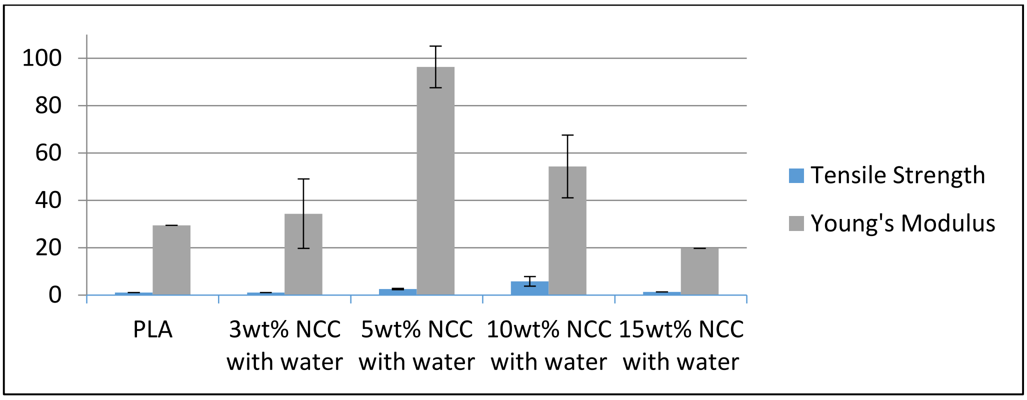

Figure 4: Graph of tensile strength, strain % and Young’s modulus for pure PLA and composites of lactic acid with 3wt%, 5wt%, 10wt% and 15wt% NCC

Conclusions

From the studies carried out, it can be concluded that in order for the polymerization of lactic acid having NCC as filler, a temperature of 110°C will be required for the polymerization to take place and a temperature of 140°C for the drying of the samples. The dispersion of NCC in water prior to be mixed with lactic acid was shown to have a larger improvement in tensile strength. Lastly, 10wt% of NCC as filler proved to have the most increment in tensile strength, with an improvement of 489%. The study also showed that addition of NCC concentration of beyond 10wt%, at 15wt% will cause adverse effects.

References

Ajioka, M., Enomoto, K., Suzuki, K. & Yamaguchi, A. 1995. The basic properties of poly(lactic acid) produced by the direct condensation polymerization of lactic acid. Journal of environmental polymer degradation, 3, 225-234.

Anderson, K. S., Schreck, K. M. & Hillmyer, M. A. 2008. Toughening Polylactide. Polymer Reviews, 48, 85-108.

Anuar, H., Zuraida, A., Kovacs, J. G. & TABI, T. 2012. Improvement of Mechanical Properties of Injection-Molded Polylactic Acid–Kenaf Fiber Biocomposite. Journal of Thermoplastic Composite Materials, 25, 153-164.

Auras, R., Harte, B. & Selke, S. 2004. An Overview of Polylactides as Packaging Materials. Macromolecular Bioscience, 4, 835-864.

Belgacem, M. N. & Gandini, A. 21. Polylactic Acid: Synthesis, Properties and Applications. Monomers, Polymers and Composites from Renewable Resources. Elsevier.

Beslikas, T., Gigis, I., Goulios, V., Christoforides, J., Papageorgiou, G. Z. & Bikiaris, D. N. 2011. Crystallization Study and Comparative in Vitro–in Vivo Hydrolysis of PLA Reinforcement Ligament. International Journal of Molecular Sciences, 12, 6597-6618.

Biagiotti, J., Puglia, D. & Kenny, J. M. 2004. A Review on Natural Fibre-Based Composites-Part I. Journal of Natural Fibers, 1, 37-68.

Bondeson, D. & Oksman, K. 2007. Polylactic acid/cellulose whisker nanocomposites modified by polyvinyl alcohol. Composites Part A: Applied Science and Manufacturing, 38, 2486-2492.

Brinchi, L., Cotana, F., Fortunati, E. & Kenny, J. M. 2013. Production of nanocrystalline cellulose from lignocellulosic biomass: Technology and applications. Carbohydrate Polymers, 94, 154-169.

Cabedo, L., Luis Feijoo, J., Pilar Villanueva, M., Lagaron, J. M. & Gimenez, E. 2006. Optimization of Biodegradable Nanocomposites Based on aPLA/PCL Blends for Food Packaging Applications. Macromolecular Symposia, 233, 191-197.

Collins, B., Cotter, P. D., Hill, C. & Ross, P. 2010. Applications of Lactic Acid Bacteria-Produced Bacteriocins. Biotechnology of Lactic Acid Bacteria. Wiley-Blackwell.

Conn, R. E., Kolstad, J. J., Borzelleca, J. F., Dixler, D. S., Filer Jr, L. J., Ladu JR, B. N. & Pariza, M. W. 1995. Safety assessment of polylactide (PLA) for use as a food-contact polymer. Food and Chemical Toxicology, 33, 273-283.

Datta, R., Tsai, S.-P., Bonsignore, P., Moon, S.-H. & Frank, J. R. 1995. Technological and economic potential of poly(lactic acid) and lactic acid derivatives. FEMS Microbiology Reviews, 16, 221-231.

Deng, M., Zhou, Q., Du, A., Van Kasteren, J. & Wang, Y. 2009. Preparation of nanoporous cellulose foams from cellulose-ionic liquid solutions. Materials Letters, 63, 1851-1854.

Drumright, R. E., Gruber, P. R. & Henton, D. E. 2000. Polylactic Acid Technology. Advanced Materials, 12, 1841-1846.

Fortunati, E., Armentano, I., Zhou, Q., Iannoni, A., Saino, E., Visai, L., Berglund, L. A. & Kenny, J. M. 2012. Multifunctional bionanocomposite films of poly(lactic acid), cellulose nanocrystals and silver nanoparticles. Carbohydrate Polymers, 87, 1596-1605.

HAL, #XE1, SZ, K., CS, #XF3 & KA, L. 2013. Plasticized Biodegradable Poly(lactic acid) Based Composites Containing Cellulose in Micro- and Nanosize. Journal of Engineering, 2013, 9.

Hartmann, M. H. 1998. High Molecular Weight Polylactic Acid Polymers. In: KAPLAN, D. (ed.) Biopolymers from Renewable Resources. Springer Berlin Heidelberg.

Hayashi, N., Sugiyama, J., Okano, T. & Ishihara, M. 1997. Selective degradation of the cellulose Iα component in Cladophora cellulose with Trichoderma viride cellulase. Carbohydrate Research, 305, 109-116.

Iwamoto, S., Kai, W., Isogai, T., Saito, T., Isogai, A. & Iwata, T. 2010. Comparison study of TEMPO-analogous compounds on oxidation efficiency of wood cellulose for preparation of cellulose nanofibrils. Polymer Degradation and Stability, 95, 1394-1398.

Iwatake, A., Nogi, M. & Yano, H. 2008. Cellulose nanofiber-reinforced polylactic acid. Composites Science and Technology, 68, 2103-2106.

Kauffman, G. B. 1992. American Scientist, 80, 402.

Klemm, D., Kramer, F., Moritz, S., Lindstrom, T., Ankerfors, M., Gray, D. & Dorris, A. 2011. Nanocelluloses: A New Family of Nature-Based Materials. Angewandte Chemie International Edition, 50, 5438-5466.

Kummerer, K., Menz, J., Schubert, T. & Thielemans, W. 2011. Biodegradability of organic nanoparticles in the aqueous environment. Chemosphere, 82, 1387-1392.

Kurcok, P., Matuszowicz, A., Jedlinski, Z., Kricheldorf, H. R., Dubois, P. & Jerome, R. 1995. Substituent effect in anionic polymerization of β-lactones initiated by alkali metal alkoxides. Macromolecular Rapid Communications, 16, 513-519.

Lee, S.-Y., Chun, S.-J., Kang, I.-A. & Park, J.-Y. 2009. Preparation of cellulose nanofibrils by high-pressure homogenizer and cellulose-based composite films. Journal of Industrial and Engineering Chemistry, 15, 50-55.

Li, H. & Huneault, M. A. 2007. Effect of nucleation and plasticization on the crystallization of poly(lactic acid). Polymer, 48, 6855-6866.

Li, W., Yue, J. & Liu, S. 2012. Preparation of nanocrystalline cellulose via ultrasound and its reinforcement capability for poly(vinyl alcohol) composites. Ultrasonics Sonochemistry, 19, 479-485.

Liu, D., Chen, X., Yue, Y., Chen, M. & Wu, Q. 2011. Structure and rheology of nanocrystalline cellulose. Carbohydrate Polymers, 84, 316-322.

Madhavan Nampoothiri, K., Nair, N. R. & John, R. P. 2010. An overview of the recent developments in polylactide (PLA) research. Bioresource Technology, 101, 8493-8501.

Maharana, T., Mohanty, B. & Negi, Y. S. 2009. Melt–solid polycondensation of lactic acid and its biodegradability. Progress in Polymer Science, 34, 99-124.

Mani-Lopez, E., Garcia, H. S. & Lopez-Malo, A. 2012. Organic acids as antimicrobials to control Salmonella in meat and poultry products. Food Research International, 45, 713-721.

Mark, J. E. 2009. Polymer Data Handbook (2nd Edition). 2 ed.: Oxford University Press.

Mazarro, R., Gracia, I., Rodriguez, J. F., Storti, G. & Morbidelli, M. 2012. Kinetics of the ring-opening polymerization of D,L-lactide using zinc (II) octoate as catalyst. Polymer International, 61, 265-273.

Moon, R. J., Martini, A., Nairn, J., Simonsen, J. & Youngblood, J. 2011. Cellulose nanomaterials review: structure, properties and nanocomposites. Chemical Society Reviews, 40, 3941-3994.

Moon, S. I., Lee, C. W., Miyamoto, M. & Kimura, Y. 2000. Melt polycondensation of L-lactic acid with Sn(II) catalysts activated by various proton acids: A direct manufacturing route to high molecular weight Poly(L-lactic acid). Journal of Polymer Science Part A: Polymer Chemistry, 38, 1673-1679.

Narayanan, N., Roychoudhury, P. K. & Srivastava, A. 2004. L (+) lactic acid fermentation and its product polymerization.

Oksman, K., Mathew, A. P., Bondeson, D. & Kvien, I. 2006. Manufacturing process of cellulose whiskers/polylactic acid nanocomposites. Composites Science and Technology, 66, 2776-2784.

Peng, B. L., Dhar, N., Liu, H. L. & Tam, K. C. 2011. Chemistry and applications of nanocrystalline cellulose and its derivatives: A nanotechnology perspective. The Canadian Journal of Chemical Engineering, 89, 1191-1206.

Petersson, L., Kvien, I. & Oksman, K. 2007. Structure and thermal properties of poly(lactic acid)/cellulose whiskers nanocomposite materials. Composites Science and Technology, 67, 2535-2544.

Pinjari, D. V. & Pandit, A. B. 2010. Cavitation milling of natural cellulose to nanofibrils. Ultrasonics Sonochemistry, 17, 845-852.

Rahman, M. M., Afrin, S., Haque, P., Islam, M. M., Islam, M. S. & Gafur, M. A. 2014. Preparation and Characterization of Jute Cellulose Crystals-Reinforced Poly(L-lactic acid) Biocomposite for Biomedical Applications. International Journal of Chemical Engineering, 2014, 7.

Rosa, M. F., Medeiros, E. S., Malmonge, J. A., Gregorski, K. S., Wood, D. F., Mattoso, L. H. C., Glenn, G., Orts, W. J. & Imam, S. H. 2010. Cellulose nanowhiskers from coconut husk fibers: Effect of preparation conditions on their thermal and morphological behavior. Carbohydrate Polymers, 81, 83-92.

Satyamurthy, P., Jain, P., Balasubramanya, R. H. & Vigneshwaran, N. 2011. Preparation and characterization of cellulose nanowhiskers from cotton fibres by controlled microbial hydrolysis. Carbohydrate Polymers, 83, 122-129.

Schwach, G. & Vert, M. 1999. In vitro and in vivo degradation of lactic acid-based interference screws used in cruciate ligament reconstruction. International Journal of Biological Macromolecules, 25, 283-291.

Shimizu, M., Fukuzumi, H., Saito, T. & Isogai, A. 2013. Preparation and characterization of TEMPO-oxidized cellulose nanofibrils with ammonium carboxylate groups. International Journal of Biological Macromolecules, 59, 99-104.

Sin, L. T., Rahmat, A. R. & Rahman, W. A. W. A. 2013. 8 - Applications of Poly(lactic Acid). In: Rahman, L. T. S. R. R. A. W. A. (ed.) Polylactic Acid. Oxford: William Andrew Publishing.

Tsioptsias, C. & Panayiotou, C. 2008. Preparation of cellulose-nanohydroxyapatite composite scaffolds from ionic liquid solutions. Carbohydrate Polymers, 74, 99-105.

Van Der Harst, E., Potting, J. & Kroeze, C. 2014. Multiple data sets and modelling choices in a comparative LCA of disposable beverage cups. Science of The Total Environment, 494–495, 129-143.

Yan, M., Li, S., Zhang, M., Li, C., Dong, F. & Li, W. 2013. Characterization of Surface Acetylated Nanocrystalline Cellulose by Single-Step Method.

MODIFICATION OF CU AND CUO NANOPARTICLES WITH OLEIC ACID AND THERMAL CHARACTERIZATION OF PARAFFINS: TOWARDS THE PREPARATION OF A STABLE NANOPCM

DIEGO VASCO, MANUEL MUÑOZ, PAULA GALVEZ, PAULA ZAPATA

Diego Vasco, Dr. MSc., Manuel Muñoz, Eng., Department of Mechanical Engineering, Paula Zapata, Dr. MSc., Paula Galvez, Department of Chemistry and Biology, University of Santiago de Chile.

Abstract

The increase of energy consumption worldwide and the lack of cheap and available energy sources have raised the interest on energy conservation. The storage of energy that otherwise would be wasted by using phase change materials (PCM) has become an active branch in the thermal researchers community. PCM can storage a great quantity of energy per volume unit in the form of latent heat in a narrow temperature range. Organic phase change materials (O-PCM), such as paraffins and oleic acids, are being used to maintain a comfort temperature in housing applications. One of the problems with O-PCM is their low thermal conductivity that increases the rate at which heat is stored and released. The modification of O-PCM with nanoparticles to improve its thermal conductivity is an approach that has been proposed by several researchers. Nevertheless, the nanoparticles surface must be modified in order to obtain more stable PCM-nanoparticle composites (nanoPCM). The present work focuses on the steps for the preparation of a stable nanoPCM. First, the thermophysical of O-PCM properties (thermal conductivity, heat capacity and density) were obtained as a function of temperature, then the surfaces of Cu and CuO nanoparticles were modified with oleic acid and finally solubility tests were performed. Although with both O-PCM the preliminary tests were not successful, further tests using glycerol as PCM and CuO allowed measuring the thermal conductivity of this nanoPCM. It was observed that for volumetric concentrations of 2%, 2.5% and 3% the thermal conductivity of glycerol is increased by 6.1%, 7.6% and 9.1%, respectively. Moreover, computational simulations of the heat loads in a house located in Chile with EnergyPlus were performed. It was found that in comparison to the implementation of a pure PCM in the envelopes of the house a potentially stable nanoPCM with CuO would not reduce the thermal peaks considerably.

Introduction

Like in many countries. Chile has presented a steady growth in demand for electricity during the last years but the country does not have sufficient energy sources to supply it. For this reason, some energy saving strategies has been implemented. In 2006-2007, the energy consumption in buildings reached 16% of the total electric energy demand (Agostini and Plottier, 2012). In Chile, the average residential energy consumption is 10.232 kWh/year (including all sources), a high value owing to the wood consumption in the southern region of the country (46.6%). Use of wood in Chile is mainly to maintain thermal comfort conditions in homes (Cámara chilena de la contrucción, 2010).

Phase change materials (PCM) are distinguished by their high latent heat, therefore they can be used to storage high quantities of energy per volume unit. PCM can storage between three and four times more energy as latent heat than as sensible heat (Mehling and Cabeza, 2008 p. 7). During the phase change process, the temperature of PCM is maintained almost constant but some of them are prone to subcooling, especially metallic oxides (García-Romero et al., 2012) and some organic compounds in confined spaces (Huang et al., 2010) The charging and discharging process of the PCM is reversible and both of them take place according to the thermal conditions of the surroundings, therefore the phase change temperature is the main characteristic which allows to choose a PCM in a particular application. PCM are mainly classified as inorganic, organic and eutectic mixtures (Zalba et al., 2003). Regarding organic PCM (O-PCM), they are classified as paraffins, fatty acids and organic mixtures (Abhat, 1983). The properties and characteristics of O-PCM make them useful in applications close to ambient temperature. In comparison with inorganic PCM, O-PCM are highly chemically stable and they spontaneously solidify without using nucleating agents, therefore they are less prone to subcooling (Tyagi and Buddhi, 2007). Nevertheless, O-PCM present certain drawbacks, they have low thermal conductivities and despite of their high autoignition points, they emit noxious gases during combustion (Sharma et al., 2009), furthermore O-PCM suffer of aging because of oxidation and they present large volume changes (ca. 10%) during solidification (Kenisarin and Mahkamov, 2007). One of the applications associated to the thermal storage ability of PCM is to control the temperature by decreasing its oscillation in an inner space during a period of time. PCM are used to raise the thermal inertia of the envelopes, mainly in buildings of low thermal inertia, therefore they can be used to decrease the energy consumption associated to heating/cooling of inner spaces.

Nanofluids are colloidal solutions of nanometric particles (metals. metallic oxides and carbon nanotubes) in a base fluid like water, ethylene glycol or paraffins. The thermal properties of a PCM can be improved by addition of nanoparticles. Some experimental studies have shown that a low quantity of nanoparticles can markedly increase the thermal conductivity of the base fluid. Wu et al. (2010) performed experimental tests to verify the increase of the heat transfer rate using nanofluid with nanoparticles (Cu, Al, C/Cu) and paraffin as base fluid. The better results were reached using stabilized nanoparticles of copper (1 wt%). heating and cooling times were reduced by 30.3% and 28.2%, respectively.

The present work focuses on the steps for the preparation of a stable nanoPCM. First, the thermophysical properties: Thermal conductivity, heat capacity and density of hexadecane and heptadecane were obtained as a function of temperature, then the surfaces of Cu and CuO nanoparticles were modified with oleic acid and finally solubility tests were performed. The preliminary tests were not successful, that is why further tests using glycerol as PCM and nanoparticles of CuO allowed measuring the thermal conductivity of the obtained nanoPCM. Moreover, computational simulations of the transient behavior heat loads in a house located in Chile with EnergyPlus were performed. It was found that in comparison to the implementation of a pure PCM in the envelopes of the house a potentially stable nanoPCM with CuO would not reduce the thermal peaks considerably.

Thermophysical properties

All the analyses were performed using reactive grade PCM (Sigma-Aldrich). Determination of latent heat, melting temperature and specific heat was done by using the thermoanalytical technique DSC (2920 Modulated), which performed a temperature sweep adding a known heat flow in a temperature range (283 K - 308 K) to certain quantity of the sample of interest.

The thermal conductivity measurement of the PCM has been performed by the transient line heat source method (KD2-Pro), which consists in an immersion probe that generates heat from its surface. The fluid absorbs part of this heat and the remainder induces an increase of the surface temperature of the sensor that in comparison with the supplied heat allows determining the thermal conductivity of the sample.

Density of the solid and liquid PCM was measured by using a picnometer (Marienfeld) with a mercury thermometer (±0.1 K), which allows measuring the temperature of the sample. To control the temperature during the measurement of thermal conductivity (283 K - 313 K) and density (283 K – 308 K) the sample was immersed in a refrigerated bath circulator (Hilab BL-20). Figure 1 shows the behavior of the specific heat of heptadecane (T_{PC} = 21°C, ΔH_{LS} = 130.400 kJ/kg) and hexadecane (T_{PC} = 18°C, ΔH_{LS} = 216.600 kJ/kg) in the temperature range between 283.15 K (10°C) and 308.65 K (35.5°C). It can be observed two trends in the liquid state, a temperature range where the heat capacity decreases until a value from which temperature raises to a constant value. Generally, the heat capacity of both solid PCM increases with temperature, however heptadecane shows a peak around 11°C where apparently a structural reordering takes place.

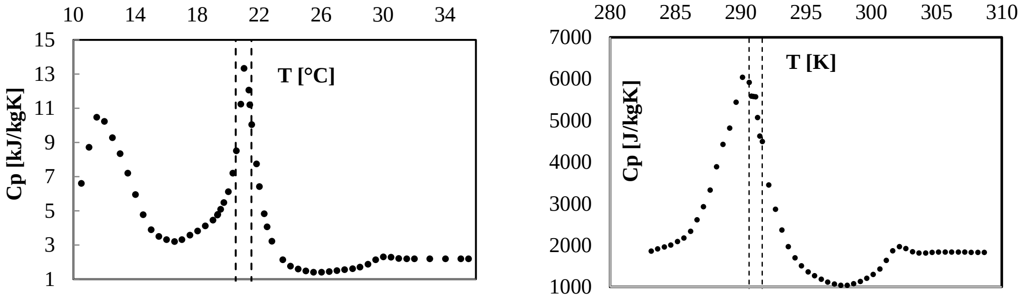

Figure 1. Heat capacity of heptadecane (left) and hexadecane (right).

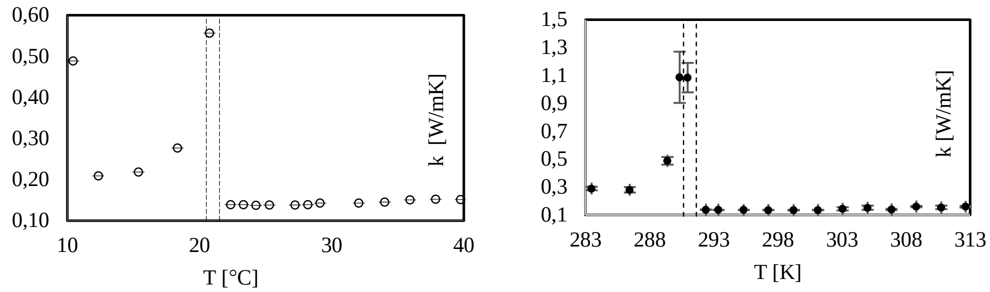

Figure 2. Thermal conductivity of heptadecane (left) and hexadecane (right).

Figure 2 corresponds to the behavior of thermal conductivity of both O-PCM in the same temperature range. It can be seen that the thermal conductivity of both liquid O-PCM is almost constant with temperature. Meanwhile in the solid range, the thermal conductivity increases with temperature from at almost constant value to a higher value close to the mushy region. In the case of heptadecane, it can be noticed a high value of thermal conductivity at 11°C. According to Figure 3, density of both PMC decreases with temperature. It can be notice that the effect of temperature is more important in the solid region, especially near to the mushy region. The variation of temperature in the liquid region can be described by a linear equation.

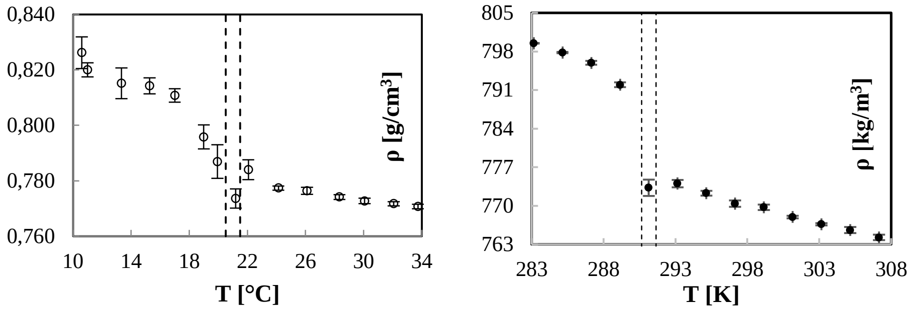

Figure 3. Density of heptadecane (left) and hexadecane (right).

Nanoparticle modification and characterization

Nanoparticles of Cu (25 nm, 99.8% pure) and CuO (40 nm, 99% pure) were obtained from Mknano. In both cases, nanoparticles are considered spherical in shape (Figure 4). To modify the nanoparticles surface in an Erlenmeyer flask 0.1 g of nanoparticles. 5 ml of hexadecane and a specified volume of oleic acid (Table 1) are added. Then the mixture is stirred during five hours at a constant temperature of 60°C. Figure 5a corresponds to an infrared spectroscopy of the different samples of modified CuO nanoparticles and oleic acid. It can be noticed that in the case of test 2 prepared with 60 µl of oleic acid, the surface of the CuO nanoparticles was modified since the characteristic signals of the ester group (C-O) at 1050 and 1300 cm^{-1} and the carbonyl group (CH_2) at 2800 and 2900 cm^{-1} were observed. All the tests performed with Cu nanoparticles were successful as can be seen in Figure 5b, since the characteristic signals of the ester group (displaced to 1416 cm^{-1}) and the carbonyl group (displaced to 1586 cm^{-1}) were detected in the corresponding infrared spectroscopy.

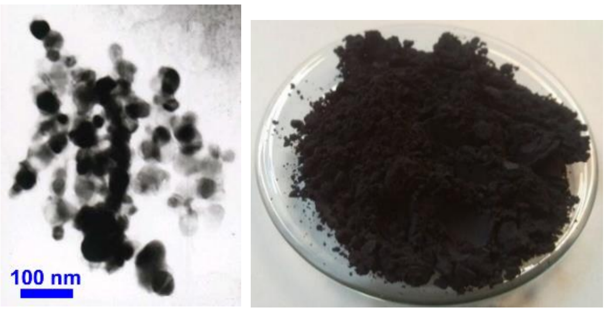

Figure 4. Nanopaticles of CuO (Courtesy of Mknano)

Test	Cu (g)	CuO (g)	Oleic acid (µl)
1	0.1071		40
2	0.1021	0.1019	60
3	0.1064	0.1008	80
4	0.1030	0.1009	100

Table 1. Specified volume of oleic acid for each nanoparticle modification test.

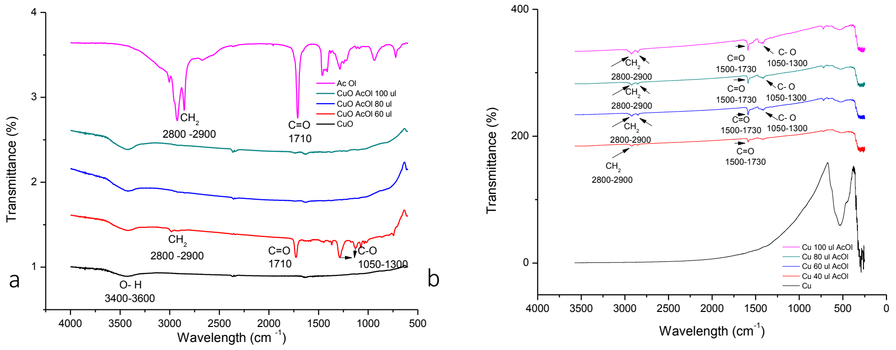

Figure 5. Infrared spectroscopy of the different CuO (a) and Cu (b) nanoparticles modification test.

Nanofluid preparation and models

The preparation of the nanofluids based on CuO nanoparticles and Glycerol as based fluid was performed by the two-step method. Using an ultrasonic processor (Hielscher UP50H) the dispersion of CuO nanoparticles in Glycerol has been done. Since the viscosity of glycerol is high in comparison with hexadecane or heptadecane, the dispersion is performed at 50 W with wave amplitude of 220 µm and a frequency of 30 kHz during 90 minutes. Since a lot of heat from the ultrasonic probe during the dispersion process is generated. a jacketed beaker with water at 15°C as refrigeration fluid was used (Figure 6). This procedure allowed that the temperature of the dispersion remained between 35°C to 40°C. Glycerol is highly hygroscopic; therefore humidity inside the process box during the dispersion process was kept low by using silica gel.

Figure 6. Experimental setup for the dispersion process of CuO nanoparticles.

To find the minimum volumetric fraction (φ) of nanoparticles that increases the thermal conductivity of glycerol over the error of the measurement method (± 5%) the Maxwell model (1) was used. Figure 6 shows the obtained thermal conductivity of glycerol as a function of temperature which can be considered constant at $k_f = 0.276$ W/mK. Considering the thermal conductivity of the nanoparticles $k_{np}= 78$ W/mK a volumetric fraction of 1.56% is needed in order to increase the thermal conductivity of the nanofluid by 5% to $k_{nf}(\varphi) = 0.289$ W/mK. According to this calculation a volumetric fraction of 2% was chosen as the threshold value. Thermophysical properties of the CuO nanoparticles are summarized in Table 2.

$$k_{nf}(\varphi)=\left(\frac{k_{np}+2k_f-2\varphi(k_f-k_{np})}{k_{np}+2k_f+\varphi(k_f-k_{np})}\right)k_f \quad (1)$$

Density (kg/m^3)	6.400
Specific heat (J/molK)	42.24
Thermal conductivity (W/mK)	78
Molecular weight (g/mol)	79.5454

Table 3. Thermophysical properties of CuO nanopaticles.

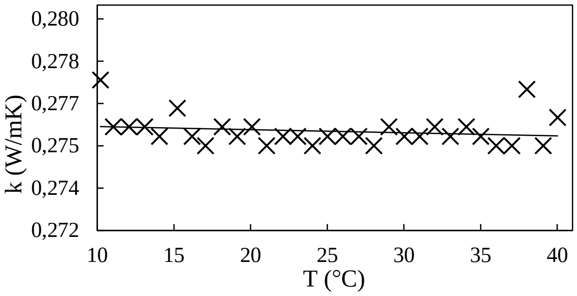

Figure 6. Thermal conductivity of glycerol.

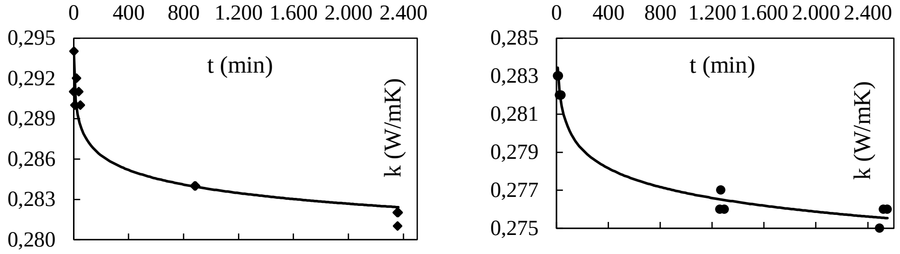

Figure 7. Transient thermal conductivity of the nanoPCM with non-modified nanoparticles (left) and modified nanoparticles (right) of CuO (φ=0.02).

Figure 7 shows the transient behavior of the thermal conductivity of the prepared nanoPCM based on the non-modified nanoparticles (nanoPCM A) and modified CuO nanoparticles (nanoPCM B). After preparation, nanoPCM A had an increment of the thermal conductivity just 2% over the predicted value by the Maxwell model, afterwards the thermal conductivity rapidly decreases showing the instability of the nanoPCM. In the case of modified CuO nanoparticles. nanoPCM B. after dispersion, the thermal conductivity reached a lower value than Maxwell's and the stability is poor. Table 4 shows the measured thermal conductivities after 24 and 48 hours and its diminution regards to the initial value.

NanoPCM	k (W/mK)		
φ =0.02	0 h	24 h	48 h
A	0.291 (0.34%)	0.284 (2.74%)	0.282 (3.42%)
B	0.283 (3.1%)	0.276 (5.48%)	0.276 (5.48%)

Table 4. Average thermal conductivity of the prepared nanoPCM with non-modified nanoparticles (A) and modified nanoparticles (B) of CuO.

Figure 8 shows the transient values of the thermal conductivity along with the predicted value using the Maxwell model. It can be seen how the first measurement of the thermal conductivity of NanoPCM A is higher than the predicted value, meanwhile for nanoPCM B, the obtained value is always lower. Figure 9 shows the surface of the nanoPCM prepared with modified nanoparticles of CuO. It can be noticed the formation of a second lighter phase that was not observed after preparation of nanoPCM A. During preparation of nanoPCM B and before ultrasonic dispersion readily agglomeration of nanoparticles was observed. This fact explain the lower thermal conductivity of the nanoPCM prepared with modified nanoparticles.

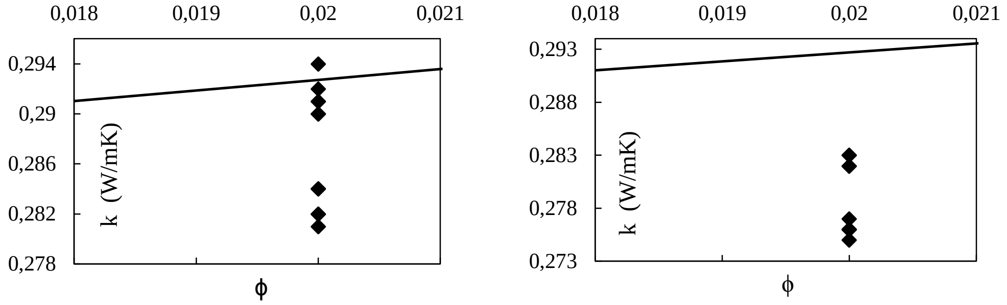

Figure 8. Thermal conductivity of the prepared nanoPCM with non-modified nanoparticles (left) and modified nanoparticles (right) of CuO. The solid line represents the predicted value by the Maxwell model.

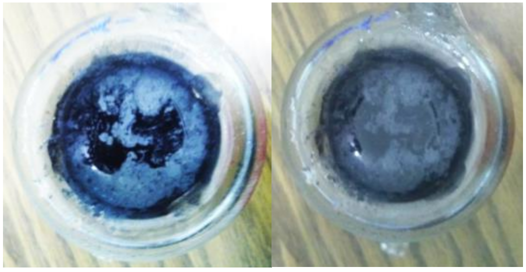

Figure 9. Formation of a second phase over the surface of the nanoPCM prepared with modified nanoparticles.

Computational Application

The main goal of this work is to use the open source software EnergyPlus to evaluate a PCM-modified thermal envelope of a house (Figure 10) located in Santiago de Chile. The modification consists on adding to the envelope a PCM (hexadecane and glycerol) layer which at the same time can be modified by adding CuO nanoparticles (Figure 11). The house thermal design follows the requirements of the Chilean normative (Decreto Supremo N° 49). In the simulations the house is submitted to environmental conditions of Santiago de Chile (predominant winds. solar radiation. temperature) to obtain the inner temperature of the house and the energy consumption of ideal (COP = 1) air conditioning equipment.

The chosen construction materials of the walls, roof, floor and windows are ruled by the general ordinance of urbanism and construction of Chile. The configuration of the thermal envelope is made of a gypsum layer in the inside followed by polystyrene foam as thermal insulation, then a structural brick block and finally a cement layer in the outside. The overall heat transfer (U) of the wall is 1.65 W/mK. The roof of the house is made of a clay tile in the outside followed by layers of pine-tree wood, polystyrene foam and a gypsum layer in the inside (U=0.44 W/mK). The considered windows are single glass and following the directives of the normative its total area is less than 25% (9%). From the total area of the perimeter walls is 99.7 m^2 from which 34.9 m^2 belongs to the inside walls.

The simulations are performed considering a layer of 1 cm of PCM or nanoPCM in the outside walls. The thermophysical properties enthalpy and thermal conductivity of the PCM used in the simulations are specified in Tables 5, 6 and 7, respectively. Respect to glycerol, thermal conductivity is considered constant with temperature (Figure 6). The charging/descharging process of the PCM takes places with the changing local environmental conditions; therefore the evaluation of the performance of the PCM is done through the calculation of the heating/cooling thermal loads and the temperature inside of the living room during a year.

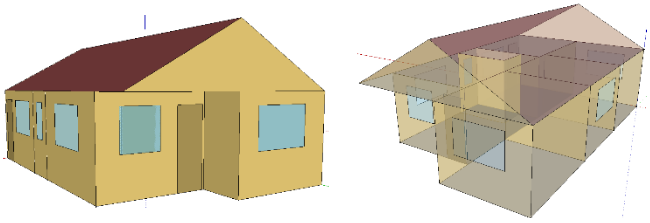

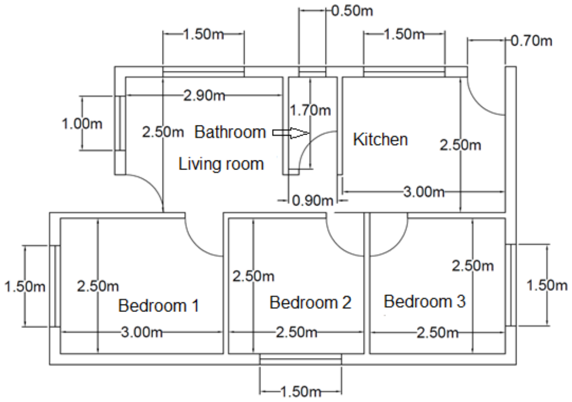

Figure 10. Sketch of the simulated house located in Santiago de Chile.

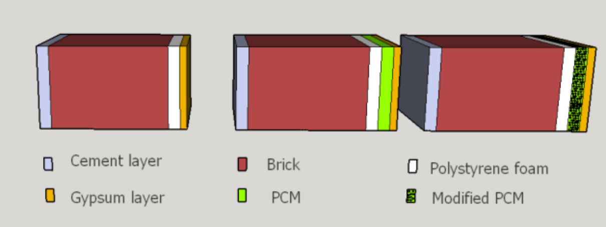

Figure 11. Configuration of the thermal envelops analyzed in the thermal simulations.

In Figure 12, it can be seen the behavior of the temperature in the living room during a fall week. The effect of the PCM is noticeable during the days where the ambient temperature is lower than the melting temperature of both PCM (18°C). During the first three days, the average diminution of the temperature fluctuation is 4.6°C that corresponds to a lesser fluctuation of 49.5% by using PCM. It can be noticed as well that the effect of the nanoparticles in the PCM is not important in the behavior of the temperature fluctuation. For this reason, the nanoPCM are not considering in the subsequent analyses.

Glycerol		Glycerol + N-CuO φ=0.02		Glycerol + N-CuO φ = 0.025		Glycerol + N-CuO φ =0.03	
T (°C)	Enthalpy (J/kgK)	T (°C)	Enthalpy (J/kgK)	T (°C)	Enthalpy (J/kgK)	T (°C)	Enthalpy (J/kgK)
-3	0.0001	-3	0	-3	0	-3	0
-1	2.771	-1	2.532	-1	2.513	-1	2.496
2	6.956	2	6.354	2	6.306	2	6.262
5	11.178	5	10.204	5	10.125	5	10.054
8	15.435	8	14.081	8	13.972	8	13.873
10	18.293	10	16.681	10	16.551	10	16.433
12	21.166	12	19.294	12	19.143	12	19.006
14	24.055	14	21.918	14	21.746	14	21.590
17.5	28.418	17.5	26.541	17.5	26.331	17.5	26.140
18.5	227.161	18.5	206.686	18.5	202.241	18.5	197.969
21	233.436	21	213.282	21	208.737	21	204.372
24	240.534	24	219.918	24	215.274	24	210.814
27	247.680	27	226.596	27	221.851	27	217.295
30	254.874	30	233.316	30	228.468	30	223.815
33	262.115	33	240.076	33	235.125	33	230.374
40	279.189	40	256.011	40	250.814	40	245.831

Table 5. Enthalpy values of non-modified and modified glycerol.

Hexadecane		Hexadecane + CuO φ =0.02		Hexadecane + N-CuO φ=0.025		Hexadecane + N-CuO φ=0.03	
T (°C)	Enthalpy (J/kgK)	T (°C)	Enthalpy (J/kgK)	T (°C)	Enthalpy (J/kgK)	T (°C)	Enthalpy (J/kgK)
-3	0	-3	0	-3	0	-3	0
-1	2.855	-1	2.612	-1	2.560	-1	2.511
2	7.746	2	7.054	2	6.907	2	6.767
5	12.804	5	11.639	5	11.390	5	11.155
8	17.874	8	16.231	8	15.881	8	15.550
10	21.423	10	19.437	10	19.013	10	18.614
12	25.372	12	22.986	12	22.477	12	21.997
14	28.123	14	25.438	14	24.869	14	24.327
17.5	44.341	17.5	39.565	17.5	38.633	17.5	37.608
18.5	260.941	18.5	224.864	18.5	217.311	18.5	210.060
21	270.621	21	233.394	21	225.600	21	218.123
24	274.020	24	236.529	24	228.680	24	221.155
27	277.449	27	239.686	27	231.783	27	224.209
30	282.701	30	244.406	30	236.393	30	228.717
33	292.266	33	249.435	33	241.003	33	233.426
40	305.076	40	260.940	40	252.232	40	244.396

Table 6. Enthalpy values of non-modified and modified hexadecane.

Hexadecane		Hexadecane + N-CuO φ=0.02		Hexadecane + N-CuO φ=0.025		Hexadecane + NCuO φ=0.03	
T (°C)	k (W/mK)	T (°C)	k (W/mK)	T (°C)	k (W/mK)	T (°C)	k (W/mK)
-2	0.289	-2	0.306	-2	0.311	-2	0.316
13	0.280	13	0.297	13	0.301	13	0.306
16	0.487	16	0.516	16	0.524	16	0.531
17	1.087	17	1.151	17	1.167	17	1.184
17.5	1.087	17.5	1.151	17.5	1.167	17.5	1.184
18	1.087	18	1.151	18	1.167	18	1.184
18.5	0.612	18.5	0.649	18.5	0.658	18.5	0.667
19	0.137	19	0.145	19	0.147	19	0.150
30	0.143	30	0.152	30	0.154	30	0.156
39	0.159	39	0.169	39	0.171	39	0.174

Table 7. Thermal conductivity values of non-modified and modified hexadecane.

During a winter week, the behavior of the temperature in the living room is quite similar to the observed in fall, the main difference is that temperature is lower during the mornings reaching values as lower as 9.5°C (Figure 13). With both pure PCM, the average diminution of the temperature fluctuation is 5.1°C that corresponds to a lesser fluctuation of 36.5%. In the case of a spring week, Figure 14 shows that there is a diminution of the temperature fluctuation during the whole week. It can be noticed as well that during the first 48 h, the temperature of the living room is higher when PCM are used in the thermal envelope.

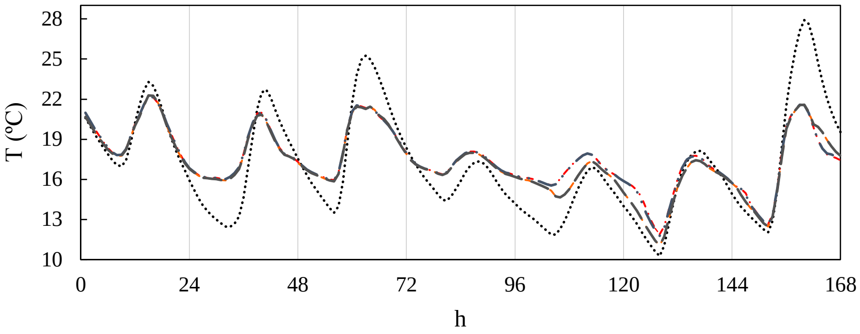

Figure 12. Temperature in the living room during a fall week. Black: No PCM, red: Glycerol, orange: Hexadecane, blue: Glycerol with n-CuO (φ=0.03), green: Hexadecane with n-CuO (φ=0.03).

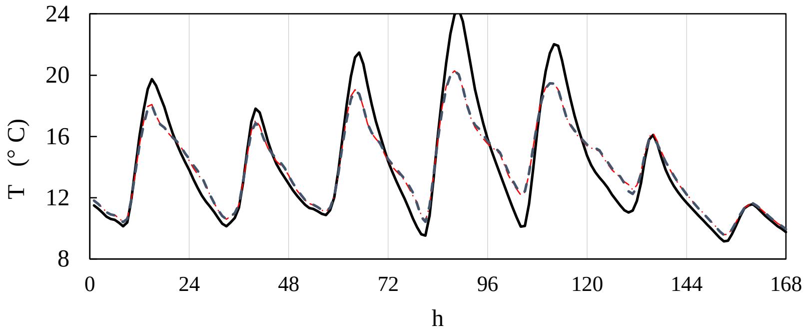

Figure 13. Temperature of the living room during a winter week. Black: No PCM, blue: Glycerol, red: Hexadecane).

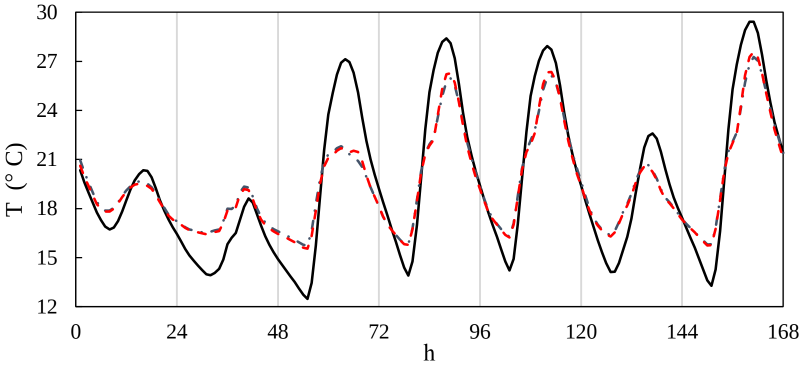

Figure 14. Temperature of the living room during a spring week. Black: No PCM, blue: Glycerol, red: Hexadecane).

Conclusions

The thermophysical properties in function of temperature of three PCM were experimentally obtained. Despite the modification of the CuO and Cu nanoparticles with oleic acid was successful, it does not improve the stability of the prepared nanoPCM. Nevertheless, the thermophysical properties were implemented in the simulation of the thermal behavior of a house located in Santiago de Chile. Generally, the modification of thermal envelops with PCM and nanoPCM causes a diminution of the temperature fluctuation inside the house, but there was not observed a significant difference between the transient temperature profiles observed in both cases.

References

Abhat, A., 1983. Low temperature latent heat thermal energy storage: Heat storage material. Solar Energy, 30, pp. 313-332.

Agostini C., Plottier M. C., Saavedra E. H., 2012. La demanda residencial de energía eléctrica en Chile. Revista de Economía Chilena, 15 , pp. 64-83.

Cámara Chilena de la Construcción, 2010. Estudio de usos finales y curva de oferta de la conservación de la energía en el sector residencia.
García-Romero A., Diarce G., Ibarretxe J., Urresti A., Sala J.M., 2012. Influence of the experimental conditions on the subcooling of Glauber's salt when used as PCM. Solar Energy Materials & Solar Cells, 102, pp. 189-185.
Huang L., Günther E., Doetsch C., Mehling H., 2010. Subcooling in PCM emulsions-Part 1: Experimental. Thermochimica Acta, 509, pp. 93-99.
Kenisarin M., Mahkamov K., 2007. Solar energy storage using phase change materials. Renewable and Sustainable Energy Reviews, 11, pp. 1913-1965.
Mehling H., Cabeza L.F., 2008. Heat and cold storage with PCM. Berlin: Springer.
Sharma A., Tyagi V.V., Chen C.R., Buddhi D., 2009. Review on thermal energy storage with phase change materials and applications. Renewable and Sustainable Energy Reviews, 13, pp. 318-345.
Tyagi V.V., Buddhi D., 2007. PCM thermal storage in buildings: A state of art. Renewable and Sustainable Energy Reviews, 11, pp. 1146-1166.
Wu S.Y., Zhu D.S., Zhang X.R., 2010. Preparation and melting/freezing characteristics of Cu/Paraffin nanofluid as phase-change material (PCM). Energy & Fuels, 24, pp.1894–1898.
Zalba B., Marín J.M., Cabeza L.F., Mehling H., 2003. Review on thermal energy storage with phase change: materials, heat transfer analysis and applications. Applied Thermal Engineering, 23, pp. 251-283.

SYNTHESIS OF CARBON SPHERULES AND PREPARATION OF DISPERSIONS BASED ON GLYCEROL: STABILITY TEST AND THERMAL CONDUCTIVITY MEASUREMENT

DIEGO VASCO, CAMILO CASTILLO, RODRIGO PIZARRO, VALDERES DRAGO

Diego Vasco, Dr. MSc, Rodrigo Pizarro, Dr. MSc., Camilo Castillo, student Eng. Departamento de Ingeniería Mecánica, Universidad de Santiago de Chile, Valderes Drago, Departamento de Física, Universidade Federal de Santa Catarina.

Abstract

There are mainly two methods of synthesis of nanoparticles, physical methods (top down) and chemical methods (bottom up). The chemical methods are the most used, since they are simpler and more efficient, moreover it is possible to control several parameters during the synthesis. Between the chemical methods, the hydrothermal and solvothermal methods can be found. The hydrothermal method, which is a homogenous reaction in a pressurized vessel, is used in the present work. Normally, the experimental factors that affect the shape and size of carbon spherules are reaction time, temperature, pressure, concentration of reactive, ionic force, dielectric constant of the solvent and pH. To maintain the values of these factors at certain levels it is important to obtain high purity nanoparticles with low size distribution. The goals of the present work are to study the effect of time of synthesis on the carbon spherules size distribution and stability of carbon spherules dispersions using glycerol as base fluid. Finally, the thermal conductivity of the most stable dispersion was measured through the transient line heat source method. The synthesis of the carbon spherules was performed according to the hydrothermal method. In this work an aqueous solution of sugar with acetic acid (5:1) was used as a precursor. The reaction was taken in a pressurized (20 atm) vessel made of stainless steel (SAE 316) with an inner covering of PTFE (polytetrafluroroethylene) at 180°C. Five reaction times were studied (1, 2, 3, 4 and 5 hours). After 1 hour of synthesis, formation of spherules was not observed. Despite the fact that after 2 hours the formation of carbon nuclei was observed by micrographic imaging, the yield was very low. After 3 (ECC03), 4 (ECC04) and 5 (ECC05) hours the yield was increased obtaining 3.04, 4.63 and 5.75 g of carbon spherules respectively. Using glycerol as base fluid and the sample ECC04 of carbon spherules as solute, three dispersions were prepared by using an ultrasonic device, afterwards solubility tests were performed by subject the samples to hot (20°C) and cold (-20°C) environments during periods of 12 hours. The dispersions with ECC05 and ECC03 underwent decantation after two and five cycles, respectively. The better stability of the dispersions with the sample of ECC03 is explained by the lower size of the carbon spherules. Nevertheless, a dispersion of ECC03 carbon spherules with 0.57 wt% did not represent an improvement higher than 5% of the thermal conductivity in respect to the base fluid. Subsequent thermal conductivity studies with higher concentrations of carbon spherules were performed.

Introduction

The use of HVAC equipment on houses and buildings is growing every year therefore a higher consumption of energy worldwide. Due to the increasing demand for energy sources, several strategies have been developed to save energy and to find new energy sources. In the case of HVAC engineers, one of their challenges is to reduce the energy consumption associated to cooling/heating without sacrifice the thermal comfort of the users. In recent years, the use of phase change materials (PCM) has raised, since they are able to store and release significant amounts of heat at a constant temperature because of their high latent heat per volume unit. There is a broad variety of PCM with phase change points close to the human comfort temperature (18°C to 22°C), allowing a greater control of the internal space temperature (less variations) and lower losses of heat to the environment. However, PCM have low thermal conductivities which can reduce the heat transfer rate. To solve this problem some authors have proposed to prepare nanoparticle – with high thermal conductivity - dispersions using PCM as base fluids (nanofluids).

Nanofluids are colloidal solutions of nanometric particles (metals, metallic oxides and carbon nanotubes) in a base fluid like water, ethylene glycol or paraffins. Some experimental studies have shown that a low quantity of nanoparticles can markedly increase the thermal conductivity of the base fluid. There are mainly two methods of synthesis of nanoparticles, physical methods (top down) and chemical methods (bottom up). The chemical methods are the most used, since they are simpler and more efficient, moreover, it is possible to control several parameters during the synthesis. Hydrothermal and solvothermal methods are two examples of chemical methods. The hydrothermal method consists in a homogenous reaction in a pressurized vessel. Normally, the factors that affect the shape and size of nanoparticles are reaction time, temperature, pressure, concentration of reactive, ionic force, solvent dielectric constant and pH. To control the values of all these factors is important to obtain high purity nanoparticles with low size distribution. The synthesis of carbon spherules of nanometric size is performed by a modified hydrothermal method proposed by Wang et al. (2002). A precursor aqueous sucrose/citric acid (molar ratio 5:1) solution is reacted in a pressurized vessel (20 atm) at 180°C. According to Sun and Li (2005), during the first stage at 140°C, aromatic and oligosaccharides are obtained, then, around 160°C, carbonization takes place. During carbonization, the formation and growth of the nuclei by diffusion of solutes through the particle surface occurs until the process is stopped. The main goals of the present work are to study the effect of the reaction time over the size and size distribution of carbon spherules and to measure the thermal conductivity of a nanofluid based on these spherules and glycerol as based fluid.

Synthesis of nanoparticles and nanofluid preparation

In this work, the hydrothermal was used for the synthesis nanoparticles. The hydrothermal method is one of the most used in the production of nanoparticles. This method – which is defined as a homogeneous chemical reaction in the presence of solvent in a closed system at high temperature and pressure– has some important advantages over conventional processes such as a lower power consumption, simplicity, and higher reaction rates. However, this method requires controlling parameters like reaction time, temperature, pressure, reactants concentration, ionic strength and pH. Small variations in one of these parameters can result in structures with undesirable morphology, size and surface, by the contrary, the control these parameters allows to obtain high purity materials with controlled stoichiometry, high homogeneity, lower distribution of particle size, controlled morphology, excellent reproducibility and mainly the production of particles at different scales.

Nanoparticles have a high surface area and consequently a high surface energy. During synthesis process, the particles tend to agglomerate and grow; therefore the total surface energy decreases. To prevent uncontrolled growth and agglomeration, two basic stabilization mechanisms are usually used: (i) repulsion by electric charge and (ii) addition of a stabilizing agent or surfactant. In this work, the addition of a surfactant makes possible to control the size, shape and dispersion of nanoparticles. One of the biggest concerns with the synthesis of carbon nanoparticles is the toxic compounds that could be released during the process. In this case, the solvent used was distilled water which implies lower power consumption and less solid or gaseous waste.

For the synthesis of the nanoparticles samples, an autoclave with an internal coating was used. The autoclave of 40 ml is made of stainless steel SAE 316 with a thickened wall of 8 mm. The autoclave is screwed in order to maintain a high internal pressure level (Figure 1). Inside of the autoclave, a polytetraflouroethylene (PTFE) vessel with a thickened wall of 3 mm is placed to avoid chemical reactions between the solution (sucrose) and the steel.

Figure 1. Autoclave and internal coating

The reactant is an aqueous solution of sucrose and citric acid in molar a ratio of 5:1. From this aqueous solution, different reaction times at 180°C were performed. Since now, the obtained products are tagged according to the nomenclature established in table 1.

Nomenclature	Reaction time [h]
ECC01	1
ECC02	2
ECC03	3
ECC04	4
ECC05	5

Table 1. Nomenclature of the different prepared samples of nanoparticles.

After one hour of synthesis, formation of spherules was not observed. Through micrographic imaging, it was observed that at least two hours are required to observe formation of carbon nuclei. The yield of carbon spherules in relation to sucrose solution for each sample after 3 (ECC03), 4 (ECC04) and 5 (ECC05) hours was 12.2%, 18.6% and 23.1% respectively, which is much more than the yield obtained by Wang et al. (2001) due to the higher sucrose and citric acid concentration.

Dispersions of 0.57 wt% with samples ECC03 and ECC05 in glycerol as fluid base were prepared using an ultrasonic processor (Hielscher UP50H). Afterwards, stability tests were performed subjecting the samples to hot (20°C) and cold (-20°C) environments during periods of 12 hours. The dispersions with ECC05 and ECC03 underwent decantation after two and five cycles, respectively. Better stability with the sample ECC03 was observed because of the lower size of the carbon spherules (Figure 2). Nevertheless, a dispersion of ECC03 carbon spherules of 0.57 wt% did not represent an improvement of the thermal conductivity higher than 5% of the thermal conductivity of the fluid base. This percentage is the error associated to the transient line heat source method (KD2-Pro). For this reason, thermal conductivity studies with higher concentrations of ECC03 carbon spherules were performed.

Figure 2. Solubility tests of carbon spherules in glycerol. From left to right, ECC04, ECC05 and ECC03 samples.

Nanofluid preparation consists on several dispersions of the sample ECC04 in glycerol. By using an ultrasonic processor (Hielscher UP50H) the dispersions of nanoparticles were done performed at 50 W with wave amplitude of 220 µm and a frequency of 30 kHz during at least one hour in a jacketed beaker refrigerated with water to avoid heat accumulation (Figure 3). The thermal conductivity measurement of the dispersions has been performed by the transient line heat source method (KD2-Pro), which consists in an immersion probe that generates heat from its surface. The fluid absorbs part of this heat and the remainder induces an increase of the surface temperature of the sensor that in comparison with the supplied heat allows determining the thermal conductivity of the sample. The measurements were done five times each ten minutes for each concentration. The aim of this study is to verify the increase of the thermal conductivity and the stability of the dispersions. The mass fractions analyzed were 0.2%, 0.4%, 0.6% and 0.8%.

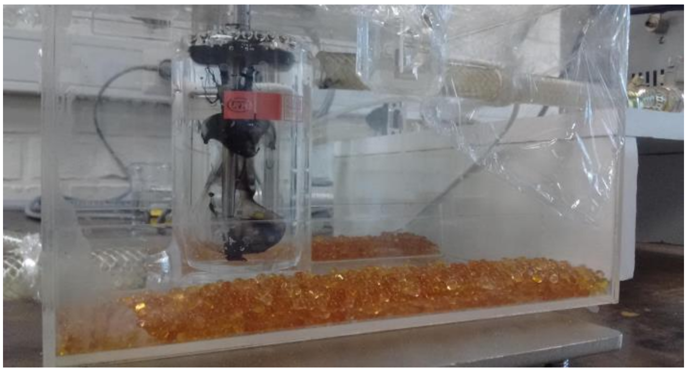

Figure 3. Experimental setup for the dispersion process of carbon spherules in glycerol.

Results: Stability and thermal conductivity

Tables 2 to 5 collect the experimental measurements of the thermal conductivities of the different dispersion of ECC04 carbon spherules in glycerol. The First measurement (after 10 minutes) is considered the increment of thermal conductivity by the addition of carbon spherules and the following measurements comprise the stability of the dispersion. At 30°C, the thermal conductivity of pure glycerol is 0.275 W/mK, according to this, the increment of thermal conductivity by carbon spherules addition were 1%, 8.7%, 5% and 2% corresponding to concentrations of 0.2 wt%, 0.4 wt%, 0.6 wt% and 0.8 wt%, respectively. Which it means that not necessarily a higher concentration of carbón spherules gives a higher thermal conductivity. This observation allows to conclude that not a single conductivity model as Maxwell's describe the thermal conductivity of the dispersions.

Measurement	Time [min]	k [W/m·K]	σ
1	10	0.278	1.88E-02
2	20	0.269	5.31E-03
3	30	0.272	2.87E-03
4	40	0.272	3.30E-03
5	50	0.276	3.09E-03

Table 2. Thermal conductivity of a dispersion of ECC04 carbon spherules in glycerol (0.2 wt%)

Measurement	Time [min]	k [W/m·K]	σ
1	10	0.299	2.83E-03
2	20	0.275	1.41E-03
3	30	0.269	7.26E-03
4	40	0.268	8.06E-03
5	50	0.274	5.31E-03

Table 3. Thermal conductivity of a dispersion of ECC04 carbon spherules in glycerol (0.4 wt%)

Measurement	Time [min]	k [W/m·K]	σ
1	10	0.289	1.31E-02
2	20	0.275	9.74E-03
3	30	0.276	6.24E-03
4	40	0.276	1.41E-03
5	50	0.280	9.43E-04

Table 4. Thermal conductivity of a dispersion of ECC04 carbon spherules in glycerol (0.6 wt%)

Measurement	Time [min]	k [W/m·K]	σ
1	10	0.280	1.48E-02
2	20	0.273	5.44E-03
3	30	0.277	8.16E-04
4	40	0.272	6.85E-03
5	50	0.278	2.05E-03

Table 5. Thermal conductivity of a dispersion of ECC04 carbon spherules in glycerol (0.8 wt%)

For each dispersion, the transient average thermal conductivity is collected in Figure 4. It can be seen how the higher thermal conductivity is reached with a concentration of 0.4 wt% and how all the dispersions are non-stable. Moreover, it can be noticed how there is no a tendency of the behavior of the thermal conductivity, after 20 minutes there was a stepped decline followed by a sudden increase. This behavior can be explained by the precipitation of the carbon spherules during the first minutes followed by a tendecy of the dispersion to reach certain equilibrium condition.

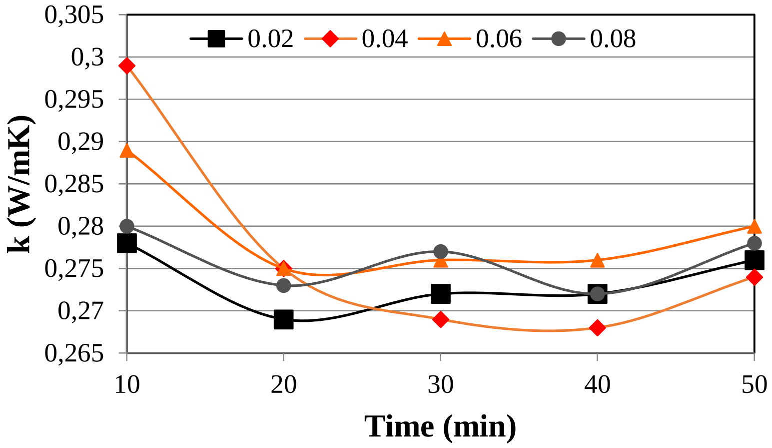

Figure 4. Transient thermal conductivity of a dispersion of ECC04 carbon spherules in glycerol.

CONCLUSIONS

The dispersion prepared with carbon spherules obtained after three hours of synthesis and glycerol showed a better stability in comparison with the other samples. Despite of that the thermal conductivity increase was low for the analyzed concentration (0.57 wt%).

The increment of thermal conductivity by carbon spherules addition were 1%, 8.7%, 5% and 2% corresponding to concentrations of 0.2 wt%, 0.4 wt%, 0.6 wt% and 0.8 wt%, respectively. Which it means that not necessarily a higher concentration of carbón spherules gives a higher thermal conductivity. This observation allows to conclude that not a single conductivity model as Maxwell's describe the thermal conductivity of the dispersions.

References

Sun X., Li Y., 2005. Hollow carbonaceous capsules from glucose solution. Journal of colloid and interface science, 291, pp. 7-12.

Wang Q., Li H., Chen L., Xuang X., 2002. Novel spherical microporous carbon as anode material for Li-ion batteries. Solid state ionics, 152-153, pp. 43-50.

Aknowledgments

To CONICYT-Chile for the support received in the Fondecyt project 11130168.

EXTRACTION OF LEAD FROM LIQUID WASTES BY EMULSION LIQUID MEMBRANE CONTAINING TRI-OCTYL PHOSPHINE OXIDE

ELSAYED FOUAD1, FAROOQ AHMAD, KHALED ABDELRAHMAN

Elsayed Fouad, Professor, Northern Border University, S. A., Farooq Ahmad, Associate Professor, Northern Border University, S. A., Khaled Abdelrahman, Assistant Professor, Northern Border University, S. A.

Abstract

An experimental design strategy is used to optimize the extraction of lead from waste water by emulsion liquid membrane. Past applications have suffered from the competing considerations of permeability and membrane stability, along with swelling. Extraction of lead is based on the complexing properties of tri-octyl phosphine oxide (TOPO). Taguchi Experimental design method was used for screening the variables. Taguchi Experimental design is defines by Response Surface Methodology (RSM) for subsequent analysis using Minitab 17 software. Parameters and their levels are TOPO concentration (0.05 - 0.25M), Span80 concentration (3 – 10 v %), external phase pH (0.5 - 5), internal phase concentration (0.1 – 1.0 M), stirring time (1 – 30 mins.) and external/emulsion volume ratio (1/1 – 20/1). Results showed that TOPO has a high contribution (73%) and Span80 has 3% on lead extraction. Our computed results using Analysis of Variance (ANOVA) shows that there is significant interaction between TOPO and Span80 concentration, internal sulfuric acid concentration, external/emulsion phase ratio, and stirring time as well as Span 80 concentration and external/emulsion phase ratio. In other way, results showed that Span80 has a highest contribution (22.5%) on emulsion breaking followed by external phase pH (11%) while Span 80, TOPO, and internal sulfuric acid concentration has a high significant effect on emulsion swelling.

Introduction

The removal and recovery of toxic heavy metals from aqueous environment have received considerable attention in recent years. Lead ions are non-biodegradable toxic heavy metal and may cause high blood pressure, kidney disease and so on. According to the World Health Organization, concentration of lead in drinking water should be less than 0.015 mg/L. The major sources of lead contamination to water come from industrial process such as aerospace, petrochemical, electroplating, batteries manufacturing, mine, metal material and many other industries. It is necessary to remove and recover this highly toxic and non-biodegradable heavy metal in order to meet increasingly stringent environmental quality standards and promote the recycling and reuse of heavy metal resources [1].

To avoid undesired accumulation of lead in aquatic environments, development of powerful treatment techniques is underway to remove lead ions from water. From this point of view, emulsion liquid membrane (ELM) has gained much attention as an advanced extraction process for the removal of contaminants present in waste water [6-18]. Compared to conventional processes, ELM contains a three-phase dispersion system, which consists of a stripping phase encapsulated by a membrane phase (organic phase), which in turn contains the extractant in organic diluents together with a surfactant to stabilize the emulsion droplet. Thus ELM process involves simultaneous extraction and stripping in one step. The metallic element present in lean solution forms a complex with the extractant at the interface of the emulsion globule and the feed phase. The complex formed is then shuttled through the organic phase to the organic phase – stripping phase interface from where it is stripped into the bulk of the encapsulated stripping phase [2].

Although this method is very effective and has been successfully applied for zinc removal, but so far its commercial applications on the removal of other heavy metals have been limited by the emulsion instability. One serious problem associated with the ELMs is their tendency to undergo swelling. For example, the globules of water-in-oil-in-water (W/O/W) membranes swell due to transfer of water from the external aqueous phase to the internal water droplets. It is widely accepted that osmotic pressure is the main driving force for swelling behavior [3].

Swelling often causes rapid increase in the volume of the internal phase. Furthermore, the swelling of membrane globules can trigger the breakdown of the globules. As a result, the process of enrichment of the solute is retarded and the efficiency of separation of the solute from the external phase becomes lower than the expected value. The swelling of the membrane globules also adversely affects the final demulsification step where the solute is recovered. The problems encountered in the demulsification step are mainly due to a sharp increase in the viscosity of emulsion, caused by swelling of internal droplets [3].

In the meantime, the membrane breakage occurs when portions of the internal phase spill into the external phase. During breakage, the stripping agent and previously extracted solute is leaked into the external phase. The most stable emulsion was obtained when there was neither swelling nor breakage of emulsion with minimum of swelling occurrence. The lack of stability of the emulsion globules will decrease extraction efficiencies. In order to solve the stability problem of emulsion liquid membrane, its formulation design is foremost important [4, 5].

Response surface methodology (RSM) is widely used for multivariable optimization studies in several processes such as optimization of process conditions, extraction, production, fermentation, biosorption of metals, etc. [19-23]. To the best of our knowledge, none of the earlier studies has optimized the extraction of lead from aqueous phase by ELM. Additionally, it is of considerable interest to optimize the two very important phenomena accompanied with ELM (Swelling and emulsion breakage). The influence of different factors such as extractant and surfactant concentrations, stirring time, external phase acidity, internal phase concentration, and volume ratio of external phase to membrane phase on the extraction of Pb by ELM is evaluated. The focus of present investigation is to study the contribution of each of the above factors on the ELM extraction in order to get the best operating conditions for efficient recovery of Pb. RSM was used to achieve the following goals:

(i) Interaction among these factors; and
(ii) A regression model which can estimate percent extraction, swelling %, and emulsion breakage.

2. Experimental

2.1 Chemicals

TOPO was obtained from Sigma Aldrich Co Ltd. Kerosene, supplied by Merck was used as diluent for organic phase. All other chemicals were of analytical grade. The nonionic surfactant, Span 80, product of Sigma-Aldrich Chemicals Co. is used as surfactant.

2.2 Emulsion Liquid Membrane Experiments

Emulsion was prepared by adding drop wise 50 ml internal sulfuric acid solution of different concentrations (Table 1) with 50 ml organic phase containing carrier, surfactant and kerosene, using an ultraturax T25 homogenizer at 10000 rpm for 5 min. The emulsion was dispersed into aqueous feed phase of Pb ions and continuously stirred with a magnetic stirrer at 400 rpm and 25°C. Mixture was separated in cylindrical separating funnels to separate the emulsion and the aqueous feed phase. Pb ions in external phase were analyzed using an ICP (Perkin Elmer, Optima 7000 DV). Extraction % was calculated according to the following equation:

$$E\% = \left[\left(C^{0}_{Pb,ext} - C^{t}_{Pb,ext}\right) / C^{0}_{Pb,ext}\right] \times 100 \tag{1}$$

After phase separation, pH of the external phase was measured by an electronic pH meter. Emulsion breakage was determined by measurement of conductivity of external phase. Concentrations of sulfuric acid in the external phase were obtained using concentration-conductivity calibration data. The %breakage (B%) can be calculated from the following equation (2) [28]:

$$B\% = \left[\left(V_e \times C_e\right) / \left(V_i \times C_i\right)\right] \times 100 \tag{2}$$

where V_e and C_e are the volume and concentration (in terms of conductivity) of the external phase, respectively, and V_i and C_i is the volume and concentration of the internal phase.

Apparent swelling ratio (S %) was expressed by the following equation:

$$S\% = \frac{V_i - V_i^0}{V_i^0} \times 100 \tag{3}$$

where V_i is the volume of the emulsion after dispersion, V_i^0 the initial volume of emulsion.

Table 1. Levels of different variables for extraction of cadmium

Independent variable	Levels 1	2	3	4	5
Carrier concentration, X_1 (M)	0.05	0.10	0.15	0.20	0.25
Surfactant concentration, X_2 (v %)	3	5	7	8	10

Internal phase concentration, X_3 (M)	0.10	0.30	0.50	0.70	1.00
External/emulsion ratio, X_4	1	5	10	15	20
Stirring time, X_5 (min)	1	5	10	20	30
External phase pH, X_6	0.5	1	2	3.5	5

2.3 Experimental design and optimization

The objective of an experimental design is to quantify the impact of the experimental factors on the three phenomena of ELM process. Taguchi Experimental design method is used for designing the experiments and RSM is used for analysis and screening the variables. Quadratic regression model design was applied to predict extraction% of Pb and swelling and breaking percentages of emulsion with a function of the concentration of TOPO (X_1) and Span80 (X_2) in the membrane phase, concentration of acid in the internal phase (X_3), external to emulsion volume ratio (X_4), stirring time (X_5), and acidity of external feed phase (X_6) according to Eq. 3.

$$Y = a_0 + \sum_{i=1}^{n} a_i X_i + \sum_{i<j}^{n} \sum_{j}^{n} a_{ij} X_i X_j + \sum a_{\ i} X_i^2 + ... \qquad (4)$$

where predicted response of the system is Y [percent of Pb extraction or emulsion breakage, B% or emulsion swelling, S%], Xi is the coded variable of associated with actual process variable i, a_i and a_{ij} are coefficients of the model. Table 1 represent coded and un-coded level for the variables used to develop the mathematical model.

The non- linear, second order regression analysis and the response surface plot of the best fitted model for coded factor level is carried out by using Minitab 17 program. The statistical analysis of the results was carried out by ANOVA. The model and its parameters were evaluated, along with the determination of the individual and interactive influences of factors on the yield of Pb extraction, B%, and S% by calculating the coefficients of Eq. (4). Statistical significance was verified by F-test. Models terms are selected or rejected based on the probability value with 95% confidence level. Eventually, response surface plots are generated in order to visualize the individual and interactive effects of the independent variables.

3. Results and discussions

Model fitting and statistical analysis

Statistical analysis indicates that the model was highly significant with low probability values (P=0.000). It was shown that the independent variables were significant at a 95% confidence level. The large p-values show that It was not significant, which suggests a significant model correlation between the variables and process responses. The correlation coefficient squared was computed as the coefficient of determination (R^2) for each response. The accuracy and variability of the model can be evaluated using R^2. This value is always between 0 and 1. The closer the value is to 1, the stronger is the model and the better the model predicts the response. From the model, R^2 was 99.48% for Pb extraction. This value ensures a satisfactory adjustment of the model to the experimental data. The adjusted R^2 (98.23%) for Pb extraction is very close to the corresponding R^2 value, which further confirms the adaptability of this model.

Both linear and quadratic terms for Pb extraction were highly significant ($p < 0.05$). The interactions between [TOPO]*external phase pH, Span 80*$[H_2SO_4]_{in}$, Span 80, *stirring time, Span 80*external phase pH, $[H_2SO_4]_{in}$*ratio, $[H_2SO_4]_{in}$*stirring time, $[H_2SO_4]_{in}$*external phase pH, ratio*stirring time, ratio*external phase pH, stirring time*external phase pH were not significant.

The responses predicted by the model were in agreement with the experimental values. This was demonstrated by plotting the predicted values against the experimental values. Fig. 1 shows the plot for predicted versus actual values for Pb extraction. This plot indicates adequate agreement between the real data and that obtained from the model and demonstrates that the model is suitable for explaining the experimental range studied.

Response surface analysis of Pb extraction

Taking into account only the significant factors (Table 2), the obtained model that shows the relationship between the E% of Pb and the extraction parameters with a satisfactory correlation coefficient is given below (Eq.5):

$$E\% = -127.082 + 196.016X_1 - 90.359X_2 - 55.34X_3 + 141.979X_5 - 2.054X_1^2 + 6.08X_2^2 + 11.108X_3^2 + 4.918X_4^2 - 16.161X_5^2 - 14.853X_6^2 - 1.056X_1X_2 - 11.227X_1X_3 - 22.622X_1X_4 - 20.834X_1X_5 + 10.207X_2X_4 \qquad (5)$$

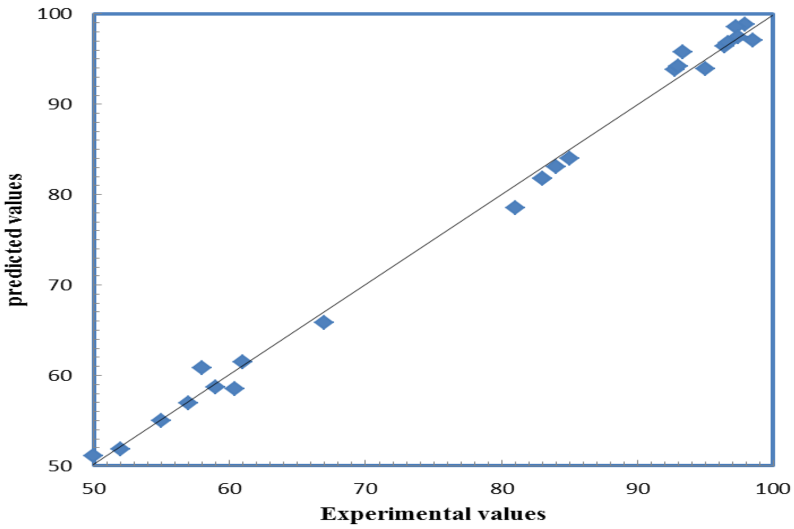

Figure 1. Predicted yield of extraction versus actual values.

The above regression equation shows TOPO concentration (X_1), stirring time (X_5), and acidity of external feed phase (X_6) have a linear positive effect on response function whereas Span80 (X_2) in the membrane phase, concentration of acid in the internal phase (X_3), and external to emulsion volume ratio (X_4) have a negative effect. The concentration of carrier, TOPO (X_1) shows both positive and negative effect (quadratic term). The quadratic term in carrier concentration shows curvature in the response surface. Hence optimal value of the response function lie between high and low levels. The constant coefficient term of the regression model (Eq. 5) represents value of response function E% at the mean values of other parameters.

Analysis of variance (ANOVA) table deducted from the results of ELM extraction of Pb, is reported in Table 2. The small p values for linear and square terms also point out that their contribution is significant to the model. But, small p values for the squared term of TOPO concentration suggest that there is curvature in the response surface. Since the response surface is explained by the second order model, it is necessary to analyze optimum setting. The graphical visualization is very helpful in understanding the second-order response surface. Figures 2-6 show the response surface plots of the pairwise interaction between the concentration of TOPO in the organic phase, concentration of Span 80 in the emulsion, concentration of H_2SO_4 in the internal phase, external to membrane ratio, stirring time and concentration of Span 80 in the emulsion and external to membrane ratio.

Table 2 Analysis of Variance for Pb extraction

Source	DF	Seq SS	Contribution, %	Adj SS	Adj MS	F-Value	P-Value
Model	17	8149.82	99.98	8149.82	479.40	1853.52	0.000
Linear	6	6461.20	79.26	4911.26	818.54	3164.75	0.000
X1	1	5961.58	73.13	2714.91	2714.91	10496.71	0.000
X2	1	321.95	3.95	63.92	63.92	247.15	0.012
X3	1	14.05	0.17	15.03	15.03	58.12	0.013
X4	1	58.33	0.72	18.25	18.25	70.57	0.117
X5	1	60.48	0.74	19.40	19.40	74.99	0.005
X6	1	44.82	0.55	21.00	21.00	81.18	0.191
Square	6	1581.95	19.41	1426.07	237.68	918.94	0.000
X1*X1	1	1466.32	17.99	1018.31	1018.31	3937.12	0.000
X2*X2	1	0.80	0.01	16.97	16.97	65.60	0.000
X3*X3	1	35.75	0.44	27.64	27.64	106.86	0.000
X4*X4	1	2.85	0.03	7.40	7.40	28.61	0.001
X5*X5	1	9.09	0.11	42.37	42.37	163.82	0.000
X6*X6	1	67.15	0.82	22.57	22.57	87.25	0.000
2-Way Interaction	5	106.67	1.31	106.67	21.33	82.49	0.000
X1*X2	1	62.92	0.77	32.87	32.87	127.10	0.000

X1*X3	1	1.09	0.01	17.11	17.11	66.16	0.000
X1*X4	1	1.54	0.02	25.48	25.48	98.53	0.000
X1*X5	1	1.84	0.02	20.92	20.92	80.88	0.000
X2*X4	1	39.30	0.48	39.30	39.30	151.93	0.000
Error	7	1.81	0.02	1.81	0.26		
Total	24	8151.63	100.00				

S = 2.44656 R-Sq = 99.48% R-Sq(pred) = 93.15% R-Sq(adj) = 98.23%

Figure 2 shows the response surface plot from the model (Eq. 12), where the other factors are kept at its mid-level 3 and the interaction between TOPO concentration and Span 80 concentration in membrane phase is examined. It is seen from Fig. 2 that the interaction between the TOPO concentration and concentration of surfactant (Span 80) in organic phase shows minimum % of extraction at around mean level of the coded variable revealed that influence of Span 80 is quadratic (nonlinear). The coefficient term is -1.056 in Eq. 5, implies negative impact on Pb extraction. This can be explained in terms of higher emulsion viscosity at high level of Span 80 concentration (within the experimental range). The increase in membrane viscosity reduces diffusivity of TOPO-Pb complex into internal strip phase of ELM. This causes reduction in mass transfer which in turn affects the yield of extraction.

Figure 3 shows that the interaction between TOPO concentration in organic phase and internal phase concentration in the membrane phase is significant, however the coefficient term is negative (-11.227) which implies negative impact on extraction of Pb. We find that the percent extraction of Pb decreases with increase in internal sulfuric acid concentration initially and beyond which there is a fall. This because interaction of TOPO concentration and internal phase concentration has a positive response regarding emulsion breaking (7.95 from Eq. 6) which implies that back diffusion occur for TOPO-Pb complex towards external phase.

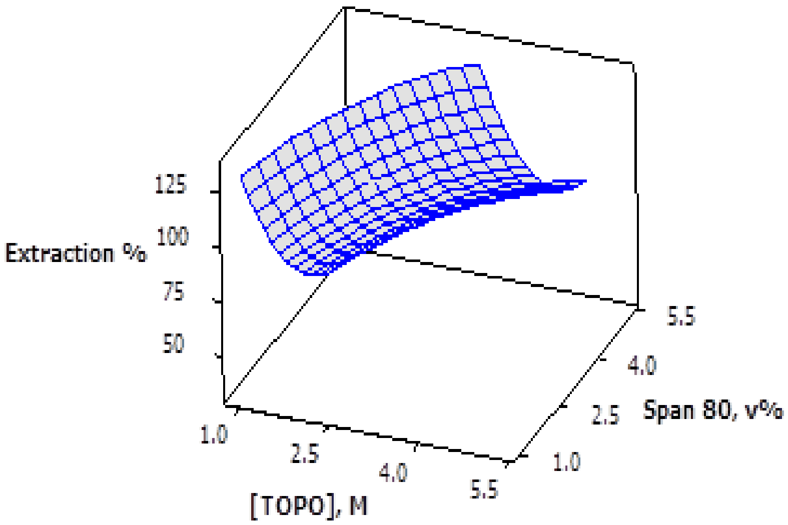

Figure 2. The 3D plot showing the effects of TOPO concentration, concentration of Span 80and their mutual interaction Response surface plot of extraction %.

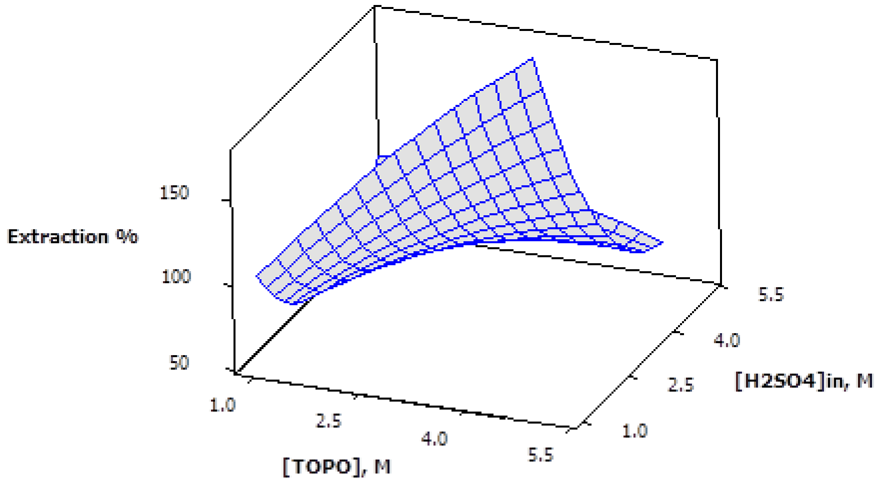

Figure 3. The 3D plot showing the effects of TOPO concentration, concentration of internal sulfuric acid concentration and their mutual interaction Response surface plot of extraction %.

Figure 4 and Eq. 5 show that interaction between concentration of TOPO(X_1) and external/emulsion ratio (X4) has a more negative effect on Pb extraction. It can be seen from this figure that when the ratio decreases, the extraction% grows significantly. For this interaction, B% has a high positive response (14.72). This means that by increasing the ratio, high breaking % was attained and back extraction occurs. In theory, it is reasonable to keep the ratio at a low value in order to obtain high extraction efficiency. However, in practice, the decrease of the ratio means the increase of the amount of emulsion required to treat each unit of Pb solution and the decrease of the concentration of Pb in internal phase. Thus the emulsion dispersed in the external phase tends to form bigger droplets, leading to the decrease of the specific surface area to extract Pb ions.

Fig. 5 shows the 3D graphic surface plot of the combined effects of TOPO concentration and stirring time (X_1X_5) on the extraction. These plots present the response as a function of two factors, keeping the other variable constant at its middle level. The surface plot shows a strong interaction between these two factors. A higher extraction% was obtained with a lower level of stirring time. Extraction % decreased with the increase of stirring time. This demonstrated that the effect of TOPO concentration (X_1) and stirring time (X_5) on extraction had a significant negative response, and was in good agreement with the coefficient in Eq. 5 (-20.834). Higher levels of stirring time lead to more breaking of emulsion.

From Eq.5, it is indicated that, the effect of the Span 80 concentration (X_2) and external phase to emulsion volume ratio (X_4) on the extraction % has a negative response. This reflects the effect of surfactant concentration on emulsion viscosity.

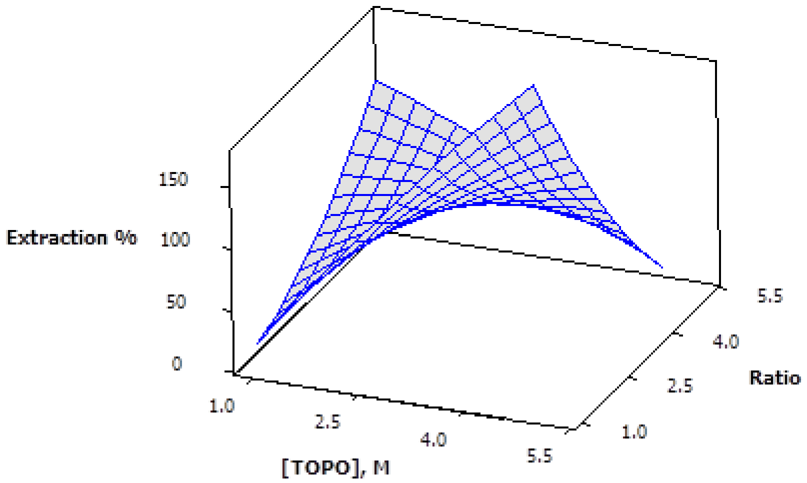

Figure 4. The 3D plot showing the effects of TOPO concentration, external/emulsion volume ratio and their mutual interaction Response surface plot of extraction %.

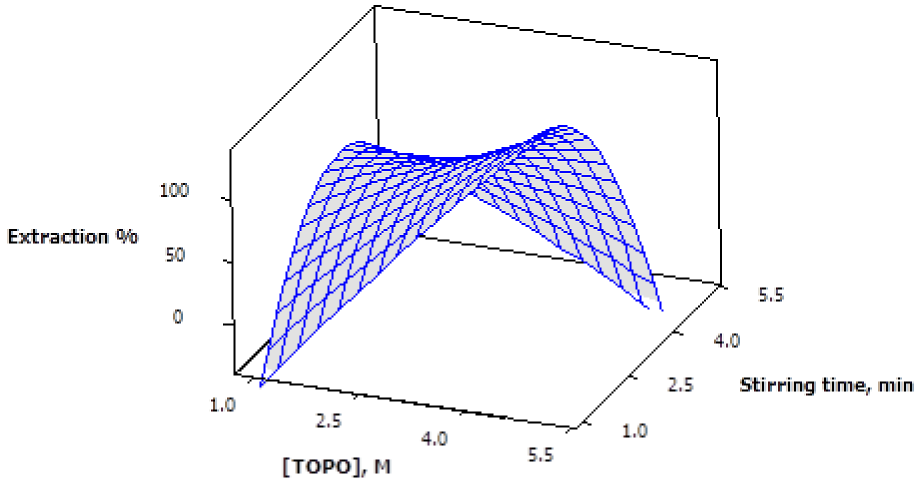

Figure 5. The 3D plot showing the effects of TOPO concentration, stirring time and their mutual interaction Response surface plot of extraction %.

3.3 Response surface analysis of emulsion breaking (B %)

The predicted data of emulsion breakage from a response surface analysis model are shown in Tab. 3. The significance and adequacy of the quadratic model were tested using ANOVA. The correlation coefficient (R^2) of the model is 0.9928, which show a good coherence between theoretical and experimental response. The model F-value of 49 implies that the model is significant and the values of P less than 0.05 indicate that model terms are significant. The model established by the regression equation can substitute the experimental real point to explain response results. The mathematical model correlating the emulsion breaking in term of significant independent variables is given below (Eq. 5):

$$B\% = 124.3 - 116.1X_1 + 58.83X_2 + 54.89X_3 - 116.8X_5 - 2.244X_1^2 - 4.994X_2^2 - 10.22X_3^2$$
$$-3.651X_4^2 + 13.79X_5^2 + 13.52X_6^2 + 2.95X_1X_2 + 7.95X_1X_3 + 14.72X_1X_4 + 16.5X_1X_5 - 7.845X_2X_4$$

(6)

From table 3, it was observed that the most effective variable in emulsion breaking are Span 80 concentration (Contribution= 22.55), External phase/emulsion volume ratio (Contribution= 11.02), and stirring time (Contribution= 4.62).

The response surface plots are plotted to understand the interaction of the variables. The response surface curves for emulsion breaking are shown in Figures 6-10. Each 3D plot represents the number of combinations of the two-test variables with the other variables maintained at mid-levels. It is evident from the surface plot that the interaction between the individual variables is significant.

From Fig. 6 it is found that as the TOPO concentration increases, B% increases. Span 80 has maxima of B% at around mean level of the coded variable revealed that influence of Span 80 concentration is quadratic (nonlinear). The increase in internal phase concentration leads to increase in B%. This is shown in Fig. 7. The same trend is observed for external to emulsion phase ratio (Fig. 8). Great influence is observed for the interaction of TOPO concentration and stirring time. From Fig. 9, increasing stirring time results in sharply increase in B% from level 1 to level 5. This is due to shear forces affecting on emulsion globules with increasing stirring time. Fig. 10 shows the interaction of Span 80 concentration and external to emulsion phase ratio. Increasing ratio shows an increase in B% until level 3 and then decreases.

Table 3 Analysis of Variance for emulsion breaking

Source	DF	Seq SS	Contribution, %	Adj SS	Adj MS	F-Value	P-Value
Model	17	7528.96	99.17	7528.96	442.880	49.00	0.000
Linear	6	2930.10	38.59	2353.83	392.304	34.41	0.000
X1	1	23.75	0.31	278.79	278.788	30.85	0.000
X2	1	1712.06	22.55	271.27	271.274	30.02	0.012
X3	1	5.96	0.08	630.56	630.561	69.77	0.013

X4	1	0.61	0.01	530.54	530.538	58.70	0.117
X5	1	351.07	4.62	575.26	575.265	63.65	0.005
X6	1	836.65	11.02	783.49	783.487	86.69	0.191
Square	6	3564.07	46.94	1968.48	328.08	36.30	0.000
X1*X1	1	1078.47	14.20	287.76	287.758	31.84	0.001
X2*X2	1	92.12	1.21	318.27	318.269	35.22	0.001
X3*X3	1	1277.16	16.82	797.63	797.626	88.26	0.000
X4*X4	1	12.13	0.16	170.10	170.103	18.82	0.003
X5*X5	1	515.55	6.79	871.50	871.497	96.43	0.000
X6*X6	1	588.64	7.75	837.47	837.468	92.67	0.000
2-Way Interaction	5	1034.79	13.63	1034.79	206.959	22.90	0.000
X1*X2	1	120.02	1.58	77.69	77.690	8.60	0.022
X1*X3	1	5.98	0.08	265.40	265.403	29.37	0.001
X1*X4	1	23.67	0.31	483.89	483.894	53.54	0.000
X1*X5	1	5.90	0.08	684.90	694.802	76.88	0.000
X2*X4	1	879.22	11.58	879.22	879.223	97.29	0.000
Error	7	63.26	0.83	63.26	9.038		
Total	24	7592.22	100.00				

S = 4.02118 R-Sq = 99.28% R-Sq(pred) = 87.54% R-Sq(adj) = 97.55%

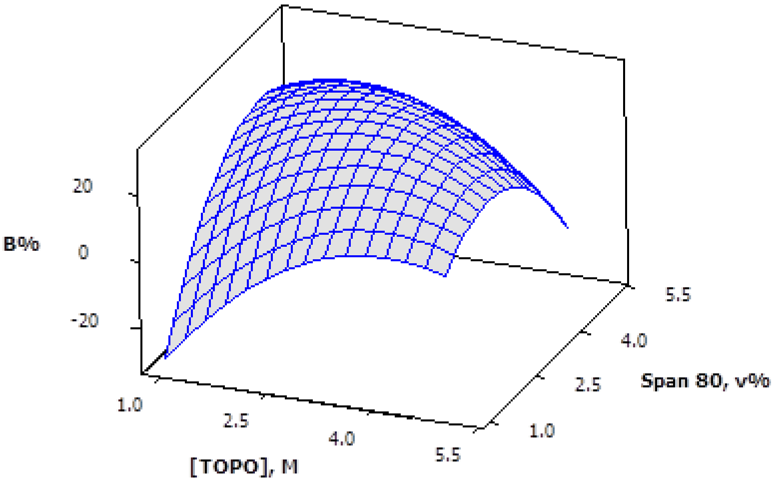

Figure 6. The 3D plot showing the effects of TOPO concentration, Span 80 and their mutual interaction on emulsion breaking.

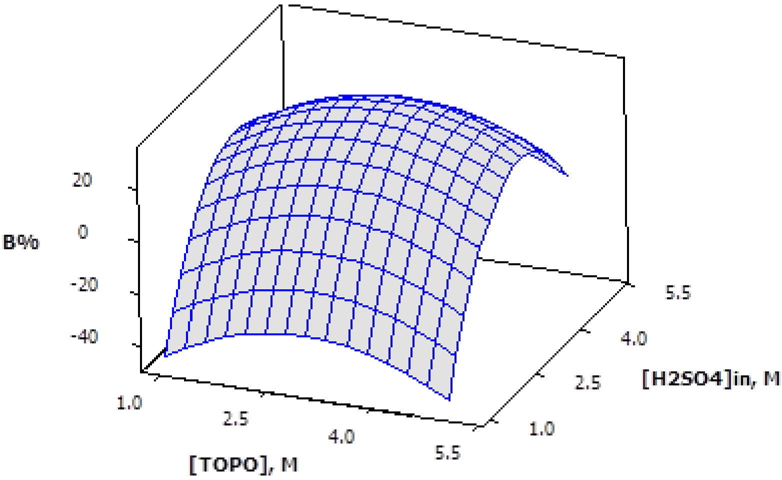

Figure 7. The 3D plot showing the effects of TOPO concentration, $[H_2SO_4]_{in}$ and their mutual interaction on emulsion breaking.

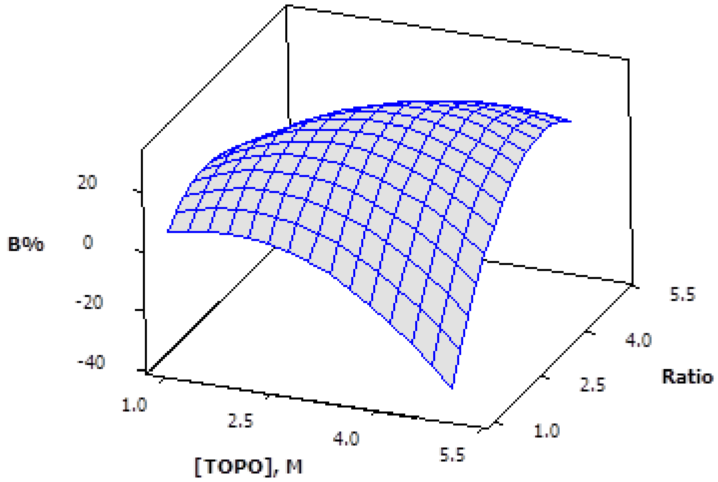

Figure 8. The 3D plot showing the effects of TOPO concentration, external to emulsion phase ratio and their mutual interaction on emulsion breaking.

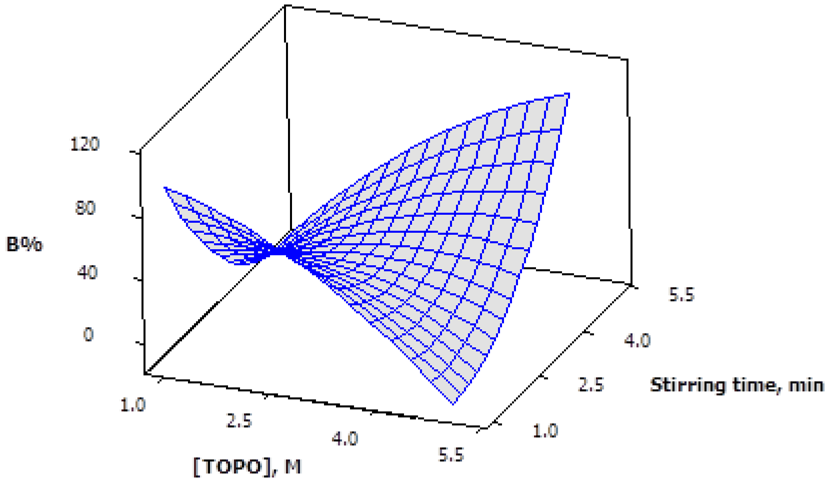

Figure 9. The 3D plot showing the effects of TOPO concentration, stirring time and their mutual interaction on emulsion breaking.

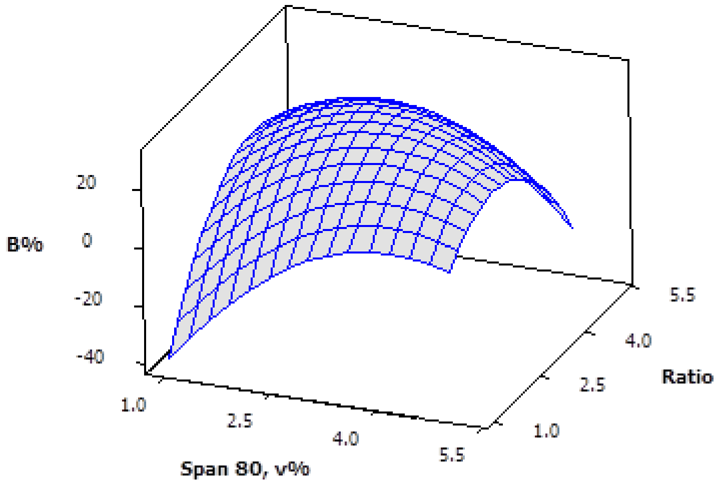

Figure 10. The 3D plot showing the effects of Span 80 concentration, external to emulsion phase ratio and their mutual interaction on emulsion breaking.

Emulsion swelling (S %)

The mathematical model correlating the emulsion swelling in term of significant independent variables is given below:

$$S\% = -24.69 - 13.295X_1 + 16.885X_2 + 13.55X_3 + 11.615X_5 - 9.45X_2^2 + 15.45X_4^2 - 22.77X_6^2$$
$$+19.44X_1X_2 + 13.02X_1X_3 - 13.96X_1X_5$$

(7)

As given in Table 4, the analysis of variance (ANOVA) of swelling pointed out a strong positive correlation (R^2 = 0.9911). In addition, according to Fisher's F-test, it can be observed that the F-value model is 1853.52. This result indicates that the model have a significant effect on the swelling of emulsion response (p Value < 0.0000). As it can be seen from table 4, that, the effective variables on emulsion swelling are Span 80, TOPO, and internal sulfuric acid concentrations. TOPO has a negative response but Span 80 concentration and internal sulfuric acid concentration have a positive response which is in agreement with the work of Wan and Zhang [24]

Table 4 Analysis of Variance for emulsion swelling

Source	DF	Seq SS	Contribution, %	Adj SS	Adj MS	F-Value	P-Value
Model	17	7132.43	99.5	7132.43	419.555	81.55	0.000
Linear	6	5479.09	76.43	1777.33	296.222	57.58	0.000
X1	1	2093.04	29.20	943.27	943.273	183.35	0.000
X2	1	2548.98	35.56	57.48	57.475	11.17	0.012
X3	1	796.00	11.10	56.42	56.424	10.97	0.013
X4	1	35.28	0.49	16.46	16.459	3.20	0.117
X5	1	0.01	0.00	81.73	81.732	15.89	0.005
X6	1	5.78	0.08	10.80	10.795	2.10	0.191
Square	6	584.25	8.15	1025.29	170.882	33.22	0.000
X1*X1	1	7.23	0.10	0.54	0.543	0.11	0.755
X2*X2	1	19.56	0.27	81.12	81.205	15.78	0.005
X3*X3	1	207.43	2.89	7.64	7.642	1.49	0.262
X4*X4	1	34.30	0.48	429.69	429.686	83.52	0.000
X5*X5	1	99.60	1.39	3.81	3.813	0.74	0.418
X6*X6	1	216.13	3.02	363.77	363.774	70.71	0.000
2-Way Interaction	5	1069.08	14.91	1069.08	213.816	41.56	0.000
X1*X2	1	350.04	4.88	420.17	420.17	81.67	0.000
X1*X3	1	12.19	0.17	32.36	32.36	6.29	0.041
X1*X4	1	512.52	7.28	9.29	9.29	1.81	0.221
X1*X5	1	169.73	2.37	106.13	106.13	20.63	0.003
X2*X4	1	15.60	0.22	15.60	15.60	3.03	0.125
Error	7	36.01	0.50	36.01	5.145		
Total	24	7168.44	100.00				

S = 2.92214 R-Sq = 99.11% R-Sq(pred) = 88.17% R-Sq(adj) = 96.95%

Conclusions

The present study shows that RSM is a useful tool to describe and predict the extraction process of lead from waste water by ELM. The experimental results adequately fit with second-order polynomial models and show significant linear, quadratic and interaction effects of the independent variables. The regression coefficients (R^2) of 0.9948, 0.9928 and 0.9911 were obtained for the response of extraction %, emulsion breaking and swelling, respectively. These values revealed good correlations between responses and independent variables. The modeling adequacy of these three responses exhibited that experimental values are in agreement with the predicted ones. From the results, it was found that the linear effects of TOPO, Span 80 concentration, internal phase concentration, stirring time, the square effects of TOPO concentration, Span 80 concentration, internal phase concentration, external to emulsion volume ratio, stirring time, external phase pH and interactive effects of TOPO concentration and internal phase concentration, external to emulsion volume ratio, stirring time had high significant influence on the extraction of lead. The most effective variables in emulsion breaking are Span 80 concentration, external phase/emulsion volume ratio, and stirring time. The effective variables on emulsion swelling are Span 80 concentration, TOPO concentration, and internal sulfuric acid concentration.

References

[1] Pei L., Wang Li-m., 2012. Transport behavior of divalent lead ions through dis-phase supplying supported liquid membrane with PC-88A as mobile carrier, International journal of chemical reactor engineering, 10 (A11), 1-24.

[2] Fouad E.A., Bart H.-J., 2008. Emulsion liquid membrane extraction of zinc by a hollow-fiber contactor, Journal of Membrane Science 307, 156–168.

[3] Yan J., Pal R., 2001. Osmotic swelling behavior of globules of W/O/W emulsion liquid membranes, Journal of Membrane Science, 190, 79–91

[4] Ahmad A.L., Kusumastuti A., Derek C.J.C., Ooi B.S., 2011. Emulsion liquid membrane for heavy metal removal: An overview on emulsion stabilization and destabilization, Chemical Engineering Journal 171, 870–882.

[5] Raja N., Raja S., Norasikin O., Nor A., Saidina A., 2014. Emulsion liquid membrane stability in the extraction of ionized nanosilver from wash water, Journal of Industrial and Engineering Chemistry 20, 3243–3250.

[6] Das D., Juvekar V.A., Bhattacharya R., 2015. Efficacy of extraction of U(VI) by liquid emulsion membrane (LEM) using TOPO, D2EHPA and TOA, Journal of Radioanalytical and Nuclear Chemistry 304(3), 1261-74.

[7] Eyupoglu V., Kumbasar R. A., 2015. Extraction of Ni(II) from spent Cr-Ni electroplating bath solutions using LIX 63 and 2BDA as carriers by emulsion liquidmembrane technique, Journal of Industrial and Engineering Chemistry 21, 303-310.

[8] Berrama T., Pareau, D., Durand G., 2015. Batch and dynamic study of lactic acid extraction using emulsion liquid membrane, Membrane Water Treatment, 6(4), 277-292.

[9] Lee S.C., 2015. Removal of acetic acid from simulated hemicellulosic hydrolysates by emulsion liquid membrane with organophosphorus extractants, Bioresource Technology, 192, 340-345.

[10] Björkegren, S., Karimi, R. F., Martinelli, A., Jayakumar, N.S., Hashim M. A., 2015. A new emulsion liquid membrane based on a palm oil for the extraction of heavy metals, Membranes, 5(2), 168-179.

[11] Anitha, M., Ambare, D.N., Singh, D.K., Singh, H., Mohapatra, P.K., 2015. Extraction of neodymium from nitric acid feed solutions using an emulsion liquid membrane containing TOPO and DNPPA as the carrier extractants, Chemical Engineering Research and Design 98, 89-95.

[12] Jingui H., , Yong Li, Xiangxin X., HongqiangR., Xiaowei H., He Y., 2015. Extraction of Ce(IV) from sulphuric acid solution by emulsion liquid membrane using D2EHPA as carrier, RSC Advances 5(91), 74961-74972.

[13] Bahram M., Kobra P., 2015. Emulsion liquid membrane for selective extraction of Bi(III), Chinese Journal of Chemical Engineering 23 (4), 641-645.

[14] Avinash B. L., Manish K. D., Vikas K. B., Sanjay P. K., Pawan D.M.,2014. Kulkarni, Prashant S., Emulsion ionic liquid membranes (EILMs) for removal of Pb(ii) from aqueous solutions, RSC Advances 4(94), 52316-52323.

[15] Eyupoglu V., Kumbasar R.A., 2015. Extraction of Ni (II) from spent Cr–Ni electroplating bath solutions using LIX 63 and 2BDA as carriers by emulsion liquid membrane technique, Journal of Industrial and Engineering Chemistry 21, 303–310.

[16] Chaouchi S., Hamdaoui O., 2015. Extraction of endocrine disrupting compound propylparaben from water by emulsion liquid membrane using trioctylphosphine oxide as carrier, Journal of Industrial and Engineering Chemistry 22, 296–305

[17] Azzoug S., Arous O., Kerdjoudj H., 2009. Cadmium(II) and lead(II) extraction and transport in supported liquid membrane using TOPO and D2EHPA as mobile carriers, Fresenius Environmental Bulletin 18 (11), 2132-2130.

[18] Mishra P. C., Islam M., Patel R. K., 2013. Removal of Lead (II) by Chitosan from Aqueous Medium, Separation Science and Technology 48, 1234–1242.

[19] Rajasimman M., Sangeetha R., Karthik P., 2009. Statistical optimization of process parameters for the extraction of chromium (VI) from pharmaceutical waste water by emulsion liquid membrane, Chem. Eng. J., 150, 275–279.

[20] Nacera B., Nasreddine B., Åke J.J., 2014. A comparative study of experimental optimization and response surface methodology of Bi(III) extraction by emulsion organophosphorus liquid membrane, Journal of Environmental Chemical Engineering 2(3), 1756-1766.

[21] Arulmozhiappan B., Sivaramu V., 2014. Optimization of Removal of Phenol from Aqueous Solution by Ionic Liquid- Based Emulsion Liquid Membrane UsingResponse Surface Methodology, Clean - Soil, Air, Water 42(1), 64-70.

[22] Chanukya, B.S., Manish K., Navin R. K., 2013. Optimization of lactic acid pertraction using liquid emulsion membranes by response surface methodology, Separation and Purification Technology 111, 1-8.

[23] Reza M., Amin M.M., Mohammad M.A., Milad R., Jahan B. G., Zohre D., 2016. Extraction optimization of pepsin-soluble collagen from eggshell membrane by response surface methodology (RSM), Food Chemistry, 190, 186-193.
[24] Wan Y., Zhang X., 2002. Swelling determination of W/O/W emulsion liquid membranes, Journal of Membrane Science, 196, 185–201

BACTERIA EFFICIENCY ENHANCEMENT FOR URANIUM RECOVERY USING DIETHYL SULFATE

FAEZEH FATEMI, MOHAMMAD ALI FIROOZE ZAREH[1], SAMANEH JAHANI
1 Nuclear Fuel Cycle Research School, Nuclear Science and Technology Research Institute, Tehran, Iran
* ffatemi@aeoi.org.ir

Abstract

In order to improve the uranium bioleaching efficiency, mutation breeding method of bacteria Acidithiobacillus ferrooxidans (At. f) was adopted to conduct the research. At. f was induced using 0.8%, 1.0% and 1.2% (volume fraction) of diethyl sulfate (DES) as mutagen factor to achieve more efficient strain for bioleaching of low-grade uranium ore. Bioleaching of uranium was carried out with low grade uranium ore sample of Saghand mine in Iran. The optimal conditions for bacterial growth were temperature at 30 °C, pH 2 and 2.5% (w/v) of uranium ore. Experiments were carried out in the flasks for examining the variations of Eh and uranium extractions. Results indicated that the mutated At. f by 0.8% DES had the best oxidative activity, as Eh of the bacteria reached to 575 mV after 72 h which increased 1.2 times as compared with the original strain. Also, the extraction of uranium reached to 100% at that time, which was 1.5 times higher than the original strain. These results suggested that the optimum mutation could significantly improve leaching ability of the At. f.

Keywords: Uranium bioleaching; Acidithiobacillus ferrooxidans; Diethyl sulfate; Mutation

1. Introduction

Uranium is an important natural resource used for several purposes such as component for anti-corrosive alloys and coloring agent for glass and porcelain [1]. Uranium is extracted conventionally using a process that employs strong acids as reagents, which often creates environmental problems, requires large amounts of energy, and involves a complex operational plant. While it is not economical to extract uranium from low-grade ores by chemical leaching, the bioleaching process, which employs microorganisms such as bacteria and fungi as the leaching catalysts, is known to be economical and environmentally acceptable [2-3]. In the microbiological leaching process, iron-oxidizing bacteria oxidize pyretic phase to ferric iron and sulfuric acid, and uranium is dissolved from the ore due to sulfuric acid attack. The recovery of heavy metals by an application of microorganisms is now a worldwide established biotechnological process. The predominant metal sulfide-dissolving microorganisms are extremely acidophilic bacteria and archaea (meaning organisms thriving at pH values below 3) that are able to oxidize either inorganic sulfur compounds and/or iron (II) ions [4-5]. For many years passed, most researches of bioleaching microorganism have been interested in Acidithiobacillus ferrooxidans, which was always considered to have the best leaching effect and is widely used in biohydrometallurgical process [6].

Bioleaching bacteria have some drawbacks such as long growth cycle and slow oxidation activity, which lead to poor effect on bioleaching which is not suitable for application in industry [7]. Such drawbacks demand the improvement of leaching bacteria. Due this, to acquire excellent bioleaching strains that grow industrially well at higher contents of metal ions, it is necessary to genetically alter bacteria with mutation [8]. Mutation is a stable, heritable change in the nucleotide sequence of a genetic nucleic acid which typically results in the generation of a new allele and a new phenotype. The generation of a mutation (mutagenesis) may occur spontaneously or may result from the activity of a mutagen. Spontaneous mutations in the DNA sequence occur when the bacterial chromosome replicates during growth. The frequency of mutations may be increased through the treatment with chemical mutagens [9].

At. f mutations by physical and chemical factors have also been increasingly applied to improving the bioleaching activity of the strains due to their simple procedure and high efficiency [10]. Study of mutagenic effect of chemical mutagens may be a useful tool in exploring the genetic variations, which might be induced by these mutagens for quantitative characters in At. f. The DES-induced mutagenesis is a frequently-used and effective method for breeding that is reported to be a monofunctional and strong alkylating agent. It is mutagenic in microorganisms and DNA damage in bacteria [11].

In this study, an original strain of At. f was processed by chemical mutagen DES, to investigate the effects of mutation on bacterial activity and bioleaching of low-grade uranium ore.

2. Materials and Methods

2.1. Microbial Strain and Culture Conditions

The At. f was cultivated in 9K liquid medium. The 9K liquid medium containing $(NH_4)_2SO_4$ 3.0 g/L; $MgSO_4·7H_2O$ 0.5 g/L; K_2HPO_4 0.5 g/L; KCl 0.1 g/L; $Ca(NO_3)_2$ 0.01 g/L and $FeSO_4·7H_2O$ 20 g/L , was the energy source for bacterial growth [12].

The optimum cultivating conditions of At. f were set at 30 °C, the initial pH value at 2.0, string speed at180 rpm and 10% inoculums. The At. f was prepared for experiments after filtering, while the concentration of At. f was adjusted to 1.6×10^8 at logarithmic phase of growth.

2.2. Induction of Mutations

In order to mutate the bacteria by DES, 10 mL of pre-cultured suspension of At. f was transferred to the plates. Then, the suspended cells were treated by 0.8, 1 and 1.2% of DES concentrations. After that, the plates were shaken for 15 min and the reaction was terminated with 25% sodium thiosulfate. In following, the aliquots were kept away from the light in the fridge at 4 ℃ for 12 h to enhance the effect of positive induction [13].

2.3. Bioleaching Experiments

Bioleaching experiments were carried out in 2 L flasks containing 900 mL of 9K liquid medium and 10% inoculums (v/v) including original At. f and induced strains as followings: 1- At. f mutated with 0.8% concentrates of DES 2- At. f mutated with 1% concentrates of DES 3- At. f mutated with 1.2% concentrates of DES. The pulp density of uranium ore was 2.5% (w/v) and the initial pH of the culture was adjusted to 2 with H_2SO_4 (10N). Flasks were incubated at 30℃ and 150 rpm in a rotary shaker. During bioleaching process, the samples were taken at regular intervals (24h) for 6 days to determine the uranium extractions and Eh values.

2.4. Analysis

The uranium extractions were analyzed by ICP method. Also, the Eh (redox potential) of the supernatants at room temperature were measured with an Eh meter.

2.5. Statistical Analysis

Data are presented as means ± Standard Error of Mean (SEM). The results were subjected to one-way ANOVA followed by Tukey's HSD using SPSS (version 22) software. Significant levels were defined as $P<0.05$.

3. Results and Discussion

3.1. Variations of Eh with DES-Treated At. F During Uranium Bioleaching

In this study, the effect of different concentrations of DES (0.8 %, 1% and 1.2%) on At. f was investigated. The results of oxidative activities in the original and induced At. f at 144h were shown in Figure 1. Results indicated that the Eh of DES-induced bacteria were better than the original one ($P<0.05$). The highest Eh value of induced At. f was 575 mV when the concentration of DES was 0.8%, which is 1.2 times higher than the original strain. The Eh of the induced At. f with 0.8, 1 and 1.2% DES reached to 575, 564, 562 mV in compare to 445 mV for original At. f at 72h. It was shown that the induced bacteria with 0.8% DES oxidized all the ferrous ions within 72 h, while the original strain needed 120h. The results indicate that the mutation treatments could significantly improve oxidation activity of bacteria ($P<0.05$). It may be due to the increasing Fe oxidation in the medium which accelerated by the involvement of bacteria, that leads to the Eh increasing. As culture time progressed, Fe^{2+} is oxidizing to Fe^{3+} and the concentration of Fe^{3+} in the medium increased, which reflected the change of Eh. In another word, Fe^{2+} is oxidized completely and the Eh reaches its highest value [14].

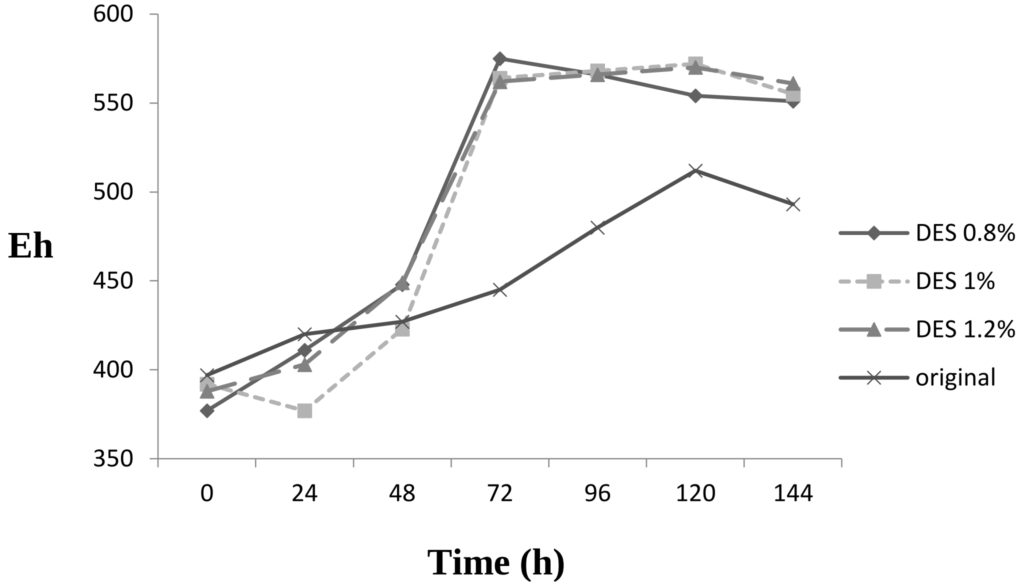

Fig. 1. Comparison of Eh value between induced At. f with different concentrations of DES and original bacteria.

3.2. Bioleaching of Uranium Ore

The yields of uranium extraction after mutation with different concentrations of DES were shown in Figure 2. The yields of uranium extractions in the presence of induced bacteria were higher than original strain ($P<0.05$). Also, after 72 h, the yields of uranium extractions in induced bacteria with 0.8, 1, and 1.2% concentrations of DES, reaches to 100, 95.08, 93.63%, respectively, while the yield of uranium extraction was 65.45% with original bacteria. In addition, the results indicated that the best concentration of DES for mutation of bacteria is 0.8% of DES, while, the extraction rate of uranium reaches 100% at 72 h which was 1.5 times higher than the original strain. In contrast, mutation with 1.2% of DES was the least effective in bioleaching process in which the yield of uranium extraction was 93.63% at 6 days, that was less than the original strain (100%) at that time ($P<0.05$). Various studies showed that, the uranium oxidation reaction requires the presence of ferric ion. The ferric ion actually oxidizes the uranium, while the bacteria (*At. f)* oxidizes ferrous ion to ferric ion [15]. In following, the dissolution of tetravalent uranium in sulfuric acid leaching system follows this equation [16]:

$UO_2 + Fe_2(SO_4)_3 \longrightarrow UO_2SO_4 + 2FeSO_4$

It can be deduced that At. f are propitious to incessancy of this reactions and mutant At. f with increasing the Fe oxidation and Eh increasing, can increase the efficiency of uranium extraction.

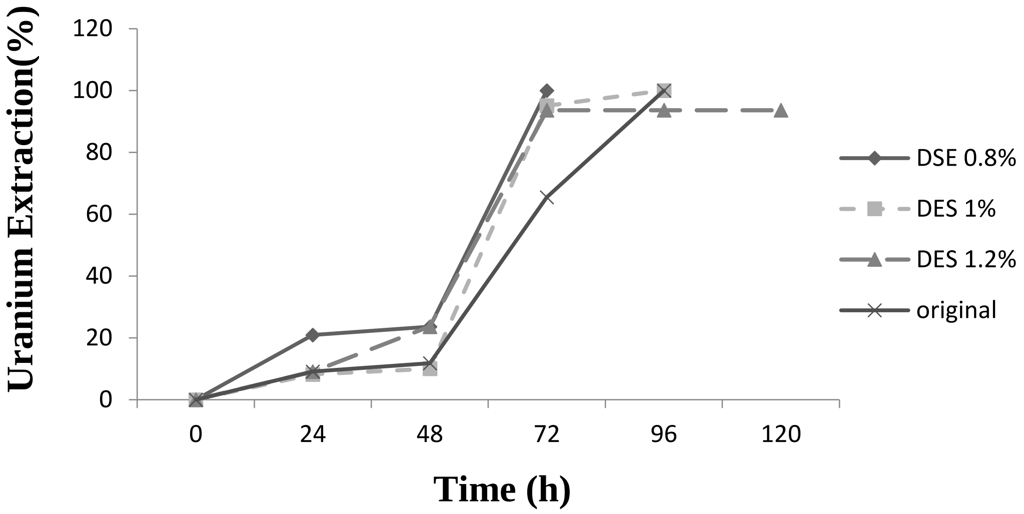

Fig. 2. Comparison of uranium extractions between induced At. f with different concentrations of DES and original strain.

4. Conclusion

1) The results of the present study showed that the bacterial mutations with variable concentrations of DES have modulating effects on uranium bioleaching rate.
2) The results proved that the At. fs pretreated by DES assist to leaching uranium from ore indirectly with the optimal concentration of 0.8%DES.
3) It was documented that in 0.8% concentration of DES, oxidative activity of mutated At. f was 575mV, which was 1.2 times higher than the original strain at 72h. Also, the uranium extraction reached 100% at 72h, which was 1.5 time higher than that of the original.
4) We can infer that the utilization of mutant bacteria can shorten the leaching time.

References

[1]- Moon S.C., Kyung. S.C. and Dong. S.K.,2005, Bioleaching of uranium from low grade black schists by Acidithiobacillus ferrooxidans, World Journal of Microbiology & Biotechnology, vol.21, pp 377–380.

[2]-Agate A.D.,1996, Recent advances in microbial mining, World Journal of Microbiology and Biotechnology, vol. 12, pp487.

[3]-Munoz J.A., Ballester A., Gonzalez F. and Blazquez M.L.,1995, A study of the bioleaching of a spanish uranium ore. part ii: orbital shaker experiments, Hydrometallurgy, vol.38, pp59.

[4]- Hedrich S., Schlömann M. and Johnson D.B., 2011, The iron-oxidizing proteobacteria, Microbiology, vol.157, pp 1551–1564.

[5]- Schippers A., Breuker A., Blazejak A., Bosecker K., Kock D. and Wright T.L., 2010, The biogeochemistry and microbiology of sulfidic mine. Waste and bioleaching dumps and heaps, and novel Fe(II)-oxidizing bacteria, Hydrometallurgy,vol.104, pp 342–350.

[6]- Ojumu T.V. and Petersen J., 2011, The kinetics of ferrous ion oxidation by Leptospirillum ferriphilumin continuous culture: The effect of pH, Hydrometallurgy, vol.106, pp 5−11.

[7]- Liu X.Y., Wang D.B., Shi W.T., Yang Y. and Zhang X.,2010, Experimental research into the mutagenic mechanism of Thiobacillus ferrooxidans, Transaction of Beijing Institute of Technology, vol.30, pp869-827.

[8]- Ying X., Jian-ping H., Bin-lan L. and Cun-jiang Z., 2001, Study on the domestication and mutagenic selection of Thiobacillus ferrooxidans, Multipurpose Utilization of Mineral Resources, vol.6, pp27−31.

[9]- Abdi D.A., 2011, Improvements of bioleaching capability of isolated strain.

[10]- Le-xian X., Jia Z., Jian-lan D., Yi Y., Bo Z., Jian-she L. and Guan-zhou Q., 2007, Comparison of three induced mutation methods for Acidiothiobacillus caldus in processing sphalerite [J], Minerals Engineering, vol.20(14), pp 1323−1326.

[11]- Lokesh G.,2008, Mutagenic effect of diethyl sulphate (DES) on the chromosomes of silkworm bombyxmori l (lepidoptera: bombycidae), J. Appl. Sci. Environ. Manage, vol.12 (3),pp45 – 50.

[12]- Silverman M.P. and Lundgren D.G.,1959, Studies on the chemoautotrophic iron bacterium ferrobacillus ferrooxidans I. An improved medium and a harvesting procedure for securing high cell yields, Journal of Bacteriology, vol.77, pp642–647.

[13]- Zai-hai Z., Dian-zuo W., Guan-zhou Q. and Yue-hua H.U., 2001, Discussion of mutation breeding for ferrous oxidation of Thiobacillus ferrooxians, Copper Engineering, vol.1, pp 12−15.

[14]- Dong Y., Lin H., Wang H. and Mo X., 2011, Effects of ultraviolet irradiation on bacteria mutation and bioleaching of low-grade copper tailings, Minerals Engineering, vol. 24, pp 870–875.

[15]- Dutrizac J.E. and Mac-Donald J.C.,1974, Ferric ion as a leaching mediu, Min scieng, vol.6, pp 59-100.

[16]- Moses C.O., Nordstrom D.K., Herman J.S. and Mills A.L., 1987, Aqueous pyrite oxidation by dissolved-oxygen and by ferric iron,Geochim. Cosmochim, vol.51 (6), pp 1561–1571.

EFFECTS OF ULTRAVIOLET IRRADIATION ON BACTERIA AND BIOLEACHING OF LOW-GRADE URANIUM ORE

FAEZEH FATEMI, SAMANEH JAHANI, SABA MIRI

1 Nuclear Fuel Cycle Research School, Nuclear Science and Technology Research Institute, Tehran, Iran.
ffatemi@aeoi.org.ir
2 Department of Biotechnology, Faculty of Life Science, Alzahra University, Tehran, Iran.
sabamiri70@gmail.com

Abstract

This paper studied the effect of ultraviolet irradiation (UV) on the mutation of Acidithiobacillus ferrooxidans (At. f) and bioleaching of low-grade uranium ore. In this study, bioleaching of uranium was carried out with low grade uranium ore sample of Saghand mine in Iran. At. f were cultivated in 9K medium containing 2.5% (w/v) uranium ore after mutation via UV radiation (60, 120 and 180 seconds). The optimum temperature and pH for growth were 35 °C and 2 for At. f. The results showed that the ultraviolet irradiation as a mutagen factor can improve bio-activity and bioleaching capability. Furthermore, the oxidative activity of At. f is greatly improved by mutants. The highest leaching rate of uranium was also obtained to be 100% via the mutant At. f with UV 120s, which is higher than the At. f without mutation at 72h. These studies showed that mutant bacteria using UV have great potential for improving uranium recovery from low-grade uranium ores.

Keywords: Bioleaching of uranium; Ultraviolet irradiation; Low-grade uranium ore; Acidithiobacillus ferrooxidans.

1. Introduction

In order to meet the demand, modern techniques are being developed for the recovery of uranium on a commercial scale from low grade ores. Presently, bioleaching is the leading mineral- processing technique where metals are dissolved from ores into solution through oxidation and decomposing processes of the ores by microorganisms followed by the extraction of these metals from the solution [1]. Bacteria oxidation has several advantages of low cost, low energy consumption and environmental protection, which shows the broad prospects for development on the treatment of low-grade uranium ores by microorganisms [2]. It is widely accepted that certain microorganisms play a major role in the leaching of basal and precious metals from various mineral resources, especially sulfide minerals [3].

At present, At. f as a kind of inorganic chemosynthetic autotrophic bacteria, is one of the mostly applied microorganisms in biological oxidation and recognized as a dominant strain to leach ores in acidic environments [4]. In addition, oxidation of ferrous ion into ferric is one of the characteristic property of At. f. The ferric ion acts as an electron acceptor and converts U^{+4} to U^{+6} states which are soluble in water, hence the metal is leached out to the liquor solution [5]:

$$UO_2 + Fe_2SO_4 \longrightarrow UO_2SO_4 + 2FeSO_4$$

Leaching reactions catalyzed by these bacteria, however, are relatively inefficient because of their slow growth rate and inhibition of iron oxidation by ferric iron [6]. As a result, such drawbacks boost demands for the improvement of leaching bacteria.

Mutation breeding is a frequently-used and effective method of obtaining excellent leaching microorganism. Therefore, mutation breeding has become the most popular method for enhancing bioleaching activity of strains. Induced UV mutation is the simplest and the most effective physical mutation method. Also, the effective UV wavelength is mainly around 255 nm which is the same with the DNA absorption spectrum of general bacteria. Hence, UV mutation has a strong bactericidal effect [7]. However, UV is the most common physical mutagen factor, excessive UV irradiation can cause loss of a large segment of DNA cells or can make the cross linked DNA unopened and prevent replication and transcription of DNA. As a result, excessive UV can induce cell death. So, there is an important issue that the amount of mutagen can influence the bacteria lethality directly, for instance large amounts of mutagen cause high lethality (about 90–99%). [8].

In this study, for the first time, At. f was processed by UV physical mutation method, to investigate the effects of mutation on the bacterial activity and process of uranium bioleaching.

2. Materials and Methods

2.1. Microbial Strain and Culture Conditions

Isolated At. f from Ramsar of Iran was grown in 9K medium (containing the following reagents: $(NH_4)_2SO_4$ 3 g/L, KCl 0.1 g/L, K_2HPO_4 0.5 g/L, $MgSO_4 \cdot 7H_2O$ 0.5 g/L, $Ca(NO_3)_2$ 0.01 g/L and $FeSO_4 \cdot 7H_2O$ 20g/L) [9]. In followings, bacteria were inoculated in 500 mL flasks containing 250 mL 9K medium with pH=2 and 10% of inoculums. Flasks were incubated at 30℃ in a rotary shaker at 180 rpm until the bacteria reached at logarithmic phase (48 h).

2.2. UV Mutation

Cultured At. f at logarithmic phase collected by filtering and the density of cells was adjusted to the concentration of 1.6×10^8 cell/mL for mutation. 10 mL of filtered culture in the logarithmic phase was transferred to the plates. The cultures were radiated by UV and stirred with bent rod. A distance of 30 cm was kept between the plates and UV light (15W). The UV wavelength was 253.7 Å and the radiation times were 60, 120 and 180s. After mutation, the samples were kept away from light and stored in the refrigerator at 4 °C for 12 h to prevent the bacteria from recovery with light [10]. Then, the mutant bacteria were cultivated in 9K liquid medium with 2.5% (w/v) uranium ore powder. In following, the effectiveness of the positive mutation in At. f was determined by Eh value and uranium extraction rates at 24 h intervals.

2.3. Bioleaching Experiments

Bioleaching experiments were carried out in 2L flasks containing 900 mL 9K liquid medium (pH = 2) with 2.5% (w/v) pulp density of uranium ore powder and 10 % of inoculums (original and mutated bacteria) incubated under shaking (150 rpm) at 35℃ for 6 days. Eh (redox potential) values and uranium concentrations in the leaching solutions were determined at 24 h intervals. The loss of water due to evaporation was compensated by water with pH =2, in order to maintain the 1L solution in the flasks.

2.4. Analysis

The uranium concentrations were analyzed by ICP method. Also, the Eh of cultures was measured with an Eh meter (Metrohm, model 827).

2.5. Statistical Analysis

Data are presented as means ± Standard Error of Mean (SEM). The results were subjected to one-way ANOVA followed by Tukey's HSD using SPSS (version 22) software. Significant levels were defined as $P<0.05$.

3. Results

3.1. Evolution of Eh by Bacteria with Different Mutation Times

The oxidative activity of mutated At. f and original bacterium calculated via the measurement of Eh in 24 h intervals for 6 days, are shown in Fig. 1. The results show that the oxidation activities of mutated bacteria were better than the original bacteria with the optimum UV radiating time at 60s ($p<0.05$). After mutation via UV (60, 120 and 180s), the Eh of bacterial cells reached to 585, 579 and 577 mV respectively, that increased by 1.31, 1.30 and 1.29 times, as compared with the original culture which was 445 mV after 3 days (Fig. 1).

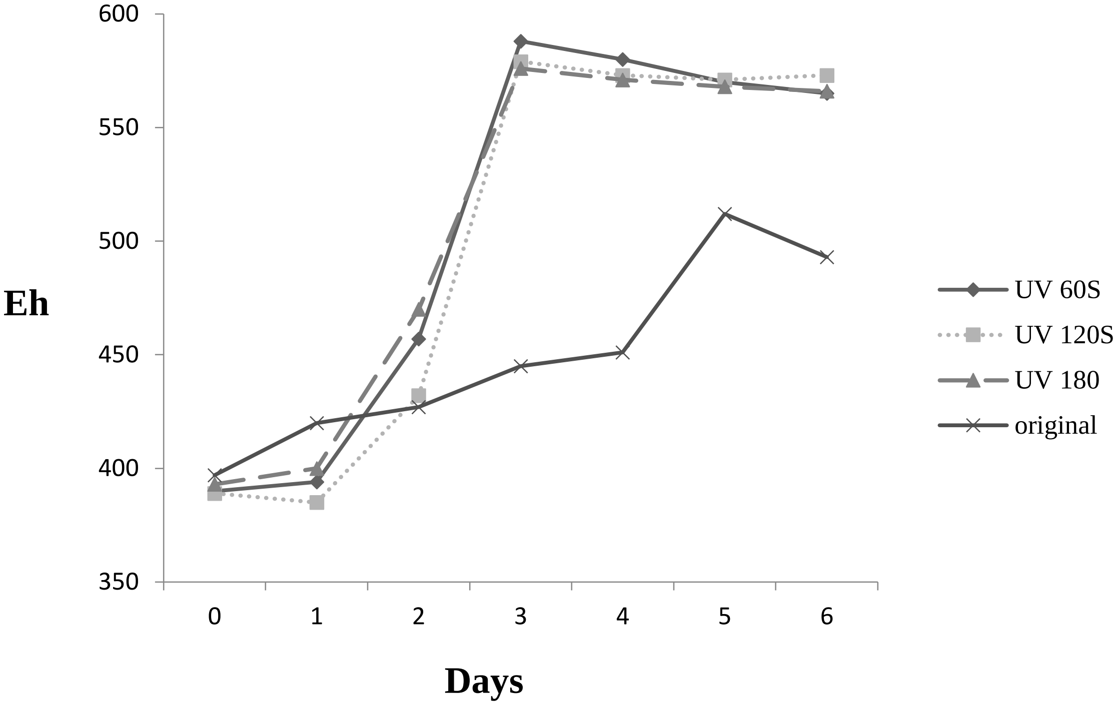

Fig. 1. Comparison of Eh value between induced At. f by UV (60,120,180s) and original bacteria.

3.2. Leaching Experiment by Mutant Strain

At. f after mutation by UV 60, 120 and 180s and also the original bacteria were used for bioleaching of uranium ore. The results of bioleaching experiments indicated that all of the mutated cultures achieve higher levels of uranium leaching yields rather than cultures without mutation ($p<0.05$). The uranium leaching rates with induced bacteria by UV (60, 120 and 180s) and original bacteria reached to 100, 96.36, 93.63 and 65.45%, respectively at 3 days (Fig. 2). It is deduced that all the mutated bacteria could improve uranium extraction as following: UV 60> UV 120> UV 180s ($p<0.05$).

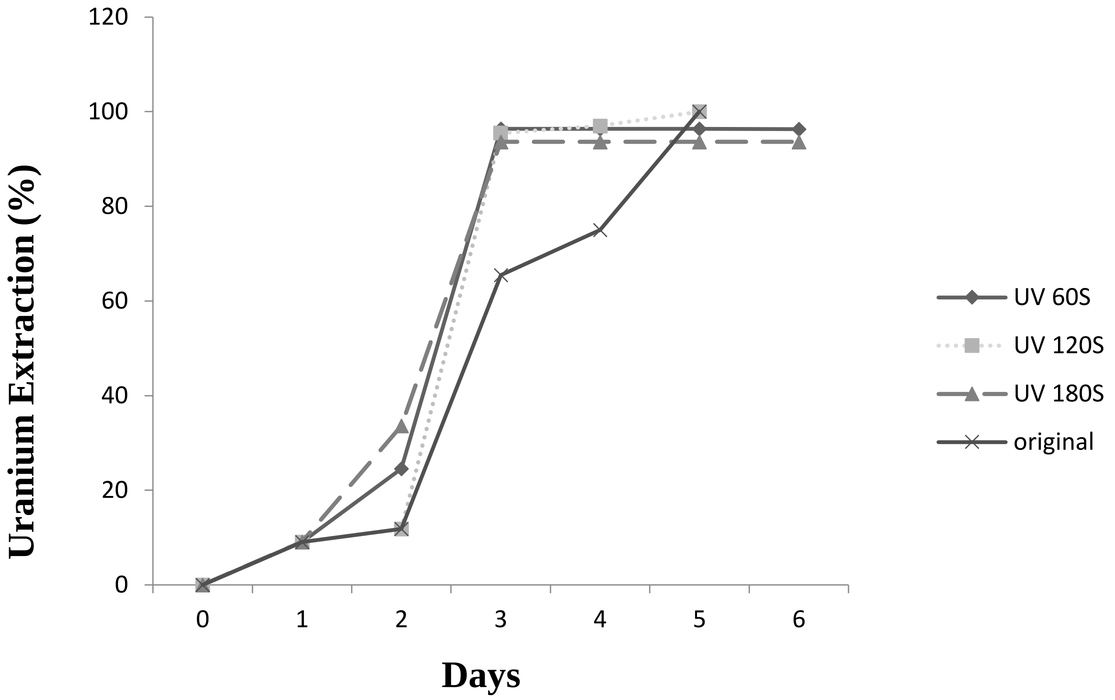

Fig. 2. Comparison of uranium extraction between induced At. f by UV (60, 120,180s) and original strain.

4. Discussion

This study indicated that the mutation could improve bacterial oxidative activity (Fe^{3+} production) which caused more extraction of uranium (Fig. 1&2). Leaching of uranium-bearing minerals is accomplished by oxidation of the insoluble U^{4+} form to the acid soluble U^{6+} form in an acid environment. The indirect mechanism by using ferric (Fe^{3+}) ions as an oxidant is proposed for the uranium bioleach process [13, 14]. In another words, the change of $[Fe^{3+}]/[Fe^{2+}]$ or the concentration of Fe^{3+} in the medium reflects the change of Eh. Furthermore, the oxidation of Fe^{2+} can provide the necessary energy for bacterial growth, so the concentration of Fe^{3+} and Eh in solution simultaneously increases gradually [7] which lead to uranium extraction. On the other hand, the increasing of Eh value (Fig. 1) may be caused by changing the structure of bacterial DNA induced by mutation. Even though, the energy of UV is very weak and the penetrability of UV cannot cause ionization, but, the UV can change the structure of DNA [11]. The main effect of UV mutation is to format thymine dimmers that change the biological activity of DNA and cause bacterial mutation [12] which may be leaded to Eh increasing resulted to more uranium extraction (Fig 1&2). Also, to confirm our results, it was documented [15] that during the whole bioleaching process, the extraction of arsenic by mutant bacteria, which used UV irradiation, was always higher than compare with the original bacteria.

5. Conclusion

In conclusion, the original bacteria after mutation processed by UV irradiation, had improved uranium extraction rate. The results prove that the optimal radiation time of UV to mutate At. f was 60s. Also, the bioleaching results showed that the mutant bacteria could increase the extraction of uranium significantly and could shorten the leaching time.

References

[1]- Xue-ling W., Guan-zhou Q. and Jian G., 2007, Mutagenic breeding of silver-resistant Acidithiobacillus ferrooxidansand exploration of resistant mechanism, Transactions of Nonferrous Metals Society of China, vol.17, pp 412-417.

[2]- Cui R.C., Yang. H.Y., Chen S., Zhang S. and Li. K.F., 2010, Valence variation of arsenic in bioleaching process of arsenic-bearing gold ore, Transactions of Nonferrous Metals Society of China, vol. 20, pp1171-1176.

[3]- Jian k., Guan-zhou Q. and Jian G., 2009, Bioleaching of chalcocite by mixed microorganisms subjected to mutation, J. Cent. South Univ. Technol, vol.16, pp 218−222.

[4]- Gleisner M., Herbert. R.B. and Kockump. C.F., 2006, Pyrite oxidation by Acidithiobacillus ferrooxidans at various concentrations of dissolved oxygen. Chemical Geology, vol. 225, pp 16−29.

[5]- Pal S., Pradhan D. and Das T., 2002, Bioleaching of low-grade uranium ore using Acidithiobacillus ferrooxidans, Indian journal of Microbiology. vol. 50, pp 70-75.

[6]- Kulpa C.F., Roskey M and Mjol I., 1986, Construction of genomic libraries and induction of iron oxidation in Thiobacillus ferrooxidans, Biotechnol Appl Biochem, vol.8, pp 330-341.

[7]- Dong Y., Lin H., Wang H. and Mo X., 2011, Effects of ultraviolet irradiation on bacteria mutation and bioleaching of low-grade copper tailings, Minerals Engineering, vol. 24, pp 870–875.

[8]- Beggs C.B.A., 2002, quantitative method for evaluating the photo reactivation of ultraviolet damaged microorganisms, Photochemistry and Photo Biology Science, vol. 1, pp 431–437.

[9]- Silverman M.P. and Lundgren D.G.,1959, Studies on the chemoautotrophic iron bacterium ferrobacillus ferrooxidans I, An improved medium and a harvesting procedure for securing high cell yields, Journal of Bacteriology, vol. 77, pp 642–647.

[10]- Yuan X., Xie X. and Fan F., 2013, Effects of mutation on a new strain leptospirillumferriphilumyxw and bioleaching of gold ore. Trans. Nonferrous Met. Soc, vol. 23, pp 2751−2758.

[11]- Pullman A. and Pullman B., 1963, On the mechanism of ultraviolet-induced mutations. Biochimica et Biophysica Acta, vol. 75, pp 269–271.

[12]- Yang Y., Zhang S., Xu A.L., Zou L.H., Li L. and Qiu G.Z., 2010 UV-induced mutagenesis and bioleaching of Acidiphilium cryptum and Acidithiobacillus ferrooxidans, Journal of Central South University (Science and Technology), vol. 41 (2), pp 393–399.

[13]- Abhilash S., Mehta K.D., Kumar., Pandey D.B. and Tamrakar K.P., 2011, Bioleaching – An alternate uranium ore processing technology for India, Energy Procedia, vol.7, pp 158–162.

[14]- Lottering J.M., Lorenzen L., Phala S.N., Smit T.J. and Schakwyk C.A.G., 2008, Mineralogy and uranium leaching response of low grade South African ores, Minerals Engineering, vol. 21, pp 16–22.

[15]- Xuehui X., Xuewu Y., Na L., Xiaoguang C,, Awad A and Jianshe L., 2013, Bioleaching of Arsenic-Rich Gold Concentrates by Bacterial Flora before and after Mutation, Hindawi Publishing Corporation, Vol.20, Article ID 969135.

DEVELOPMENT OF A THERMAL KINETIC DEGRADATION MODEL FOR LINEAR LOW DENSITY POLYETHYLENE (LLDPE) BLENDS WITH POLYSTARCH-N (PSN)

F.A. Al-TURKI, S.M. Al-SALEM, A. BUMAJDAD, A.R. KHAN

F.A. Al-Turki, Ms., College of Graduate Studies, Kuwait University, S. M. Al-Salem, Dr., Environment and Life Sciences Research Centre, Kuwait Institute for Scientific Research, A. Bumajdad, Prof., Department of Chemistry, Faculty of Science, Kuwait University, A.R. Khan, Dr., Environment and Life Sciences Research Centre, Kuwait Institute for Scientific Research.

Abstract

Compounded blends of linear low density polyethylene (LLDPE) with polystarch-N (PSN) were subjected to thermogravimetry (TGA) using five different heating rates (β=5, 10, 15, 20 and 25 °C min^{-1}), in order to study their thermal degradation kinetics. A pyrolysis setup was used in the experiments with a nitrogen (N_2) jacket in a constant flow of 50 ml min^{-1}. Results were compared with virgin LLDPE, in order to study the difference in the degradation behaviour of the blends simulating biodegradable compounds used in polymeric products. An analytical solution approach was used in developing a novel mathematical model for the blends degradation dependant on the inflection point (T_{if}) of the two stages of PSN and LLDPE degradation in the TGA curves. The kinetic parameters obtained, i.e. pre-exponential factor (A_o) and apparent activation energy (E_a), were compared with those of the virgin LLDPE. The degradation reaction was assumed to be of nth order. Multi variable non-linear optimisation was used in this work. The objective function set in the analytical solution had three variables: the pre-exponential factor (A_o), apparent energy of activation (E_a) and reaction order (n); which were optimized to match experimental weight fractions as function of time and temperature based on the pre-set constant heating rate (β) with the model computed values. Results of the blends studied (20 and 40 wt% PSN) were comparable to each other, in terms of kinetic parameters showing a PSN and LLDPE reaction orders between 1 and 2, respectively, in line with expectations of virgin material behaviour and ready-made biodegradable product with additives (i.e. PSN). The E_a for both stages of the blends were estimated between 150 and 200 kJ mol^{-1}, compared with an average of some 220 kJ mol^{-1} for LLDPE.It can be concluded that degradation of biopolymers in blends is best described in sequential degradation mechanisms rather than isocoversion kinetics or integral solution results which were used to estimate single rate kinetic parameters. Amount of PSN in the blends did not show impact on kinetic results indicating that rate of degradation and mechanisms is independent of starch content in the LLDPE blend. Results of this work can point towards developing green industrial practices for thermo-chemical reactor design based on degradation kinetic work conducted.

Keywords: Degradation Kinetics, TGA, Polymer, Starch, LLDPE, Blends.

Introduction

Plastics production has increased by an estimated 3.9% from the year 2012 to almost 299 mtpa in 2013 [1]. From the year 1950 to 2012, plastic production has increased on average by 8.7% per year [1]. This could be justified due to the versatility plastics, consequently polymers, have when compared to metals and wood. The continuous production of plastics threatens the natural resources, e.g. coal, oil and natural gases. Furthermore, it could lead to the accumulation of plastic solid waste (PSW) due to high consumption rates. PSW poses concerns on state level in the state of Kuwait. This is related to the practice of landfilling, which is considered to be the standard method of disposal in the country for solid waste.

---

*Corresponding Author: Dr. Sultan Al-Salem, Environment and Life Sciences Research Centre, Kuwait Institute for Scientific Research, P.O. Box: 24885, Safat 13109, Kuwait. Tel:+965-2495-6877, Fax: +965-2398-7673,
Email: ssalem@kisr.edu.kw.

Packaging is the major sector for plastics uses [2-4] and biodegradable bags have been offered as a practical solution in the area. Thermo-chemical treatment (TCT) is one of the best process for polymers treatment and energy recovery. Pyrolysis, gasification and hydrogenation are all included under TCT, which is qualified for energy rehabilitation and products recovery such as gases, tars and char [5]. Fig.1. illustrates different thermolysis schemes with reference to the main technologies falling under TCT applied technologies [6]. Nonetheless, to understand the impact and efficiency of TCT methods of different polymeric fractions, the degradation kinetics have to be established for the materials intended to be treated. In this case, biodegradable polymers have been chosen to thermally characterize and establish its kinetics. This is done to enable the determination of the optimal degradation kinetics of such materials, in order to, develop and design optimal engineering units in the future that can treat such polymers. To the best of our knowledge, no attempt has been conducted in the past for studying the thermal degradation of biodegradable polymers and establishing its kinetics.

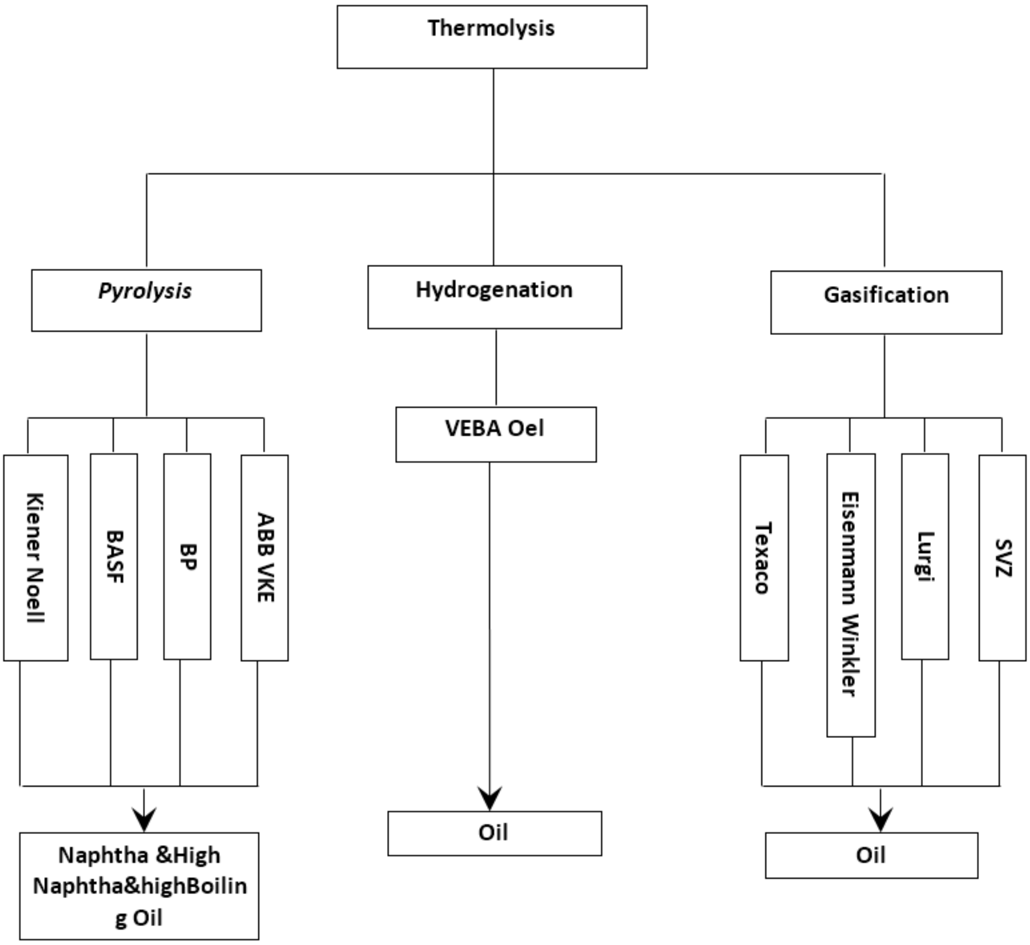

Fig.1. Different thermolysis schemes with reference to the main technologies [6].

Experimental procedure

Materials

Virgin linear low density polyethylene (vLLDPE) film extrusion grade donated by a local supplier in pellets form (3 mm) with a melting point (T_m) of 124°C, melt flow index (MFI) of 2 g/10 min and a density of 0.918 g/cm^3, was used. Flakes of Polystarch-N (PSN) were purchased from Willow Ridge Plastics (USA) with masterbatch properties as follows: T_m =110°C, MFI =10 g/10 min and a density =1.17 g/cm^3. PSN contained 0.5 wt% of starch as per suppliers materials safety data sheet (MSDS).

LLDPE/PSN compounding

A Collin Tech single screw extruder (D = 26 mm, L/D = 32) was used for compounding the samples. The LLDPE/PSN dry blends were processed under 30 bar pressure with a rotational speed of 800 rpm. Zone temperatures were maintained between 155 to 165°C, with a die head temperature of 165°C. Two dry blends (i.e. without chemical additives) were prepared containing 20% and 40% by weight of PSN, respectively. Extruded strands were pelletized using a Collin Tech Line pelletizer(CSG 171T) to approximately 3 mm pellets for further testing. All samples were stored in laboratory conditions at 23°C/50% relative humidity in the dark between sample formulation and testing.

Thermogravimetric analysis (TGA)

Thermogravimetry in non-isothermal (dynamic) setup was performed for the LLDPE and LLDPE/PSN blends in a Shimazdu model (DTG-60) thermogravimetric analyzer (TGA) coupled with data acquisition software (TA analysis 1.51). Weight loss and weight derivative against temperature curves were recorded. Samples were heated from room temperature (25°C) to 800°C. Five heating rates (β) were used in conducting the experiments as follows: 5, 10, 15, 20 and 25°C/min. The ICTAC recommendations were followed in performing the experiments [7]. A constant flow of dry nitrogen with a flow rate of 50 ml/min was maintained throughout using 7-8 mg samples. Duplicate experiments were performed showing high repeatability.

Development of analytical solution

An analytical solution was developed in this work for the purpose of evaluating the kinetic parameters of the thermal degradation reaction of the LLDPE and PSN blends. Rearranging the decay expression of kinetics previously explained in Al-Salem and Khan [6] results in the following expression for a known reaction time (t, min):

$$\frac{dx_P}{x_p^n} = -k\,dt \qquad (1)$$

The degradation reaction is assumed to be of n^th order and both sides of Eq.(1) are integrated for time equals to zero (i.e. for a polymer fraction (x_p) equal to 1) to time equals to (t) assumed to be the end of the experimental run, as the real integral limits results in the following expression:

$$\frac{x^{-n+1}}{-n+1} = -k\,t \qquad (2)$$

Substituting k with the Arrhenius expression shown in Eq.(2) and rearranging the denominator results in Eq.(3).

$$x = \left((n-1)A\exp(-E/RT)t+1\right)^{(-1/(n-1))} \qquad (3)$$

In mathematical terms, the optimisation problem is posed as follows:

$$\text{Objective Function (O.F.)} = \min\sum_{i=1}^{N}\left|\frac{x_{P(\text{exp})} - x_{P(\text{th})}}{x_{P(\text{exp})}}\right| \qquad (4)$$

Where N is the number of time steps for the model solution. The O.F. is the summation of the expression in Eq.(4) where $x_{p(exp)}$ and $x_{p(th)}$ are the experimental values and model values corresponding to the solution at each given time subject to the following constraints:

$$E_a \geq 0 \qquad (5)$$

$$t_o = 0 \qquad (6)$$

$$x_p(t_o) = 1 \qquad (7)$$

The objective function has three variables: the pre-exponential factor (A_o), apparent energy of activation (E_a) and reaction order (n); which are optimized to match experimental weight fraction as a function of time and temperature based on pre-set constant heating rate (β) with model computed values. Multi variable non-linear optimisation was used to solve the problem.

Results and discussion

In this study, various dynamic pyrolytic degradation TG curves have been modelled (i.e. Figure 2) for the five different heating rates (β) used comparing with the experimental TG curves of vLLDPE, blend with PSN (20 wt% and 40wt%, respectovley). Figure 3.a depicts experimental data for PSN20/80 for all successive rates and Figure 3.b reflects corresponding model results for all heating rates. It was observed that with the increase of PSN fraction in blends, the TG curve showed a shift to lower value in the degradation temperature. The pure LLDPE, 20/80 and 40/60 (wt% PSN/wt% LLDPE) blends began decomposing at nearly 415°C, 291°C and almost 267°C respectively. The apparent activation energies (E_a) estimated are reported in Tables 1-2 1 and 2 for PSN20% and LLDPE, respectively.

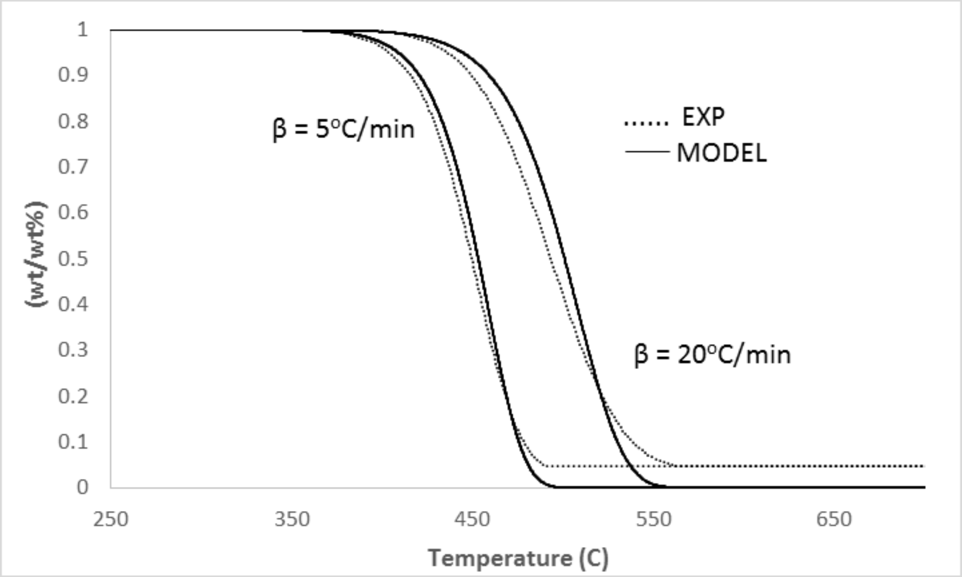

Fig.2. Model vs experimental results for LLDPE at β = 5 and 20 °C/min.

Fig.3.(a) Experimental results for PSN20% showing at different heating rates (β). (b) Model results for PSN20% showing at different heating rates (β).

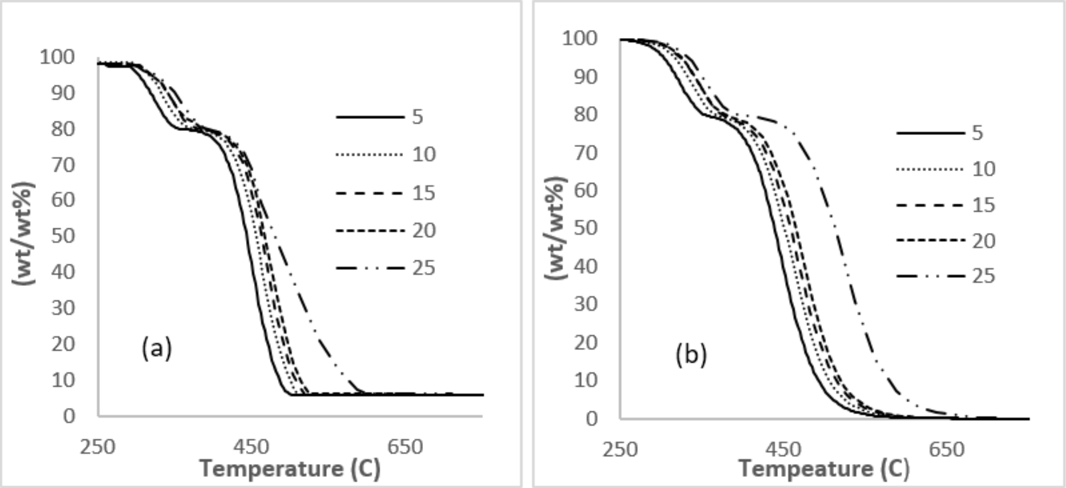

	PSN (20/80) (wt/wt%)				
	Ea_1 (kJ/mol)	Ea_2 (kJ/mol)	A_1 (min^{-1})	A_2 (min^{-1})	r^2
β = 5 °C/min	150	200	$1.96x10^{11}$	$3.27\ x10^{12}$	0.9991
β = 10 °C/min	150	200	$1.91\ x10^{11}$	$3.72\ x10^{12}$	0.9988
β = 15 °C/min	150	200	$1.89\ x10^{11}$	$4.01\ x10^{12}$	0.9988
β = 20 °C/min	150	200	$4.58\ x10^{11}$	$8.21\ x10^{12}$	0.9988
β = 25 °C/min	150	200	$1.93\ x10^{11}$	$6.04\ x10^{11}$	0.9928

Table 1. Apparent activation energy for PSN20% (Ea_1 and Ea_2), pre-exponential factors (A_1 and A_2) and regression coefficient (r^2) between experimental and theoretical fits.

	LLDPE (wt/wt%)		
	Ea (kJ/mol)	A (min^{-1})	r^2
β = 5 °C/min	232.44	6.97 x10^{12}	0.9993
β = 10 °C/min	221.13	9.02 x10^{11}	0.9987
β = 15 °C/min	213.11	2.41 x10^{11}	0.9995
β = 20 °C/min	202.98	2.43 x10^{10}	0.9979
β = 25 °C/min	189.82	1.76 x10^{9}	0.9963

Table 2. Apparent activation energy for LLDPE (Ea), pre-exponential factors (A) and regression coefficient (r^2) between experimental and theoretical fits.

There was a common trend observed where the higher the heating rate (β), the lower the activation energy (E_a) for LLDPE polymer (Table 2). This could be attributed to pyrolytic reaction occurring at elevated temperatures with shorter time, plummeting the energy required for the degradation of the materials [8]. As past studies confirmed the effect of heating rate on apparent activation energy [9-10]. By using the comparison between the model and experimental results, theoretical curves are plotted (i.e. Fig.2. shows the LLDPE TG experimental curve for two heating rates, 5°C/min and 20°C/min with model results). It was also observed by the regression coefficients at all heating rates as mentioned in Table 1 and 2 that the theoretical data were in close proximity to the experimental data points. Energy of activation for PSN20% and 40% are less than LLDPE as shown in the tables. For the all polymeric materials, the thermal degradation reactions are endothermic in nature, where the lower energy of activation occurred with the lower melting polymers, and vice versa. Temperature inflection point (T_{if}) is a point on a TG curve at which the slope (rate of degradation) reaches to maximum and then decreases to negligible rate. For LLDPE, T_{if} is at 453°C, PSN20% is at 316°C for the first stage and 525°C for the second stage, and it is at 321°C and 457°C for PSN40%. It was noted that T_{if} for LLDPE>PSN20%>PSN40%. It is also worth noting that the degradation effect was modelled and consequently mathematically represented optimally through the two stage model presented in this communication, in a more efficient manner than past published models established in literature. This could be attributed to the nature of polymeric blends, and the way interactions occur in the polymer matrix, making it a complex process to be represented via past models that rely upon iso-conversion kinetics or classical integral solutions. The experimental results also depicted the loss of moisture clearly at first stages, due to water absorption from the atmosphere by the starch content in the polymeric blend. Such an effect could be considered in mathematical terms in future work. However, the efficiency of the model established here was with acceptable engineering solution limits of ±5%.

Conclusions

A general mathematical expression based of the integral solution developed by utilizing thermogravimetric analysis (TGA) in inert atmosphere for biodegradable polymer blends in comparison to a commercial grade virgin one (LLDPE). The experimental data fitted the model very well depicting the true pyrolytic reaction behaviour, indicating clearly the degradation mechanism as the two stage decay are shown. As the heating rate increased, the activation energy decreases, reflecting the progression of the reaction. LLDPE activation energy was higher than the PSN blends at all studied heating rates. The degradation of the PSN blends started at lower temperatures then the blends with higher fraction of LLDPE, 40 wt% of PSN, which has resulted in the lowest energy of activation estimated.

Acknowledgments

The authors would like to acknowledge the support of Kuwait University (KU) to Ms. F.A Al-Turki in her MSc thesis project with grant no. PSPU GS 01/01. Ms. F. Jassem of the Kuwait Institute for Scientific Research (KISR) is gratefully acknowledged for supplying test specimens used in this work.

References

Gourmelon, G. (2015). Global Plastic Production Rises, Recycling Lags | Vital Signs Online. [online] Vitalsigns.worldwatch.org. Available at: http://vitalsigns.worldwatch.org/vs-trend/global-plastic-production-rises-recycling-lags

USEPA, 2002. Municipal Solid Waste in the United States: 2000 Facts and Figures. Executive summary. United States Environmental Protection Agency, Office of solid waste management and emergency response (5305W), EPA530-S-02-001, June.

USEPA, 2008. Municipal Solid Waste in the United States: 2007 Facts and Figures. Executive summary, United States Environmental Protection Agency, Office of solid waste management and emergency response (5306P), EPA530-R-08-010, November.

Waste Watch, 2003. Plastics in the UK economy: A guide to polymer use and the opportunities for recycling. Final report of the Program of sustainable use (UK); Waste Watch group.

Al-Meshan, A.M. and Mahros, F., 2001. Recycling of Municipal Solid Waste in the State of Kuwait. Arabian J Sci Eng, 26(2C): 3-10.

Al-Salem, S., Lettieri, P. and Baeyens, J. 2009. Recycling and recovery routes of plastic solid waste (PSW): A review. Waste Management, 29(10), pp.2632

Sergey Vyazovkin , Alan K. Burnham ,José M. Criado , Luis A. Pérez-Maqueda , Crisan Popescu , Nicolas Sbirrazzuoli, 2011. ICTAC Kinetics Committee recommendations for performing kinetic computations on thermal analysis data. pp.5.

Al-Salem, S.M., Khan, A.R, 2014. On the degradation kinetics of poly(ethylene terephthalate) (PET)/poly(methyl methacrylate) (PMMA) blends in dynamic thermogravimetry. Polymer degredation & stability 104:28-32.

Holland BJ, Hay JN. 2002. The value and limitations of non-isothermal kinetics in the study of polymer degradation. Thermochim Acta 2002; 388:253-73.

Motaung TE, Luyt AS, Saladino ML, Martino DC, Caponetti E. 2012. Morphology, mechanical properties and thermal degradation kinetics of PMMA-zirconia nanocomposites prepared by melt compounding. Express Polym Lett 2012; 6:871-81.

SUSTAINABILITY ASSESSMENT OF RICINUS COMMUNIS BIODIESEL USING LCA APPROACH

MOHAMMED AMOURI, TOUDERT AHMED ZAID, MAJDA AZIZA

Abstract

The actual energy consumption, production and industrial growth is not sustainable because fossil carbon is finite and not renewable. Developing a sustainable bio-based economy that uses eco-efficient bioprocesses and renewable bioresources is one of the key strategic challenges. As one of the biofuels policy goals is a sustainable production and use of bioenergy crops, all potential feedstock need to be assessed for their effectiveness to achieve this goal, and this assessment is to be made part of the sustainability standards for bioenergy feedstock crops. Biofuels are eco-friendly fuels and their utilization would contribute address global concerns about containment of carbon emissions and to promote the rural region development particularly in developing countries. In this context, the life cycle assessment (LCA) is a tool that can be used effectively in evaluating various renewable energy sources for their sustainability and can help policy makers choose the best energy source for specific purpose.

In this study, we have studied the life cycle sustainability of second generation biodiesel derived from Ricinus communis feedstock. The lifecycle of Castor bean based biodiesel production includes the stages of cultivation, oil extraction, biodiesel production. The functional unit of this study was 1 ton of biodiesel production and the impact categories studied were global warming, energy balance, human health and ecosystem quality. We have used the impact 2000+ as evaluation method.

Our results obtained from this study show that the use of Ricinus communis as feedstock for biodiesel production is a very promising alternative. This life cycle analysis study revealed that the use of castor for biodiesel production could have many advantages as a positive net energy value and a net energy ratio (NER) of 2.45. Moreover, Life cycle assessment of biodiesel derived from castor oil shows a positive contribution to climate change reduction revealed by a positive carbon balance.

The results obtained from the analysis of the whole production system revealed that among all the stages, the cultivation process of Ricinus communis is the largest contributors to most of environmental impact categories. It contribute for 47.1% for ecosystem quality, 83.1% for human health, 48.2% for climate change and 39.9% for resources consumption.

These results suggest the enhanced usage of this renewable feedstock in future with inclusion of further technological improvement in farming practices and production process.

A USE OF ACTIVATED CARBON DEVOLOPPED FROM JUJUBE STONE FOR THE REMOVAL OF A LEAD FROM AQUEOUS SOLUTIONS BY SORPTION

NESMA BOUCHELKIA, LOTFI MOUNI , LAZHAR BELKHIRI , ABDELKRIM BOUZAZA

[a] Laboratoire de Gestion et Valorisation des Ressources Naturelles et Assurance Qualité. Faculté SNVST, Université Akli Mohand Oulhadj, Bouira 10000, Algerie.
[b]Département d'Hydraulique, Université de Batna, 05000, Algerie
[c] Laboratoire Sciences Chimiques de Rennes – Equipe Chimie et Ingénierie des Procédés, UMR 6226 CNRS, ENSCR, Avenue du Général Leclerc, 35700 Rennes, France.
*Corresponding author. E-mail address: lotfimouni@gmail.com
Tel: +213559829379

Abstract

The preparation of activated carbon from Jujube stone with H_2SO4 activation and its ability to remove lead from aqueous solutions were reported in this study. The performance of the activated carbon was characterized by N_2 adsorption–desorption isotherms, Brunauer–Emmett–Teller equation, scanning electron microscopy, Fourier transform infrared analysis (FTR), X-ray diffraction (XRD) and scanning electron microscopy (SEM) in ordre to determine the surface morphology of prepared ACJJ. Adsorption studies were carried out by varying the initial metal ion and the pH. The amount of Pb (II) ions adsorbed increased with increasing pH and initial Pb (II) ions concentration. The removal of lead ions was quick and the kinetic adsorption can be well described by pseudo-second-order model. The Langmuir model fit the data better than the other models used in this study and the monolayer adsorption capacity of Pb (II) ions was determined as 71.43 mg g^{-1} pH 6.0. Thermodynamic parameters, such as standard Gibbs free energy (ΔG°), standard enthalpy (ΔH°) and standard entropy (ΔS°) were calculated. The adsorption of Pb onto ACJJ was found to be spontaneous and exothermic in nature.

Keywords: Sorption, lead, Jujube stone, Chemical activation, Isotherms, Kinetics

Introduction

Removal of heavy metals from waste water by adsorption process is a very common.Although activated carbon is a preferred adsorbent, its application is often restricted due to its high cost. Thus, there is a growing demand to find low-costand efficient, locally available adsorbent for the adsorption of lead such as activated carbon prepared by apricot stone[4], date stone [5], pine bark [6], wheat bran [7], tobacco stems [8], sago waste [9]. While several researchers have adopted various low-cost adsorbents,there is still a need to develop activated carbon from cheaper and readily available materials, which can be effective and economical for the removal of heavy metals from aqueous solutions.Activated carbon production from agricultural waste has two advantages. First, waste material is converted to useful, value-added adsorbents. Disposal of agricultural by-products has become a major, costly waste disposal problem. Second, produced activated carbons are used for removing organic chemicals and metals from waste water. Basically, there are two different processes for the preparation of activated carbon: physical activation and chemical activation. In comparison with physical activation, there are two important advantages of chemical activation. One is the lower temperature in which the process is accomplished. The other is that the global yield of the chemical activation tends to be greater since burn-off char is not required.

The aim of this study was to investigate the application of activated carbon prepared from the Jujube stone for the removal of lead from aqueous solutions. This tree is widely distributed in deciduous forests of center Algeria. The products were characterized by N_2 adsorption, scanning electron microscopy (SEM), fourier transform infrared spectroscopy (FT-IR).There is no information in the literature on the use of Jujube as adsorbent. In this work, the kinetics of sorption for the use of Jujube as sorbent for lead ion removal from solution is investigated. In addition, pseudo-isotherms were also presented for the sorption system.

2. Materials and methods

2.1. Preparation of activated carbon

Jujube stone was used in this study a source of activated carbon, collected from Bouira, Algeria. It was harvested between September and December. Hundred grams of the selected fraction was impregnated with concentrated H_2SO_4. Then it was activated in a hot air oven at 600 °C for 02 h.

2.2. Batch adsorption experiments

Stock solution of Pb(II) ions (1000 mg/L) was prepared by dissolving the analytical reagent grade lead nitrate (Plasma Pure Standard Solutions, Leeman Labs) in deionized water. The stock solution was further diluted to the required concentrations before used. A known weight of activated carbon is left in contact with 100 mL of each solution (10, 20, 30, 50, 70, 90 mg/L) during 2 h. The initial solution pH was adjusted to 6.0 with HNO_3. Small volume liquid samples are withdrawn at different time intervals and immediately filtered to remove adsorbent particles.The concentrations of Pb(II) ions were measured by atomic adsorption spectrometer (Shimadzu AA6500). Amount of Pb(II) ions adsorbed at equilibrium was calculated using the following equation:

$$qe = \frac{(C0 - Ce) \times V}{m} \qquad (1)$$

where q_e($mg.g^{-1}$) is the equilibrium adsorption capacity of lead adsorbed per gram of the ACJJ,C_0 and Ce are the initial lead concentration (mg L^{-1}) and lead concentration (mg L^{-1}) at equilibrium, respectively; V is the volume of the lead solution (L); and m is the weight of the ACJJ (g). The sorption percentage (% removal) of metal ions from aqueous solution is calculated as follows

$$\text{Removal \%} = \frac{(C0 - Ce)}{C0} \times 100 \qquad (2)$$

2.3. Sorption kinetic study

The kinetic experiments were performed in 100 mL batch reactors at 25.0 ± 0.5 °C. First, 0.5g of JAC was introduced in 100 mL of deionized water. After the introduction of the metal ions, samples were collected at suitable time intervals, filtered through a 0.45 µm cellulose acetate membrane filter, and then analyzed for lead with an atomic absorption spectrophotometer (Shimadzu AA6500).

3. Results and discussion

3.3. Boehm titration

Parameter	Value
Yeild (%)	52.1
ph_{pzc}	4.68
CEC	2.84
Ash (%)	3.32
Density (g/ml)	1.41
Textural properties	
S_{BET} (m^2/g)	418
Mesopore volume (ml/g)	0.52
Mesopore area (m^2/g)	138.47
Micropore volume (ml/g)	0.21
Surface functional groups (mmol/g)	
Acidic groups	3.12
Carboxylic	1.78
Lactonic	0.94
Phenolic	0.52
Basic groups	1.23
iodine number mgg^{-1}	103

Table 1 summarizes the results of Boehm titration and shows that most of acidic functional groups are carboxylic, followed by lactonic and phenolic. The total number of the surface basic sites was calculated to be 1.23 mmol/g and is smaller than the total number of the acidic surface sites.

Table.1 Physical properties of activated carbon derivedfrom the Jujube stone.

3.1. Effect of pH

pH is an important parameter affecting metal adsorption onto the adsorbent. This is du to the fact that H^+ ions themselves are strongly competing with the adsorbate. Effect of pH was studied by varying the initial pH of solution from 2 to 10. The pH was adjusted by 0.1M NaOH or 0.1M HCl and measured by using a pH meter (Jenway 3010). The adsorbent dosage, rotation speed, solution temperature and initial lead concentration were fixed at 0.5g, 140rpm, 25ºC and 50mg/L respectively. The results indicate that the maximum lead fixed by ACJJ is obtained at pH 6. At low pH values, there is an excessive protonation of the carbon surface resulting in a decrease in the sorption of Pb(II) ions. Fig. 1 shows the pH influence on the sorption. The uptake of Pb(II) increases with increasing pH from 2 to 6, reaches a maximum, and decreases from pH 6.0 to 10.

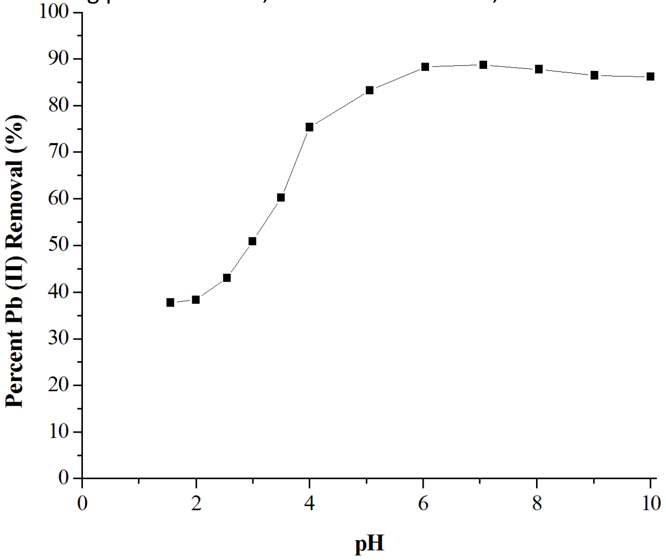

Fig.1. Effect of initial pH on adsorption capacity of lead solution (initial concentration 50 mg/L, contact time 140 min and adsorbent dose 0.5 g/100 mL).

3.2. Effect of contact time

Fig.5 shows that the Pb(II) adsorption approaches to plateau smoothly and continuously, suggesting the monolayer coverage of Pb(II) on the outer surface of the ACJJ [16]. During the initial first 10 min, the adsorption of Pb (II) is fast due to a available vacant surface sites. After a this time (i.e 10 min), the adsorption sites become unavailable and there maining free surface sites are difficult to be occupied due to repulsive forces between the solute molecules on the solid and bulk phases [17].

3.3. Effect of initial concentration

A range of lead concentrations (10–90 mgl^{-1}) (adjusted to pH 7) were used, and the flasks agitated for 140 minutes. A 0.5g sample of ACJJ was added to each 100 ml volume of lead solution and agitated at 140 rpm and the temperature was set at 25°C for all experiments. Samples (10.0 ml) were withdrawn at suitable time interval and the filtrate analysed by atomic absorption spectrophotometry (AAS).The lead adsorption experiments display a direct relationship between the metal uptake and initial concentration of the metal ions present in the solution up to a certain limiting initial concentration and inverse relationship between the removal percentage and initial metal concentration Fig.2. Whereas the latter takes into account the adsorbent dosage and reveals the genuine lead adsorption efficiency of the material at different initial concentrations.

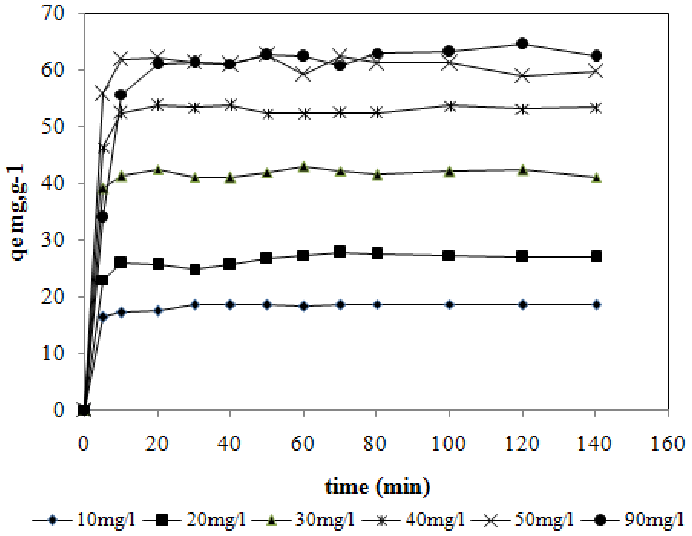

Fig.2. Effect of agitation time and initial concentration of Pb(II) on the sorption of lead by activated carbon. (pH 6.0, adsorbent dose 0.5 g/100mL, contact time 140 rpm and 25 °C).

3.4. Effect of adsorbent dosage

The results of the experiments with varying adsorbent concentrations are presented in Fig. 3. Increase in the adsorbent concentration, from 0.5 to 10 g/l, increases removal of lead(II) ions from 7.16 % to 99.95%. With increasing adsorbent dosage more surface area is available for the adsorption due to increase in active sites on the adsorbent and its availability for adsorption, making easier penetration of ions to the adsorption sites [3]. Thus, optimum dosage of ACJJ for adsorption of lead(II) ions is found to be 5.0 g/l. All active sites on the adsorbent surface are then occupied and increase in adsorbent dosage do not provide higher uptake of lead (II) ions.

3.5. Sorption thermodynamics

Thermodynamic considerations of an adsorption process are necessary to conclude whether the process is spontaneous or not.0.5 g of ACJJ was added to a 100 ml of 50 mgl^{-1}of lead (pH 6.0) stirred at 140 rpm and at temperature 298 K. Samples (10 ml) were withdrawn at suitable time intervals and the filtrate analysed by Atomic Absorption Spectrophotometer (AAS). The experiment was repeated at 303, 308 and 318°K. Thermodynamic behaviour of the sorption of lead on ACJJ is evaluated by the thermodynamic parameters including the change in free energy (ΔG°), enthalpy (ΔH°) and entropy (ΔS°). These parameters are calculated from the following equation [41]:

$\Delta G° = -RT \ln K_D$ (16)

where, R is the universal gas constant (8.314 J mol^{-1}K^{-1}), T istemperature (°K) and K_D is the distribution coefficient for the adsorption calculated from the following equation :

$K_D = C_{ads}/C_e$ (17)

Where C_{ads} is the amount of lead (mg) adsorbed on the adsorbent per litre of the solution at equilibrium and Ce is the equilibrium concentration (mg L^{-1}) of the lead in the solution.The enthalpy (ΔH°) and entropy (ΔS°) parameters are estimated from the following equation:

$\ln K_D = (\Delta S°/R)-(\Delta H°/RT)$ (18)

The constants of thermodynamics as shown in Table 6 (i.e., thechange of enthalpy ΔH°, entropy ΔS° and free energy ΔG°), can be determined from the slope and intercept of the linearization of the test data asshown in Fig..The negative ΔHº value indicates the exothermic nature of the process. Moreover, the negative ΔSº value corresponds to a decrease in the degree of freedom of the adsorbed species [42-44]. A negative ΔG° value confirmed the feasibility of the process and the spontaneous nature of adsorption, which decreased with increasing of temperature, indicating that reducing the temperature was beneficial to theadsorption process.

Table. 2
Predicted thermodynamic constants for lead adsorption on ACJJ.

Metal	ΔH°(kj/molK)	ΔS°(kj/molK)	ΔG°(kj/mol)		
			293	298	303
Pb^{2+}	-3.62	-0.108	-3.61	-2.91	-1.43

4. Conclusion

Jujube stone can be used as a highly suitable raw material with H_2SO_4 used as an activation agent to prepare ACJJ. From the kinetics studies it is observed that adsorption of Pb(II) is very rapid in the initial stage and decreases while approaching equilibrium. The results of this research reveal that the adsorption process is strongly dependent on pH of solution. At the same time, the adsorption kinetics fitting results also show that the reaction process accord with the pseudo-second-order kinetic model well (R^2= 0.9999) and demonstrated that intra-particle diffusion plays a significant role in the adsorption mechanism, which suggests that the main rate determining step was chemisorptions.

References

[1] L.Mouni, D. Merabet, A. Bouzaza, L. Belkhiri, Adsorption of Pb(II) from aqueous solutions using activated carbon developed from Apricot stone, Desalination .276 (2011) 148–153.

[2] R. Ayyappan, A.C.Sophia, K. Swaminathan, S. Sandhy, Removal of Pb(II) from aqueous solution using carbon derived from agricultural wastes. Process Biochem. 40, (2005) 1293–1299.

[3] L.A. Teles de Vasconcelos, C.G. Gonz´ alez Bec¸a, Adsorption equilibria between pine bark and several ions in aqueous solution, 1. Pb(II), Eur.Water Poll. Control 4 (1) (1994) 41–51.

[4] Y. Bulut, Z. Baysal, Removal of Pb(II) from wastewater using wheat bran, J.Environ. Manage. 78 (2006) 107–113.

[5] W. Li, L. Zhang, J. Peng, N. Li, Tobacco stems as a low cost adsorbent for the removal of Pb(II) from wastewater: equilibrium and kinetic studies, Ind. Crops Prod. 28 (2008) 294–302.

[6] S.Y. Quek, D.A.J. Wase, C.F. Forster, The use of sago waste for the sorption of lead and copper, Water SA 24 (1998) 251–256.

[7] A. Mittal, A. Malviya, D. Kaur, J. Mittal, L. Kurup, Studies on the adsorption kinetics and isotherms for the removal and recovery of Methyl Orange from waste waters using waste materials, J. Hazard. Mater. 148 (2007) 229-240.

[8] M.N. Ibrahim, W.S. Ngah, M.S. Norliyana, W.R. Daud, M. Rafatullah, O. Sulaiman, R. Hashim, A novel agricultural waste adsorbent for the removal of lead (II) ions from aqueous solutions, J. Hazard. Mater. 182 (2010) 377-385.

HYDROGEN STORAGE IN A RECYCLABLE ORGANIC HYDRIDE: THE DEHYDROGENATION OF METHYLCYCLOHEXENE

MUHAMMAD R USMAN

Associate Professor, Institute of Chemical Engineering and Technology, University of the Punjab, Lahore 54590, Pakistan. Email: mrashidusn@gmail.com, Phone: +92 42 99230462

Abstract

Methylcyclohexane-Toluene-Hydrogen (MTH) system is safe and economical way of hydrogen storage and its utilization. The dehydrogenation of methylcyclohexane (MCH) is the essential reaction in the MTH system. The dehydrogenation of MCH is believed to occur in a series of dehydrogenation reactions where methylcyclohexane is first dehydrogenated to methylcyclohexene (MCHe) and methylcyclohexene so formed is then dehydrogenated to methylcyclohexadiene (MCHde) and finally methylcyclohexadiene is dehydrogenated to toluene. In the present study, the dehydrogenation reaction of 1-methylcyclohexene is carried out over an in-house 1.0wt% Pt/γ-Al_2O_3 catalyst. The reaction is studied in a plug flow fixed bed reactor under integral conditions. The methylcyclohexene has been found to be highly reactive even at low temperatures and under all the conditions of experimentation methylcyclohexene has virtually gone to completion. The results are useful in understanding the mechanism (rate-controlling step) involved in the dehydrogenation of MCH and may be helpful in recognizing the possibility of using MCHe as an organic hydride.

Introduction

Nations around the world are finding ways of energy supplies that are not only sustainable and economical but benign to the environment. Hydrogen based energy system is the one among such feasible solutions. However, cheap and safe storage of hydrogen is the greatest hurdle in the success of hydrogen to be used as a source of energy. Methylcyclohexane-Toluene-Hydrogen (MTH) system is a safe and economical way of hydrogen storage and its utilization (Usman and Cresswell, 2013). In the MTH system, methylcyclohexane is dehydrogenated to toluene to give off three hydrogen molecules which can be used as a source of energy. The toluene so produced is hydrogenated to give back methylcyclohexane to complete the MTH cycle. Obviously, the dehydrogenation reaction is the essential reaction and needs to be carried out at a low temperature and fast rate requiring an efficient catalyst (Usman, 2011) and an appropriate reactor system. The dehydrogenation of MCH to toluene (TOL) is considered to occur in a series of dehydrogenation steps. It is believed that in each step, a molecular hydrogen is removed and the corresponding hydrogen deficit molecule is produced. At first, methylcyclohexane is converted to methylcyclohexene (MCHe) which then undergoes further dehydrogenation to produce methylcyclohexadiene (MCHde) and final hydrogen removal results in the formation of toluene. In the present study, the dehydrogenation of methylcyclohexene is carried out over an in-house 1.0wt% Pt/γ-Al2O3 catalyst. The experiments are carried out to study the product composition and the reversibility of the reaction. The effect of various variables such as temperature, pressure, and feed composition is studied on the dehydrogenation reaction. The study is useful in recognizing the possibility of using methylcyclohexene as an organic hydride and in understanding the mechanism (rate controlling step) involved in the dehydrogenation of methylcyclohexane.

Experimental

The experimental setup was consisted of a stainless steel tube of 1.02 cm ID in which the catalyst, 1.0wt% Pt/γ-Al_2O_3, was packed in the form of discrete particles (–450 +710 μm) to form a fixed bed of catalyst. 1-methylcyclohexne (97% purity) was obtained from Sigma-Aldrich and used as feed as received. The experiments were performed in the range of 280°C–380°C reactor wall temperature, at a constant total pressure of 5.0 bar, and at constant W/F_{D0} of 32.8 h·g-cat/mol MCHe. All the experiments were performed in the presence of hydrogen. The details of the experimental setup and the catalyst preparation procedure are given elsewhere (Usman, 2010; Usman et al., 2012).

Results and discussion

Fig. 1 shows the outcomes of the methylcyclohexene (MCHe) dehydrogenation. With hydrogen in the feed, the reactant MCHe is found very reactive. At wall temperatures of 340°C and 380°C, complete conversion is the result, however, at wall temperature of 280°C and 300°C conversion is nearly completed. With hydrogen in the feed both hydrogenation and dehydrogenation reactions are important which is confirmed by the presence of methylcyclohexane and toluene in the product (no methylcyclohexadiene is observed in the products). The figure (Fig. 1) shows how the increase in the temperature causes a decrease in the concentration of MCH and an increase in the toluene concentration. In other words, dehydrogenation reaction becomes increasingly dominated with an increase in wall temperature that results in greater toluene yield, and reverse is true for the hydrogenation reaction. The yield of TOL is always ahead of the yield of MCH, noticeably at higher temperatures, which shows domination of dehydrogenation reaction instead of hydrogenation reaction at higher temperatures. Not shown here, the effect of space time on the MCHe conversion is not found appreciable (Usman et al., 2012). The effect is quite noticeable for conversion to toluene and MCH. With hydrogen in the feed, conversion to methylcyclohexane increases, while the conversion to toluene decreases with decrease in W/F_{D0}, both at wall temperature of 341°C and 380°C. The results obtained, here, with methylcyclohexene need to be kinetically analysed to methodically understand the mechanistic of the reaction and to determine the role of the intermediates in the dehydrogenation of methylcyclohexane (MCH).

Though methylcyclohexene (MCHe) almost certainly dehydrogenates indirectly to toluene through the intermediate step involving methylcyclohexadiene (MCHde), the latter is not observed as discussed above. Therefore, it seems appropriate to describe the overall hydrogenation/dehydrogenation scheme by the pair of the following two reactions:

$$\mathrm{MCHe} + \mathrm{H_2} \rightleftharpoons \mathrm{MCH} \qquad \text{(I)}$$

$$\mathrm{MCHe} \rightleftharpoons \mathrm{TOL} + 2\mathrm{H_2} \qquad \text{(II)}$$

Let us assume the conversion of MCHe by reaction (I) be X_I and that by reaction (II) be X_{II}. It may be shown from the overall stoichiometry that the mole fractions of the components in the gas stream are that shown in Table 1.

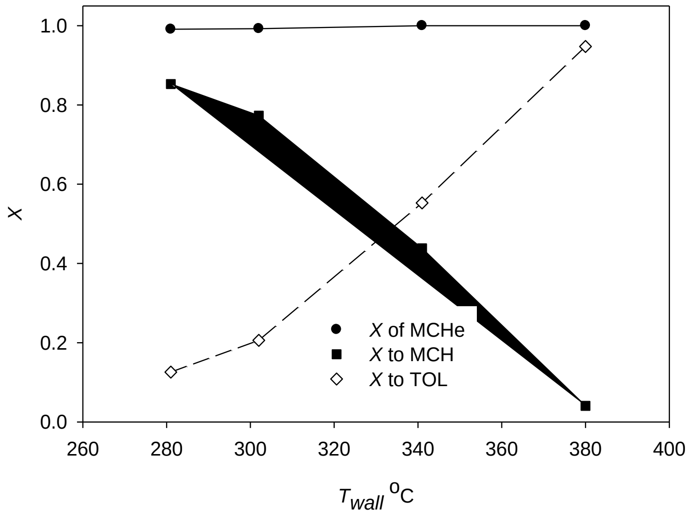

Figure 1. Effect of reactor wall temperature on the composition of reaction products for the dehydrogenation of MCHe. p = 5.0 bar, H_2/MCHe feed molar ratio = 8.0, and W/F_{D0} = 32.8 h·g-cat/mol MCHe.

Component	Representation	Mole fraction
MCH	A	$\frac{y_{A0}+y_{D0}\cdot X_{\mathrm{I}}}{1-y_{D0}\cdot(X_{\mathrm{I}}-2\cdot X_{\mathrm{II}})}$
TOL	B	$\frac{y_{B0}+y_{D0}\cdot X_{\mathrm{II}}}{1-y_{D0}\cdot(X_{\mathrm{I}}-2\cdot X_{\mathrm{II}})}$
H_2	C	$\frac{y_{C0}-y_{D0}(X_{\mathrm{I}}-2\cdot X_{\mathrm{II}})}{1-y_{D0}\cdot(X_{\mathrm{I}}-2\cdot X_{\mathrm{II}})}$
MCHe	D	$\frac{y_{D0}\cdot(1-X_{\mathrm{I}}-X_{\mathrm{II}})}{1-y_{D0}\cdot(X_{\mathrm{I}}-2\cdot X_{\mathrm{II}})}$
Inert	I	$\frac{y_{I0}}{1-y_{D0}\cdot(X_{\mathrm{I}}-2\cdot X_{\mathrm{II}})}$

Table 1. Stoichiometric mole fractions for reactions (I) and (II).

The equilibrium conversions X_{Ie} and X_{IIe} for reactions (I) and (II), respectively, can be obtained by solving the following equations simultaneously written for an ideal gas mixture:

$$K_{\mathrm{I}}\cdot p=\frac{y_{Ae}}{y_{De}\cdot y_{Ce}}=\frac{(y_{A0}+y_{D0}\cdot X_{\mathrm{I}e})\cdot\left(1-y_{D0}\cdot(X_{\mathrm{I}e}-2\cdot X_{\mathrm{II}e})\right)}{y_{D0}\cdot(1-X_{\mathrm{I}e}-X_{\mathrm{II}e})\cdot\left(y_{C0}-y_{D0}\cdot(X_{\mathrm{I}e}-2\cdot X_{\mathrm{II}e})\right)} \tag{1}$$

$$\frac{K_{\mathrm{II}}}{p^2}=\frac{y_{Be}\cdot y_{Ce}{}^2}{y_{De}}=\frac{(y_{B0}+y_{D0}\cdot X_{\mathrm{II}e})\cdot\left(y_{C0}-y_{D0}\cdot(X_{\mathrm{I}e}-2\cdot X_{\mathrm{II}e})\right)^2}{y_{D0}\cdot(1-X_{\mathrm{I}e}-X_{\mathrm{II}e})\cdot\left(1-y_{D0}\cdot(X_{\mathrm{I}e}-2\cdot X_{\mathrm{II}e})\right)^2} \tag{2}$$

where, K_I and K_{II} are the equilibrium constants of reactions (I) and (II), respectively. These constants can be defined in terms of change in Gibbs free energy for the reactions (I) and (II) by the following expressions:

$$\ln K_{\mathrm{I}}=\frac{-\Delta G_{\mathrm{I}}{}^{\mathrm{o}}(T)}{R\cdot T} \tag{3}$$

$$\ln K_{\mathrm{II}}=\frac{-\Delta G_{\mathrm{II}}{}^{\mathrm{o}}(T)}{R\cdot T} \tag{4}$$

Values of $\Delta G_{\mathrm{I}}{}^{\mathrm{o}}(T)$ and $\Delta G_{\mathrm{II}}{}^{\mathrm{o}}(T)$ can be calculated using the values of standard Gibbs free energy of formation of the reacting species. The superscript "o" defines values at low pressure representing an ideal gas. These values are tabulated in Table 2.

Formula: $\Delta G_{f,i}^{\mathrm{o}}(T)=a+bT+cT^2+dT^3$, kJ/mol (5)

Component	Coefficients				Ref.
	a	b	c	d	
MCH	–160.038	0.61255	4.6303×10^{-5}	0	Y*
TOL	47.813	0.23831	3.1916×10^{-5}	0	Y
MCHe	–36.7437	0.416113	1.166×10^{-4}	-4.0818×10^{-8}	L**

Table 2. Stoichiometric mole fractions for the reactions (I) and (II). For H_2 $\Delta G_f{}^{\mathrm{o}}(T)$ is zero.

*(Yaws, 1999) ,**Liessmann et al., 1995)

Eq. 3 and Eq. 4 are used to find out the values of ln Ki. Fig. 2 is plot of these values against 1000/T, K^{-1}. A straight line fit is the result between the values and the following equations are obtained for K_I and K_{II}:

$$\ln K_{\mathrm{I}} = -19.10 + 14.09 \times \frac{1000}{T} \tag{6}$$

$$\ln K_{\mathrm{II}} = 27.51 - 11.25 \times \frac{1000}{T} \tag{7}$$

These two equations (Eq. 6 and Eq. 7) can be used to measure the equilibrium constants and hence the equilibrium extent of reactions I and II for any specified operating conditions.

Summary

1-methylcyclohexene undergoing the dehydrogenation reaction has been found to be highly reactive and in all the cases the reaction is virtually completed. With hydrogen in the feed, the reversible (hydrogenation) reaction is also important, however, the yield of toluene (forward reaction) is always greater than methylcyclohexane (reverse reaction). No methylcyclohexadiene has been observed in the reaction products. As methylcyclohexene and methylcyclohexadiene are the intermediates in the overall dehydrogenation reaction of methylcyclohexane, this study may be helpful in understanding the mechanism of the overall dehydrogenation reaction.

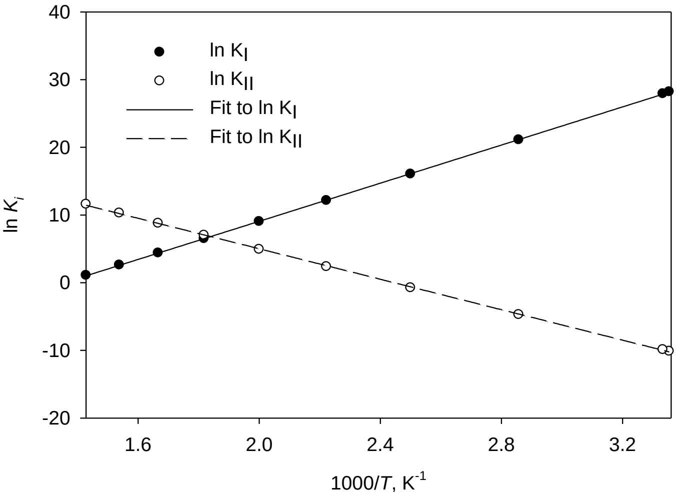

Figure 2. Variation of K_i with absolute temperature.

Nomenclature

F_{D0}	molar flowrate of 1-methylcyclohexene, mol/s
G_f^o	Gibbs free energy of formation of an ith component at low pressure, mol/s
G_i^o	Gibbs free energy of reaction of an ith reaction at low pressure, mol/s
K_i	equilibrium constant of the ith reaction
p	pressure, bar
R	universal gas constant, kJ/mol
T	temperature, K
T_{wall}	reactor wall temperature, K
W	weight of catalyst, kg
X	fractional conversion
X_{ie}	equilibrium conversion of the ith reaction
y_{ie}	equilibrium mole fraction of the ith component
y_{i0}	initial mole fraction of the ith component

References

Liessmann, G.; Schmidt, W.; Reiffarth, S., 1995. Data compilation of the Saechsische Olefinwerke Boehlen. Berlin: Fiz Chemie.

Usman, M.R., 2010. Kinetics of methylcyclohexane dehydrogenation and reactor simulation for on-board hydrogen storage. PhD Thesis. Manchester: The University of Manchester.

Usman, M.R., 2011. The catalytic dehydrogenation of methylcyclohexane over monometallic catalysts for on-board hydrogen storage, production, and utilization. Energy Sources, Part A, 33(24), pp.2231–2238.

Usman, M.R.; Cresswell, D.L., 2013. Options for on-board use of hydrogen based on the methylcyclohexane-toluene-hydrogen system. International Journal of Green Energy, 10(2), pp.177–189.

Usman, M.; Cresswell, D.; Garforth, A., 2012. Detailed reaction kinetics for the dehydrogenation of methylcyclohexane over Pt catalyst. Industrial and Engineering Chemistry Reserach, 51(1), pp.158–170.

Yaws, C.L., 1999. Chemical properties handbook. New York: McGraw-Hill.

SYNTHESIS OF AG-TIO2 BIMETALLIC NANOPARTICLES WITHIN PS-B-PAA REVERSE MICELLE CORES

NUMAN HODA, BURÇIN ACAR ÇAKIR, ÖNDER TOPEL, LEYLA BUDAMA

Abstract

In order to synthesize nanoparticles with small and controlled size, it has been well-known that micellar templating technique has been more advantaged comparing with the other techniques such as sol-gel technology, vapor deposition, micro emulsion systems. Especially, block copolymers are of great interest in this respect which may form micellar aggregates called nanoreactor depending on the selecting solvent. The nanoreactors can be used to fabricate nanoparticles having certain size and size distribution by encapsulating ions such as metal salts. After collecting the metal ions within the cores of micelles, controlled size nanoparticles can be produced by chemical reduction or oxidation.

Moreover, it is also possible to produce bi-metallic core-shell nanoparticles by loading another metal ion into the cores. By regarding the phenomena, silver and titanium oxide bi-metallic nanoparticles were synthesized using reverse micelles of polystyrene-blockpolyacrylic acid as a nanoreactor in the present work. After arranged PS-b-PAA reverse micelles in toluene with PAA cores and PS coronas, silver nanoparticles were synthesized within the cores by using AgNO3 precursor salts as first step. Then, Ti(OBu)4 precursor was loaded in the silver including cores and hydrolyzed by controlled water and acid addition. Formation of bi-metallic nanoparticles within micelle cores was confirmed by X-ray diffraction and transmission electron microscopy. The average size of bimetallic nanoparticles was determined as 23±5 nm.

COMPREHENSIVE STUDY ON GEOTHERMAL POWER PLANT BY MIXTURE FLUIDS

TALIEH RAJABLOO, PAOLO IORA AND COSTANTE MARIO INVERNIZZI

Abstract

Organic Rankine cycles (ORC) are suitable for conversion of heat to power. One of the important hot source available for ORC is geothermal fluid, which have variable temperature and well known to be exploited by mixtures. As a reference case for our analysis, we consider a geothermal ORC plant established by the ORMAT [1]. This plant works with n-pentane at heat source temperature of 104 ° C.

Based on our previous results [2], linear hydrocarbons are thermally stable at this temperature range. Therefore, we designed a new system to improve the efficiency and controlling the cycle. Furthermore, this new system has been investigated to select the optimized working fluid. In general, ORC system with saturated vapor at the turbine inlet is desirable for low temperature applications, simplifying turbine design and producing the greatest turbine power.

The ORC is composed of a pump, an evaporator, a turbine, and a condenser. Results showed that fan consumption and mass flow rate of cooling air decreased significantly in the case of mixtures of working fluid which is due to the glide match of temperature profiles in both, condenser and evaporator. Moreover, heat recovery efficiency was increased in the case of optimized mixtures. Furthermore, the pool boiling evaporation was feasible in the as designed plant showing the acceptable performance of cycle.

References:

1. Quoilin, S. and V. Lemort. in 5th European conference economics and managment of energy in industry. 2009. Portugal.
2. Pasetti, M., C.M. Invernizzi, and P. Iora, Applied Thermal Engineering, 2014. 73(1): p. 764-774.

STEEL SLAG AS FERTILIZER

PEGAH MOGHADAM, MOHSEN NASR ISFAHANI

Abstract

In the past several decades, the recovery of byproducts and wastes, generated in the industry, has increased dramatically. Furthermore, environmental protection agencies ratified some sever rules for recovering industrial wastes to prevent industrial pollutions and also to maintain energy recovery in the industry cycle.

Byproduct recovery in the steelmaking industry has always been considered as one of the requirements of this industry. Steel Slag is one of the key byproducts in this industry and is produced in large amounts. For this reason, manufacturers decided to restore these products and use it in various industries, in order to partly recover wasted energy and costs and avoid environmental problems in disposal or storage of this product. On the other hand, the increase of slags recovery and use in different fields of application, such as in agriculture, allowed to reduce landfill slags and to preserve natural resources. One of the applications of steel and iron slag is using it as a fertilizer. This fertilizer had to compete with other fertilizers of the same chemical properties which were cheap and readily available. However, manufacturers by applying new techniques, provided a condition in which using slag as a fertilizer increases the quality of product and soil and eliminate the deficiencies of agricultural soils (e.g. some needed metals, the need to increase pH, stabilizing soil conditions, est.) in comparison with other fertilizers. This used steel slag the Current study, using documentary method, explores the new ways of producing iron and steel slag and their using conditions.

In Japan and some of the European country are using steel slag as fertilizer in their Cultivations rice. The analyses on quality of rice products showed all the benefit of using steel slag as fertilizer in comparing to other fertilizers which was used before.

EFFECTS OF CURING TIME ON CORROSION RESISTANCE OF HYBRID SILANE COATING FOR LOW CARBON STEEL

ALI RAHIMI FERDOSINEZHAD, LOH HWEI LING, POOVARASI BALAN

[1, 2, 3] Chemical Engineering Discipline, School of Engineering, Monash University, Jalan Lagoon Selatan, Bandar Sunway, 46150 Selangor Darul Ehsan, Malaysia
[A*] rahimi.ali@aol.com, [B] hlloh1@student.monash.edu, [C] poovarasi.balan@monash.edu
Keywords: Silane, Corrosion, Curing time, Low Carbon Steel, FTIR

Abstract

This work is aimed to investigate the barrier properties of GPTMS-TEOS hybrid silane as a function of curing time using Fourier transform infra-red spectroscopy (FTIR), scanning electron microscopy (SEM), and electrochemical impedance spectroscopy (EIS). The hybrid silane was synthesized using 3-glycidoxy-propyl-methyldiethoxysilane (3-GPTMS) and tetraethyl orthosilicate (TEOS) as main precursors while 0.05M nitric acid was used as catalyst. The mixture was left to hydrolyse before low carbon steel was dip-coated in the resultant sol-gel and cured for different time durations (i.e. 1, 2, 5, and 24 hours) at 90˚C. It was found that the absorbance intensity recorded by FTIR for Si-O-Si (siloxane), observed in the range of 1000 cm^{-1} and 1100cm^{-1}, increased with increasing curing time. Surface morphology images observed under the SEM also produced similar observations in which the degree of delamination and cracking of silane coating was reduced as the curing time increased. EIS was used to study the electrochemical behaviour of the coated carbon steels. After 24 hours of immersion of coated steel carbon in a corrosive environment, results further confirmed that impedance values of the coated metals cured for 24 hours is significantly higher than others (1E6 ohm.cm^2), implying a better corrosion barrier properties. It was therefore concluded that a longer curing time produced a silane film with a higher degree of cross-linking, subsequently forming a crack free and evenly distributed surface which could better protect low carbon steel against corrosion.

1. Introduction

Hybrid silanes have emerged as one of the leading alternatives for replacement of currently used toxic chromate-based pre-treatment. Since mid-1980's, the sol-gel derived hybrid silanes have been the centre of intensive research for their unique application in corrosion prevention; the progress of which has been thoroughly reported by Wang and Bierwagen (2009). Hybrid silanes, in particular, have the advantage of both organic and inorganic silanes, thus allowing for the formation of thin films with superior corrosion barrier properties.

Silanes are synthesised through a two-step process comprising of hydrolysis and condensation. During hydrolysis, the hydrolysable groups (Si-OR) of precursors react with water molecules to form silanol groups (Si-OH). These silanol groups can then form hydrogen bonding with the existing hydroxyl groups (Me-OH) present on the metal surface and adhere to it. During condensation, the hydrogen bonding between the silane film and metal surface is replaced and strengthened by covalent Si-O-Me and Si-O-Si bonds as water molecules are removed (Woo, Reucroft et al. 1993). The formation of metallo-siloxane groups (Si-O-Me) increases the adhesion strength between the metal surface and silane film while effectively reducing the number of active sites on the metal surface that would otherwise attract corrosive water molecules (Yang, Feng et al. 2010; Hernández-Escolano, Ramis et al. 2012). On the other hand, the formation of siloxane network (Si-O-Si) creates a dense hydrophobic silane film that would suppress the water uptake and thus protects the metal substrate from corrosion.

Curing of silane pre-treated metal substrates by placing the metal substrates in a furnace further encourages the transition of hydrogen bonds to covalent bonds which intensifies the production of dense siloxane network. During this process, the metal substrates are placed in a furnace at a certain temperature for a set amount of time. Curing temperature is generally selected based on thermal stability of the precursors and therefore is not the subject of investigation in this study.

The present work aims to study the barrier properties of GPTMS-TEOS hybrid silane film on low carbon steel upon changing the duration of curing time. Analytical characterization of the pre-treatment was conducted via Fourier Transform Infra-Red spectroscopy (FTIR) and Scanning Electron Microscopy (SEM) while Electrochemical

Impedance Spectroscopy (EIS) was used to monitor the silane barrier properties in the initial stages of corrosion (i.e. first 24 hours after the initiation of corrosion).

2. Methodology

2.1 Surface Preparation

The substrate used for the present investigation were low carbon steel supplied by Q-Panel (U.S.A) with dimensions of 6 cm x 2 cm x 1mm thickness. The steel strips were cleaned ultrasonically with soap water, deionized water (DI), and acetone for 2 minutes in room temperature before alkaline cleaning using NaOH solution (pH 10.8) for 5 minutes at 50˚C. The steel strips were then rinsed with DI water and dried using compressed air.

2.2 Silane Preparation and Application

The silane solution was prepared by mixing 3-glycidoxy-propyl-methyldiethoxysilane (3-GPTMS, 98%, Gelest) and tetraethyl orthosilicate (TEOS, 99%, Sigma Aldrich) precursors and dissolving them in 0.05 nitric acid (HNO_3, 69%, Friendemann Schidt). The hybrid silane was prepared using a GPTMS: TEOS: 0.05 M HNO_3 molar ratio of 2: 1: 10 which was chosen based on a published work by Metroke et al. (2002) and Balan et al. (2013). The resulting sol-gel was then stirred vigorously for an hour at 250 rpm for homogenization and was stored for three days before being coated on the surface of metal panels.

The primary method to coat the metal panels was dip-coating. The panels were dipped into the sol-gel solution thrice, with each immersion lasting one minute. The low carbon steel panels were then cured in an oven at 90 ℃ for 1 hour, 2 hours, 5 hours, and 24 hours. The curing temperature was selected based on the understanding that 3-GPTMS has a relatively low thermal stability. Nemeth and Liu (2009) found that a 3-GPTMS sols had a higher thickness when cured at 90˚C as compared to samples that were cured at higher temperatures.

2.3 Characterization

Fourier Transform Infra-Red spectroscopy (FTIR) tests were conducted on the coated samples to monitor changes in the chemical structure and bonding of the silane film after curing has taken place. Measurements were carried out on a Thermo Scientific Research Instruments Nicolet iS10 with a spectral resolution of 4 cm^{-1} in the mid-IR range of 500-4000 cm^{-1}. For each measurement, the number of scans was 64.

Scanning Electron Microscopy (SEM) tests were conducted to observe the morphology of the hybrid silane film on the metal substrate after curing. These tests were repeated after the exposure of metal panels to 0.05 M sodium chloride solution for 24 hours to observe the changes in the silane film morphology after the initial stages of corrosion. These changes were observed with a Hitachi S-3400N scanning electron microscope at a potential of 15 kV.

Electrochemical Impedance Spectroscopy (EIS) measurements were employed to monitor the corrosion barrier performance of the hybrid silane film in different samples to understand the influence of modification of curing time on its corrosion barrier performance. EIS tests were conducted by exposing the metal panels to 0.05 M sodium chloride solution at room temperature for 24 hours. The data were obtained as a function of frequency using a sine wave of 10 mV amplitude peak to peak. Frequency scans were taken at a range of 100 kHz to 0.01 Hz. A total of 10 impedance sample points were taken.

3. Results and Discussion

Fig. 1 shows the results obtained from FTIR for hybrid films cured at 90˚C for various durations. Strong absorptions were observed along the FTIR spectra at different wavenumbers with varying intensities. The absorption at 3000 cm^{-1} and 3700 cm^{-1} is due to OH vibrations (from Si-OH groups) that are formed during the hydrolysis of 3-GPTMS and TEOS. It is seen that the absorption peak is the strongest for the sample cured for 24 hours, followed by samples cured for 2 and 5 hours while the samples cured for 1 hour exhibit the lowest intensity. Assuming constant absorption coefficient for the Si-OH groups, this implies that the concentration of OH groups is the highest for 24 hours cured sample while the samples cured at 2 and 5 hours have almost the same concentration of such groups and finally samples cured for 1 hour has a significantly lower OH group concentration. The same trend is observed for the absorption at 2937 cm^{-1} and 2879 cm^{-1} which are due to C-H vibration in glycidoxy-propyl moiety of 3-GPTMS. Silica network is characterized by the strong absorption occurring between 1000 cm^{-1} and 1100 cm^{-1} corresponding to the Si-O-Si anti-symmetric stretching. The intensity of this band is particularly the strongest for 5 hours and 24 hours cured samples and the weakest for the 1 hour cured sample. The increase in the intensity of this siloxane band (Si-O-Si) indicates the extent of the condensation. This infers that the condensation reaction is driven closer to completion upon a longer period of curing as more silanol is consumed to form the siloxane network. Aside to normal increase of intensity in this region, there is also a shift to the left in the spectra which could be the result of structural changes due to rearrangement of Si-O-Si groups. This effect is well documented in literature (Innocenzi 2003; Nemeth and Liu 2009). Similarly, with the increase of curing time, the absorption intensity at 950 cm^{-1} is higher which is attributed to the stretching vibration of Si-OH or Si-O-Fe (Almeida, Guiton et al. 1990). The lowest part of the spectra it is seen that the peak at 560 cm^{-1} is at its maximum for 2, 5, and 24 hours cured samples while the sample cured for only 1 hour exhibit the lowest intensity. This band is associated with the vibration of oxygen atoms in Si-O-Si and therefore the observed trend infers that 24 hours has undergone the most cross-linking through the oxygen atom.

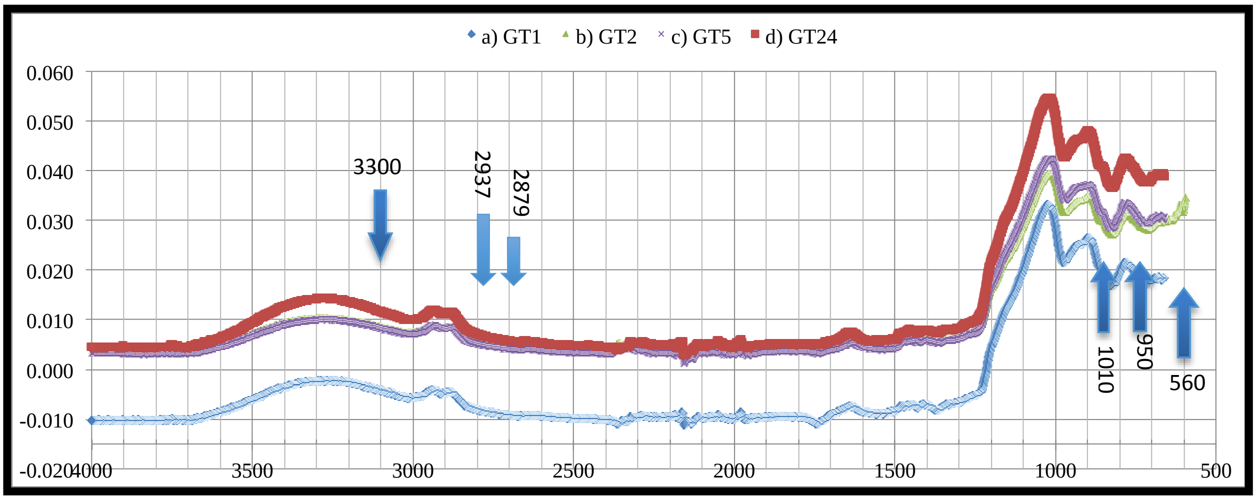

Figure 1- FTIR spectra for coated substrates cured for (a) 1 hour; (b) 2 hours; (c) 5 hours; (d) 24 hours.

SEM was used to investigate the effects of curing time on the morphology of the hybrid silane pre-treatment. Fig. 2 shows the surface morphology of the silane pre-treatment at various curing time immediately after adsorption of silane film to the metal surface. It is revealed that all samples that had undergone 1 hour, 2 hours, and 5 hours of curing exhibit cracks while the sample cured for 24 hours (Fig. 2a) appears crack-free. Furthermore, it is seen that the severity of the cracks in the first 3 samples decreases with the increasing curing time.

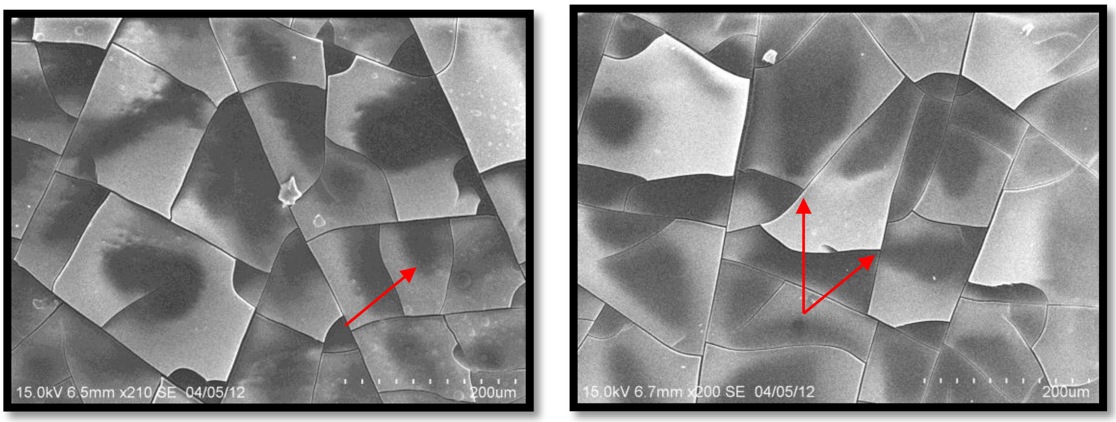

(a)

(b)

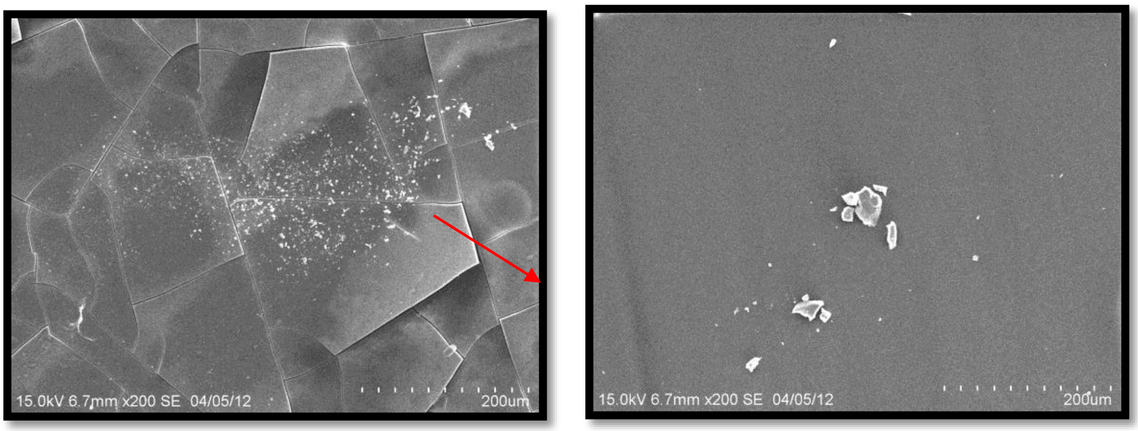

(c) (d)

Figure 2: SEM images before corrosion at 200x magnification for (a) GT1; (b) GT2; (c) GT5; (d) GT24

Similar SEM images were captured after the samples were exposed to 0.5M sodium chloride solution for about 24 hours which are shown in Fig. 3. It is seen that cracks are present in all samples as shown in Fig. 2. The severity of the cracking however decreases with increasing curing time. In Fig. 3a, the surface of the metal is visible as a result of severe delamination leaving the metal surface completely unprotected against corrosive environments. Only the sample cured for 24 hours (Fig. 4d) shows no significant cracking of the silane film.

It has been suggested that the existing cracks are the result of stresses applied on the film due to the agglomeration of corrosion products (Zandi Zand, Verbeken et al. 2012). Therefore a lower degree of cracking can be associated to fewer corrosion products underneath the coating. This infers that the sample cured for 24 hours has gone through minimum corrosion as compared to other samples. The effects of corrosion and its progress can be monitored by observing the pictures in Fig. 4 in reverse chronological order i.e. GT24 > GT5 > GT2 > GT1.

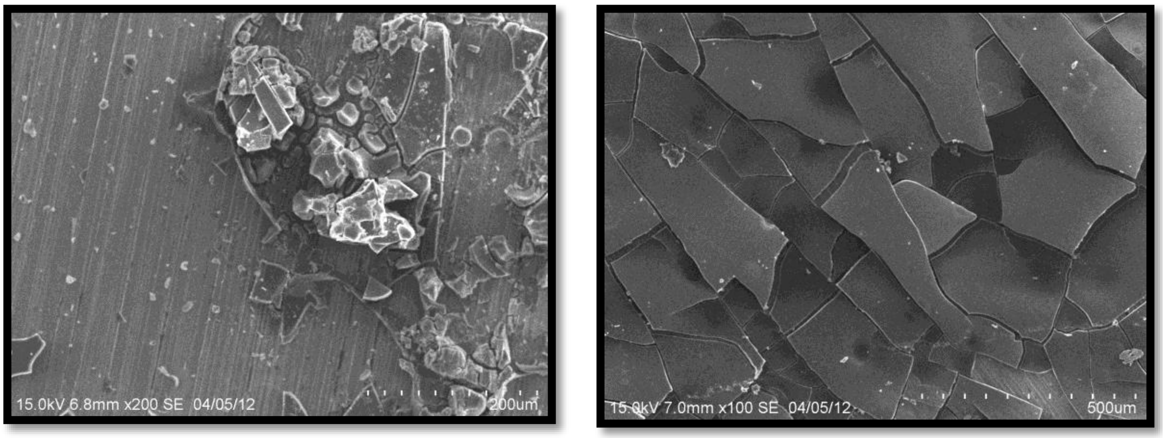

(a) (b)

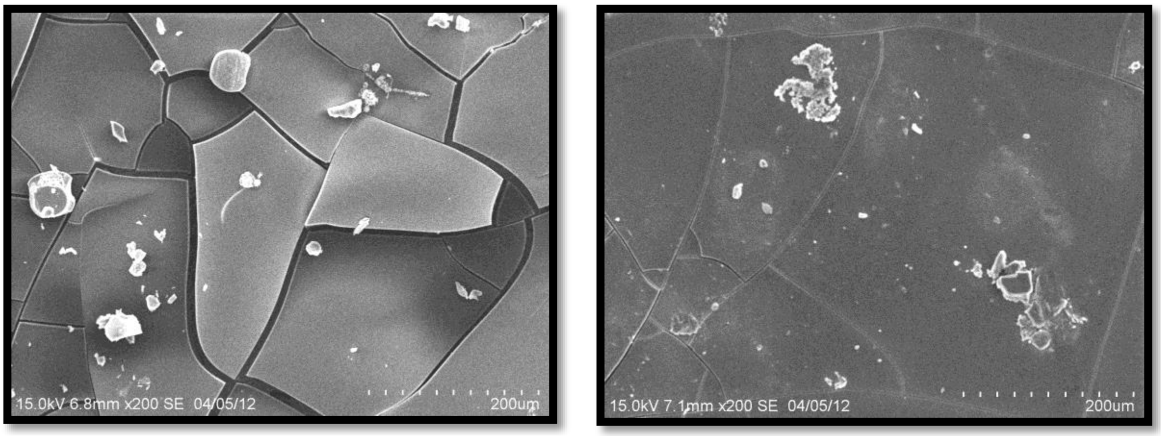

(c) (d)

Figure 3: SEM images after corrosion at 200x magnification for
(a) GT1; (b) GT2; (c) GT5; (d) GT24

Fig. 5 and Fig. 6 show the impedance response of silane pre-treated low carbon steel in 0.05 M sodium chloride electrolyte after 24 hours of exposure. In Fig. 5, it can be seen that the overall impedance is increased with longer curing time, indicating that the corrosion resistance is enhanced. However the results present no upper threshold at which longer curing time no longer contributes to the enhancement of coating's barrier properties. This finding does not agree with the results obtained by Lampke's studies in which an upper threshold for curing time is obtained after 3 hours to produce the best performing film (Lampke, Darwich et al. 2008). Results obtained in Fig. 1 are nevertheless in line with the hypothesis that when a silane is cured longer, further cross linking would take place. As a result of cross linking, a majority of pores in the film will be sealed and thus improves the overall resistance of the film.

In Fig. 6, two distinct time constant are observed for GT1, one at low and another at higher frequency. The time constant at low frequency is ascribed to the electrochemical activity at the low carbon steel surface suggesting that the corrosive electrolyte has already reached the surface of the metal and that corrosion has already initiated. The time constant at higher frequency was associated with the capacitance of the hybrid silane film, hinting water uptake in the film and poor barrier performance (van Ooij, Zhu et al. 2005). On the other hand, only a single time constant was detected at middle frequency (10-100 Hz) for GT2, GT5, and GT24. Such behaviour is hypothesized to be the result of the formation of the Si-O-Fe interfacial layer between the metal substrate and the siloxane network. This interfacial layer thus posed an additional resistance against the onset of corrosion (Yang, Feng et al. 2010).

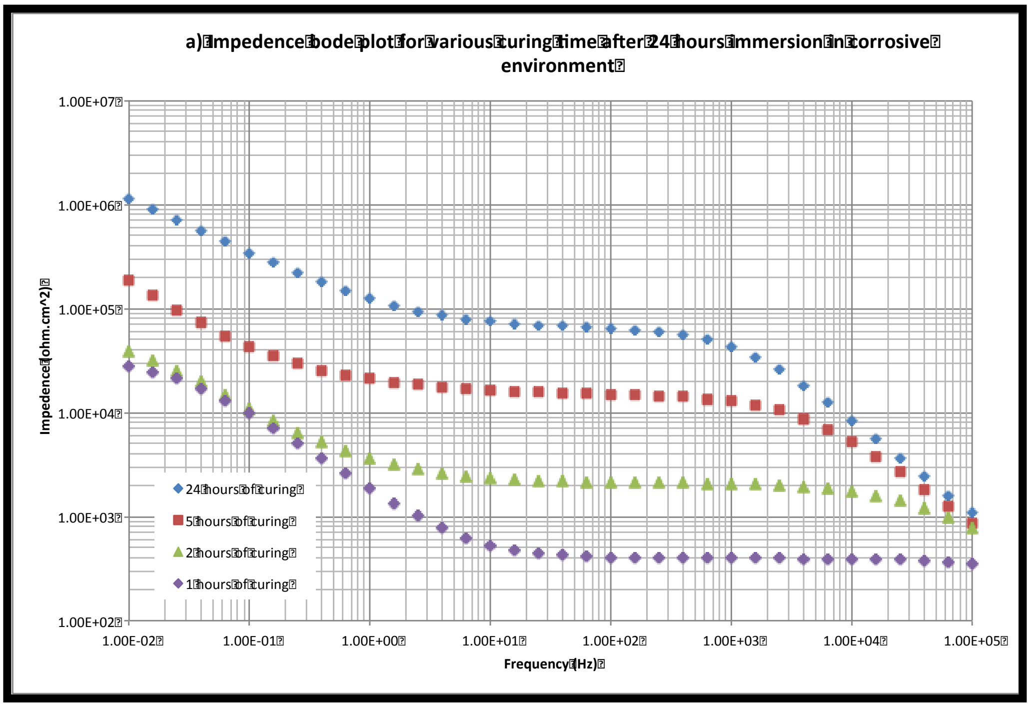

Figure 5: Impedance bode plot for various curing time after 24 hours immersion in corrosive environment

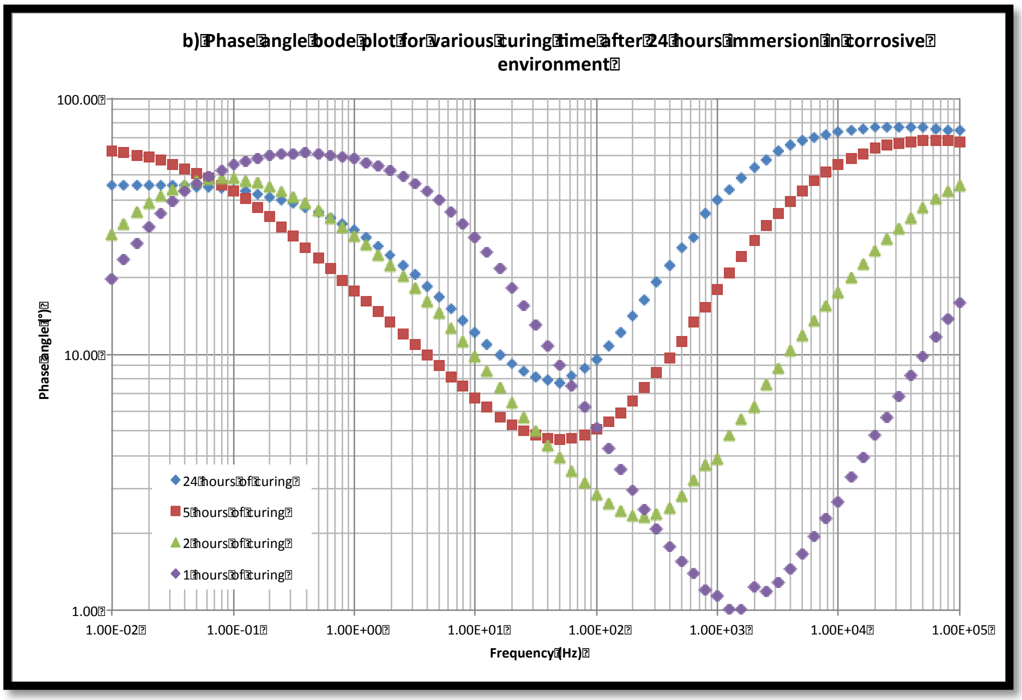

Figure 6: Phase angle bode plot for various curing time after 24 hours immersion in corrosive environment

4. Conclusion

Based on the results obtained from FTIR, SEM, and EIS, it was found that a longer curing time, specifically for 24 hours, could produce a denser Si-O-Si bonding silane film indicating a strongly bonded silane network with the low carbon steel. Evidently such pre-treatment could better protect low carbon steel against corrosive environments. This was confirmed by the observations of SEM images in which the silane film cured for 24 hours produced the least cracking and no delamination after being exposed to a corrosive environment for 24 hours. Higher impedance values of EIS measurements for the 24 hours cured pre-treatment also proved further confirmation that the corrosive electrolytes could not penetrate the silane film as easily as compared to others.

Despite these findings no upper threshold for the curing time was found which would produce the optimal overall barrier properties. This infers the necessity to conduct further studies to truly understand the implication of curing time on the synthesis and the network of hybrid silane films.

References

lmeida, R., Guiton, T. and Pantano, C. (1990). Characterization of silica gels by infrared reflection spectroscopy. Journal of Non-Crystalline Solids, 121(1-3), pp.193-197.

Balan, P., Ng, A., Beng Siang, C., Singh Raman, R. and Eng Seng, C. (2013). Effect of Nanoparticle Addition in Hybrid Sol-Gel Silane Coating on Corrosion Resistance of Low Carbon Steel. AMR, 686, pp.244-249.

Hernandez-Escolano, M., Ramis, X., JimÃ©nez-Morales, A., Juan-DÃaz, M. and Suay, J. (2011). Study of the thermal degradation of bioactive solâ€“gel coatings for the optimization of its curing process. J Therm Anal Calorim, 107(2), pp.499-508.

Innocenzi, P. (2003). Infrared spectroscopy of solâ€“gel derived silica-based films: a spectra-microstructure overview. Journal of Non-Crystalline Solids, 316(2-3), pp.309-319.

Lampke, T., Darwich, S., Nickel, D. and Wielage, B. (2008). Development and characterization of sol-gel composite coatings on aluminum alloys for corrosion protection. Mat.-wiss. u. Werkstofftech., 39(12), pp.914-919.

Metroke, T., Kachurina, O. and Knobbe, E. (2002). Spectroscopic and corrosion resistance characterization of GLYMOâ€“TEOS Ormosil coatings for aluminum alloy corrosion inhibition. Progress in Organic Coatings, 44(4), pp.295-305.

Nemeth, S. and Liu, Y. (2009). Mechanical properties of hybrid solâ€“gel derived films as a function of composition and thermal treatment. Thin Solid Films, 517(17), pp.4888-4891.

van Ooij, W., Zhu, D., Palanivel, V., Lamar, J. and Stacy, M. (2006). Overview: The Potential of silanes for chromate replacement in metal finishing industries. Silicon Chemistry, 3(1-2), pp.11-30.

van Ooij, W., Zhu, D., Stacy, M., Seth, A., Mugada, T., Gandhi, J. and Puomi, P. (2005). Corrosion protection properties of organofunctional silanes 2014; An overview. Tinshhua Sci. Technol., 10(6), pp.639-664.

Wang, D. and Bierwagen, G. (2009). Solâ€“gel coatings on metals for corrosion protection. Progress in Organic Coatings, 64(4), pp.327-338.

Woo, H., Reucroft, P. and Jacob, R. (1993). Electrodeposition of organofunctional silanes and its influence on structural adhesive bonding. Journal of Adhesion Science and Technology, 7(7), pp.681-697.

XIAO, K., DONG, C., LI, X. and WANG, F. (2008). Corrosion Products and Formation Mechanism During Initial Stage of Atmospheric Corrosion of Carbon Steel. Journal of Iron and Steel Research, International, 15(5), pp.42-48.

Yang, L., Feng, J., Zhang, W. and Qu, J. (2010). Experimental and computational study on hydrolysis and condensation kinetics of Î³-glycidoxypropyltrimethoxysilane (Î³-GPS). Applied Surface Science, 257(3), pp.990-996.

Zandi Zand, R., Verbeken, K. and Adriaens, A. (2012). Corrosion resistance performance of cerium doped silica solâ€“gel coatings on 304L stainless steel. Progress in Organic Coatings, 75(4), pp.463-473.

MEASUREMENTS AND MODELING OF TERNARY SYSTEMS CONTAINING THIOLS (ORGANIC SULFUR SPECIES) IN HYDROCARBON AND WATER AT 303, 335, AND 365 K AND PRESSURE UP TO 9 MPA

JAVEED A. AWAN, CHRISTOPHE COQUELET, IOANNIS TSIVINTZELIS, GEORGIOS M. KONTOGEORGIS

[1]Institute of Chemical Engineering and Technology, University of the Punjab, Lahore, Pakistan, [2] CEP, Mines ParisTech, Fontainebleau, France, [3] Department of Chemical Engineering, Aristotle University of Thessaloniki, GR-54124, Thessaloniki, Greece, Department of Chemical Engineering, Aristotle University of Thessaloniki, GR-54124, , Thessaloniki, Greece, [4]CERE, Chemical Engineering, Lyngby, Denmark

---

Abstract

New vapor-liquid-liquid equilibrium (VLLE) data for methanethiol + methane + water, ethanethiol + methane + water, 1-propanethiol + methane+ water, and1-butanethiol + methane + water ternary systems have been measured at three temperatures (303, 335, and 365 K) and pressures up to 9 MPa. A"static-analytic"method was used for performing all the measurements. The total system pressure was maintained by CH_4. All the experiments have been performed at Mines Paris Tech France. The objective of this work is to provide new experimental VLLE data with thermodynamic modeling for mixtures of mercaptans (thiols) with other natural gas contents at its crude form, for which no data are available in the open literature. Such data will help the industrial modeling of processes relevant to reduction of sulfur emissions. The Cubic-Plus-Association (CPA) equation of state was applied to describe the phase behavior of the investigated systems. It is shown that the CPA EoS satisfactorily describes the solubilities of mercaptans (thiols) in all phases. It is observed from the experimental data that the solubility of CH_4in the aqueous and organic phase increases with an increase of the total system pressure and decreases with an increase of the temperature. However, the solubility of CH_3SH in the aqueous and organic phases decreases slightly with an increase of the total system pressure and increases significantly with an increase of the temperature. The new VLLE data of ternary system were compared with predictions of the cubic-plus-association equation of state. The model tends to under predict the concentration of CH3SH in all phases, particularly the vapor phase. However, the model underestimates the water content of the vapor phase, especially at low pressures and at the highest investigated temperature, i.e., at 365 K. Only the ethanethiol + methane + water system showed significant cross-association effects. Furthermore, no cross association (solvation) was found to be significant in 1-propanethiol + methane + water and1-butanethiol + methane +water ternary systems.

Corresponding Author: javeedawan@yahoo.com. (Dr. Javeed A. Awan Associate Professor), Phone : +92 42 992 304 62, Fax: +92 42 992 311 59

SYNTHESIS OF NOVEL N SULFONAMIDOXAZOLIDIN-2-ONES

RADIA BOUASLA, MALIKA BERREDJEM AND NOUR-EDDINE AOUF

LCOA, Bioorganic Chemistry Group, Sciences Faculty, Chemistry Department, Badji-Mokhtar; Annaba University, BP 12, 23000, Algeria.
Corresponding author E-mail: *rbouasla@yahoo.fr*

Abstract

The oxazolidinones are an important class of synthetic antimicrobial compounds [1]. Linezolid, the only marketed agent in this class, was approved in 2000 for use in the treatment of skin and skin-structure infections [2].
The sulfonamide groupe is considered as a pharmacophore which is present in number of biologically active molecules, particularly antimicrobial agent [3, 4].
In this work, we report the synthesis and the structural analysis of N-sulfonamidoxazolidinones. Modified oxazolidinones were prepared from natural amino acids. The reduction of the latter leads to the formation of amino alcohols. Intramolecular cyclization under mild conditions allows access to chiral oxazolidin-2-ones.The N-sulfonamidoxazolidinones were synthesized by the introduction of sulfonyle group into chiral oxazolidin-2-one. The synthesis of N-sulfonamidoxazolidinones was performed in four-steps, using chlorosulfonyl isocyanate (CSI).

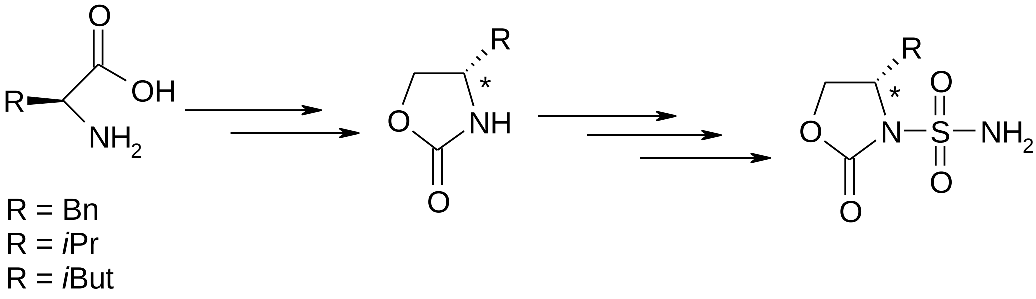

The structures of all compounds synthesized were unambiguously confirmed by usual spectroscopic methods 1H NMR, 13C NMR and IR.

Keywords: Oxazolidinones, Chlorosulfonyl isocyanate, tert-butanol, Sylfonyle.

[1] G. Hostetler, D.Dunn, B. A. Mckenna, K. Kopec, S. Chatterjee. Bioorg. Med. Chem. Lett. 2014, 24, 2094.
[2] M.R, Barbachyn, C.W. Ford. Angew Chem Int Ed Engl. 2003, 42, 2010.
[3] R. Bouasla, M. Berredjem, A. Allaoui, H. Berredjem, M. Lecouvey, N.E. Aouf. J. Het. Chem. 2013, 50, 1328. [4] C. Barbey, R. Bouasla, M. Berredjem, N. Dupont, P. Retailleau, M. Lecouvey, N.E. Aouf. Tetrahedron. 2012, 68, 9125.

THE FLUORESCENCE QUENCHING OF DNA-ETHIDIUM BROMIDE BY TETRABUTYLAMMONIUM BROMIDE-BASED DEEP EUTECTIC SOLVENTS

RIZANA YUSOF, KHAIRULAZHAR JUMBRI, HASLINA AHMAD, MOHD BASYARUDDIN ABDUL RAHMAN

Rizana Yusof, MSc, [1]Department of Chemistry, Faculty of Science, Universiti Putra Malaysia, 43400 UPM Serdang, Selangor, Malaysia, [2]Department of Chemistry, Faculty of Applied Sciences, Universiti Teknologi MARA (UiTM), 40450 Shah Alam, Selangor, Malaysia. Khairulazhar Jumbri, PhD Doctor, [1]Department of Chemistry, Faculty of Science, Universiti Putra Malaysia, 43400 UPM Serdang, Selangor, Malaysia, Haslina Ahmad, PhD Doctor, [1]Department of Chemistry, Faculty of Science, Universiti Putra Malaysia, 43400 UPM Serdang, Selangor, Malaysia, Mohd Basyaruddin Abdul Rahman, PhD Professor, [1]Department of Chemistry, Faculty of Science, Universiti Putra Malaysia, 43400 UPM Serdang, Selangor, Malaysia, [2]Enzyme and Microbial Technology Research Centre (EMTech), Universiti Putra Malaysia, 43400 UPM Serdang, Selangor, Malaysia.

Abstract

The binding properties of the tetrabutylammonium bromide (TBABr)-based deep eutectic solvents (DESs) with calf thymus DNA (ct-DNA) have been investigated by fluorescence quenching studies. The competitive study with ethidium bromide (EB) shows that the DES can displace EB from the DNA-bound EB and has a significant degree of binding to DNA. The ability of DES to quench EB from DNA was determined quantitatively with the Stern-Volmer equation. The effect of using different hydrogen bond donors (HBDs) in DES, in terms of chain length and presence of hydroxyl group (^-OH) into quenching EB from DNA were reported. It was found that the value of Stern-Volmer quenching constant (K_{SV}) increase with the longer HBDs used in DES. The K_{SV} values of DESs were reported in range of 4.15 to 6.36 M^{-1}. The electrostatic interactions between the TBA^+ cation and the DNA phosphate group occurred along with hydrophobic interactions between the TBA^+ cation and the DNA phosphate group. This study reports important aspects of the DNA-DES interactions, and is expected to be of help in the development of new DES.

Introduction

In recent years, deep eutectic solvent (DES) has been considered as new alternatives to the traditional toxic organic solvents. Generally, DES is formed from an eutectic mixture; that composed of quaternary ammonium salt and hydrogen bond donor (HBD)(Abbott et al., 2003). A great attention toward DESs as a new medium solvent is due to their unique properties such as low vapour pressure, low flammability, good recyclability, high thermal stability and wide range of solubility (Abbott et al., 2003, 2004; Smith et al., 2012). DESs were introduced in many of applications such as electrochemistry, biocatalysis, biomass processing, metal dissolution and extraction (Abbott et al., 2006; Francisco et al., 2012; Gorke et al., 2010).

In DNA technologies, DES was also been used to dissolve and solvate DNA with an expectation it did not disrupt the helical structure. The ability of DNA to maintain stable is strongly influenced by the interactions of DES to DNA (Zhao, 2014). As reported by Sharma et al., (2015) the existence of electrostatic attraction and hydrogen bonding interaction between DES and DNA will result for DNA to maintain stable even after a long storage in DES mixtures. There are many techniques have been used to study the interactions between DNA and small molecules, such as circular dichroism (CD) spectroscopy, ultra-violet (UV) spectroscopy, electrochemical method, dynamic light scattering (DLS), isothermal titration calorimetry (ITC) and fluorescence quenching (Ding et al., 2010; Mamajanov et al., 2010; Xie et al., 2008).

The fluorescence quenching is one of the effective techniques used to study the quenching mechanism, mode and strength of the interaction between small molecules and DNA. The most common fluorophore used to intercalate DNA is ethidium bromide (EB), which the molecular structure is shown in Figure 1 (Ding et al., 2010; Izumrudov et al., 2002). In the presence of DNA, EB emission spectra increases resulted from strong intercalation of EB into base pairs and stretches the double helix structures of DNA (Ding et al., 2010; Sirajuddin et al., 2013;

Street, 1995). The quenching process occurred when small molecules that have strong affinity toward DNA were added into solution, which leads to a decrease of EB-DNA emission spectra. The informations obtain from interaction of DES and DNA is very crucial in understand the ability of DES to stabilize DNA native structures. However, there are limited of study discussed the interaction and mechanism between DES and DNA.

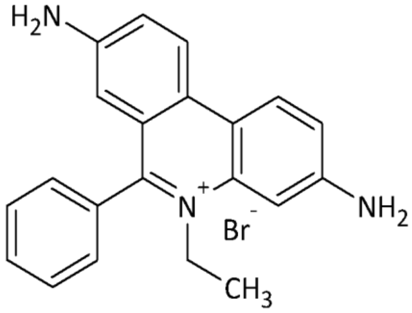

Figure 1. The structure of Ethidium Bromide

In this work, we have investigated the fluorescence quenching behavior of DESs of different length and number of hydroxyl group, -OH on HBD with DNA-bound EB. For this purpose, we synthesized four different DESs that contained different of HBDs; ethylene glycol (EG), 1,3-propanediol (1,3-PD), 1,5-pentanediol (1,5-PD) and glycerol (Gly). The effects of different HBDs on DES in quenching process were reported quantitatively by Stern volmer quenching constant, K_{SV}.

Materials and methods

Materials

Tetrabutylammonium bromide (TBABr), 1,3-propanediol (1,3-PD) and 1,5-pentanediol (1,5-PD) were supplied by Fluka Chemical (Reidstr, Steinheim, Germany) with 98% purity. Ethylene glycol (EG) was purchased from R&M (Essex, UK) and glycerol (Gly) from J.T.Baker. All chemicals were used without further purification. Calf-thymus DNA (ct-DNA, B10 kbp, D1501) was purchased from Sigma and used without further treatment since the purity was high as determined by UV-visible spectroscopy. Ethidium bromide (EB) was also purchased from Sigma. Deionized water type III was used (Super Q Millipore system, conductivity lower than 18 mscm^{-1}) for the preparation of reagents. All the solutions were prepared without a buffer.

Synthesis of Tetrabutylammonium bromide-based DES.

DESs were synthesized through mixing the TBABr salt with different HBDs, ethylene glycol (EG), 1,3-propanediol (1,3-PD), 1,5-pentanediol (1,5-PD) and glycerol (Gly). The syntheses were carried out at molar ratios of 1 to 3 (TBABr to HBD). The mixtures were heated at 60°C and stirred at 250 rpm for three to five hours until a clear liquid appeared. The mixtures were then cooled to room temperature and sealed tightly. DES mixtures were prepared accordingly to the method previously reported (Yusof et al., 2014). The structure of synthesized DES as shown in Figure 2 were labeled as followed: Tetrabutylammonium bromide: ethylene glycol (TBABr:EG), Tetrabutylammonium bromide: 1,3-propanediol (TBABr:1,3-PD), Tetrabutylammonium bromide: 1,5-pentanediol (TBABr:1,5-PD) and Tetrabutylammonium bromide: glycerol (TBABr:Gly).

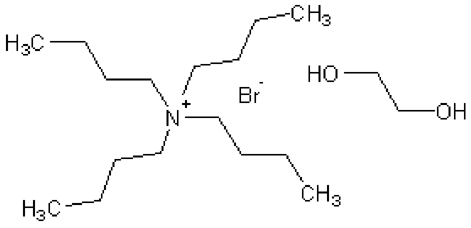

TBABr:EG

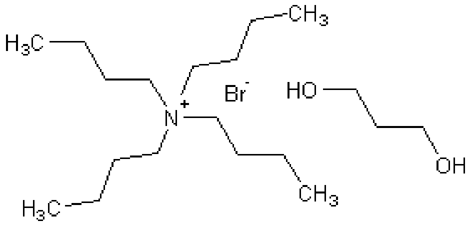

TBABr:1,3-PD

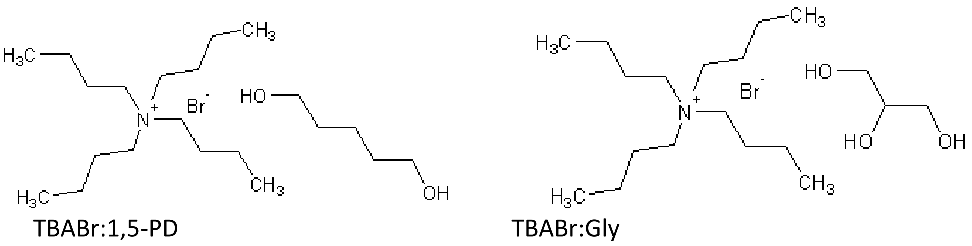

Figure 2. The structures of synthesized DESs

Fluorescence Quenching of DES into DNA-bound EB

The fluorescence quenching of DNA-bound EB by DES was performed. The DNA-bound EB solution was prepared freshly by adding a portion of 1µL of DNA stock solution (2.5 x 10^{-3} M) into 3 mL of 0.5 µM EB. The intensity of the solution was measured after 3 minutes of incubation. The titration of DNA into EB was continued by increasing the DNA concentration from 8.3 x 10^{-7} M to 1.25 x 10^{-5} M while keeping the concentration of EB constant (0.5 µM). The fluorescence emission spectra were recorded after each successive addition of DNA solution. Subsequently, the DES solution was slowly titrated into the DNA-bound EB solution. The titration of the DES into the DNA-bound EB solution was done by increasing the concentration of the DES (0.025, 0.075, 0.175, 0.30, 0.45, 0.63 and 0.83M), while the concentration of DNA-bound EB was kept constant. The excitation wavelength for EB was set at 510 nm and the emission spectra was recorded in the wavelength range from 550 to 750 nm. Both the excitation and emission slits were set at 5 nm.

In this experiment, EB was used as a fluorescent probe in a quenching study. The extent of binding between the DES and DNA was measured through the addition of DES to the DNA-bound EB. The ability of DES to bind and quench the EB from DNA-bound EB was studied by recording the extent of fluorescence quenching. Figure 3 showed the emission spectrum of free EB (5 x 10^{-7} M) (curve a) at 610 nm when excited at 510 nm. The addition of DNA (0.83 x 10^{-7} to 1.25 x 10^{-5} M) into the EB solution increased the emission and shifted to 595 nm (curve b). The shifted of about 15 nm indicated the effect of the intercalation EB into DNA. The change was observed because of the intercalation of EB into hydrophobic environment between the DNA base pair that isolated EB from the water molecules. The intercalation of EB into DNA leading to lengthening of the ethidium excited-state lifetime, that increase the emission spectrum (Ding et al., 2010; Pasternack et al., 1991).

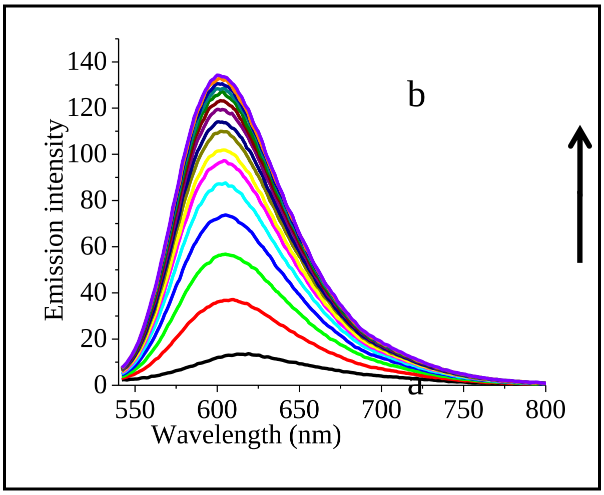

Figure 3. Fluorescence emission spectra of free EB (curve a) and DNA-bound EB (curve b). The arrow indicates the change in emission upon increasing the DNA concentration.

When DNA-bound EB was saturated, TBABr:EG was titrated continuously into the DNA-bound EB solution. It was suggested that the TBA^+ cation attracted to the negative DNA phosphate group through electrostatic attraction. As shown in Figure 4, TBABr:EG was continued added from concentration of 0.025M to 0.830M (curves c-i). The stronger electrostatic attraction was formed and resulted for DNA compaction (Satpathi et al., 2015). Hence, there are insufficient spaces for EB probe, which lead for the release of EB from DNA. This can be observed through a decreased of EB emission spectra (Ding et al., 2010; Ghosh et al., 2014; Manojkumar et al., 2015). The results indicated that the electrostatic attraction between DES and DNA is not only strong, but also able to remove EB from DNA. The similar findings were observed from previous studies by Ding et al. (2010). They stated that the intercalation of EB into DNA was prevented due to the compaction of DNA by ionic liquids (ILs). When increasing DES's concentration, the emission spectra also red shifted to a longer wavelength from 600 to 616 nm as indication of EB release from DNA. The quenching process of DNA-bound EB with other DESs, TBABr:1,3-PD, TBABr:1,5-PD and TBABr:Gly are shown in Figure 5,6 and 7 respectively.

However, there were differences in the concentration of DES required to induce an equal extent of fluorescence quenching even similar fluorescence quenching were observed in the addition of all synthesized DES into DNA-bound EB. To quantitatively compare the quenching efficiency, the fluorescence data were analyzed by the Stern-Volmer equation (equation 1) (Anjomshoa et al., 2014):

$$\frac{I_o}{I} = 1 + K_{SV}[Q] \qquad (1)$$

K_{sv} is the Stern-Volmer quenching constant and Q is the DES. The value of K_{sv} is obtained from the slope of the Stern-Volmer plot of I_o/I vs. [DES]. The DESs quenching of DNA-bound EB were in good agreement with the linear Stern-Volmer equation. The linear correlation coefficient (r^2) for each curve was found to be 0.98 to 0.99, which represented excellent linearity. Figure 8 shows the Stern-Volmer plot of different DESs plotted in one graph to compare the ability of each DES to quench DNA-bound EB. It was observed that TBABr:1,5-PD (6.36 M^{-1}) had the highest K_{sv} value, followed by TBABr:1,3-PD (5.90 M^{-1}), TBABr:EG(5.69 M^{-1}) and TBABr:Gly (4.15 M^{-1}) (Table 1).

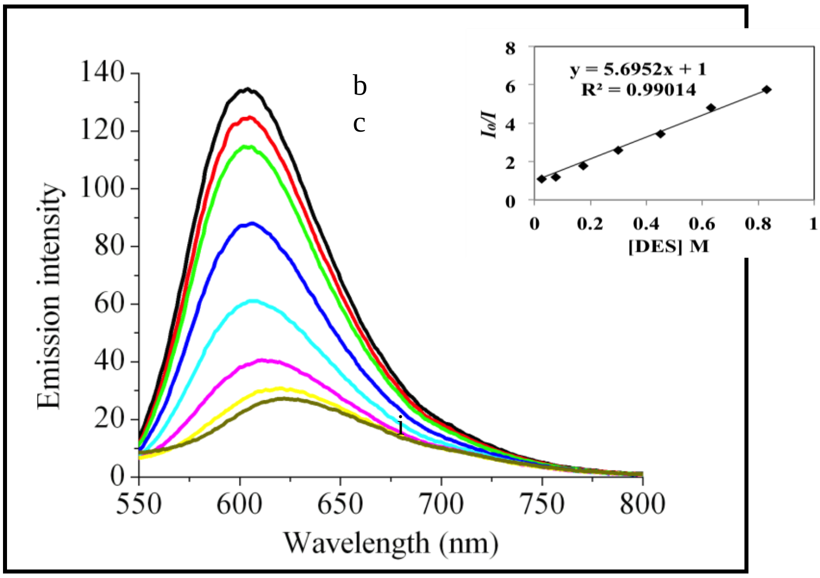

Figure 4. Fluorescence emission spectra of DES quench DNA-bound EB containing different concentrations of TBABr:EG with [DNA]=0.0025M, [EtBr]=0.5 µM, [DES]=0 M(curve b) to 0.83M (curve i). The arrow indicates the change in emission upon increasing the DNA concentration.

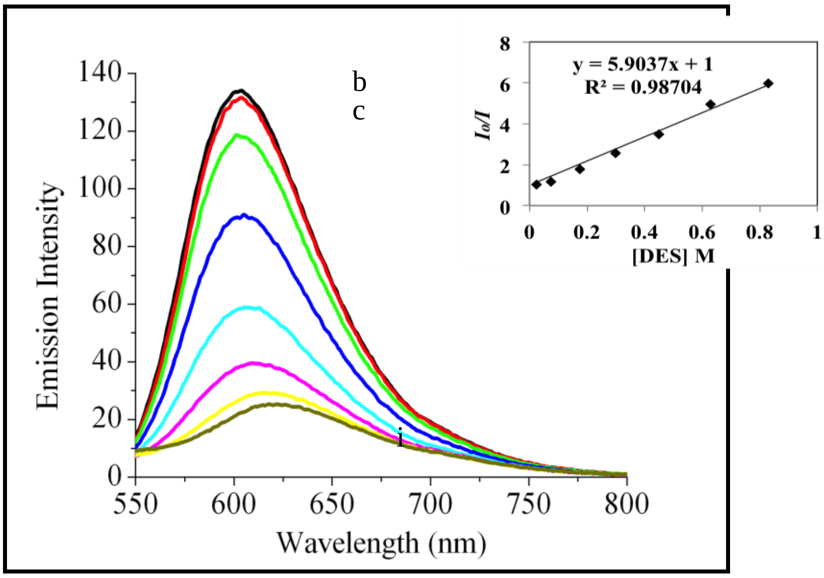

Figure 5. Fluorescence emission spectra of DES quench DNA-bound EB containing different concentrations of TBABr:1,3-PD with [DNA]=0.0025M, [EtBr]=0.5 µM, [DES]=0 M(curve b) to 0.83M (curve i). The arrow indicates the change in emission upon increasing the DNA concentration.

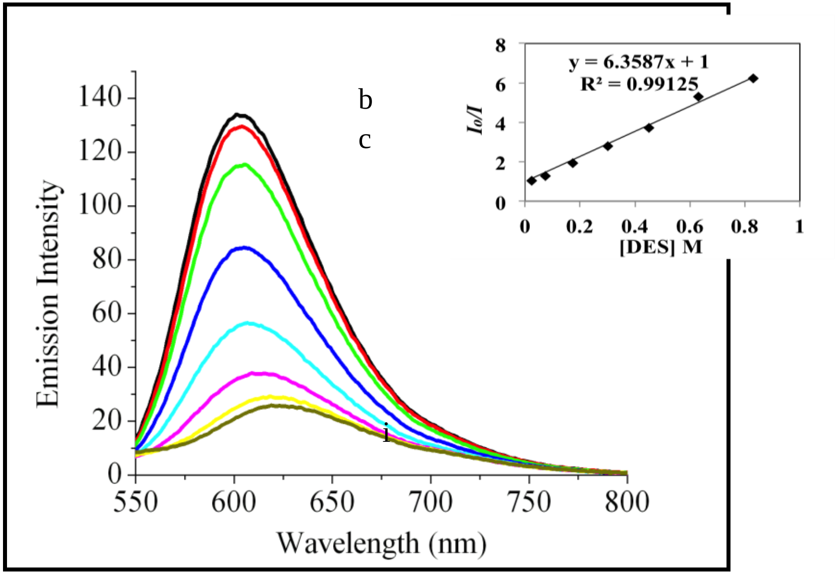

Figure 6. Fluorescence emission spectra of DES quench DNA-bound EB containing different concentrations of TBABr:1,5-PD with [DNA]=0.0025M, [EtBr]=0.5 µM, [DES]=0 M(curve b) to 0.83M (curve i). The arrow indicates the change in emission upon increasing the DNA concentration.

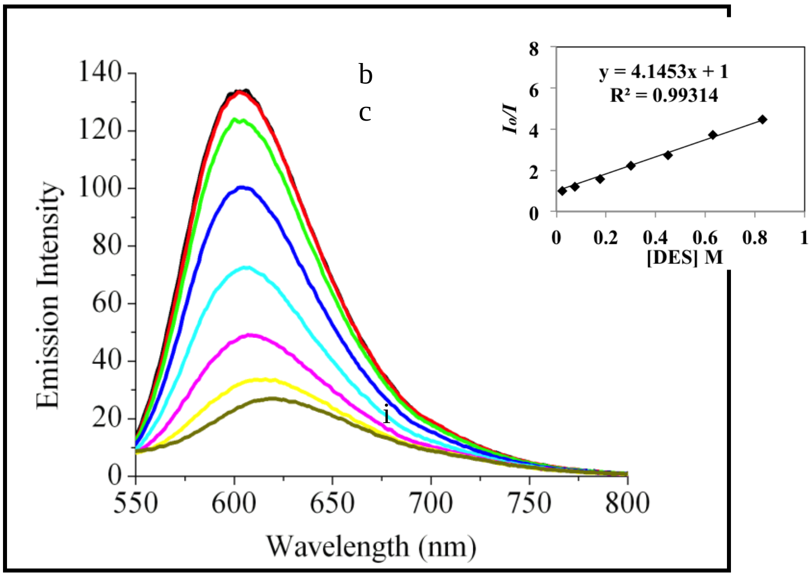

Figure 7. Fluorescence emission spectra of DES quench DNA-bound EB containing different concentrations of TBABr:Gly with [DNA]=0.0025M, [EtBr]=0.5 µM, [DES]=0 M(curve b) to 0.83M (curve i). The arrow indicates the change in emission upon increasing the DNA concentration.

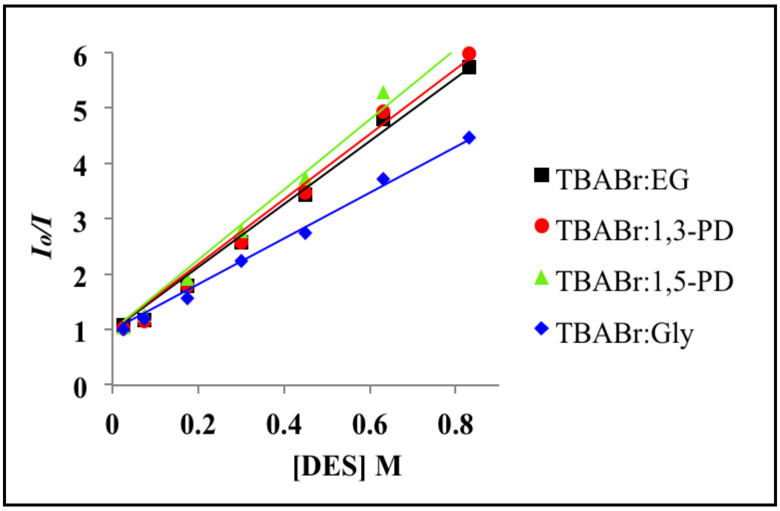

Figure 8. The Stern-Vomer plots for the quenching of different DESs to DNA-bound EB.

Table 1. The Stern-Volmer quenching constant (K_{sv}) of different DES to DNA-bound EB.

DES	K_{sv} (M^{-1})
TBABr:EG	5.69
TBABr:1,3-PD	5.90
TBABr:1,5-PD	6.36
TBABr:Gly	4.15

As shown in Table 1, the DES with the longest HBD, TBABr:1,5-PD had the highest quenching efficiency in removing EB from DNA. This finding is in agreement with the previous studies of binding between the cationic surfactants and DNA. The big cationic surfactant such as dihexadecyldimethylammonium bromide (DHDAB) and cetyltrimethylammonium chloride (CTAC) were more effective in dissociating the EB from complex compare to the smaller cationic surfactant; tetramethylammonium chloride (TMAC) (Bhattacharya and Mandal, 1997). The release of EB from DNA was attributed from the hydrophobic interactions between the hydrocarbon chains of TBA^+ cation on DES with the bases of DNA (Ding et al., 2010).

Hence, these results proposed that other than $-CH_2$ group on cation, the $-CH_2$ group on HBD also interacts with DNA to quench EB from DNA, at different level. The quenching efficiency increased with more $-CH_2$ unit on DES, owed to hydrophobic interaction to dissociate DNA. The efficiency of TBABr:EG and TBABr:1,3-PD to quench EB was almost similar due to the difference of only one unit of $-CH_2$ on HBD. Meanwhile, TBABr:Gly had the weakest ability to quench EB from DNA, although the number of $-CH_2$ groups on HBD was similar to TBABr:1,3-PD. The glycerol on TBABr:Gly consists of 3 -OH group compare to other DESs, only 2 –OH group. The presence of extra $^-$OH group on glycerol had reduced the hydrophobic effect on DES, hence decreased the ability of the TBABr:Gly to remove EB from DNA. The result confirmed the importance of hydrophobic effect of DES to destabilize of the DNA-bound EB complex.

Conclusions

The binding and interactions between TBABr-based DES and DNA were studied by fluorescence quenching technique. The fluorescence quenching of DESs; TBABr:EG, TBABr:1,3-PD, TBABr:1,5-PD and TBABr:Gly into DNA-bound EB were done to prove the ability of DESs to interact with DNA. When DESs were added, TBA^+ cation compacted DNA structure and led for the released of EB from DNA. The mechanism proved that TBA^+ cation could bind to DNA phosphates to form DES-DNA complexes through the electrostatic attraction. The process confirmed that DES is sufficiently strong to remove EB from DNA. Through studies, it was concluded that DES with the longest HBD, TBABr:1,5-PD had the highest quenching efficiency in removing EB from DNA. Hence, other than electrostatic interaction, it was suggested that the hydrophobic interaction occurred between the hydrocarbon chains of TBA^+ cation on DES with the bases of DNA. The quenching efficiency increased with the increased of hydrophobic part on DES, due to hydrophobic interaction to dissociate DNA from EB. Therefore, the studies on the interaction between DES and DNA will help in understanding the mechanisms of quenching since it could be used as a basis for future development of specific DESs for nucleic acid technology.

Acknowledgements

This work was supported by the Research University Grant Scheme (RUGS 9341900) from Universiti Putra Malaysia. Rizana Yusof thanks the Universiti Teknologi MARA (UiTM) and the Ministry of Education, Malaysia for the award of a scholarship. Mohd Basyaruddin Abdul Rahman acknowledges the Genetic and Molecular Biology Initiative, Malaysia Genome Institute (MGI), Malaysia for the facilities provided.

References

Abbott, A. P., Capper, G., Davies, D. L., McKenzie, K. J., and Obi, S. U. (2006). Solubility of Metal Oxides in Deep Eutectic Solvents Based on Choline Chloride. Journal of Chemical & Engineering Data, 51(4), 1280–1282.

Abbott, A. P., Capper, G., Davies, D. L., and Rasheed, R. K. (2004). Ionic liquid analogues formed from hydrated metal salts. Chem. Eur. J., 10(15), 3769–3774.

Abbott, A. P., Capper, G., Davies, D. L., Rasheed, R. K., and Tambyrajah, V. (2003). Novel solvent properties of choline chloride/urea mixtures. Chemical Communications, (1), 70–71.

Anjomshoa, M., Fatemi, S. J., Torkzadeh-Mahani, M., and Hadadzadeh, H. (2014). DNA- and BSA-binding studies and anticancer activity against human breast cancer cells (MCF-7) of the zinc(II) complex coordinated by 5,6-diphenyl-3-(2-pyridyl)-1,2,4-triazine. Spectrochimica Acta - Part A: Molecular and Biomolecular Spectroscopy, 127, 511–520.

Bhattacharya, S., and Mandal, S. S. (1997). Interaction of surfactants with DNA. Role of hydrophobicity and surface charge on intercalation and DNA melting. Biochimica et Biophysica Acta - Biomembranes, 1323(1), 29–44.

Ding, Y., Zhang, L., Xie, J., and Guo, R. (2010). Binding characteristics and molecular mechanism of interaction between ionic liquid and DNA. The Journal of Physical Chemistry. B, 114(5), 2033–2043.

Francisco, M., van den Bruinhorst, A., and Kroon, M. C. (2012). New natural and renewable low transition temperature mixtures (LTTMs): screening as solvents for lignocellulosic biomass processing. Green Chemistry, 14(8), 2153–2157.

Ghosh, S., Banik, D., Roy, A., Kundu, N., Kuchlyan, J., and Sarkar, N. (2014). Spectroscopic investigation of the binding interactions of a membrane potential molecule in various supramolecular confined environments: contrasting behavior of surfactant molecules in relocation or release of the probe between nanocarriers and DNA surfa. Physical Chemistry Chemical Physics : PCCP, 16(45), 25024–38.

Gorke, J., Srienc, F., and Kazlauskas, R. (2010). Toward advanced ionic liquids. Polar, enzyme-friendly solvents for biocatalysis. Biotechnology and Bioprocess Engineering, 15(1), 40–53.

Izumrudov, A., Zhiryakova, V., and Goulko, A. (2002). Ethidium Bromide as a Promising Probe for Studying DNA Interaction with Cationic Amphiphiles and Stability of the Resulting Complexes. Langmuir, 18(3), 10348–10356.

Mamajanov, I., Engelhart, A. E., Bean, H. D., and Hud, N. V. (2010). DNA and RNA in anhydrous media: duplex, triplex, and G-quadruplex secondary structures in a deep eutectic solvent. Angewandte Chemie, 49(36), 6310–6314.

Manojkumar, K., Prabhu Charan, K. T., Sivaramakrishna, A., Prakash, C., Jha, V.M.K, Siva, R., Jayaraman, G., and Vijayakrishna, K. (2015). Biophysical Characterization and Molecular Docking Studies of Imidazolium Based Polyelectrolytes–DNA Complexes: Role of Hydrophobicity. Biomacromolecules, 16, 894–903.

Mukesh, C., Mondal, D., Sharma, M., and Prasad, K. (2013). Rapid dissolution of DNA in a novel bio-based ionic liquid with long-term structural and chemical stability: successful recycling of the ionic liquid for reuse in the process. Chemical Communications, 49(61), 6849–6851.

Pasternack, R. F., Caccam, M., Keogh, B., Stephenson, T. a, Williams, a P., and Gibbs, E. J. (1991). Long-Range Fluorescence Quenching of Ethidium Ion by Cationic Porphyrins in the Presence of DNA. J. Am. Chem. Soc., 113(18), 6835–6840.

Satpathi, S., Sengupta, A., Hridya, V. M., Gavvala, K., Koninti, R. K., Roy, B., and Hazra, P. (2015). A Green Solvent Induced DNA Package. Scientific Reports, 5, 1–9.

Sharma, M., Mondal, D., Singh, N., Trivedi, N., Bhatt, J., and Prasad, K. (2015). High concentration DNA solubility in bio-ionic liquids with long-lasting chemical and structural stability at room temperature. RSC Adv., 5(51), 40546–40551.

Sirajuddin, M., Ali, S., and Badshah, A. (2013). Journal of Photochemistry and Photobiology B : Biology Drug – DNA interactions and their study by UV – Visible , fluorescence spectroscopies and cyclic voltametry. Journal of Photochemistry and Photobiology B: Biology, 124, 1–19.

Smith, E. L., Abbott, A. P., and Ryder, K. S. (2012). Deep Eutectic Solvents (DESs) and Their Applications. Chem. Rev, 114(21), 11060-11082

Street, N. S. (1995). Criteria for the Mode of Binding of DNA Binding Agents. Bioorganic & Medicinal Chemistry, 3(6), 723–728.

Xie, Y. N., Wang, S. F., Zhang, Z. L., and Pang, D. W. (2008). Interaction between room temperature ionic liquid [bmim]BF4 and DNA investigated by electrochemical micromethod. The Journal of Physical Chemistry. B, 112(32), 9864–9868.

Yusof, R., Abdulmalek, E., Sirat, K., and Rahman, M. B. A. (2014). Tetrabutylammonium Bromide (TBABr)-Based Deep Eutectic Solvents (DESs) and Their Physical Properties. Molecules (Basel, Switzerland), 19(6), 8011–8026.

Zhao, H. (2014). DNA stability in ionic liquids and deep eutectic solvents. Journal of Chemical Technology & Biotechnology, 90, 19-25

SUPERHYDROPHOBIC SURFACE DEVELOPMENT BASED ON POLYURETHANE CHEMISTRY FOR COATING MATERIALS

SEHER ŞENADA, SENNUR DENIZ

Seher Şenada ,MSc Degree,Yıldız Technical University, Sennur Deniz, Assist.Prof.Dr., Chemical Engineering Deparment,Yıldız Technical University
Davutpaşa Cd., 34210, Esenler- Istanbul/Turkey

Abstract

The work is based on the superhydrophobic surfaces has been developed for the textile and construction applications, and related with the preparation of fluorine-modified polyurethanes (FPUs) as coating material.

Polymeric structure of FPUs is formed by reacting an excess of aliphatic diisocyanates (IPDI, HDI and H12MDI) with a polyether polyol (Voranol 2000 L, Mw: 2000 g/mol) to form a prepolymer. Reactions were maintained by different NCO/OH molar ratios with the presence of tin based catalyst because of aliphatic diisocyanates is less reactive. Then the prepolymer is modified by fluorinated diols. To increase the molecular weight of FPUs, a low molecular weight diol (1,4 butandiol) was used as chain extender in all reactions.

The effects of NCO/OH molar ratio and diisocyanate type on the thermal and structural properties of FPUs were characterized by using differential scanning calorimeter (DSC) and FTIR. Dynamic contact angles of FPU films were measured to investigate the surface hydrophobicity.

Keywords: fluorine; polyurethane; hydrophobic surface

Introduction

Polyurethanes (PUs) consisting of alternating soft and hard segments are one of the most actively investigated polymers because of their wide range of properties (Lelah, Cooper, 1986).These polymers find applications in many different fields, including breathable waterproof textiles, synthetic leathers, shrink-proof wools, adhesives, and fine chemicals (Yen,Tsai,Hong,2006)

Generally, superhydrophobic surfaces are created through the combination of surface roughening and lowering of the surface energy (Miwa, Nakajima, Fujishima, Watanabe, Hashimoto, 1999). It is well known that a fluorinated polymer has a low wettability due to its low surface energy. Therefore, it is an ideal building block to develop a superhydrophobic coating. On the other hand, the low wettability is basically a surface property, so it is unnecessary to have fluorine in the bulk.

Fluorine polymers, commonly referred to as fluoropolymers, can greatly enhance the properties of coatings used in modern industrial, household and construction products. The qualities of fluoropolymer resins and oligomeric additives make them an ideal solution for applications requiring a high resistance to solvents, acids and bases, and most importantly an ability to significantly reduce friction (James,2008)

Polyfluorourethanes can be produced from fluorinated diols and a traditional diisocyanate, or a fluorinated diisocyanates and traditional diols. Polymers manufactured via the latter process have been shown to be nonflammable with good low temperature flexibility while providing excellent corrosion resistance (Rochow and Stump, 1971). The hardness can be controlled by changing the ratio of perfluorinated diisocyanate to diol. Coatings based on some fluorourethane resins exhibit hydrophobic and super hydrophobic properties and find applications in textile and construction.

Experimental

2.1. Materials:

The specifications of chemicals used for the synthesis of FPUs are given in Table 1.

Materials	Specifications	Supplier
Voranol 2000 L	Average Molecular Weight : 2000 g/kg Hydroxyl Number : 56.0mg KOH/g Water, max : %0.05	Dow Chemicals
Isophorone diisocyanate (IPDI)	Average Molecular Weight : 222 g/kg NCO content (%) :37.8%	Evonik
Dicyclohexylmethane diisocyanate (H12MDI)	Average Molecular Weight : 262 g/kg NCO content (%) :32.0%	Bayer
1,6-hexamethylene diisocyanate (HDI)	Average Molecular Weight : 168 g/kg NCO content (%) :50.0%	Bayer
Dibutyltin dilaurate (DBTDL)	Appearance : Yellowish Liquid Average Molecular Weight : 632 g/kg	Ruikechem
Fluorolink Polymer Modifier	Average Molecular Weight : 700 g/kg Fluorine content (%) :61.0% Appearance: Clear, colorless liquid	Solvay
1,4-Butandiol	% Moisture (Karl Fischer) : <=0.04 % Purity (GC) : >=99.5 % B1D Monocyclic Acetal (GC) : <=0.1 Carbonyl Number : <=0.5 mg KOH/g	ISP

Table 1.Chemicals Used for Synthesis of FPU

2.2. Synthesis of fluorine-containing polyurethane (FPU):

Nine fluoromodified polymer dispersions with different hard to soft segments molar ratios (NCO/OH = 1.5, 1.8 and 2.0) were prepared by the melting process.

All the reactions were carried out in a 500 mL three necked round-bottom glass reactor at isothermal conditions in a flask heating mantle. The reactor was equipped with a mechanical stirrer and a nitrogen inlet. In the first step, the polyol and diisocyanate were added to a glass reactor equipped with a mechanical stirrer to obtain the prepolymer. The reactions were carried out at 90°C under nitrogen atmosphere. The mixture was stirred for 2 hours at 90°C then the amount of residual NCO groups estimated by n-dibutylamine titration. After that, DBTDL and fluorolink polymer modifier were added into the reactor at 90°C. The reaction was followed under nitrogen purging at a mixing rate of 200 rpm until a visible viscosity change was observed; otherwise, it was continued for 1 hour and free NCO determined by n-dibutylamine titration. Afterwards, the chain extender (1,4-butanediol) was added to complete the reaction with the unreacted NCO groups. Finally, synthesized FPUs were casted with a casting knife on stainless steel plate to form the FPU films.

Sample Number*	Diisocyanate Type	r (NCO/OH)	Reaction Temperature (°C)	Film Property	Appearance
PU1-2.0	H_{12}MDI	2.0	90	√**	White viscous liquid
PU1-1.8		1.8	90	√	White viscous liquid
PU1-1.5		1.5	90	√	White viscous liquid
PU2-2.0	HDI	2.0	90	√	White viscous liquid
PU2-1.8		1.8	90	√	White viscous liquid
PU2-1.5		1.5	90	√	White viscous liquid
PU3-2.0	IPDI	2.0	90	n.a***	White low viscous
PU3-1.8		1.8	90	n.a	White low viscous
PU3-1.5		1.5	90	n.a	White liquid

Table 2. Specifications of Synthesized FPU.

* The nomenclature of the waterborne polyurethane dispersions consists in the capital letters PU followed by the NCO/OH ratio

** √: Film occurred

***n.a: Film did not occur

2.3. Characterization of the polyurethane films

2.3.1. Infrared Spectroscopy (FTIR spectroscopy).

The FTIR spectra of the polyurethane films were obtained in PerkinElmer Spectrum One model. Measurements were carried out in the attenuated total reflectance mode by using a ZnSe prism. An incidence angle of the IR radiation of 45° was used, and 100 scans were averaged with a resolution of 4 $cm^{-1.}$

2.3.2. Differential Scanning Calorimeter (DSC).

DSC experiments were carried out in PerkinElmer Jade DSC model instrument. Aluminum pans containing 10–15mg of sample were heated from 25°C to 400 ◦C under nitrogen atmosphere (flow rate: 50 ml/min). The heating rate was 10°C/min. The melting points (Tm) in a DSC, you get not only the onset of melting, the Tm, but also the peak temperature, which corresponds to complete melting in organics and the energy that the melting transition needs in order to occur. This is the enthalpy of the transitions, and it is associated with the crystallinity of materials.

2.3.3. Contact Angle Measurement

Contact angle, θ, is a quantitative measure of the wetting of a solid by a liquid. It is defined geometrically as the angle formed by a liquid at the three-phase boundary where a liquid, gas and solid intersect. As shown below it is the angle between the solid and the tangent to the drop profile at the intersection point.

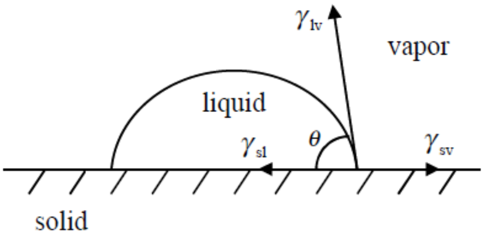

Figure 1. A water droplet on smooth surface.

Contact angle is defined as the angle between the surface of the solid and the liquid at the
point where the liquid surface touches the solid.
Low values , θ of indicate that the liquid spreads, or wets, well while high values indicate
poor wetting. If the angle is less than 90° the liquid is said to wet the solid. If it is greater than 90° it is said to be non-wetting. A zero contact angle represents complete wetting. The values of static contact angles (where the drop is not in motion) are found to depend on the recent history of the interaction. When the drop has recently expanded the angle it is said to represent the advanced contact angle. When the drop has recently contracted the angle is said to represent the receded contact angle. These angles fall within a range with advanced angles forming a maximum value and receded angles forming a minimum value.
If the three-phase boundary is in actual motion the angles produced are called dynamic
contact angles and are referred to as advancing or receding angles. The difference between advanced and advancing (or receded and receding) is that in the static case motion is incipient and in the dynamic case motion is actual. Dynamic contact angles may be measured at various speeds and low velocities they should be equal to static angles. The difference between an advanced and a receded contact angle is known as contact angle hysteresis. Hysteresis can be used to characterize surface heterogeneity, roughness and mobility.
Contact angles were measured using a Sigma 700 Tensiometer instrument at room temperature. Measurement method is defined as follow: Measuring contact angles with a tensiometer is done by lowering a solid sample from above the liquid to a certain depth in the liquid and then out again. This cycle can be repeated several times to identify variations in surface structure and notice adsorption phenomena. Force readings are taken throughout the cycle. The force on the balance is given by the following equation.
F_{TOTAL} = wetting force + weight of probe – buoyancy
The weight of the probe is obtained from the force reading at the start of the experiment
before the probe touches the liquid (wetting force = buoyancy = 0). Buoyancy is directly proportional to the depth of immersion and thus it can be extrapolated from the force readings during immersion. Wetting force is defined as:

wetting force = $\gamma_{LV} P \cos\theta$

Where P is the perimeter of the probe. The actual experiment consists of four phases.

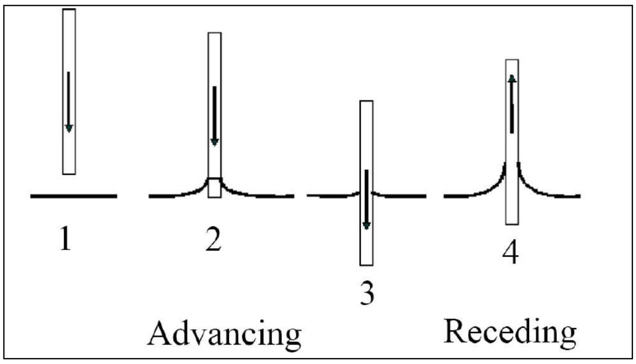

Figure 2. The experiment consists of four phases.

Dipping a plate into a liquid to calculate contact angle data when contact angle is less than 90°. The force readings measured for each phase is shown below.

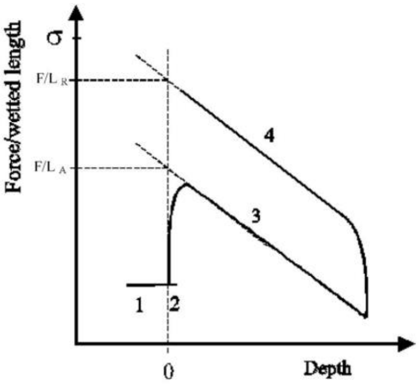

Figure 3. Graph of force per wetted length against depth of immersion.

Phase 1) The probe is above the water and is lowered until the probe touches the surfaces. The force/length reading is zeroed.
Phase 2) The probe hits the surface, indicated by the change in force. The depth is zeroed. In this case the contact angle is less than 90°.
Phase 3) The probe is immersed into the liquid until a set depth, and the force/length value decreases due to the increase in buoyancy. Data on advancing angles is obtained.
Phase 4) The probe reverses direction and is pulled up. Force/length increases as buoyancy decreases, and data on receding angles is obtained.
When the probe is pulled above the water the recorded data points are same as those in phase 1, and if the probe is pushed into the water again a new loop begins.
Once the effects of buoyancy are removed, the force/length reading consists of only the wetting force as explained above. As surface tension and perimeter are constant the difference between the advancing (F/L a) and receding (F/L r) values is accounted for by the difference in the contact angle.

Result and Discussion
Characterization of the polyurethane films
The syntheses of FPUs were confirmed by FTIR analysis as shown in Fig. 4. In IPDI spectrum, there were characteristic absorptions of –NCO group (2256 cm^{-1}). In Voranol 2000 L spectrum, there were characteristic absorptions of –OH group (3481 cm^{-1}) and aliphatic C–H stretch (2868–2970cm^{-1}), C–F stretch (1274 cm^{-1}). The characteristic absorptions of N–H stretching (3318 cm^{-1}) and C O (1715 cm^{-1}) appeared; it proved carbamoyl NHCOO– was formed in FPU.
The chemistry of the polyurethane films was analyzed by FTIRs spectroscopy. The most relevant IR bands correspond to N–H stretching at 3338cm^{-1}, C-N stretching and N-H stretching at 1531cm−1, C–H stretching at 2938 and 2855cm−1, and C O stretching due to urea (1700–1648cm−1) and urethane (1739–1717cm−1) groups .On the other hand, the FTIR spectra show the characteristic C–O and N–CO–O stretching (1242 and 1035cm−1), and C–O–C stretching (1162 and 955cm−1) bands of the polyol.

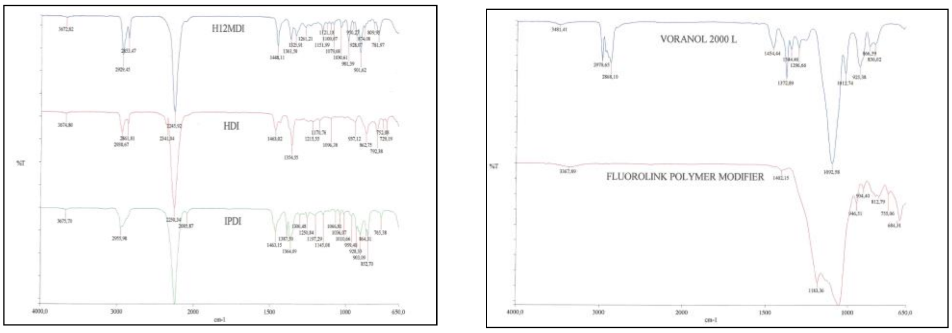

(b)

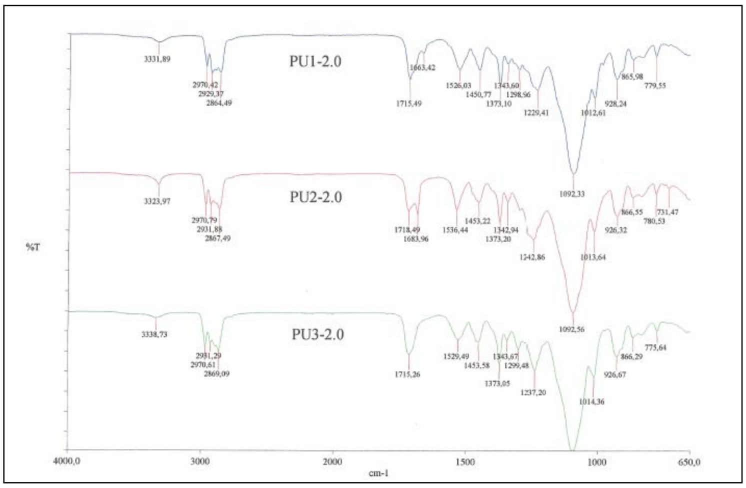

(c)

Figure 4. FTIR spectrums of raw materials and FPUs

Aliphatic isocyanates: hexamethylene diisocyanate (HDI), isophorone diisocyanate (IPDI)
and (4,4'–diisocyanatodicyclohexylmethane (H12MDI), improve thermal and hydrolytic stability, resistance to UV degradation and they do not yellow (Bechara, 1998). Aliphatic diisocyanates are less reactive than aromatic ones and they must be used with certain catalysts.

PU are synthesized by the prepolymer reaction of a diisocyanate and a polyol (mainly polyethers and polyesters). If a diol of low molecular weight reacts with –NCO-terminated prepolymers in the chain extension reaction step, urethane linkages will also be formed. In this case, poly(urethaneurea)s, which are the most important class of polyureas, are produced. These copolymers show reduced plasticity in comparison to homopolyurethanes. The resulting PU or poly(urethaneurea) chains consist of alternating short sequences forming soft (flexible) and hard (rigid segments). The soft segments, originated from the polyol, impart elastomeric characteristics to the polymer. The hard segments are mainly produced by reacting the isocyanate and the chain extender. They are polar and impart mechanical properties to PU. The hard segments contain the highly polar urethane linkages.

Polyether polyol reacted with aliphatic isocyanates with different NCO/OH molar ratio.Contact angle and T_m values are shown in Table 3.

Sample Number*	Diisocyanate Type	r (NCO/OH)	Contact Angle,θ (°)	T_m(°C)
PU1-2.0	H_{12}MDI	2.0	110	265
PU1-1.8		1.8	100	-
PU1-1.5		1.5	-*	-
PU2-2.0	HDI	2.0	80	200
PU2-1.8		1.8	-	-
PU2-1.5		1.5	-	-
PU3-2.0	IPDI	2.0	n.a**	140
PU3-1.8		1.8	n.a	-
PU3-1.5		1.5	n.a	-

Table 3. Results of Contact Angle Measurement and T_m

*- : no measurement

**n.a: Not acceptable

Conclusion

In this work, we designed and synthesized a novel fluorinated macro polymer. The superhydrophobic FPU coating materials were synthesized with a polyether polyol, flurionated modifed polyol and different types of aliphatic diisocyanates. It was found that NCO/OH molar ratio and aliphatic diisocyanate type are most effective on film formation and contact angle values of FPU films. The water contact angle value of smooth FPU film based on H12MDI about 110° were obtained from PU1-2.0 sample which was synthesized with NCO/OH ratio: 2. Of course there are still many challenges ahead for optimization of these superhydrophobic coatings.

Acknowledgment

The authors are thankful to the authority of the Yıldız Technical University for providing necessary facility for doing our research work. Financial and experimental support by CHT Tekstil Kimya is gratefully acknowledged.

References

[1]M.D. Lelah, S.L. Cooper, Polyurethane in Medicine, CRC Press, Boca Raton, FL, 1986.

[2]Masashi Miwa, Akira Nakajima,Akira Fujishima,Kazuhito Hashimoto,and Toshiya Watanabe Received December 20, 1999. In Final Form: March 22, 2000 Various

[3]M.S. Yen, H.C. Tsai, P.D. Hong, J. Appl. Polym. Sci. 100 (2006) 2963.

[4]Barry Jones,'' Halocarbon Products Corporation'',September 2008; JCT CoatingsTech Magazine

[5]Rochow, S. E.; Stump, E. C., Jr., "Preparation of highly fluorinated polyurethanes," 1971; NASA Technical Reports Server

[6]M.A. Pérez-Limiñana, F. Arán-Aís, A.M. Torró-Palau, A.C. Orgilés-Barceló, J.M. Martín-Martínez, Int. J. Adhes. Adhes. 25 (2005) 507–517.

[7]Bechara I. (1998) Formulating with polyurethane dispersions. Eur. Coat. J., 4, pp. 236–243.

INCORPORATING PROTEIN FLEXIBILITY IN THE IDENTIFICATION OF SMALL MOLECULES AS PROTEIN ARGININE DEIMINASE IV (PAD4) INHIBITORS

ZALIKHA IBRAHIM, BIMO A. TEJO, MUHAMMAD ALIF MOHAMMAD LATIF, MOHD BASYARUDDIN ABDUL RAHMAN

Abstract

Protein arginine deiminase type IV (PAD4) is a promising target in the treatment of rheumatoid arthritis. Virtual screening against a single receptor structure is a conventional practice. However, binding site flexibility information is unattainable using this method. In this work, an ensemble-based virtual screening approach was employed to screen small molecules as PAD4 inhibitors. The binding interactions between PAD4 and top compounds were analyzed. The effect of protein flexibility in the screening was also discussed. The information reported could serve as the basis for future works targeting this enzyme.

THERMAL AND MECHANICAL PROPERTIES OF COMPRESSION-MOLDED POLY (LACTIC ACID)/GLUTEN/CLAYS BIO(NANO)COMPOSITES

ABDELLATIF MOHAMED

Abstract

Poly (lactic acid) (PLA), wheat vital gluten (VG), and 3, 6, and 9% clays (NC1 or NC2) were mixed in a Haake Rheocord torque rheometer at 170°C for 10 min. Blends were compression molded and tested using modulated DSC (MDSC), thermogravimetric analysis (TGA), Instron, FTIR, and HPLC. Neat PLA profile exhibited a glass transition (Tg) and exothermic (Cry) followed by endothermic (Mel) transitions. The profile showed a Tg of 0.46 J/g/°C, Cry with 29.6 J/g, whereas Mel exhibited 28.3 J/g. Vital wheat gluten displayed a single Tg (0.45 J/g/°C). Enthalpic relaxation of PLA was noted in the presence of clays, where the overall DSC profiles of PLA were different especially during melting. The hydrophobic nature of NC1 clay created shoulders during PLA melting. The degradation kinetics of the blends followed a multistep mechanism as shown by the TGA data. The tensile strength dropped because of processing and due to the addition of clay, whereas elongation was reduced by NC1. Higher Young's modulus value due to NC1 or NC2 indicates stiffer bio(nano)composite. Proteinase-K enzyme treatment indicated better biodegradability in presence of NC1. Due to the hydrophobic nature of NC1, the amount of the acetic acid extractable protein was reduced. The FTIR analysis showed no evidence of chemical reaction between PLA, gluten and the clays, but suggested the occurrence of significant non-covalent intermolecular interactions.

PHYTOREMEDIATION OF PETROLEUM RELEASES BY PHRAGMITE AUSTRALIS

AMEL NASRI, SEGNI LADJEL, FATIHA DJAFRI, AYADA DJAFRI

Laboratory of Process Engineering , University Kasdi Merbah Ouargla.
Laboratory of Material Chemistry, University of Oran1.
Laboratory of Applied Organic Chemistry, University of Oran1.
mmeamelsalem@yahoo.com

Abstract

To remediate to pollution, new methodes are placed to assure the obtention of the best yields with the most possible reduced costs. among these methods we have choose phytoremediation because of the important scale of pollutants wich remediating plants can judiciously absorb. they are chosen according to concentrations and pollutants types to extract, and according to the type of soil and climatic conditions.

According to the types of pollutants present in the petrolium releases, we can fix our work on an overwhelming plant with rhizomes the common reed « phragmite australis » wich on top of his rhizoremediating character can resist to an extreme climatic conditions, to assure maximum of remediation according to the concentrations of pollutants.

For the realization of this study, the stumps of common reed have been harvested in the region of Ouargla in south east of algeria, cultivated in an experimental basin. To prepare this experimental basin, we have used a container as growing environment identical to the natural one wich contains 3 layers of soil, the first one is a waterproof layer (waterproof film, clay…………….), this layer is overcomed by a layer of several calibers of gravel wich is overcomes by sand to allow plantation of the plants.

The taked releases waters from several petroleum industrial sites in Ouargla as the plant stumps have not undergo any treatment and have been analysed before and after plant contact.

In order to eliminate the possibility of the intervention of the prepared soil in depollution, as well as some external parameters, we have proceed to the same handlings with a virgin container (without plant).

Two variable factors imposed themselves during water- plant contact, the first one is the quantity of deversed polluted water in the container, and the other one is its staytime, wich allow to determinate that the ideal values for the best depollution with respect of survival needs of the plant.

This study allow us to observe large variability of results according to volume of deversed water, and its staytimes. after several tests we have observed that the ideal staytime is 39 hours for a maximum volume of 2000ml of water for 100gr of hardy plant.

The pollution parameters analyzes (nitrites, nitrates, dbo, dco….) of the petrolum releases waters have been carried out according to the conventionnal experimental protocols before and after water-plant contact. The obtained results prove efficacity of the rhizoremediation by phragmite australis in all staytimes starting from the first 4 hours of contact. the average of the yields of pollutants retentions is 95%.

Keywords : phytoremediation, phragmite australis, pollution, green chemistry

X RAYS ANALYSIS OF MICROSTRUCTURE IN AL-LI ALLOYS

RACHIDA AMICHI, SMAINE BOURAHLA

Abstract

The superplastic behavior required a fine grain structure. This could be obtained by either static recristallization before superplastic deformation or for dynamic recristallization during the first stages of superplastic deformation (SPD).

The aluminum alloys witch develop a fine and equiaxed grain structure by the two previous recristallization modes, are Al-Li alloys. However these alloys remain partially recristallized during the first mode.

The object of the present work is to study the effect of natural aging and annealing on texture evolution of Al-Li alloy (8090) for a fixed temperature 530°C (superplastic deformation temperature). The experimental techniques used for texture evolution are X ray diffraction (XRD) and microhardness. For metallographic and electronic observations, optical and scanning electron microscopes (SEM have been used).

The observed results show the existence of three structurechanges of the studied material. The first one corresponds to the restoration stage followed by recristallization process.

However a grain growth structure is seen in the last stage .The only texture change is observed with grain growth.

Keywords: Al-Li, superplasticity, static recristallization, XRD

Introduction

The first priority of the twenty first century in aerospace transport is the use of light materials. The reasons are purely ecological in order to decrease greenhouse gas emissions and mostly economical in order to reduce energy consumption. Aluminum Lithium alloys was then developed. Indeed lithium addition in aluminum alloys diminishes their weights and increases Young modulus (1). This alloys show a superplastic behavior (2) .This is related to a fine and equiaxed grain structure developed in the alloy by static recristallization (before superplastic deformation SPD) or by dynamic recristallization (during the first stages of SPD). The required structure for superplastic flow can be obtained by both routes in only Al-Li alloys. However the alloy shows a resistance to static recristallization (3). The material shows a partially recristallized structure. Thus the object of this work is to study the effect of annealing time and temperature on the evolution of static recristallization process of Al-Li alloys.

Experimental procedure

The studied material is Al-Li alloy designed by 8090 lital A having a nominal chemical composition (weight %) showed in Table 1.

Table 1: Chemical composition of Al-Li alloy (weight %)

Al	Li	Cu	Mg	Zr
balance	2.5	1.2	0.6	0.1

The material was received in sheet form of 2 mm thickness. The samples were aged for two years then annealed at a fixed temperature i.e. 530°C (T_{SPD}) for various times within the range 4 to 48 hours. The heat treatments were performed in a furnace type Nabertherm. For metallographic observation and x rays analysis, the specimens were mechanically polished with different grades. The samples were cleaned in ultrasonic container then polished with diamant paste using different grades between 6-1/4 µm. In order to reveal the microstructure the samples were etched using Keller’s solution. X rays diffraction and microhardness were used for recristallization process study.

Results and discussions

Heat treatment effect

A/ Static recristallization

Figure1. shows x rays diffraction diagram for the as-received material .The different identified picks correspond to α-Al- matrix , whereas additional picks observed correspond to phase picks present in the alloy as β (Al_3Zr) and Ɵ (Al_2Cu). The main orientation is α (220) with relatively high intensity.

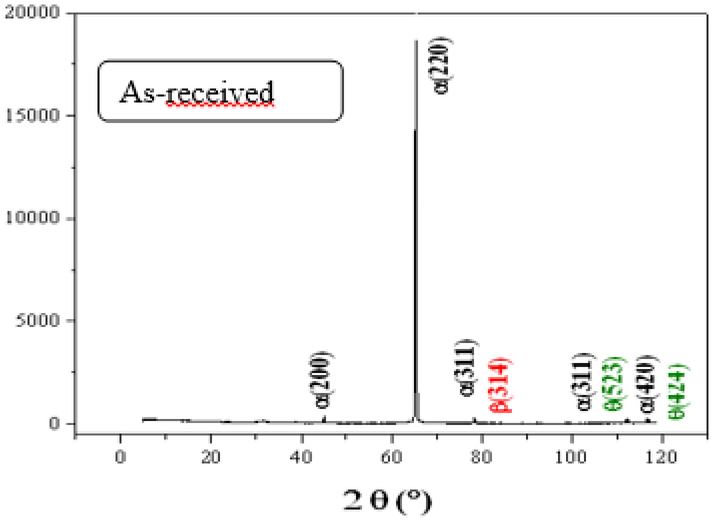

Figure 1: X rays diffraction diagram of as received material

The x rays diffraction patterns obtained for annealed samples at 530°C at various times within the interval 4 to 48 hours, are presented in Figure 2. It is shown that the preferential orientation remains α (220) for specimens annealed at 530°C from 4hs to 16 hours and 48hs similar to as seen in the as received material. It is noticed that its intensity drops as time increases. The only texture change appears in the specimen annealed during 24 hours where the major orientation passes to α (311). Similar studies (3,4) show the same behavior where the main orientation in naturally aged or heat treated alloy is α(220).

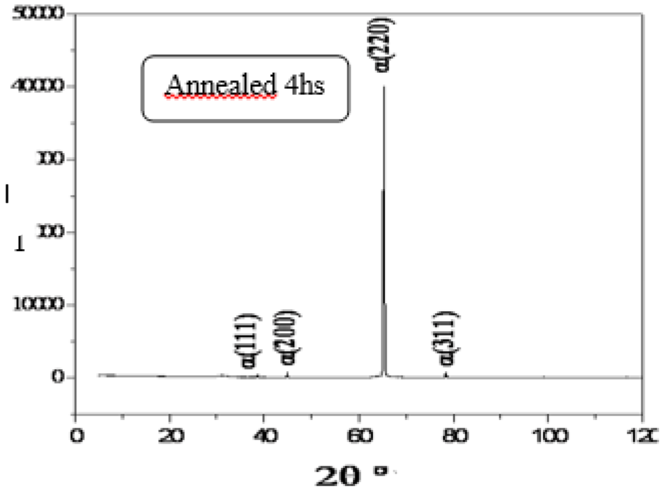

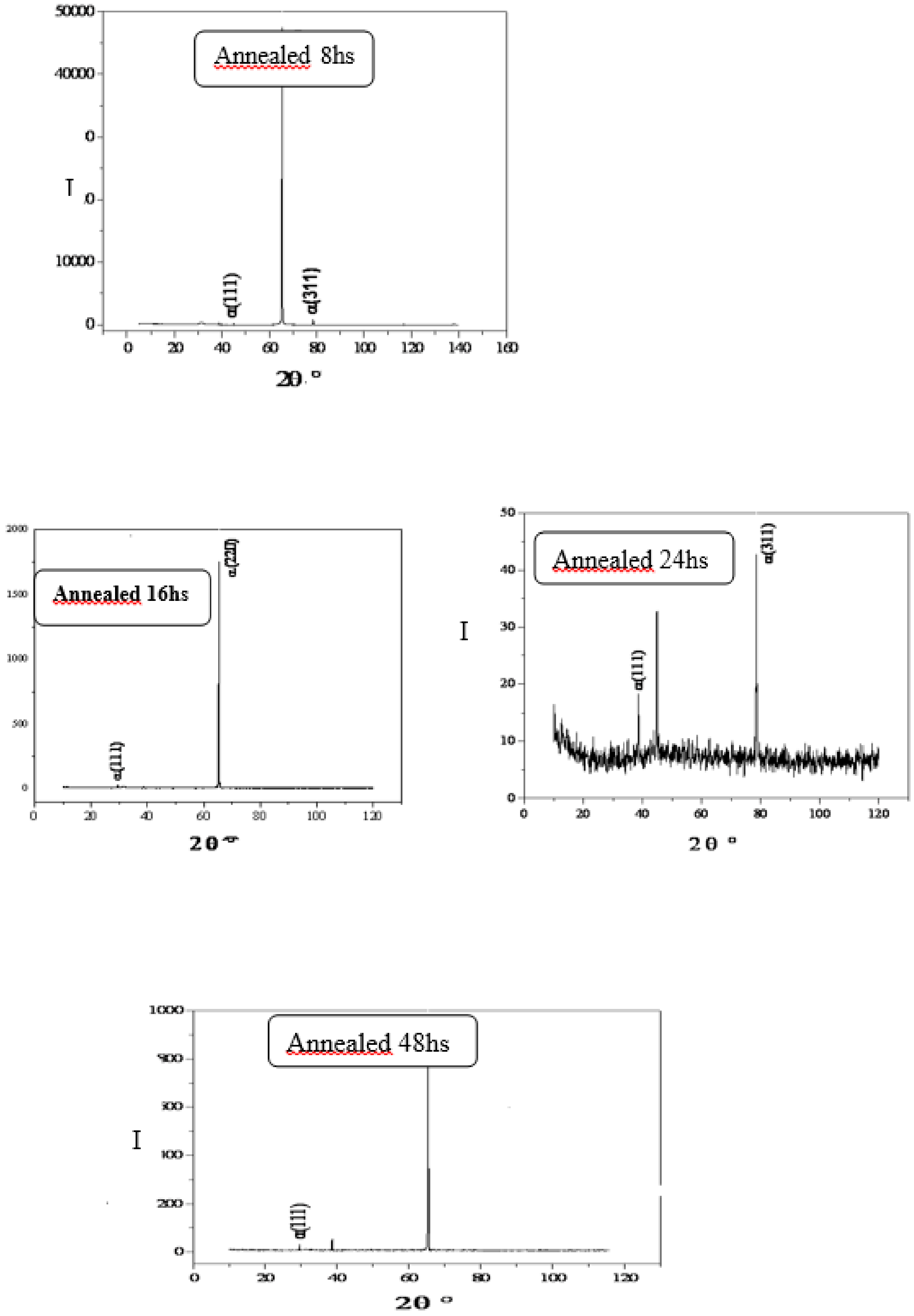

Figure 2: X rays diffraction patterns of annealed specimens at 530°C from 4hours to 48 hours.

B/ Microstructure evolution

Figure 3 shows the different structure taken with light and scanning electron microscopes (SEM) for as-received specimen and samples annealed at 16hs and 24hs and etched with Keller4s solution. It is clearly seen that the microstructure changes in the interval 16hs to 24hs. The recristallization takes place within this time interval with a mean grain size of about 10µm without any texture change. Similar observation was made in a previous work

(5) where dynamic recristallization was observed without giving any new texture. This is characteristic of a superplastic material. Whereas a grain growth is observed for specimen annealed at 24hs with an average grain size exceeding 15µm.

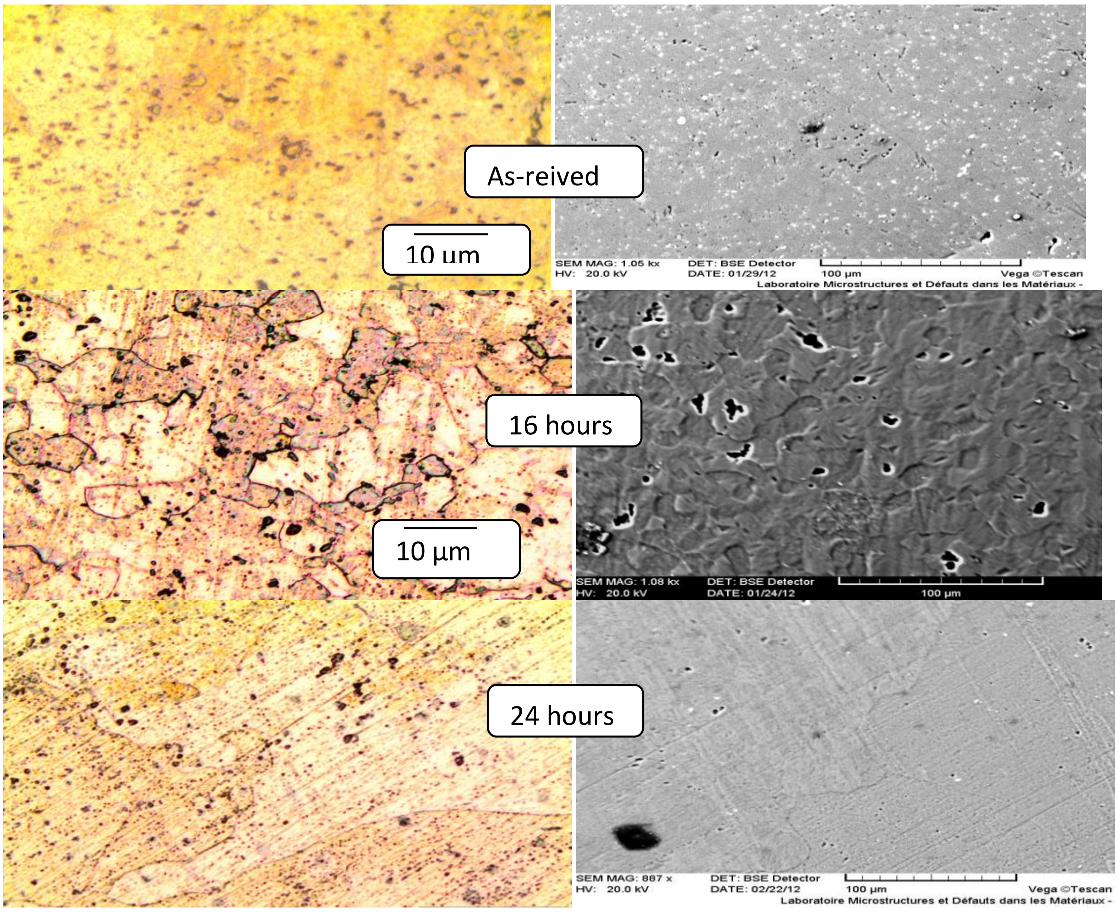

Figure 3: Microstructure observed for as-received and annealed specimens
at 530°C for 16 and 24 hours respectively

C/ Microhardness study

The microhardness variation as a function of annealing time and taking into consideration the as received microhardness, is shown in Figure 4. It presents two variations. It is noticed a slight increase up to 8hs, then the microhardness drops down continuously to reach a lower value at 48hs. The increase could be associated to structural hardness of the material with could be related to the presence of β(Al_3Zr) observed only in samples annealed up to 8hs . It is thought that the initial fall of the microhardness in the range 8hs to 16hs could be due to the restoration process which led to the recristallization seen in specimen annealed for 16hs. The important and continuous decrease observed in the alloy heat treated for 24hs is attributed to the grain growth of the material.

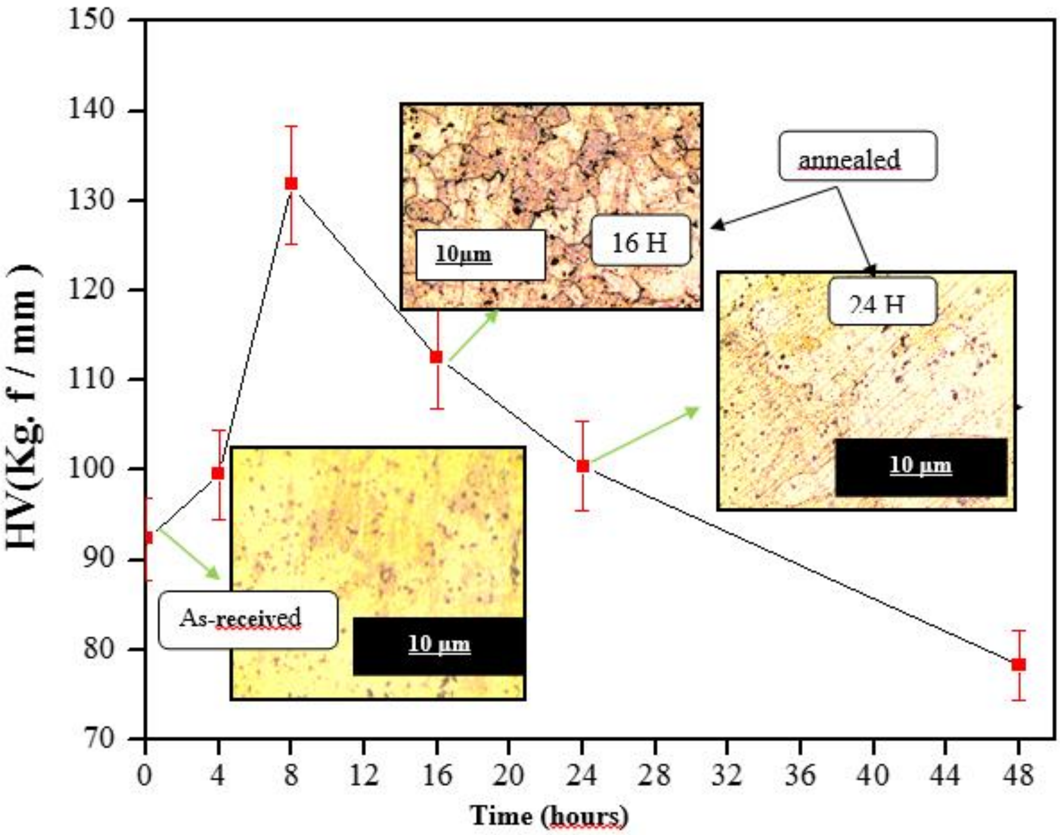

Figure 4: Microhardness as a function of annealing time at a fixed temperature 530°C

Conclusion

It is clearly seen that the material maintains its initial and principal orientation i.e. α (220) in both as-received and annealed materials for various times. Natural aging does not make any effect on texture. However static recristallization process takes place at 530°C within the time range 16hs-24hs without showing any texture change. The main orientation remains α (220).Finally, in the specimen annealed for 24hs, it is noticed a grain growth and a change in the main orientation which passes from α (220) to α (311) .

References

[1] B.Noble, S.J.Harris, K.Dinsdale, Matière des Sciences, N°17, (1982) ,461-468.
[2] R.Grimes ,Proc.4th Int.Al-Li conf. Paris, ed.,G.Champier, 1987 ,239-250
[3] R.Amichi, N.Ridley, Sciences and Technologies, N°12, (1999).
[4] S.Bourahla, thèse de Magister, Influence des traitements thermiques sur la recristallisation des alliages superplastiques, Université de Constantine, Algérie, 2007
[5] F.Moulla. thèse de Magister, Evolution de la texture des alliages superplastiques, Université de Constantine, Algérie, 2010

SPECTROSCOPIC STUDIES OF INCLUSION COMPLEX OF 2-BENZOTHIAZOLETHIOL AND Β- CYCLODEXTRIN

SONIA BADI, ACHOUR SERIDI, MEKKI KADRI

Abstract

The 2-benzothiazolethiol is important in medicinal chemistry [1]. It is virtually insoluble in water, in which its manipulation is difficult, but the problems may be alleviated by cyclodextrin inclusion. Cyclodextrins are known to form inclusion complex with many kinds of hydrophobic compounds because their molecular structure generates a hydrophilic exterior surface and a hydrophobic cavity interior [2]. The inclusion complex formation of β-CD and 2-benzothiazolethiol was carried out by spectrophotometric measurements at 25 0C. The stoichiometrie and stability constants of complex have been determined .the thermodynamic parameters (ΔG, ΔH) and (ΔS) of inclusion process are also determined. The results indicate that the interactions of phenothiazines with β -CDs are very strong.

[1] : M. Kidwai et al, European Journal of Medicinal Chemistry 45 (2010) 5031e5038
[2] : N.V. Roik et al, Journal of Molecular Structure 987 (2011) 225–231

GROWTH OF METAL OXIDE (TIO2/AG) THIN FILMS SPUTTERED BY HIPIMS EFFECTIVE IN BACTERIAL INACTIVATION: PLASMA CHEMISTRY AND ENERGETIC

OUALID BAGHRICHE, ABDENOUR ZERTAL, JUAN KIWI

Abstract

High-Power Impulse Magnetron Sputtering (HIPIMS) is a technology that belongs to the field of Ionized PVD of thin films. This study shows the first complete report on ultrathin TiO2/Ag nano-particulate films sputtered by highly ionized pulsed plasma magnetron sputtering (HIPIMS) leading to fast bacterial loss of viability. The Ag and the TiO2/Ag sputtered films induced complete Escherichia coli inactivation in the dark, which was not observed in the case of TiO2. When Ag was present, the bacterial inactivation was accelerated under low intensity solar simulated light and this has implications for a potential for a practical technology. The design, preparation, testing and surface characterization of these innovative films are described in this study. The HIPIMS sputtered composite films present an appreciable savings in metals compared to films obtained by conventional sputtering methods. HIPIMS sputtering induces a strong interaction with the rugous polyester 3-D structure due to the higher fraction of the Ag-ions (M+) attained in the magnetron chamber. The immiscibility of Ag and TiO2 in the TiO2/Ag films is shown by High Angular Dark Field (HAADF) microscopy.

The ionization degree of the film forming species is significantly increased and film growth is assisted by an intense ion flux. Reports have revealed the significant enhancement of the film properties as the HIPIMS technology is used. However, a decrease of the deposition rate, as compared to the conventional DC magnetron sputtering Pulsed (DCMSP) process, is commonly observed during HIPIMS.

COMPARATIVE STUDY OF CDS/PS AND CDS/PMMA COMPOSITE FILMS

HARIECHE, BOUBEKEUR BOUDINE, M SEBAIS

Abstract

Nanocrystalline CdS particles have been dispersed in both polystyrene (PS) and poly-methyl methacrylate matrices in the form of thin composites films by ex situ methodology. These films were successfully prepared by spin coating technical. The structural characterization was performed by X-ray diffraction and .The UV–VIS measurements showed blue shift of the absorption threshold, proving the presence of nanoparticles, but the shift in CdS/PS samples is more than that those of CdS/PMMA composites films.

PL spectrum showed that the elaborate samples present bands of luminescence in the visible field from where the possibility of regarding these samples as optically active mediums. We can also show that the photoluminescence bands of CdS/PS films are blue shifted than those of CdS/PMMA composites films, this difference is due to the matrix effect.

ANTIMICROBIAL ACTIVITY OF MENTHA ROTUNDIFOLIA ESSENTIAL OILS AND METHANOLIC EXTRACTS

RACHID BELHATTTAB, SIHAM FERDJIOUI

Abstract

Lamiaceae family, a large variety of aromatic plants, is essentially distributed over countries with moderate climate. It consist of almost 220 genus and more than 4000 species. Among them Mentha rotundifolia. The essential oil from the aerial parts of the plant was obtained by hydrodistillation using a cleavenger type apparatus whereas methanol extracts were obtained by maceration (MME) and Soxhlet apparatus (SME). The yields were 0,7 %(v/w), 16,05% (w/w) and 9,2% (w/w) respectively. The chemical composition of the oil was determined by GC and GC/MS allowing the identification of 43 compounds with transpiperiton oxyde as the main constituent (66,39%). Antimicrobial activity was evaluated according to the disc diffusion test against seven microbial strains (four bacteria and three fungi). Methanolic extracts exhibited no antimicrobial effect whereas essential oils developped strong effects against fungal strains and moderate ones against bacteria.

RELATIONSHIP BETWEEN MICROSTRUCTURE, MICROHARDNESS AND CORROSION RESISTANCE OF ALUMINUM ALLOY TYPE 2017A

SOFIA BENAMIROUCHE, ABDEREZAK ABDI, MOHAMED EL AMINE BELOUCHRANI

Sofia Benamirouche, PhD Student, *Electrochemistry and Corrosion Laboratory, EMP, Algiers, Algeria, Abderezak Abdi, Dr., Electrochemistry and Corrosion Laboratory, EMP, Algiers, Algeria, Mohamed El Amine Belouchrani, Pr., Material Engineering Laboratory, EMP, Algiers, Algeria.*

Abstract

The present study has been conducted to investigate the effects of different tempers on the electrochemical behavior of aluminum alloy 2017A, by means of three thermal states: natural aging T4, artificial ageing T6 at 165°C and T7 at 200°C. The microstructural analysis and the electrochemical behavior were carried out by electrochemical, mechanical and metallographic techniques. It has been determined that the T4-naturally heat treatment specimen with 20 days of maturation has better nobility, strength and low bias current of corrosion compared to the other considered treatments.

1. Introduction

Nowadays, aluminum and its alloys are important engineering materials due to their high strength-to-weight ratio, easy workability and low cost [MARTINS, 2008]. They are widely used in construction and aerospace industries [DING, 2010]. However, due to the presence of impurities and alloying elements, they have a highly heterogeneous microstructures compared to other metal alloys [VALDEZ, 2014]. Specifically, in 2xxx alloys series, the alloying elements Mg and Cu are added to improve the mechanical properties. However, after artificial ageing, the existence of this impurities provoke the formation of new Cu-rich intermetallic (IM) precipitates Al-Cu-Mg witch reduce significantly the corrosion resistance [QUEIROZ, 2008]. In addition, the presence of a small amount of Fe leads to the formation of Al-Cu-Fe phase and reduce the amount of Cu required for structural hardening. The morphology of the intermetallic precipitates that may being observed as well as their dimensions, proportions and spatial distributions vary with the approved heat treatment. Nevertheless, there have been significant advances to understanding of both the heterogeneous microstructure of some high strength alloys as well as its influence on behavior against corrosion phenomena. The present work was carried out to study the coupled effects of the microstructure and the micro-hardness on the electrochemical behavior in NaCl medium (3%) of 2017A aluminum alloy specimens, elaborated by mean of different heat treatments, including a T4-natural aging and artificial age-hardening T6 and T7 in Argon atmosphere. It allow us both to establish a correlation between the electrochemical behavior with their micro-structure and micro-hardness, and to identify the best heat treatment conditions for a good corrosion resistance.

2. Experimental procedure

2.1. Specimens preparation

A rectangular specimens (40×15×4 mm^3) of 2017A aluminum alloy (wt. % composition: 3.89 Cu, 0.81 Mg, 0.78 Mn, 0.84 Si, 0.48 Fe, 0.04 Pb, 0.04 Cr, 0.06 Zn and balance of Al) were used. First, they were annealed at 300 °C for 30 minutes and then cooled at room temperature for 3 days to erase previous thermal and/or mechanical treatments and to limit the machining effects (residual stress and structural changes in the surface). The specimens were divided in three sample groups which were subjected to a series of heat treatment process given in table1. The solution heat-treatments for all samples were carried-out at 530 °C for 55 minutes in a furnace under Ar atmosphere.

Table1. Heat treatment process of 2017A aluminum alloy samples.

Samples ID	Treatment process	Condition
I	Natural ageing-T4	Solution heat-treating, water quenching, aging at room temperature for 10 and 20 days.
II	Artificial ageing-T6	Solution heat-treating, water quenching, tempering at 165 °C for 6, 8, 10 and 12 hours.
III	Artificial ageing-T7	Solution heat-treating, water quenching, over-tempering at 200°C for 6, 8, 10 and 12 hours.

2.2. Microstructural and micro-hardness characterizations

Various characterization methods are used to highlight the metallurgical microstructure (formation and distribution of precipitates, grain size, etc.) to understand phenomenon involved in corrosion, including optical microscopy (OM) by mean of Leica DM 2500M microscope, scanning electron microscopy (SEM) using a Quanta 600 FEG unit, equipped with a quantitative Energy Dispersive Spectrometer (EDS) capable of chemical analysis. For the highlighting of the size of grains and the various phases formed, the specimens are subjected to a mechanical polishing using the abrasives paper 1000, 1200, 2400 and 4000, than with 1 micron diamond past, and finally, a chemical etching with Keller's reactant for 100 seconds. Vickers indentation tests were performed using a High Wood HWDM-1 micro-hardness tester at 300 g force, with a Vickers diamond pyramid and the average values of impression diagonals were recorded. For a better estimate of the micro-hardness values, 18 tests are performed in matrix form for each specimen and the two extreme values are removed from the calculation of the average. The standard deviation σ is generally in the order of 2 Hv.

2.3. Electrochemical measurements

To provide more information about corrosion behavior, the electrochemical measurements were performed at room temperature in a standard three-electrode cell in aerated NaCl solution (3% wt.), using Autolab 128 N potentiostat coupled to a PC and controlled by Nova 1.0 software. This characterization was performed over an exposed area of 1 cm^2. A Pt-foil serves as the counter electrode and Ag/AgCl (3 M KCl) as reference electrode (0.210 V vs. NHE). The polarization curves were recorded from -150 to 150 mV around OCP, with 10 mV/s scan rates. The electrochemical impedance spectroscopy (EIS) was performed in a.c.-frequency using BioLogic SP-150 Potentiostat, in the range of 1 MHz-10 mHz with a perturbation amplitude of 10 mV (rms) around the open circuit potential (OCP).

3. Results and discussion

3.1. Microstructure characterization

The SEM image (Figure 1) shows the distribution of intermetallic particles in the 2017A aluminum alloy after a natural age-hardening for 20 days. The EDS characterization reveals three main intermetallic particles which differ in their morphologies and chemical compositions, one is light and glossier with a irregular shape Al–Cu–Mn–Fe–Si(Mg) (length ⍰ 40 µm) and the others are smaller and gray, ⍰-Al_2Cu phase (length⍰ 1 µm) in spherical shape and Al-Cu-Mg precipitate corresponding to S-Al_2CuMg phase, according the phase diagram of the system Al-Cu-Mg [RINGER, 2010]. This later kind of particles is often described in the literature and represent about 60% of all particles in the intermetallic alloy 2024 [YESPICA, 2012], more than 2017A alloy. The exact stoichiometry of the coarse particles Al-Cu-Fe-Si (Mg) has not been determined since it differs according the analyzed particle, as also stated in the literature [GUILLAUMIN, 1998; BUCHHEIT, 1997]. The nominal composition in Table 2, obtained by EDS for 2017 alloy specimen's heat treated according to T4 (20 days), T6 (12 hours) and T7 (12 hours), confirms the existence of the intermetallic particles Al-Cu-Mn-Fe-Si(Mg).

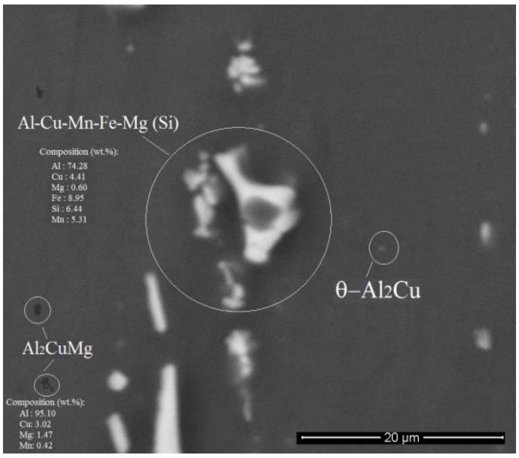

Figure 1. SEM micrograph of the 2017A alloy after T4 heat treatment for 20 days. Inset: EDS characterization of the intermetallic particles.

Table 2. EDS characterization of Al-Cu-Mn-Fe-Si(Mg) particles in the 2017A alloy specimens after heat treatments T4 (20 days), T6 and T7 (12 hours).

	Nominal composition (wt. %)					
Heat treatment	Cu	Mg	Fe	Si	Mn	Al
T4 (20 days)	4.41	0.60	8.95	6.44	5.31	balance
T6 (12 hours)	6.64	0.66	10.21	6.65	5.37	balance
T7 (12 hours)	3.45	1.27	4.36	1.69	2.62	balance

The morphology and the grain sizes are highlighted by optical microscopy. The micrographs are similar for all the heat treatments with a difference in the particle size and dispersion of precipitates. The presence of elongated grains is observed and the grain morphology is typical of the materials obtained by hardening. On the micrographs, there is also the presence of coarse intermetallic particles as small black spot distributed in random way. In enclose grains, coarse precipitation is observed.

The average grain sizes in Table 3 were determined by means of the mean linear intercept method according to ASTM Standard E 112, "Standard Test Methods for Determining Average Grain Size". Table 3 brings the average values of different measurements.

Table3. Values of average grain size of the alloy heat treated.

State	T4		T6				T7			
	10days	20days	6h	8h	10h	12h	6h	8h	10h	12h
d (µm)	18.78	17.45	10.02	15.15	10.24	12.91	17.11	17.75	22.71	11.42

Table 3 shows that the alloy in the T6 state has the finest grain then the T4 state and T7 state. The refinement of grains in T6 treatment is mainly due to the formation of fine precipitates which are relatively distributed in a homogeneous manner which prevents the growth of grains [PAUSE, 2008]. T4 heat treatment product precipitates more distant and larger size which stimulates the grain growth kinetics. In addition, the T7 state present larger size of precipitates by artificial treatment effect of temperature (200 °C). At this temperature, coalescence of the fine precipitates occur giving precipitates larger and distant. The grain growth is therefore favored. In this state, the average grain size is the largest compared to other tempers.

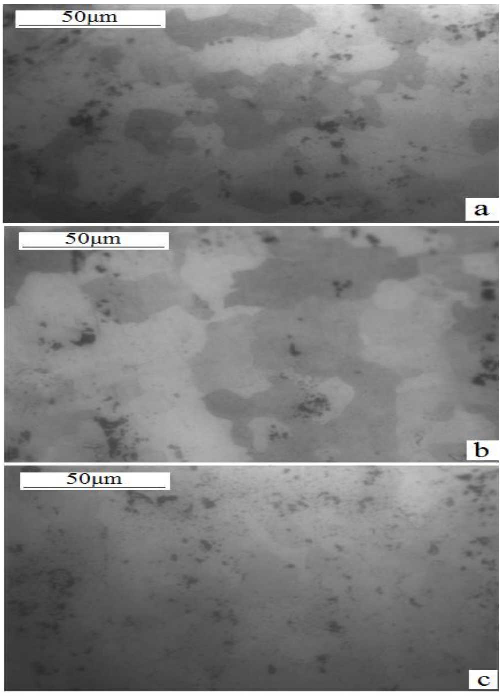

Figure 2. Optical micrographs of 2017A aluminum alloy specimens
a) T4(20 days), b) T6(12 h), c) T7(12 h).

3.2. Micro-hardness

Samples are first polished (up to 1 µm particle size) to avoid maximum hardening surface. Table 4 summarizes the measured values of the average micro-hardness of the various samples.

Table 4. Values of micro-hardness of the alloy heat treated specimens.

State	T4		T6				T7			
Treatment	10d	20d	6h	8h	10h	12h	6h	8h	10h	12h
Hv	138	142	144	125	133	149	135	144	118	120

Specimen T4-naturally treated

The specimen T4-naturally aged for 10 days is softer than the one treated for 20 days. The acceleration of the precipitation of hardening phases is caused by the effect of temperature and that will make it harder than T6 alloy. The material under T4 state is constituted of a solid solution and Guignier-Preston (GP) zones which are not an effective storage sites for dislocation and may cause the high observed hardness, resulting from interactions between dislocations, the limitation of dynamic recovery by the high solute concentration in solid solution, and optionally by a dynamic precipitation induced by the plasticity.

Specimen T6-artificially treated (165°C)

The specimen T6-artificially aged during 6 and 12 hours is harder than the one treated under naturally aging T4. The hardness value decrease considerably after 8 hours (125 Hv), and increase for 12 hours to reach a maximum value of 149 Hv. This hardening is caused by the refining of the grain sizes which becomes dominant. The grain size is progressively reduced for the times 10 and 12 hours, causing a gradual increase in hardness owing to the possible dissolution of particles θ'. These later are almost completely dissolved after 10 hours of treatment, after which the grain refinement occurs leading to a lowest particle size. It is well known that the precipitates constitute the main barrier to the movement of dislocations. They are potential sites for storage of dislocations and also accelerate the dynamic recovery phenomenon by changing the solid solution. This has already been studied on the alloys Al-1.7% Cu by Murayama et al. [MURAYAMA, 2001].

Specimen T7-artificially treated (200°C)

The specimen T7-artificially treated at 200°C results in a significant decrease in micro-hardness which is inversely proportional to the grain size and the size of precipitates [PAUSE, 2008; ASHBY, 1991]. At this stage, the material comprises precipitates θ and S circumvented by dislocations. This bypass results in the formation of geometrically necessary dislocations, which in accumulating, favor a smaller micro-hardness, this has been explained for the alloys of the 7000 series by Dumont [DUMONT, 2001]. This is essentially due to the higher tempering temperature. According to the theory, phase θ'' and S'' appear earlyon, but they are gradually replaced by new phases metastable (θ' and S'). The θ'-phase dimensions are significantly greater (2 µm) with a partial cohesion with the matrix and does not substantially opposes the path of the dislocations through the material. The appearance of this phase can therefore be softening generator [ASHBY, 1991].

3.3. Electrochemical Characterization

OCP measurement

Figure 3 represents the open circuit potential (OCP) recorded over 3 hours in NaCl solution (3%). These curves show after a potential step towards evolution of higher values, high stability. The recorded OCP values are summarized in Table 5.

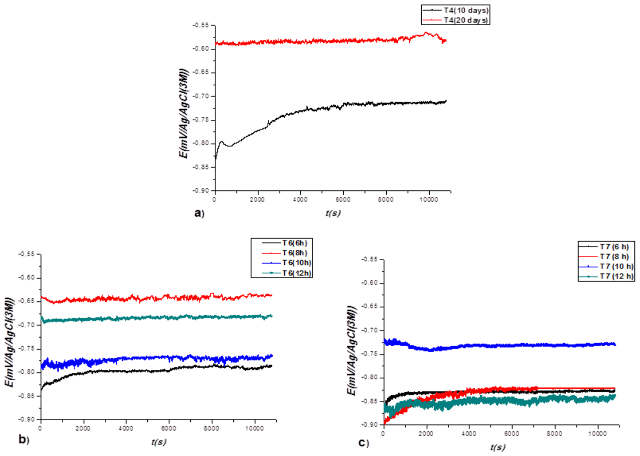

Figure 3. Evolution of free potential in NaCl solution (3%) for the different heat treatments: (a) T4, (b) T6 (c) T7.

Table 5. OCP values of the alloy heat treated specimens in NaCl medium (3%).

state	T4		T6				T7			
	10days	20days	6h	8h	10h	12h	6h	8h	10h	12h
OCP$_{mV/Ag/AgCl(3M)}$	710	580	785	636	764	681	826	823	730	838

This difference of potential can have several origins: it may simply reflect a more or less marked location of the attack, which changes the active surface, seat of the anodic dissolution and / or come from a difference in corrosion potential of these different states. This second hypothesis seems the most likely. Indeed, as shown by the results metallography, all samples contain the S phase (Al_2CuMg) in round shape. Therefore, following the immersion in NaCl, we have dissolution of Mg which leads to a sustained ennoblement of the surface [ZHU, 2003]. The results of the enrichment of the composition of the matrix of copper, resulting in a change of behavior on the macroscopic electrochemical dissolution and fragmentation of precipitates, are also given in the references [MURAYAMA, 2001; CABIBBO, 2005]. It is generally accepted that the inter-granular corrosion in alloys of 2xxx series to open circuit conditions in environments containing chloride, begins with the dissolution of the particles in S phase (Al_2CuMg) on the grain boundaries which is favored not only by coupling micro-galvanic [GUILLAUMIN, 1998; BRUNNER, 2012], but also by the active nature of the S phase [BUCHHEIT, 1997; BIRBILIS, 2005]. A detailed study on the electrochemical characteristics of the S phase is given by Buchheit et al. [BUCHHEIT, 2000], where they mounted the S phase does not dissolve as a single entity, but may be subject to selective dissolution of Mg and Al of the intermetallic . The result of this may be that the enrichment of Cu which may allow the S phase of behaving like a local cathode after some duration.

Polarization curves

And the corrosion potentials and the corrosion current densities were determined by Tafel extrapolation method. Figure 4 shows the polarization curves obtained in NaCl medium (3%) ventilated. Whatever the heat treatment used, the current-potential curves are formed in the cathode region, a bearing corresponding to the oxygen reduction reaction with current densities of the order of 10 $^{-6}$ A.cm $^{-2}$ for all the metallurgical states studied.

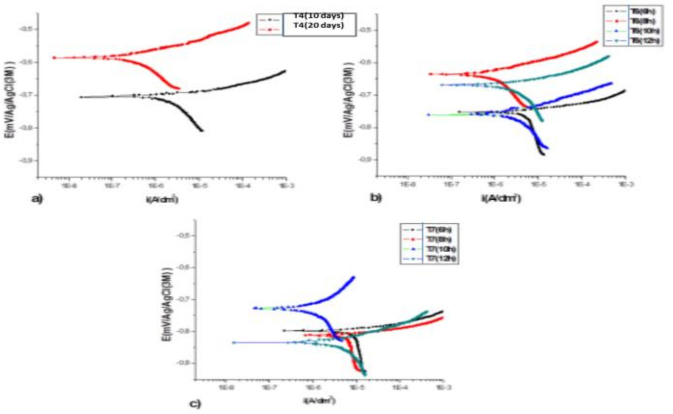

Figure 4. Linear polarization curves obtained in a solution of 3% by weight NaCl for different metallurgical states: (a) T4, (b) T6, (c) T7.

The values of the electrochemical characteristics obtained from these curves are shown in Table 6.
Table 6. Values of the electrochemical characteristics of the alloy
heat treated in a 3% NaCl medium.

State	Time	E_{corr}(mV/Ag/AgCl(3M))	i_{corr} (µA/cm^2)
T4	10 days	-705	0,34
	20 days	-584	0,09
T6	6 hours	-753	10,92
	8 hours	-673	2,49
	10 hours	-758	0,51
	12 hours	-668	0,70
T7	6 hours	-797	12,64
	8 hours	-810	9,33
	10 hours	-727	3,10
	12 hours	-835	1,41

In terms of current, it should be noted that with the T4 state, the higher current is recorded when the maturation period is 10 days, whereas the lower corresponds to a longer maturation period. For the T6, the corrosion currents are higher than for the T4, except for artificial treatment duration of 10 hours in which it is registered a similar behavior to that of T4 (10 days) with a current of 0.51 µA / cm^2. However, with the T7, it seems that this treatment does not improve the behavior. In contrast to a treatment time of 6 hours, the corresponding current is highest compared to the other treatments.

From Table 6, we see that the material has a low corrosion current density. Especially since its equilibrium potential is larger, and it has better resistance of polarization. The evolution of the corrosion potential of the alloy according to the thermal treatment, is more complex to be analyzed, this alloy contains two stages in the form of intermetallic particles, a cathode compared to the mother phase rich in copper or iron, and the other anodic compared to the mother phase rich in magnesium. Lacroix showed that the dissolution of the S phase of the particles is accompanied by an enrichment with copper that increases the corrosion potential [LACROIX, 2008]. Moreover, it appears that the corrosion potential can be considered a characteristic parameter of the degree of progress of the dissolution of the particle S. Several researchers have studied the corrosion of this alloy. These researchers attributed this corrosion to the presence of cathode intermetallic particles, but Kiryl et al. [KIRYL, 2007], after the monitoring of the evolution of anodic intermetallics particles versus time found that they dissolve and leave microcrevasses on the metal surface. We think that these can be, thereafter, the seat of localized corrosion.

The introduction of heat treatment brings a big change on the shape and composition of the intermetallic particles and this makes it even more complex problem [NACER, 2011].

Presumably, during the period of the experiment, the behavior of one phase predominates, resulting so periods of growth or decay of the corrosion potential.

Impedance spectroscopy curves

The electrochemical impedance spectroscopy (EIS) was successfully applied to study the mechanisms of corrosion of aluminum alloys. It makes it possible to separate the various contributions of the corrosion mechanism by their kinetics. Fast phenomena are observed at high frequency while the slower phenomena are analyzed for lower frequencies.

Diagrams EIS Nyquist representation (a) and Bode (b and c), obtained for the various heat treatments of the 2017A alloy in 3% NaCl medium are shown in Figures 5, 6 and 7.

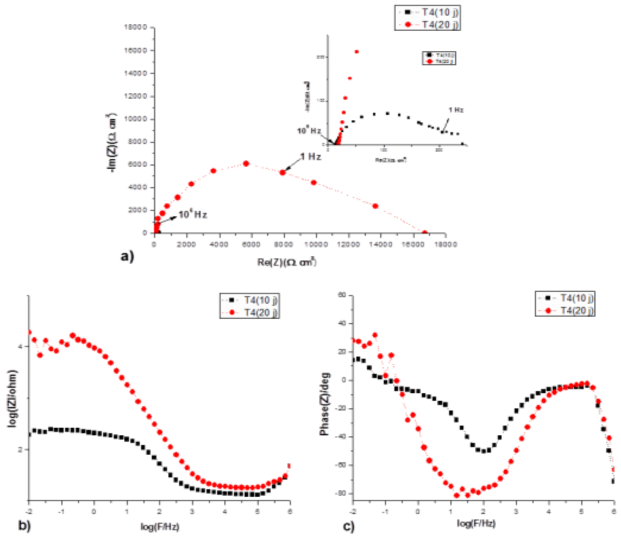

Figure 5. Electrochemical impedance Nyquist diagrams in planes (a) and Bode (b and c) obtained for the T4 condition at different maturation period.

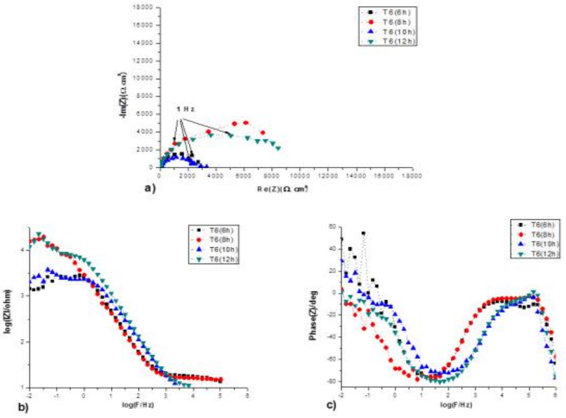

Figure 6. Electrochemical impedance Nyquist diagrams in planes (a) and Bode (b and c) obtained for the T6 condition at different maturation period.

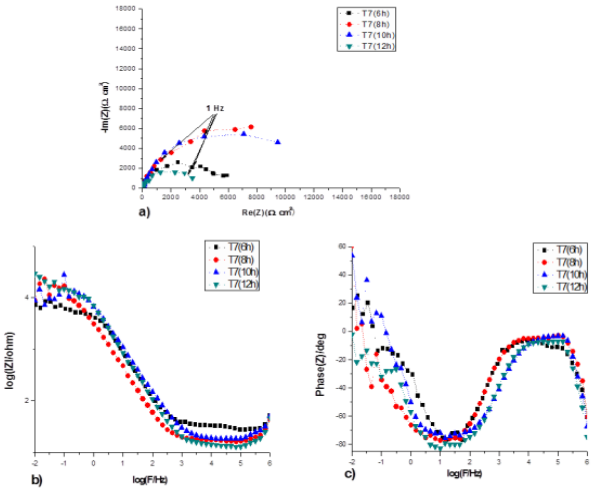

Figure 7. Electrochemical impedance Nyquist diagrams in planes (a) and Bode (b and c) obtained for the T7 condition at different maturation period.

All results of this technique are modeled in this study by equivalent electronic circuit (PEC), presented in Figure 8.

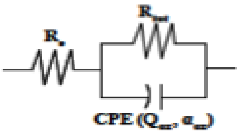

Figure 8. Electrical circuit used.

The kinetic parameters deduced from these diagrams are given in Table 7. A good correlation is obtained between the experimental and simulated data not only on the observed spectra, but also through the value of the correlation factor, χ^2, which the values are close to 10^{-3}. This figure represents the average of the squared deviations between the model and the experimental values and gives the evaluation of the adequacy of modeling [ORAZEM, 2006].

Table7. Electrical parameters obtained by data fitting.

State	Time (h)	R_e(Ω. cm^2)	R_p (k Ω. cm^2)	C_{dc} (µF. cm^{-2})	n
T4	10 d	13.36	0,2052	114,70	0,8055
	20 d	18.27	14,192	12,010	0,9216
T6	6 h	16.52	3,2320	42,580	0,9300
	8 h	15.82	11,030	6,6800	0,8957
	10 h	8,424	2,6730	32,340	0,8750
	12 h	10,13	8,8240	19,440	0,9193
T7	6 h	32,17	5,7070	24,870	0,9138
	8 h	17,05	13,784	25,693	0,8945
	10 h	18,44	14,061	23,330	0,8801
	12 h	9,597	4,0080	32,110	0,8779

From the table above, which shows the evolution of parameters Re, Rp, Cdc and n obtained from the adjustment of impedance diagrams, we note that for all tempers, the capacity grows parallel to a decrease in the polarization resistance. This indicates dissolution of the passive layer and an acceleration of the corrosion of material [BELLENGER, 2002].

Increasing in the capacity generally refers to the reduction in the thickness of the passive film [BATAILLON, 1994]. The observed capacity difference (Table 7) suggests that some heat treatments produce a defective oxide, with higher conductivity, which allows the incorporation of Cl^- ions in the oxide film. Thus the film becomes soluble and its break occurs. These treatments may also increase the dissolution rate of the metal by increasing the amount of free metal ions in the solution within the crevice formed by stitching. The diffusion of ions Cl^- inward causes the evacuation of metal cations outwards.

The sloping medium frequency determined by the exponent n of the previous relation, is between 0.8055 and 0.93, corresponding to a compact and passive oxide film. This pure capacitive behavior is associated with a high resistance of corrosion for the samples, but with preponderance to the state T4.

The resistance of the electrolyte, which is the actual value of the high impedance frequency, is low. It is substantially constant and does not change with the heat treatment thus the chloride ion concentration is large enough to ensure good conductivity of the electrolyte.

In conclusion, it is possible to say that the maximum of the polarization resistance is obtained for T4 treatment with a 20 days maturation period with a value of 14.192 kW. In the same state, it is recorded a hardness of 142 Hv and remains the largest compared to the rest of the samples.

III.4. Metallography observation

Figures 9, 10 and 11 show micrographs of the surface of the alloy 2017A treated thermally obtained by scanning electron microscope after the test of polarization with an immersion of about 3 hours in a solution of NaCl 3%. The surface of the alloy has the appearance of localized corrosion. The expansion of a region of its surface shows a compact film that has significant cracks which will lead to incorporation or greater and easier diffusion of chloride ions. In other words, an increase in the rate of dissolution of the material. Thus, according to the electrochemical behavior of the intermetallic, we distinguish two types of behavior, one of the cathodic and anodic particles.

Cathode particles: Al_2Cu, Al-Cu-Mn- Si -Fe (Mg) and the dispersoids have a cathode character compared to the matrix [GUILLAUMIN, 1998; RINGER, 2000]. Thus, the area adjacent to these precipitates will dissolve preferentially during immersion in a solution aggressive, to the point that some particles are loosened. The anode particles, Al_2CuMg, have a less well-defined electrochemical behavior. Anodic compared to the matrix [WEI, 1998]. These particles and the adjacent aluminum matrix underwent dissolution. The particles have a porous structure, often mentioned in the literature [KOLICS, 2001]. So the observations made above are clearly visible here. This porous structure is in perfect agreement with a phenomenon of preferential dissolution of aluminum and magnesium contained in the particles resulting in an enrichment of the copper particle.

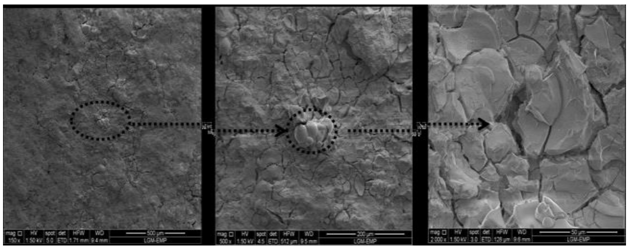

Figure9. SEM micrograph after immersion in the 3% NaCl during the polarization matured for sample (T4).

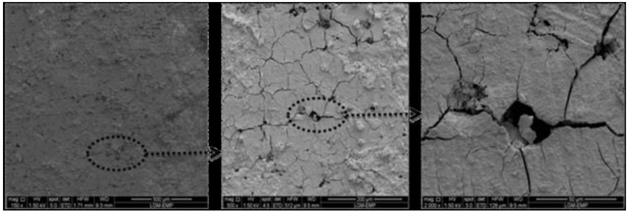

Figure10. SEM micrograph after immersion in the 3% NaCl during the polarization matured for sample (T6).

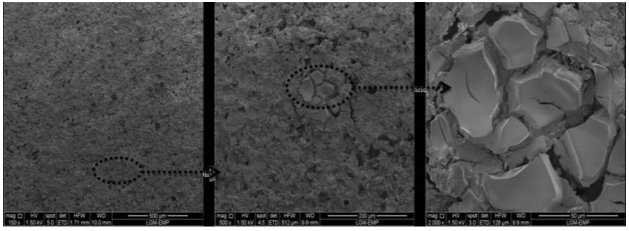

Figure11. SEM micrograph after immersion in the 3% NaCl during the polarization matured for sample (T7).

Conclusion

The microstructural and electrochemical analysis used in these experiments show the influence of heat treatments on the grain sizes, specifically the distribution and the size of precipitates. The micro-hardness test linked the size of the precipitates to the average grain size as well as mechanical properties. Thus, large precipitates stimulate grain growth and therefore provide low hardness.

Examination of the results shows the improvement of electrochemical behavior characterized by the evolution of free potential. Corrosion current decreases and a good polarization resistance is attributed to the maturation treatment with duration of 20 days. Moreover, a correlation between the electrochemical overall behavior and hardness of the alloy and the grain size is clearly demonstrated; therefore, it is noticed that for improved corrosion behavior a medium hardness with high grain size are required.

References

Martins, N.C.T., Moura Silva, T., Montemor, M.F., Fernandes, J.C.S., Ferreira, M.G.S., 2008. Electrodeposition and characterization of polypyrrole films on aluminum alloy 6061-T6, Electrochimica Acta 53, 4754-4763.

Ding, H.-y., Dai, Z.-D., Skuiry, S.-C., Hui, D., 2010. Corrosion wear behaviors of micro-arc oxidation coating of Al_2O_3 on 2024Al in different aqueous environments at fretting contact, Tribology International 43, 868-875.

Valdez, B., Kiyota, S., Stoytcheva, M., Zlatev, R., Bastidas, J.M., 2014. Cerium-based conversion coatings to improve the corrosion resistance of aluminum alloy 6061-T6, Corrosion Science 87, 141-149.

Queiroz, F.M., Magnani, M., Costa, I., de Melo, H.G., 2008. Investigation of the corrosion behaviour of AA 2024-T3 in low concentrated chloride media, Corrosion Science 50, 2646-2657.

Ringer, S. P., Hono, K., 2000. Microstructural evolution and age hardening in aluminum alloys: atom probe field-ion microscopy and transmission electron microscopy studies, Materials Characterization, 44-101.

Yespica, W.J.P., 2012. Comparative study of the electrochemical behavior of aluminum alloys 2024 and 7075 T351 T7351 in neutral sodium sulfate, PhD Thesis, University of Toulouse.

Guillaumin, V., Mankowski, G., 1998. Localized corrosion of 2024 T351 aluminum alloy in chloride media, Corrosion Science.

Buchheit, R., Grant, R., Hlava, P., Mckenzie, B., Zender, G., 1997. Local dissolution phenomena associated with S phase (Al_2CuMg) particles in aluminum alloy 2024-T3, J. ElectrochemSoc, 144, 2621-2627.

Pause, N., 2008. Fatigue-corrosion dans le sens travers court des tôles d'aluminium 2024-T351 présentant des défauts de corrosion localisée, PhD Thesis, Ecole Nationale Supérieure des Mines de Saint-Etienne.

Murayama, M., Horita, Z., Hono, K., 2001. Microstructure of two-phase Al 1.7 at% Cu alloy deformed by Equal Channel Angular Pressing, Acta Mater. 49, 21-29.

Ashby, M. F., Jones, H., 1991. Matériaux, tome 2. Microstructure et mise en œuvre, DUNOD.

Dumont, D., 2001. Relations Microstructure / Ténacité dans les alliages aéronautiques de la série 7000, PhD Thesis, Institut National Polytechnique de Grenoble.

Zhu, D., Van Ooij, W.J., 2003. Corrosion protection of AA 2024-T3 by bis-[3-(triethoxylsilyl)propyl] tetrasulfide in neutral sodium chloride solution. Part 1: corrosion of AA2024-T3, Corrosion Science, 45, 2163-2175.

Cabibbo, M., Evangelista, E., Vedani, M., 2005. Influence of severe plastic deformations on secondary phase precipitation in a 6082 Al–Mg–Si alloy, Metall. Mater. Trans. A 36A, 1353-1364.

Brunner, J.G., Birbilis, N., Ralston, K.D., Virtanen, S., 2012. Impact of ultrafine-grained microstructure on the corrosion of aluminum alloy AA2024, Corrosion Science, 57, 209-214.

Birbilis, N., Buchheit, R.G., 2005. An experimental survey of electrochemical characteristics for intermetallic phases in aluminum alloys, J. ElectrochemSoc, 152, B140-B151.

Buchheit, R. G., Martinez, M.A., Montes, L.P., 2000. Evidence for Cu Ion Formation by dissolution and Dealloying the Al_2CuMg Intermetallic Compound in Rotating Ring-Disk Collection Experiments, J. ElectrochemSoc, 147(1), 119.

Lacroix, L., 2008. Mécanisme de corrosion localisée de l'alliage d'aluminium 2024 apport de la microscopie à force atomique (AFM) couplée au mode kelvin (KFM) et des alliages modèles, PhD Thesis, Institut National Polytechnique de Toulouse.

Kiryl, A., Zheludkevich, L., Lamaka, V., Ferreira, G.S., 2007. Role of intermetallic phases in localized corrosion of AA5083, Electrochem Acta 52, 7651-7659.

Nacer, Z., 2011. Influence des effets de vieillissement et du laminage à froid sur la microstructure, associés aux propriétés mécaniques et chimiques des alliages Aluminium-Magnésium, PhD Thesis, Université de Mouloud Mammeri Tizi-Ouzou, Algérie.

Orazem, M. E., Pebere, N., Tribollet, B., 2006. Enhanced Graphical Representation of Electrochemical Impedance, J. ElectrochemSoc 153(4), B129–B136.

Bellenger, F., 2002. Etude et contrôle de la corrosion feuilletante des alliages d'aluminium 2024 et 7449 par bruit électrochimique et émission acoustique. Analyse microstructurale et caractérisation de l'endommagement, PhD Thesis, Institut National des Sciences Appliquées de Lyon.

Bataillon, C., Brunet, S., 1994. Electrochem Acta, 39, 455.

Wei, R. P., Liao, C. M., Gao, 1998. M., A transmission electron microscopy study of constituent, particle, induced corrosion in 7075,T6 and 2024,T3 aluminum alloys, Metallurgical and Materials Transactions A 29, 1153-1160.

Kolics, A., Besing, A. S., Wieckowski, A., 2001. Interaction of Chromate Ions with Surface Intermetallics on Aluminum Alloy 2024-T3 in NaCl Solutions, J. Electrochem Soc, 148(8), B322.

STEEL CORROSION INHIBITION BY ELAEOSELINUM THAPSIOIDES EXTRACT IN ACID SOLUTION

MERZOUG BENAHMED, NOUREDDINE DJEDDI, BRAHIM HARKATI, SALAH AKKAL

Merzoug Benahmed, Dr, Laboratoire des Molécules Bioactives et Applications, Université de Tébessa,Noureddine Djeddi, Mr, Laboratoire des Molécules Bioactives et Applications, Université de Tébessa,Brahim Harkati, Dr, Laboratoire des Molécules Bioactives et Applications, Université de Tébessa, Salah Akkal, Pr, Laboratoire de Phytochimie et Analyses physicochimiques et Biologiques, Département de Chimie, Faculté de Sciences exactes, Université Mentouri Constantine.

Abstract

The n-butanol extract of the aerial parts of Elaeoselinum thapsioides is tested as corrosion inhibitor of Carbon steel in 1.0 M HCl solution using weight loss measurement, electrochemical impedance spectroscopy (EIS) and potentiodynamic polarization techniques. The corrosion inhibition efficiency increases on increasing Elaeoselinum thapsioides extract concentration. Potentiodynamic polarization curves indicated that the plants extract behaves as mixed-type inhibitor. The adsorption of inhibitor on carbon steel surface was found to follow Langmuir isotherm.

Keywords: Carbon steel, Elaeoselinum thapsioides extract, Weight loss, Polarization, EIS.

Introduction

Carbon steel is one of the most important alloys which are frequently used in wide industrial applications, due to its excellent to its excellent properties and low cost. Corrosion is one of the problems facing industrial processes, leading to high financial losses. The use of organic inhibitors for preventing corrosion is a promising alternative solution. Most of the well-known acid inhibitors are synthetic compounds especially those with electron donating group N, O and S showed an effective corrosion inhibition (Bentiss, 2000, Elayachi, 2006). However, the use of these synthetic inhibitors has been limited because of the environmental threat. Hence use of natural products which are ecofriendly and harmless (El-Etre, 2001; El-Etre, 1998; Bouyanzer, 2006) has become popular.

Plant extracts are an incredibly rich source of natural chemical compounds that can be extracted by simple procedures with low cost and are biodegradable in nature. Corrosion inhibition of the extracts of Azadirachta indica (Valek, 2007), Olea europaea (El-Etre, 2008), Zenthoxylum alatum (Chauhang, 2007) and Ferula harmonis (El-Etre, 2008) were studied as corrosion inhibitors in HCl medium.

Elaeoselinum thapsoides has been screened for its anticorrosion effect in the present study using weight loss measurement, potentiodynamic polarization and electrochemical impedance spectroscopy.

Experimental:

2.1. Plant Extraction and isolation

The air-dried aerial parts of Elaeoselinum thapsioides were extracted with boiling methyl alcohol (70 %). The hydro-alcoholic solution was concentrated under reduced pressure to dryness and the residue was dissolved in hot water and kept in cold overnight. After filtration, the aqueous solution was successively treated with ethylacetate and n-butanol, then the ethylacetate and n-BuOH extracts were concentrated to dryness (Benahmed, 2006; Akkal, 2010).

2.2. Materials:

CS carbon steel, composed of C 0.23 wt.%, Mn 0.85 wt.%, P 0.024 wt.%, S 0.030 wt.%, Si 0.4 wt.%, and Fe balance was used in the present study. Coupons of CS with an exposed surface area of 2 cm^2 were used for weight loss measurements. For electrochemical measurements, a steel cube embedded in epoxy resin, leaving an exposed surface area of 1.1 cm^2 as the working electrode. The coupons were polished with different grade of emery papers, degreased and rinsed, before its immersion in the test solution.

2.3. Corrosion tests:

a- Weight loss measurements:

The polished and pre weighed CS specimens were suspended in 150 ml test solutions with and without the inhibitor at different concentrations. After a period of 7 h, the coupons were taken out, washed in distilled water, dried and then weighed. Each experiment was repeated at least three times to confirm reproducibility. From the weight loss values, corrosion rates (CR), surface coverage and the inhibition efficiency (IE %) were calculated.

Potentiodynamic polarization measurement:

All electrochemical measurements were carried out using a computer controlled Voltalab PGZ 301 instrument with Voltamaster (version 7.0.8) software at room temperature. Open circuit potential (E_{ocp}), was measured for 60 min to allow stabilization of the steady state potential. The potential of the potentiodynamic polarization curves ranged from a cathodic potential of -250 mV to an anodic potential of +250 mV versus OCP at a scan rate of 1 mV s^{-1}.

Electrochemical impedance spectroscopy :

Eelectrochemical impedance spectroscopy measurements were carried out using the same instrument described above (section above) with the open circuit potential, of every sample was immersed for 60 min over a frequency range of 100 kHz to 0.01 Hz with applied potential signal amplitude of 5 mV.

Results and discussion

Weight loss measurements:

The values of inhibition efficiency and corrosion rates obtained from weight loss measurements for CS in acid solutions containing different concentrations of BEET at different temperatures are presented in Table 1. From the values of Table 1, it is clear that the presence of inhibitor leads to decrease the corrosion rate. It is indicated that inhibition efficiency of CS increases with increasing of BEET concentration up to 81 % at 293 K (Figure. 1). The increase in inhibition efficiency may be attributed to the adsorption of the molecules at the CS surfaces (Tang, 2013). As the temperature increases, the corrosion rate (CR) increases and inhibition efficiency decreases (Figure. 2). This suggests possible desorption of some adsorbed inhibitor from the steel surface at higher temperature. Such behavior shows that the phytochemical components are physically adsorbed on the carbon steel surface (Djeddi,2015).

C (mg L^{-1})	Temperature											
	293 K			303 K			313 K			323 K		
	CR (mg cm^{-2}h^{-1})	θ	IE (%)	CR (mg cm^{-2}h^{-1})	θ	IE (%)	CR (mg cm^{-2}h^{-1})	θ	IE (%)	CR (mg cm^{-2}h^{-1})	θ	IE (%)
0	0.1485	-	-	0.1858	-	-	0.2971	-	-	0.6958	-	-
100	0.1016	0.3160	31.60	0.1299	0.3010	30.10	0.2180	0.2663	26.63	0.5329	0.2341	23.41
200	0.0730	0.5082	50.82	0.0984	0.4704	47.04	0.1766	0.4057	40.57	0.4173	0.4003	40.03
300	0.0566	0.6220	62.20	0.0772	0.5845	58.45	0.1403	0.5277	52.77	0.3525	0.4934	49.34
400	0.0445	0.700	70.00	0.0622	0.6654	66.54	0.1173	0.6050	60.50	0.2986	0.5709	57.09
500	0.0359	0.758	75.80	0.0519	0.7203	72.03	0.1045	0.6483	64.83	0.2600	0,6264	62.64
600	0.0335	0.7742	77.42	0.0455	0.7549	75.49	0.0926	0.6883	68.83	0.2360	0.6608	66.08
800	0.0290	0.8042	80.42	0.0371	0.8002	80.02	0.0813	0.7264	72.64	0.2036	0.7074	70.74
900	0.0280	0.8110	81.10	0.0361	0.8054	80.54	0.0722	0.7569	75.69	0.1901	0.7268	72.68

Table 1: Corrosion rate data of CS in 1 M HCl for various concentrations of BEET

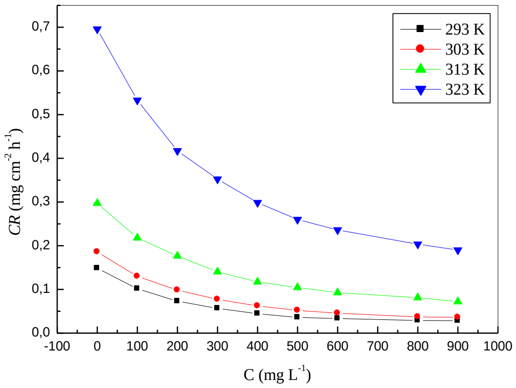

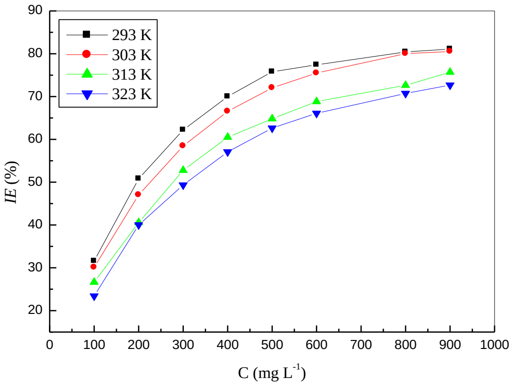

Figure. 1 Relationship between corrosion rate and concentration of BEET in 1 M HCl

Figure. 2 Effect of temperature and concentration on the inhibition efficiency of BEET in 1 M HCl

3.1.1 Adsorption isotherm

The mechanism of corrosion inhibition may be explained on the basis of adsorption behavior. The degrees of surface coverage (θ) for different inhibitor concentrations were evaluated by weight loss data. The θ values were fitted to different adsorption isotherm models, including Langmuir, Frumkin, Freundlich and Temkin isotherms, and the best results judged by the correlation coefficient (r^2) were obtained with the Langmuir adsorption isotherm at all studied temperatures.

Freundlich adsorption isotherm could be represented using the following equation:

Langmuir: $\frac{C}{\theta} = \frac{1}{K}$ +c (1)

Where θ is the surface coverage, C is the inhibitor concentration and k is the adsorption constant. The k values presented in the Table 2 were calculated from the intercept lines on the C/ θ axis.

Temperature (K)	r^2	k ($L.mg^{-1}$)
293	0,998	0.0053
303	0,999	0.0045
313	0,999	0.0037
323	0,999	0.0033

Table 2 : Parameters of the linear regression

Results in the Table indicate that k values are seen to decrease with increasing temperature. Such behavior can be interpreted on the basis that increases in temperature results in desorption of some adsorbed components of the extracts on the surface and is consistent with the proposed physisorption mechanism (Djeddi, 2015).

3.1.2 Thermodynamic parameters

Thermodynamic parameters are important to further understand the adsorption process of BEET on steel/solution interface. The standard adsorption free energy (ΔG^0_{ads}) can be calculated on the basis equation (El Bribri, 2013; Yaro, 2013):

$$\Delta G^0_{ads} = -RTln(C_{H_2O} . k) \quad (2)$$

where R is the gaz constant, T the absolute temperature (K) and C_{H_2O} is the concentration of water with an approximate value of 10^6 mg L^{-1}. It should be noted that the unit of C_{H_2O} lies in that of k (Li, 2012).

The standard adsorption enthalpy (ΔH^0_{ads}) could be calculated on the basis of the Van't Hoff equation (Li, 2013):

$$\frac{dlnk}{dT} = \frac{\Delta H^{\circ}_{ads}}{RT^2} \quad (3)$$

Equation (3) can be rewritten as :

$$lnk = -\frac{\Delta H^{\circ}_{ads}}{RT} + I \qquad (4)$$

where I is a constant of integration. Figure. 3 presents straight lines of lnk versus 1/T with good linear relationship (the linear correlation coefficients is 0.9970). ΔH^{0}_{ads} values were calculated from the slope ($-\frac{\Delta H^{\circ}_{ads}}{R}$) and are listed in Table 4.

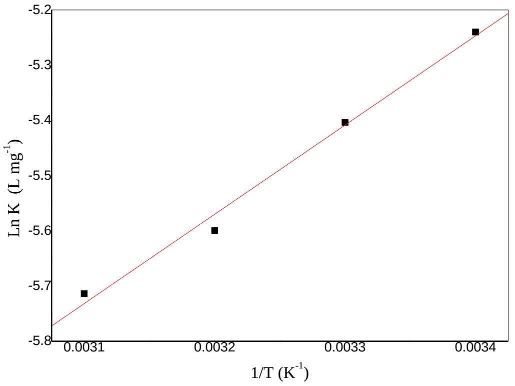

Figure. 3: Straight line of ln$k$ versus 1/T for BEET.

From the obtained values of parameters of ΔG^{0}_{ads} and ΔH^{0}_{ads}, the standard adsorption entropy (ΔS^{0}_{ads}) can be calculated using the thermodynamic Gibbs-Helmholtz equation:

$$\Delta S^{\circ}_{ads} = \frac{\Delta H^{\circ}_{ads} - \Delta G^{\circ}_{ads}}{T} \qquad (5)$$

All the standard thermodynamic parameters are listed in Table 3. The negative values of ΔG^{0}_{ads} indicates the spontaneity of the adsorption process (Deyab, 2013). In the present work, the calculated values of free energy of adsorption lie between -16.45 and -7.34 kJ mol-1, less than the threshold value (-40 kJ mol^{-1}) required for chemical adsorption and the IE% decreased with increasing temperature. These support the mechanism of physical adsorption (Hamdy, 2013). The negative sign of ΔH°_{ads} suggests that the adsorption of inhibitor is an exothermic process (Li, 2012; Ostavory, 2009). In an exothermic process, physisorption can be distinguished from chemisorption by considering the absolute value of ΔH°_{ads}. For physisorption, ΔH°_{ads} is lower than 40 kJ mol^{-1} while for chemisorption, ΔH°_{ads} approaches 100 kJ mol^{-1} (Pournazari, 2013).

T (K)	ΔG°_{ads} (kJ mol^{-1})	ΔH°_{ads} (kJ mol^{-1})	ΔS°_{ads} (J mol^{-1} K^{-1})
293	- 20,89	-13.44	25.43
303	- 21,19		25.58
313	- 21.40		25.43
323	- 21.78		25.82

Table 3: Standard thermodynamic parameters of the adsorption of BEET in 1 M HCl solution.

3.1.3 Activation parameters of the corrosion process

Temperature has a great effect on the rate of metal electrochemical corrosion. It is evident that from the figure. 2, the inhibition efficiency decreases with increasing temperature. The dependence of corrosion rate on temperature can be expressed by the Arrhenius equation (Lebrini, 2011):

$$ln\ CR = -\frac{E_a}{RT} + lnA \qquad (6)$$

Ea is the apparent activation energy of the CS dissolution and A is the Arrhenius preexponential factor. The logarithm of the CR versus 1/T can be represented as straight-lines and the activation energy values were calculated from Arrhenius plots.

The values of activation energy listed in Table 4 are higher in the presence of the BEET than in their absence. It may be attributed to the geometric blocking effect of adsorbed inhibitive species on the metal surface (Tebbji, 2007). Further inspection of Table 5 also revealed that Ea increases with increase in BEET concentration. This means that the corrosion reaction will further be pushed to surface sites that are characterized by progressively higher values of Ea in the presence of extracts (Behpour, 2012).

The enthalpy, $\Delta H^{\circ}_{a}$and entropy, ΔS°_{a} of activation for the corrosion process, the alternative formulation of Arrhenius equation was used (Behpour, 2012; Tebbji, 2007) :

$$lnV_{corr} = \frac{RT}{N_A h} exp\frac{\Delta S_a}{R} exp -\frac{\Delta H_a}{RT} \qquad (7)$$

Where h is the plank's constant, NA is Avogadro's number. A plot of ln(Vcorr/T) vs. 1/T gave a straight line with a slope of $-\frac{\Delta H_a}{RT}$ and an intercept of ($ln\frac{R}{N_A h}+\frac{\Delta S_a}{R})$, from which the values of ΔS_a and ΔH_a were calculated and listed in Table 4. The positive signs of enthalpies reflect the endothermic nature of the dissolution process (Hodaifa, 2013).

	Ea, ΔH°_{a} and ΔS°_{a} at (293 – 323) K		
C. (mg l^{-1})	E_a (kJ mol^{-1})	ΔH°_{a} (kJ mol^{-1})	ΔS°_{a} (J mol^{-1} K^{-1})
0	42.42	39.72	46.97
100	45.64	42.94	54.68
200	48.34	45.64	61.27
300	50.58	47.89	66.69
400	52.76	50.05	72.07
500	55.31	52.50	78.68
600	54.60	51.90	75.85
800	55.13	52.43	76.27
900	53.53	50.83	70.57

Table 4: Activation parameters Ea, ΔH°_{a} and ΔS°_{a} for CS in 1M HCl at different concentrations of BEET at different temperatures

The values of ΔS°_{a} given in Table 4 are positive and increased in the presence of extracts. This behavior can be explained as a result of the replacement process of water molecules during adsorption of BEET on the steel surface (Zarrok, 2012).

3.2 Polarization measurements

The anodic and cathodic polarization curves of CS steel in 1 M HCl solution devoid and containing increasing concentrations of BEET are traced and represented in Figure. 4. The respective kinetic parameters derived from the above plots are given in Table 5. It was illustrated from the data that the addition of BEET decreased the corrosion current density (icorr). The decrease may be due to the adsorption of the inhibitor on metal/acid interface (Ahamad, 2010).

In presence of BEET both cathodic and anodic Tafel slopes (βc, βa) decrease. This result indicating that the BEET is a mixed type inhibitor acting on both the hydrogen evolution reaction and metal dissolution (Bobina, 2013).

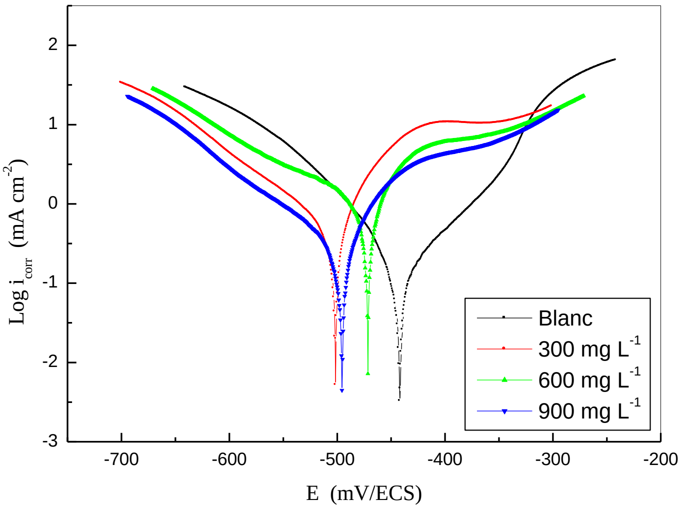

Figure. 4: Potentiodynamic polarization curves for CS in 1 M HCl containing different concentrations of BEET.

Polarization parameters at 293 K						
C. (mg L^{-1})	- E$_{corr}$ (mV)	i$_{corr}$ (mA cm^{-2})	β$_a$ (mV dec^{-1})	- β$_c$ (mV dec^{-1})	θ	IE_p (%)
Blanc	441.7	1.9129	123.5	167.2		-
300	501.3	0.7353	61	113.6	0.6156	61.56
600	471.5	0.4123	75.1	117.1	0.7845	78.45
900	483.1	0.3493	75.8	113.4	0.8174	81.74

Table 5 Potentiodynamic polarizations parameters of CS in 1M HCl for various concentrations of BEET.

		Polarization parameters at (293–323) K					
T (K)	C. (mg L^{-1})	- E$_{corr}$ (mV)	i$_{corr}$ (mA cm^{-2})	β$_a$ (mV dec^{-1})	- β$_c$ (mV dec^{-1})	θ	IE_p (%)
293	Blanc	441,7	1,9129	123,5	167,2	-	-
	900	483.1	0.3493	75.8	113.4	0.8174	81.74
303	Blanc	481,9	2,1830	164,0	108,2	-	-
	900	499.6	0.4718	51.8	104.8	0.7839	78.39
313	Blanc	504,1	2,5495	157,2	121,1	-	-
	900	398.4	0.6091	63.0	118.1	0,7611	76.11
323	Blanc	458,0	2,6891	224,6	266,3	-	-
	900	395.4	0.6878	60.9	121.4	0,7442	74.42

Table 6 Polarization parameters and corresponding inhibition efficiency for the corrosion of CS in 1 M HCl without and with 900 mg l-1 of BEET at (293–323) K

3.3 Electrochemical impedance spectroscopy

The corrosion of CS steel in 1 M HCl solution in the presence of plant extract was investigated by EIS at room temperature after an exposure period of 60 min. Impedance diagrams are obtained for frequency range 100 kHz to 0.01 Hz at the open circuit potential for steel in 1 M HCl in absence and presence of BEET. Nyquist plots for steel in 1 M HCl at various concentrations of BEET is presented in Figure. 5. Table 7 gives values of charge transfer resistance (R_{ct}) and double-layer capacitance (C_{dl}). Figure. 5 showed that the impedance spectra exhibit only one capacitive loop which indicated that the corrosion of steel is mainly controlled by a charge transfer process (Behpour, 2012; Deng, 2012). It is also clear that these are not perfect semicircles and this difference has been attributed to frequency dispersion and the heterogeneity of the metal surface (Lebrini, 2011). On the other hand, it is clear from the plots that the size of these loops increases on increasing the plant extract concentration. This suggested that the formed inhibitive film was strengthened by addition of plant extract (Hazwan, 2011).

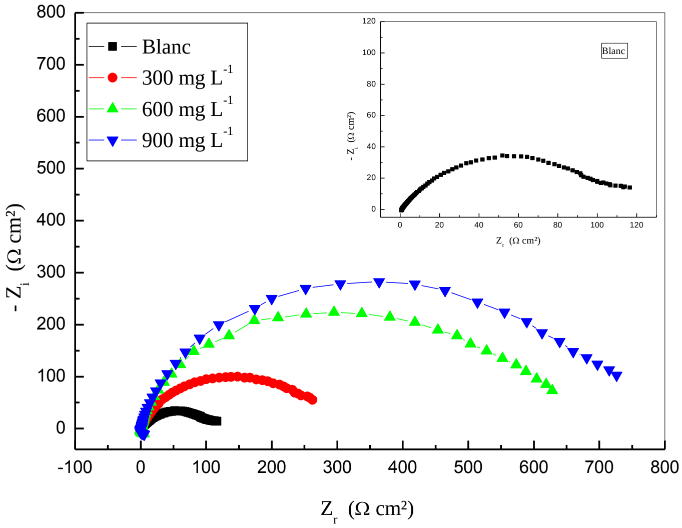

Figure. 5: Nyquist plots for CS in 1 M HCl containing different concentrations of BEET.

A simple electrical equivalent circuit (EEC) has been proposed to model the experimental data. Generally, when a non-ideal frequency response is present, it is commonly accepted to replace the double-layer capacitance by the constant phase element (CPE) (Bobina, 2013).

The values of the Cdl can be calculated from CPE parameter and Rct according to the following equation (El Bribri, 2013):

$$C_{dl} = R_{ct}^{\frac{1-n}{n}} Q^{\frac{1}{n}} \quad (8)$$

n is the deviation parameter of the CPE: $0 \leq n \leq 1$, for $n=1$, equation (8) agrees to the impedance of an ideal capacitor, where Q is identified with the capacity. The EEC depicted in Figure. 6 is employed to analyze the impedance spectra, where R1 represents the solution resistance, R_2 denotes the charge-transfer resistance, and a CPE instead of a pure capacitor represents the interfacial capacitance.

From the impedance parameters (Table 7), it is clear that the R_{ct} values increase with inhibitor concentration and consequently the inhibition efficiency increases to 82 % at 900 mg L^{-1}. The values of double layer capacitance are also brought down to the maximum extent in the presence of BEET and the decrease in the values of C_{dl} follows the order similar to that obtained for icorr in this study. The decrease in C_{dl} is due to the adsorption of the BEET on CS surface leading to the formation of a film from the acidic solution (Fouda, 2011).

Conc. (mg L^{-1})	R_{ct} (Ω cm²)	C_{dl} (µF cm^{-2})	IE (%)
0	129,6	465	-
300	324.3	186	60.04
600	576.1	107	77.50
900	719.6	88	82.00

Table 7: Electrochemical impedance spectroscopy parameters of CS in 1 M HCl for various concentrations of BEET.

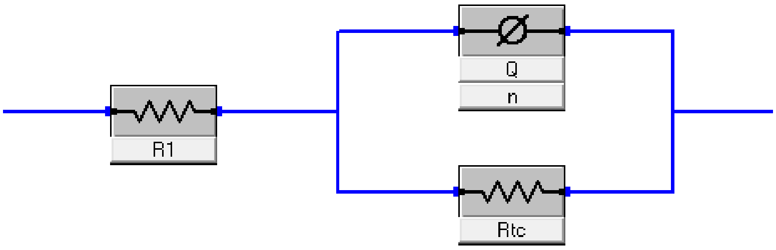

Figure. 6: Equivalent circuit used to fit the capacitive loop

T (K)	Conc. (mg L^{-1})	Electrochemical impedance parameters R_{ct} (Ω cm^2)	 C_{dl} (µF cm^{-2})	 IE (%)
293	0	129,6	465	-
	900	719.6	84	82.00
303	0	115.8	470	-
	900	604.9	94	80.86
313	0	83.68	516.2	-
	900	322.9	135	74.08
323	0	77.71	556.5	-
	900	286.4	158	72.87

Table 8 Impedance parameters and inhibition efficiency values for CS without and with 900 mg L^{-1} of BEET at (293–323) K

Corresponding data are given in Tables 6 and 8. It was observed that the i_{corr} increased and the R_{ct} decreased with increasing temperature. The inhibition efficiencies, calculated from the electrochemical impedance parameters, showed the same trend as obtained from polarization measurements and the weight loss measurements discussed above. The decrease in inhibition efficiency reveals that the film formed on the metal surface is less protective at higher temperatures, since the desorption rate of the inhibitor is greater at higher temperatures (Bayol, 2008).

Conclusion

From the overall experimental results, the following conclusions can be deduced:

Results obtained through weight loss measurements and electrochemical tests demonstrated that the butanolic extract of Elaeoselinum thapsioides acts as efficient corrosion inhibitors of the carbon steel in acid solution.

Potentiodynamic polarization measurements demonstrate that BEET acts as mixed-type inhibitor.

The adsorption of BEET on the CS surface obeys Langmuir adsorption isotherm. The negative values of free energy of adsorption (ΔGads) indicate that the adsorption process is spontaneous and physically adsorbed on the CS surface.

Reference

Ahamad I., Prasad R., Quraishi M. A., 2010. Corros. Sci. 52, 1472.
Akkal S., Louaar S., Benahmed M., Laouer H., Duddeck H., 2010. Chem. Nat. Comp. 46, 5.
Bayol E., Gurten A.A., Dursun M., Kayakirilmaz K., 2008. Acta. Phys-Chim. Sin. 24(12), 2236.
Behpour M., Ghoreishi S. M., Khayatkashani M., Soltani N., 2012. Mater. Chem. Phys. 131, 621.
Benahmed M., Akkal S., Louaar S., Laouer H., Duddeck H., 2006. Biochem. Syst. Ecol. 34, 645.
Bentiss F., Traisnel M., and Lagrenee M., 2000. Corros. Sci., 42, 127.
Bobina M., Kellenberger A., Millet J.P., Muntean C., Vaszilcsin N., 2013. Corros. Sci. 69, 389.
Bouyanzer B., Hammouti, L. Majidi, 2006. Mater. Lett. 60, 2840.
Chauhan L. R., Gunasekaran G., 2007. Corros. Sci. 49, 1143.
Deng S., Li X., 2012. Corros. Sci. 55, 407.
Deyab M.A., Abd El-Rehim S.S. J. Taiwan Inst. Chem. Eng. (2013). doi: 10.1016/j.jtice.2013.09.004
Djeddi N., Benahmed M., Akkal S., Laouer H., Makhloufi E., Gherraf N., 2015. Res Chem Intermed. 41, 4595.
El Bribri A., Tabyaoui M., Tabyaoui B., El Attari H., Bentiss F.. 2013. Mater. Chem. Phys. 141, 240.
Elayyachy M., El Idrissi A., Hammouti B., 2006. Corros. Sci. 48, 2470.
El-Etre A.Y., 2007. Corros, Sci. 314,578.
El-Etre A.Y., 1998. Corros. Sci. 40, 1845.
El-Etre A.Y., 2001. Corros. Sci.43,1031-1039.
El-Etre A.Y., 2008. Mater. Chem. Phys. 108, 278–282.
Fouda A.S., Wahed H. A., Arab. J. of chem. 2011. doi: 10.1016/ arabjc2011.02.014
Hamdy A., El-Gendy N.Sh., 2013. Egyptian. J. Petr. 22, 17.
Hazwan Hussin M., Jain kassim M., 2011. Chem. phys. 125, 461.
Hodaifa G., Ochando-Pulido J.M., Alami S.B.D., Rodriguez-Vives S., Martinez-Ferez A.. 2013. Ind. Crop. Prod. 49, 526.
Lebrini M., Robert F., Lecante A., Roos C., 2011. Corros. Sci, 53, 687.
Li L., Zhang X., Lei J., He J., Zhang S., Pan F. 2012. Corros. Sci. 63 82.
Li X., Deng S., Fu H., 2012. Corros. Sci. 62, 163.
Ostovari A., Hoseinieh S. M., Peikari M., Shadizadeh S. R., Hashemi S. J., 2009. Corros. Sci. 51, 1935.
Pournazari Sh., Moayed M. H., Rahimizadeh M., 2013. Corros. Sci. 71, 20.
Tang Y., Zhang F., Hu S., Cao Z., Wu Z., Jing W. 2013. Corros. Sci. 74, 271.
Tebbji K., Faska N., Tounsi A., Oudda H., Benkaddour M., Hammouti B., 2007. Mater. Chem. Phys. 106, 260.
Valek A., Martinez S. A., 2007. Corros. Sci. 61, 148.
Yaro A. S., Khadom A. A., Wael R. K., 2013. Alexandria Engineering Journal 52, 129.
Zarrok H., Zarrouk A., Hammouti B., Salghi R., Jama C., Bentiss F., 2012. Corros. Sci. 64, 243.

SYNTHESIS AND CHARACTERIZATION OF SOME CHLORINATED 3, 5-DIARYL-2-PYRAZOLINES ANALOGUE OF NATURAL PRODUCT AS ANTIMICROBIAL AGENTS

BENMEKHBI LOTFI , BENCHARIF LEILA

[1] Laboratoire de Catalyse et Organométalliques,: CNRS–Université de Rennes 1, Campus de Beaulieu, 35042 Rennes Cedex, France.
[2] Laboratoire de chimie des matériaux Université de Constantine1 Algérie.
[3]Département de Chimie Université constanine 3.
Email : mekhbi@yahoo.fr

Abstract

Variously substitued pyrazolines and their derivatives analogue of natural product isolated from various medicinal plants are important biological agents and a significant amount of research activity has been directed towards this class; their prominent effects are antimicrobial[1] antifungical antiviral, antiparasitic, anti-tubercular[2] and insecticidal agents[3].

A series of chlorinated 3, 5-diaryl-2-pyrazolines has been synthesized by the reaction of appropriately substituted chlorochalcones (analogue of flavonoids) and phenyl hydrazine in hot acetic acid solution. The structures of all compounds have been elucidated by microanalysis and ^{1}H- and ^{13}C- NMR spectroscopic measurements. The antibacterial activites of the synthesized compounds against staphylococcus aures ATCC 6538, Escherichia coli ATCC 8739, klebsiella pneumoniae ATCC 4352, pseudomonas aeruginosa ATCC 1539, proteus mirablis, were tested using disk diffusion method and the minimum inhibitory concentration (MIC) Method. All the déterminations tests were performed in triplicate and the results were taken as a mean of at least three determinations. The tested compounds exhibited different degrees of antibacterial activities or inhibition actions.

Keywords : pyrazolines, biological agents , chlorochalcones, antibacterial activites

References :

Ramalingham K, Thyvekikakath G X, Berlin K D, Chesnut R W, Brown R A, DurhamN N and Ealick AE J. Med. Chem. 1977, 20, 847.
Holla B, Shivarama, Akberali P M and Shivanada M K, Farmaco 2000, 55, 256.
Palaska E, Aytemir M, Tayfun I, Erol K, and Dilek E, Eur. J. Med. Chem. Ther. 2001, 36, 639.

ENVIRONMENTAL WASTEWATER IMPACT ON THE WATER RESOURCES OF THE REGION OF KHENCHELA (EASTERN ALGERIA)

BENRABAH SAMIA, ATTOUI BADRA, HANNOUCHE MANI

Université Badji Mokhtar, Faculté des sciences de l'ingénieur, Département de Géologie, Laboratoire de Géologie, Annaba, 23 000, Algérie
hydroannaba@hotmail.fr

Abstract

The vulnerability of groundwater Northeast Algerian and particularly watersheds Khenchela region depends on agricultural and urban context in the first place then the industrialist. Despite a relative abundance of water resources, high urban and agricultural growth has led to a considerable increase in water needs and therefore a high degree of pollution.

This study aims to determine the overall quality of groundwater oriented to the drinking water supply of the wilaya of Khenchela, particularly the concentration of mineral salts in order to assess their spatial and temporal variability. This area has been the subject of several previous studies, given the importance of its watershed. Some of these studies have focused on hydrology, geology and geomorphology of the watershed, this one was interested in the determination of physicochemical parameters, organic, revealing the vulnerability of waters of the North and North West part of watershed in strong mineralization, which requires a term priority during monitoring and the use of other means of evaluation for the protection of its quality.

Keywords: Vulnerability, wells, groundwater, mineral salts, assessment.

EFFECTS OF COPPER AND COBALT CO-DOPING ON STRUCTURAL, OPTICAL AND ELECTRICAL PROPERTIES OF TIO2 THIN FILMS PREPARED BY SOL GEL METHOD

BADREDDINE. TOUBAL, RABAH. BENSAHA, FAHRETTIN YAKUPHANOGLU

Badreddine. TOUBAL, Laboratoire de Céramique, Département de Physique, Université des frères Mentouri , Constantine, Algérie.
Rabah. BENSAHA, Laboratoire de Céramique, Département de Physique, Université des frères Mentouri ,Constantine, Algérie.
Fahrettin YAKUPHANOGLU, Nanoscience and Nanotechnology laboratory, Physics Departement, Firat University Elazig, Turkey.

Abstract
Un-doped TiO_2, Co single doped TiO_2 and (Cu-Co) co-doped TiO_2 thin films have been growth on silicon substrates by the sol-gel dip coating technique. We mainly investigated both effects of the dopants and annealing temperature on the structural, optical and electrical properties of TiO_2 films using X-ray diffraction (XRD), Raman and FTIR spectroscopy, Atomic force microscopy (AFM), Scanning electron microscopy (SEM), UV–Vis spectroscopy. The chemical compositions of Co-doped and (Cu-Co) co-doped TiO_2 films were confirmed by XRD, Raman and FTIR studies. The average grain sizes of $CoTiO_3$-TiO_2 nanocomposites were increased with annealing temperature. AFM and SEM reveal a completely the various nanostructures of $CoTiO_3$-TiO_2 nanocomposites thin films. The films exhibit a high optical reflectance with a large band gap. The highest electrical conductivity was obtained for the (Cu-Co) co-doped TiO_2 films. The polyhedral surface morphology might possibly improve the surface contact between particle sizes and then contribute to better electron mobility as well as conductivity. The obtained results suggest that the prepared TiO_2 films can be used for optoelectronic applications.

1. Introduction

Over the last few years, a great attention has been focused on the metal compounds thin films for various industrial and technological applications. Titanium dioxide (TiO_2) is one of the widely studied oxide materials because of its excellent optical and electrical properties (possess high transmittance and high refractive index in the visible region. exhibit a semiconductor character with a wide-band-gap 3.2 eV). (Subramaniana,2008 p.76 - Ganesh, 2012 p.21), extended stability against photo- and chemical corrosion (Pomoni, 2005 p.160). These properties make this material a candidate for a large number of prime applications such as photocatalytic purifier (Pomoni, 2005 p.160), optical thin film devices like antireflection coating for solar cell (Fujishima, 1972 p.37). TiO_2 films are used as a sensor material and also in the capacitors devices (Hara, 2001 p.151- Tang, 1995 p.71). It has been demonstrated that the properties of TiO_2 thin films can be improve by mono and co-doping with foreign elements. Copper (Sreethawong, 2005 p.661 - Aguilar, 2013 p.49), has drawn much attention because it can enhance the photocatalytic activity of TiO_2 by preventing the photo-excited electron–hole recombination. Cobalt doped TiO_2 thin films have gained much importance as they exhibit ferromagnetism at room temperature conditions which are suited for spintronic applications (Matsumoto, 2001 p.854 - Bryan, 2004 p.1640). In addition, some reports have been well suggesting that both Cu- based and Co-based catalysts were especially promising for the reduction of nitric oxide NO with carbon monoxide (CO) (Ding, 2005 p.275 -CHEN, 2009 p.1296- Stoyanova, 1998 p.233).

However, the growing interest of researchers in metal titanates compounds $MTiO_3$ (M= Fe, Co, Ni, Cu, and Zn) is also due to a series of its physiochemical properties permitting its application as photocatalysts (Chen, 2007 p.2891 - Iwasaki, 2000 p.202 - Kapoor, 2005 p. 145), gas sensors (Siemons, 2006 p.110 -Siemons, 2007 p.595), magnetic recorders (Schoofs, 2013 p.67), and electronic components (Pan, 2001 p.3447 - Kim, 2003 p.1874 - Anjana, 2006 p.2114). $CoTiO_3$ exhibits some excellent properties among them. $CoTiO_3$ is stable and can be applied in high-temperature environments (Kim, 2003 p.1874 -Liu, 2009 p.323). Moreover, the band gap of $CoTiO_3$ (~ 2.25 eV) (Xu, 2000 p.543), is narrower than that of TiO_2. Therefore, $CoTiO_3$ has strong optical absorption in visible light region (Liu, 2009 p.323- Lin, 2006 p.789). The colored semiconducting materials often indicate that they selectively absorb visible light (Wei Li, 2013 p.3). Considering its potential applications in various fields, many different synthetic routes have been adopted to fabric $CoTiO_3$ compounds, such as solid state methods (Klemme, 2011 p.54), pulsed laser deposition (Schoofs, 2013 p.67), the Pechini process (Lin, 2006 p.789) and stearic acid gel (Enhessari, 2010 p.61). Among these, sol–gel is one of the most successful methods to manufacture $CoTiO_3$ thin films, its simplicity and speed, the possibility of coating the both sides and forming multilayer and mixed compounds under different preparation conditions (Abbas, 2015 p.671).

In this study, Co doped TiO_2 and (Cu-Co) co-doped TiO_2 thin films were prepared by sol-gel technique on silicon substrates as a function of effect co-doping and annealing temperature. Structural evolutions with annealing temperature are investigated by X-ray Diffraction (XRD), Raman Spectroscopy and FTIR confirmed Spectroscopy. The optical band-gap energies of our films have been estimated from optical reflectance spectra. Finally, the current–voltage (I–V) measurements of Co doped TiO_2 and (Cu-Co) co-doped TiO_2 thin films were carried at room temperature. The electrical conductivity results of the TiO_2 thin films are presented and discussed in this paper for its possible application in the opto-electronics devices.

2. Experimental details

2.1. Samples preparation

Un-doped TiO_2, Co doped and (Cu-Co) co-doped TiO_2 thin films have been prepared by sol-gel method, which is based on the polycondensation reactions of alkoxides, in alcoholic solutions, in the presence of an acid catalyst, in three steps. The first step consists to prepare un-doped thin films of TiO_2 by following the standard procedure previously provided in (Bensouyad, 2011 p.25 - Mechiakh, 2006 p.464). In the second step, solutions of 7 wt % Co and 7 wt % (Cu-Co) were prepared separately. The total concentration of each metal ion in co-doped sols was fixed to 3.5 Wt%. 7 wt% Co and 7 wt % (Cu-Co) acetate salt were weighed in appropriate amount and dissolved in bath contained 15 ml absolute methanol and 5 ml distilled water by using continuous magnetic stirring at room temperature.

In the last step, the solution of TiO_2 were doped and co-doped with 7% of a Co and 7% (Cu- Co) solutions. Then, the resultant solutions were ready to use.

The un-doped TiO_2, Co doped and (Cu-Co) co-doped TiO_2 thin films were deposited on single crystal silicon (001) substrates by dip coating method. The substrates were dip-coated in the solutions at a constant rate of 6.25 cm s^{-1}. After each dipping, the un-doped TiO_2, Co doped and (Cu-Co) co-doped thin films were dried for 30 min at a drying temperature equal to 100 °C. The deposition process was repeated several times to increase the thickness of thin films. The coated films were annealed at 800 and 1000°C for 1 h using a furnace.

2.2. Characterization studies

The crystalline structure and the phase composition of un-doped TiO_2, Co doped TiO_2, (Cu-Co) and co-doped TiO_2 thin films deposited on silicon was analyzed by XRD with a Siemens D5000 diffractometer using CuK_α radiation (λ=1.540598 Å) The patterns were scanned at room temperature, over the angular range $20° < 2\theta < 80°$. Raman spectra experiments were performed in the region 100–800 cm^{-1} in the back scattering mode using SENTERRA R200L and OPUS as software. Infrared spectra (IR) from all films were recorded in the region of 400–4000 cm^{-1} using a Fourier Transform-Infrared Spectrometer JASCO FT/IR 6300. The micrographs of the films were examined using AFM (MFP 3D- ASYLUM RESEARCH an Oxford Instrument Company), a scanning electron microscope coupled with an energy-dispersive scanning SEM-EDX (JEOL JSM 7001F). A surface profiler ALTI SURF 500/ ALTI MAP was used to determine film thicknesses. The percentage reflectance of un-doped TiO_2, Co single doped and (Cu-Co) co-doped TiO_2 thin films were measured using a UV-Vis spectrophotometer JASCO V-670, equipped with a UV–vis–NIR integrating sphere ILN-725 in the wavelength range of 260–800 nm. The electrical properties of thin films were obtained by using I-V Measurement (Keithley, HIOKI 3532-50 LCR HIT ESTER).

3. Results and discussion

3.1. Structural properties of the films

3.1.1. X-ray diffraction analysis

Fig. 1 show the XRD patterns of un-doped TiO_2, Co single doped TiO_2 and (Cu-Co) co-doped TiO_2 thin films prepared on Si substrates and annealed at 800 and 1000°C for 1 h. The XRD pattern of un-doped TiO_2 thin film and annealed at 800°C, was a mixture of anatase and rutile phases of TiO_2. It can be noted that after Co doping and (Cu-Co) co-doping a new reflection peaks in the XRD patterns at 2Θ = 24.37 and 33.04 correspond to the (012) and (104) planes of the rhombohedral $CoTiO_3$ phase appear (Barakat, 2005 p.1 -Ehsan, 2012 p.493 - CHEN, 2009 p.1296). However, the relative intensities of the anatase peaks decrease with Co doping and (Cu-Co) co-doping. As the annealing temperature increases at 1000°C, the XRD pattern of un-doped TiO_2 film converted completely to rutile phase of TiO_2 and no anatase-related peak was detected. Comparing XRD patterns of Co doped and (Cu-Co) co-doped TiO_2 films annealed at 800°C, with those annealed at 1000°C, It can be seen that the main diffraction peak of both $CoTiO_3$ and rutile phases shifted toward larger angles and their diffraction peak intensities increased. No other phase, such as CoO, CuO or mixed Cu-Co oxide was detected indicating that there is complete solubility of Cu rutile TiO_2 (Zulfiqar, 2013 p.1271).

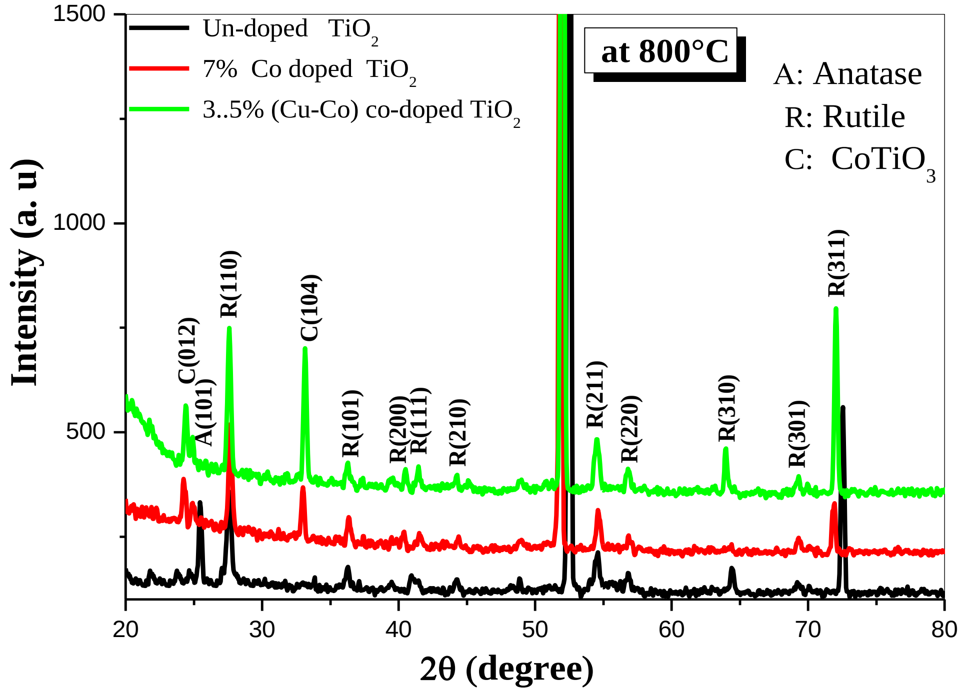

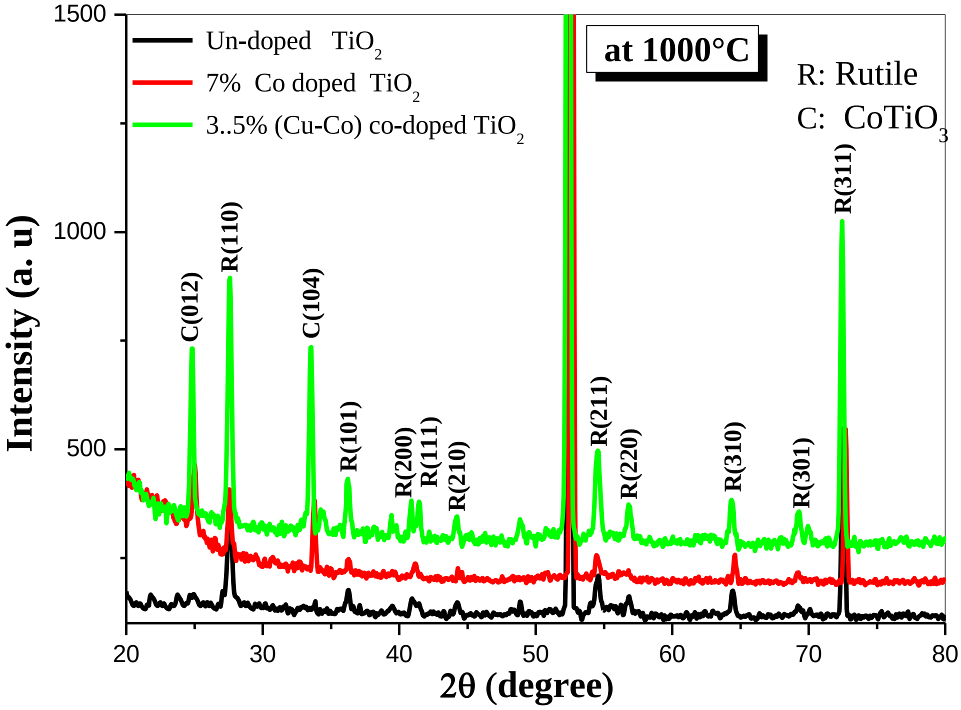

Fig.1. X-ray diffraction patterns of un-doped TiO_2, 7% Co doped TiO_2 and 3.5% (Cu-Co) co-doped TiO_2 thin films prepared on Si substrates and annealing at 800 and 1000°C.

The crystallite size values for all the deposited thin layers were calculated from XRD patterns, using the Scherrer equation yielded (West, 1992), which are listed in table 1.

$$L = \frac{k\lambda}{\beta \cos\theta} \qquad (1)$$

Where L is the crystallite size, k is a constant (=0.94 assuming that the particles are spherical), λ is the wavelength of the X-ray radiation, β is the full width at half maximum (FWHM) of (hkl) diffraction peak and θ is the angle of diffraction.

Annealing temperature T (°C)	TiO_2 films	DRX analysis calculated			Surface roughness RMS (nm)
		Phase	(hkl)	L (nm)	
800	Un-doped	Anatase	(101)	32.1	4.624
		Rutile	(110)	23.9	
	7% Co doped	Anatase	(101)	10.0	4.330
		Rutile	(110)	30.2	
		$CoTiO_3$	(104)	33.1	
	3.5% (Cu-Co) co-doped	Anatase	(101)	28.9	4.446
		Rutile	(110)	27.7	
		$CoTiO_3$	(104)	29.2	
1000	Un-doped	Rutile	(110)	25.3	4.936
	7% Co doped	Rutile	(110)	36.2	9.539
		$CoTiO_3$	(104)	33.1	

3.5% (Cu-Co)	Rutile	(110)	28.5	12.960
co-doped	CoTiO₃	(104)	32.3	

Table.1 Grain size and surface roughness of un-doped TiO_2, Co doped TiO_2 and (Cu-Co) co-doped TiO_2 films annealed at 800°C and 1000°C.

3.1.2. Raman spectroscopy analysis

Fig. 2 shows the Raman spectra of the un-doped TiO_2, Co single doped TiO_2 and (Cu-Co) co-doped TiO_2 thin films prepared on Si substrates and annealed at 800 and 1000°C for 1 h. The characteristic frequency region of the Raman spectrum for un-doped TiO_2 display different Raman active modes of anatase and the rutile phases of TiO_2 (Colmenares, 2006 p.120 - Onfroy, 2007 p.184 - Periyat, 2008 p.13). The anatase main bands are at 145, 195, 396, 640 and 797 cm^{-1} corresponding to E_g, E_g, B_{1g}, A_{1g}, B_{1g}, and E_g modes, and the rutile bands are at 446 and 609 cm^{-1} corresponding to E_g, E_g modes respectively. A large peak located at 237 cm^{-1} was often observed for rutile TiO_2 and was assigned to either second-order scattering or dynamic disorder of TiO_6 octahedra (Balachandran, 1982 p.276 - Chisaka, 2013 p.697). In addition to bands due to anatase and rutile phases presented in Raman spectrum of Co single doped and (Cu-Co) co-doped films, some additional Raman bands at 268, 334 and 693 cm^{-1} were observed. These letter bands are attributed to $CoTiO_3$ (Zhou, 2006 p.368 -Bassi, 2005 p.74305). However, with increasing annealing temperature, it can be seen that mixtures of $CoTiO_3$ and rutile are presented (fig. 2b). The rutile main peaks are at 142, 443 and 612 $cm^{-1}$and the $CoTiO_3$ bands are at 236,268, 334, 384 and 695 cm^{-1}. It has been reported that $CoTiO_3$ has ten Raman active fundamental modes ($5A_g + 5E_g$) at 696, 604, 520, 478, 456, 383, 336, 267, 238 and 208 cm^{-1} (Ganesh, 2012 p.220). The most typical feature is the strong Raman mode observed at 696 cm^{-1}. This arises from the highest frequency vibrational mode of CoO_6 octahedra units of $CoTiO_3$ and is the symmetric stretching mode (Zhou, 2006 p.368 - Pärna, 2011 p.6897- Ganesh, 2012 p.220). The main vibration typical bands and peaks of un-doped TiO_2, Co doped TiO_2 and (Cu-Co) co-doped TiO_2 thin films are shown in table 2.

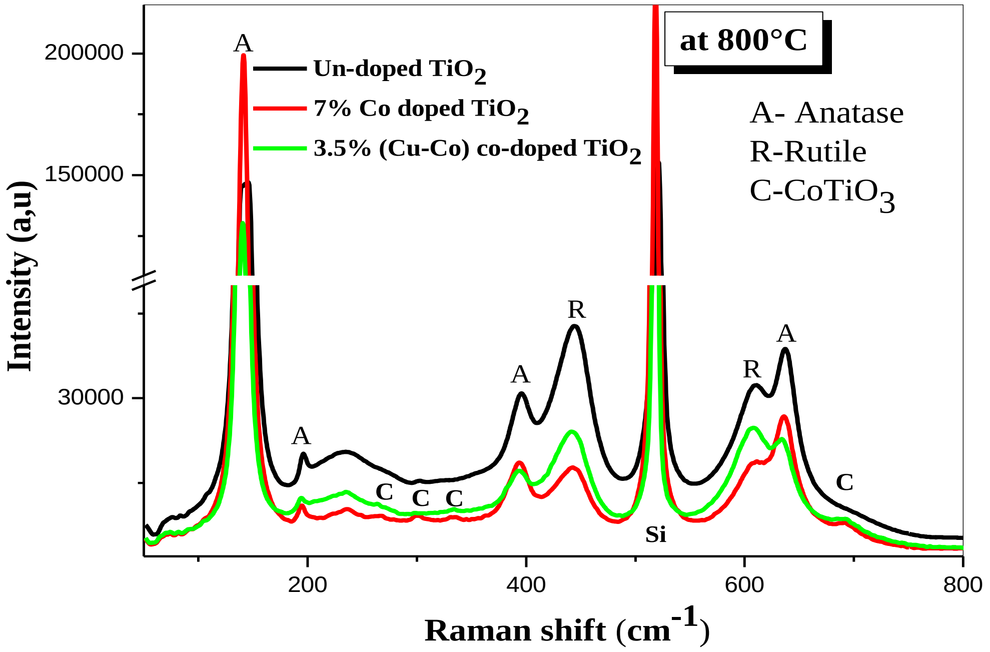

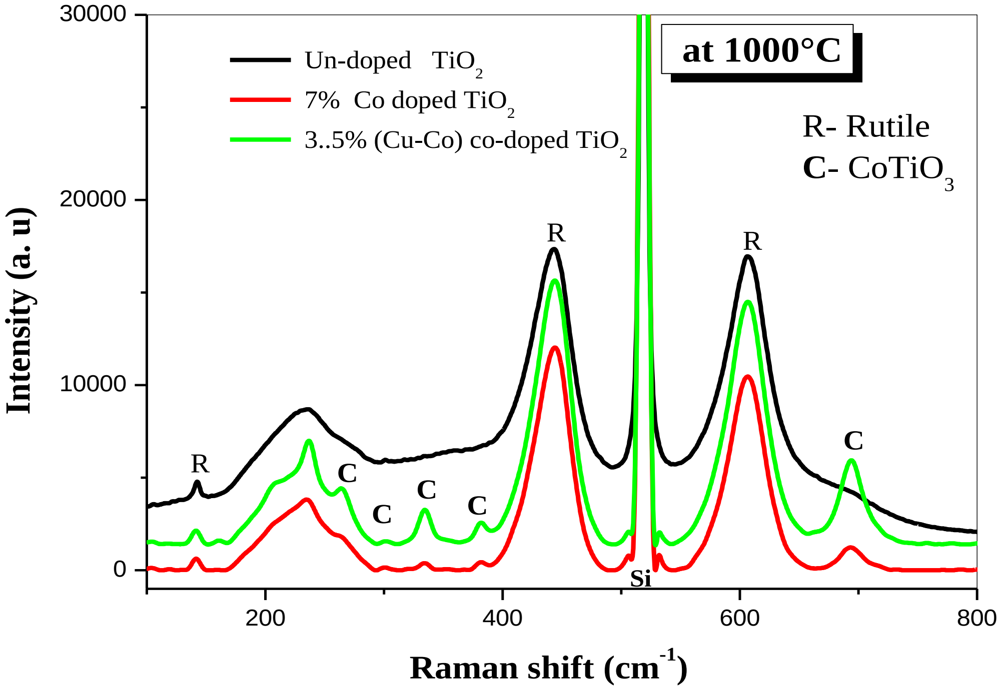

Fig.2. Raman spectra of un-doped TiO₂, 7% Co doped TiO₂ and 3.5% (Cu-Co) co-doped TiO₂ thin films prepared on Si substrates and annealing at 800 and 1000°C.

3.1.3. FTIR analysis

Fig.3 shows the infrared absorption spectrum of un-doped TiO₂, Co doped TiO₂ doped and (Cu-Co) co-doped TiO₂ thin films annealed at 800 and 1000°C respectively. These spectra were used for the detection of the presence of functional groups in the material. In the case of the films annealed at 800°C, weak absorption band observed at 1517 cm^{-1} was attributed to stretching vibration of the carboxylic group coordinated to Ti (Nolan, 2009 p. 16151). The absorption bands at 1256 cm^{-1} and 735 cm^{-1}, are characteristic of stretching vibration of Ti–OH (Liao, 2006 p.2020). The strong absorption peak at 1087 cm^{-1} is indicative of the formation of SiO₂ at the Si interface (Almeida, 1998 p.51 - Parra, 2008 p. 143). Absorption bands observed at 813 cm^{-1} and 894 cm^{-1} have attributed for the vibration mode of Si–OH and Ti–O–C respectively (Liao, 2006 p.2020 - Parra, 2008 p.143). In the low energy region below 700 cm^{-1}, a very strong absorptions at 613 cm^{-1} and 459 cm^{-1} have been observed, which are the characteristic peaks of Ti–O–Ti and O–Ti–O polymeric chains corresponding to the crystalline titania in the rutile and anatase structure (Reddy, 2001 p.205 - Reddy, 2001 p.6227).

As the annealing temperature increases, the FTIR spectra of un-doped TiO₂, Co doped TiO₂ and (Cu-Co) co-doped TiO₂ films annealed at 1000°C exhibit similar characteristic absorption bands to that of the films annealed at 800°C and the shape of these absorption bands becomes sharper with slight shift towards lower frequencies as the incorporation of dopants into crystal lattice of TiO₂. We think that the small band shifts to the lower wavenumbers, observed in our FTIR spectra may be due to increase in size of the nanoparticles or may be due to asymmetric stretching with the formation of Ti–O–Co band (Goswami, 2013 p.14480 - Alamgir, 2014 p.278). In addition, there are no absorption band assigned to the CoO, CuO or mixed Cu-Co oxide were detected in both Co doped TiO₂ and (Cu-Co) co-doped TiO₂. We assume that the possible presence of bridging ligands of such species in the TiO₂ framework, and their presence can be correlated to signal shift of characteristic bands in the FTIR and Raman spectra and in the XRD patterns of our films.

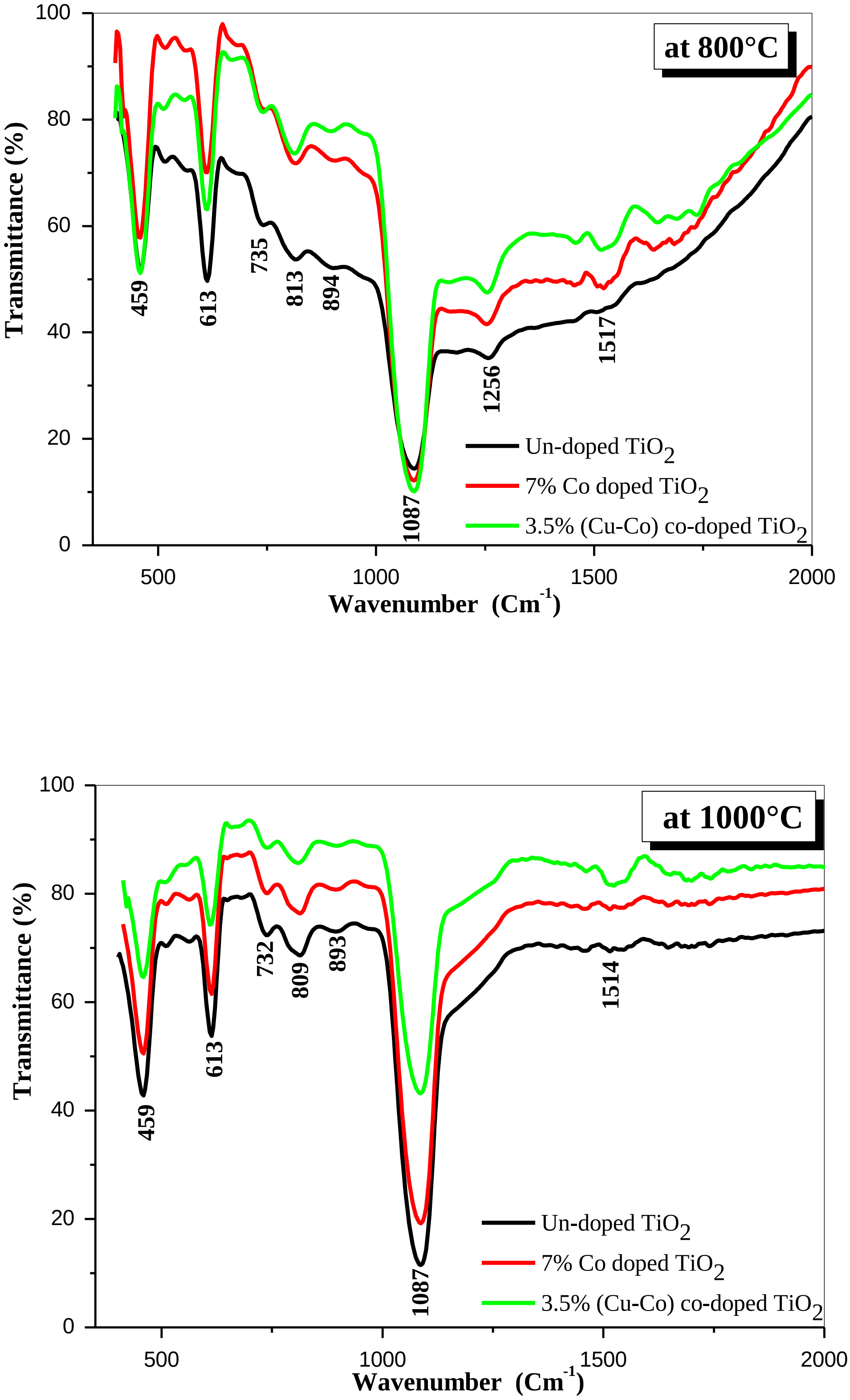

Fig.3. FT-IR spectra of un-doped TiO_2, 7% Co doped TiO_2 and 3.5% (Cu-Co) co-doped TiO_2 thin films prepared on Si substrates and annealing at 800 and 1000°C.

Annealing temperature T (°C)	TiO_2 films	Raman Shift (cm^{-1}) Anatase	Rutile	$CoTiO_3$	FT IR bands (cm^{-1}) Ti–O–Ti vibration mode
800	Un-doped	142.2	444.3	-	613.0
	7% Co doped	142.2	441.6	689.6	610.9
	3.5% (Cu-Co)	140.4	440.8	692.1	611.4
1000	Un-doped	-	443.3	-	612.8
	7% Co doped	-	444.3	693.28	612.3
	3.5% (Cu-Co)	-	444.1	694.77	611.1

Table.2 Comparison of Raman and Infrared absorption characteristic bands of un-doped TiO_2, Co doped TiO_2 and (Cu-Co) co-doped TiO_2 films annealed at 800°C and 1000°C.

3.2. Morphology observation

3.2.1. AFM analysis

The typical 2D AFM images (size 2µm x 2µm) of the un-doped, Co single doped and (Cu-Co) co-doped TiO_2 thin films prepared on Si substrate and annealed at 800, 1000°C are shown in fig.4. It was found that by increasing the annealing temperature the average grain size and roughness of the films increase as is summarized in table 1. The maximum grain size was found to be equal 30 nm for un-doped TiO_2, Co doped and (Cu-Co) co-doped TiO_2 films annealed at 800°C. The RMS roughness values were 5.033, 4.330 and 4.446 nm respectively. Fig (4d), (e) and (f) show the surface structure of the thin films annealed at 1000°C. A dependence of the grain shape on the annealing temperature can clearly be seen. Large grains appear surrounded by smaller grains. The maximum grain size was estimated to be in the range of 40 to 80 nm and the RMS roughness value was found to be in the range of 5 to 13 nm. The SEM images of both (Cu-Co) co-doped TiO_2 thin films annealed at 800 and 1000°C were taken and the results are given in fig.5.

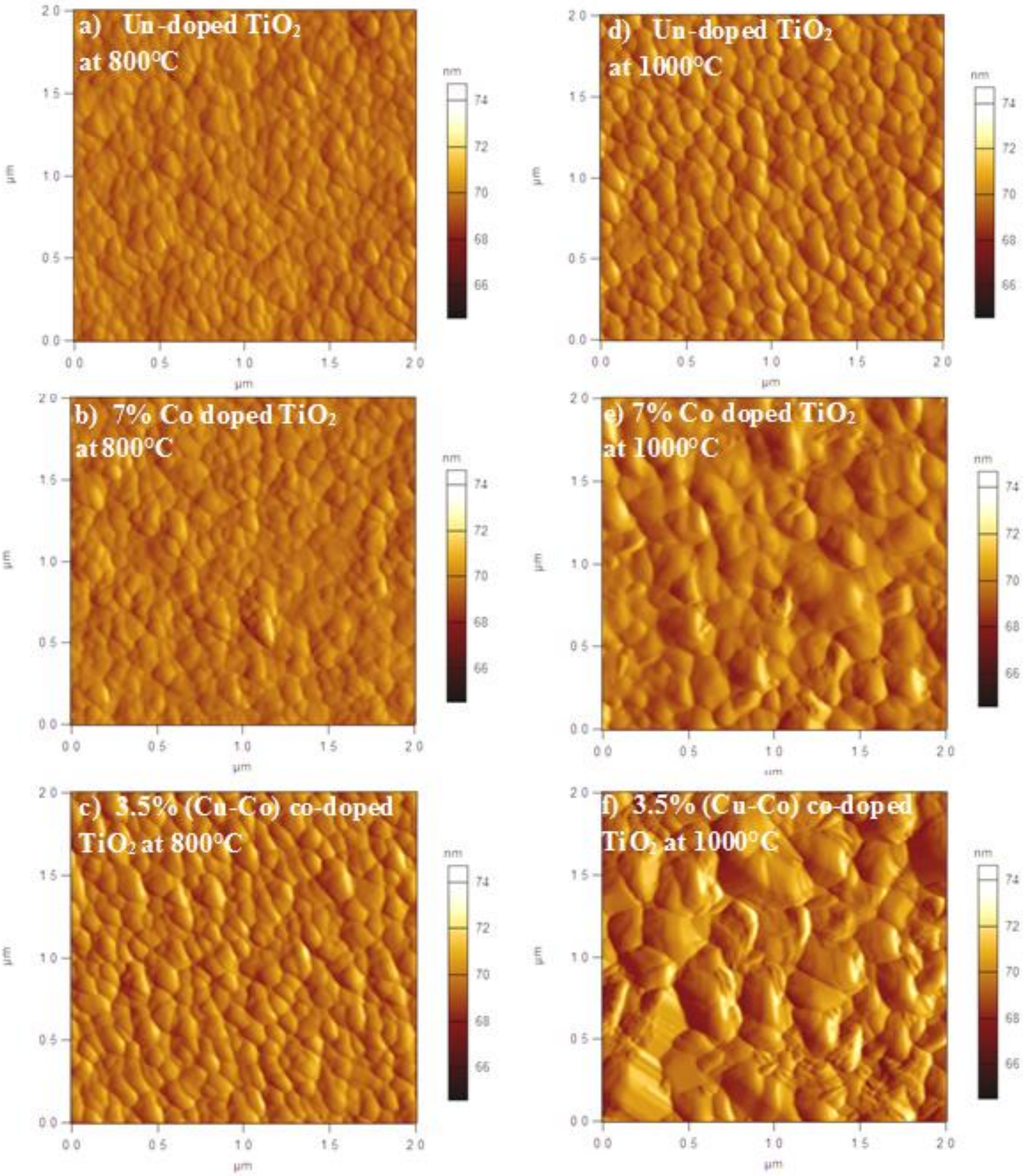

a) Un-doped TiO_2 at 800°C

d) Un-doped TiO_2 at 1000°C

b) 7% Co doped TiO_2 at 800°C

e) 7% Co doped TiO_2 at 1000°C

c) 3.5% (Cu-Co) co-doped TiO_2 at 800°C

f) 3.5% (Cu-Co) co-doped TiO_2 at 1000°C

Fig.4. AFM images of un-doped TiO_2, 7% Cobalt single doped TiO_2 and 3.5% (Cu-Co) co-doped TiO_2 thin films prepared on Si substrate and annealing at 800, 1000°C.

3.2.2. SEM analysis

SEM observations have shown differences in morphology between films annealed at 800 and 1000°C. It is clear from the fig.5 that the particles have irregularly shaped and the grains appeared to be flat, indicating coalescence process (growth) of grains. It can also be seen, some smaller particles are nearly spherical. Comparing with the film annealed at 1000°C, the (Cu-Co) co-doped film reveal a completely different morphology, the TiO_2 nanoparticles reveals a polyhedral structure, and the surface of the polyhedron was level and smooth. In addition, the (Cu-Co) co-doped film annealed at 1000°C reveal higher number of pores comparing with the film annealed at 800°C.

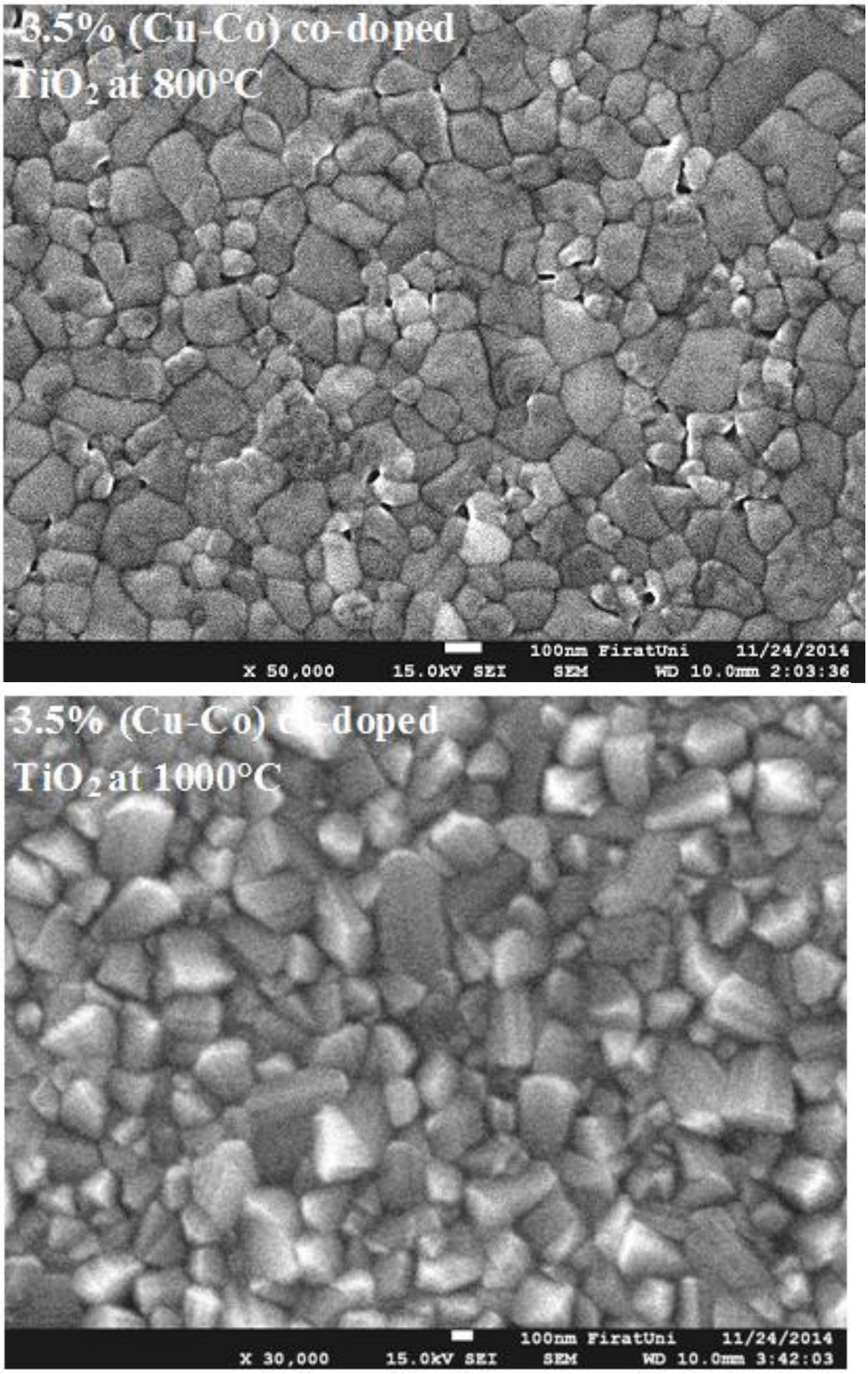

Fig.5. SEM micrographs of 3.5% (Cu-Co) co-doped TiO_2 thin films prepared on Si substrate and annealed at 800, 1000°C.

3.3. Optical properties of the films

Fig.6. Shows the reflectivity spectra of un-doped TiO_2, Co single doped and (Cu-Co) co-doped TiO_2 thin films deposited on Si substrates and annealed at 800°C and 1000°C. It is clear to see that the reflectance of films has been observed to increase with increasing in the annealing temperature, Co doping and (Cu-Co) co-doping. The most significant differences between the un-doped TiO_2, Co doped and (Cu-Co) co-doped TiO_2 films annealed at 1000°C and those annealed at 800°C in the optical reflection (fig.6) manifest in the wavy nature in the visible light

region is due to interference effect which means that our films are sufficiently thick (Sreemany, 2004 p.169 - Mahanty, 2004 p.77).

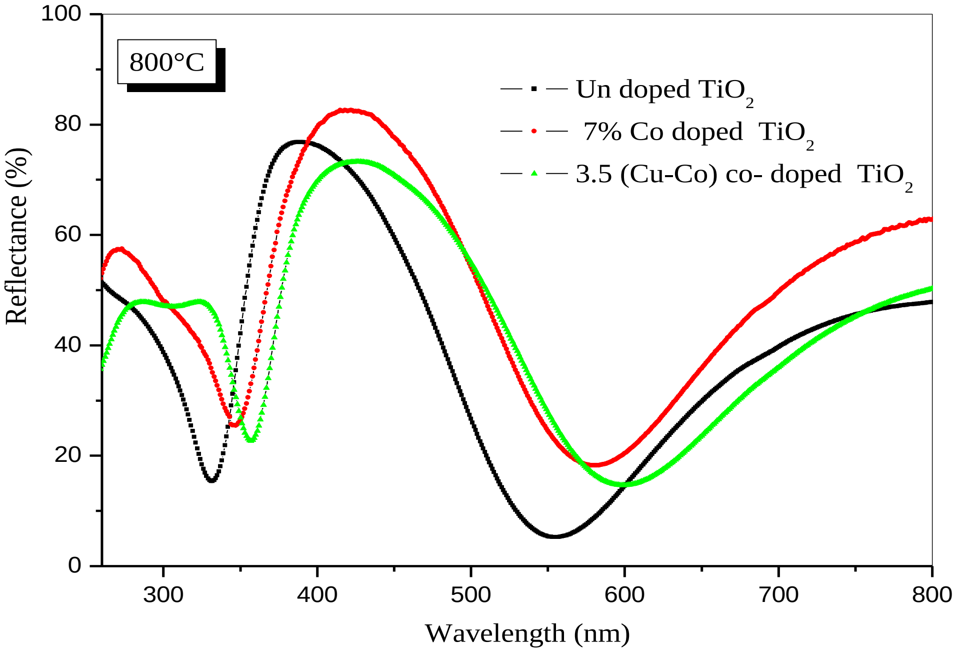

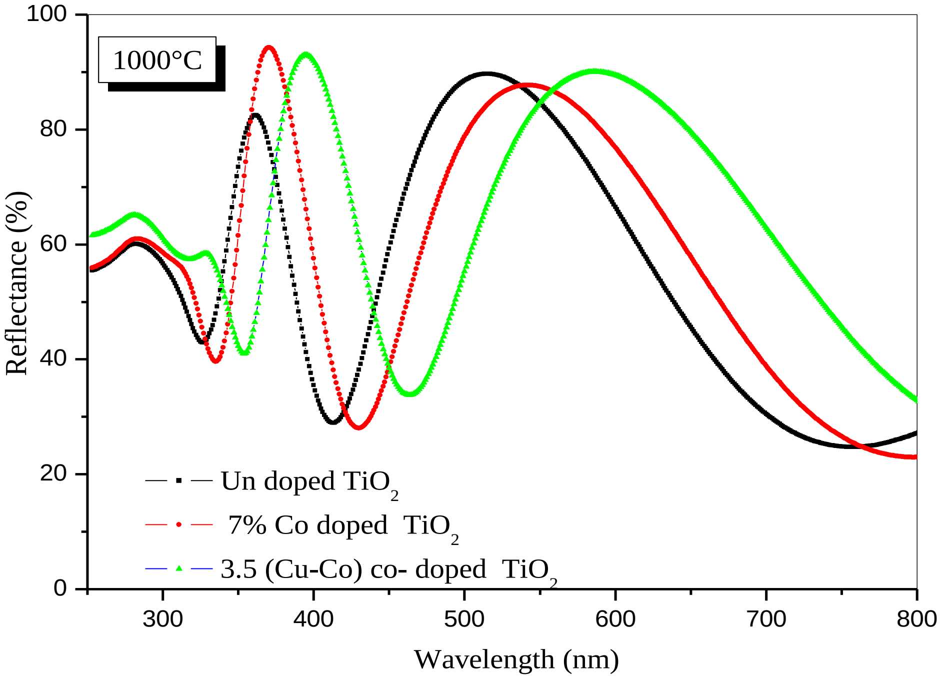

Fig.6. Reflectance spectra of un-doped TiO_2, 7% Co doped TiO_2 and 3.5% (Cu-Co) co-doped TiO_2 thin films deposited on Si and annealed at 800°C and 1000°C.

Both the reflectance coefficient of Co doping TiO_2 films annealing at 800°C and 1000°C have found to be higher compared to the un-doped and (Cu-Co) co doping TiO_2 films. We also note that the Co doped and (Cu-Co) co-doped reflectance spectra show a slightly to longer wavelength, associated with a dramatic decrease in the optical gap.

The band gap values of our films were determined from the equation reported in (Mechiakh, 2010 p670 - Abbas, 2014 p 1176) and tabulated in table.3.

$$E_g = \frac{1239.8}{\lambda} \qquad (2)$$

Where, E_g is the optical band gap (eV) and λ (nm) is the wavelength of the absorption edge in the spectrum (Grätzel, 1991 p.737).

Annealing temperature T (°C)	TiO_2 films	Layer thickness d (nm)	Ban gap energy Eg (eV)
800	Un-doped	135	3.32
	7% Co doped	139	3.05
	3.5% (Cu-Co) co-doped	134	3.08
1000	Un-doped	96	3.47
	7% Co doped	99	3.39
	3.5% (Cu-Co) co-doped	98	3.20

Table.3 Film thickness d (nm) and Band gap (eV) of un-doped TiO_2, Co doped TiO_2 and (Cu-Co) co-doped TiO_2 films for the same numbers of dipping.

The band gap values of the un-doped TiO_2 and the Co doped TiO_2 and (Cu-Co) co-doped TiO_2 thin films annealed at 800°C were found to be lower than films annealed at 1000°C. This reflects an anatase-to-rutile phase transformation and also can be attributed to the increase in crystallite size of both $CoTiO_3$ and rutile TiO_2 phases, the energy levels of the valence and conduction bands are shifted (Hamden, 2014 p.910), with increasing of the energy gap between the valence and conduction bands (Bouattour, 2010 p.818). We think that the effect of Co doping and (Cu-Co) co-doping can be distinguished from the reorganization of nanostructures from the flat grains to polyhedral structure as seen in SEM images and in the improvement in the crystalline quality of the films along with change in the film density and porosity.

3.4. Electrical analysis

In order to have information about the electrical conductivity (σ) and electrical resistivity (ρ) of un-doped TiO_2, Co doped TiO_2 and (Cu-Co) co-doped TiO_2 thin films annealed at 800 and 1000°C, respectively. The current-voltage measurements at room temperature were performed between the two metallic contacts applied to the surface of the films coated on silicon substrates. The I-V variations of un-doped TiO_2, Co doped TiO_2 and (Cu-Co) co-doped TiO_2 thin films at room temperature are illustrated in Fig.7.

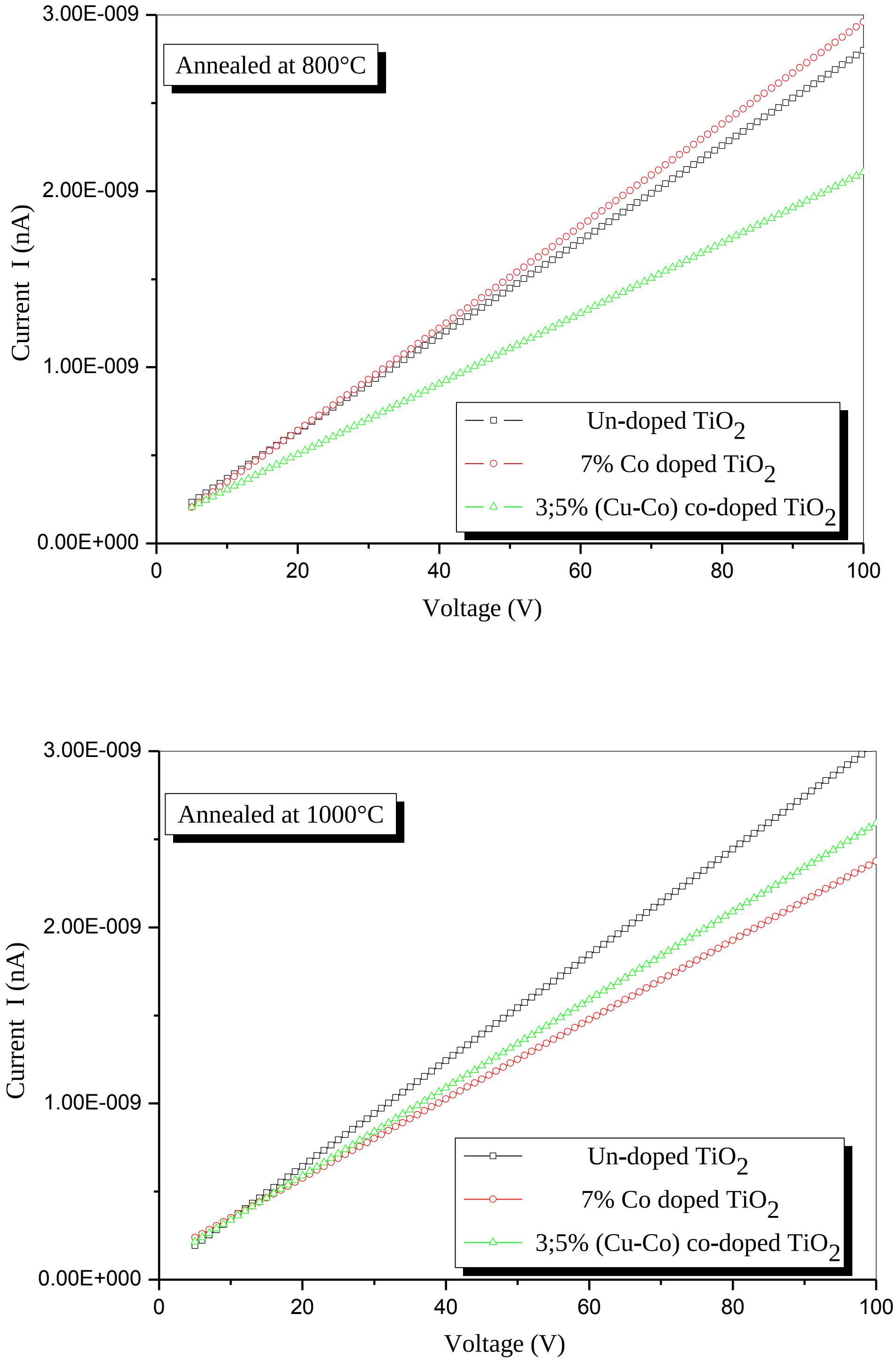

Fig.7. Room temperature I-V measurements for the un-doped TiO_2, Co doped TiO_2 and (Cu-Co) co-doped TiO_2 thin films annealed at 800 and 1000°C, respectively.

These plots indicate that linear increase of current with increase voltage, depicting the ohmic nature of the contacts as shown in the below equation

$$V = IR \qquad (3)$$

The electrical resistance (R) was calculated from the slope of the linear fit and the electrical conductivity (σ) and resistivity (ρ) of our films were deduced using the equation (4).

$$\sigma = \left(\frac{1}{\rho}\right) = Slope \left(\frac{Td}{A}\right) \qquad (4)$$

Where, (σ) is the electrical conductivity, (ρ) is the electrical resistivity, slope is the 1/R, T is the thickness of film, d is the distance between metallic contact and A is the circular area of the metallic contact (A= π r^2, with r =0.325 mm).

Table.4 present electrical resistance (R), resistivity (ρ) and conductivity (σ) values of un-doped TiO_2, Co doped TiO_2 and (Cu-Co) co-doped TiO_2 films annealed at 800°C and 1000°C, deduced from equations (3) and (4).

Annealing temperature T (°C)	TiO_2 films	resistance (R) (Ω)	Resistivity (ρ) (Ω. cm)	Conductivity (σ) (Ω. cm)$^{-1}$
800	Un-doped	4.00 10^{10}	4.54 10^{11}	2.20 10^{-12}
	7% Co doped	3.70 10^{10}	4.16 10^{11}	2.40 10^{-12}
	3.5% (Cu-Co) co-doped	3.60 10^{10}	4.00 10^{11}	2.50 10^{-12}
1000	Un-doped	5.38 10^{10}	4.29 10^{11}	2.33 10^{-12}
	7% Co doped	4.79 10^{10}	3.93 10^{11}	2.54 10^{-12}
	3.5% (Cu-Co) co-doped	4.31 10^{10}	3.70 10^{11}	2.70 10^{-12}

Table.4 Electrical resistance (R), resistivity (ρ) and conductivity (σ) (at room temperature) of un-doped TiO_2, Co doped TiO_2 and (Cu-Co) co-doped TiO_2 films annealed at 800°C and 1000°C.

For the TiO_2 films annealed at 800°C, the resistivity was calculated to be in the range 4.54 10^{11} to 4.00 10^{11} (Ω cm), the conductivity was also determined to in the range 2.20 10^{-12} to 2.50 10^{-12} (Ω cm)$^{-1}$. As the annealing temperature increases, the electrical resistivity (ρ) and conductivity (σ) values of un-doped TiO_2, Co doped TiO_2 and (Cu-Co) co-doped TiO_2 films annealed at 1000°C, were found to be in the same factor (($\rho \sim 10^{11}$) and ($\sigma \sim 10^{-12}$)) as the TiO_2 films annealed at 800°C, with a little reduction in the value of electrical resistivity (increasing in the conductivity values). Alam et al (Alam, 2002 p.137) and Sta et al (Sta, 2014 p.421) have reported similar values of electrical conductivity. In the other hand, TiO_2 is generally considered to be an insulator at lower temperatures (T < 200°C) (Fasakin, 2013 p.1) and the conduction process in TiO_2 films is due to oxygen vacancies which act as donors. Rastogi et al (Rastogi, 2000 p.1011) have shown that the room temperature conductivity of their pure TiO_2 films increased by five times after increasing oxygen vacancies.

Compared the electrical conductivity values of un-doped TiO_2 films with those of Co single doped and (Cu-Co) co-doped TiO_2 films leads us to deduce that the conduction process at room temperature in the Co doped and (Cu-Co) co-doped TiO_2 appears to be dominated by the TiO_2 matrix independent of the dopant addition. We can also observed that different thicknesses with polyhedral shapes structures also affect the conductivity of thin films

4. Conclusion

In this study, sol-gel dip coating process was employed to prepare Co single doped TiO_2 and (Cu-Co) co-doped TiO_2 thin films on silicon (001) substrates. The aim of this study is to examine both the influence of the metal ions doping and annealing temperature effect on the electrical and optical performances at room temperature. The electrical characteristics of $CoTiO_3$-TiO_2 nanocomposite films revealed that the conduction process appears to be dominated by the TiO_2 matrix independent of the (Cu, Co) dopant addition and the structural defects play a critical role to enhance the electrical conductivity of films. Formation of $CoTiO_3$-TiO_2 nanocomposites are confirmed by XRD, Raman and FTIR studies in both Co-doped and (Cu-Co) co-doped TiO_2 films annealed at 800 and 1000°C respectively. Significant differences were detected on the TiO_2 particles morphology of Co and (Cu-Co) co-doped TiO_2 thin films. A dependence of the grain shape on the annealing temperature can also clearly be seen. It has been observed the surface roughness of films increase with both the calcination temperature and (Cu-Co) doping. The films exhibit also a high optical reflectance with a large band gap. The band-gap energy of the Co-doped and (Cu-Co) co-doped TiO_2 films is found to increase with increasing annealing temperatures.

References

Subramaniana, M., Vijayalakshmi, S., Venkataraja, S., Jayavel, R., 2008.Thin Solid Films.

Ibram Ganesh, Polkampally, P. Kumar, Abhishek K. Gupta, Panakati S.C. Sekhar, Kalathur Radha, Gadhe Padmanabham, Govindan Sundararajan, 2012. Processing and Application of Ceramics.

K. Pomoni, A. Vomvas, C. Trapalis, 2005. Thin Solid Films.

A. Fujishima, K. Honda, 1972: Nature

Hara, K. Horiguchi,T. Kinoshita, T. Sayama, K. Arakawa.H. 2001. Energy Mater. Sol. Cells Tang, H. Prasad, K. Sanjinés, R. Lévy,F. 1995. Sens. Actuators, B, Chem.

Sreethawong T., Yoshikawa, S. 2005. Catal. Commun.

Aguilar, T. Navas, J. Alcántara, R. Fernández-Lorenzo, C. Gallardo,J.J. Blanco, G. Martín Calleja J., 2013. Chem. Phys. Lett.

Matsumoto,Y. Murakami, M. Shono, T. Hasegawa, T. Fukumura,T. Kawasaki,M. Ahmet, P. Chikyow, T. Koshihara,S.-Y. Koinuma,H. 2001 Science.

Daniel Bryan, J. Heald,S.M. Chambers,S.A. Gamelin,D.R. Am. J. 2004 Chem. Soc.

Ding G H, Jiang X Y, Zheng X M, 2005 Chinese Chemical Letters.

CHEN Xia, ZHANG Junfeng *, HUANG Yan, TONG Zhiquan, HUANG Ming, 2009 Journal of Environmental Sciences.

Stoyanova D, Christova M, Dimitrova P, Marinova J, Kasabova N, Panayotov D, 1998. Applied Catalysis B.

Chen, X. Mao, S.S. 2007. Chem. Rev.

M. Iwasaki, M. Hara, H. Kawada, H. Tada, S. Ito, 2000. J. Col- loid Interface Sci.

Kapoor, P.N. Uma, S. Rodriguez, S. Klabunde,K.J. Mol.J. 2005. Catal. A Chem

Siemons, M. Simon, U. 2006. Actuat. B Chem.

Siemons, M. Simon, U. 2007. Actuat. B Chem.

Schoofs F, Egilmez M, Fix T, MacManus-Driscoll JL, 2013. J Magn Magn Mater.

Pan, T.M. Lei, T.F. Chao,T.S 2001. J. Appl. Phys.

Kim, H.T. Lanagan, M.T. Am. 2003. J. Ceram. Soc,

Anjana, P.S. Sebastian, M.T. J. Am. 2006. Ceram. Soc.

Liu,X.C. Hong,R. Tian,C. 2009 J. Mater. Sci. Mater El.

Xu,Y. Schoonen, M.A.A. 2000. Am Mineral.

Y.-J. Lin, Y.-H. Chang,W.-D. Yang, B.-S.Tsai, 2006. J. Non Cryst Solids.

Ming-Wei Li, Xiao-Mei Gao, Yin-Ling Hou, Cheng-Yang Wang, C 2013. Journal of Nano-and Electronic Physic.

Klemme S, Hermes W, Eul M, Wijbrans CH, Rohrbach A, Pottgen R, 2011. Chem Cent J. Enhessari M, Parviz A, Ozaee K, Karamali E, 2010. J Exp Nanosci.

Abbas F., Bensaha R., Taroré H., 2015. Optik.

Bensouyad,H. Adnane, D. Dehdouh, H. Toubal, B. Brahimi, M. Sedrati,H. Bensaha, R. 2011. Journal of Sol-Gel Science and Technology.

Mechiakh R , Bensaha R, 2006. C. R. Physique.

Barakat, M.A. Hayes,G. and Ismat Shah,S. 2005. Journal of Nanoscience and Nanotechnology.

Muhammad Ali Ehsan, Muhammad Adil Mansoor, Muhammad Mazhar, Asif Ali Tahir , Mazhar Hamid and K. G. Upul Wijayantha, 2012. Applied Organometallic Chemistry.

CHEN Xia, ZHANG Junfeng, HUANG Yan, TONG Zhiquan, HUANG Ming, 2009. Journal of Environmental Sciences.

Zulfiqar Ali Muhammed, Nawaz Chaudhry, Syed Tajammul, Hussain, Syad Adila Batool, Syed Mustansar Abbas, Nisar Ahmad, Nisar Ali, Niaz Ahmad Niaz, 2013. Digest Journal of Nanomaterials and Biostructures.

A.R. West, 1992. Solid State Chemistry and its applications, Wiley, Chichester.

Colmenares, J.C. Aramendıa, M.A. Marinas, A. Marinas, J.M. . Urbano, F. 2006. JAppl.Catal. A: Gen.

Onfroy, T. Manoilova, O. V Bukallah, S.B. Hercules,D.M. Clet, Houalla, G. M. 2007. Appl. Catal. A: Gen.

Periyat, P Baiju,K.V. Mukundan,P. Pillai,P.K. Warrier, K.G.K. 2008. Applied Catalysis A: General.

Balachandran U., Eror, N.G. 1982. Journal of Solid State Chemistry.

Mitsuharu Chisaka, Akimitsu Ishihara, Kazuaki Suito, Ken-ichiro Ota, Hirokazu Muramoto, 2013. Electrochimica Acta.

Zhou, G.W. Lee, D.K. Kim, Y.H. Kim, C.W. Kang, Y.S. 2006. Bull. Korean Chem. Soc.

Li Bassi, A. Cattaneo, D. Russo, V. Bottani, C.E. Barborini, E. Mazza, T. Piseri, P. Milani, P. Ernst, F.O. Wegner, K. Pratsinis, S.E. SE, 2005. J. Appl. Phys.

Pärna, R. Joost, U. Nõmmiste, E. Käämbre, T. Kikas, A. Kuusik, I. Hirsimäki, M. Kink, I. Kisand, V. 2011 Applied Surface Science..

Ibram Ganesh, Gupta, A.K. P.P. Kumar, Chandra Sekhar, P.S. Radha, K. Padmanabham, G. Sundararajan, G. 2012. Materials Chemistry and Physics.

Nolan, N. T.; Seery, M. K.; Pillai, S. C, 2009. Journal of Phys. Chem. C.

Liao, M.H., Hsu, C.H., Chen, D.H. 2006 J. Solid State Chem.
Almeida, R.M. 1998. J. Sol–Gel Sci. Technol.
Parra, R. Góes, M. S. Castro, M. S. Longo, E. Bueno, P. R. Varela, 2008. J. A Chemistry of Materials.
Reddy, B.M. and Ganesh, I. 2001. Journal of Molecular Catalysis A: Chemical.
Reddy,B.M. Ganesh, I. Reddy, Fernandez, E.P. A. and Smirniotis, P.G. 2001. Journal of Physical Chemistry B.
Goswami, P. Ganguli, J.N. 2013. Dalton Trans.
Alamgir, AHN. Khan,Wasi . Shabbir Ahmad, Mehedi Hassan, M. 2014 Optical Materials.
Sreemany, Monjoy. Suchitra Sen, 2004. Materials Chemistry and Physics.
Mahanty, S. Roy, S. and Suchitra Sen, 2004. J. Cryst. Growth.
Mechiakh,R. Ben Sedrine, Chtourou, N. R. Bensaha, R. 2010. Applied Surface Science.
Abbas, F. Bensaha, R. Tarore, H .2014. C. R. Chimie.
Grätzel, M, and O'Regan, B, 1991 Nature.
Hamden, Z. Boufi, S. Conceicão, D.S. Ferraria, A.M. Botelho do Rego, A.M. Ferreira, D.P. Vieira Ferreira, L.F. Bouattour, S. 2014. Applied Surface Science.
Bouattour, S. Botelhodo Rego, A.M. Vieira Ferreira, L.F. 2010. Mater. Res. Bull.
Alam M.J. and Cameron, D.C. 2002. Journal of Sol-Gel Science and Technology.
Sta, I. Jlassi, M. Hajji, M. Boujmil, M.F. Jerbi, R. Kandyla, M. Kompitsas, M. and Ezzaouia, H. 2014. Journal of Sol-Gel Science and Technology.
Oladepo Fasakin, Marcus Adebola Eleruja, Olumide Oluwole Akinwunmi, Bolutife Olofinjana, Emmanuel Ajenifuja, Ezekiel Oladele Bolarinwa Ajayi, 2013. Journal of Modern Physics.
Rastogi, A C. Sharma, S.,N and Sandeep Kohli, 2000. Semicond. Sci. Technol.

CHEMICAL COMPOSITION, ANTIMICROBIAL AND ANTIOXIDANT PROPERTIES OF MARGOTIA GUMMIFERA ESSENTIAL OIL

BOUCHEKRIT MOUFIDA, LAOUER HOCINE, HAJJI MOHAMED, NASRI MONCEF, FLAMINI GUIDO

BOUCHEKRIT MOUFIDA, Laboratory of Natural Resources Valorization, Department of biology and ecology, University Ferhat Abbes, 19000 Setif, Algeria. LAOUER HOCINE, Laboratory of Natural Resources Valorization, Department of biology and ecology, University Ferhat Abbes, 19000 Setif, Algeria. HAJJI MOHAMED, Laboratory of Enzyme Engineering and Microbiology, National School of Engineers of Sfax, B.P. ‘’W” 3038 Sfax, Tunisia. NASRI MONCEF, Laboratory of Enzyme Engineering and Microbiology, National School of Engineers of Sfax, B.P. ‘’W” 3038 Sfax, Tunisia. FLAMINI GUIDO, Department of Pharmaceutical Sciences, Office of Bioorganic Chemistry and biopharmaceuticals, University of Pisa, Via Bonanno 33, 56126 Pisa, Italy.

Abstract
Several aromatic plants and their essential oils are known to possess antimicrobial and antioxidant properties. The aims of this study were to examine the chemical composition of the essential oil of Margotia gummifera, collected in Algeria, and to test the efficacy of the essential oil as antimicrobial and antioxidant potentials. The essential oil of the aerial parts of this plant has been extracted by hydrodistillation in a Clevenger type apparatus, and analyzed by gas chromatography and gas chromatography coupled to mass spectrometry. A total of 30 compounds have been identified, representing 96.8% of the essential oil. The main constituents of the oil were found to be β-pinene (41.6%), α-pinene (34%), γ-terpinene (3.6%), myrcene (3.5%) and p-cymene (2.8%). The antibacterial activity of M. gummifera essential oil was studied by the agar diffusion method against 11 bacterial strains and one yeast, the essential oil obtained from the aerial parts revealed a moderate activity against Pseudomonas aeruginosa ATCC 27853 (9mm), Staphylococcus aureus ATCC 25923 (9mm), Salmonella enterica ATCC 43972 (8mm) and Candida albicans ATCC 1024 with 8 mm. In the DPPH scavenging assay, the IC_{50} values of the essential oil and butylated hydroxyanisole (BHA) as a reference were 51.059mg/ml and 11µg/ml respectively.

Keywords: Margotia gummifera, essential oil, antimicrobial activity, antioxidant activity and chemical composition.

Introduction
Food poisoning is still an essential concern for both consumers and the food industry despite the use of various preservation methods. Natural products provide a significant source of potential drugs from which human kind has identified not only phytomedicines and herbal remedies, but also most of our current antibiotics and antioxydant drugs. The medicinal properties of plants from the Apiaceae (Umbelliferae) family are known since immemorial times. Nowadays, more than 100 cultivated Apiaceae species are registered for several uses, mainly as medicinal plants (41%), particularly due to their essential oils (Khoshbakht, Hammer and Pistrick, 2007; Edris, 2007; Tavares, et al., 2010, Valente, et al., 2013). Many natural compounds such as secondary metabolites, namely monoterpenes, sesquiterpenes and phenylpropanoids were isolated from Apiaceae family (Moreno-Dourado, et al., 2000; Valente, et al., 2013). Nowadays, the EOs have established draw materials for food, beverages, cosmetics, agrochemicals and pharmaceuticals industries (Scott, 2005; Breitmaier, 2006; Newman and Crag, 2007; Lucera, et al., 2012; Rajashekar, Bakthavatsalam and Shivanandappa, 2012; Evergetis and Haroutounian, 2014).

Margotia gummifera (Desf.) Lange (synonym Elaeoselinum gummiferum), commonly known as bruce-fetid, is the only species of the genus Margotia (Apiaceae) (Valente, et al., 2013). Regarding its essential oil composition, only too detailed study has been performed (Valente, et al, 2013; Pala-Paul, Perez-Alonso and Velasco-Negueruela, 2001), and it identifies α-pinene, myrcene, β-pinene, sabinene and β-phellandrene as the main compounds. That study comprised plant samples from Spanish and Portugal regions, justifying further analytical investigations with plants growing in other localities. However, to the best of our knowledge, no biological assays of M.gummifera have been performed (except the anti-inflammatory activity which was studied by Valente, et al. (2013).

Because of the resistance that pathogens build against antibiotics, there is a growing interest about the use of natural antibacterial products for food preservation. Reichling, et al. (2009) have compiled the most important results about antibacterial and antiviral properties of essential oils published in the last decade. In addition, the antioxidant activity of essential oils is another biological property of great interest because it may preserve foods from the toxic effects of oxidants (Maestri, et al., 2006; Miguel, 2010).

Therefore, the aim of this present study is (a) to examine the chemical composition of the essential oils isolated from the aerial part of M. gummifera by GC–MS, and (b) to evaluate the antibacterial and the antioxydante activity of essential oils.

MATERIALS AND METHODS

Chemicals

1,1-diphenyl-2-picrylhydrazyl (DPPH), butylatedhydroxyanile (BHA) were purchased from Sigma-aldrich (St Louis, MO, USA), potassium ferricyanide (LOBA chemicals), trichloroacetic acid (TCA: Scharlau chemicals, Espagne), Dipotassium Phosphate (K_2HPO_4: ACROS, USA), Monopotassium phosphate (KH_2PO_4: Panreac, Espagne) ferric chloride (Biomedicals) and other solvents, DMSO.

Preparation of the plant material

The aerial parts of M. gummifera are collected in the region of Bijaia, in September 2013 during the period of blooming. Then, it is freed from the impurities then dried in the shade in an ambient temperature. The plant colected has been identified by Pr. LAOUER Hocine, "Laboratory of Natural Resources Valorization, Department of biology and ecology, University Ferhat Abbes, Setif. Algeria. Voucher specimens of the plant material are deposited in the Herbarium at the department of biology and ecology, University of Setif (UFAS).

Extraction of the essential oil

The dried aerial parts of the studied plants M.gummifera were submitted for 3 hours to hydrodistillation using a French-type Clavenger apparatus. The obtained essential oils were dried over anhydrous sodium sulphate, then stored at 4°C until tested and analysed.

Gas chromatography analysis

The GC analyses were accomplished with a HP-5890 Series II instrument equipped with DB-WAX and DB-5 capillary columns (30 m x 0.25 mm, 0.25 µm film thickness), working with the following temperature program: 60°C to 240°C at 3°C/min; injector and detector temperatures 220°C; carrier gas helium (2 ml/min); detector dual FID; split ratio 1:30; injection of 0.5 µl). The identification of the components was performed, for both the columns, by comparing their retention times with those of pure authentic samples and by means of their linear retention indices (lri) relative to the series of n-hydrocarbons.

GC-EIMS analyses were performed with a Varian CP-3800 gas-chromatograph equipped with a DB-5 capillary column (30 m x 0.25 mm; coating thickness 0.25 µm) and a Varian Saturn 2000 ion trap mass detector. Analytical conditions: injector and transfer line temperatures 220 and 240°C respectively; oven temperature programmed from 60°C to 240°C at 3°C/min; carrier gas helium at 1 ml/min; injection of 0.2 µl (10% hexane solution); split ratio 1:30. Identification of the constituents was based on the comparison of the retention times with those of authentic samples, comparing their linear retention indices relative to the series of n-hydrocarbons, and on computer matching against commercial (NIST 98 and ADAMS) and home-made library mass spectra built up from pure substances and components of known oils and MS literature data (Stenhagen, Abrahamsson and McLafferty, 1974; Massada, 1976; Jennings and Shibamoto, 1980; Swigar and Silverstein, 1981; Davies, 1990; Adams, 1995). Moreover, the molecular weights of all the identified substances were confirmed by GC-CIMS, using MeOH as CI ionizing gas.

Antimicrobial activity

Microbial strains

Antibacterial activity of M. gummifera essential oils were tested against 11 strains of bacteria: Staphylococcus aureus ATCC 25923, Micrococcus luteus ATCC 4698, Escherichia coli ATCC 25922, Pseudomonas aeruginosa ATCC 27853, Klebsiella pneumonia ATCC E47, Salmonella typhi ATCC 19430, Salmonella enterica ATCC 43972, Staphylococcus aureus resistant against the Méthyciline ATCC 43300 (S.A.R.M.), Listeria inocula CIP ATCC 74915, Bacillus cereus ATCC 11778 and Enterococcus faecalis ATCC 29212. Antifungal activity was tested using Candida albicans.

Agar diffusion method

Antimicrobial activity was performed according to the method described by Berghe and Vlietinck (1991). M.gummifera essential oils were dissolved at 100 mg/ml in 100% dimethylsulfoxide (DMSO). Culture suspension (200µl) of the tested microorganisms 10^6 colony-forming units (CFU)/ml of bacteria cells (estimated by absorbance at 600 nm) and 10^8 spores/ml of fungal strains (measured by Malassez blade) were spread on Muller-Hinton agar and Luria-Burtani medium respectively. Then, bores (3 mm depth, 6 mm diameter) were made using a sterile borer and were loaded with 60 µl of each sample essential oil. A well with only 60 µl of DMSO (without E.O.) was used as a negative control. Gentamycin and nystatine were used as positive references for bacteria and fungi respectively. The Petri dishes were kept, first, for 3 h at 4°C, and then incubated for 24 h at 37 °C for bacteria, 48 h at 30 °C for C. albicans strain. Antimicrobial activity was evaluated by measuring the diameter of the growth inhibition zones in millimeters (including well diameter of 6 mm). The measurements of inhibition zones were carried for two sample replications, and values are the averages of two replicates.

Antioxidant activity

DPPH assay

The DPPH radical-scavenging activity of M. gummifera essential oils is determined by the method of Kirby and Schmidt (1997) with some modifications. A volume of 500µl of essential oils at different concentrations (1 - 30mg/ml) was added to 375µl of 99,8% ethanol and 125µl of DPPH solution (0,02%) as free radical source. The mixtures were incubated for 60 min in the dark at room temperature. Scavenging capacity was measured spectrophotometrically by monitoring the decrease in absorbance at 517nm. In its radical form, DPPH has an absorption band at 517nm which disappears upon reduction by an antiradical compound. Lower absorbance of the reaction mixture indicated higher free radical-scavenging activity. BHA was used as positive control. DPPH radical-scavenging activity was calculated as:

DPPH radical scavenging activity% = $[(A_c – A_s) / A_c] \times 100$

Where:

- $A_{control}$ is the absorbance of the control reaction (containing all reagents except the sample).
- A_{sample} is the absorbance of M. gummifera essential oils.

Ferric-reducing activity

The reducing power of M. gummifera essential oils was determined by the method of Yildirim, Mavi and Kara (2001). Sample solutions (0.5ml) with different concentrations (0.5-10mg/ml) of the essential oil were mixed with 1.25ml of 0.2M phosphate buffer (pH 6.6) and 1.25ml of (10g/l) potassium ferricyanide solution. The mixtures were incubated for 30 min at 50°C. After incubation, 1.25ml of (100g/l) trichloroacetic acid was added. A 1.25ml aliquot of the supernatant from each sample mixture was mixed with 1.25ml of distilled water and 0.25ml of (1.0g/l) ferric chloride solution in a test tube. After a 10 min reaction time, the absorbance was measured at 700nm. Higher absorbance of the reaction mixture indicated higher reducing power.

RESULTS AND DISCUSSION

Essential oil composition

The hydrodistillation of the aerial parts of M. gummifera species collected in Algeria yielded white oil with a strong perfumery odour. The yield of the volatile oil obtained was 1.76% in relation to the dry weight of the plant, which confers an industrial potential interest. The essential oil obtained was analysed by using the gas chromatography (GC) and GC/mass spectrometry (MS) techniques. The results of the qualitative and quantitative oil analyses were listed in Table 1. From the data obtained, 30 compounds were identified, representing 96.8% of the total oil.

The highest percentages of compounds (Table 1) were Monoterpene hydrocarbons (88.9%), followed by Oxygenated monoterpenes (7.6%). The lowest percentage of compound was found for Sesquiterpene hydrocarbons (0.3%).

To the best of our knowledge, there are few reports on the chemical composition of the essential oil isolated from the plant belonging to the genus Margotia. In the essential oil obtained from ripe umbels with mature seeds of M. gummifera collected from three different regions of Portugal (Cabo Sardao, Cabo de S. Vicente and Sagres), the yield varied from 1.3% to 1.8% (v/w) with high contents of monoterpene hydrocarbons (85.0–88.1%) (Valente, et al., 2013). Results obtained from the present study are similar to the data published before.

As can be seen in the Table 1, β-pinene (41.6%) was found as the major component of aerial part essential oil, followed by α-pinene (34%). β-pinene was detected in the essential oils of M. gummifera umbels (6.2-8.1%), which contained the sabinene as the most abundant substance (23.5-21%) (Valente, et al., 2013).

α-pinene had been previously identified as one of the main compounds in M. gummifera ripe umbels (12.5-11%) (Valente, et al., 2013), this compound also dominated in the oil obtained from the same plants growing in Spain (37.4%) (Pala Paul, Perez-Alonso and Velasco-Negueruela, 2001; Valente, et al., 2013). Bader, Cioni and Flamini (2010) reported α-pinene (60.8%), sabinene (12.8%) and β-pinene (8.2%) as the main compounds obtained from Elaeoselinum asclepium subsp. Meoides recolted in Sicily, Italy.

γ-terpinene (3.6%), myrcene (3.5%), p-cymene (2.8%) and myrtenol (2.3%) were other important constituents of this oil. Valente, et al. (2013) found also that limonene (7.5-8.8%) and γ-terpinene (5-5.6%) were dominant in the rupe umbels. Whereas, p-cymene was in form of traces (1-1.3%) and myrtenol was completly absent. In addition, myrcene showed the higher concentration in the oils obtained from Spain and Portugal plants with 22.8% and 23-20.3% respectively. (Pala-Paul, Perez-Alonso and Velasco-Negueruela, 2001; Valente, et al., 2013).

Our study revealed the presence of a low concentration with sabinene (0.5%), this compound was present in the essential oil of M. gummifera harvested in Spain (fruits) and Portugal (rupe umbels) with 16.3% and 23.5-20.4% respectively (Bader, Cioni and Flamini, 2010).

Pinar, Rodriguez and Alemany (1978) have examined the roots of Margotia gummifera (Desf.) Lange (= Elaeoselinum gummiferum (Desf.) Tutin) from which two diterpenic compounds have been isolated. One of these diterpenoids is the previously known ent-kaur-16-en-19-oic acid (Henrlck and Jefferies, 1964) and the other one is a new substance, gummiferolic acid. (Pinar, Rodriguez and Alemany, 1978). Kaurane flavonoids have also been detected, such as luteolin in E. foetidum and E. meoides, quercetin in E. gummiferum, and kaempferol in E. tenuifolium (Crowden, Harborne and Heywood, 1969; Bader, Cioni and Flamini, 2010).

As reported in the literature, many factors such as the geographical origin, the genetic factors, the plant material, and the season in which the plants were collected may be responsible for the variation of the chemical composition of the essential oils (Sivropoulou, et al., 1997; Hajji, et al., 2010).

Table 2. Chemical composition of the essential of M. gummifera from Algeria.

Constituents	EO of Margotia gummifera	l.r.i.	
α-thujene	0.2	933	4.57
α-pinene	34.0	941	4.75
Camphene	0.3	955	5.09
Thuja-2,4(10)-diene	0.2	959	5.22
Sabinene	0.5	977	5.71
β-pinene	41.6	981	5.79
Myrcene	3.5	993	6.15
α-phellandrene	0.1	1006	6.55
δ-3-carene	0.3	1013	6.73
p-cymene	2.8	1028	7.17
Limonene	1.6	1032	7.30
γ-terpinene	3.6	1063	8.30
Terpinolene	0.2	1090	9.36
6-camphenone	0.1	1092	9.43
6,7-epoxymyrcene	0.1	1096	9.54
Perillene	0.1	1101	9.85
α-campholenal	0.6	1127	10.79
cis-verbenol	0.2	1142	11.38
Trans-verbenol	1.3	1146	11.52
Trans-pinocamphone	0.1	1162	12.15
Pinocarvone	0.6	1164	12.23
p-mentha-1,5-dien-8-ol	0.6	1168	12.43
4-terpineol	0.3	1179	12.84
cis-pinocarveol	0.2	1185	13.19
α-terpineol	0.4	1191	13.41
Myrtenol	2.3	1195	13.64
Verbenone	0.3	1206	14.18
Trans-carveol	0.3	1219	14.61
Perilla alcohol	0.1	1297	18.09
γ-muurolene	0.3	1478	25.74

Monoterpene hydrocarbons	88.9		
Oxygenated monoterpenes	7.6		
Sesquiterpenehydrocarbons	0.3		
Oxygenated sesquiterpenes	0.0		
Phenylpropanoids	0.0		
Non-terpene derivatives	0.0		
Total identified	96.8		

Antimicrobial activity

The antibacterial activity of M. gummifera essential oil was evaluated against Gram positive (L. inocula, B. cereus, E. faecalis, S. aureus, S.A.R.M and M. luteus), Gram negative (S. typhi, S. enterica, P. aeruginosa, E. coli and K. pneumoniae) bacteria and one fungy C. albicans. The results of the antimicrobial test of the essential oils are presented in Table 2. The control disk with DMSO showed no activity at all.

As can be seen from the Table 2, essential oil showed remarkable activity against the test microorganisms (bacteria and fungy). According to the results, the most sensitive microorganisms were SARM, B.cereus, L.inocula, E. faecalis and M.luteus (G^+) which have the lowest diameters of inhibition (6mm) compared to Gentamycin control positive (27, 30, 26, 30 and 24mm respectively). However, we observed a moderate inhibition of the crude extract at its dilutions on S. aureus with diameters of inhibition of 9 mm (Gentamycin =.25mm). Surprisingly, dilutions of the essential oil was devoid a moderate activity againts Gram negative bacteria, S. enterica and P. aeruginosa with inhibition zone of 8 and 9mm respectively. Notwithstanding, no activity was observed on E. coli and S. typhi. Regarding the antifungal effect, the oils obtained from aerial parts were effective against the pathogenic yeast C. albicans with a diameter of inhibition around 8mm in comparison to Nystatin (21mm).

Apiaceae essential oils are known to possess antimicrobial activity against a wide spectrum of microorganisms (Ekiert, 2000; Di Pasqua, et al., 2005; Kosalec, Pepeljnjak and Kustrak, 2005; Ozcan, et al., 2006; Demirci, et al., 2007; Tavares, et al., 2008; Oroojalian, et al., 2010; Tavares, et al., 2010).

Accordingly, our results demonstrated that the antimicrobial activity of M. gummifera essential oil might be related to their Monoterpene hydrocarbons components which constitute more than 88.9% of the oil, such as α-pinene, β-pinene and myrcene. However, Non-terpene derivatives, Phenylpropanoids and Oxygenated sesquiterpenes were absent in this oil, Sesquiterpene hydrocarbons and Oxygenated monoterpenes represent low concentration (0.3% and 7.6%, respectively). Many studies have demonstrated that sesquiterpenes (α-bisabolol, α-curcumene) possess various biological activities, including antibacterial, cytotoxic and antifungal activities (Seto, et al. 1988; Selles, et al. 2013; Meliani, et al., 2013). Pauli (2006) reported that α-bisabolol from Matricaria chamomilla (asteraceae) may inhibit fungal growth via specific inhibition of ergosterol biosynthesis. Sadashiva, et al. (2010) reported that α-curcumene possesses antibacterial properties. Moreover, other components such as farnesene, farnesol, pinene, sabinene and limonene, cubebene may also contribute to the antimicrobial activity of the oil (Maria-Rose, et al., 2004; Togashi, et al., 2008; Su Jian-Yu, Zhu and Ying-Juan, 2012; Merghache, et al., 2014). It has been shown that the phenolic components of essential oils showed the strongest antimicrobial activity, followed by aldehydes, ketones and alcohols (Arora and Kaur, 1999; Marino, Bersani and Comi, 1999; Özcan, 1998; Özkalp and Özcan, 2009; Hajji, et al., 2010). In this respect, Skaltsa, et al. (2003) reported that aldehydes and alcohols from essential oils are known to be active, with different specificities and levels of activity, which is related not only to the functional groups present but also to hydrogen bonding parameters (Hajji, et al., 2010). Tavares, et al. (2010) found that the antifungal activity of Distichoselinum tenuifolium oil was superior compared to that of its main compound assayed individually, myrcene (77.4%). Tirillini, et al. (2009), the strong antifungal activity of L. garganicum could be due to the presence of the oxygenated components.

The conclusion that can be drawn from the obtained results is that the essential oil of M. gummifera has a moderate capacity to inhibit the growth of both Gram positive and Gram negative bacterial strains and yeasts, the sensitivity of Gram positive bacteria may be explained according to their cell wall structure. Moreover, differences in susceptibility among the microorganisms to the antimicrobial activity of essential oils may be explained by inherited genes on plasmids (Askari, et al., 2009), the active fraction is probably responsible for the antimicrobial activity of the essential oil (Özkalp and Özcan, 2009). In our opinion, it is also possible that the antimicrobial activity of the oil is a synergistic effect of the major and minor constituents present in the essential oil (Merghache, et al., 2014; Tavares, et al., 2010). It should be noted that DMSO at the concentration used does not present any inhibitory activity against the bacteria and yeasts tested.

According to our literature survey, we could reach no report for the antimicrobial activity of the essential oil and/or plant extracts of M. gummifera. From this point of view, data presented here could be assumed as the first report on this topic and will introduce a significant contribution into the literature.

Table 2: Antimicrobial activity of essential oil of M. gummifera

Test organisms	Inhibition zone diameter of E.O. (mm)	Standard Gentamycin Nystatin	DMSO T-
Salmonella typhi ATCC 19430	0	35.0 ± 1.0	-
Escherichia coli ATCC 25922	0	29.0 ± 1.0	-
Micrococcus luteus ATCC 4698	0	24.0 ± 1.0	-
Salmonella enterica ATCC 43972	8	13.0 ± 2.0	-
Staphylococcus aureus ATCC 25923	9	25.0 ± 1.0	-
Enterococcus faecalis ATCC 29212	0	30.0 ± 2.0	-
S.A.R.M. ATCC 43300	0	27.0 ± 1.0	-
Bacillus cereus ATCC 11778	0	30.0 ± 2.0	-
Listeria inocula cip ATCC 74915	0	26.0 ± 1.0	-
Pseudomonas aeruginosa ATCC 27853	9	35.0 ± 2.0	-
Klebsiella pneumonia ATCC E47	0	16 ± 1.0	-
Candida albicans ATCC1024	8	21	-

- E.O: the essential oil of aerial part of Margotia gummifera during the flowering stage.
- Gentamycin was used as a standard for antibacterial activity.
- Nystatin was used as a standard for antifangal activity.
- DMSO (Dimethyl sulfoxide) was included as a negative control.

Antioxidant activity

Antioxidant properties of the essential oil were evaluated to find a new natural source of antioxidant. In this research, two most widely used assays, namely 2,2-diphenyl-l-1- picrylhydrazil (DPPH) and Reducing power (RP) methods, were applied to evaluate the antioxidant potentials of the essential oil extracted from the aerial parts of M. gummifera. DPPH measures the free radical scavenging ability of the oil, whereas reducing power measures the ability of the essential oil to reduce metal ions. DPPH is a very stable radical, able to accept an electron or a hydrogen atom creating the diamagnetic molecule (non radical), while in Reducing power there is a single electron transfer (Prior, Wu and Schaich, 2005). The activities of the essential oil were compared with the synthetic antioxidants BHA which was used as antioxidant references.

DPPH radical-scavenging assay

The DPPH method was evidently introduced nearly 50 years ago by Blois (1958) and it is widely used to test the ability of compounds to act as free radical scavengers or hydrogen donors, and to evaluate antioxidant capacity (Proestos, et al., 2013).

The antioxidant activity of the essential oil of M. gummifera was determined by the DPPH test system. DPPH is a stable nitrogen centered free radical, the color of which changes from violet to yellow upon reduction by either the process of hydrogen -or electron- donation. Substances which are able to perform this reaction can be considered as antioxidants and therefore radical scavengers (Ebrahimzadeh, et al., 2009; Nabavi, et al., 2008; Nabavi, et al., 2011).

The parameter EC_{50} (Efficient Concentration‖ Value), is used for the interpretation of the results from the DPPH method and is defined as the concentration of substrate that causes 50% loss of the DPPH activity (color) (Proestos, et al., 2013), the lower is the EC_{50}, the higher is the antioxidant power (Hamdy Roby, et al., 2013).

Figure 1 demonstrates DPPH scavenging activity, expressed in percentage, caused by different concentrations of essential oil from M. gummifera in comparison with BHA as standard, free radical scavenging capacity increased with a higher extract concentration. In this system, The IC_{50} value of the synthetic antioxidant butylated hydroxyanisole (BHA) was 11µg/ml, whereas, the Ec_{50} of M. gummifera essential oil was 51.059mg/ml. The free radical scavenging activity of M. gummifera essential oil was weaker than Periploca laevigata root barks (PLRB) essential oil which had an IC_{50} value of 0.76 mg/ml (Hajji, et al., 2010) and D. setifolius essential oil collected in Algeria withe IC_{50} = 41.895 mg/mL (Laouer, et al., 2013). The free radical scavenging activity of M. gummifera essential oil was also lower than that of Marrubium globosum essential oil which had an IC_{50} value of 1.20 mg/ml (Sarikurkcu, et al., 2008).

The activities changed according to the chemical composition, low activity was attributed to the absence or to the very low concentrations of some compounds responsible for antioxidant activity (Miguel, 2010).

Jukié M. and Milos M. (2005) have demonstrated that the thym phenolic chemotype possesses stronger antioxidant properties than the non phenolic one (Laouer, et al., 2013).

Ruberto G. and Baratta M.T. (2000) studied the antioxidant activity of 98 pure essential oils chemical components and showed that monoterpene hydrocarbons had a significant protective effect, with several variants due to the different functional groups. Furthermore, some researchers have shown that some essential oils rich in non-phenolic compounds also have antioxidant potential (El-Massry, El-Ghorab and Farouk, 2002; Mighri, et al., 2010). Table 1 showed that essential oil of M. gummifera is rich on Monoterpene hydrocarbons components.

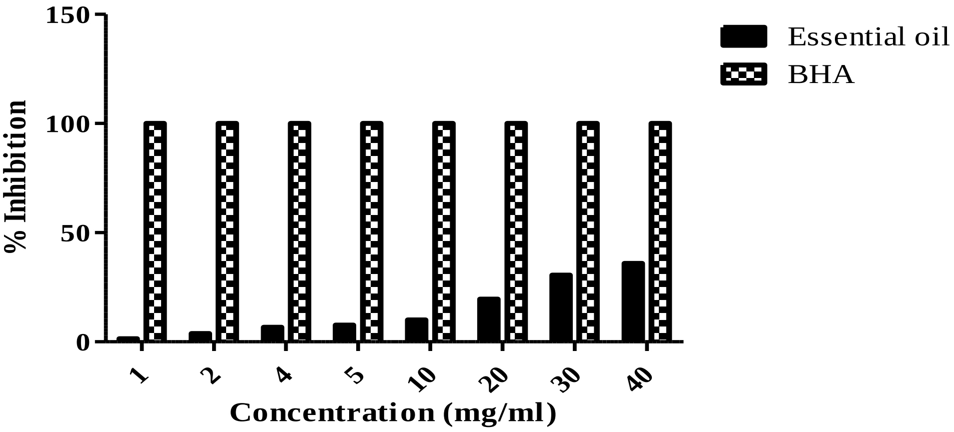

Figure 1. DPPH radical scavenging activities of M. gummifera essential oil. BHA was used as positive control.

Pouvoir réducteur

Free radicals are able to attack the highly unsaturated fatty acids of membrane system inducing lipid peroxidation. An over production of TBARS, the end product of the lipid peroxidation process, occurs after an increase of free radicals. The inhibitory effects of samples on lipid peroxidation in liposomes is generally estimated after the incubation of these liposomes with an Fe^{3+}/ascorbate system and then the determination of the amount of TBARS accumulated after an interval of time (Du, Tu and Yen, 1999; Şerbetçi, et al., 2012; Tefiani, et al., 2015). Different studies have reported that there is a direct correlation between antioxidant activities and reducing power of certain bioactive compounds. It has been widely accepted that the higher the absorbance at 700 nm, the greater is the reducing power (Joshi, Verma and Mathela, 2010; Miguel, 2010).

In this study, the ability of the essential oil, and BHA as a positive control, to reduce Fe^{3+} to Fe^{2+} was determined (Shimada, et al., 1992). As can be seen in Fig. 2, the reducing capacity of the essential oil and BHA increased with increasing concentration. The reducing power activity of the essential oil from PLRB was similar to that of Thymus algeriensis essential oil (Hazzit, et al., 2009). However, the essential oil of M. gummifera showed lower reducing power activity than did BHA. The reducing powers of M. gummifera essential oil at a concentration of 1mg/ml was 0.631, whilst those of essential oil of PLRB, Salvia palaestina and Salvia Ceratophylla were 1 (Hajji, et al., 2010), 0.362 and 0.248 (Gürsoy, Tepe and Aşkın Akpulat, 2012) respectively. Reducing powers of BHA was measured as 2.02 at 0.2 mg/mL concentration.

All aromatic plants exhibited low reducing power (Proestos, et al., 2013), this reductive potential may be related to the presence of phenolic compounds, such as isothymol and carvacrol, due to hydroxyl substitutions in the aromatic ring, which possess potent hydrogen donating abilities, as described by Shimada, et al. (1992) (Gürsoy, Tepe and Aşkın Akpulat, 2012).

Antioxidant properties of carvacrol and terpinene were reported also by Ruberto G. et al. (2000). Nevertheless, our results seem to reveal the existence of some minor components responsible for the reductive ability of the oils.

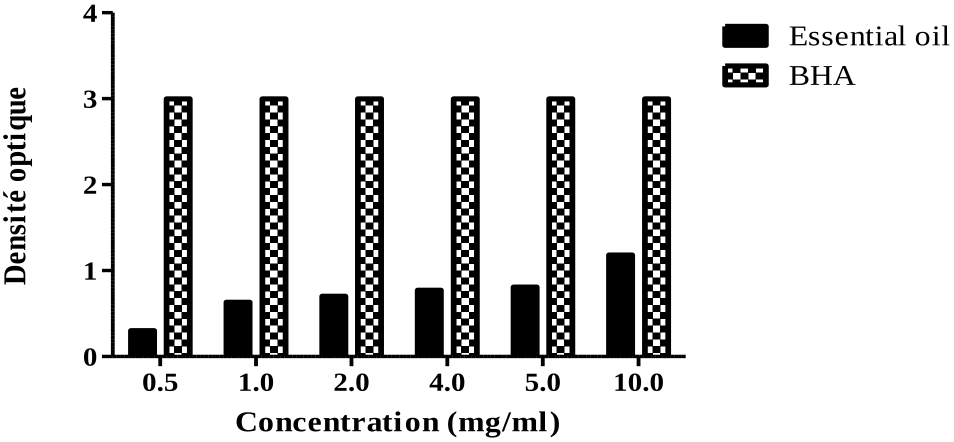

Figure 2. Reducing power of M.gummifera essential oil at different concentrations. BHA was used as positive control.

CONCLUSION

The manufacturers of foods, cosmetics and pharmaceuticals are increasingly in need of natural products. Thus the importance of conducting studies on essential oils, lies not only on the chemical characterization but also on the possibility of linking the chemical contents with particular functional properties. The essential oil of M. gummifera collected in Algeria is mainly characterized by the presence of α-pinene, β-pinene, γ-terpinene and myrcene as the major components. Furthermore, the M. gummifera oil exerted weak antimicrobial and moderate antioxidant activities. In fact, the results presented in this study are the first information on the antioxidant and antimicrobial activities of essential oil of M.gummifera.

ACKNOWLEDGEMENT

The authors are thankful to Professor Moncef Nasri, Director of Laboratory of Enzyme Engineering and Microbiology, National School of Engineers of Sfax, Tunisia for providing facilities for this work. The authors wish to thank Professor Guido Flamini, Department of Pharmaceutical Sciences, Office of Bioorganic Chemistry and biopharmaceuticals, University of Pisa, Italy for the GC/MS analysis.

References

Adams, R. P., 1995. Identification of essential oil components by gas chromatography/mass spectroscopy. Carol Stream: Allured.

Arora, D.S. and Kaur, I., 1999. Antimicrobial activity of spices. Int. J. Antimicrob. Agent, 12: 257-262.

Askari, F., Sefidkon, F., Teimouri, M. and Yousef Nanaei, S., 2009. Chemical Composition and Antimicrobial Activity of the Essential Oil of Pimpinella puberula (DC.) Boiss. J. Agr. Sci. Tech., Vol. 11: 431-438

Bader, A., Cioni, P.L. and Flamini, G., 2010. GC-MS Analysis of the essential oils of ripe fruits, roots and flowering aerial parts of Elaeoselinum asclepium subsp. meoides growing in Sicily. Natural Product Communications, Vol. 5 (7), 111-1114.

Berghe, V. A. and Vlietinck, A. J., 1991. Screening methods for antibacterial and antiviral agents from higher plants. Method for Plant Biochemistry, 6: 47–68.

Blois, M.S., 1958. Antioxidant determinations by the use of a stable free radical. Nature; 181: 1199–1200.

Breitmaier, E., 2006. Terpenes. Willey-VCH Verlag GmbH and Co, Morlenbach, Germany, p. 214.

Crowden, RK., Harborne, JB. and Heywood, VH., 1969. Chemosystematics of the Umbelliferae-General survey. Phytochemistry, 8: 1963-1984

Davies, N. W., 1990. Gas Chromatographic retention indexes of monoterpenes and sesquiterpenes on methyl silicone and Carbowax 20M phases. J. Chromatogr., 503: 1–24.

Demirci, B., Kosar, M., Demirci, F., Dinç, M. and Baser, K.H.C., 2007. Antimicrobial and antioxidant activities of the essential oil of Chaerophyllum libanoticum Boiss. Et Kotschy. Food Chemistry, 105: 1512–1517.

Di Pasqua, R., De Feo, F., Villani, F. and Mauriello, G., 2005. In vitro antimicrobial activity of essential oils from Mediterranean Apiaceae. Verbenaceae and Lamiaceae against food borne pathogens and spoilage bacteria. Annals of Microbiology, 55: 139–143.

Du, P.D., Tu, Y.Y. and Yen, G.C., 1999. Antioxidant activity of water extract of Harng Jyur (Chrysanthemum morifolium Ramat). LWT-Food Sci. Technol., 32: 269–277.

Ebrahimzadeh, MA., Nabavi, SM., Nabavi, SF. and Eslami, B., 2009. Free radical scavenging ability of methanolic extract of Hyoscyamus squarrosus leaves. Pharmacology online, 2: 796-802.

Edris, A.E., 2007. Pharmaceutical and therapeutic potentials of essential oils and their individual volatile constituents: a review. Phytother. Res., 21: 308–323.

Ekiert, H., 2000. Medicinal plant biotechnology: the Apiaceae family as the example of rapid development. Pharmazie, 55: 561–567.

El-Massry, K. F., El-Ghorab, A. H. and Farouk, A., 2002. Antioxidant activity and volatile components of Egyptian Artemisia judaica L. Food Chemistry, 79: 331–336.

Evergetis, E. and Haroutounian, S. A., 2014. Exploitation of Apiaceae family plants as valuable renewable source of essential oils containing crops for the production of fine chemicals. Industrial Crops and Products, 54: 70–77.

Gürsoy, N., Tepe, B. and Aşkın Akpulat, H., 2012. Chemical Composition and antioxidant activity of the essential oils of Salvia palaestina (Bentham) and S. ceratophylla (L.). Rec. Nat. Prod., 6:3, 278-287.

Hajji, M., Masmoudi, O., Souissi, N., Triki, Y., Kammoun, S. and Nasri, M., 2013. Chemical composition, angiotensin I-converting enzyme (ACE) inhibitory, antioxidant and antimicrobial activities of the essential oil from Periploca laevigata root barks. Food Chemistry, Available at: http://dx.*doi*.org/*10.1016/j.foodchem.2010.01.021*.

Hamdy Roby, M. H., Sarhan, M. A., Selim, K. A.-H. and Khalel, K. I., 2013. Antioxidant and antimicrobial activities of essential oil and extracts of fennel (Foeniculum vulgare L.) and chamomile (Matricaria chamomilla L.). Elsevier, Industrial Crops and Products, 44: 437– 445, Available at: http://dx.doi.org/10.1016/j.indcrop.2012.10.012.

Hazzit, M., Baaliouamer, A., Verissimo, A. R., Faleiro, M. L. and Miguel, M. G., 2009. Chemical composition and biological activities of Algerian Thymus oils. Food Chemistry, 116: 714–721.

Henrlck, C. A. and Jefferies, P.R., 1964. Aust.J. Chem., 17, 915.

Jennings, W. and Shibamoto, T., 1980. Qualitative Analysis of Flavor and Fragrance Volatiles by Glass Capillary Chromatography. New York: Academic Press.

Joshi, S.C., Verma, A.R. and Mathela, C.S., 2010. Antioxidant and antibacterial activities of the leaf essential oils of Himalayan Lauraceae species. J. Chem. Toxicol., 48: 37-40.

Jukié, M. and Milos, M., 2005. Catalytic oxidation and antioxidant properties of thym essential oils (Thymus vulgarea L.). Croatica chemical acta, 78 (1): 104–10.

Khoshbakht, K., Hammer, K. and Pistrick, K., 2007. Eryngium caucasicum Trautv. Cultivated as a vegetable in the Elburz Mountains (Northern Iran). Genet. Resour. Crop. Ev., 54: 445–448.

Kirby, A. J. and Schmidt, R. J., 1997. The antioxidant activity of Chinese herbs for eczema and of placebo herbs. Journal of Ethnopharmacology, 56: 103–108.

Kosalec, I., Pepeljnjak, S. and Kustrak, D., 2005. Antifungal activity of fluid extract and essential oil from anise fruits (Pimpinella anisum L., Apiaceae). Acta Pharmaceutica, 55: 377–385.

Laouer, H., Bouheda, A., Haroutounian, S., Evergetis, E., Bouchekrit, M., Sahli, F., Boulaacheb, N. and Akkal, S., 2013. Chemical and Biological Study of Essential oils of two populations of Algerian Daucus setifolius Desf. Pharmacognosy Communications, Volume 3/Issue 1.

Lucera, N., Costa, C., Conte, A. and Del Nobile, M.A., 2012. Food applications of natural antimicrobial compounds. Front. Microbiol., V. 3:287, doi: 103389/fmicb.00287.

Maestri, D.M., Nepote, V., Lamarque, A.L. and Zygadlo, J.A., 2006. Natural products as antioxidants. In Phytochemistry: Advances in Research; Imperato, F., Ed.; Research Signopost: Kerala, India, pp. 105-135.

Maria-Rose, JRA., Elnatan, BS., Maria-Usileide, DSL., Nadja, APN., Telma-Leda, GL. and Edilberto, RS., 2004. Composition and antimicrobial activity of the essential oil from aerial parts of Baccharis trinervis (Lam.) Pers. Arkivoc., 6:59–65.

Marino, M., Bersani, C. and Comi, G.J., 1999. Antimicrobial activity of the essential oils of Thymus vulgaris L. measured using a bioimpedometric methad. J. Food Prot., 62: 1017-1023.

Massada, Y., 1976. Analysis of essential oils by gas chromatography and mass spectrometry. New York: J. Wiley & Sons.

Meliani, N., Dib, M. El-A., Djabou, N., Costa, J., Allali, H., Tabti, B. and Muselli, A., 2013. Chemical composition and antimicrobial activity of Daucus aureus essential oils from Algeria. Natural Product Communications, Vol. 8 (6).

Merghache, D., Boucherit-Otmani, Z., Merghache, S., Chikhi, I., Selles, C. and Boucherit, K., 2014. Chemical composition, antibacterial, antifungal and antioxidant activities of Algerian Eryngium tricuspidatum L. essential oil, Natural Product Research, DOI: 10.1080/14786419.2014.883392.

Mighri, H., Hajlaoui, H., Akrout, A., Najjaa, H. and Neffati, M., 2010. Antimicrobial and antioxidant activities of Artemisia herba-alba essential oil cultivated in Tunisian arid zone. Elsevier Masson SAS, C. R. Chimie, 13: 380–386.

Miguel, M. G., 2010. Antioxidant and Anti-Inflammatory Activities of Essential Oils: A Short Review, Molecules, 15, 9252-9287, doi:10.3390/molecules15129252

Moreno-Dourado, F.J., Guerra, F.M., Aladro, F.J., Bustamante, J.M., Jorge, Z.D. and Massanet, G.M., 2000. Synthesis of (±)-11α-hydroxy-3-oxo-6αH,7αH,10βMeendesman-1,2-4,5-dien-6,12-olide. J. Nat. Prod., 63: 934–938.

Nabavi, S.M., Ebrahimzadeh, M.A., Nabavi, S.F., Eslami, B. and Dehpour, A.A., 2011. Antioxidant and antihaemolytic activities of Ferula foetida regel (Umbelliferae). European Review for Medical and Pharmacological Sciences, 15: 157-164.

Nabavi, SM., Ebrahimzadeh, MA., Nabavi, SF. and Jafari, M., 2008. Free radical scavenging activity and antioxidant capacity of Eryngium caucasicum Trautv and Froriepia subpinnata. Pharmacology online, 3: 19-25.

Newman, D.J. and Crag, G.M., 2007. Natural products as sources of new drugs over the last 25 years. J. Nat. Prod., 70: 461–477.

Oroojalian, F., Kasra-Kermanshahi, R., Azizi, M. and Bassami, M.R., 2010. Phytochemical composition of the essential oils from three Apiaceae species and their antibacterial effects on food-borne pathogens. Food Chemistry, 120: 765–770.

Özcan, M., 1998. Inhibitory effects of spice extracts on the growth of Aspergillus parasiticus NRRLR 2999 strain. Springer-Verlag, Z. Lebensm Unters Forsch, Vol. 207, pp. 253-255.

Ozcan, M.M., Chalchat, J.-C., Arslan, D., Ates, A. and Unver, A., 2006. Comparative essential oil composition and antifungal effect of Bitter Fennel (Foeniculum vulgare ssp. piperitum) fruit oils obtained during different vegetation. Journal of Medicinal Food, 9: 552–561.

Özkalp, B. and Özcan, M.M., 2009. Antibacterial activity of several concentrations of Sater (Satureja hortensis L.) essential oil on spoilage and pathogenic food - related microorganisms. World Appl. Sci. J., 6 (4): 509-514.

Pala-Paul, J., Perez-Alonso, MJ. and Velasco-Negueruela, A., 2001. A contribution to the knowledge of the oil of Elaeoselinum gummiferum (Desf.) Tutin. J Essent Oil Res., 13:362–363

Pauli, A., 2006. α-Bisabolol from chamomile-a specific ergosterol biosynthesis inhibitor. Int. J. Aromather., 16:21–25. Pimenov MG., Leonov MV. (1993). The genera of the Umbelliferae. A nomenclator. Kew: Royal Botanic Gardens, p. 156.

Pinar, M., Rodriguez, B. and Alemany, A., 1978. Gummiferolic Acid, A New Ent-Atis- 6-Ene diterpenoid from Margotia Gummifera. Phytochemestry, Vol. 17, pp. 1736-1637

Prior, RL., Wu, X. and Schaich, K., 2005. Standardized methods for the determination of antioxidant capacity and phenolics in foods and dietary supplements. J. Agric. Food. Chem., 53:4290–4302.

Proestos, C., Lytoudi, K., Mavromelanidou, K. O., Zoumpoulakis, P. and Sinanoglou, V.J., 2013. Antioxidant Capacity of Selected Plant Extracts and Their Essential Oils. Antioxidants, 2, 11-22, doi:10.3390/antiox2010011.

Rajashekar, Y., Bakthavatsalam, N. and Shivanandappa, T., 2012. Botanicals as grain protectants. Psyche, http://dx.doi.org/10.1155/2012/646740, art ID 646740,13 pages.

Reichling, J., Schnitzler, P., Suschke, U. and Saller, R., 2009. Essential oils of aromatic plants with antibacterial, antifungal, antiviral and cytotocic properties-an overview. Forsch. Komplementmed, 16: 79-90.

Ruberto, G., and Baratta, M. T., 2000. Antioxidant activity of selected essential oils components in two lipid model systems. Food Chemistry, 69: 167–174.

Sadashiva, CT., Sharanappa, P., Remashree, AB., Raghu, AV., Udayan, PS. and Balachandran, I., 2010. Chemical composition and antimicrobial activity of the essential oil from bark of Pittosporum dasycaulon Miq. Adv. Biol. Res., 4(6):301–304.

Sarikurkcu, C., Tepe, B., Daferera, D., Polissiou, M. and Harmandar, M., 2008. Studies on the antioxidant activity of the essential oil and methanol extract of Marrubium globosum subsp. Globosum (Lamiaceae) by three different chemical assays. Bioresource Technology, 99: 4239–4246.

Scott, R.P.W., 2005. Essential oils. Encyclopedia of Analytical Science, Elsevier, pp.554–561.

Selles C., Dib MA., Djabou N., Beddou F., Muselli A., Tabti B., Costa J. and Hammouti B. (2013). Antimicrobial activity and evolution of the composition of essential oil from Algerian Anacyclus pyrethrum L. through the vegetative cycle. Nat Prod Res., doi:10.1080/14786419.2013.811409.

Şerbetçi, T., Özsoy, N., Demirci, B., Can, A., Kültür, Ş. and Can Başer, H., 2012. Chemical composition of the essential oil and antioxidant activity of methanolic extracts from fruits and flowers of Hypericum lydium Boiss. Ind. Crops Prod., 36: 599–606.

Seto, M., Miyase, T., Umehara, K., Ueno, A., Hirano, Y. and Otani, N., 1988. Sesquiterpene lactones from Cichorium endivia L. and C. intybus L. Chem. Pharm. Bull., 36:2423–2429.

Shimada, K., Fujikawa, K., Yahara, K., and Nakamura, T., 1992. Antioxidative properties of xanthum on the autoxidation of soybean oil in cyclodextrin emulsion. Journal of Agricultural and Food Chemistry, 40: 945–948.

Sivropoulou, A., Nikobu, C., Papanikolaou, E., Kokkini, S., Lanaras, T. and Arsenakis, M., 1997. Antimicrobial, cytotoxic and antiviral activities of Salvia fruticosa essential oil. Journal of Agricultural and Food Chemistry; 45: 3197–3201.

Skaltsa, H. D., Demetzos, C., Lazari D. and Sokovic, M., 2003. Essential oil analysis and antimicrobial activity of eight Stachys from Greece. Phytochemistry, 64: 743–752.

Stenhagen, E., Abrahamsson, S. and McLafferty, F. W., 1974. Registry of Mass spectral data. New York: J. Wiley & Sons.

Su Jian-Yu, L., Zhu, L. and Ying-Juan, T., 2012. Chemical composition and antimicrobial activities of essential oil of Matricaria songarica. Int. J. Agric. Biol., 14(1):107–110.

Swigar, A. A. and Silverstein, R. M., 1981. Monoterpenes. Milwaukee: Aldrich Chem. Comp.

Tavares, A.C., Gonc alves, M.J., Cavaleiro, C., Cruz, M.T., Lopes, M.C., Canhoto, J.M. and Salgueiro, L., 2008. Essential oil of Daucus carota subsp. halophilus: chemical composition, antifungal activity and citotoxicity. Journal of Ethnopharmacology, 119: 129–134.

Tavares, A.C., Gonçalves, M.J., Cruz, M.T., Cavaleiro, C., Lopes, M.C., Canhoto, J. and Ribeiro Salgueiro, L., 2010. Essential oils from Distichoselinum tenuifolium: Chemical composition, cytotoxicity, antifungal and anti-inflammatory properties. Journal of Ethnopharmacology, 130: 593–598

Tefiani, C., Riazi, A., Youcefi, F., Aazza, S., Gago C., Faleiro, M.L., Pedro, L.G., Barroso, J.G., Figueiredo, A.C., Megías, C., Cortés-Giraldo, I., Vioquef, J. and Miguel, M.G., 2015. Ammoides pusilla (Apiaceae) and Thymus munbyanus (Lamiaceae) from Algeria essential oils: Chemical composition, antimicrobial, antioxidant and antiproliferative activities. Journal of Essential Oil Research, http://dx.doi.org/10.1080/10412905.2015.1006739.

Tirillini, B., Pagiotti, R., Angelini, P., Pintore, G., Chessa, M. and Menghini, L., 2009. Chemical composition and fungicidal activity of the essential oil of Laserpitium garganicum from Italy. Chemistry of Natural Compounds, Vol. 45, No. 1.

Togashi, N., Inoue, Y., Hamashima, H. and Takano, A., 2008. Effects of two terpene alcohols on the antibacterial activity and the mode of action of farnesol against Staphylococcus aureus. Molecules, 13:3069–3076.

Valente, J., Zuzartea, M., Liberal, J., Gonçalves, M.J., Lopes, M.C., Cavaleiro, C., Cruz, M.T. and Salgueiro, L., 2013. Margotia gummifera essential oil as a source of anti-inflammatory drugs. Industrial Crops and Products, 47, 86–91.

Yildirim, A., Mavi, A. and Kara, A. A., 2001. Determination of antioxidant and antimicrobial activities of Rumex crispus L. extracts. Journal of Agricultural and Food Chemistry, 49: 4083–4089.

RELIABILITY OF HYDROCARBONS TRANSPORT PIPELINES SUBJECTED TO CONTINUOUS DEGRADATION

BOUZID RACHID, BOUALI ELAHMOUNE, GACEB MOHAMED

BOUZID Rachid, Doctor, Université M'Hamed Bougara de Boumerdes – Algeria -, BOUALI Elahmoune, Doctor, Université M'Hamed Bougara de Boumerdes – Algeria -, GACEB Mohamed, Doctor, Université M'Hamed Bougara de Boumerdes – Algeria –

Abstract

It is at the projection stage of a hydrocarbons transport pipeline that its reliability is constituted through the choice of patterns of the correct components, technological solutions, as well as the correct values of safety reserves taking into account various influential factors. It is at this point that verification opportunities are offered through experimental methods and calculation of the rationality of the technical resolutions made and the possibility to choose the alternative that is best suited. In this work physico-statistics and functional approaches will be considered.

These methods allow us to obtain the reliability characteristics of the constructive elements of a pipeline taking into account the nature of external actions, the deterministic and random properties of the elements, technological, techno-economic and other factors. The constructive elements of an in-service pipeline are subjected to a set of external and internal factors which constitute its surrounding environment. Under the combined action of all these factors, physico-chemical process (corrosion, ageing, distortion...) take place, in the material of the pipeline elements. These lead to the deterioration of the state of the pipeline elements up to the limits where the element no longer meets the standards required in the relevant technical documents. This situation leads us to the idea of considering the behavior of the pipeline as a random process and States limits as breaks of random variation jumps outside the realm of tolerable States.

Among the functional models of the reliability theory, the basic model called "parametric reliability of the elements" has been used. In the calculation results of the parametric reliability, the likelihood that the parameters determining the State of good functioning of the element do not go out beyond the boundary of the field of tolerances is first considered.

Introduction

The projection stage is a decisive phase in the life cycle of a pipeline. It is at this stage that its reliability is constituted by the choice of correct components patterns, technology solutions, as well as the choice of the correct values of the security reserves taking into account various influential factors. Reliability issues must be resolved during the projection and the completion of a project. It is at this point that verification opportunities are offered by experimental methods and calculation of the rationality of adopted technical resolutions (schema, material...) and the possibility to choose the alternative that best suits the concrete case considered [2].

For the resolution of the problem of determining the of the reliability characteristics of the pipeline constructive elements, there are various mathematical and physic-statistical methods [4]. In this work physic-statistical and functional approaches will be considered. The physic-statistical approach to the determination of the reliability characteristics of the pipeline constructive elements is based on two designs [4]:

The first design is the use of physic-statistical methods for the analysis of the processes leading to the failure of the pipeline constructive elements. The analysis of these processes makes it possible to obtain the necessary mathematical models for functional reliability models.

The second design is the functional approach to the determination of the reliability characteristics of the pipeline constructive elements; in this case information is used about the parameters of the materials bearing capacity of the tubes, the actual loads, and finally about the technological parameters of the pipeline elements in general.

In contrast to the conventional methods of calculation of systems reliability using the rate of elements' failures, the above approaches allow to obtain the characteristics of reliability of the pipeline constructive elements taking into account the nature of external actions, the deterministic and random properties of the elements, technology, techno-economic and other factors. The in-service pipeline constructive elements are subject to a set of external and internal factors which constitute its surrounding environment. Under the action of all these factors, in the pipeline elements materials physic-chemical processes (corrosion, ageing, distortion...) take place, which lead to the deterioration of the State of the pipeline elements up to the limits where the element no longer meets the required standards in the relevant technical documents. This situation leads us to the idea of considering the behavior of the pipeline as a random process and States limits as breaks of random variation outside the realm of tolerable States.

Among the functional models of the reliability theory, the basic model called "parametric reliability of the elements has been used. The results of calculation of the parametric reliability, it is first found the likelihood that the parameters determining the State of the element functioning do not go out beyond the boundary of the field of tolerances. To do this, parameters such that: stresses and pipeline strength reserves [1] are used.

Theoretical approach to the problem under consideration

During pipeline operation, the tubes are solicited by in-service pressure, after which the mechanical stress in the pipe walls is S(t). At the same time the pipe strength threshold is R(t). It is considered that S(t) is a deterministic quantity and resistance is random in its value and deterministic over time. The probability of pipe good functioning is given by the expression [3]:

$$\boldsymbol{P(R > S) = \int_S^{\infty} f_R(R)dR} \qquad (1)$$

Where: $\boldsymbol{f_R(R)}$ is the distribution density of the variable R probability

Following deteriorations of the pipe state over time their strength threshold decreases according to $\boldsymbol{R - G(t)}$ where $\boldsymbol{G(t)}$ is the pipe deterioration function. In this case the good functioning probability takes the following form:

$$\boldsymbol{P\big[\big(R - G(t)\big) > S(t)\big] = P[R > S - G(t)]}$$

Where: $$\boldsymbol{P(R > S) = \int_{S-G(t)}^{\infty} f_R(R)\, dR} \qquad (2)$$

For a normal distribution of R, we have:

$$\boldsymbol{f_R(R) = \frac{1}{2\pi\, \sigma_R}\, ex \left\{\frac{[R - m_R(t)]^2}{2\, \sigma_R^2}\right\}} \qquad (3)$$

Where: $\boldsymbol{m_R(t)}$ is the mathematical expression of the strength threshold which decreases over time due to the pipes deterioration (corrosion).

$\boldsymbol{\sigma_R}$: is the quadratic deviation of the pipes strength threshold

Taking into account expressions (2) and (3) and after some transformations, we get the final form of the expression of the good functioning probability as follows:

$$\boldsymbol{P[R(t) > S(t)] = 0,5 + \Phi\left[\frac{m_R(t) - S(t)}{\sigma_R}\right]} \qquad (4)$$

Where: $\boldsymbol{\Phi}$ is the Laplace function

In using the expression (4), the relationship between the permissible minimum value of the pipe good functioning probability P_{ad} and the strength reserve $\boldsymbol{\Delta = \frac{m_R(t) - S(t)}{\sigma_R}}$ is obtained in the form:

$$\boldsymbol{P_{ad} = 0,5 + \Phi(\Delta)} \qquad (5)$$

In fixing the pipeline service duration and the minimum permissible value of the good functioning probability, the value of the required strength reserve $\boldsymbol{m_R}$ at the time of pipeline projection studies is obtained from expression (5). On the other hand for given laws of functions $\boldsymbol{S(t)}$ and $\boldsymbol{R(t)}$ features laws the pipeline good functioning probability was assessed in terms of the service duration. The $\boldsymbol{S(t)}$ and $\boldsymbol{R(t)}$ laws are formulated by a stochastic process based on two random variables that follow a Gaussian distribution [5]:

$$\boldsymbol{S(t) = A_1 + B_1(t)}$$
$$\boldsymbol{R(t) = A_2 + B_2(t)}$$

Where: $\boldsymbol{A_1, B_1, A_2, B_2}$- are random variables

The random variables $\boldsymbol{S(t)}$ and $\boldsymbol{R(t)}$ are distributed according to a normal distribution, described by the mathematical expectation and the mean quadratic deviation given respectively by the expressions:

$$\boldsymbol{\mu_x(t) = \mu_0 + \alpha t} \quad \text{and} \quad \boldsymbol{\sigma_x(t) = \sigma_0 + \beta t}$$

Where α, β are constants

Results and discussion

A pipe section 1220 mm in diameter, connecting two compression stations 70 km apart is considered. The nominal working pressure is 74 kgf/cm^2 and the pipes constituting the pipeline are made of X52 steel. At the time $\boldsymbol{t_1, t_2, \ldots, t_N}$ the mathematical expectations and the quadratic deviations of the processes $\boldsymbol{S(t)}$ and $\boldsymbol{R(t)}$ are determined from available data on changes in the operating pressure and the State of degradation of the considered pipeline section over a 40 years period.

The linear regression technique has been implemented. Validation of regression models used is verified by analysis of residues. The expressions below give the estimation of the parameters of the regressions of the average of the observations:

$$\boldsymbol{\mu_S(t) = 48 + 10^{-2}t \quad in\ kgf/mm^2}$$
$$\boldsymbol{\mu_R(t) = 53 - 0,8\,t \quad in\ kgf/mm^2}$$

t: is the service life in years

The variation of the good functionning probability of the segment of the pipeline section in terms of its service life is represented in figure 1. It shows, that the good functioning probability of the section considered of the pipeline falls abruptly after 20 years of service; It is the influence of the rate of degradation on the good functioning probability of the segment which becomes very important and therefore the frequency of the inspections of the state of the section must be increased. For a given pipeline period of service T and good functioning probability of the concerned section, greater or equal to $\boldsymbol{P_{ad}}$= 0,9998,, expression (5) yields the value of the strength reserve required $\Delta_{exigée}$= $\boldsymbol{3,55\ kgf/mm^2}$. The initial pipe strength required at the projection stage of is determined by the expression:

$$\boldsymbol{\left(m_R^0\right)_{exigée} = \sigma_R \Delta_{exigée} + (1,2)\left(0,048 + 10^{-5}T\right)}$$

This last expression to determine by a reliability approach necessary pipe wall overthickness of similar pipelines to those considered in this work which is 5.5 mm in the case.

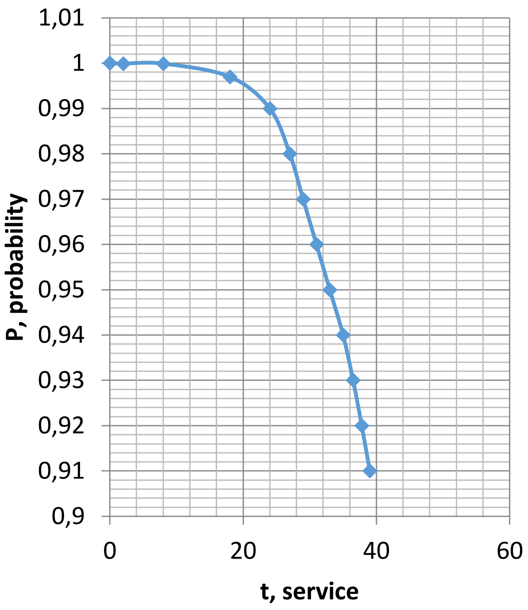

Fig 1: Good functioning probability of a pipeline section of in terms of its service life

Conclusion

Functional modes for the determination of the reliability characteristics of components at the base of the failure physics are currently little used. The main difficulties associated with the use of functional models for the reliability characteristics determination are:

First, there exists complexity to take account of the influence of a large number of internal and external factors on physico-chemical processes.

Second, the wide diversity of construction materials and internal processes makes it difficult to develop generalized mathematical models taking into account the complex influence of exploitation factors on the defects initiation and propagation. But despite the mentioned difficulties, this route is an interesting perspective.

Références

[1] Abdelbaki N., Gaceb M., Bouali E., Bettayeb M., Bouzid R; Reliability approach to choice of dimensions and materials of tubes used in hydrocarbons transport network; Chemical Engineering Transaction, Vol 39, 2014 – p1339-1344.

[2] Hopkins P., Corder I. and Corbin P., The resistance of gas transmission pipelines to mechanical damage; Paper VIII-3, International Conference on Pipeline Reliability,Calgary,Canada, 1992

[3] Melchers R. E; Structural Reliability Analysis on Prediction; Second Edition, John Willey and Sons, Chichester, 1999.
[4] Procaccia H., Morilhat P; Fiabilité des Structures des installations Industrielles, Eyrolles 1996
[5] Xue and Yang ; Upper and Lower Bounds of Stress-Strength Interference Reliability with Random Strength-Degradation; IEEE, Transaction of Reliability. V46,1.142-145

MODELING OF DESWELLING BEHAVIORS OF PH AND TEMPERATURE SENSITIVE POLY(N-ISOPROPYL ACRYLAMIDE-ACRYLIC ACID) INTERPENETRATING HYDROGELS BY ARTIFICIAL INTELLIGENCE SYSTEM

CIHANGIR BOZTEPE, MEHMET YÜCEER, ASIM KÜNKÜL

[1]İnönü University, Engineering Faculty, Department of Chemical Engineering, Malatya/Turkey
e-mail: cihangir.boztepe@inonu.edu.tr

Abstract

The water storage capacity of hydrogels can be as much as 1000 times their dry weight. pH and thermo sensitive hydrogels can be applied in many fields, such as controlled drug release applications, separation systems, bioreactors, sensors, and tissue engineering [1]. For predicting the swelling–deswelling behaviors of hydrogels, one approach could be to identify the input–output relationship between these parameters based on experimental data. Artificial neural networks (ANN) are powerful tools that can recognize complex relationships in input–output data [2].

In this study, Thermosensitive poly(NIPAAm) micro hydrogels were synthesized by free radical emulsion polymerization. Then, poly(NIPAAm-co-AAc) IPN hydrogels were prepared by free radical polymerization in the presence of poly(NIPAAm) microgels. The unit mass ratio between poly(NIPAAm) and poly(NIPAAm-AAc) was chosen to be 30:70 because the IPN complex between two macromolecules was better at this ratio. pH and temperature sensitive hydrogels obtained in soft, elastic, in long cylindrical shapes were cut into pieces of 20 mm length. All deswelling tests of hydrogels were applied to equilibrium swelling state of them. For developing ANN model of deswelling behavior of Poly(N-Isopropyl acrylamide-Acrylic acid) Interpenetrating Hydrogels, feed-forward back propagation neural network algorithm with Multi-Layer Perceptron (MLP) was used. Experimentally developed 1404 observations for each input and output parameters were taken for development of the model. The data set was randomly divided into three subsets for training (70%), validation (15%), and testing (15%). The developed model with two hidden layers having thirty neurons in the first layer and twenty neurons in the second layer gave best result as (R=0.9995 and MSE=1.6278). Transfer function for hidden layers was tangent sigmoid while for the output layer was pure linear function. The predictions from the ANN model, which associated input parameters, including the different temperature, pH, and deswelling values with time, produce results that show good agreement with experimental data. Table 1 gives the ANN performance in terms of: mean squared error (MSE) and the correlation coefficient (R) between the experimental data and neural network outputs.

Table 1. Statistical Evaluation of Learning, Validation and Test Data

	Training	Validation	Test
R	0.9995	0.9988	0.9986
MSE	1.6278	3.8148	4.7823

Model analysis indicated that the ANN models could accurately describe the nonlinear, multivariable deswelling behaviors of highly swellable hydrogels. Therefore, it is evident from the study that simulated neural networks can be used to predict deswelling behavior of Poly(N-Isopropyl acrylamide-Acrylic acid) Interpenetrating Hydrogels

Keywords: ANN, pH and temperature sensitive hydrogel, modeling, deswelling behavior

References:

[1] Gerlach, G. and Arndt, K.F. (2009) In Hydrogel sensors and actuators (General Properties of Hydrogels), edited by O. Okay; Berlin Heidelberg: Springer.

[2] Boztepe, C., Solener, M., Yuceer, A. M., Kunkul, A. and Kabasakal, O. S. (2015), Journal of Dispersion Science and Technology, 36:1647–1656.

THE SYNTHESIS, CHARACTERIZATION AND INVESTIGATION OF ANTIMICROBIAL INHIBITION KINETICS OF ACRYLAMIDE BASED HYDROGEL-SILVER NANOCOMPOSITE SYSTEM

CIHANGIR BOZTEPE, EMIR TOSUN, TUĞÇA BILENLER, KÜBRA ŞIŞLIOĞLU

[1] İnönü University, Engineering Faculty, Department of Chemical Engineering, Malatya/Turkey
[2] İnönü University, Engineering Faculty, Department of Food Engineering, Malatya/Turkey
E-Mail: cihangir.boztepe@inonu.edu.tr

Abstract
The design and development of polymer-silver nanostructure composite materials have gained much attention in recent years due to their unique and versatile properties such as a non-toxic and environmentally friendly antibacterial materials, have high surface area and high surface atom fraction [1, 2].

In this study, poly(AAm-co-VI-co-AMPS) hydrogels were prepared by free radical polymerization in the presence of N,N'-methylenebisacrylamide. Silver nanoparticles loaded to hydrogels systems via in situ reduction of silver nitrate in the presence of sodium borohydride as a reducing agent. The synthesized hydrogel–silver nanocomposites were characterized by using FT-IR, scanning electron microscopy (SEM) equipped with an energy-dispersive X-ray spectrometer (EDX mapping). The antimicrobial activity of hydrogel-silver nanocomposite were determined by using well agar and broth dilution tests. The hydrogel -silver nanocomposite that stand out with high it's antimicrobial effect was tested in order to examine more detail by broth dilution technique against E.coli as model microorganisms. A continuous bioreactor system for this test was formed and operative dose that decision made previous test was used. The inactivation kinetics of Hydrogel-Silver nanocomposite against E.coli were adjust to a Weibull distribution model, by Eq. (1) and estimated parameters are given in Table 1.

$$\log_{10}\left(\frac{N}{N_0}\right) = -\frac{1}{2.303}\left(\frac{t}{\alpha}\right)^{\beta} \qquad (1)$$

Table1. Estimated parameters of Weibull distribution function

Bacterial Strain	α(min)	ß	R^2 (%)	MAPE
E.coli	53.7312	1.8033	99.30	0.1144

Keywords: Antimicrobial Hydrogel, Hydrogel-Silver nanocomposite materials, İnhibition kinetic.

References:
[1] Babu A.C., Prabhakar M.N., Babu A.S., Mallikarjuna B., Subha M.C.S. and Chowodji R., 2013, International Journal of Carbohydrate Chemistry, 2013:8.
[2] Hebeish A., Hashem M., Abd El-Hady M.M., and Sharaf S. 2013, Carbohydrate Polymers, 92: 407– 413

HYDROGEL SUPPORTED NHC-PD CATALYST SYSTEMS FOR THE SUZUKI REACTION

CIHANGIR BOZTEPE, ASIM KÜNKÜL, ISMAIL ÖZDEMİR, NEVIN GÜRBÜZ

[1]İnönü University, Engineering Faculty, Department of Chemical Engineering, Malatya/Turkey
[2]İnönü University, Catalysis Research and Application Center, 44280, Malatya, Turkey
e-mail: cihangir.boztepe@inonu.edu.tr

Abstract

In recent years, the stable N-heterocyclic carbene (NHC) complexes of Pd^{II} or Pd^0 have been used as catalysts for Suzuki reactions. In contrast to the widely used phosphine complexes, NHC' s have shown remarkable stability towards heat, oxygen and moisture, and represent a remarkable improvement with respect to the catalytic activity. The Suzuki reaction is usually carried out with a homogeneous Pd catalyst but, in order to use the Suzuki reaction in a wide range of industrial applications, a heterogeneous Pd catalyst must be developed [1]. Hydrogels are three-dimensional crosslinked polymeric materials that can absorb and hold large amounts of water without undergoing dissolution. Hydrogel catalyst supports have several advantages, such as big surface area, fast recovery and the simple recycling of the catalysts by filtration, which in turn prevents the contamination of the ligand and decreases the environmental pollution caused by residual metals in the waste [2].

In this study, novel two NHC-Pd polymerizable carbene complexes having catalytic activity, have been prepared and immobilized on poly(Acrylamide) crosslinked hydrogel by free radical polymerization. Synthesized heterogeneous polymeric catalysts were used in Suzuki-Miyaura coupling reactions of various aryl bromides and aryl boronic acid. We investigated the effects to catalytic performance of these catalysts type in the Suzuki-Miyaura cross-coupling reactions and illustrated in Table 1. Acrylamide based polymeric hydrogel NHC-Pd catalysts exhibited good recyclability and could be reused at least five times without remarkable loss of its catalytic activity.

Table 1. Suzuki- Miyaura coupling reactions of various aryl bromides and aryl boronic acid with the catalyst at 80 ^0C in water.

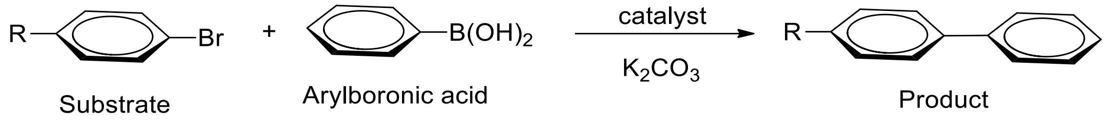

Catalyst Type	Yields (%) as a Substrates				
	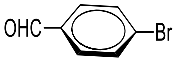	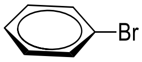	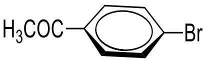	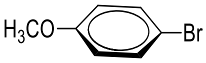	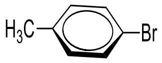
Catalyst 1	96	91	95	91	94
Catalyst 2	86	69	90	60	62

Reaction conditions: bromobenzene (0.25 mmol), phenylboronic acid (0.375 mmol, 1.5 eq.), K_2CO_3 (0.75 mmol, 3 eq.), H_2O (5 mL), and 1 equimolar % Pd catalyst, 2 hours.

Keywords: Hydrogel, Heterogeneous Catalyst, N-Heterocyclic carbene, Suzuki-Miyaura reaction.

References:

[1] Kang, T., Feng, Q., Luo, M., 2005, Synlett, 15, 2305–2308

[2] Lee, Y., Hong, C. H., Ahn, H., Yu, J. and Rhee, H. 2014, Journal of Organometallic Chemistry 769: 80-93

THE CATALYTIC ACTIVITIES OF SOME NOVEL POLYMERIC NHC-PD HYDROGEL SYSTEMS

CIHANGIR BOZTEPE, ASIM KÜNKÜL, ISMAIL ÖZDEMİR, NEVIN GÜRBÜZ

[1]İnönü University, Engineering Faculty, Department of Chemical Engineering, Malatya/Turkey
[2]İnönü University, Catalysis Research and Application Center, 44280, Malatya, Turkey

e-mail: cihangir.boztepe@inonu.edu.tr

The Suzuki reaction is one of the most powerful synthetic pathways for Cabon-Carbon bond formation that involves a palladium-catalyzed coupling reaction between an aryl halide and an arene boronic acid. The Suzuki reaction is usually carried out with a homogeneous Pd catalyst but, in order to use the Suzuki reaction in a wide range of industrial applications, a heterogeneous Pd catalyst must be developed [1]. Hydrogels are three-dimensional networks of cross-linked polymers, which can hold up to 1000 times of water. Hydrogel catalyst supports have several advantages, such as big surface area, fast recovery and the simple recycling of the catalysts by filtration, which in turn prevents the contamination of the ligand and decreases the environmental pollution caused by residual metals in the waste. And, hydrogels have also been used as a scaffold to in situ synthesize inorganic nanoparticles within the three-dimensional hydrogel networks [2]. In this studuy, novel NHC-Pd complex having catalytic activity, have been prepared and immobilized on three different acrylamide based polymeric hydrogel supports which consist from poly(acrylamide) (Poly(AAm)), poly(acrylamide-co-vinyl imidazole) (Poly(AAm-co-VI)) and poly(acrylamide- co-2-acrylamido-2-methylpropane sulfonic acid) (Poly(AAm-co-AMPS)) by free radical polymerization method. And, we described the effects to catalytic performance of these supports in the Suzuki-Miyaura cross-coupling reactions and illustrated in Table 1.

Table 1. Suzuki- Miyaura coupling reactions of various aryl bromides and aryl boronic acid with the catalyst at 80 ^{0}C in water.

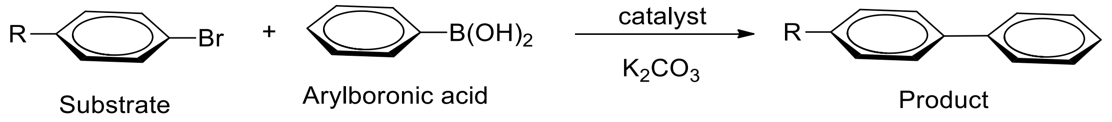

	Yields (%) as a Substrates				
Catalyst Support Type	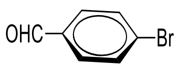	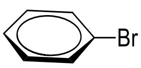	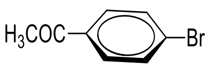	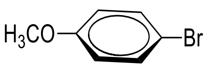	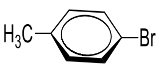
Poly(AAm)	96	91	95	91	94
Poly(AAm-co-VI)	33	17	28	23	19
Poly(AAm-co-AMPS)	99	96	99	95	97

Reaction conditions: bromobenzene (0.25 mmol), phenylboronic acid (0.375 mmol, 1.5 eq.), K_2CO_3 (0.75 mmol, 3 eq.), H_2O (5 mL), and 1 equimolar % Pd catalyst, 2 hours.

Keywords: Hydrogel, Heterogeneous Catalyst, N-Heterocyclic carbene, Suzuki-Miyaura reaction.

References:

[1] Hong, M. C., Choi, C. M., Chang, W. Y., Lee, Y., Kim, J., Rhee, H., 2012, Adv. Synth. Catal.,354:1257 – 1263
[2] Lee, Y., Hong, C. H., Ahn, H., Yu, J. and Rhee, H. 2014, Journal of Organometallic Chemistry 769: 80-93

EFFECT OF TEMPERATURE AND TIME ON VULCANIZING A FABRIC CONVEYOR BELT WITH A COLD VULCANIZING ADHESIVE

DENIZ AKIN SAHBAZ, CAGLAYAN ACIKGOZ, OMER METE KOCKAR

Deniz Akın Şahbaz, Res. Asst., Afyon Kocatepe University, Çağlayan Açıkgöz, Assoc. Prof. Dr., Bilecik Şeyh Edebali University, Ömer Mete Koçkar, Prof. Dr., Anadolu University

Abstract

Conveyor belts are the most commonly used for transport of solid objects and bulk materials due to the simplicity in construction, flexibility in transport system configuration, and versatility in use. If a belt is removed from service because of carcass breakdown or injury, in most cases belt repairs will be one of three types: vulcanized, metal fasteners and cold vulcanization. It is known to repair rubber conveyor belts by a cold vulcanizing process instead of a hot vulcanizing process. Cold vulcanization provides belt splicing without requiring vulcanization heater equipment. The cold vulcanizing adhesives are commonly used in jointing conveyor belts and bonding rubber to metal surfaces. With high adhesive strength and fire-resistant, cold vulcanizing cement has become necessary adhesive for coal mine assembly line and been widely used in coal mines, power plants, cement plants. These adhesives are composed of two separate components which are mixed immediately before use. One of the components usually contains chloroprene based liquid rubber cement, while the other component contains hardener. The components are advantageously in the liquid phase. After the actual making of cold cure repairs, long time is necessary for the chemical action to reach minimum useful strength, often four hours or more. However, cold-chemical splice quality is affected by ambient temperatures. Low temperature can adversely affect the strength of cold-chemical bonds. This study investigated the optimum conditions for vulcanizing a fabric conveyor belt with better adhesive strength at different curing temperature (25, 35, 45°C) and time (4, 8, 24 hours) at 0.001 kg/mm^2 curing pressure by using HB Fuller and Özer SY 2000 cold vulcanizing cements. Measurements of shear strength of spliced fabric conveyor belt were carried out on the tensile testing machine (Devotrans DVT). The results show that mechanic properties of spliced belts vary considerably with temperature and time. The optimum conditions for vulcanizing a fabric conveyor belt by using the cold vulcanizing cements with a better shear strength included: curing time of 24 hours and curing temperature of 45°C. The conditions for cold vulcanizing a fabric conveyor belt presented herein are helpful to the manufacturers and user of the fabric conveyor belt.

Keywords: cold vulcanizing adhesive, conveyor belt, low temperature curing, shear strength

Introduction

Conveyor belts are transportation equipments, which are rubber based with cord fabric, used for transporting various substances from one place to another. Conveyor belts are used in many industries, such as in mining, natural resource processing, smelting, cement and lime production, pulp and paper production, sea and river ports, civil engineering, agriculture, sugar factories, power plants and others, they are the most commonly used transportation tools (Mazurkiewicz, 2008).

Figure 1. A typical belt conveyor used for transport (ÖZERBAND, 2015)

Conveyor belts consist of two parts, first part is the carcass and second part is the rubber covering. Carcass part is the one which bears the weight, rubber part is the one which composes the outer appearance of the belt and also is subject to outer effects (BİLLAS, 2014). Conveyor belt's exposure to light, heat, humidity, chemicals and gaseous pollutants causes a decrease in the degree of polymerization and a change in chemical composition in rubber structure of conveyor belts (Dobrota, 2013). Because of the aging, conveyor belts lose their tensile strenght and remove from service. Most belt conveyor operations rely on one or both the three following methods of splicing: high temperature vulcanization, room temperature (cold) vulcanization or mechanical fastening. Mechanical belt fastening is the process of joining belt ends by metal hinges or plates, whereas vulcanization is the process of joining belt ends through heat and/or chemicals (Flexco, 2015).

A continuous loop conveyor belt (Figure 2), which half length is used for delivering materials , and other half is the return run, consist of sections joined by cold vulcanization and heat curing (Mazurkiewicz, 2009). Joining of belts using these methods is an onerous and time-consuming process. Choice of a vulcanizing method depends on a number of factors including the structure of conveyor belt, required strength of the adhesive joint, ambient conditions.

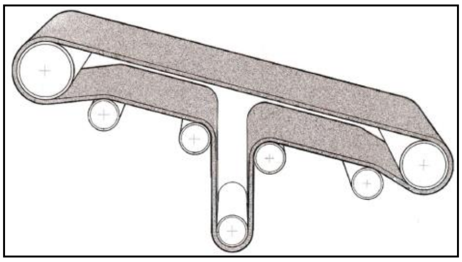

Figure 2. Schematic of a continuous loop conveyor belt (ÖZERBAND, 2015)

In cold vulcanization of high-performance belt transport systems (Figure 3), plies are opened at lengths specified as per fabric type and number of plies. Cold vulcanized adhesive mixed with hardener is applied both surfaces prepared for splicing. Great care is required in gathering two belts and all the steps should be coincided together. Because in contrary to the hot vulcanization, subsequent adjustment is not possible (ÖZERBAND, 2015).

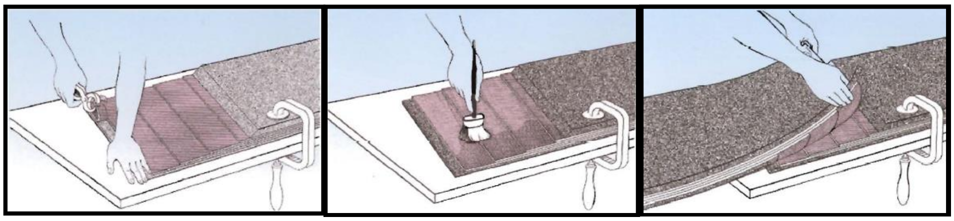

Figure 3. Splicing of textile belts by cold vulcanization (ÖZERBAND, 2015)

Some studies related to vulcanizing a fabric conveyor belt with adhesives and adhesion properties were presented. Chou, Liu and Tseng (2012) have investigated that the optimum conditions of splicing (or vulcanizing) a fabric conveyor belt with a better capability of elongation using the vulcanizing method and the analysis of mean of the Taguchi method. Chou, Liu and Chuang (2013) also have indicated that the optimum conditions for vulcanizing a fabric conveyor belt with better adhesive strength and less abration. Mazurkiewicz (2008) has investigated the ageing impact on the strength of adhesive sealed joints of conveyor belt. Also, the strength parameters of conveyor belt bonded joints during different periods of use has obtained.

The aim of the present study is to investigate the effect of temperature and time on adhesion property of HB Fuller and Özer SY 2000 cold vulcanizing cements. This work is novel as no author has studied about the adhesion property of cold vulcanizing adhesives.

Materials and Methods

The conveyor belt used in this study is made of natural rubber (NR). In the laboratory studies, test pieces with width of 30 mm and length of 150 mm, which were cut from the same area of the fabric conveyor belt were used for measuring adhesive properties (Figure 4).

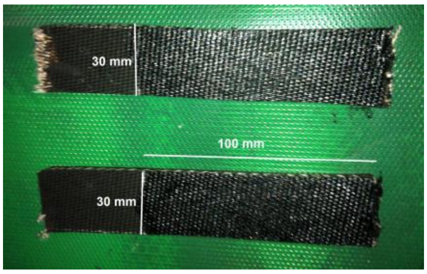

Figure 4. Test pieces of the fabric conveyor belt used in experiments

HB Fuller and Özer SY 2000 cold vulcanizing cements were used as the adhesives to investigate the adhesion conditions of conveyor belt. Özer SY 2000 was supplied by OZERBAND Conveyor Belt Industry and Trade Inc. (Afyonkarahisar, Turkey) whereas HB Fuller was provided by AGA Machine and Rubber (İstanbul,Turkey).

Measurements of shear strength of spliced fabric conveyor belt samples were carried out on the tensile testing machine (Devotrans DVT). The tension rate was 100 mm/min.

Results and Discussion

In the joint area obtained by a cold vulcanizing adhesive, there must be a structure with mechanical features as close as possible to the original conveyor belt. Temperature and time which are technological parameters, have a large influence on the tensile strenght of the conveyor belt and play important roles in adhesion of vulcanizing cement. The dependence of shear strength of spliced conveyor belt by Özer SY 2000 and HB Fuller cold vulcanizing adhesives on time and temperature are shown in Figure 5 and 6.

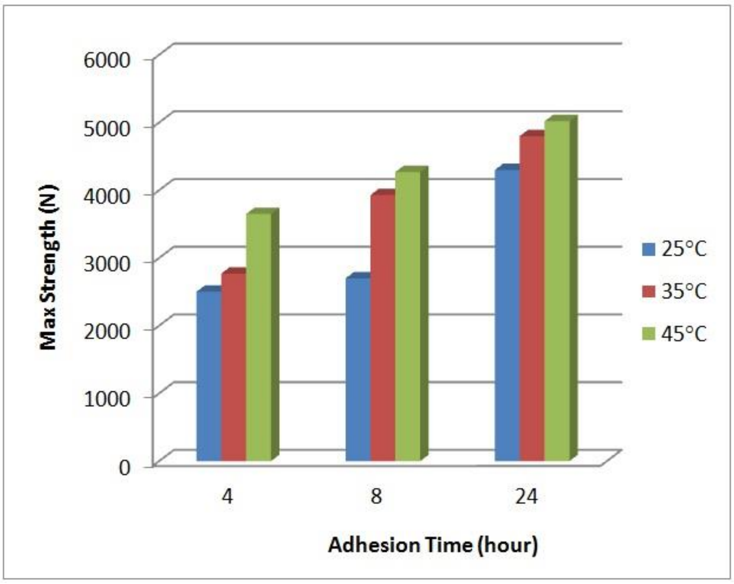

Figure 5. Variation of maximum strenght values of spliced conveyor belt with adhesion time (Cold vulcanizing adhesive: Özer SY 2000; Temperature: 25, 35, 45°C)

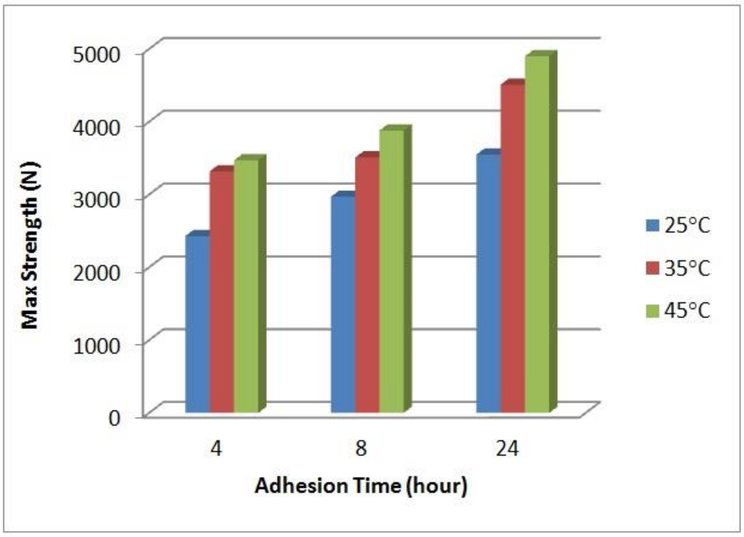

Figure 6. Variation of maximum strenght values of spliced conveyor belt with adhesion time (Cold vulcanizing adhesive: HB Fuller; Temperature: 25, 35, 45°C)

From the figures, it is seen that shear strength increases with time. This observation is attributed to increasing cross-linking structure of rubber component present in the spliced area which enhances the shear resistance of the adhesives.

Shear strength of the spliced conveyor belt also increases with increasing temperature. At low temperatures of testing, the solvent of adhesive need time to remove from the applied adhesive layer whereas at higher temperatures, evaporation of the organic solvent proceeds more quickly. The mechanical properties are maximum when the ambient temperature is 45°C.

Conclusions

The article presents the results of a study on the use of cold vulcanizing adhesive for repair of a fabric conveyor belt at various conditions and the effect of the temperature and time of curing on the mechanical properties of the bonded layer.

Best results in cold vulcanization by adhesive were obtained for a curing pressure, a vulcanization time of 24 hours and a vulcanization temperature of 45°C. To obtain good results in splicing process of textile belts by cold vulcanization, longer curing time may be needed because of continuing the vulcanization of chloroprene rubber, unlike the other rubbers, with zinc oxide and magnesium oxide.

Acknowledgement

This study is supported by Scientific Project 2015-01.BŞEÜ.03-03 from Bilecik Seyh Edebali University, Turkey. The authors would like to thank BILLAS Tire & Rubber Industry and Trade Inc. and OZERBAND Conveyor Belt Industry and Trade Inc., Turkey for assisting this research.

References

Billas Lastik ve Kauçuk San. Tic. A.Ş., 2014. Product Catalogue. [Online] Available at: http://www.billas.com.tr/konveyor/katalog/billas-konveyor/ .

Chou, C.-S., Liu, C.-L., Tseng, C.-S., 2012. Optimum conditions for field vulcanizing a fabric conveyor belt with a better capability of elongation. Materials and Design, 34, 279-284.

Chou, C.-S., Liu, C.-L., Chuang, W.-C., 2013. Optimum conditions for vulcanizing a fabric conveyor belt with better adhesive strength and less abrasion. Materials and Design, 44, 172-8.

Dobrota, D., 2013. Adhesion degradation of rubber and steel insert for conveyor belts. Journal of Adhesion Science and Technology, 27(2), pp.125-35.

Flexco, 2015. Get The Facts About Conveyor Belt Splicing Techniques. [Online] Available at: www.flexco.com/filebase/en/log/File3693 .

Mazurkiewicz, D., 2008. Analysis of the ageing impact on the strength of the adhesive sealed joints of conveyor belts. Journal of Materials Processing Technology, 208, pp.477-85.

Mazurkiewicz, D., 2009. Problems of numerical simulation of stress and strain in the area of the adhesive-bonded joint of a conveyor belt. Archives of Civil and Mechanical Engineering, 9(2), pp.75-91.

Özer Konveyör Band Sanayii ve Ticaret A.Ş., 2015. Online Catalog. [Online] Available at: http://ozerbant.com/katalog/ .

PATH INTEGRAL TREATEMENT OF THE DEFORMED GENERALIZED DENG-FAN POTENTIAL PLUS THE DEFORMED ECKART POTENTIAL IN D-DIMENSIONS

DIAF AHMED, HADJER BAKHTI, HADDA BADANI

[1] Khemis Miliana University,Khemis Miliana, Algeria.
[2] Médéa University, Algeria.

Abstract

In this work, path integral formalism is used to solve an exponential-type potential. An analytical expression, for the energy eigenvalues of the deformed generalized Deng-Fan potential plus the deformed Eckart potential for l-states, is derived by an approximation to the centrifugal term of the potential , in the framework of the Duru-Keinert method. Nonlinear space-time transformations in the radial path integral are applied. A transformation formula is derived that relates the original path integral to the Green function of a new quantum solvable system. The energy spectrum and the normalized eigenfunctions are both obtained for the application of this technique to the studied potential. Our results are in very good agreement with those found by the Schrödinger formalism.

Keywords: Deng-Fan Potential , Energy spectrum, l-states.

✉ Corresponding Author Email : s_ahmed_diaf@yahoo.fr

VOLUMETRIC THERMODYNAMIC'S PROPERTIES OF DILUTE ANALGESIC SUBSTANCES IN ALCOHOLS AT DIFFERENT TEMPERATURES

SAÉDA DIDAOUI, AHCÈNE DOUAS, AHMED AIT-KACI

Laboratoire de Thermodynamique et Modélisation Moléculaire. Faculté de chimie,
Université des Sciences et Technologie Houari Boumediène
B.P.32 El-Alia Bab-Ezzouar 16111 Alger, Algérie

Keywords: salycilamide, volumetric properties, density, thermal coefficients

Corresponding author : E-mail: sdidaoui@hotmail.com[1]

Abstract

Salicylamide or 2-hydroxybenzamiden is a mild analgesic with anti-inflammatory and antipyretic properties. It has been used in protections against fungus in, for example, oils, soaps and lotions.

The study of volumetric properties in various solvents may be helpful in investigating the molecular phenomenon and interesting for numerous applications.

The apparent molar volume of salicylamide in alcohols (C1 – C8) as solvents in the range temperature 288.15 to 318.15 K with an interval of 5K and at a pressure of 101.325 kPa were determined from the density data obtained using vibrating-tube Anton Paar DMA 5000 densimeter.

The partial molar volume, of salicylamide in these solvents at different temperatures was evaluated by extrapolating the apparent molar volume versus molality plots to m = 0. In addition, the partial molar expansivity , the isobaric coefficient of thermal expansion and water transfer volume – alcohol at infinite dilution of salicylamide and for comparison of salicylic acid and acetylsalicylic acid with the same alcohols have been computed. The expansivity data show dependence of the values on the structure of the solute molecules.

ADSORPTION AND CORROSION INHIBITIVE PROPERTIES OF RUTA CHALEPENSIS ON API X52 STEEL IN HYDROCHLORIC ACID MEDIA

MERYEM AMAL BENGHALIA, CHAHINEZ FARES, MOHAMED HADJ MELIANI, ABDELKADER KHADRAOUI

Meryem Amal BENGHALIA: Laboratory for theoretical physics and material physics; Department of Process Engineering, Faculty of Technology, Hassiba Ben Bouali University of Chlef, B.P. 151, 02000 Chlef, Algeria.
Laboratory of water & Environnement Faculty of Technology, Hassiba Ben Bouali University of Chlef, B.P. 151, 02000 Chlef, Algeria
Chahinez FARES: Laboratory for theoretical physics and material physics; Department of Process Engineering, Faculty of Technology, Hassiba Ben Bouali University of Chlef, B.P. 151, 02000 Chlef, Algeria.
Mohamed HADJ MELIANI: Laboratory for theoretical physics and material physics; Department of Mechanics Engineering, Faculty of Technology, Hassiba Ben Bouali University of Chlef, B.P. 151, 02000 Chlef, Algeria
Abdelkader KHADRAOUI: Laboratory for Valuation of Natural Substances, University Djilali Bounaama, Khemis-Miliana, Algeria.
Presenting and corresponding author: *chahinezfares@yahoo.fr*

Abstract

The extract of Ruta Chalepensis leaves was tested as a corrosion inhibitor of steel in 1M HCl using Tafel polarization and weight loss methods. The results showed that when the concentration of the extracts is increased the corrosion rate of steel sample is decreased, which indicates that the inhibition of the corrosion takes place. The polarization results showed that the extracts of Ruta Chalepensis plant acts as mixed type inhibitor; they retarded both cathodic and anodic corrosion reactions. The electrochemical parameters (E_{corr}, Icorr, β_c and β_a) and the inhibition efficiency were calculated. The Ruta Chalepensis efficiency was, also, studied in the range 298 and 353 K. Ruta Chalepensis extract was adsorbed on the steel surface in accordance with a Temkin adsorption model. The thermodynamic data of activation: constant of adsorption K_{ads} and the standard free energy of adsorption $\Delta G°_{ads}$, for the extracts were calculated.

Keywords: Corrosion; Green inhibitors; Ruta Chalepensis extract; Acid medium; Adsorption.

1. Introduction

Steel pipelines play an extremely important role throughout the world as a means of transporting gases and liquids from their sources to the ultimate consumers [1]. In fact, steel pipelines are susceptible to corrosion problem in acid media. The largest end uses for acid solutions, especially hydrochloric acid, are steel pickling to remove the undesirable scales and rusts on steel surface, and oil well acidizing to enhance oil/gas recovery [2–6]. These operations usually induce serious corrosion of equipment, tubes, and pipelines made of steel [7, 8].

The use of inhibitors is one of the most practical methods for metals protection against corrosion in acidic media. The majority of the well-known inhibitors are organic compounds containing heteroatoms, such as nitrogen-base materials and their derivatives, sulphur-containing compounds, aldehydes, thioaldehydes, acetylenic compounds, which allow adsorption on the metal surface [9]. Unfortunately, many common corrosion inhibitors that are still in use today are toxic to the environment and hazardous to health [10]. Restrictive environmental regulations have now made researchers to focus on the need to develop cheap, non-toxic and environmental friendly natural products as inhibitors [11-34].

The natural product, extracted by simple procedures with low cost, serve as an incredibly rich source of naturally synthesized chemical compounds [11-34]. Various mechanisms of action mode adsorption have been postulated for the corrosion inhibition property of the natural products [13, 27, 35-39]. Both physical as well as chemical adsorption mechanisms were been confirmed by the thermodynamic parameters analysis. Generally, values of the free energy of adsorption up to −20 kJ mol^{-1} are consistent with electrostatic interaction between charged molecules and a charged metal (which indicates physisorption), while those around -40 kJ/mol^{-1} or higher involves charge sharing or transfer from the organic molecules to the metal surface to form a co-ordinate type of bond (chemisorption).

This study aims to gain some insight into the corrosion of API X52 pipeline steel in HCl in the presence of Ruta Chalepensis extract (RC) as a corrosion green inhibitor. Ruta Chalepensis, which has the current Algerian name ''Fidjel'', is an aromatic plant, widely used in traditional medicine and is generally found in humid regions of Algeria. The inhibition effect of the extract of Ruta Chalepensis leaves on the corrosion of steel in 1 M HCl solution by gravimetric, electrochemical polarization methods. In order to elaborate adsorption mechanism, a various thermodynamic parameters of dissolution processes were evaluated in the temperature range of 298 and 353 K.

2. EXPERIMENTAL

2.1. Steel specimen

Tests were performed on a pipeline steel of the following chemical composition (wt.%): C: 0.103%, P: 0.012%, Si: 0.12%, Mn: 0.97%, Cr: 0.02%, Cu: 0.01%, Al: 0.032%, Ni: 0.005%, Mo: 0.005%, S: 0.002%, Ti: 0.002%, V: 0.002% and the remainder is Fe. This material was made according to API 5L grade X52 specifications.

2.2. Solutions Preparation

The aggressive solution, 1 M HCl, was prepared by diluting the analytical grade 37% HCl with distilled water.

The tested extract was prepared by boiling 10 g of Ruta Chalepensis seed in 1 L of 1 M HCl for 10 min. The solutions were cooled, filtered using Whatman filter paper No. 1, and adjusted to 1 L of volume to obtain a stock solution (10 g L^{-1}).

Different concentrations of the extract (5%, 10%, 20% and 30%) were prepared by diluting the stock solution with the respective blank corrodent of 1 M HCl.

2.3. Electrochemical Measurements

The electrochemical tests were performed using PGP 201 potentiostat with Volta Master 4 software, a three-electrode cell was used for the electrochemical experiments. The counter-electrode (CE) was a large grid of platinum and the saturated calomel electrode (SCE) was also used as a reference electrode (RE) The working electrode (WE) was a piece of API X52 steel pipeline.

The open circuit potential (OCP) was measured for 1 hour until stabilization. After measuring the OCP, potentiodynamic polarization curves were obtained with a scan rate of 0.5 mV/s in the range of ±1000 mV from OCP.

The inhibitory efficacy of the corrosion E (%) is derived from the knowledge of the corrosion current of the samples with and without inhibitor as shown in eq. (01).

$$E\ (\%) = \frac{i_{corr-i_{corr}^{inb}}}{i_{corr}}.100 \qquad (1)$$

Where: i_{corr} and i_{corr}^{inh} respectively represent the corrosion current in the absence and presence of inhibitor.

2.4. Weight loss measurements

The gravimetric method consists of exposing samples to a corrosive environment for a specified time 6 hours after measuring its initial mass. After the immersion period, the sample was removed, and then cleaned with distilled water. The corrosion products were removed from the metal surface by immersion in a pickling solution containing HCl for some seconds. Sample mass difference before and after each test is used to determine the inhibitory efficiency according to the relation (02):

$$E\ (\%) = \frac{\Delta m - \Delta m^{inh}}{\Delta m} * \mathbf{100} \quad (2)$$

Where E (%) is the inhibitory efficiency $\boldsymbol{\Delta m}$ (g) is the mass loss (the rate of corrosion) of the sample without inhibitor $\boldsymbol{\Delta m^{inh}}$ (g) is the sample mass loss with inhibitor.

3. RESULTS AND DISCUSSION

3.1. Polarization Measurements

The anodic and cathodic polarization curves of the APIX52 steel 1M HCl at different temperatures, in the absence and presence of inhibitor at concentrations of 5%, 10%, 20% and 30%, are shown in Figure 1.

Potentiodynamic polarization experiments were undertaken to determine the effect of the anodic ($Fe \rightarrow Fe^{2+} + 2e$) and cathodic ($2H^{+} + 2e \rightarrow H_2$) partial reactions of the corrosion process. The polarization curves reveal that APIX52 specimen is seen to exhibit active dissolution with no distinctive transition to passivation within the studied potential range in the acidic environment. The plots also show that the anodic and cathodic reactions in blank acid and upon the addition of Ruta Chalepensis extract follow Tafel's law.

The plots indicate that the corrosion current density decreases markedly in the presence of Ruta Chalepensis extract compared to the blank solution and also decreases with an increase in the concentration of the extract. It is also observed that the presence of Ruta Chalepensis extract does not shift Ecorr remarkably; therefore, this inhibitor could be regarded as a mixed-type inhibitor, and inhibition of APIX52 corrosion by RC occurred by the geometric blocking effect mechanism [35].

The values of the corrosion current density in the absence (i^{o}_{corr}) and presence (i_{corr}) of inhibitor were used to estimate the inhibition efficiency. Figure 2 showed the inhibition efficiency function of inhibitor concentration at different temperatures.

From the figure 2, it is seen that the inhibition efficiency increases with an increase in the concentration of Ruta Chalepensis extract, reaching a maximum value of 79.3% Ruta Chalepensis extract at 50°C.

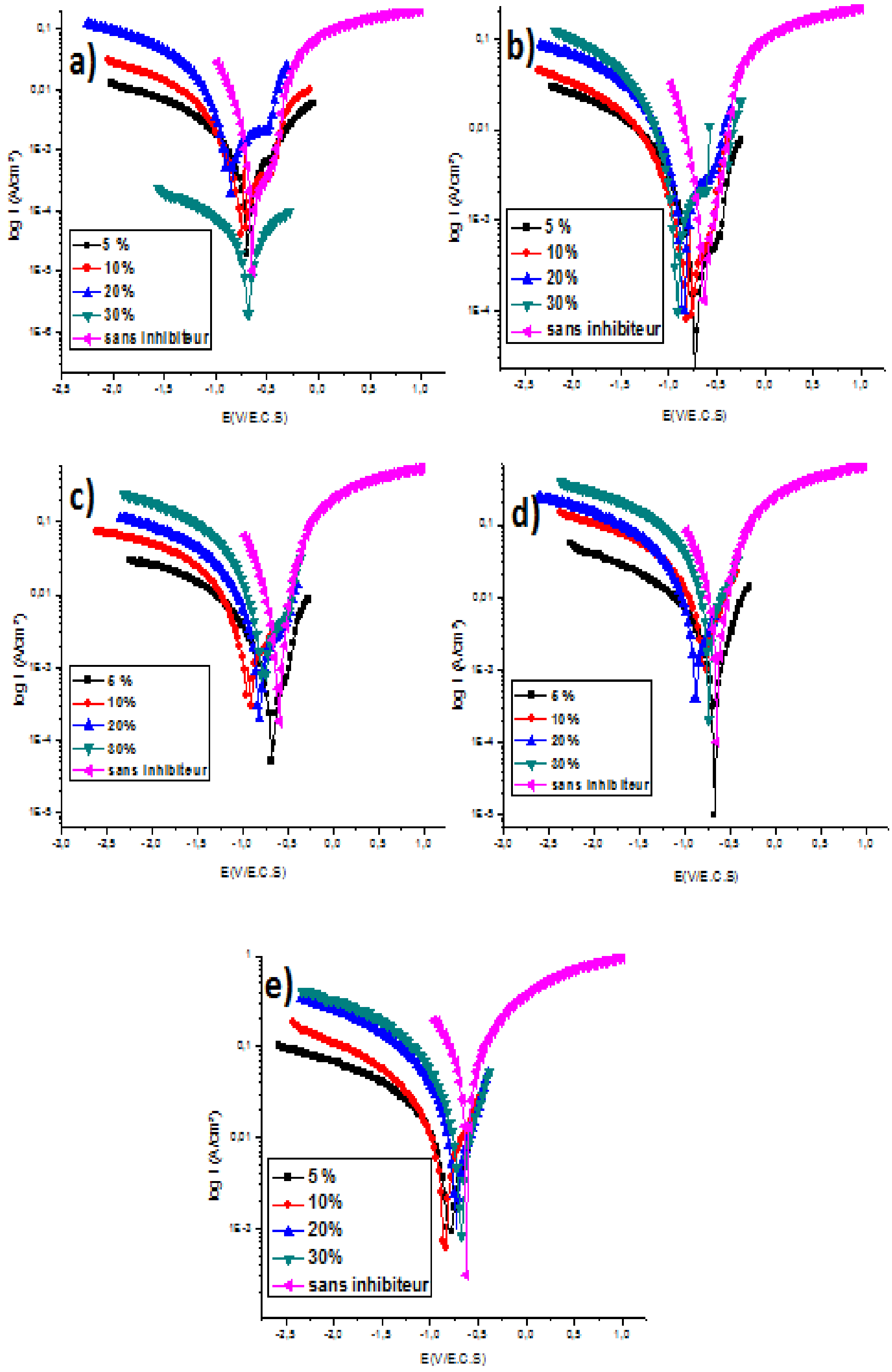

Figure 1: Polarization curves of the X52 steel with and without addition of the inhibitor for the extract of Ruta Chalepensis in HCl medium at different temperatures. a) Tamb, b) T = 35 ° C, c) T = 50 ° C, d) T = 65 ° C, e) T = 80 ° C.

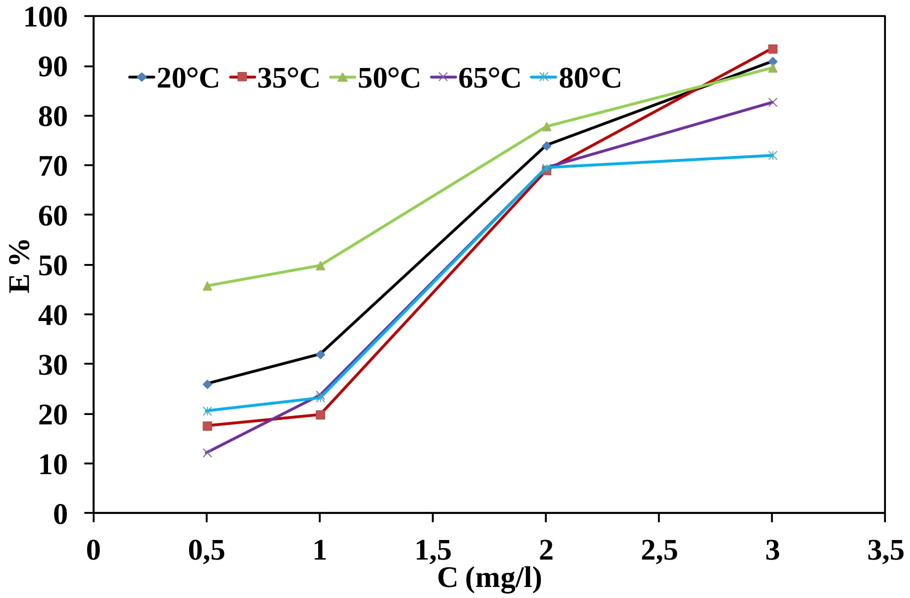

Figure 2: Inhibition efficiency against the inhibitor concentration at different temperatures for APIX52 steel in 1 M HCl from Polarization measurements.

3.2. Weight loss measurements

The effect of the addition of RC extract tested at different concentrations on the corrosion of steel in 1 M HCl solution was studied using weight loss at different temperature after 6 h of immersion period. Inhibition efficiency E (%) is calculated using equation 2. Table 1 gives the values of the inhibition efficiency (E %) for steel corrosion in 1 M HCl and in the presence of inhibitors tested at different concentrations.

Table 1: Gravimetric results of the steel corrosion with and without addition of Ruta Chalepensis after 6 h of immersion in 1 M HCl at different temperature

	Concentrations Temperatures	5%	10%	20%	30%
E%	20°C	22,1	47,82	87,25	77,35
	35°C	15,66	22,22	62,33	79,11
	50°C	40,54	45,12	71,16	97,23
	65°C	20,64	20,15	59.05	55,47
	80°C	13,82	19,25	50,89	58,75

From Table 1, it can be seen that corrosion rate values in 1 M HCl solution containing Ruta Chalepensis extract decreased as the concentration of inhibitor increased. This result is due to the adsorption of components of the extract as coverage of inhibitor on the steel surface increases with inhibitor concentration. The highest inhibition efficiency of 97.23% was obtained at 30% Ruta Chalepensis extract at 50°C. The efficiency obtained by gravimetric measurements, are in excellent agreement with those obtained from the extrapolation of the cathodic Tafel lines.

3.3. Adsorption Considerations

It is accepted that inhibitors adsorb onto the APIX52 steel surface to inhibit corrosion processes. The types of adsorption can be physisorption or chemisorption. It is well known that the coverage of corrosion inhibitor on metal surface (θ) is the most useful parameter for the study of the adsorption behaviour of the inhibitor which is calculated as θ = E%/100 [36]. The values of surface coverage (θ) for different concentration of the studied inhibitor (1M) were obtained from Tafel polarization data and have been used to determine the appropriate isotherm and the adsorption process (Figure 3).

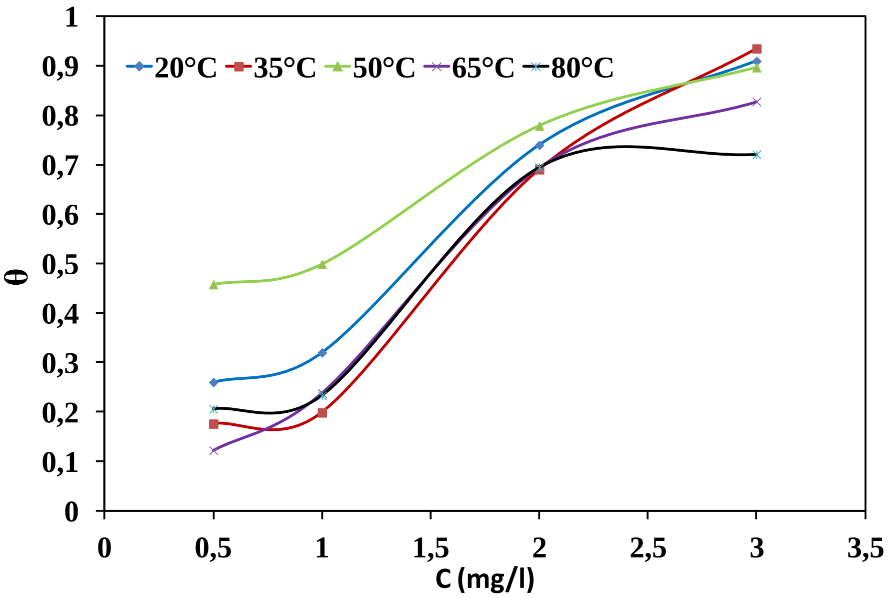

Figure 3: Adsorption curves of the Ruta Chalepensis on APIX52 in 1M HCl.

Attempts were made to fit θ values to the Frumkin [37], Langmuir [38] and Temkin [39, 40] isotherms. The value of the correlation coefficient (R^2) was used to determine the best-fit isotherm. The best result was obtained with Temkin isotherm according to the following equation:

$$exp(f\theta) = KC_{inh} \qquad (3)$$

Where θ is the surface coverage, C is the concentration, and K_{ads} is the adsorption equilibrium constant and f is the molecular interaction constant. The equilibrium constants for adsorption process are related to the free energy of adsorption, ΔG_{ads}, by:

$$K = \frac{1}{55,5} exp\left(-\frac{\Delta G_{ads}}{RT}\right) \qquad (4)$$

Where 55.5 is the concentration of water expressed in mol dm^{-3}, R is the molar gas constant, and T is the absolute temperature.

Figure 4 shows the plot of θ against Ln C. Linear plots were obtained that show that adsorption of the constituents of Ruta Chalepensis onto a APIX52 surface follows the Temkin adsorption isotherm.

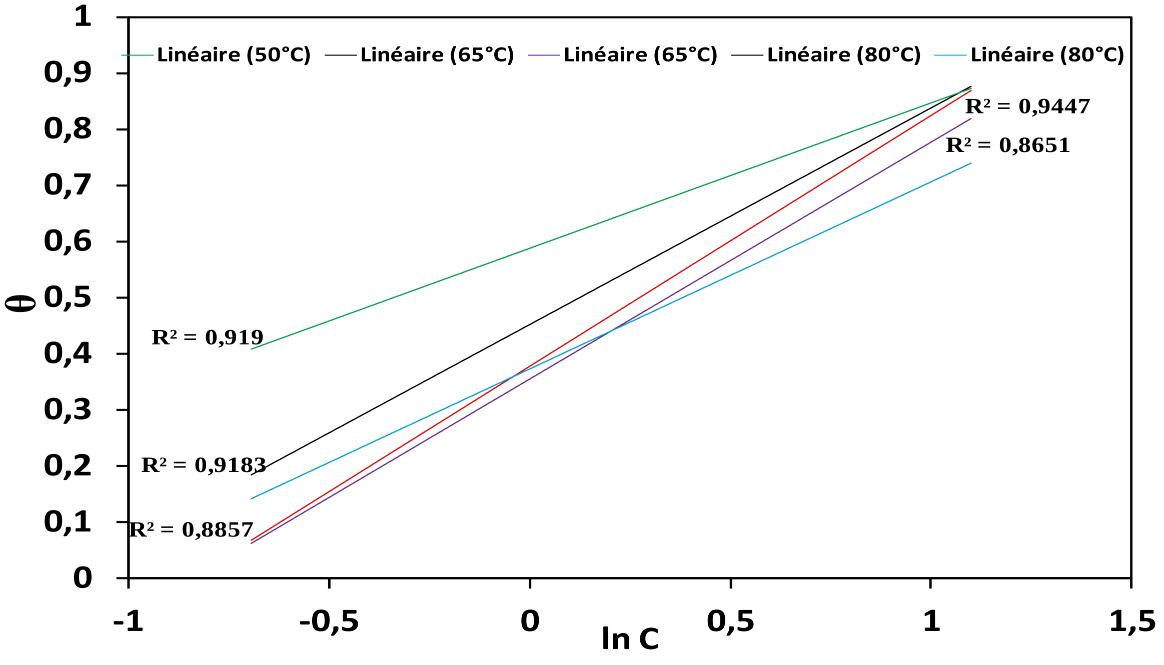

Figure 4: Temkin adsorption isotherm for Ruta Chalepensis extract on APIX52 in 1M HCl at different temperatures.

Adsorption parameters derived from the plots are listed in the Table 2. The results in the table indicate that K_{ads}, whose values indicate the binding power of the inhibitor to the metal surface, is seen to decrease with increasing temperature. Such behavior can be interpreted on the basis that increases in the temperature result in desorption of some adsorbed constituents of the extracts on the metal surface and are consistent with the proposed physisorption mechanism.

The large negative value of ΔG_{ads} implies that the adsorption of Ruta Chalepensis extract on the steel surface is allowed from thermodynamics point of view and indicates that the inhibitor is strongly adsorbed. The adsorption of 1M HCl on the API X52 steel could be mainly attributed to the physisorption one, because the values of the free energy of adsorption, are between −10.66 and −14.51 kJ mol^{-1}.

Other thermodynamic parameters, such as adsorption enthalpy, ΔH, and adsorption entropy, ΔS, can be derived from these data. Since $\Delta G = \Delta H - T\ \Delta S$, a plot of ΔG versus T should be a straight line with a slope of 0.0333 kJ mol^{-1} K^{-1}, this value it is ΔS, the enthalpy of adsorption, ΔH_{ads}, −10.950 kJ mol^{-1} were determined.

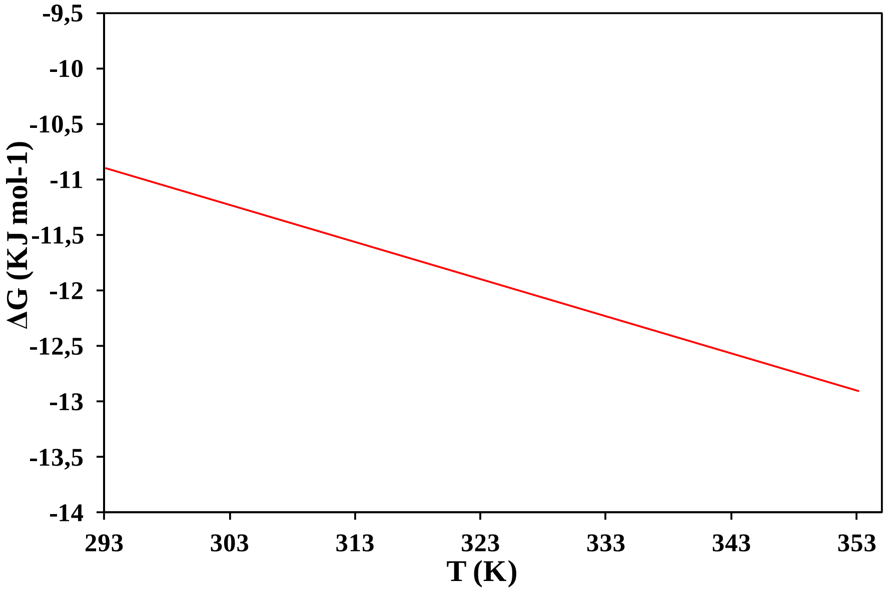

Figure 5: Thermodynamic parameters for the adsorption of Ruta Chalepnsis extract on APIX52

The obtained negative values of ΔH_{ads} confirm the exothermic behavior of the adsorption process of the extract on the API X52 steel pipeline surface in 1 M HCl solution. While, an endothermic adsorption process ($\Delta H_{ads} > 0$) is attributed unequivocally to chemisorption. An exothermic adsorption process ($\Delta H_{ads} < 0$) may involve either physisorption or chemisorption or a mixture of both processes [41, 42]. The values of the obtained enthalpy therefore suggest physical adsorption of the inhibitors on the surface of the metal. Typically, enthalpy of physical adsorption process is lower than 80 $KJmol^{-1}$, while the enthalpy of chemisorption process approaches 100 $KJmol^{-1}$ [32]. The values of the obtained enthalpy therefore suggest physical adsorption of the inhibitors on the surface of the metal.

The standard adsorption entropy values obtained that the sign of ΔS_{ads} is positive. This is opposite to what would be expected, since adsorption is always accompanied by a decrease of entropy. The reason could be explained as follow: The adsorption of the extract is accompanied by desorption of water molecules from the surface. Thus, when the adsorption process for the inhibitor is believed to be associated with a decrease in entropy of the solute, the opposite is true for the solvent. The thermodynamic values obtained are the algebraic sum of the adsorption of organic molecules and desorption of water molecules [43]. Therefore, the gain in entropy is attributed to the increase in solvent entropy. The positive values of ΔS_{ads} also mean that an increasing in disordering takes place in reactants adsorption form inhibitor to the metal/solution interface, which is the driving force for the adsorption of inhibitor onto steel surface [44].

Table 2: Thermodynamic adsorption values of the *Ruta Chalepensis* extract on APIX52 steel in 1M HCl solution.

Inhibitor conc. (mg/l)	20°C				35°C				50°C				65°C				80°C			
	E	θ	K	- ΔG KJ mol^{-1}	E	θ	K	- ΔG KJ mol^{-1}	E	Θ	K	- ΔG KJ mol^{-1}	E	θ	K	- ΔG KJ mol^{-1}	E	θ	K	- ΔG KJ mol^{-1}
5%	26	0,26	**1,43**	**10,66**	17,59	0,1759	**1,02**	**10,34**	45,8	0,458	**3,99**	**14,51**	12,2	0,122	**1,02**	**11,35**	20,6	0,206	**1,35**	**12,67**
10%	32	0,32			19,85	0,1985			49,9	0,499			23,8	0,238			23,3	0,233		
20%	74	0,74			69,06	0,6906			77,9	0,779			69,5	0,695			69,48	0,6948		
30%	91	0,91			93,52	0,9352			89,7	0,897			82,8	0,828			72,1	0,721		

4. CONCLUSION

In this work, the inhibitive action of Ruta Chalepensis extract, an inexpensive, eco-friendly, and naturally occurring substance, on the corrosion behavior of steel in 1 M HCl has been studied by using various methods. The results obtained are in good agreement and are given as follows.

The Ruta Chalepensis extract inhibited the corrosion of API 5L X52 steel in 1M HCl solution and the extent of inhibition was concentration dependent and inhibition efficiency increased with increase in concentration of inhibitor.

The results of potentiodynamic polarization investigations revealed that 1M functioning as a mixed inhibitor showing anodic and cathodic behaviour. Also, it was noticed that the adsorption of 1M on the steel surface followed the Temkin adsorption isotherm.

The values of Gibbs free energy of adsorption indicated that 1M was physically adsorbed on the surface of the steel.

REFERENCES

[1] Ghareba S., Omanovic S., Interaction of 12-aminododecanoic acid with a carbon steel surface: Towards the development of 'green' corrosion inhibitors, j. Corros. Sci, 2010, 52, 2104–2113.

[2] Hernandez-Espejel A., Dominguez-Crespo M.A., Cabrera-Sierra R., Rodriguez-Meneses C., Arce-Estrada E.M., Arce-Estrada E.M., Investigations of corrosion films formed on API-X52 pipeline steel in acid sour media, j. Corros. Sci, 2010, 52, 2258–2267.

[3] Hegazy M.A., Ahmed H.M., El-Tabei A.S., Investigation of the inhibitive effect of p-substituted 4-(N,N,N-dimethyldodecylammonium bromide)benzylidene-benzene-2-yl-amine on corrosion of carbon steel pipelines in acidic medium, j. Corros. Sci., 2011, 53, 671–678.

[4] Sadeghi Meresht E., Shahrabi Farahani T., Neshati J., Failure analysis of stress corrosion cracking occurred in a gas transmission steel pipeline, j. Eng. Failure Anal, 2011, 18 , 963-970.

[5] Abiola O.K., Adsorption of 3-(4-amino-2-methyl- 5-pyrimidyl methyl)-4-methyl thiazolium chloride on mild steel, j. Corros. Sci, 2006, 48, 3078–3090.

[6] Ali J.Z., Guo X.P., Qu J.E., Chen Z.Y., Zheng J.S., Adsorption Behaviour and Synergistic Mmechanism of a Cationic Inhibitor and KI on the Galvanic Electrode, j. Colloids & Surfaces. A: PhysicoChemical. Engineering. Aspects, 2006, 281, 147–155.

[7] Dehri I., Ozcan M., The effect of temperature on the corrosion of mild steel in acidic media in the presence of some sulphur-containing organic compounds, Mater, j. Chem. Phys, 2006, 98, 316–323.

[8] Tang L., Li X., Li Lin, Mu G., Liu G., j. Mater. Chem. Phys, 2006, 97 , 301–307.

[9] Oguzie E. E., Enenebeaku C. K, Akalezi C. O., Okoro S. C., Ayuk A. A., Ejike E. N., Adsorption and corrosion-inhibiting effect of Dacryodis edulis extract on low-carbon-steel corrosion in acidic media, j. Colloid Interface Sci., ,2010, 349, 283−292.

[10] Obot I. B., Obi-Egbedi N. O., Adsorption properties and inhibition of mild steel corrosion in sulphuric acid solution by ketoconazole: Experimental and theoretical investigation, j. Corros. Sci., 52, 2010, 198−204.

[11] Kalpana M., Mehta G.N., j. Trans. SAEST, 2003, 38-40.

[12] Al-Sehaibani H., Evaluation of extracts of henna leaves as environmentally friendly corrosion inhibitors for metals, j. Mater. Wissen. Werkst. Tech., 2000, 31, 1063.

[13] El-Etre A.Y., Abdallah M., El-Tantawy Z.E., Corrosion inhibition of some metals using lawsonia extract, j. Corros. Sci., 2005, 47, 385.

[14] El-Etre A.Y., Colloid J., Inhibition of acid corrosion of carbon steel using aqueous extract of olive leaves, j. Interface Sci., 2007, 314, 578.

[15] Chetouani A., Hammouti B., Benkaddour M., Corrosion inhibition of iron in hydrochloric acid solution by jojoba oil, j. Pigment Resin Technol., 2004, 33, 26.

[16] Raja P.B., Sethuraman M.G., Inhibitive effect of black pepper extract on the sulphuric acid corrosion of mild steel, j. Mater. Lett., 2008, 62, 2977.

[17] Oguzie E.E., Studies on the inhibitive effect of Occimum viridis extract on the acid corrosion of mild steel, Mater. j. Chem. Phys., 2006, 99, 441.

[18] Ramesh S.P., Kumar K.P.V.,. Sethuraman M.G, j., Extract of Andrographis Paniculata as corrosion inhibitor of mild steel in acid medium, Bull. Electrochem., 2001, 17, 141.

[19] Okafor P.C., Ikpi M.E., Uwah I.E., Ebenso E.E., Ekpe U.J., Umoren S.A., Inhibitory action of Phyllanthus amarus extracts on the corrosion of mild steel in acidic media, j. Corros. Sci., 2008, 50, 2310.

[20] Parikh K.S., Joshi K.J., Natural Compound Onion (Allium Cepa), Garlic (AlliumSativum) and Bitter Gourd (Momordica Charantia) As Corrosion Inhibitors for Mild Steel In Hydrochloric Acid, j. Trans. SAEST, 2004, 39, 29.

[21] Smita A.V., Mehta G.N., j. Trans. SAEST, 1997, 32, 89.

[22] Sakthivel P., Nirmala P.V., Umamaheshwari S., Antony A.A.A., Kalaignan G.P., Gopalan A., Vasudevan T., Corrosion inhibition of mild steel by extracts of Pongamia Glabra and Annona Squamosa in acidic media, j. Bull. Electrochem., 1999, 15, 83.

[23] El-Etre A.Y., Inhibition of aluminum corrosion using Opuntia extract, j. Corros. Sci., 2003, 45, 2485.

[24] Chaieb E., Bouyanzer A., Hammouti B., Benkaddour M., Inhibition of the corrosion of steel in 1 M HCl by eugenol derivatives, j. Appl. Surf. Sci., 2005, 246, 199.

[25] Gunasekaran G., Chauhan L.R., Eco friendly inhibitor for corrosion inhibition of mild steel in phosphoric acid medium, j. Electrochim. Acta, 2004, 49, 4387.

[26] Orubite K.O., Oforka N.C., Inhibition of the corrosion of mild steel in hydrochloric acid solutions by the extracts of leaves of Nypa fruticans Wurmb, j.Mater. Lett., 2004, 58, 1768.

[27] Lebrini M., Robert F., Lecante A., Roos C., Corrosion inhibition of C38 steel in 1 M hydrochloric acid medium by alkaloids extract from Oxandra asbeckii plant, j. Corros. Sci., 2011, 53, 687.

[28] Behpour M., Ghoreishi S.M., Khayatkashani M.,. Soltani N, The effect of two oleo-gum resin exudate from Ferula assa-foetida and Dorema ammoniacum on mild steel corrosion in acidic media, j. Corros. Sci., 2011, 53, 2489.

[29] Abiola O.K., James A.O., The effects of Aloe vera extract on corrosion and kinetics of corrosion process of zinc in HCl solution, j. Corros. Sci., 2010, 52, 661–664.

[30] Halambek J., Berkovic´ K. , Vorkapic´-FuracˇJ., The influence of Lavandula angustifolia L. oil on corrosion of Al-3Mg alloy, j. Corros. Sci., 2010, 52, 3978.

[31] Satpathy A.K., Gunasekaran G., Sahoo S.C., Kumar A., Rodrigues P.V., Corrosion inhibition by Justicia gendarussa plant extract in hydrochloric acid solution, j. Corros. Sci., 2009, 51, 2848.

[32] Abiola O.K., Otaigbe J.O.E., The effects of Phyllanthus amarus extract on corrosion and kinetics of corrosion process of aluminum in alkaline solution, j. Corros. Sci., 2009, 51, 2790.

[33] Znini M., Bouklah M., Majidi L., Kharchouf S., Aouniti A., Bouyanzer A., Hammouti B., Costa J., Al-Dyab S.S., Chemical Composition and Inhibitory Effect of Mentha Spicata Essential Oil on the Corrosion of Steel in Molar Hydrochloric Acid,J.Int. Electrochem. Sci., 2011, 6, 691.

[34] Abdel-Gaber A.M., Abd-El-Nabey B.A., Saadawy M., The role of acid anion on the inhibition of the acidic corrosion of steel by lupine extract, j. Corros. Sci., 2009, 51, 1038.

[35] Li X., Deng S., Fu H., Mu G., Inhibition effect of 6- benzylaminopurine on the corrosion of cold rolled steel in H2SO4 solution, j. Corros. Sci., 2009, 51, 620−634.

[36] Zhang X., Wang F., He Y., Du Y., Study of the inhibition mechanism of imidazoline amide on CO2 corrosion of Armco iron, j. Corros. Sci., 2001, 43, 1417–1431.

[37] Oguzie E.E., Li Y., Wang F.H., Corrosion inhibition and adsorption behavior of methionine on mild steel in sulfuric acid and synergistic effect of iodide ion, j. Corros. Sci., 2007, 310, 90–98.

[38] Okafor P.C., Liu C.B., Liu X., Zheng Y.G., Wang F., Liu C.Y., Wang F., ORIGINAL PAPER Corrosion inhibition and adsorption behavior of imidazoline salt on N80 carbon steel in CO2-saturated solutions and its synergism with thiourea, J. Solid State Electrochem., 2010, 14, 1367–1376.

[39] Okafor P.C., Zheng Y.G.,, Synergistic inhibition behaviour of methylbenzyl quaternary imidazoline derivative and iodide ions on mild steel in H2SO4 solutions, j. Corros. Sci., 2009, 51, 850–859.

[40] Okafor P.C., Liu X., Zheng Y.G., Corrosion inhibition of mild steel by ethylamino imidazoline derivative in CO2-saturated solution, j. Corros. Sci., 2009, 51, 761–768.

[41] Durnie W., Marco R.D., Jefferson A., Kinsella B., Development of a structure-activity relationship for oil field corrosion inhibitors, J. Electrochem. Soc., 1999, 146, 1751–1756.

[42] Ali S.A., El-Shareef A.M., Al-Ghamdi R.F., Saeed M.T., The isoxazolidines: the effects of steric factor and hydrophobic chain length on the corrosion inhibition of mild steel in acidic medium, j. Corros. Sci., 2005, 47, 2659–2678.

[43] Branzoi V., Branzoi F., Baibarac M., The inhibition of the corrosion of Armco iron in HCl solutions in the presence of surfactants of the type of N-alkyl quaternary ammonium salts, j. Mater. Chem. Phys., 2000, 65, 288–297.

[44] Li X.H., Deng S.D., Fu H., Li T.H., Adsorption and inhibition effect of 6-benzylaminopurine on cold rolled steel in 1.0 M HCl, j. Electrochim. Acta, 2009, 54, 4089–4098.

INVESTIGATION OF METHYLENE BLUE ADSORPTION OF AGRICULTURAL WASTES WITH ELOVICH ADSORPTION KINETICS IN FIXED BED

FATIH KILIÇ, ÇIĞDEM SARICI ÖZDEMİR

FATIH KILIÇA,* ÇIĞDEM SARICI ÖZDEMİRB

[a]Tunceli University,Tunceli,62100
[b]Inonu University,Malatya,44100
[*] Correspondence author: Tunceli University,Tunceli,62100,ffatihkilicc@gmail.com

Abstract

During adsorption, adsorbing the substances in the liquid phase is carried by the adsorbent. The adsorption rate is always determined by the slowest step. If the adsorbent's phase is stationary, there is a case where the mixing has not been done. Porous solids such as molecular sieve which has more complex activated diffusion. Therefore, the diffusion into the pores is negligible for porous and microporous solids. In this case, adsorption kinetics is determined through the outward diffusion and molecular adsorption-desorption processes. Adsorption kinetics model was created to determine the adsorption behavior[1]. Elovich kinetic model is one of the adsorption kinetic models. This equation describes the chemical adsorption that occurs in heterogeneous solid surface [2]. In this study; for the agricultural waste of almond shell and peanut shell characterization studies were made by boehm titration. Thus the value of adsorption capacity was found to be sufficient for two agricultural wastes. Two agricultural waste has become a standard particle size of 0.250 mm to 0.125 mm. For both adsorbent, elovich kinetic model was studied at 25, 40 and 50 ºC for 2 hours. The high R^2 values were obtained for both adsorbent. α and β values were obtained from graphics. β values are increasing with temperature for both adsorbent. α values showed a linear increase in temperature for the BK adsorbent but there has beeen decline for FK.

Keywords: Agricultural Waste, Peanut shell, Almond shell, Adsorption

REFERENCES

[1] Ho, Y.S. ve McKay G. 1998-a, Sorption of dye from aqueous solution by peat, Chemical Engneering journal,70:115-124.
[2] Bhattacharyya, K.G. and Gupta, S.S. 2006. Adsorption of Fe(III) from water by natural and acid activated clays: Studies on equilibrium isotherm, kinetics and thermodynamics of interactions.Adsorption,12(3):185–204.

REMOVAL OF PHARMACEUTICAL COMPOUNDS USING ACTIVATED CARBON CLOTH FROM AQUEOUS SOLUTIONS

FIRDEVS MERT, SADIK ÇALIK, LEYLA BUDAMA AKPOLAT, NUMAN HODA

Abstract

Ibuprofen, is a non-steroidal anti-inflammatory drug used for relieving pain, helping with fever and reducing inflammation and also sulfadiazine eliminates bacteria that cause infections by stopping the production of foliate inside the bacterial cell. These compounds are commonly used in pharmaceutical industries. So they are major pollutants for environment especially from waste water. There are some prevalent methods to remove pharmaceutical compounds from waste water such as chemical oxidation, coagulation, liquid membrane permeation and adsorption. Among these methods adsorption is the most effective method to remove pharmaceutical compounds. Activated carbon is most widely used adsorbent material for adsorption because of its efficiency. Activated carbon can be in the form of powder, granular, fiber or cloth form. Activated carbon cloth is becoming popular because of having very high specific surface area, adsorption kinetics and capacity, uniform pore size and mechanical strength. In this work; the removal of ibuprofen and sulfadiazine from their aqueous solutions was studied by using a new product of activated carbon cloth. Their experimental adsorption data evaluated using Langmuir and Freundlich models. The fits of experimental data to the models that are applied were discussed. It is found that Langmuir model fits to experimental adsorption data more precisely with r2 (regression coefficient) of 0,94 and 0,99 for ibuprofen and sulfadiazine, respectively.

MATHEMATICAL MODELING OF PLATFORMING

K. HACHAMA , R. KERFAH

K. HACHAMA*,1 , R. KERFAH1

[1] University of Khemis-Miliana, road of Thenia Elhad, Khemis-Miliana 44225, Algéria.
E-mail: hachama_k@yahoo.fr

Abstract

In this study, we were interested to present a mathematical model to simulate a Flat-Forming section of a refinery that produces vehicle fuel. This unit essentially comprises three fixed bed reactor, a flash tank and a distillation column (debutanizer). Between each reactor a preheating furnace is required to compensate the heat loss due to the endothermic reactions. The pseudo-components so that all reactants and products involved in the process are linked together by a network of chemical reactions.

In a first step, we addressed the thermodynamic aspect. The method proceeds in the presence of high hydrogen content gas and at elevated pressure and temperature. The knowledge of the state of the reaction mixture is fundamental and essential to simulate a chemical engineering process. The second stage is dedicated to chemical reactions producing aromatics and isoparaffins which contribute to the increase of the octane rating of the feedstock. These reactions occur in heterogeneous phase in the presence of a metal catalyst impregnated on an alumina or silica support and involve very diverse and often complex mechanisms.

Integrating the equations of energy and mass balances based on the choice of mathematical models of chemical reactions and equations of state. Finally an optimum choice can be made taking into account the deactivation of the catalyst used, the severity (temperature) and the product quality (octane rating).

Keywords: Mathematical modeling, platforming, fixed bed reactor.

References

[1] FISCHER (B.) 'Modélisation mathématique de la réformation catalytique' Thèse Doc. Ing., Uni. Claude Bernard, Lyon (1977).

[2] RIAZI (M.R.) et DAUBERT (T.E) 'Characteristion parameters for petrolum fractions' Ind. Eng. Chem. Res., 26, 759-762, (1987).

[3] BOMMANNAN (D.), SRIVASTAVA (R.D.) et SARAF (D.N.) 'Modelling of catalytic naphta reformers' The Canadian Journal of Chemical Engineering, Vol 67, 405-411, June (1989).

[4] VAN TRIMPOT (P.A.), MARIN (G.B.) et FROMENT (G.F.) 'Reforming of C_7 hydrocarbons on a sulfired commercial Pt/Al_2O_3 catalyst' Ind. Eng. Chem. Res., 27, 51-57, (1988).

[5] TASKAR (U.) et RIGGS (J.B.) 'Modeling and optimization of a semiregenerative catalytic naphtha reformer' AiChE Journal, Vol. 43, No. 3, (1997).

STRUCTURAL AND OPTICAL PROPERTIES OF LEAD OXIDE/POLYSTYRENE NANOCOMPOSITE FILMS

B. TROUDI, O. HALIMI, M. SEBAIS, B. BOUDINE, B. HARIECHE, B. KEHAL

Laboratory of Crystallography, Department of Physics, University Frères Mentouri, Constantine, Algeria

ABSTRACT

The structural and optical properties of highly transparent and thermally stable lead oxide (PbO)/polystyrene (PS) nanocomposite films have been investigated. The samples in the form of thin films are deposited on glass substrates by spin-coating technique using a colloidal solution prepared by dissolving the polystyrene and dispersing the PbO nanocrystallites. The characterization of nanocomposite films PbO:PS by the X-ray diffraction (XRD) showed the incorporation of PbO crystallites (orthorhombic phase) in the amorphous matrix PS. The PbO crystallite size was estimated to 28.21 nm. Analysis of nanocomposite PbO:PS by Raman and infrared spectroscopies confirmed the results of X-ray diffraction by revealing vibration modes which are specific to the Pb-O bond. Surface morphology and topography of the PbO:PS nanocomposite thin films were highlighted with the help of atomic force microscopy (AFM). Optical absorption in the UV-Visible allows to observe a band at 320 nm which is related to the presence of PbO nanocrystallites in the PS matrix. The optical gap of the nanocomposite PbO:PS was estimated to 3.46 eV. Some discrepancies with respect to the gap of polystyrene and bulk PbO are due to the nanosized crystallites of PbO. This variation of the gap is a result of the new optical behaviour of PS when it is doped with PbO nanocrystallites. The photoluminescence (PL) has showed strong emission band at 338 nm in the UV and weak bands at 411, 448, 473 and 518 nm in the visible domain.

Keywords: PbO nanocrystals, polystyrene, nanocomposite, Thin films, Spin-coating, XRD, AFM, Absorption UV-Visible, Photoluminescence, Raman and infrared spectroscopy.

1. INTRODUCTION

Nowadays, nanocomposites are present in the most part of industrial sectors. They offer new technology and business opportunities and in addition they are environmentally friendly. As grain dimensions of phases in the nanocomposite reach the nanometer level, interactions at phase interfaces become preponderant, and this is an important factor to enhance materials properties. Nanocomposites manufacturing must address the challenges related to chemical composition and to grain size of phases which are directly responsible of optical, electrical, thermal and mechanical properties of materials [1] In this work we fabricate lead(II)-polystyrene (PbO:PS) nanocomposite in order to study its structural features and especially highlight its optical characteristics. In the literature, few studies are devoted to PbO:polymer nanocomposites and particularly to their optical properties. PbO and PS have large optical gap whose values are 3.81 eV for direct band gap of PbO nanoparticles [2] and 4.2 eV for PS [3] respectively. Both are optically active in the UV range, which can promote the absorption and the luminescence of the hybrid nanocomposite PbO:PS. To realize this study, PbO:Polystyrene thin film nanocomposites were deposited onto glass substrate using a colloidal solution. Structural and optical properties were investigated by X-ray diffraction, AFM microscopy, FT-IR and Raman spectroscopy, UV-Visible absorption and photoluminescence.

2. EXPERIMENTAL

2.1. PREPARATION OF SAMPLES

The polystyrene, with chemical formula ($CH2=CH-C6H5$), is insoluble in water but soluble in many organic solvents such as toluene, tetrahydrofuran (THF), acetone, benzene and particularly in chloroform. In our work we used chloroform to dissolve the polystyrene and get a colloidal solution (1mg/mL). To accelerate the dissolution and improve the homogenization, this first solution is heated to 50°C and stirred for 1 hour. On the other hand, a certain amount of PbO nanoparticles (50 mg) is introduced into chloroform solvent (10 mL). This second solution is stirred for 30 minutes to ensure a homogeneous dispersion and to avoid the agglomeration of PbO nanoparticles. After standing for 5 mn, we suck up only the solution near the free surface which contains in suspension the lightweight particles of PbO and to obtain the composite PbO:PS we add it to the first solution then the mixture is stirred for 30 mn. Mass proportions of the polystyrene and PbO nanoparticles in the solvent are chosen so as to have unagglomerated, homogeneous and stable solution. Glass slides used as a substrate were degreased and thoroughly rinsed with distilled water before deposition of few droplets of PbO NCs doped PS solution. Thin films were deposited by spin coating technique performed under various conditions depending on the viscosity of the mixture. The rotational speed ranged from 300 to 2000 rpm in order to control the thickness. The deposition principle is based on homogeneous spreading using appropriate conditions. All experiments were performed at ambient pressure and room temperature.

2.2. CHARACTERIZATION TECHNIQUES

The structural characterization of the as deposited thin films of PbO:PS nanocomposite was performed on an X'pert PRO PANalytical X-ray diffractometer using CuKα radiation (λ=1.54059 Å). The chemical analysis, by Fourier transform infrared spectroscopy, was carried out using a JASCO FT-IR 6300 spectrophotometer. Raman spectra were recorded in a back scattering configuration with a RENISHAW 1000 micro-Raman spectrometer using an excitation wavelength of 633nm (He-Ne laser) and an output of 10 mW. The surface morphology was studied by atomic force microscopy (AFM) using A100-AFM with SPM control system PROGRAM version 6.4.3. The optical properties were investigated by the UV-Visible absorption using a Shimadzu UV-3100PC Spectrophotometer and photoluminescence spectra were obtained by exciting the samples, at room temperature, with a 325 nm radiation generated by an Argon laser.

3. RESULTS AND DISCUSSIONS

3.1. X-RAY DIFFRACTION ANALYSIS

X-ray diffraction patterns of pure PS and PbO:PS nanocomposite thin films are shown in Figure 1. For the Pure PS (spectrum (a)) there are no diffraction peaks which mean it has an amorphous structure. However for the PbO:PS composite (spectrum (b)) several diffraction peaks can be observed at 2θ=32.65°, 36.49°, 38.05°, 48.54° and 65.50° which may be assigned to the diffraction lines corresponding to the (020), (120), (002), (202), and (410) planes of orthorhombic structure of ß-PbO with lattice parameters : a = 5.876 Å, b = 5.476 Å, c = 4.743 Å and space group Pbcm in agreement with data reported in JCPDS card 72-0093 of PbO orthorhombic.

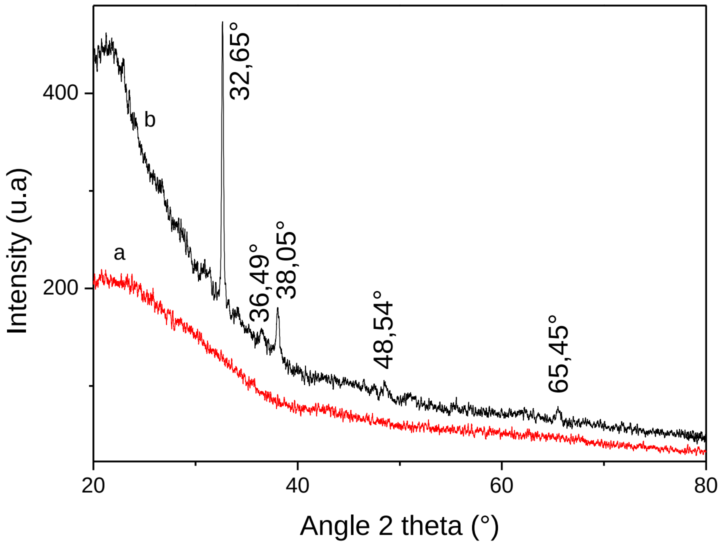

Figure 1: X-Ray spectra of (a) pure PS and (b) PbO:PS nanocomposite

These peaks confirm the incorporation of PbO crystallites in PS matrix with a random orientation and the peaks resolution reflects the good crystallinity of the PbO crystallites. All peaks belong to the PbO orthorhombic structure (no others peaks detected) which means that there was no chemical reaction between the PS matrix and PbO crystallites. Also peaks have relatively wide profiles indicating that the crystallites have a small (nanometric) size. The sizes of PbO crystallites are estimated using formula of Debye-Scherrer:

$$D = \frac{0.9\,\lambda}{\beta\cos\theta}$$

Where ‘λ’ is wavelength of X-Ray (0.15406 nm), ‘β’ is FWHM (full width at half maximum), ‘θ’ is the diffraction angle and ‘D’ is the size of particles. The average crystallite size is found in the range 28.21 nm (Table. 1).

Diffraction angle (θ) (˚2Th)		Planes (hkl)	FWHM (˚2 Th)	Size (nm)
Observed	JCPDS 72-0093			
32 .65	32.68	(020)	0.18	47.19
36.49	36.16	(120)	0.33	26.01
38.05	37.91	(002)	0.31	27.81
48.54	49.34	(202)	0.46	19.44
65.50	65.76	(410)	0.47	20.62

Table 1: Nanometric sizes of PbO nanocrystals embedded in PS matrix

3.2. AFM ANALYSIS

For more information on the structural properties of PbO:PS nanocomposite thin films we have analysed the topography of their surface and distribution of PbO nanoparticles. The AFM technique is applied to investigate the surface profiles of the films. Figures 2a and 2b show respectively three-dimensional (3D) and two-dimensional (2D) topographical images of PbO:PS nanocomposite. Aggregates of PbO particles are clearly visible on the surface of films and are spread uniformly. These aggregates form grains of PbO with different dimensions. The nanoparticle size of PbO, leads to a high surface energy which promotes their coalescence. Line profile (Figure 2c) obtained by Gwyddion-2.39.win32.exe software reveals that the approximate size of PbO particles is around 25 nm, which is in good agreement with results of X-ray diffraction. AFM reveals the granular nature and agglomeration of particles which are observed from the 3D micrographs. The surface roughness of PbO:PS nanocomposite thin film was estimated to 1.8 nm. The micrographs show that the surface morphologies and surface roughness of the films are strongly dependent on the crystallite size variations.

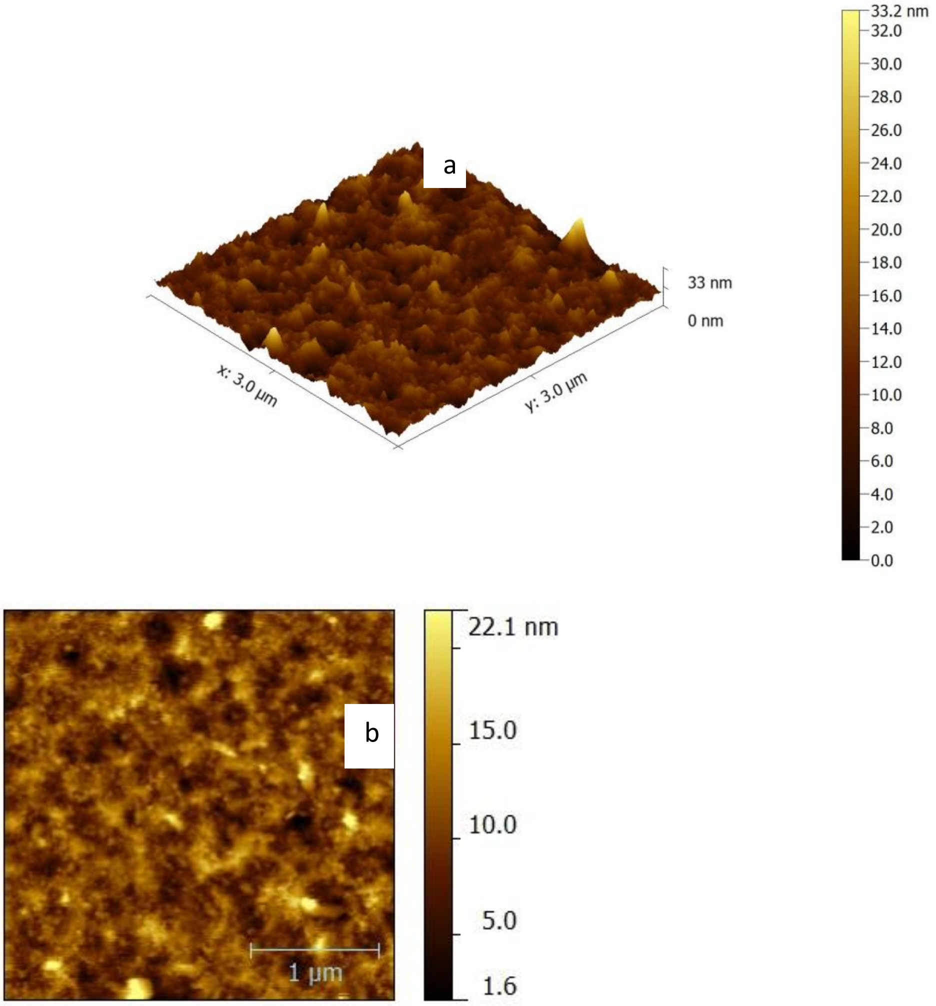

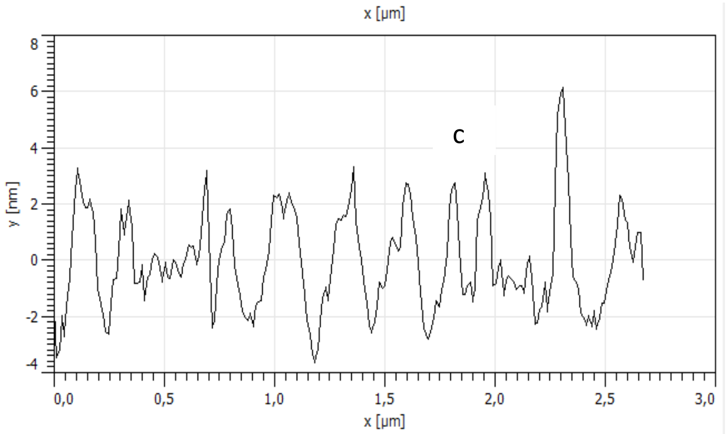

Figure 2: AFM images (3 µm x 3 µm) of as prepared PbO:PS nanocomposite thin film (a) 3D, (b) 2D, and (c) line profile of PbO. From (a) and (b), it is confirmed that PbO nanoparticles are uniformly distributed on polymer host. In addition, line profile (c) reveals that the size of PbO is around 25 nm.

3.3. RAMAN ANALYSIS

Figure 3 shows the Raman spectrum of the PbO:PS nanocomposite. It displays one intense band at 145 cm^{-1} and three weak bands at 290, 342 and 387 cm^{-1}. The frequencies of the PbO vibration modes determined from DFT calculations are listed in Table 2 [4] and are in a good agreement with those observed in the Raman spectrum of the fabricated nanocomposite PbO:PS.

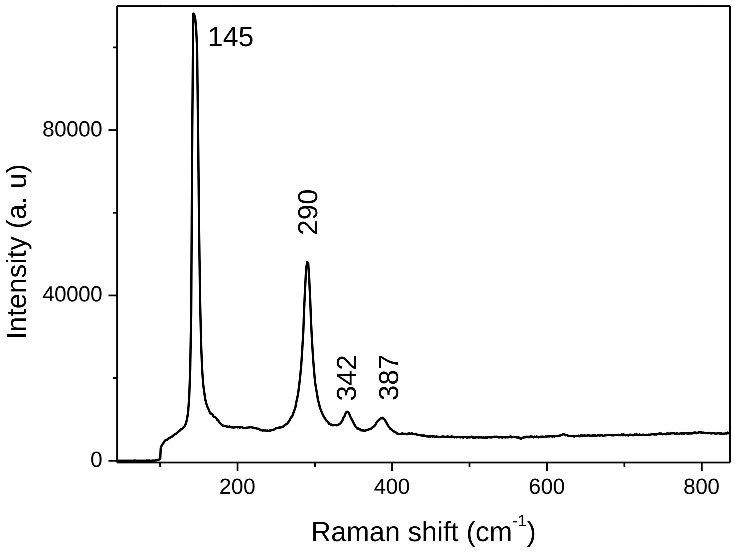

Figure 3: Raman spectrum of PbO:PS nanocomposite

Modes assignment	Theoretically predicted frequencies (cm^{-1}) [5]	Experimental frequencies (cm^{-1}) [6]	PbO:PS nanocomposite (cm^{-1})
Ag	390-255-167-89	384.5-250-171-87.5	387
B1g	345-288-147-71-57	289.5-143-71.5-52.5	342-290-145
B2g	217-91	217-91	

Table 2: Compared frequencies of vibration modes of PbO

3.4. FT-IR ANALYSIS

Fourier Transform Infrared spectroscopy is a technique for the chemical analysis. It is based on the measurement of the vibrational frequencies of bonds in molecules. The FT-IR spectrum of PbO:PS nanocomposite thin film, in low frequencies, is shown in Figure 4. One can observe peaks at 570, 639, 667 and 848 cm^{-1}. They are associated with vibrations of Pb-O bond as reported earlier by A. V. Borhade et al [7] And S. Gnanam et al [8]. This result, once again, confirms the incorporation of PbO crystallites in the PS host matrix.

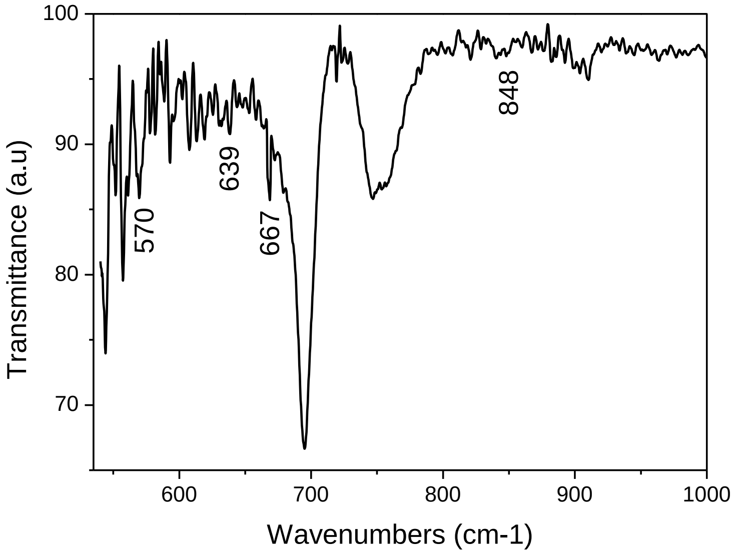

Figure 4: FT-IR spectrum of PbO:PS nanocomposite

3.5. OPTICAL ABSORPTION ANALYSIS

The absorption spectra of the PS polymer and of the PbO:PS nanocomposite films are compared in Figure 5. Optical absorption measurements were performed at room temperature in the range wavelengths going from 280 nm to 600 nm. In this range the Polystyrene matrix is optically transparent. For the pure PS films we observe a very low absorption between 325 and 425 nm which may be due to intrinsic defects, but for the nanocomposite PbO:PS an appreciable absorption band is observed in the range 300-450 nm with a maximum at 320 nm. Absorption is enhanced by the presence of the nanoparticles PbO. Similar results were found by B. Karthikeyana et al [9] for ZnO oxide incorporated in the PVA polymer. The energy band gap of PbO:PS nanocomposite, determined by using the method of the second derivative of absorbance [10] is of 3.46 eV (Figure 6). It is larger than the value of 2.7 eV for bulk PbO [11] and it reveals a blue-shift of fundamental absorption edge to shorter wavelengths due to quantum confinement effect. The band gap increases when particle size decreases toward nanometric scale. The large band gap found (3.46 eV) confirms the nanometric size of PbO crystallites as estimated earlier by X-ray analysis.

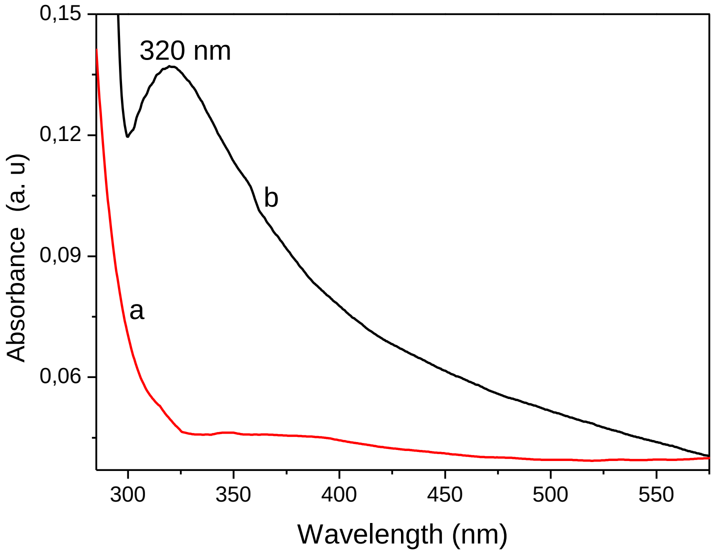

Figure 5: UV-Visible absorption of (a) pure PS and (b) PbO:PS nanocomposite

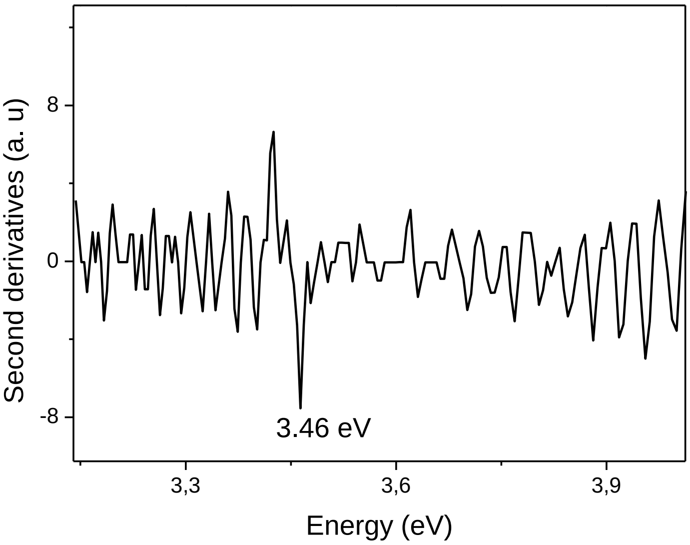

Figure 6: Optical gap of PbO:PS nanocomposite

3.6. PHOTOLUMINESCENSE ANALYSIS

The photoluminescence spectra of as prepared thin films of pure PS and PbO:PS nanocomposite are shown in figure 7. The photoluminescence measurements are performed at room temperature and under excitation wavelength of 325 nm (3.81 ev) which is lower than band gap energy of PS. The PL spectrum of pure PS shows very weak luminescence whereas PL spectrum of PbO:PS nanocomposite exhibits UV strong emission peak at 338 nm and visible emission peaks at 411, 448, 473, 518 and 530 nm. The strong emission band around 338 nm is due to the exchange of excitonic recombination of electrons [12]. The blue emission is usually related to the transition of electrons from the conduction band edge to holes, trapped at different deeps, of interstitial Pb^{2+} sites [13]. Also blue emission could be attributed to recombination of electrons in the conduction band with deep doubly ionized oxygen vacancies [14]. For the nanoparticles, the surface defect levels depend on the method of synthesis and of the interactions with host matrix. The band observed at 473 nm relates to surface defects [12]. The oxygen vacancies may be neutral, singly ionized or doubly ionized [15].The green emission at 518 and 530 nm from the PbO:PS nanocomposite could be ascribed to the single ionized oxygen vacancy in PbO nanoparticles [12]. The PbO nanoparticles, in combination with PS, can bring about functionalities suitable for the realization of efficient optoelectronic devices.

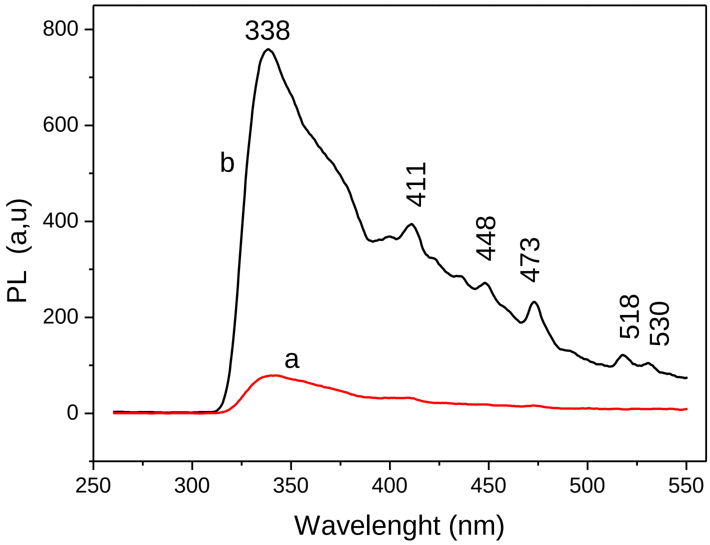

Figure 7: PL spectra of (a) pure PS and (b) PbO:PS nanocomposite

4. CONCLUSION

A simple method was used to fabricate PbO:PS nanocomposite thin films, which is based on spin coating of colloidal solution of polystyrene in which were dispersed PbO nanocrystallites. It was found from X-ray investigation that PS host matrix is in amorphous state and the filler particles are of orthorhombic phase of PbO with an average nanometric size in the range 19.44 to 47.19 nm. The Raman and FT-IR spectroscopic analysises confirm the incorporation of PbO particles in PS matrix. The wide UV-Visible absorption band centered at 320 nm indicates a relatively important size dispersion of PbO nanoparticles. The enrgy band gap of PbO:PS nanocomposite was estimated at 3.46 ev. The incorporation of PbO nanoparticles in the PS matrix increases the absorption of UV-visible wavelengths and promotes the photoluminescence intensity of the nanocomposite PbO:PS. The emission bands observed in the visible range are due to electronic transitions toward defects of different energy levels.

REFERENCES

[1] Camargo P.H.C., Satyanarayana K.G. and Wypych F, 2009, Nanocomposites: synthesis, structure, properties and new application opportunities ; Materials Research, Vol. 12, No. 1, pp 1-39.

[2] Mythili N. and Arulmozhi K.T., 2014 , A comparative study on the structural and optical properties of PbO and Zn doped PbO nanocrystals, Journal of Materials Science: Materials in Electronics, Volume 25, Issue 9, pp 3984-3989.

[3] Tariq J. A., 2010, Refractive Index Dispersion and Optical Properties of Dye Doped Polystyrene Films, Malaysian Polymer Journal, Vol. 5, No. 2, pp 204-213.

[4] Cortez-Valadez M., Vargas-Ortiz A., Rojas-Blanco L. et al, 2013, Additional active Raman modes in α-PbO nanoplates, Physica E: Low-dimensional Systems and Nanostructures, Volume 53, pp 146-149.

[5] Vigouroux J.P., Calvarin G. and Husson E., 1982, Etude vibrationnelle des oxydes PbO α et PbO β: Interpretation en relation avec la dilatation thermique, Journal of Solid State Chemistry, Volume 45, Issue 3, pp 343-352.

[6]: Baleva M. and Tuncheva V., 1994, Optical Characterization of Lead Monoxide Films Grown by Laser-Assisted Deposition, Journal of Solid State Chemistry, Volume 110, Issue 1, pp 36-42.

[7] Borhade A., Uphade B. and Tope D., 2013, PbO as an efficient and reusable catalyst for one-pot synthesis of tetrahydro benzo pyrans and benzylidene malonitriles, J. Chem. Sci. Vol. 125, No. 3, pp. 583–589.

[8] Gnanam S. and Rajendran V., 2011, Optical properties of capping agents mediated lead oxide nanoparticles via facile hydrothermal process, International Journal of Nanomaterials and Biostructures 1 (2) pp 12-16.

[9] Karthikeyana B. , Pandiyarajanb T. and Mangalarajab R.V., 2016 , Enhanced blue light emission in transparent ZnO:PVA nanocomposite free standing polymer films, Spectrochimica Acta Part A: Molecular and Biomolecular Spectroscopy, Volume 152, 5 , pp 485–490.

[10] Othmani A., Plenet J.C., Berstein E. et al, 1994, Nanocrystals of Cds dispersed in a sol-gel silica glass: Optical properties, J. Cryst. Growth 144, pp 141-149.

[11] Kowshik M., Vogel W., Urban J. et al, 2002, Microbial Synthesis of Semiconductor PbS Nanocrystallites, Advanced Materials, Volume 14, Issue 11, pp 815–818.

[12] Mythili N. and Arulmozhi K.T., 2014, Characterization Studies on the Chemically Synthesized α and β Phase PbO Nanoparticles, International Journal of Scientific & Engineering Research, Volume 5, Issue 1, pp 412-416]

[13} Liu X, Wu X, Cao H et al, 2004, Growth mechanism and properties of ZnO nanorods synthesized by plasma-enhanced chemical vapor deposition, J. Appl. Phys. 95, pp 3141-3147.

[14] Aliakbari A, Najafi E, Amini M.M. et al,2014, Structure and photoluminescence properties of lead(II) oxide nanoparticles synthesized from a new lead(II) coordination polymer, Monatshefte fuer Chemie, 145 (8) pp 1277-1285.

[15] Gong Y., Andelman T., Neumark G.F. et al, 2007, Origin of defect-related green emission from ZnO nanoparticles: effect of surface modification, Nanoscale Res. Lett., 2, pp 297–302.

PHYTOCHIMICAL STUDY AND ANTIOXIDANTS ACTIVITY OF PLANTAGO ALBICANS L.

BRAHIM HARKATI, ALI KALLA, MERZOUG BENAHMED, HOCINE LAOUER, SALAH AKKAL

harkatib@yahoo.fr

BRAHIM HARKATI Laboratoire des molécules actives et applications, Université Larbi Tebessi-Tébessa, Route de Constantine 12000 Tébessa, Algérie. MERZOUG BENAHMED Laboratoire des molécules actives et applications, Université Larbi Tebessi-Tébessa, Route de Constantine 12000 Tébessa, Algérie, ALI KALLA Laboratoire des molécules actives et applications, Université Larbi Tebessi-Tébessa, Route de Constantine 12000 Tébessa, Algérie. HOCINE LAOUER Laboratoire de Valorisation des Ressources Naturelles Biologiques, Département de Biologie, Université Ferhat Abbas de Sétif, Algérie. SALAH AKKAL Laboratoire de Phytochimie et Analyses physicochimiques et Biologiques, Université Mentouri Constantine, Route d'Ain el Bey, 25000 Constantine, Algérie.

Abstract
The aerial parts of Plantago albicans L (Asteraceae) are used in folk medicine for blood clotting in case the surgeon when diabetic in Eastern Algeria. In this study, we report the phytochemical studies using standard methods of analysis and these investigations revealed the presence of two triterpenoids: Lupeol acetate, 3-O-acetyl pseudotaraxasterol and one flavonoid named 5, 7, 4'-Trihydroxy 3',6-dimethoxy flavones. Their structures were determined using spectroscopic methods 2D NMR, ESI-MS and UV, chemical transformation and comparison with the related known compounds. The antioxidant activities of extracts non-polar and polar were also investigated.

Keywords: Plantago albicans L.; triterpenoid; flavonoid; NMR; activities antioxidants.

1. Introduction

The family of Plantaginaceae usually includes three genus of very different importance: Plantago (over 260 ssp) Littorella (3 ssp) and Bougeria (1 sp). The genus Plantago is divided into two sub-genres: subg. Plantago with alternate leaves and subg. Psyllium with opposite leaves (Lewalle, 1978 p 69-74). The Plantago L. is a genus of annual, perennial herbs and with a worldwide distribution (Pilger et al, 1937 p 269). it is high medicinal value (Brigges, 1977 p 181-1-35). With an aim of better knowing the secondary metabolism of the genus of Plantago albicans L and of discovering natural compounds. TLC analyses followed by chemical detection, together with VLC, and CC experiments, showed the presence of two triterpenoid in extract non-polar and flavonoid in the methanol extract. This procedure led to the isolation of 3 natural products, which were then characterized by spectroscopic means (^{1}H-NMR, ^{13}C-NMR, DEPT, HMBC, HSQC, COSY, ESI-MS and UV). The extracts non-polar and polar were submitted to chemical and biological screening.

2. Extraction and isolation

The aerial parts of Plantago albicans L (1030 g) of were macerated with CH_2Cl_2 three times for 24 h at room temperature and CH_2Cl_2 extract was evaporated under reduced (diminished) pressure. The filtrate was then evaporated to yield 21.7 g of the extract was obtained. The CH_2Cl_2 soluble extract (10.8 g) was then subjected to a gradient elution VLC on silica gel using the solvents Hexane: CH_2Cl_2 to give six fractions. Fraction F3 was subjected to Si gel CC and eluted with Hexane: CH_2Cl_2 to give sixteen fractions. Fraction F3.6 was subjected to Si gel CC and eluted with hexane: CH_2Cl_2 to obtain Lupeol acetate (Fig. 1) (Jamal et al, 2008 p 45–50). F5 was subjected to Si gel CC and eluted with hexane: CH_2Cl_2, to give four fractions. F5.3 is 3-O-acetyl pseudotaraxasterol (Fig. 2) (William et al, 1986 p 3349-3729). The MeOH soluble extract was subjected to column chromatography on Sephadex LH-20 eluting with MeOH, to give seven fractions. Fraction A2 was further separated by silica gel column chromatography eluting with Hexane: EtOAc to give fourteen fractions. A2.8 purified to obtain 5, 7, 4'-Trihydroxy 3', 6-dimethoxy flavones (jaceosidine) (Fig. 3) (Sang-Jun et al, 2008 p 3325-3329).

3. Structure elucidation and identification

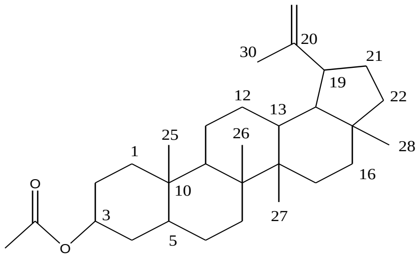

Figure 1 : Lupeol acetate

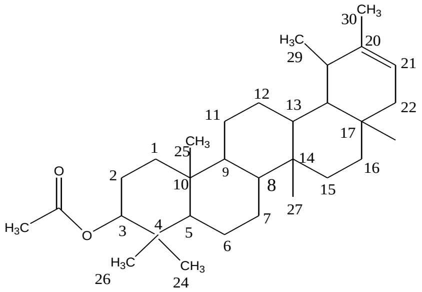

Figure 2 : 3-O-acetyl pseudotaraxasterol

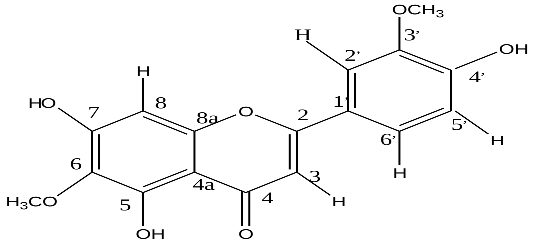

Figure 3: 5, 7, 4’-Trihydroxy 3’,6-dimethoxy flavones

Lupeol acetate was isolated as white needles (6.7 mg). ESI-MS for $C_{32}H_{52}O_2$ m/z: 468 (17.2%), 453 (2.9%), 408 (1.7%), 218 (15.2%), 43 (100 %). 1H NMR (300 MHz, $CDCl_3$): δ 4.69 (1H,s, H-29b), 4.57 (1H,s, H-29a), 4.46 (1H, m, H-3), 2.05 (3H, s, H-2′), 1.69 (3H, s, H-30), 1.04 (3H, s, H-25), 0.94 (3H, s, H-28), 0.84 (3H, s, H-23), 0.83 (3H, s, H-24), 0.83 (3H, s, H-26), 0.79 (3H, s, H-27). ^{13}C NMR 171.3 (C-1′), 151.2 (C-20), 109.6 (C-29), 81.2 (C-3), 55.6 (C-5), 50.5 (C-9), 48.5 (C-18), 48.2 (C-19), 43.2 (C-17), 43.0 (C-14), 41.1 (C-8), 40.2 (C-22), 38..6 (C-1), 38.0 (C-4), 37.3 (C-10), 36.6 (C-13), 35.8 (C-16), 34.4 (C-7), 30.0 (C-21), 28.2 (C-2′), 27.6 (C-23), 25.3 (C-15), 24.0 (C-12), 21.7 (C-2), 21.1 (C-11), 19.5 (C-30), 18.4 (C-6). 18.2 (C-28′), 16.7 (C-24), 24.4 (C-25), 16.2 (C26), 14.7 (C-27) (Sholichin et al, 1980 P 1006-1008; Chaturvedula et al, 2012 P 23-27).

3-O-acetyl pseudotaraxasterol was isolated as colorless needles (5.2 mg): ESI-MS for $C_{32}H_{52}O_2$ m/z: 468 (22), 408 (15), 249 (18), 204(20), 189 (100). 1H NMR (300 MHz, $CDCl_3$): 4.46 (1H, m, H-3), δ 4.58 (1H, t, J = 3.59 , H-20), 2.05 (3H, m, H-2′), 1.69 (3H, s, H-30), 0.84 (3H, s, H-24), 0.84 (3H, s, H-26), 1.04 (3H, s, H-25), 1.04 (3H, s, H-27), 0.95 (3H, s, H-28), 0.95 (3H, s, H-29). ^{13}C NMR : 171.0 (C-1′), 139.87 (C-20), 118.88 (C-21), 80.66 (C-3), 55.39 (C-5), 50.33 (C-9), 48.69 (C-18), 44.05 (C-22), 42.34 (C-14), 41.09 (C-8), 39.21 (C-13), 38.42 (C-1),*37.03* (C-10), 36.70 (C-16/C-19), 34.39 (C-7/C-17), 27.99 (C-23), 27.61 (C-2/C-12), 27.03 (C-15), 22.52 (C-29), 22.42 (C-30), 21.64 (C-11), 18.20 (C-6), 17.71 (C-28), 16.61 (C-25), 16.35 (C-24), 16.05 (C-26), 14.72 (C-27) (William et al, 1986 p 3349-3729 ; Viviane et al, 2011 p 615-621).

5, 7, 4’-Trihydroxy 3’, 6-dimethoxy: (5.3 mg). ESI-MS for $C_{17}H_{14}O_7$ m/z: 330 (100) $[M]^+$, 329 (8) $[M-H]^+$, 315 (63) $[M-Me]^+$, 167 (19) [A-15], 148 (8) $[B_1]$, 151 (8) $[B_2]$. ^{1}H NMR ($CDCl_3$) δ 7.46 (dd, J=8.4 , 2,1, H-6′), 7,34 (d, J=2.1, H-2′), 6.97(d, J=8.3, H-5′), 6.56 (s, H-3), 6.54 (s, 6.54, H-8), 3.98 (s, 6-OCH_3), 3.94 (s, 3′-OCH_3). ^{13}C NMR 183,8 (C-4), 165,5 (C-2), 123,8 (C-1′), 148,5 (C-4′), 158,5 (C-7), 95.5 (C-8), 151,3 (C-3′), 132,3 (C-6), 121,0 (C-6′), 112,9 (C-2′), 104,5 (C-4a). 154,5 (C-8a), 104,2 (C-3), 153,6 (C-5), 116,5 (C-5′), 62,0 (C-6), 56,7 (C-6) (Husni et al, 1983 p 299-314).

4. Antioxidant activities

The antioxidant activity was investigated with the 2,2-diphenyl-1-picrylhydrazyl (DPPH) radical scavenging method using Blois method modified by Brand-Williams et al. (Brand, 1995p 25-30).and Molyneux (Molyneux, 2004 p 211-219).

5. Results and discussion

In this study, the parts of Plantago albicans L. were extracted and, fractionated, and a total of three compounds were obtained. These compounds were identified by spectroscopic methods, such as 2D NMR, and ESI-MS and UV, and by comparison with the literature values (Fig. 1-3). All the compounds were isolated from this plant for the first time.

The methanol extract showed significant antioxidant activity compared to the reference antioxidant trolox and the TEAC value found in our study (TEAC = 1.35). Non-polar extract showed no measurable antioxidant activities when assayed with the method (DPPH).

6. REFERENCES

Brand-Williams, W., Cuvelier, M.E., and Berset, C., 1995. Use of a free radical method to evaluate antioxidant activity, Lebensm. Wiss. Technol. p 25-30.

Brigges, B.G., Carolin, R.C., and Pulley, J.M., 1977, Flora of new South Wells. Plantaginaceae p 181-1-35.

Chaturvedula, Venkata. S., and Indra P., 2012. Isolation and Structural Characterization of Lupane Triterpenes from Polypodium Vulgare. Research Journal of Pharmaceutical Sciences p 23-27.

Husni, A. A., Twaij, H. A. A., Kery, A., and Niran. K. Al-Khazraji, N. K., 1983. Some pharmacological, toxicological and phytochemical investigations on Centaurea phyllocephala. Journal of Ethnopharmacology p 299-314.

Jamal, A.K., Yaacob, W.A., and Laily B. Din., 2008. A Chemical Study on Phyllanthus reticulates. Journal of Physical Science p 45–50.

LEWALLE, J., 1978. Bulletin de l'Institut Scientifique p 69-74

Molyneux, P., 2004. The use of the stable free radical diphenylpicrylhydrazyl (DPPH) for estimating antioxidant activity, Songklanakarin J. Sci. Techn p 211-219.

Pilger, R., 1937. Plantaginaceae. In: Engler A. (ed.) Das Pflanzenreich IV 269 (102). Wilhelm Engel-mann, Leipzig.

Sabrin, R.M., Gamal, A. M., Lamiaa. A. S., Laetitia, M. Y., Gwendoline V. G., Robert. K, and Diaa T.A., 2012. New ursane-type triterpenes from the root bark of Calotropis procera. Phytochemistry Letters p 490–495.

Sang-Jun, L., Ha-Yull, C., Camelia, G. A., Angela, R. W., Richard, A. D., and Tom, J. M., 1998. Estrogenic Flavonoids from Artemisia vulgaris L. J. Agric. Food Chem p 3325-3329.

Sholichin. M., Yamasaki, K., Kasai, R., and Tanaka. O., 1980. 13C Nuclear magnetic ressonance of lupane-type triterpenes 1980. Lupeol, betulinic acid. Chem Pharm Bull p 1006-1008.

Viviane, G.C., Jacqueline, A., Lucienir. P., Dorila. P. V., Policarpo, A.S., Rosana O, Alves A. J, and Antônia F.C. 2011. Evaluation of the bactericidal and trypanocidal activities of triterpenes isolated from the leaves, stems, and flowers of Lychnophora pinaster. Brazilian of Journal pharmzcognosy p 615-621.

William, F. Reynolds, Stewart. Mc L., Janusz.P,, Raul. G., Enriquez, L. E., and Ismael, L., 1986. Total assignment of ^{13}C and ^{1}H spectra of three isomeric triterpenol derivatives by 2D NMR: an investigation of the potential utility of 1H chemical shifts in structural investigations of complex natural products. Tetrahedron p 3349-3729.

JUNIPERUS SABINA L. OF ALGERIA: CHEMICAL COMPOSITION AND ANTIBACTERIAL ACTIVITY OF THE AERIAL PARTS ESSENTIAL OILS

ABDENOUR ADJOUAD, HOCINE LAOUER, ROBERT P. ADAMS, SALAH AKKAL

Abstract

The essential oil composition of Juniperus sabina L. (Cupressaceae), collected from Djurdjura Mountain (Algeria) was studied. The aerial parts (twigs and leaves) essential oils were analyzed by means of gas chromatography and gas chromatography-mass spectrometry. Two main components were identified. Oil from twigs and leaves contained mainly sabinene (53.7%), while the essential oil from the one individual same organ is rich in sabinene (34.2%) and terpinen-4-ol (19.6%). All the oils tested in the disc-diffusion method showed antibacterial activity in dilution of ½ (v/v). K. pneumoniae E47 Resistant to quinolones is the best sensitive bacteria among the tested micro-organism. The oil showed the lowest MIC (0.03%) against S. thyphimurium NCCB1808 and S. aureus resistant to penicillin ATCC25923. P. aeruginosa ATCC27853 did not show MIC in range of essential oil concentration studied. E. coli ATCC25922, S. aureus ATCC 25923, S. aureus resistant to penicillin ATCC25923, pneumoniae E47 resistant to quinolones, K. pneumoniae E47 resistant to quinolones, B. subtilis NCCB1090 and E. coli NCCB1 are very similar, with a MIC of 0.12%.

MICROPOROUS SYNTHETIC CO-SILICALITE-1 FROM LUDOX SILICA PREPARED BY A HYDROTHERMAL PROCESS AS A CATALYST FOR OXIDATION OF CONGO RED

IMÈN BENCHIKH, FATIHA DJAFRI, AYADA DJFRI , FRANCK LAUNAY

Imèn BENCHIKH [1], Fatiha DJAFRI [1], Ayada DJFRI[2] , Franck LAUNAY [3]
[1] Laboratoire de Chimie des Matériaux LCM, Université d'Oran 1, Algérie
[2] Laboratoire de Synthèse Organique Appliquée LSOA, Université d'Oran 1, Algérie
[3] Sorbonne Universités, UPMC-Paris 06, UMR 7197, Laboratoire de Réactivité de Surface, site Le Raphael, Bat. A/B, 3 rue Galilée, 94200 Ivry-sur-Seine, France
Corresponding author. E-mail: benchikh_imene @yahoo.fr.Tel :00213658337844

Abstract

The choice of zeolite is the economic and ecological factor for they are regular alterative and applied in the environment (1). The presence of dyes in textile discharge causes damage to the environment because they are toxic even at low concentrations. Our main objective is developed an inexpensive and effective oxidation process to bleach effluents from the textile industry. To achieve this goal, we used the H_2O_2 as oxidant (2) and Co-silicalite-1 MFI type microporous material as a catalyst. . CoS-1 with Co / Si = 1 (XRF) is prepared by a hydrothermal method and characterized by X-ray diffraction (XRD) confirmed the silicalite crystalline phase. Fourier transform infrared (FTIR) analysis showed a band at 995 cm^{-1} probablement due to Si-0-Co links, in addition to other bands characteristic of the MFI structure. The results obtained when processing aqueous solutions. At room temperature without and with catalysts and as model molecule organic azo dye Congo red dyes for an initial concentration of $2.2\ 10^{-5}$ M dye, Reaction parameters such as pH, time and the type catalysts influence the effectiveness of the color and the volume O_2 rain.

Keywords: Co-Silicalite-1, MFI, catalysis, oxidation, organic dye.

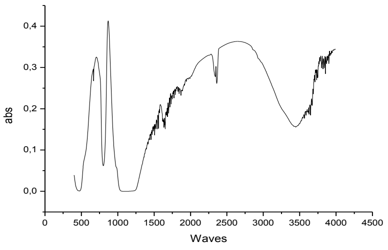

IR spectrum (transmission) of CoS-1.

Reference:

1. "New Solid Acids and Bases. Tanabe K, Misono M, Ono Y, Hattori H. 1989, Stud.Sur.Sci Catal,58.c .
2. M Muruganandham, M Swaminathan. Photochemical oxidation of reactive azo dyes with UV-H2O2 process, Dyes and pigments. 2004, pp. 269-275.

EFFECT OF CONSTRUCTION, METEOROLOGICAL AND OPERATIONAL PARAMETERS ON THE FRESH WATER YIELD OF A CONDENSATION CHAMBER OF A MODULAR SOLAR STILL

RABAH KERFAH, NOURA BELKHEIR, ZAARAOUI ABDEL KADER, EL GHALIA FILALI

RABAH KERFAH[1], NOURA BELKHEIR[1], ZAARAOUI ABDEL KADER[1] EL GHALIA FILALI[2]
Rabah Kerfah, Doctor, FIMA Laboratory, University of Khemis Miliana, Algeria, Noura Belkheir, Doctor, FIMA Laboratory, University of Khemis Miliana, Algeria, Zaaraoui Abdel kader, Doctor, FIMA Laboratory, University of Khemis Miliana, Algeria, El Ghalia Filali, Advanced Mechanics Laboratory, U.S.T.H.B. Algiers, Algeria.

[1]rkerfah@yahoo.fr

Abstract.

In this paper, we present the effect of different parameters construction (height and width of the condensation chamber), meteorological (relative humidity) and operational (cooling water flow rate) on the fresh water production of an condensation chamber of a modular solar distillation system working in natural convection mode. This still is comprised of two modules. The fist is a streaming plan solar collector and the second is a condensing chamber. Equations governing the heat and mass exchange are established using the nodal method. Results show that increasing different parameters leads to a great fresh water yield, in one hand. On the other hand, there are a cooling water flow rate and a fist compartment height value for from which any increases leads to a weak augmentation to the fresh water yield.1. Introduction

Desalination is one of many processes available for water purification, and sunlight is one of several forms of energy that can be used to power the process. Although of simple design, the basin solar still gives a low daily production. So many techniques have been used to improve the performance of such still. For instance, by coupling the basin solar still with a flat plate [0], parabolic concentrator collector [0], vertical flat plate reflector 0, the reuse of the latent heat of condensation 0 and increased condensing surface by fins 0. It is the same for the evaporation surface, which is modified for example with the addition of sponge cubes and fins on the bottom of the basin [**Hata! Bilinmeyen anahtar değişkeni.**,0]. The addition of stones, coal, red brick pieces, iron pieces and sand in brackish water can store energy in sensible heat form 0.

The separation of the evaporation chamber from the condensation leads to a higher temperature difference between the glass cover and the brackish water. A decrease in pressure of water vapors compared to that of a conventional still results. The absence of condensate on the cover increases the solar radiation absorbed by the bottom of the still, thus generating an increase in the distilled water amount [0,0,0,0].

This article is concerned with a numerical study of a condenser chamber of a modular solar still composed of a streaming solar collector and a condensation chamber.

2. Description of the condensing chamber

The condensing chamber is a vertical channel of rectangular section composed of three compartments. In the first, the water vapour, which is generated by the evaporation of water film in the solar streaming collector, condenses on a plane wall cooled from the outside by forced water flow. This forced flow circulates in a channel (1 mx1 mx2.5 cm) insulated from the ambient medium by a layer of glass wool (2 cm thick). To reject the non-condensed water vapour to the atmosphere, the device contains above the condensing chamber, a compartment comparable to a solar air heater, composed of an glass cover (2.3 mx1 mx4 mm), a sheet steel galvanized (2.3 mx1 mx0.4 mm) painted in black and insulated by a layer of glass wool (2cm thick). The third compartment which appeared as a channel. It is used to increase the chimney effect.

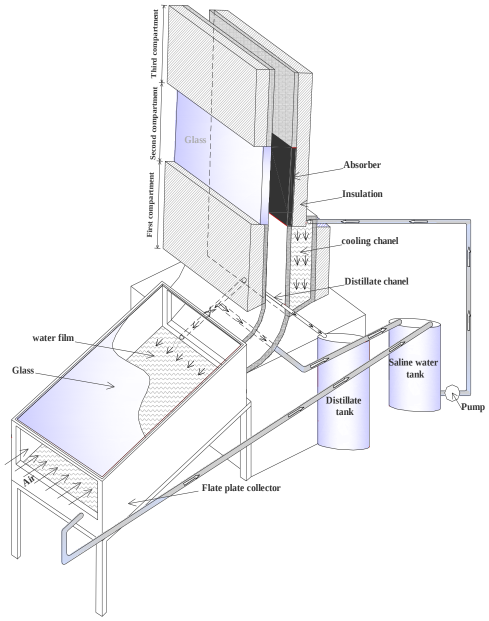

Figure 5: schematic view of still

3. Thermal analysis

3.1. Simplifying assumption

Transfers are one-dimensional.
Air is perfectly transparent to solar radiation.
Materials are assimilated to grey bodies.
Sky is assimilated to a black body.
The ground temperature is equal to the ambient temperature.
The effect of the condensing chamber’s shadow on the collector is neglected.

3.2. Transfer Equations

The condenser chamber of the still is divided to perpendicular fictive parts in the flow’s direction. Based on the electrical analogy 0, a heat balance is established in each part, in order to describe the transfer equations.
By considering each part as an independent entity, it is possible to describe the evolution of thermal transfer in the still. The instantaneous energy variation in a part (i) of the still is equal to the algebraic sum of the exchanged flow densities inside each part:

$$\frac{M_i Cp_i}{S}\cdot\frac{\partial T_i}{\partial t}=\phi_{soi}+\sum_{i=1}^{n}\sum_{x}\varphi_{ij}+\phi_{ch} \qquad (1)$$

Where: φ_{ij} is exchanged heat flux density by the transfer mode x (conduction, convection or radiation) between elements i and j (w/m 2).

$$\phi_{soi}=\alpha_i\varphi_i \qquad (2)$$

$$\varphi_{ch}=\overset{\bullet}{m}L_V \qquad (3)$$

The heat flux density (ϕ_{xij}) by the transfer mode x (convection, conduction and radiation) can be written as:

$$\varphi_{xij}=h_{xij}\left(T_j-T_i\right) \qquad (4)$$

Thus, Eq. 1 can be reduced to;

$$\frac{M_i Cp_i}{S}\cdot\frac{\partial T_i}{\partial t}=\phi_{soi}+\sum_{i=1}^{n}\sum_{x}h_{xij}\left(T_j-T_i\right)+\overset{\bullet}{m}L_V \qquad (5)$$

The radiation heat transfer coefficients between, on the one hand, the external surface of the cover and sky, and the other hand, the insulation and the ground, are deduced from 0. The natural convection heat transfer coefficients between the external sides of the glass, the external sides of insulators and the ambient air (h_{cvent}) are calculated from their correlations 0.

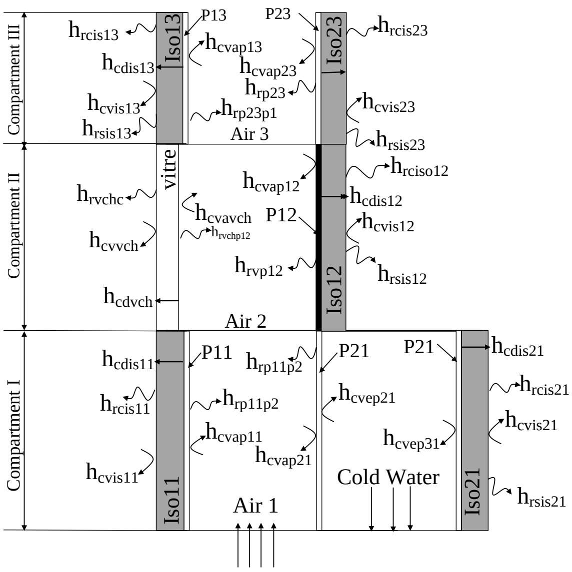

Figure: 6 a schematic view of heat and mass transfer in the condenser chamber

The coefficients of heat transfer by natural convection are computed using correlations reported in 0. The forced convection heat transfer coefficients between the cooling water and the channel walls ($h_{cvep_{21}}$, $h_{cvep_{31}}$) are deduced by the reported correlations in 0.
The mass calculation of the condensed water is obtained from 0:

$$\dot{m}_c = \frac{85.0\ (T_a - T_P)\ HR}{L_v} \qquad (6)$$

The air flow is deduced from the expression below 0:

$$Q_m = Cd\ \ A \left[g\ \ L \left(\frac{T_{asr} - T_{aen}}{T_{aen}} \right) \right]^{1/2} \qquad (7)$$

4. Numerical methodology

Transfer equations are solved using a numerical implicit finite-difference scheme method. An iterative calculation is necessary because the heat and mass transfer coefficients depend on the temperatures of the different media which are unknown. Moreover, the air flow through the still depends on the air temperature at the still outlet. It is also necessary to use an iterative method for the calculation of this flow.

5. Results and discussions

The simulation of the condensation chamber is carried out under the following condition:
Inlet cooling water temperature equal to 12°C
Inlet water vapor temperature equal to 24°C
Solar radiation equal to 600W m-2
Cooling water Flow rate equal to 0.03 m3 s-1
The effect of t he relative humidity on the fresh water yield was represented on figure 7. It shows that an increase in the relative humidity of the air at the inlet of the chamber condensation increases the amount of condensed water vapour. In fact, an air more humid includes a greater amount of water vapor which is cooled. Consequently, it gives a larger condensed fresh water yield.
figure 8 shows the effect of the width of the condensation chamber (gap between of P11 and P21). It is will be noted that the expansion of this space has a positive effect on the amount of condensed water vapor. The increase of this space enhances the section flow area in the condensation chamber. Thus, an augmentation of the vapour flow rate, which contributes to increased the fresh water yield.

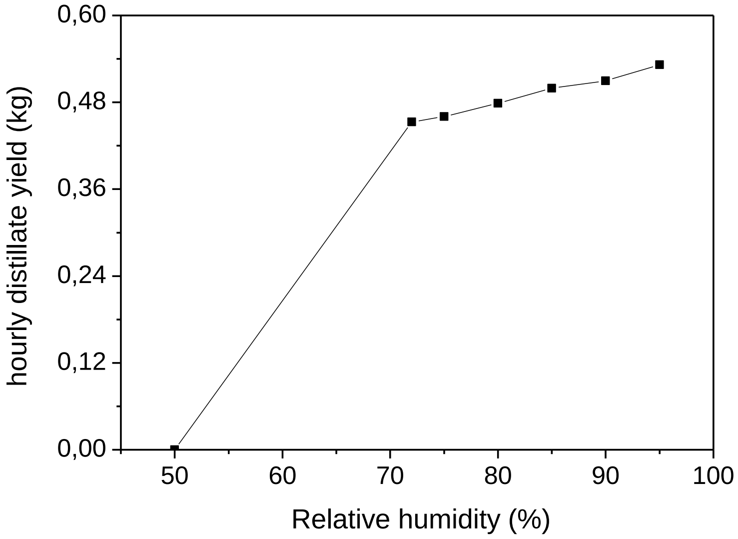

Figure 7 : Effect of the relative humidity at the inlet of the condensation chamber on the hourly distillate yield

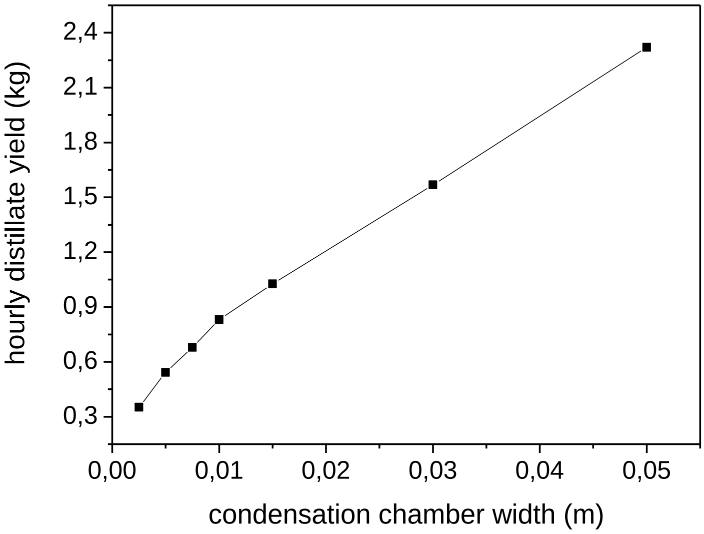

Figure 8 : Effect of the width of the condensation chamber on the hourly distillate yield

From figure 9 it can be noted that the brackish flow rate flowing along one wall of the condensing unit for which the amount of condensing vapour is maximal is about 0.0045m3 s−1. These values correspond to the optimum daily distillate.

The effect of the fist compartment of the condensation chamber height on the fresh water yield was represented on Figure 10. It noted that increasing the fist compartment height leads to rise the total height of the condensation chamber which will enhance the water vapour flow rate. Thus, the water fresh water yield increased. However, there is an optimum value (1.2 m) of the height of the first compartment from which any increases leads to a weak augmentation to the fresh water yield.

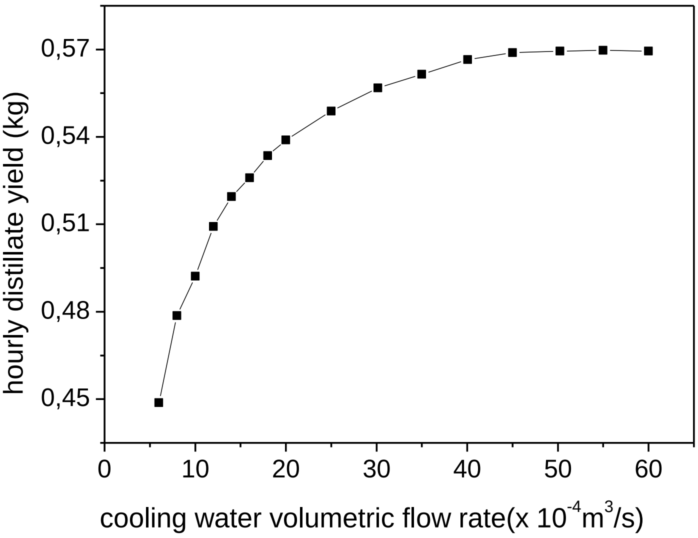

Figure 9 : effect of water volumetric flow rate on the hourly distillate yield

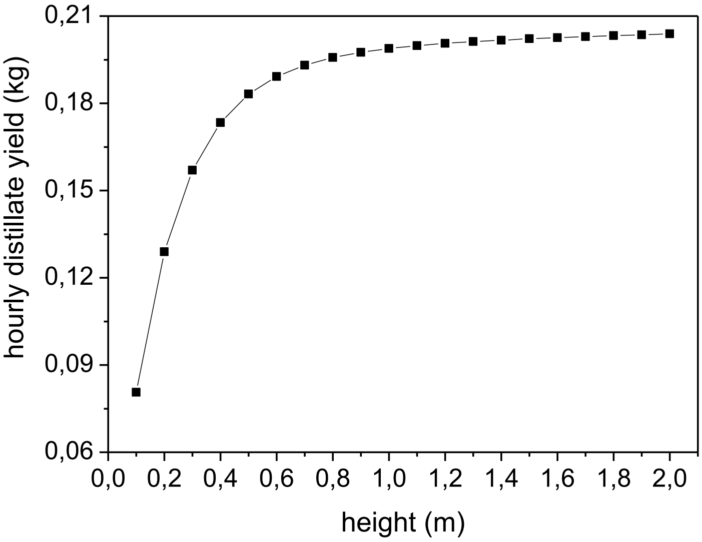

Figure 10 : Influence of fist compartment height on the hourly distillate yield

6. Conclusion

We have modeled and simulated a condenser chamber of modular still. The modeling was carried out by using the electrical analogy. Transfer equations are solved using an implicit finite-difference scheme method and "Diabolo Sablier" method. The obtained results through this research show that:

The fresh water yield increase with increasing the water flow rate, the fist compartment of the condensation chamber height, the relative humidity of the humid air at the inlet, the condensation chamber width and the cooling flow water flow rate.

There is an optimum value of the cooling flow rate and the first compartment height for from which any increases leads to a weak augmentation to the fresh water yield.

Nomenclature

A	Cross sectional area (m ^{2})	indice	
Cd	Coefficient of discharge of air channel.	a :	Water vapor
Cp :	Specific heat capacity at constant pressure (J/kg K)	amb :	ambient
g :	Gravitational constant (m/s ^{2}).	c :	condensed
h :	Coefficient of heat transfer (W/m^{2}K)	cd :	Conduction
HR :	Relative humidity (%).	ch :	chamber, change of state
L :	Still Length (m).	cv :	Convection
Lv :	Specific latent heat of vaporization (J/kg).	e :	Water
M :	Mass (kg)	ev :	Evaporated
$\dot{m}$:	Rate of mass flow (kg/s m^2)	en	inlet
P :	Pressure (Pa)	ij :	i : wall number j : level number
Pu :	Output power (W)	p :	Wall
Qm	Volumetric air flow rate (m^3/s)	r :	Radiation
T :	Temperature (K).	s :	Saturation
grec		sr	outlet
αi :	Absorptivity	soi :	Solar
ϕ:	flux density (W/m2)	v :	Glass

References

Rai, S.N.; Tiwari, G.N.: 1983. *Single basin solar still coupled with water flat collector*, Energy Conversion and Management, Vol 23, p.145-149.

Singh, S. K.; Bhatnagar: V. P.; Tiwari G. N. 1996. *Design parameters for concentrator assisted solar distillation*, Energy Conversion and Management, Vol. 37, p. 247-252.

Tanaka, H.; Nakatake, Y. 2007, *Improvement of the tilted wick solar still by using a flat plate reflector,* Desalination, Vol. 216(), p.139-146.

Al-Karaghouli, A. A.; Minasian, A. N. 1995; *Technical note a floating-wick type solar still*, Renewable Energy, Vol. 6, p.77-79.

Fath, H. E. S.; Hosny, H. M. 2002; *Thermal performance of a single-sloped basin still with an inherent built-in additional condenser*, Desalination, Vol. 142 ; p.19-27.

Abu-Hijleh, B. A/K.; Rabah, H. M. 2003. *Experimental study of a solar still with sponge cubes in* basin, Energy Conversion and Management, Vol. 44; p.1411-1418.

Velmurgan, V.; Gopalakrishnan, M.; Raghu, R., Srithar, K. 2008; *Single basin solar still with fin enhancing productivity*, Energy Conversion and management, vol.49 p. 2602-2608.

Murugavel, K. K.; Chockalingam, K.; Srithar, K. 2008; *An experimental study on single basin double slope simulation solar still with thin layer of water in the basin*, Desalination, Vol. 220 p. 687-693.

Zayouti, E.; Bouirden, L.; Aharoune, A.; Banouni, M. 2002; *Distillation Solaire: Amélioration de la Condensation de la Vapeur d'Eau dans les Distillateurs Solaires*, International Forum on Renewable Energies, Agadir, Maroc

El-Bahi, A.; Inan, D. 1999; *A solar still with minimum inclination coupled to an outside condenser*. Desalination, Vol. 123 ; p. 79-83.

El-Bahi, A.; Inan, D. 1999; *Analysis of a parallel double glass solar still with separate condenser,* Renewable Energy, Vol. 17 p. 509-521.

Tiwari, G. N.; Kupfermann, A.; Aggarwal, S. 1997; *A new design for a double-condensing chamber solar still*, Desalination, Vol. 114 ; p. 153-164.

Duffe, J. A., Beckman, W. A. 2006; *Solar engineering of thermal Processes*, edited by Jhon wily and Sons, 3rd edition, New York

Incropera, F.P., DeWitt, D.P. 2007; *Fundamentals of Heat and Mass Transfer,* , edited by Wiley, 6th edition ,New York .

Edwards, D.K., Denny, V. E., Milles, A. F. 1979; *Transfer processes an introduction to diffusion convection, and radiation*, McGraw Hill publication, 2nd edition ; p.166-168.

Aybar, H. Ş*. 2006; Mathematical modeling of an inclined solar water distillation system*, Desalination, vol.190 , p. 63-70.

Bansal, N. K., Mathur, R., Bhandari, M. S. 1993; *Solar chimney for enhanced stack ventilation*, Building and Environment, Vol. 28 ; p. 373-377.

KINETICS OF INHIBITION OF XANTHINE OXIDASE BY LYCIUM ARABICUM AND ITS PROTECTIVE EFFECT AGAINST OXONATE-INDUCED HYPERURICEMIA AND RENAL DYSFUNCTION IN MICE

NAOUEL BOUSSOUALIM, HAYAT TRABSA, IMANE KRACHE, ABDERRAHMANE BAGHIANI, SEDDIK KHENNOUF, NOUREDDINE CHAREF, LEKHMICI ARRAR

1Laboratory of Applied Biochemistry, 2Laboratory of Phytotherapy Applied to Chronic Diseases, Faculty of Nature and Life Sciences, Univ. Setif, Setif 19000, Algeria

Abstract

To evaluate the in-vitro inhibition of xanthine oxidase (purified from bovine milk) by extracts of Lycium arabicum, as well as it is in vivo hypouricemic and renal protective effects. Four extracts of Lycium arabicum, methanol (CrE), chloroform (ChE), ethyl acetate (EaE) and aqueous (AqE) extracts, were screened for their total phenolics and potential inhibitory effects on purified bovine milk xanthine oxidase (XO) activity by measuring the formation of uric acid or superoxide radical. The mode of inhibition was investigated and compared with the standard drugs, allopurinol, quercitin and catechin. To evaluate their hypouricemic effect, the extracts were administered to potassium oxonate-induced hyperuricemic mice at a dose of 50 mg/kg body weight.The results showed that EaE had the highest content of phenolic compounds and was the most potent inhibitor of uric acid formation (IC50 = 0.017 ± 0.001 mg/mL) and formation of superoxide (IC50 = 0.035 ± 0.001 mg/ml). Lineweaver-Burk analysis showed that CrE and EaE inhibited XO competitively, whereas the inhibitory activities exerted by ChE and AqE were of a mixed type. Intraperetoneal injection of L. arabicum extracts (50 mg/kg) elicited hypouricemic actions in hyperuricemic mice. Hyperuricemic mice presented a serum uric acid concentration of 4.71 ± 0.29 mg/L but this was reduced to 1.78 ± 0.11 mg/L by EaE, which was the most potent hyporuricemic extract. L. arabicum fractions have a strong inhibitory effect on xanthine oxidase and and also have a significantly lowering effect on serum and liver creatinine and urea levels in hyperuricemic mice.

Keywords: Lycium arabicum, Uric acid, Creatinine, Superoxide, Phenolic compounds, Flavonoids, Hyperuricemia

MODELING OF THE SOLUBILITY OF ANTILIPEMIC AGENTS IN SUPERCRITICAL CARBON DIOXIDE APPLICATION TO CLOFIBRIC ACID

ABDESLAM-HASSEN MENIAI, ISMAHENE HALOUI, ABIR BOULEDJOUIDJA, AHMED ZERMANE, OUASSILA LARKECHE, RANIA DJERAFI, ELISABETH BADENS

Abdeslam-Hassen Meniai, Professor, Laboratoire de l'Ingénierie des Procédés de l'Environnement, Université Constantine 3 Algeria, Ismahene Haloui, PhD student, Laboratoire de l'Ingénierie des Procédés de l'Environnement, Université Constantine Algeria, Abir Bouledjouidja, PhD student, Laboratoire M2P2, Aix-Marseille Université, France, Ahmed Zermane, Assistant Professor, Laboratoire de l'Ingénierie des Procédés de l'Environnement, Université Constantine 3 Algeria, Ouassila Larkeche, Assistant Professor, Laboratoire de l'Ingénierie des Procédés de l'Environnement, Université Constantine 3 Algeria Institution, Rania Djerafi PhD student, Laboratoire M2P2, Aix-Marseille Université, France, Elisabeth Badens Professor, Laboratoire M2P2, Aix-Marseille Université, France

Abstract

The present study is concerned with the modeling of the solubility of antilipemic agents such as clofibric acid in supercritical carbon dioxide using Peng Robinson equation of state (Pr-EOS) in combination with the van der Waals one fluid mixing rule.

The calculations were performed at three different temperatures of 308.2, 318.2 and 328.2 K with pressure varying in the range from 10 to 22 MPa. These conditions were adopted in experimental works reported in the literature, and therefore offered an opportunity for the assessment of the model reliability.

A priori the required physicochemical and critical properties of the antilipemic agent were predicted using well known methods based on the group contribution concepts.

The necessary interaction parameters k_{ij} were obtained from experimental data reported in the literature and concerning the considered compounds, by the optimization of a well defined objective function using the Nelder-Mead version of the simplex technique.

Keywords: Antilipemic agent; Clofibric acid; Solubility; Supercritical Fluid; Mixing rule; Equation of state

Introduction

A great number of various chemical processes do operate at high pressure and very often do involve liquid-vapor, liquid-liquid or solid -liquid phase equilibria, with the latter being the main interest of this study. In certain cases the operating conditions go up to the supercritical state, particularly for systems dealing with pharmaceutical compounds where in fact in the aim to make use of the fact that if compressed up to their critical conditions, supercritical fluids behave as solvents with powerful properties such as interesting combinations of liquid like density and solvency, and gas like viscosity, diffusivity, compressibility. However the main difficulty in calculating the solubilities of solid compounds in supercritical fluids is the choice of the most appropriate combination of an equation of state (EOS) and a mixing rule (MR), for the given conditions as well as the availability or not of the required interaction parameters such as k_{ij}.

In fact the solubility of materials in supercritical fluids has been extensively discussed in the literature, due to its importance and concerns a great number of various applications where CO_2 is the mostly used fluid due to its friendly behaviour towards the environment, avoiding the use of organic solvents.

The general conclusion is that the calculations or predictions of supercritical equilibria are not easy even when experimental data is available to improve the adopted equations. This has encouraged the development of new theoretical models by introducing new parameters in the model equations as confirmed in (Haselow, et al. 1986) where a number of cubic and non cubic equations of state were tested for the prediction of supercritical fluid equilibria. Also for the prediction of the solubilities of high boiling compounds in supercritical fluids, the results given by the Soave-Redlich-Kwong equation of state were slightly better that those obtained by using the perturbed hard sphere equation that incorporates Carnahan–Starling repulsive and the Soave attractive terms, confirming the importance of the choice of the most appropriate equation (Yamamoto, et al. 1987). Many studies revealed that the choice of the most appropriate mixing rule can be more important and difficult that the selection of the equation of state itself (Zhong and Masuoka, 1997) and (Lee, et al. 1989). As pointed out in (Ashour and Aly, 1996), the adopted calculation techniques can also greatly influence the accuracy of the phase equilibrium predictions.

Consequently the present study deals with the modeling of the solubility of an antilipemic agent, namely clofibric acid in supercritical carbon dioxide. This active pharmaceutical ingredient along with other compounds like Fenofibrate and Gemfibrozil are frequently recommended for concerned patients to reduce lipids in general and cholesterol and triglyceride levels in particular. They are poor water-soluble substances (Yasuji, Takeuchi and Kawashima, 2008) and therefore supercritical carbon dioxide can provide a good alternative for processes like the supercritical anti-solvent (SAS) and the rapid expansion of supercritical solution (RESS), generally used for the micronization of these active pharmaceutical ingredients (Martin and Cocero, 2008).

Thermodynamic modeling

Similarly to vapor-liquid phase equilibria, the condition for solid-liquid equilibria, assuming a pure solid phase, is expressed by the following isofugacity criterion (Reid, Prausnitz and Poling, 1978):

$$f_i^s = f_i^F \tag{1}$$

Where f_i^F is the fugacity of solute i in the fluid mixture and f_i^s is the fugacity of pure solute i at the same conditions of temperature and pressure in the solid phase and expressed as:

$$\boldsymbol{f_i^S = P y_i \varphi_i^F} \tag{2}$$

With P the pressure, y_i the solute molar fraction and $\boldsymbol{\varphi_i^F}$ the fugacity coefficient of the solute in the fluid phase.

Considering the solid phase as pure, the fugacity of solute can be expressed as (Peng and Robinson, 1976):

$$\boldsymbol{f_i^S = P_i^{sat}(T)\varphi_i^{sat} exp\left[\int_{P_i^{sat}}^{P} \frac{v_i^{sat}}{RT} dP\right]} \tag{3}$$

With $\boldsymbol{P_i^{sat}}$ the pressure and pressure at saturation, respectively, $\boldsymbol{v_i^{sat}}$the molar volume of the solute at saturation and $\boldsymbol{\varphi_i^{sat}}$ the fugacity coefficient of solute I at saturation.

Combining Eqns. 1 & 2 gives the solute mass fraction in the fluid as (Peng and Robinson, 1976):

$$\boldsymbol{y_i = \frac{P_i^{sat}(T)}{\varphi_i^F P} exp\left[\frac{v_i^S(P - P_i^{sat}(T))}{RT}\right]} \tag{4}$$

In this work, $\boldsymbol{\varphi_i^F}$ is in calculated using Peng-Robinson equation along with two different mixing rules, namely those due to van der Waals as described in the next section.

The equation of state (EOS)

The common two parameter cubic equations can be expressed in a general manner as follows (Reid, Prausnitz and Poling, 1978):

$$P = \frac{RT}{V - b} + \frac{a}{V^2 + ubV + wb^2} \tag{5}$$

For these equations u and w are integer taking values of 2 and -1, respectively, to lead to the following Peng-Robinson equation (Reid, Prausnitz and Poling, 1978) and (Peng and Robinson, 1976):

:

$$P = \frac{RT}{V - b} + \frac{a}{V(V + b) + b(V - b)} \tag{6}$$

Where a and b are the attractive and repulsive parameters, respectively, and for a pure substance they are expressed in terms of the critical properties and the acentric factor as follows:

$$\boldsymbol{b = \frac{0.07RT_c}{P_c}} \tag{7a}$$

$$\boldsymbol{a = \frac{0.45724R^2T_c^2}{P_c}\left(1 + f_\omega(1 - T_r^{\frac{1}{2}})\right)^2} \tag{7b}$$

$$\boldsymbol{f_\omega = 0.37464 + 1.542274\omega - 0.2699\omega^2} \tag{7c}$$

The van der Waal's one fluid mixing rule

Two different mixing rules were used in the present paper and they are expressed as follows (Prausnitz, Lichtenthaler and De Azevedo, 1999):

$$a_{ij} = \sum_i \sum_j (a_i a_j)^{1/2}(1-k_{ij}) \tag{8a}$$

$$b_{ij} = \frac{b_i + b_j}{2} \tag{8b}$$

$$a_m = \sum_i \sum_j y_i y_j a_{ij} \tag{8c}$$

$$b_m = \sum_i \sum_j y_i y_j b_{ij} \tag{8d}$$

Where a_i and b_j are the attractive and repulsive parameters, respectively, for pure substances, a_{ij} and b_{ij} are the corresponding unlike parameters which are calculated for Peng-Robinson of state as follows (Reid, Prausnitz and Poling, 1978):

$$\boldsymbol{b_i = \frac{0.07RT_c}{P_c}} \tag{9a}$$

$$\boldsymbol{a_i = \frac{0.45724R^2T_c^2}{P_c}\left(1 + f_\omega(1 - T_r^{\frac{1}{2}})\right)^2} \tag{9b}$$

$$\boldsymbol{f_\omega = 0.37464 + 1.542274\omega - 0.2699\omega^2} \tag{9c}$$

The fugacity coefficient

Using the explicit form of any equation of state the most adequate relation to find explicitly the fugacity coefficient is as follows (Prausnitz, Lichtenthaler and De Azevedo, 1999):

$$\ln \varphi_i^V = \frac{1}{RT}\int_V^\infty \left[\left(\frac{\partial P}{\partial n_i}\right)_{T,V,n_j} - \frac{RT}{V}\right] dV - \ln Z \tag{10}$$

Where V is the total volume of the system, n_i and n_j are the number of moles of component i and j, respectively and Z the compressibility factor.

Introducing the Peng-Robinson equation of state into Eqn.11 leads to the following expression of the fugacity coefficient (Reid, Prausnitz and Poling, 1978):

$$\boldsymbol{ln\varphi_i \frac{b_i}{b_m}(Z-1) - ln\left[Z\left(1 - \frac{b_m}{V}\right)\right] + \frac{a_m}{2.828RTb_m}\left(\frac{b_i}{b_m} - \frac{2}{a_m}\sum_j x_i a_{ij}\right) ln\left(\frac{1+2.414\frac{b_m}{V}}{1-0.414\frac{b_m}{V}}\right)} \tag{11}$$

The compressibility factor for the liquid phase is calculated by resolving numerically the following cubic equation obtained by replacing V by ZRT/P in Eqn. 6:

$$\boldsymbol{Z^3 - (1-B)Z^2 + (A - 2B - 3B^2)Z - (AB - B^2 - B^3) = 0} \tag{12}$$

With A and B are as follows:

$$\boldsymbol{A = \frac{aP}{R^2T^2} = 0.45724\frac{P_r}{T_r^2}} \tag{13a}$$

$$\boldsymbol{B = \frac{bP}{RT} = 0.07780\frac{P_r}{T_r}} \tag{13b}$$

It should be noted that most of the equations of state are very sensitive to the size and energy parameters of the different components in a given mixture.

Results and discussion

Physical properties

The necessary physical properties such as the critical properties, the acentric factor, the saturation pressure and the molar volume at saturation of the considered antilipemic agent, namely clofibric acid in supercritical carbon dioxide were a priori calculated using the well known Joback's group contribution methods (critical properties), Bhirud and Riedel methods for (molar volume and saturation pressure, respectively) and lee-Kesler for the acentric factor (Reid, Prausnitz and Poling, 1978). The results are shown in Table 1.

Critical properties		
Pc (MPa)	Tc (K)	ω
2.1	663.91	0.8539
Molar volume and pressure at saturation		
T (K)	Solute molar volume V_m (cm^3/mol)	Saturation pressure P_{sub} (MPa)
308.2	278.946	1.56E-10
318.2	273.312	1.09E-10
328.2	268.149	6.44E-09

Table 1: Estimated physical properties of clofibric acid

The critical temperature and pressure and the acentric factor are 304.15 K, 7.38 MPa and 0.239, respectively.

Solubility calculation

The solubility of clofibric acid in the gas phase is calculated according to an iterative procedure consisting on guessing an initial value for the solute molar fraction in the supercritical fluid which is used to calculate the solute fugacity coefficient which in turn is used to calculate the new solute molar fraction. Both values, the previous and the new one are compared and if the deviation is important the previous calculation steps are repeated starting with the calculated molar fraction as the new initial guess. The calculations are halted when a negligible deviation is reached.

However the values of the interaction parameter in the different mixing rules must a priori be calculated from the experimental data reported in the literature (Chen, et al.,2010). Therefore in this work the initiative was taken coupling the simultaneous calculation of the interaction parameters and the solute molar fraction in the gas phase.

The Local approach

The calculations are performed at each given pressure and temperature and starts by a guess of the interaction parameters k_{ij} for the case of van der Waal's mixing rule and two binary parameters k_{ij} and k_{ji} for that of Panagiotopoulos and Reid. This is followed by the determination of the solute molar fraction in the gas phase. The k_{ij} values are adjusted according to a minimization of the following objective function by means of the Nelder-Mead simplex technique:

$$\boldsymbol{F} = \sum_{1}^{N}\left(\boldsymbol{y}_{exp} - \boldsymbol{y}_{calc}\right)^{2} \qquad (15)$$

The results for the two different mixing rules used are shown in the following tables and figures as follows:

van der Waal's mixing rule

The obtained results are shown in Table 2 and Figures 1-3

T	308.2 K	318.2 K	328.2 K
P (MPa)	k_{ij}	k_{ij}	k_{ij}
10.01	-.19077	-.39277	-.29183
12.02	-.16838	-.30190	-.18726
14.02	-.15256	-.26067	-.15789
16.02	-.14252	-.24240	-.13972
18.02	-.13413	-.22960	-.12196
20.03	-.12753	-.21862	-.11148
22.01	-.12343	-.20943	-.10262

Table 2: Calculated interaction parameter values

For each pressure and temperature, the objective function was forced to practically a value equal to 0 leading to a perfect agreement between the experimental clofibric solubility values reported in (Chen, et al., 2010) and the calculated results.

Since the antilipemic agents are used in specified temperature and pressure ranges of [308.2 - 328.] and [10.1 - 22.02], respectively, the initiative was taken to perform a double regression analysis to end up with a final function $k_{ij}(P,T)$ with correlation factors very close to unity. A polynomial fit was adopted, increasing its order whenever necessary to force the correlation factor near to unity.

A priori the polynomials representing $k_{ij}(P)$ were calculated and the obtained expressions are as follows:

T, K Coefficients	308.2	318.2	328.2
C_1	3.221680	-3.079912E-01	-13.886570
C_2	-1.429855	-5.766020E-01	4.293788
C_3	2.394091E-01	1.562671E-01	-5.460806E-01
C_4	-2.068863E-02	-1.684446E-02	3.571548E-02
C_5	9.828203E-04	9.077886E-04	-1.245428E-03
C_6	-2.443436E-05	-2.442298E-05	2.134463E-05
C_7	2.489356E-07	2.621478E-07	-1.316659E-07

Table 3: Polynomial coefficients of the function $k_{ij}(P)$

$$k_{ij} = \sum_{i=1}^{7} C_i P_i^{i-1} \qquad (16)$$

The $C_{i's}$ coefficients of the above seven polynomials are used in the second regression analysis to end up with the functions in terms of temperature as shown in the follows:

$$C_k = \sum_{j=1}^{3} C_{kj} T_j^{j-1} \qquad (17)$$

$$k_{ij}(T,P) = \sum_{k=1}^{k=7} C_k P_k^{k-1} = \sum_{k=1}^{7}\left(\sum_{j=1}^{3} C_{kj} T_j^{j-1}\right) P_k^{k-1} \qquad (18)$$

The $C_{kj's}$ coefficients of the above polynomials are shown in the following table:

	C_{kj}		
j k	1	2	3
1	-4815.43750942712	31.1202114832	-5.02445381E-002
2	1942.060750369399	-12.496347784	2.0085685E-002
3	-300.82331647334	1.9310380524	-3.0960285E-003
4	23.74842675017399	-1.5219337464E-001	2.4357885E-004
5	-1.01573477131838	6.5013719368E-003	-1.03909245E-005
6	2.241160841522599E-002	-1.4330737436E-004	2.2878115E-007
7	-1.997418677705801E-004	1.2761263388E-006	-2.0351295E-009

Table 4: Polynomial coefficients in terms of temperature

$$\overline{k_{ij}} = \frac{1}{P_b-P_a} X \frac{1}{T_a-T_b} \int_{P_a}^{P_b}\int_{T_a}^{T_b} \sum_{k=1}^{7}\left(\sum_{j=1}^{3} C_{kj} T_j^{j-1}\right) P_k^{k-1}\, dPdT \qquad (19)$$

$$\overline{k_{ij}} = \frac{1}{P_b-P_a} X \frac{1}{T_a-T_b} \sum_{k=1}^{7}\left.\left.\left(\sum_{j=1}^{3} C_{kj} \frac{T_j^j}{j}\right)\right]_{T_a}^{T_b} \frac{P_k^k}{k}\right]_{P_a}^{P_b} \qquad (20)$$

This is a very useful correlation since the value of the interaction parameter k_{ij} is available at any given values of T and P with the fixed ranges. It has also the advantage to avoid the usual difficulties encountered when the function converges to a local minimum rather than a global one during the minimization process. It has been tested in the present case leading to the results shown in the following figures:

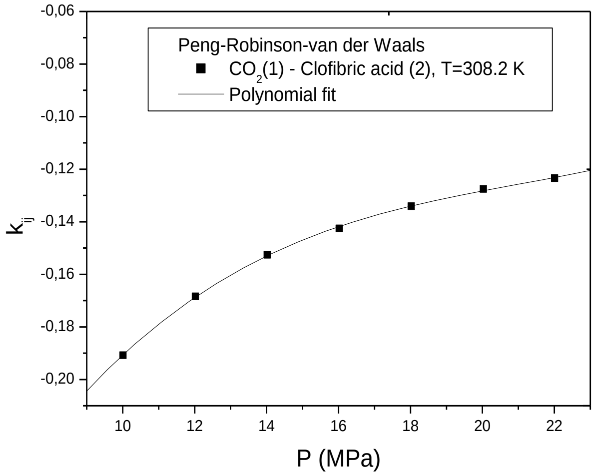

(a)

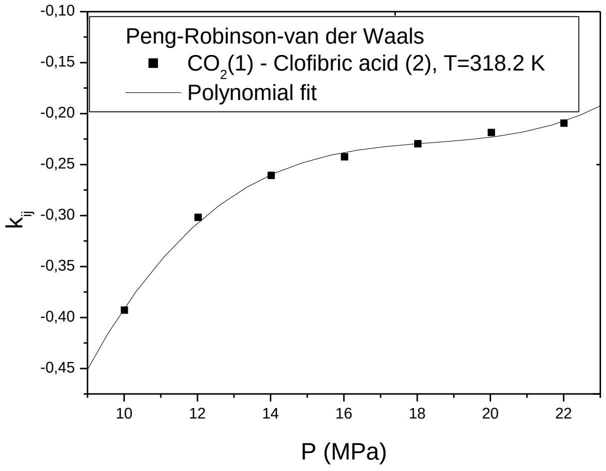

(b)

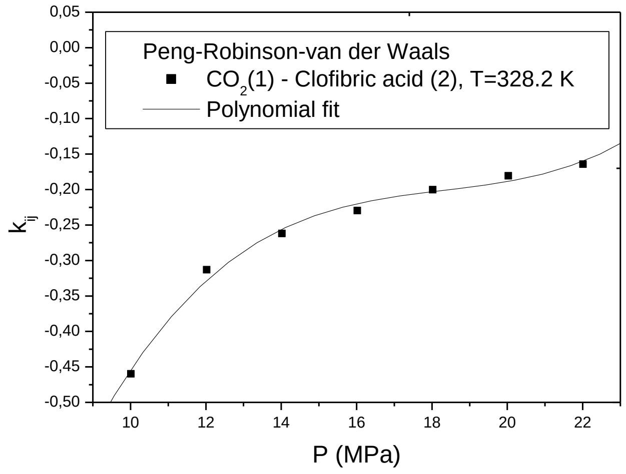

(c)

Figure 1. Variation of k_{ij} with three different temperatures

Figure 1a, b & c shows the variations of the clofibric acid with the pressure at the three temperatures where the usual typical curve trends are observed. From this figure it can also be confirmed that the temperature effect is not regular as shown by the curve corresponding to T= 308.2 K. Also for a given pressure, the curve for to T= 318.2 K is showing a better solubility than the one corresponding to T= 328.2 K. This can be explained by the resulting 'force' balance between pressure and temperature.

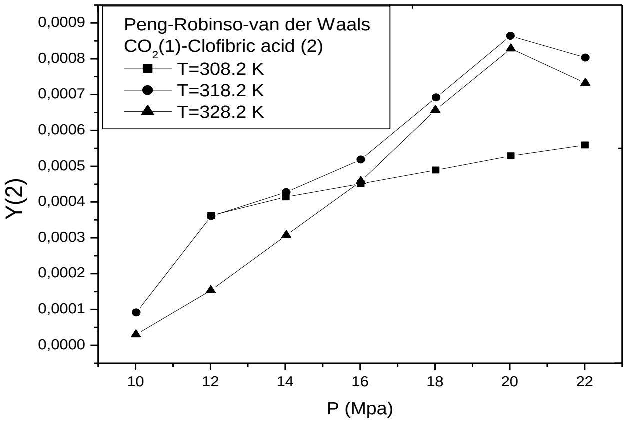

Figure 2. Comparison of Clofibric acid at the three temperatures

In order to examine the reliability of the developed function $\boldsymbol{k_{ij}(P,T)}$ the obtained solubility results are compared with the experimental values reported in (Chen, et al., 2010) as shown by the following figure 3:

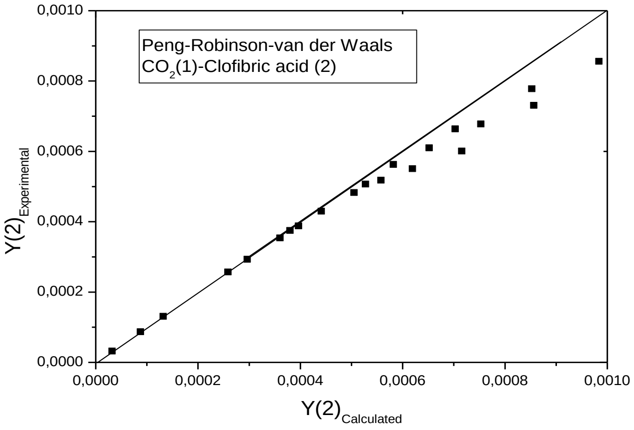

Figure 3. Model assessment

From this figure it can be concluded that the obtained results are in a quite good agreement the experimental values. The absolute mean deviation (AMD) was calculated as 4.67x 10^{-5} which is very encouraging to develop further the proposed approach.
A mean average value for $\boldsymbol{k_{ij}}$ calculated according to the following expression:

$$\overline{k_{ij}} = \frac{1}{P_b - P_a} \cdot \frac{1}{T_b - T_a} \int_{P_a}^{P_b} \int_{T_a}^{T_b} k_{ij}(P,T)\, dP dT$$

A numerical value of -0.2265 was obtained and it can at least be used as an initial value for the minimization of a global objective function, since one of the main difficulties is the choice of this starting point which may influence the convergence.

Conclusion

Through this study one can see the complexity of the problem of calculating solid solubility in supercritical fluids. The main contribution of the present study is the proposition of the locally based approach to obtain the interaction parameters, avoiding the convergence problems always encountered in data prediction.

The obtained results were reasonable and compared fairly well with experimental values with an absolute mean deviation of $4.67.10^{-5}$. Therefore the approach is to be extended further to involve other equations of state and mixing rules, considering a great number of different systems. It can also support a global approach helping to initiate the problem by providing an initial average value of the interaction parameter.

Nomenclature

a	Attractive parameter	[/]
b	Repulsive parameter	[/]
f	Fugacity	[Mpa]
P	Pressure	[MPa]
P_c	Critical Pressure	[MPa]
P_r	Reduced Pressure	[/]
P_{sat}	Saturation Pressure	[MPa]
T	Temperature	[K]
T_c	Critical Temperature	[K]
T_r	Reduced Temperature	[/]
k_{ij}	Interaction Parameter	[/]
R	Universal gas constant	[m]
V	Volume	[m^3]
y	Solute molar fraction	[/]
Z	Compressibility factor	[/]
φ	Fugacity coefficient	[/]
ω	Acentric factor	[/]

References

Ashour, I., Aly, G., 1996, J. Comp. Chem. Eng. 20(1), pp. 79–91.

Chen, Y. M., Lin, P. C., Tang, M., Chen, Y. P., 2010, J. of Supercritical Fluids, 52, pp. 175–182.

Haselow, J. S., Han, S. J., Greenkorn, R. A., Chao, K. C., 1986, ACS Symp. Ser. 300, pp.156–178.

Lee, Y. Y., Kim, H., Lee, H., Hong, V.-H., 1989, Korean J. Chem. Eng. 6(2) pp. 131–137.

Martin, A., Cocero, M.J., 2008, Micronization processes with supercritical fluids: fundamentals and mechanism, Adv. Drug Deliv. Rev. 60, pp. 339–350.

Peng, D. Y., Robinson, D.B., 1976, Ind. Eng. Chem. Fundam., 15, pp. 59–64.

Prausnitz, J. M., Lichtenthaler, R. N., De Azevedo, E. G., 1999, Molecular Thermodynamic of Fluid Phase Equilibria, Third edition, Prentice-Hall, Inc.

Reid, R. C., Prausnitz, J. M., Poling, B. E., 1978, The Properties of Gases and Liquids, 4th edition New York: Mc Graw –Hill book.

Yamamoto, H., Kanegae, F., Mishima, K., Iwai, Y., Arai, Y., 1987, Mem. Fac. Eng., Kyushu Univ. 47(2), p. 95.

Yasuji, T., Takeuchi, H., Kawashima, Y., 2008, Particle design of poorly water-soluble drug substances using supercritical fluid technologies, Adv. Drug Deliv. Rev. 60, pp. 388–398.

Zhong, C., Masuoka, H., 1997, Fluid Phase Equilibria. 141, pp. 13–23.

ANTIOXIDANT ACTIVITY OF ARISTOLOCHIA LONGA L. EXTRACTS

MEROUANI N, BELHATTAB R.

MEROUANI N[1]. , BELHATTAB R[2].
1-Department of Vegetal Biology and Ecology, Faculty of Nature and Life Sciences. University Ferhat Abbas – Setif 1– 19000, Setif, Algeria
2- Dept. Biochemistry, Faculty of Nature and Life Sciences. University Ferhat Abbas –Setif 1– 19000, Setif, Algeria

Abstract

Aristolochia longa L. (Aristolochiacea) is a native plant of Algeria used in traditional medicine. This study was devoted to the determination of polyphenols, flavonoids, and condensed tannins contents of Aristolochia longa L. after their extraction by using various solvents with different polarities(methanol, acetone and distilled water) .these extracts were prepared from stem, leaves, fruits and rhizome. The antioxidant activity was determined using three in vitro assays methods: scavenging effect on DPPH, the reducing power assay and ß-carotene bleaching inhibition (CBI). The results obtained indicate that the acetone extracts from the aerial parts presented the highest contents of polyphenols. The results of The antioxidant activity showed that all extracts of Aristolochia longa L., prepared using different solvent, have diverse antioxidant capacities, however The aerial parts methanol extract exhibited the highest antioxidant capacity of DPPH and reducing power(Respectively 55,04ug/ml±1,29 and 0,2 mg/ml±0,019), But the aerial parts acetone extract showed the highest antioxidant capacity in the test of ß-carotene bleaching inhibition with 57%.These preliminary results could be used to justify the traditional use of this plant and their bioactives substances could be exploited for therapeutic purposes such as antioxidant and antimicrobial.

Keywords: Aristolochia longa L., Polyphenols ,Flavonoids ,Condensed tannins ,Antioxidant Activity.

SYNTHESIS OF NEW MATERIALS DERIVES OF (Z) 2 - (2 PHENYL-3-THIENYL) ACRYLONITRILE) CARACTERISATIONS: CYCLIC VOLTAMMETRY AND IMPEDANCE SPECTROSCOPY

S. MOSBAH, M.BENCHARIF, L.BENCHARIF

Laboratoire de Chimie des Matériaux de Constantine, Equipe d'électrochimie, Département de Chimie, Faculté des Sciences exacte, Université des frères Mentouri, Route de Aïn El Bey, Constantine.
Email: salimacne@yahoo.fr
Fax: 031 905580

Abstract:
Since the band E of gap for example governs the electronic and optical properties intrinsic conjugated polymers, much of work was carried out during the 10 last years for synthesizes the conducting polymers with the lowest band gap [1].

In the last few years, the scientists seek to synthesize organic molecules having gaps similar to those of metals. Recent studies showed that the family of the poly (thienylen vinylen) (PTV) presents a gap electronic Eg lower than that of polythiophen (Pt), 1.8 and 2.1eV respectively.

Other work showed that the introduction of the groupings acceptors into the combined chain has an advantage in the control of this forbidden band. Indeed, the substitution of the grouping cyano in the double connection of the poly (thienylen vinylene leads to a polymer with a great electronic affinity, poly (thienylen-cyanovinylen) (PTCV), conferring a new property to him which found its application in the diodes electroluminescent [1].

The poly (Z) 2 (2-phenyl-3-thienyl) acrylonitrile is synthesized electrochemically by anodic way in an electrolytic bath BU_4BNF_4 (0,2M)/CH_2Cl_2 with conditions anhydrous and under inert atmosphere.

Theoretical calculations carried out show the sites of polymerization in the monomeric reason [2-3-4].

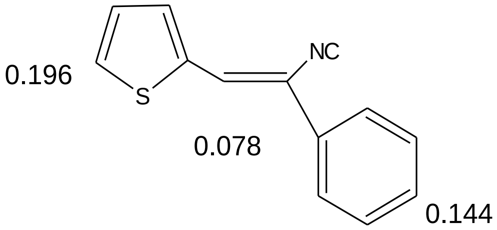

The polymer is formed on Pt electrode, either by cyclic voltametry, or by potentiostatic method and is characterized by spectroscopic methods NMR, IR, UV.

Impedance spectroscopy of a polymer deposit carried out on an electrode consisted a film of Pt. show the semicircle which characteristic of charge-transfer resistance at the electrode/polymer interface at high frequency and the diffusion process at low frequency.

Keywords: Poly ((Z) 2 (2-penyl-3-thienyl) acrylonitrile, cyclic voltametry, impedance spectroscopy.

References:
[1]. J Roncali, Chem. Rev. 97 (1997) 173.
[2]. J Rault-Berthelot, C. Rozé, M.M. Granger, E Raoult, J Electroanal. Chem., 466 (1999) 144-154.
[3]. GianniZotti, Sandro Zecchin, and Gilberto Schiavon
Anna Berlin, Giorgio Pagani, and Michela Borgonovo
R. Lazzaroni, Chem. MATER. 1997, 9, 2876-2886.
[4]. Smoth, J R., Campbell, S.a., Ratcliffe, N.M.., Synth. Put, 73(2) (1995) 171-182.

FIRST-PRINCIPLES CALCULATIONS OF THE PHASE STABILITY AND SURFACE ENERGY OF TIO2 (100) AND (110)

MOURAD AZIBI, NADIA SAOULA

Mourad Azibi, Center for Development of Advenced Technologies (C.D.T.A), Cité 20 août 1956 Baba Hassen, 16303,Algiers, Algeria, Nadia Saoula, Center for Development of Advenced Technologies (C.D.T.A), Cité 20 août 1956 Baba Hassen, 16303, Alger, Algeria

Abstract

First-principles calculations of the crystal structures, bulk moduli, and relative stabilities of TiO_2 rutile and anatase were successfully calculated and simulated by plane wave pseudopotential. The minimum total energy of the structure is achieved by relaxing automatically the internal coordinates using the Broyden-Fletcher-Goldfarb-Shanno (BFGS) algorithm.

The calculated unit cell data agree to within 2% of the corresponding experimental determination and calculated bulk moduli are within 5 % of the most reliable experimental results. Rutile TiO_2 (100) and (110) slabs are constructed before the calculation by cleaving a bulk TiO_2 after geometry optimization. A vacuum region with the thickness of 15 Å is included in the supercell to prevent the interaction between the slab and its periodic images.

The calculated results of structural relaxation and surface energy for TiO_2 (110) and (100) slab indicate that a 10 and 12 layers slab, respectively, were found to be a good surface model.

The surface energy of TiO_2 (100) and (110) are calculated to be 1.11 J/m^2 and 0.78 J/m^2, respectively. Our investigated results are in good accord with the existing theoretical results.

Other properties like Raman spectrum were also investigated.

Keywords – TiO_2, Ab initio calculations, elastic properties, surface energy.

Introduction

TiO_2 has received more and more attention as a promising material for catalyst carrier, biomaterials (Moseke, et al., 2012; Uhm, et al., 2013; Guo, et al., 2014; Zhao, et al., 2011; Lan, et al., 2013), dye-sensitized solar cells and photochemical applications (Jones, 2001; Molinari, et al.,2000; Zuo, et al., 2009; Haruta, et al., 1998; Takanabe, et al., 2005). It is well known that knowledge of the elastic properties of materials is important because of their closely relations with various fundamental physical properties. In particular, they provide information on the stability and stiffness of the materials.

The adsorption of ions, molecules and chemical reactions at interfaces between the oxide surfaces and the aqueous medium are central among many natural phenomena and industrial processes, including catalysis.

First principle studies are optimistic approaches, which provide better experimental parameters leading to rapid material improvements economically. Extensive theoretical research on the electronic, elastic, optical and phonon studies of rutile titanium dioxide have been reported in the previous research articles (Labat, et al., 2007; Islam, Bredow, and Gerson, 2007; Fox, et al., 2010; Cho, et al., 2006; Mattioli, et al., 2008; Shirley, Kraft and Inderwildi, 2010; Person and da Silva,2005).

In the present work we propose a more comprehensive study about elastic properties of anatase and rutile and the surface properties of (110) and (100) surface of rutile TiO_2 obtained by ab initio study.

Computational details

CASTEP (Cambridge Serial Total Energy Package) software (Segall, et al., 2002)was utilized in our calculations, based on density functional theory (DFT). CASTEP uses a plane wave basis set for the expansion of the single particle Kohn-Sham as implemented and ultra-soft pseudo potentials to describe ionic cores. The minimum total energy of the structure is achieved by relaxing automatically the internal coordinates using the Broyden-Fletcher-Goldfarb-Shanno (BFGS) algorithm.

The atomic configurations of Ti and O generated from the ultra-soft pseudo potential are $3s^2$ $3p^6$ $3d^2$ $4s^2$ and 2s $2p^4$, respectively. The exchange correlation energy is described by the local density approximation of Ceperley and Alder. Brillouin zone sampling is performed using 3×5×1 and 5×2×1 Monkhorst-Pack k-points meshes for (100) and (110) surface calculations, respectively. The plane wave cutoff energy in our calculations is 380 eV, which assures a total energy convergence of 5.0×10^{-7}eV/atom.

TiO_2 (100) and (110) slab is constructed before the calculation by cleaving a bulk TiO_2 after geometry optimization, as shown in Fig. 1. A vacuum region with the thickness of 15 Å is included in the supercell(Han, et al., 2006) to prevent the interaction between the slab and its periodic images.

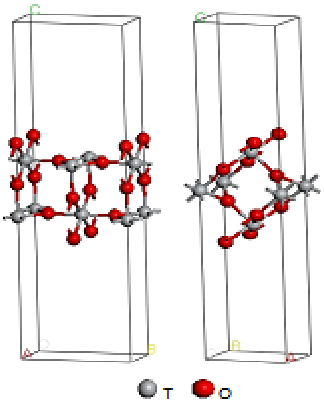

(a) (b)

Figure1. Crystal structures of (a) unrelaxed (100) and (b) unrelaxed (110) with O-terminated.

Upon attaining a critical thickness, the surface energy will converge to a fixed value, indicating that the TiO_2 slab possesses a bulk-like interior. After structure optimization, we have calculated the surface energy of the (100) and (110) surfaces for the slabs of sizes ranging from 2 to 11 layers using the following equation:

$$E_{surf} = \frac{E_0 - N_{TiO_2} E_{TiO_2}}{2S}$$

Where E_0 is the total energy of N-layer slab, $E_{TiO_2}$is the energy of one motif TiO_2 in the rutile unit cell, N_{TiO_2} is the number of TiO_2 motif contained in the N-layer slab and S is the surface.

Results and discussion

In Table 1, we present the relaxed structure of rutile and anatase TiO2. For comparison, we also list experimental results. It is shown that the optimized structural parameters are in good agreement with experimental values.

	a(Å)	c(Å)
rutile	4.645 4.593 (Asahi, 2000)	2.968 2.958 (Asahi, 2000)
anatase	3.802 3.782 (Abrahams and Bernstein, 1971)	9.701 9.502 (Abrahams and Bernstein, 1971)

Table1.The relaxed structure of the rutile and anatase, compared to experiment results

Elastic constants of tetragonal crystal system can be calculated using a Taylor expansion of the total energy E (V,ε) (Tian, 2004; Fast, et al., 1995; Liu, et al., 2010), is written as

$$E(V, \varepsilon) = E(V_0, 0) + V_0 \left[\sum_i \tau_i \varepsilon_i \xi_i + \frac{1}{2} \sum_{ij} C_{ij} \varepsilon_i \xi_i \varepsilon_j \xi_j \right]$$

Whereas $E(V_0, 0)$ is the energy of the unstrained system with equilibrium volume V_0, τ_i is an element in the stress tensor, ξ_i is a factor to take care of Voigt index and C_{ij} represents elastic constants. The linear elastic constants form a 6 × 6 symmetric matrix, having 27 unlike components. These components will reduce to six elements C_{11}, C_{12}, C_{13}, C_{33}, C_{44} and C_{66} according to the symmetry of tetragonal structure(Alton and Barlow, 1967). The Born stability conditions (Grimsditch, et al., 1998; Sinko and smirnov, 2002; Born and Huang, 1982; Ferrer, 1941)for the elastic constants of tetragonal structures are $(C_{11}-C_{12}) > 0$, $C_{11}> 0$, $C_{33}> 0$, $(C_{11}+C_{33}-2C_{13}) > 0$,

$(2C_{11}+C_{33}+2C_{12}+4C_{13}) > 0$, $C_{44} > 0$, $C_{66} > 0$. Our rutile and anatase TiO2 satisfies these criteria showing its phase stability under zero pressure.

Table 2 and 3 represents the comparison of calculated elastic constants; Hill bulk modulus and Hill shear modulus with previously reported theoretical and experimental results.

Our results for cut-off energy of 380 eV are in excellent agreement with the experimental results and previous first principle studies as a whole

	C_{11}	C_{33}	C_{44}	C_{66}	C_{12}	C_{13}	B	G
Present work	278.65 +/- 1.43	490.49 +/- 1.17	122.96 +/- 0.48	223.46 +/- 0.44	182.44 +/- 1.92	157.89 +/- 0.43	222	116
Isaak (1998)	268	484	124	190	175	147	212	113
Jun (2008)	292	471	114	236	192	174	233	133
Ogata (1999)	412	519	136	119	107	123		
Ma (2009)	267	483	122	212	165	152	217	128

Table2. Calculated elastic constants C_{ij} (GPa), Hill bulk modulus B (GPa) and shear modulus G (GPa) for rutile TiO_2 together with theoretical and experimental results at zero pressure.

	$C_{11} + C_{12}$	C_{33}	C_{44}	C_{66}	C_{13}	B	G
Present work	497.55	202.88 +/- 2.11	61.28 +/- 1.42	62.81 +/- 0.12	146.16 +/- 1.51	182	66
Iuga (2007)	471	190	54	60	143	174	58
Yin (2010)	501	187			148		
Dubrovinsky (2001)						178	
Arlt (2000)						179	

Table3. Calculated elastic constants C_{ij} (GPa), Hill bulk modulus B (GPa) and shear modulus G (GPa) for anatase TiO_2 together with theoretical and experimental results at zero pressure

As can be seen in Figure 2, the surface energy oscillates with the number of layers. Nevertheless, the amplitude of these oscillations decreases and as the number of layers increases until convergence.

The calculated surface energy of TiO_2 (100) is 1.11 J/m^2 and 1.12 J/m^2 for 6 and 7 layer slab, respectively, and of TiO2 (110) is 0.78 J/m^2 and 0.77 J/m 2 for 10 and 11 layer slab, respectively, only 0.01 J/m^2 difference between the two slabs, which means that it has converged as the number of atomic layers is 6 and 10 for TiO2 (100) and TiO2 (110), respectively.

The values obtained are in good agreement with the literature (Table 4).

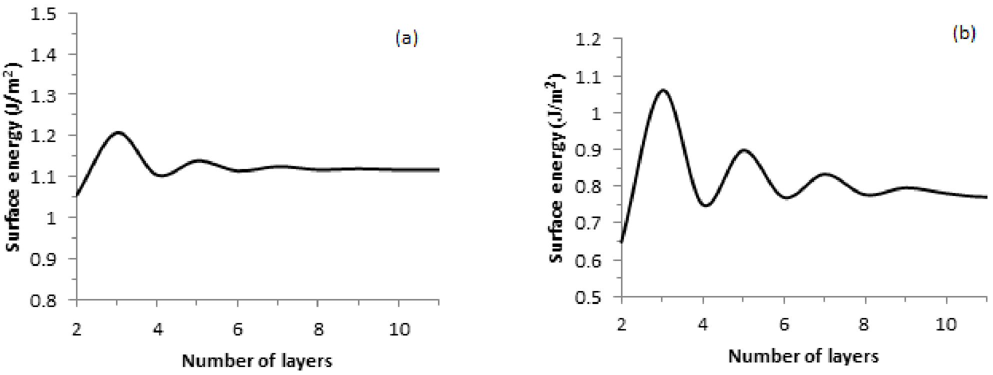

Figure 2. Surface energy as a function of number of layers: (a) TiO_2 (100) and (b) TiO_2 (110)

(b)

	TiO_2 (100)	TiO_2 (110)
Present work	1.11	0.78
Muscat (1999)	1.30	-
Ramamoorthy (1994)	1.12	0.89
Lazzeri (2001)	-	0.84
Albaret (2000)	-	0.66

Table4. Calculated surface energy (J/m2) of TiO2 (100) and TiO2 (110) together with theoretical results

The Raman spectrum of rutie and anatase TiO_2 is observed in the present research and shown in Figure 3, where all four Raman peaks theoretically expected appear distinctly. The frequencies of these Raman peaks, listed in Table 5 are well compared with experimental data. Raman line intensities at zero pressure, on the other hand, cannot be easily compared to the experimental line intensities.

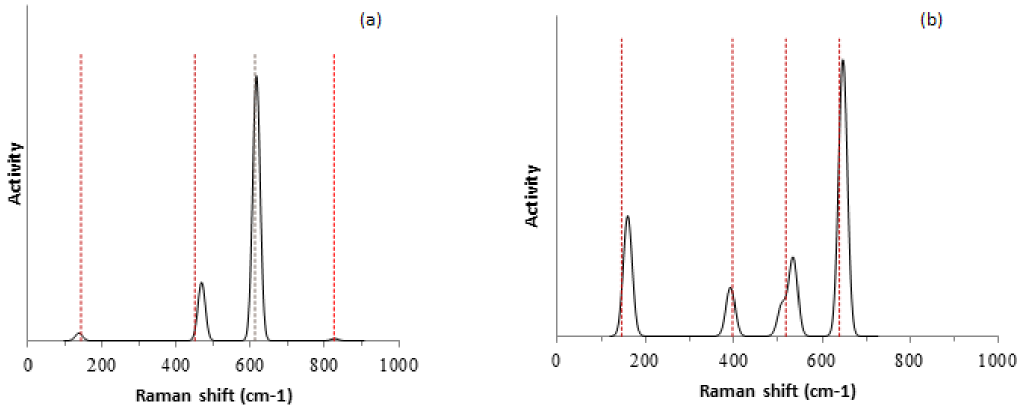

(b)

Figure 3. Raman spectra in the: (a) rutile and (b) anatase TiO_2 at zero pressure

	A_{1g}	E_g	B_{1g}	B_{2g}
Present work rutile	616	469	137	828
Merl (1980)	612	450	143	826
Lukacevic (2012)	636	482	117	844
Present work anatase	----	159-647	382-534	----
Zhang (2012)	----	145-639	397-518	----

Table 5.Raman active phonon frequencies (in cm^{-1}) for rutile and anatase TiO_2 together with experimental results.

Conclusion

The structural properties of rutile and anatase TiO_2 and the surface energy of rutile TiO_2 (100) and (110) are explored using the first principles total energy plane wave pseudo potential method based on density functional theory.

The structural parameters, elastic and mechanical properties for both rutile and anatase are in good agreement with available experimental and theoretical results.

The oscillation amplitude of the energy of the (100) face is less low than the face (110), convergence is reached more quickly. However, the value of the TiO_2 surface energy (110) is less than that of TiO_2 (100), which explain the stability of the face (110).

References

Abrahams, S. (1971). Rutile: Normal Probability Plot Analysis and Accurate Measurement of Crystal Structure. *The Journal of Chemical Physics*, 55(7), p.3206.

Albaret T., 2000. Thèse de l'Université de Paris 11.

Alton, W. (1967). Acoustic-Wave Propagation in Tetragonal Crystals and Measurements of the Elastic Constants of Calcium Molybdate. *J. Appl. Phys.*, 38(10), p.3817.

Arlt, T., Bermejo, M., Blanco, M., Gerward, L., Jiang, J., Staun Olsen, J. and Recio, J. (2000). High-pressure polymorphs of anatase TiO 2. *Phys. Rev. B*, 61(21), pp.14414-14419.

Asahi, R., Taga, Y., Mannstadt, W. and Freeman, A. (2000). Electronic and optical properties of anatase TiO 2. *Phys. Rev. B*, 61(11), pp.7459-7465.

Born M., Huang K., 1982. Berlin: Dynamical Theory and Experiment I, Springer-Verlag, Berlin.

Cho, E., Han, S., Ahn, H., Lee, K., Kim, S. and Hwang, C. (2006). First-principles study of point defects in rutile TiO 2 − x. *Phys. Rev. B*, 73(19).

Dubrovinsky, L., Dubrovinskaia, N., Swamy, V., Muscat, J., Harrison, N., Ahuja, R., Holm, B. and Johansson, B. (2001). Résultats de la recherche revue scientifique - Cite This For Me. *Nature*, 410(6829), pp.653-654.

Fast, L., Wills, J., Johansson, B. and Eriksson, O. (1995). Elastic constants of hexagonal transition metals: Theory. *Phys. Rev. B*, 51(24), pp.17431-17438.

Ferrer W.L., 1941. Algebra, Clarendon Press, Oxford, England, p.138.

Fox, H., Newman, K., Schneider, W. and Corcelli, S. (2010). Bulk and Surface Properties of Rutile TiO 2 from Self-Consistent-Charge Density Functional Tight Binding. *J. Chem. Theory Comput.*, 6(2), pp.499-507.

Grimsditch, M., Polian, A., Brazhkin, V. and Balitskii, D. (1998). Elastic constants of α-GeO. *J. Appl. Phys.*, 83(6), p.3018.

Guo, Z., Chen, C., Gao, Q., Li, Y. and Zhang, L. (2014). Fabrication of silver-incorporated TiO2 nanotubes and evaluation on its antibacterial activity. *Materials Letters*, 137, pp.464-467.

Han, Y., Dai, Y., Shu, D., Wang, J. and Sun, B. (2006). First-principles study of TiB 2 (0001) surfaces. *Journal of Physics: Condensed Matter*, 18(17), pp.4197-4205.

Haruta, M., Uphade, B., Tsubota, S. and Miyamoto, A. (1998). Selective oxidation of propylene over gold deposited on titanium-based oxides. *Res. Chem. Intermed.*, 24(3), pp.329-336.

Isaak, D., Carnes, J., Anderson, O., Cynn, H. (1998). Elasticity of TiO2 rutile to 1800 K. Phys. Chem. Miner., 26, p.31.

Islam, M., Bredow, T. and Gerson, A. (2007). Electronic properties of oxygen-deficient and aluminum-doped rutile Ti O 2 from first principles. *Phys. Rev. B*, 76(4).

Iuga, M., Steinle-Neumann, G. and Meinhardt, J. (2007). Ab-initio simulation of elastic constants for some ceramic materials. *The European Physical Journal B*, 58(2), pp.127-133.

Jones, F. (2001). Teeth and bones: applications of surface science to dental materials and related biomaterials. *Surface Science Reports*, 42(3-5), pp.75-205.

Jun, Z., Jing-Xin, Y., Yan-Ju, W., Xiang-Rong, C. and Fu-Qian, J. (2008). First-principles calculations for elastic properties of rutile TiO 2 under pressure. *Chinese Physics B*, 17(6), pp.2216-2221.

Labat, F., Baranek, P., Domain, C., Minot, C. and Adamo, C. (2007). Density functional theory analysis of the structural and electronic properties of TiO[sub 2] rutile and anatase polytypes: Performances of different exchange-correlation functionals. *The Journal of Chemical Physics*, 126(15), p.154703.

Lan, M., Liu, C., Huang, H. and Lee, S. (2013). Both Enhanced Biocompatibility and Antibacterial Activity in Ag-Decorated TiO2 Nanotubes. *PLoS ONE*, 8(10), p.e75364.

Lazzeri, M., Vittadini, A. and Selloni, A. (2001). Structure and energetics of stoichiometric TiO 2 anatase surfaces. *Phys. Rev. B*, 63(15).

Liu, Q., Liu, Z., Feng, L. and Tian, H. (2010). First-principles study of structural, elastic, electronic and optical properties of rutile GeO2 and α-quartz GeO2. *Solid State Sciences*, 12(10), pp.1748-1755.

Lukačević, I., Gupta, S., Jha, P. and Kirin, D. (2012). Lattice dynamics and Raman spectrum of rutile TiO2: The role of soft phonon modes in pressure induced phase transition. *Materials Chemistry and Physics*, 137(1), pp.282-289.

Ma, X., Liang, P., Miao, L., Bie, S., Zhang, C., Xu, L. and Jiang, J. (2009). Pressure-induced phase transition and elastic properties of TiO 2 polymorphs. *physica status solidi (b)*, 246(9), pp.2132-2139.

Mattioli, G., Filippone, F., Alippi, P. and Amore Bonapasta, A. (2008). Ab initio study of the electronic states induced by oxygen vacancies in rutile and anatase TiO 2. *Phys. Rev. B*, 78(24).

Merle, P., Pascual, J., Camassel, J. and Mathieu, H. (1980). Uniaxial-stress dependence of the first-order Raman spectrum of rutile. I. Experiments. *Phys. Rev. B*, 21(4), pp.1617-1626.

Molinari, A., Amadelli, R., Antolini, L., Maldotti, A., Battioni, P. and Mansuy, D. (2000). Phororedox and photocatalytic processes on Fe(III)–porphyrin surface modified nanocrystalline TiO2. *Journal of Molecular Catalysis A: Chemical*, 158(2), pp.521-531.

Moseke, C., Hage, F., Vorndran, E. and Gbureck, U. (2012). TiO2 nanotube arrays deposited on Ti substrate by anodic oxidation and their potential as a long-term drug delivery system for antimicrobial agents. *Applied Surface Science*, 258(14), pp.5399-5404.

Muscat, J., Harrison, N. and Thornton, G. (1999). Effects of exchange, correlation, and numerical approximations on the computed properties of the rutile TiO 2 (100) surface. *Phys. Rev. B*, 59(3), pp.2320-2326.

Ogata, S., Iyetomi, H., Tsuruta, K., Shimojo, F., Kalia, R., Nakano, A. and Vashishta, P. (1999). Variable-charge interatomic potentials for molecular-dynamics simulations of TiO[sub 2]. *J. Appl. Phys.*, 86(6), p.3036.

Persson, C. and Ferreira da Silva, A. (2005). Strong polaronic effects on rutile TiO[sub 2] electronic band edges. *Appl. Phys. Lett.*, 86(23), p.231912.

Ramamoorthy, M., Vanderbilt, D. and King-Smith, R. (1994). First-principles calculations of the energetics of stoichiometric TiO 2 surfaces. *Phys. Rev. B*, 49(23), pp.16721-16727.

Segall, M., Lindan, P., Probert, M., Pickard, C., Hasnip, P., Clark, S. and Payne, M. (2002). First-principles simulation: ideas, illustrations and the CASTEP code. *Journal of Physics: Condensed Matter*, 14(11), pp.2717-2744.

Shirley, R., Kraft, M. and Inderwildi, O. (2010). Electronic and optical properties of aluminium-doped anatase and rutile TiO 2 from ab initio calculations. *Phys. Rev. B*, 81(7).

Sinko, G. and Smirnov, N. (2002). Ab initio calculations of elastic constants and thermodynamic properties of bcc, fcc, and hcp Al crystals under pressure. *Journal of Physics: Condensed Matter*, 14(29), pp.6989-7005.

TAKANABE, K., NAGAOKA, K., NARIAI, K. and AIKA, K. (2005). Influence of reduction temperature on the catalytic behavior of Co/TiO2 catalysts for CH4/CO2 reforming and its relation with titania bulk crystal structure. *Journal of Catalysis*, 230(1), pp.75-85.

Uhm, S., Song, D., Kwon, J., Lee, S., Han, J., Kim, K. and Kim, K. (2013). E-beam fabrication of antibacterial silver nanoparticles on diameter-controlled TiO2 nanotubes for bio-implants. *Surface and Coatings Technology*, 228, pp.S360-S366.

Yin, W., Gong, X. and Wei, S. (2008). Origin of the unusually large band-gap bowing and the breakdown of the band-edge distribution rule in the Sn x Ge 1 − x alloys. *Phys. Rev. B*, 78(16).

Zhang, T., Hu, X., Fang, M., Zhang, L. and Wang, Z. (2012). Synthesis of hierarchical TiO2 nanotube arrays assembled by anatase single crystal nanoparticles. *CrystEngComm*, 14(22), p.7656.

Zhao, L., Wang, H., Huo, K., Cui, L., Zhang, W., Ni, H., Zhang, Y., Wu, Z. and Chu, P. (2011). Antibacterial nano-structured titania coating incorporated with silver nanoparticles. *Biomaterials*, 32(24), pp.5706-5716.

Zuo, Z., Huang, W., Han, P., Li, Z. and Huang, J. (2009). A DFT study on the interaction of Co with an anatase TiO2 (001)-(1×4) surface. *Journal of Natural Gas Chemistry*, 18(1), pp.78-82.

ABSORPTION SPECTROSCOPY OF SINGLE GOLD NANOPARTICLES

MUSTAFA YORULMAZ, SARA NIZZERO, ANNELI HOGGARD, LIN-YUNG WANG, YI-YU CAI, WEI-SHUN CHANG AND STEPHAN LINK

Abstract

Plasmonic nanoparticles exhibit interesting radiative and non-radiative properties when they are optically excited [1]. These properties have been widely exploited for a variety of intriguing applications in fields ranging from chemistry to biology and photonics [2,3]. For example, gold nanoparticles can be used for optical probing and sensing, waveguiding, local heating, and optical data storage [4-6].

Single-particle methods have been utilized to understand the interesting properties of nanoparticles [7]. The obtained information is very helpful in order to make rational designs using nanostructures for specific applications. Moreover, these methods make the distribution of variables accessible which otherwise is averaged out in an ensemble of particles. While the radiative properties are well-characterized using fluorescence and scattering spectroscopy tools, studying the non-radiative properties still keeps challenging [8,9].

Photothermal microscopy is a very sensitive technique that can be used to detect a single nano-object by the heat it generates. Even detection of a single chromophore by its absorption using the photothermal contrast has been shown in literature [10]. However, all these measurements have been performed using a single excitation wavelength. The knowledge of pure absorption as a function of wavelength for an individual nano-object is therefore not [11, 12].

Here, we introduce the absorption spectroscopy, which is performed by using the well-studied photothermal microscopy technique. In order to achieve that, we incorporate photothermal microscopy with a supercontinuum laser source and a correction procedure which accounts for the effects of chromatic aberration and wavelength dependent excitation efficiency on the measured absorption spectrum.

The single-particle absorption spectroscopy we present can benefit applications of individual plasmonic nanostructures in photonics and optoelectronic devices.

[1] Chang et al. Acc. Chem. Res. 45, 1936 (2012); Gaiduk et al. ChemPhysChem 12, 1536 (2011). [2] Yuan et al. Faraday Discuss. 167, 515 (2013); Dominguez-Medina et al. Langmuir 28, 9131 (2012). [3] Yuan et al. Angew. Chem. Int. Ed. 52, 163 (2013). [4] Solis et al. Nano Lett. 12, 1349 (2012). [5] El-Sayed et al. Cancer Lett. 239, 129 (2006). [6] Zijlstra et al. Nature 459, 410 (2009). [7] Zijlstra et al. Rep. Prog. Phys. 74, 106401 (2011). [8] Fang et al. ACS Nano 6, 7177 (2012), Yorulmaz et al. Nano Lett. 12, 4385 (2012). [9] Boyer et al. Science 297, 1160 (2002); Gaiduk et al. Chem. Sci. 1, 343 (2010); Chang et al. J. Phys. Chem. Lett. 12, 3967 (2012). [10] Gaiduk et al. Science 330, 353 (2010). [11] Tcherniak et al. Nano Lett. 10, 1398 (2010); Berciaud et al. Phys Rev. B 73, 045424 (2006). [12] Chang et al. Nano Lett. 12, 3967 (2012); Maier et al. Nature Mater. 2, 229 (2003).

SYNTHESIS AND CHARACTERIZATION OF MG-AL-CO3-LDHS: A HIGHLY EFFICIENT CATALYST FOR THE SYNTHESIS OF 3,4-DIHYDROPYRIMIDIN-2(1H)-ONES AND THIONES ANALOGS BY BIGINELLI REACTION UNDER SOLVENT-FREE CONDITIONS

MUSTAPHA DIB, SOUFIANE AKHRAMEZ, ABDELLATIF ESSOUMHI, HAJIBA OUCHETTO, KHADIJA OUCHETTO, ABDERRAFIA HAFID AND MOSTAFA KHOUILI

Abstract

Synthesis of 3,4-dihydropyrimidin-2(1H)-ones/thiones (DHPMs), a multicomponent Biginelli reaction, has been carried out by using ethyl acetoacetate, aromatic aldehydes, substituted urea/thiourea and in the presence of Mg-Al-CO3-LDH as a reusable solid catalyst. This latter is prepared, at pH=10, by a co-precipitation method with ratio of Mg2+/Al3+ =3.

Our method has advantage of excellent yield, short reaction times at temperature 90°C , reusability and being environmentally friendly. Mg-Al-CO3-LDHs are easy to separate and to recycle and they could be reused without any decrease in the yield of the reactions. The physicochemical techniques XRD and IR were used to characterize this catalyst.

STRUCTURAL AND OPTICAL PROPERTIES OF PURE AND SN, IN AND CU DOPED ZNO

OUILI ZEINEDDINE, ALLIOUCHE HAYETTE, BOUDINE BOUBEKEUR, SEBAIS MILOUD AND HALIMI OUAHIBA

Abstract

Semiconductor nanomaterials have attracted a huge interest. These materials have been extensively studied in order to develop new electronics and optoelectronics devices. Among these materials, ZnO have several interesting physical properties such as strong diffusion and absorption of ultraviolet radiation and non-toxicity that makes its utilization free from any biological risks.

This work consists to the fabrication and characterization of pure and Sn, In and Cu doped ZnO thin films. The sample preparation was carried out by the colloidal method. The pure and doped solutions were prepared at room temperature. The films were deposited using a dip-coating technique on glass matrix. The XRD and Raman characterizations show that the ZnO thin film crystallize with a wurtzite structure. The optical properties of pure and doped ZnO thin films reveal that doping changes the optical properties of ZnO.

THEORETICAL STUDY OF THE DOPAMINE: β CD COMPLEX USING DFT-ONIOM METHODS

RAYENNE DJEMIL, DJAMELEDDINE KHATMI

Department of Material Sciences
Faculty of Mathematical, Informatics, and Material Sciences
Laboratory of computational chemistry and nanostructures
BP: 401, University of Guelma, Algeria
messdjem@gmail.com
khatmi.djameleddine@gmail.com

Abstract: In this work, we studied the complexation of a dopamine DA: β-cyclodextrin complex via different ONIOM approaches using both mixed (DFT: HF) and non-mixed (DFT: DFT) combinations. We applied the hybrid functional B3LYP. The complexation, and deformation energies were determined, and compared to those obtained with Full B3LYP/6-31G (d) level. The intermolecular hydrogen bond interactions of the complex have been analyzed with the Natural Bond Orbital (NBO) methodology.

Keywords: Dopamine, β Cyclodextrin, Inclusion complexes, ONIOM2, DFT.

Introduction:

Noncovalent interactions are ubiquitous and are a main source for many molecular complexes in nanoscience, materials chemistry, and biochemistry [1] . The ability to describe these interactions computationally is crucial for modeling structure.

Computational chemistry is a powerful tool that analyzes inclusion complexes. It has been found to be an efficient method to assess non-covalent intermolecular interactions and to predict structural geometrical models [2, 3].

Quantum mechanics, especially density functional theory (DFT) is considered as the most effective method for inclusion complexes calculations. It has gained more popularity for displaying molecular structures and also for predicting physio-chemical properties [4-11].

The choice of method and the computational cost has been a particularly important concern in theoretical research or it must be ensured the best-fit method precision and computational cost. However, the accurate quantum modeling of chemical systems containing a large number of atoms is still a challenging task. One of the remedies to circumvent this problem is to use the ONIOM method [12, 13] . Which has drastically extended the regime of chemical and biological systems.

Through this work, we aim to find the best method can accurately describe the inclusion complexes using the approach ONIOM2 to ensure a reasonable computational cost. Then, we compared ONIOM results with Full DFT in which we used only DFT in two layers [14-17].

We have studied the DA-CD complex in order to describe its geometry using ONIOM (B3LYP/6-31g (d): HF/3-21G*) hybrid calculations [18,19]. Here, we studied this system via ONIOM2 method using two ONIOM combinations in order to find the most effective combination relatively to the standard method [full B3LYP/6-31G(d)].

The choice of guest molecules has focused on the dopamine (3,4-dihydroxyphenethylamine, DA) which is a neurotransmitter molecules belonging to catecholamines in mammalian central nervous [20], these simple molecules containing organic functions can establish hydrogen bonds and give Van der Waals interactions and the manifestation of hydrophobicity is provided by the aromatic ring of neurotransmitter.

In practice, the formation of inclusion complexes between the cyclodextrin molecule and neurotransmitter serves as a means of analysis of these neurotransmitters because they react differently to the cyclodextrin [21–26]. The formation of an inclusion complex will depend mainly on the size of the guest and the size of the cavity of the cyclodextrin and the polarity of the guest molecule [27.28] . The polarity of the guest molecule is a critical parameter due to the hydrophobic nature of the internal cavity of the cyclodextrin. 29 Implemented interactions between the host and the guest can be of various types, such as Coulomb interactions, dipole, van der Waals or hydrogen bonding [30].

In order to analyze the intermolecular hydrogen bond interactions, we used the Natural Bond Orbital (NBO) [16] .

Computational methods:

The calculations in this work were performed using the Gaussian 09 and Mopac software (versions 2009) [31, 32] . The software Cambridge Bio Chem 3D Ultra (version 12.0) was used for building structures starting neurotransmitters that are then optimized with the method B3LYP / 6-31G (d), and the construction of the whole process of training of inclusion complexes. The β-CD was extracted from the database of the same software.

A systematic searching approach, described by Liu and Guo [33], is used to find the minimum energy of dopamine-β-CD complex. It consists of exploring the conformational space along an axis passing through the center of the cyclodextrin cavity where the dopamine molecule is moved to the β-CD molecule. Once the minimum energy structure is obtained, its geometry is re-optimized with ONIOM2 method using different DFT functionals. To be simple, when the aromatic ring of dopamine is firstly inserted into β-CD, we call this 'head orientation' and when the functional group is firstly introduced this orientation is called 'tail orientation'.

In order to assign atoms to layers for the ONIOM calculations, using Gauss view, different layers are indicated by the different display formats. Here, the CD atoms are selected for low layer represented by wire frame, and the guest for high layer represented by ball and sticks (fig.1). In Gaussian calculation, we assigned each layer to the corresponding method [34].

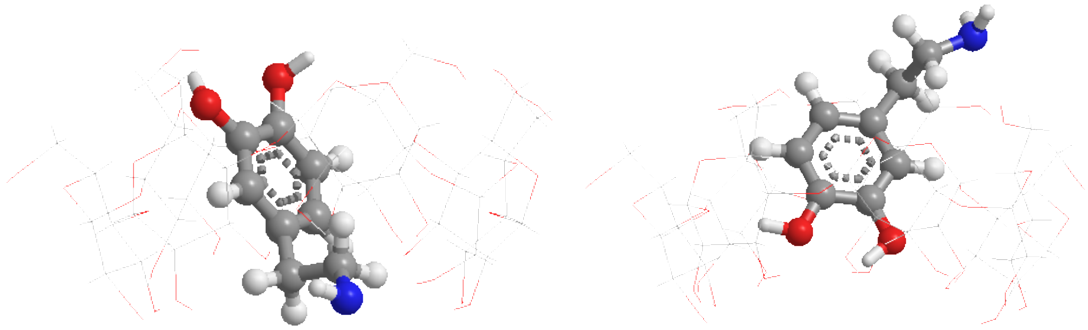

(b)

Fig.1: The two approaches of DA from the wide secondary cyclodextrin cavity: (a) head orientation and b) tail orientation.

In order to find the best method to better predict the energies and geometries of the inclusion complexes we applied two variants of ONIOM2 using the B3LYP functional on the inclusion complex DA: β CD, with a basis set of 3-21G * on the cyclodextrin and a basis set 6-31G (d) on dopamine. We also applied full DFT B3LYP /6-31G (d) for comparison with the ONIOM approach.

All ONIOM results are compared to those obtained with full DFT [B3LYP/6-31G(d)] which is chosen as a target method.

The Natural Bond Orbitals (NBO) theory [35] analyzes the orbital interactions. The donor–acceptor interactions for hydrogen bonds, donate from a filled orbital of the electron donor to an empty orbital of the electron acceptor. The NBO calculations were performed using NBO 3.1 program, it is implemented in the Gaussian 09 package [36].

Results and discussion:

Two ONIOM2 approaches were selected to assess mixed and non-mixed combinations compared to the standard method, full DFT [B3LYP/6-31G(d)].

When the [DFT: HF] combination is applied for the guest (DFT) and the host (HF) molecules, this is known as the mixed combination. It is known as non-mixed combination when the [DFT: DFT] combination is applied to both molecules, with the same density functional but with different basis set.

The results highlighted in table 1 represent the complexation and the deformation energies obtained in both orientations.

Table 1: ONIOM energies and full DFT of complex DA: β CD and strain energies of the guest and host molecules calculated for both orientations at B3LYP functional.

	Full B3LYP	Mixed ONIOM B3LYP/6-31G(d) : HF/3-21g*	Not mixed ONIOM B3LYP6-31G(d): B3LYP/3-21g*	HF
$E_{complexation}$ Head	-26.35	-38.7	-66.3	-16.80
DEF(DA)	4.45	8.5	9.5	2.75
DEF(CD)	1.18	9.9	17.20	0.35
$E_{complexation}$ Tail	-23.58	-29.7	-45.7	-12.64
DEF(DA)	0.55	4.2	6.0	2.67
DEF(CD)	1.57	5.6	7.1	1.35
ΔE	-2.76	-9.0	-20.7	-4.16

$$E_{complexation} = E_{complex} - (E_{\beta-CD} + E_{dopamine})$$

$$E_{deformation}(dopamine) = E[dopamine]_{sp}^{opt} - E[dopamine]_{opt}$$

$$E_{deformation}(\beta - CD) = E[\beta - CD]_{sp}^{opt} - E[\beta - CD]_{opt}$$

$E_{deformation}(dopamine)$ stands the deformation energy of dopamine, $E[dopamine]_{sp}^{opt}$ is the single point energy of dopamine using its geometry in the optimized complex, and $E[dopamine]_{opt}$ is the energy of the optimized geometry of dopamine.

Based on the complexation energy values obtained with ONIOM2 combinations or standard method (full DFT), it can be seen that head orientation process is more favorable.

More explicitly, head orientation is found more stable in full DFT [B3LYP/6-31G(d)] calculation with the complexation energy's difference between the two orientations equal to 2.76 kcal/mol. The value of the energy gap obtained with HF/6-31G (d) method is equal to 4.16 kcal. While, ONIOM2 approaches give more substantial energy differences. Thus, mixed combination [B3LYP: HF] gives complexation energy's difference between the two orientations equal to 9 kcal/mol. Therefore, for not-mixed combination, [B3LYP/6-31G(d): B3LYP/3-21G(d)] gives a value of complexation energy's difference around 20 kcal/mol.

Overall, we can say that mixed combination [DFT: HF] gives important complexation energy values relatively to the standard method full B3LYP, and HF results is situated between the both. While, not-mixed combination gives significantly an overestimate values of these energies.

As it can be seen from table 1, the deformation energy value of dopamine in the most favorable orientation calculated with full DFT is found equal to 4.45 kcal/mol. Whereas, the value obtained with HF method is less (2.75 kcal). Therefore, the two ONIOM combinations mixed and not-mixed give values equal to 8.5 and 9.9 kcal/mol, respectively.

However, the deformation energy of β-CD is found equal to 1.18 kcal/mol with full DFT, and is lower with HF method. Also, [B3LYP: HF] combination gives the value (9.9 kcal/mol). However, with the not-mixed combination the values of deformation energies were overestimated 17.20 kcal/mol.

Table2: The electron donor orbitals, electron acceptor orbitals and corresponding E$^{(2)}$ energies, distances and angles for head orientation.

Donor	Acceptor	d(Å)	Angle(°)	$E^{(2)}$ (kcal/mol)
Lp O47	BD*O154-H162	1.646	167.4	1.65
LpO69	N158-H169	2.162	166.7	3.33
LpO155	O47-H129	1.907	135.4	0.44
Lp O54	C150-H160	2.570	144.9	070
LpO154	C41-H124	2.326	167	1.42

The formation of hydrogen bonds in the geometry of mixed [B3LYP: HF] combination, and the energy of H-bond evaluated by E^2 energy of stabilization were obtained with NBO analysis.

Thus, the mixed ONIOM combination geometry form two intermolecular hydrogen bonding established between O47 as acceptor and H162 of H162-O154, the second as proton donor (O47-H129…O155) bond with interaction energies equal to 1.65, and 0.44 kcal, respectively. The third one is between O69 and N158-H169 with interaction energy $E^{(2)}$ equal to 3 kcal/mol.

Finally, regarding weak H-bond (C-H···O) one bond (O154···H124-C41) is detected in this geometry between oxygen atom O154 and hydrogen atom (H124) with energy equal to 1.42. However, a second weak H-bond (O54···H150-C167) established between the oxygen atom (O54) and a hydrogen atom (H150) of (C150-H167) bond. The energy of this bond (O54···H150-C167) is estimated equal to 0.70 kcal/mol.

Conclusion:

We studied dopamine/β-CD complex via ONIOM2 method using B3LYP density functional and two ONIOM combinations in order to find the most effective combination. The results were compared to those obtained with standard method [full B3LYP/6-31G (d)]. In point view of geometry, complexation and deformation energies of the complex and H-bond interactions, the mixed [B3LYP: HF] combination gave closer results than the not-mixed one in relative comparison with full DFT [B3LYP/6-31G (d)]. The most driving forces detected in this inclusion process are hydrophobic interactions (aromatic ring inside the cyclodextrin cavity) and hydrogen bond interactions between dopamine and β-CD.

REFERENCES

Bryan M. Wong. J. Comput.Chem. 2009, 30, 51.

Zhou, Y.; Liu, C.; Yu, H.; Xu, H.; Lu, Q.; Wang, L. Spectrosc. Lett. 2006, 39 (5), 409.

Jursic, B. S. Zdravkoxski, Z., and French, A. D. Mol. Struct. 1996, 366, 113.

Hohenberg, P. and Kohn, W. Phys. Rev. 1964, 136, B864.

Kohn, W. and Sham, L. Phys. Rev. 1965, 140, A1133.

Segall, M. Lindan, P. Probert, M. Pickard, C. Hasnip, P. Clark, S. and Payne, M. J. Phys. Condens. Matter. 2002, 14, 2717.

Liu, W. Karpov, E. Zhang, S. and Park, H. Comput. Methods Appl. Mech. Eng. 2004, 193, 1529.

Martin, R. Electronicn Structure: Basic Theory and Practical Methods (Cambridge University Press, 2004)

Capelle, K. Braz. J. Phys. 2006, 36, 1318.

Hafner, J. Wolverton, C., and Ceder, G. (GuestEditors), MRS Bull. 2006, 31.

Hafner, J. J. Comput. Chem. 2008, 29, 2044.

Froese, R.D.J.; Morokuma, K. Chem. Phys. Lett. 1996, 263, 393.

Dapprich, S.; Komromi, I.; Byun, K. S.; Morokuma, K. et Frisch, M. J. J. Mol. Struct. (THEOCHEM). 1999, 1, 461.

Holt, J. S . J. Mol. Struct. 2010, 965, 31.

Huang M.J., Quan Z. and Liu Y.M. Int. J. Quantum Chem, 2009; 109(1): 8.

Attoui Yahia , O., Khatmi .D.E. J. Mol. Struct: THEOCHEM 2009, 912, 38.

Benghodbane, S. Khatmi, D.E. J Incl. Phenom. Macrocycl. Chem. 2012.

Djemil, R. and Khatmi, D.E. Can. J. Chem. 2011, 89: 1519.

Lachi, N. Khatmi, D.E. and Djemil, R. C. R. Chimie 17 (2014) 1169–1175

Cui, H., Wu, L., Chen, J., Lin, X.: Multi-mode in situ spectroelectrochemical studies of redox pathways of adrenaline. J. Electroanal. Chem. 504, 195–200 (2001)

Izaoumen, N., Bouchta ,D., Zejli H.,. El Kaoutit ,M. et Temsmani ,K. R. Analytical lett, 1869-1885, 12 (2005).

Bouchta ,D. ; IZaoumen ,N.; Zejli, H.; El Kaoutit ,M.;. Tensamani ,K. R. Biosensors and Bioelectronics 20 2005.2228-2235

Yu ,Y; Cun-Xi, L; Zhi-Min ,L; Yan-Li ,L; Guo-Li ,S ; Ru-Qin, Y. Analytical lett V.37 N.11 2004.2267-2282

Wang Ge-Yun; Liu; Xiu-juan; Luo; Guo-An Wang; Zong-Hua.chineses .J. chem; 2005; 23; 297-302

Majewska, U. E.; Chmurski, K.; Biesiada, K.; Olszyna, A. R. et Bilewicz, R. Electroanalysis. 2006, 18, 1463.

Fragoso, A.; Almirall, E.; Cao, R.; Echegoyen, L. et Jonte, R. G. Chem. Commun. 2004, 19, 2230.

Dang, X.-J.; Nie, M.-Y.; Jian T. et Li, H.-L. J. Electroanal. Chem. 1998, 448, 61.

Danel, C.; Azaroual, N.; Brunel, A.; Lannoy, D.; Vermeersch, G.; Odou, P. and
Vaccher, C. J. Chromatogr. A 2008, 1215, 185.

Mrozek, J.; Banecki, B.; Sikorska, E.; Skwierawska, A.; Karolczak, J. et Wiczk, W.
Chem. Phys. 2008, 354, 58.

Tanji. Y, Wanzhi .W, Jinxiang.Z. Anal.Bioanal.chem 2006, 386.2087-2090.

Frisch, M.J.; Trucks, G.W.; Schlegel, H.B.; Scuseria, G.E.; Robb, M.A.; Cheeseman, J.R.; Montgomery, J.A.; Vreven, Jr., T.; Kudin, K.N.; Burant, J.C.; Millam, J.M.; Iyengar, S.S.; Tomasi, J. ; Barone, V. ; Mennucci, B. ; Cossi, M. ; Scalmani, G. ; Rega, N. ; Petersson, G.A.; Nakatsuji, H.; Hada, M.; Ehara, M. ; Toyota, K. ; Fukuda, R. ; Hasegawa, J. ; Ishida, M.; Nakajima, T.; Honda, Y.; Kitao, O.; Nakai, H.; Klene, M.; Li, X. ; Knox, J.E. ; Hratchian, H.P.; Cross, J.B.; Adamo, C.; Jaramillo, J.; Gomperts, R.; Stratmann, R.E.; Yazyev, O.; Austin, A.J.; Cammi, R.; Pomelli, C.; Ochterski, J.W.; Ayala, P.Y.; Morokuma, K.; Voth, G.A.; Salvador, P.; Dannenberg, J.J.; Zakrzewski, V.G.; Dapprich, S.; Daniels, A.D.; Strain, M.C.; Farkas, O.; Malick, D.K.; Rabuck, A.D.; Raghavachari, K.; Foresman, J.B.; Ortiz, J.V.; Cui, Q.; Baboul, A.G.; Clifford, S.; Cioslowski, J.; Stefanov, B.B.; Liu, G.; Liashenko, A.; Piskorz, P.; Komaromi, I.; Martin, D.J.; Fox, T.; Keith, M.A.; Al-Laham, C.Y.; Peng, A.; Nanayakkara, M.; Challacombe, R.L.; Gill, P.M.W.; Johnson, B.; Chen, W.; Wong, M.W.; Gonzalez, C. and Pople, J.A. Gaussian 03, Revariision E01, Gaussian, Inc., Pittsburgh, PA, 2003.

Stewart, J. J. P. J. MOPAC 2007; Stewart Computational Chemistry, Colorado Springs, CO, USA, 2007

Liu, L.; Guo, Q.X. J. Incl. Phenom. Macro. 2004, 50, 95.

Lundberg, M. Kawatsu, T. Vreven, T. Frisch M. J. and Morokuma, K. JCTC 5. 2009, 222.

Reed, A. E.; Curtiss, L. A.; Weinhold, F. Chem. Rev. 1988, 88, 899.

Glendening, E. D.; Reed, A. E.; Carpenter, J. E.; Weinhold, F. NBO Version 3.1.

EVALUATION OF FLOCCULANTS FOR THE RECOVERY OF CHAETOCEROS GRACILIS MICROALGAE

LETICIA PÉREZ, ROCÍO MACEIRAS, J. LUIS SALGUEIRO, ÁNGELES CANCELA, ÁNGEL SÁNCHEZ

Leticia Pérez, University of Vigo, Rocío Maceiras, Defense University Center, J. Luis Salgueiro, University of Vigo, Angeles Cancela, University of Vigo, Angel Sáchez, University of Vigo

Abstract

Microalgae are being considered an attractive alternative as a feedstock for biodiesel production. However, some previous steps for biodiesel production are necessary. The first step involves the harvesting of microalgae after their cultivation. There are several methods that can be applied in this step, such as: centrifugation, flocculation, filtration, gravity sedimentation or flotation.

Flocculation consists in the coalescence of dispersed microalgal cells to form large particles for settling. A large number of flocculants have been tested to induce flocculation of microalgae cells. The flocculants can be classified according their chemical compositions as follows: inorganic flocculants and organic flocculants or polyelectrolyte flocculants.

In this paper, the flocculation of Chaetoceros Gracilis microalgae with two type of flocculants (organic and inorganic) has been carried out. The used organic flocculants were: chitosan, agar-agar, calcium lactate, arabic gum and sodium alginate. The following inorganic salts were used: calcium chloride, copper sulphate, potassium hydroxide, potassium iodide, alum, aluminium chloride, ferric sulphate and ferric chloride. Different tests were carried out with the same flocculant concentration (200 mg/L) and with a total flocculation time of 510 min. For determining the influence of flocculants on the process, the microalgae was settled down by gravidity in absence of flocculant. The recovery efficiency was determined during the process in all experiences with the aim to establish the optimum period of sedimentation. The obtained results allow to conclude that $FeCl_3$ was the most suitable flocculant for this microalga achieving close to 100 % biomass recovery. Moreover, an economic analysis was done with the aim to choose the most appropriated flocculant from different points of view.

Keywords: microalgae; harvesting, inorganic flocculants, organic flocculants

Introduction

The growth of world population, the high price of fossil fuels and pollution derived from them are factors that require the search and development of new and clean sources of renewable energy. So, the European Union (EU) by Directive 2009/28/CE has defined ambitious climate and energy targets by 2020, known as the 20-20-20 targets, setting three key objectives: reduce greenhouse gas emissions by 20% from 1990 levels, a 20% improvement in the EU's energy efficiency and increase the share of renewable resources to 20% (Ribeiro, da Silva et al. 2015). In order to achieve this goal, numerous studies concerning the microalgae have been carried out due to the many benefits of these photosynthetic microorganisms. So, microalgal based biofuels show many economical and eco-friendly advantages (Barros, Gonçalves et al. 2015). A high growth and high lipid accumulation make them the ideal feedstock for biofuels production.

In recent years, microalgae have been widely studied for biodiesel production. Several stages are involved in the production process of this biofuel: culture, harvesting, dewatering, oil extraction and transesterification reaction. Effective microalgae harvesting with minimal cost and energy consumption is basic to achieve a profitable biodiesel production process.

The high costs involved in microalgal biomass recovery is one of the main problems for large-scale biodiesel production (Wan, Alam et al. 2015). Thus, low cost technologies are required to process the microalgae. In this line, flocculation of microalgae, which consists of removal of a low amount of biomass from a large volume of culture medium, is presented as the most promising harvesting method (Vandamme, Foubert et al. 2013).

In this study, a comparison of efficiency of different inorganic and organic flocculant agents in the recovery of Chaetoceros Gracilis marine microalgae was conducted. Tested flocculants included metal salts such as ferric chloride, aluminium chloride or copper sulphate among others. In addition, organic polymers like chitosan or sodium alginate were also proved. And finally, the economic analysis of harvesting process was performed.

Materials and methods

Microalgae and culture conditions

Chaetoceros Gracilis microalgae were obtained from the Culture Collection of Algae at ECIMAT (Estación de Ciencias Marinas de Toralla) belonging to University of Vigo. The microalga presents rectangular shape, is oval in cross section and it has flat ends. This centric diatom was cultured in 50 litres photobioreactor bag of polyethylene under artificial illumination with 17/7 light/dark cycle. Strain of Chaetoceros Gracilis microalgae were cultivated in a natural salinity water at a temperature of 21 °C for 8 days. The measured cells concentration once the culture was completed was 6.200 cells/microliter and its pH value was 7.95. All experiments carried out in this research were performed with cells from a single culture.

Goldmedium of Aqualgae was the culture medium used for Chaetoceros Gracilis microalgae and that consists on the mixture of two different macronutrients solutions. Solution A containing $NaNO_3$ and $NaH_2.PO_4{\cdot}2H_2O$, and Solution B containing Na_2-EDTA, $C_6H_5FeO_7$ (III), H_3BO_3, $MnCl_2.4H_2O$, $Na_2MoO_4.2H_2O$, $ZnCl_2$, Cr_2O_3, $CuSO_4.5H_2O$, $CoCl_2.6H_2O$, SeO_2. Vitamin: thiamine-HCl, cyanocobalamin, biotin.

Flocculants

Chemical flocculation is highly efficient for biomass removal. In recent years, many flocculating agents have been used for efficient harvest of different microalgae species. So, in this research chemical flocculation experiments to harvest Chaetoceros Gracilis marine microalgae were carried out. The flocculants used were grouped according to their chemical composition into inorganic and organic flocculants and the same dosage of 200 mg/L was used for all them. The inorganic flocculants employed were: calcium chloride, copper sulphate, potassium hydroxide, potassium iodide, alum, aluminium chloride, ferric sulphate and ferric chloride. On the other hand, the organic flocculants used were: chitosan, agar-agar, calcium lactate, arabic gum and sodium alginate. All these flocculants of analytical grade were provided locally.

Flocculation experiments

The effect of the flocculant type on harvest efficiency was determined using 1 L glass beakers. Each flocculant was directly added up to a final concentration of 200 mg/L, except for chitosan that it was previously dissolved in 10 millilitres of hydrochloric acid 0.1 molar and subsequently it was added to culture medium. Next, the microalgae suspension was severely mixed for 4 minutes at a stirring speed of 1000 rpm using HANNA HI 190M Magnetic Mini-Stirrer with the aim to distribute the coagulant through the water and to favour coagulation. Then, the suspension was slowly mixed for 1 minute at 100 rpm to induce the flocculation. Finally, when stirring stopped the biomass was allowed to settle down for eight and half hours at room temperature. All experiments were done in duplicates each time.

The absorbance of microalga in all experiences was measured at 680 nm using a spectrophotometer Spectro 22 (Labomed, USA) at the following times: 0, 5, 10, 15, 20, 30, 40, 50, 60, 90, 120, 150, 210, 270, 330, 390, 450, and 510 minutes. Based on the difference in absorbance between the initial Chaetoceros Gracilis suspension and the absorbance measured at each of the times listed above, biomass recovery percentage was calculated according to the following equation (Gerde, Yao et al. 2014):

$$\%\ \mathbf{Biomass\ Recovery} = \left(\mathbf{1} - \frac{\mathbf{Sample\ absorbance}}{\mathbf{Initial\ absorbance}}\right)\ \mathbf{x\ 100} \qquad (1)$$

So, biomass recovery percentage represents the efficiency of flocculation process for Chaetoceros Gracilis microalgae.

Results and discussion

Algae sedimentation

In order to optimize the flocculation of Chaetoceros Gracilis microalga, sedimentation experiments with this microalgae individually were conducted. Thus, these control experiments were performed as reference.

As shown in Figure 1, in the natural sedimentation experiments performed, no significant sedimentation of C. Gracilis was discovered. The marine microalgae cells exhibited difficulty to form an agglomerate by itself without addition of any flocculant. Only a recovery close to 7% was obtained. These data suggest that the addition of a coagulant is needed to promote flocs formation and to enable an efficient recovery of alga studied. Stable suspensions of microalgae cells can be achieved by addition of flocculating agents to facilitate the neutralization of the negatively charged surface of microalgae (Brady, Pohl et al. 2014).

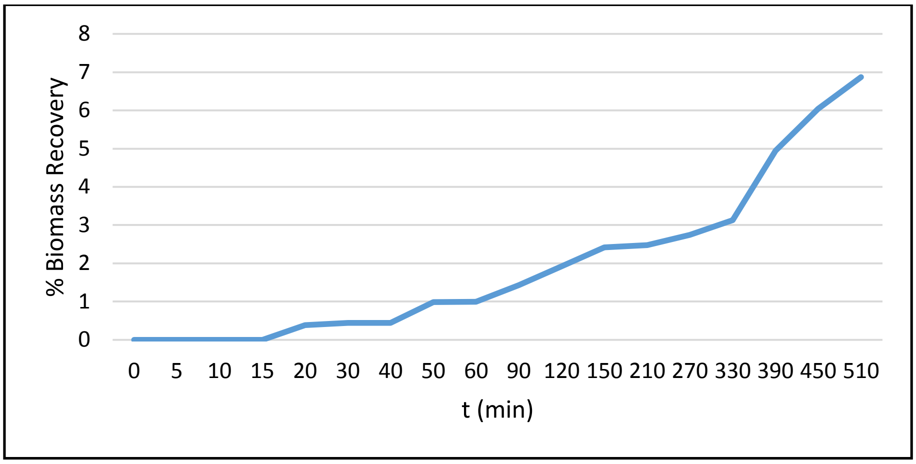

(A)

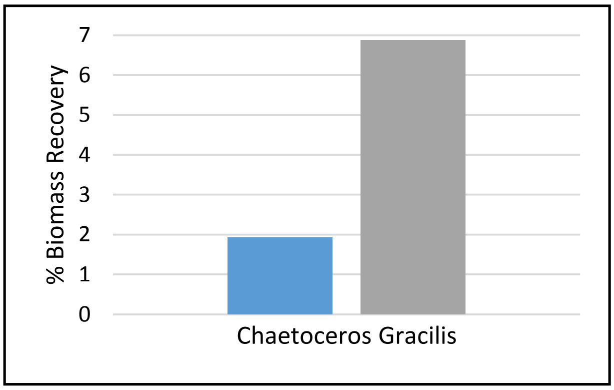

(B)

Figure 11. % Biomass recovery for Chaetoceros Gracilis microalgae: (A) along time, (B) at 120 minutes and 510 minutes. Where:

🟦t=120 min ▨ t=510 min

Flocculation experiments

Inorganic flocculants

The effect of eight inorganic flocculants on microalgal flocculation was studied at room temperature. Biomass recoveries higher than 95% were obtained when the suspension of Chaetoceros Gracilis was mixed with ferric chloride and aluminium chloride (metal salt). In addition, good biomass removal (70%) were reached using another ferric salt, ferric sulphate.

These biomass recovery values were similar to those obtained by Chen, Wang et al. (2013) with ferric chloride dose of 150 mg/L to harvest Scenedesmus sp. For their part, Sanyano, Chetpattananondh et al. (2013) accomplished a full recovery of Chlorella sp. biomass with 143 mg/L of ferric chloride in just 40 minutes. Pirwitz, Rihko-Struckmann et al. (2015) also achieved a very high flocculation efficiency (90-97%) for Dunaliella Salina marine microalgae when ferric chloride or aluminium chloride were used as coagulants in a dose of 1 mM.

Thus, the data obtained in this research and those obtained by other authors suggest that both ferric chloride and aluminium are two highly efficient flocculants, even in a short time, that accomplish almost total recovery of algal biomass existing in the culture medium.

The high efficiency of harvesting process reached can be explained as the interaction and neutralization of negatively charged cells through the cations released by the metal salts when they are hydrolysed. These mechanisms are basic to attain the flocs formation and get a good coagulation process (Renault, Sancey et al. 2009).

This study revealed that alum, calcium chloride, copper sulphate, potassium hydroxide and potassium iodide were not suitable for harvesting C. Gracilis marine microalgae. Very low biomass recoveries were obtained by

these inorganic flocculants (around 10 to 15%). Nevertheless, high flocculating ability was shown by calcium chloride and alum in other studies conducted by other authors (Kim, La et al. 2011, Uduman, Qi et al. 2010).
Recoveries attained confirm that chemical flocculation is efficiently induced using appropriate inorganic flocculants, and flocs formation is achieved.

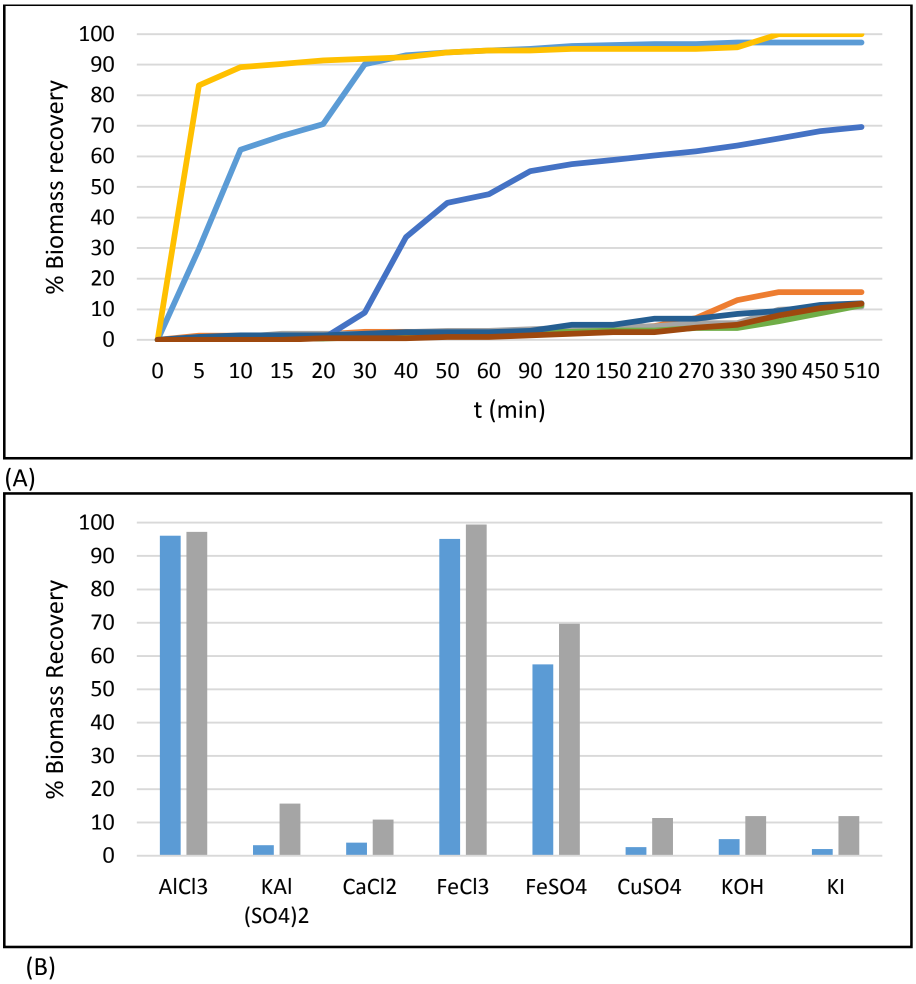

Figure 12. % Biomass recovery for different inorganic flocculants used: (A) along time, (B) at 120 minutes and 510 minutes. Where:

🟦$AlCl_3$ 🟧 $KAl(SO_4)_2$ ⬜$CaCl_2$ 🟨 $FeCl_3$ 🟦 $FeSO_4$ 🟩 $FeCl_3$ 🟦 KOH 🟫 KI
🟦 t=120 min ⬜ t=510 min

Organic flocculants
In comparison with the common chemical flocculants, bioflocculants are safer, cleaner and they do not produce environmental pollution. For this reason, organic flocculants were tested in this study.
According to data shown in Figure 3, all organic flocculants proved, except chitosan, showed an efficiency of flocculation process equal or lower than 12%. The highest biomass recovery (23%) was obtained using chitosan. This polysaccharide presents valuable properties such as high density of cationic charge, long polymeric chains or biodegradability that make it an efficient coagulant agent (No, Meyers 2000). However, in this research biomass recovery values were very low in contrast with those obtained by Rashid, Rehman et al. (2013) with 92% of Chlorella Vulgaris biomass removal with a lower dose of chitosan than that used in this research (120 mg/L).
By other hand, when calcium lactate or arabic gum were used as flocculant agents a recovery obtained was similar to the values achieved without addition of the flocculant (data shown in Figure 1). These results argue that both organic flocculants should not apply to flocculation of Chaetoceros Gracilis marine microalgae.
It is important to note that, the advantage of this type of flocculants in comparison with other inorganic compounds applied is that it does not require the subsequent descontamination of culture medium and therefore avoids additional costs and prevents undesired contaminations.

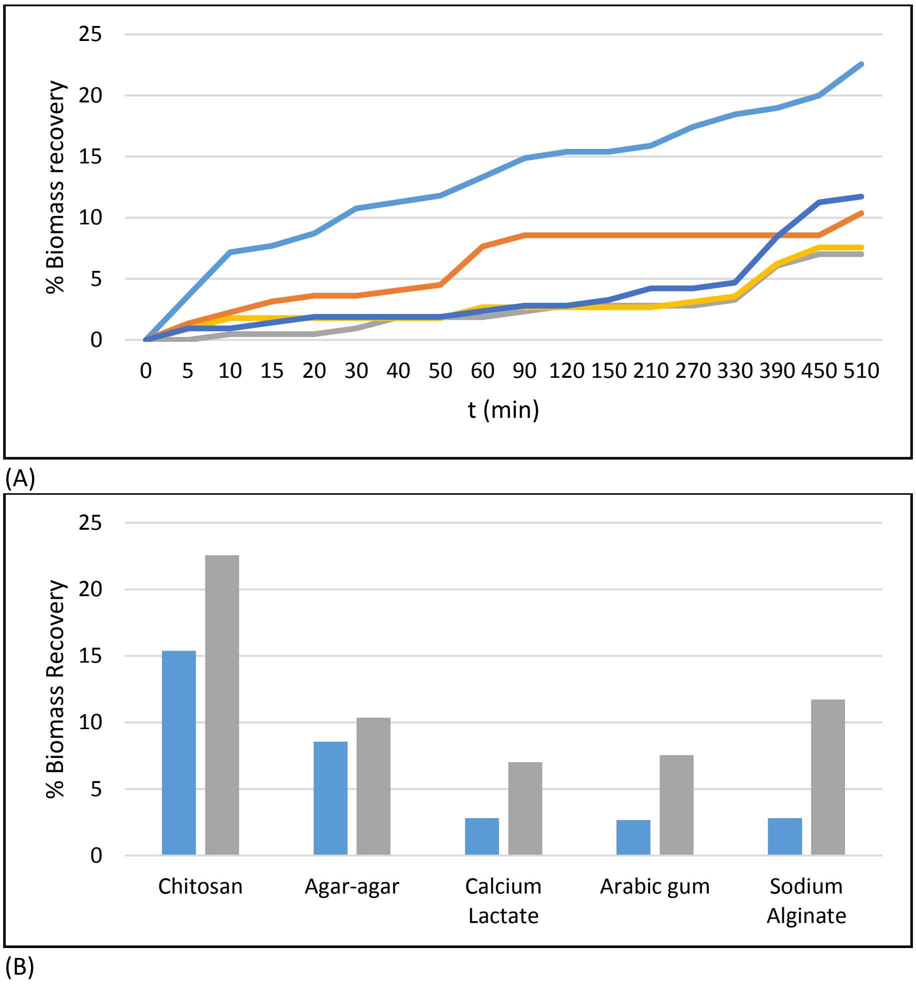

Figure 13. % Biomass recovery for different organic flocculants used: (A) along time, (B) at 120 minutes and 510 minutes. Where:

🟦Chitosan 🟧 Agar-agar ⬜ Calcium lactate 🟨 Arabic gum 🟦 Sodium alginate
🟦 t=120 min ⬜ t=510 min

Economic analysis of harvesting process

Cost of flocculation technique for harvesting microalgae is an important factor to take into consideration (Vandamme, Foubert et al. 2013). Therefore, an economic analysis of the different used flocculants has been carried out.

In this study, an only dose of 200 mg/L of several types of flocculants (five organics and eight inorganics) was employed. However, the biomass recovery efficiency of Chaetoceros Gracilis microalga was very different.

In order to estimate the cost of processing per litre of culture broth of each type of flocculant, the equation 2 is proposed considering the dose of flocculant used (200 mg/L) and the flocculation efficiency achieved in each case (% biomass recovery). Table 1 presents the percentage of algal biomass recovered in the preceding sections according to the different types of flocculating agents tested. In addition, prices of flocculants used are shown.

Cost (€/L) = Flocculant dose (g/L) x Flocculant price (€/g) x (100/%Biomass recovery) (2)

INORGANIC FLOCCULANT	% Biomass recovery	Flocculant price (€/kg)	ORGANIC FLOCCULANT	% Biomass recovery	Flocculant price (€/kg)
Aluminium chloride	97.3	24.16	Chitosan	22.6	520.60
Alum	15.6	8.90	Agar-Agar	10.4	104.00
Calcium chloride	10.9	8.93	Calcium Lactate	7.0	14.28

Ferric chloride	99.5	13.66	Arabic gum	7.6	56.50
Ferric sulphate	69.6	33.50	Sodium alginate	11.7	18.50
Copper sulphate	11.4	23.20			
Potassium hydroxide	11.9	10.62			
Potassium iodide	11.9	144.00			

Table 1. % Biomass recovery for different organic and inorganic flocculants used at 510 minutes and their prices.

Table 2 presents the associated costs to the harvesting process obtained with equation 2. Considering the obtained results, it can be said that ferric chloride is the cheapest coagulant agent employed to harvest biomass cells of marine microalgae Chaetoceros Gracilis. This inorganic flocculant exhibited high capacity for removal biomass under marine conditions (97%). Furthermore, it presents a competitive price compared with other inorganic flocculants such as aluminium chloride or ferric sulphate. Thus, processing for example 1000 litres of culture broth, an efficient biomass recovery would take place with only 2 g of $FeCl_3$ and an associated cost of 2.7 €. Nevertheless, the cost would be almost double (5€ per litre) if $AlCl_3$ was used to form aggregates and conduct to flocs formation.

FLOCCULANT TYPE	INORGANIC FLOCCULANT	ORGANIC FLOCCULANT	COST (€/L)
Ferric chloride	X		0.0027
Aluminium chloride	X		0.0050
Ferric sulphate	X		0.0096
Alum	X		0.0114
Calcium chloride	X		0.0164
Potassium hydroxide	X		0.0178
Sodium alginate		X	0.0316
Copper sulphate	X		0.0407
Calcium Lactate		X	0.0408
Arabic gum		X	0.1487
Agar-Agar		X	0.2000
Potassium iodide	X		0.2420
Chitosan		X	0.4607

Table 2. Harvesting process cost per liter of culture broth.

These inorganic flocculants are widely used because of its high effectiveness, low cost and ease to use. However, the toxicity associated with them is being increasingly questioned. For these reasons, the use of flocculants environmentally friendly such as chitosan or sodium alginate is growing. In this way and based on the obtained data in this research, the yield reached in harvesting process is lower than that achieved by inorganic flocculants and their cost is much higher. For example, in the case of sodium alginate would be necessary assign 31.6 € to process 1.000 litres of algal culture. Twelve times more that using ferric chloride.

Thus, metal salts would be the most effective in the harvesting of Chaetoceros Gracilis cells from an economic point of view. In contrast, from an environmental standpoint, organic flocculants would be more suitable. Therefore, processing large amounts of algal culture are necessary for large-scale biodiesel production. Just like that, a good choice of coagulant agent can greatly reduce the costs associated with harvesting process. Consequently, an economic biofuels production could be managed.

Conclusions

The choice of the type of flocculant agent to use in harvesting process depends on the species of microalgae, its biomass recovery efficiency and the associated costs and derivative pollution. In this research, the flocculation efficiencies of Chaetoceros Gracilis microalgae using organic flocculants were much lower than in the case of inorganic flocculants.

The results displayed on this paper have demonstrated that metal salts of iron and aluminium (FeCl3 and AlCl3) are a suitable candidates to flocculate and harvest the centric diatom Chaetoceros Gracilis cultured under marine conditions. Thus, the interaction with the negatively charged surface cells was more effective in the case of metalic cations of iron or aluminium that in the case of positively charged polymers as chitosan. Thus, from an economic point of view, FeCl3 is the cheapest and most efficient metal salt to removal Chaetoceros Gracilis biomass.

References

BARROS, A.I., GONÇALVES, A.L., SIMÕES, M. and PIRES, J.C.M., 2015. Harvesting techniques applied to microalgae: A review. Renewable and Sustainable Energy Reviews, 41, pp. 1489-1500.

BRADY, P.V., POHL, P.I. and HEWSON, J.C., 2014. A coordination chemistry model of algal autoflocculation. Algal Research, 5, pp. 226-230.

CHEN, L., WANG, C., WANG, W. and WEI, J., 2013. Optimal conditions of different flocculation methods for harvesting Scenedesmus sp. cultivated in an open-pond system. Bioresource technology, 133(0), pp. 9-15.

GERDE, J.A., YAO, L., LIO, J., WEN, Z. and WANG, T., 2014. Microalgae flocculation: Impact of flocculant type, algae species and cell concentration. Algal Research, 3, pp. 30-35.

KIM, D., LA, H., AHN, C., PARK, Y. and OH, H., 2011. Harvest of Scenedesmus sp. with bioflocculant and reuse of culture medium for subsequent high-density cultures. Bioresource technology, 102(3), pp. 3163-3168.

NO, H.K. and MEYERS, S.P., 2000. Application of chitosan for treatment of wastewaters. Rev Environ Contam Toxicol., 163, pp. 1-27.

PIRWITZ, K., RIHKO-STRUCKMANN, L. and SUNDMACHER, K., 2015. Comparison of flocculation methods for harvesting Dunaliella. Bioresource technology, 196, pp. 145-152.

RASHID, N., REHMAN, S.U. and HAN, J., 2013. Rapid harvesting of freshwater microalgae using chitosan. Process Biochemistry, 48(7), pp. 1107-1110.

RENAULT, F., SANCEY, B., BADOT, P.-. and CRINI, G., 2009. Chitosan for coagulation/flocculation processes – An eco-friendly approach. European Polymer Journal, 45(5), pp. 1337-1348.

RIBEIRO, L.A., DA SILVA, P.P., MATA, T.M. and MARTINS, A.A., 2015. Prospects of using microalgae for biofuels production: Results of a Delphi study. Renewable Energy, 75, pp. 799-804.

SANYANO, N., CHETPATTANANONDH, P. and CHONGKHONG, S., 2013. Coagulation–flocculation of marine Chlorella sp. for biodiesel production. Bioresource technology, 147(0), pp. 471-476.

UDUMAN, N., QI, Y., DANQUAH, M.K., FORDE, G.M. and HOADLEY, A., 2010. Dewatering of microalgal cultures: A major bottleneck to algae-based fuels. Journal of Renewable and Sustainable Energy, 2(1),.

VANDAMME, D., FOUBERT, I. and MUYLAERT, K., 2013a. Flocculation as a low-cost method for harvesting microalgae for bulk biomass production. Trends in biotechnology, 31(4), pp. 233-239.

WAN, C., ALAM, M.A., ZHAO, X., ZHANG, X., GUO, S., HO, S., CHANG, J. and BAI, F., 2015. Current progress and future prospect of microalgal biomass harvest using various flocculation technologies. Bioresource technology, 184(0), pp. 251-257.

DEFECTS EVOLUTION IN CVD ZINC CHALCOGENIDES AT DOPING PROCESS BY TRANSITION METALS

EUGENI GAVRISHUK, VLADIMIR IKONNIKOV, DMITRY SAVIN, ELENA MOZHEVITINA, ROMAN AVETISOV

Abstract

At a present time a development of effective media for tunable solid-state diode-pumped lasers is one of the most actual problems of laser physics and optical materials technology. Lasers based on zinc chalcogenides doped with chromium and iron are of great scientific and practical interest, due to their compact size, wide range of adjustment, and the ability to operate at room temperature. Comparing with zinc selenide, zinc sulfide matrix has a number of potential advantages that may facilitate obtaining outstanding characteristics for ZnS:Cr(Fe) lasers.

Of all the known methods for producing of A2B6 crystals doped by transition metal a diffusion technique is the most popular due to the opportunities of precision doping. It is very promising to carry out the diffusion process under barothermal impact using a hot isostatic pressing (HIP), which is a technique of simultaneous exposure of high temperatures (up to 1500ºC) and high pressures (up to 200 MPa) in order to change material properties. Application of HIP-treatment enables to increase the temperature of the diffusion process in comparison with annealing at atmospheric pressure. Another most important consequence of the HIP-treatment is a change of the defect structure of the samples.

The research was supported by the Russian Science Foundation grant N 15-13-10028

The goal of the research was to study the effect of Fe (Cr) doping during a HIP-treatment on a defects evolution in zinc chalcogenides obtained by CVD technique. In the investigation of transmission spectra, it was determined that during the HIP process we carried out an efficient doping of chalcogenides of zinc by divalent iron ions of chromium, and at the same time while in the ZnS decreased the number of bulk defects. This resulted to radiation scattering in a short wavelength region.

X-ray diffractometry and original extraction technique made it possible to analyze a samples nonstoichiometry. It was found out that for as-grown CVD samples of ZnS and ZnSe a deviation from stoichiometry was about 10-3-10-4 mol.%. The HIP processing of the samples decreased the nonstoichiometry up to 10-6-10-7 mol.%.

The purity of the samples was analyzed by ICP-MS and SIMS techniques before and after doping. The total impurity level was less than 10-5 wt.%. However the HIP-treatment decreased this value in one order due to hardware materials pollutants. Studies of the luminescence in 2-5 microns range revealed that the samples were perspective as laser materials.

Thus, in the process of doping with zinc chalcogenides the HIP-treatment results in a reduction of the concentration of volume, structural, and point defects affecting the material properties and improved their stoichiometry. The impurities from the hardware materials have no appreciable effect on the optical characteristics of the samples.

NEW FLUORESCENT HYBRID MATERIALS BASED ON Eu-COMPLEXES IN OXYFLUORIDE GLASS AND GLASSCERAMIC MATRIX

OLGA PETROVA, ILYA TAYDAKOV, MARİA ANUROVA, ALİNA AKKUZİNA, ROMAN AVETİSOV, ANDREW KHOMYAKOV, IGOR AVETİSSOV

Olga Petrova, PhD, Ilya Taydakov, PhD, Maria Anurova, Alina Akkuzina, Roman Avetisov, PhD, Andrew Khomyakov, Igor Avetissov Prof.,
D. Mendeleyev University of Chemical Technology of Russia

Abstract

The hybrid materials were synthesized using a high temperature reaction. We used $80PbF_2$-$20B_2O_3$ glass as an inorganic matrix and various phenanthroline complexes europium (III) - as organic phosphors. The photoluminescence spectra of hybrid materials were measured just after synthesis and after heat treatment. We suggested that an exchange reaction between a Eu-complex and a glass matrix had occurred.

Introduction

Hybrid materials (HM) based on metal-organic phosphors and inorganic glasses are promising materials for developing of new light emitting devices (Lebeaua and Innocenzi 2011, Avetisov, et al., 2014, Petrova et al., 2015). Organic luminescent materials are highly efficient under optical and electric excitation. However, most of them are extremely unstable in air and need protection. An embedding of organic materials into transparent matrices may solve the degradation problem and lead to the creation of new materials. Inorganic glass matrices are stable at higher temperatures than organic polymers, lacquers and compounds, and their thermal expansion coefficients are less than those of organic matrices. In general, glasses are characterized by a high hardness and chemical resistance, as well as a resistance to radiation (especially UV).

In our previous research concerning the fabrication of bulk and film hybrid materials, we considered boron oxide (Avetisov, et al., 2014, Petrova, et al., 2015) as a glass matrix. However, boron oxide is not an ideal candidate for application as a glass matrix: its melt viscosity at 400–500 °C is very high (~2×10^4 Pa·s), and its chemical resistance is insufficient. We made glasses in the PbF_2–B_2O_3 system in the 25-80 mol % PbF_2 composition range (Rao, Baskaran and Kumar, 2013, Courrol, et al., 2003). These glasses have lower melting temperatures and melts viscosities.

Experimental

Different methods of preparation of europium (III) complexes have been described (Yu, et al., 2011, Fernandes, et al., 2005). Syntheses of organic ligands were carried out according to a slightly modified procedure (Taydakov and Krasnoselskiy, 2011, Li, Yan and Yang, 2008) using dichloromethane as a solvent.

The glasses were synthesized of 10 g batches using PbF2, B2O3, and EuF3 as initial materials (99.99 wt.% purity grade for all). Syntheses were conducted at 850–900 °C during 0.25 to 0.5 h in closed corundum crucibles. The melt was poured into a steel mold. To compare HM properties, we synthesized the 79 PbF_2-20 B_2O_3-1 EuF_3 glass as a standard. At synthesis up to 50% of the fluorine volatilized from melt and up to the 10 wt.% of aluminum oxide had been dissolving in glass.

The HM’s were synthesized using a high temperature reaction of lead fluoroborate glass melt with organo-metallic phosphors in corundum crucibles at the 500-600°C during 30 seconds at melt stirring. The samples were obtained by rapid cooling in a steel mold. The produced HM’s were shaped as transparent yellowish glassy plates without visible bubbles and trace inclusions.

A heat treatment of samples was performed in several temperature–time regimes at temperatures above T_g and various durations from 0.5 to 4 h. Scanning Electron microscopy (SEM, Tescan VEGA3-LMU) equipped with a detector for energy-dispersive spectroscopy (EDS Oxford Instruments X-MAX-50) and AZTec software were used for data gathering and processing. The glass and HM’s were analyzed by SEM-EDX with a beam energy of 30 KeV after surface carbonization.

The transmission spectra of glasses and HM's were studied using a UNICO 2800 (UV/VIS) spectrophotometer in the 200-1100 nm range.

A Fluorolog FL3-22 spectrofluorimeter (Horiba Jobin Yvon) with double-grating excitation and emission monochromators was used for luminescence measurements of the inorganic glass, organic phosphors Eu (III) complexes, synthesized HM's and HM's after a heat treatment (the 400 to 700 nm wavelength range with the 0.1 nm step). PL was excited by a pulsed diode laser (λ = 370 nm, Δτ = 1.5 ns). All of the luminescence measurements were carried out at room temperature.

Results and dıscussıon

To produce HM's we used different asymmetric organic phosphors phenanthroline based Eu (III) complexes (Table 1).

Photoluminescence (PL) spectra of Eu-complexes demonstrated narrow lines in the red spectrum range with maximum at λ=611 nm corresponding to the $^5D_0 \rightarrow {}^7F_2$ transition in Eu^{3+}ion (Fig. 1).

All the obtained complexes contained Eu^{3+} ion in an asymmetric position. This resulted to the higher PL intensity of a hypersensitive electron-dipole $^5D_0 \rightarrow {}^7F_2$ transition in contrast with a $^5D_0 \rightarrow {}^7F_1$, transition. The ratio of the intensities is as high as 20-30. The $^5D_0 \rightarrow {}^7F_0$ band was not splitted which proved a phase purity of the analyzed complexes (Weber, 1967).

An easy melting $80PbF_2$-$20B_2O_3$ glass was used as a glassy matrix for HM's creation. It is proved that the phosphor powders have the brightest luminescence lines. In the cases of the glass and HM's PL lines are significantly broadened comparing with powder phosphors. The broadening is attributed to a formation of several luminescence centers with similar structures. HM's demonstrated PL with varying intensities in the range of emission colors from red to green. The PL spectra of the HM's based on fluoro-substituted Eu-complexes (Fig. 2 lines 1, 2) had a distinguished line of Eu^{3+} ion transition (λ_{max}=611 nm), but for the HM's based on a naphthyl ligand (Fig. 2 lines 3, 4), the PL in the short-wave part (λ=400-580 nm) was more intense (Fig. 2).

We have assumed that there is an exchange reaction which accompanied by a partial decomposition of the organic complexes. The similar reaction was described in (Petrova, et al., 2015) for the HM based on tris(8-hydroxyquinoline) aluminum (Alq_3) with boron oxide. During the reaction Eu^{3+} ions embedded into a glass matrix and this causes the reduction of the PL intensity to values typical for inorganic glasses doped by Eu^{3+} ion. Simultaneously, the ligands were bonding into complexes with Pb^{2+} ions.

N	Phosphor	Abbreviation	Structures of complexes
1	4,4,5,5,6,6,7,7,8,8,9,9,9-tridecafluoro-1-(1-methyl-1H-pyrazol-4-yl) nonane-1,3- dionato-(1,10-phenanthroline) europium	**Eu(L^2)$_3$ (Phen)**	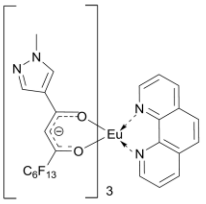
2	4,4,5,5,6,6,6-heptafluoro-1-(1-methyl-1H-pyrazol-4-yl)hexane-1,3- dionato-(1,10-phenanthroline) europium	**Eu(L^1)$_3$ (Phen)**	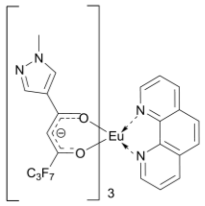
3	Tris(4,4,4-trifluoro-1-(2-naphthyl) butane-1,3-dionato-(4,7-diphenyl-1,10-phenantroline) europium	**Eu(NTA)$_3$ (Bath)**	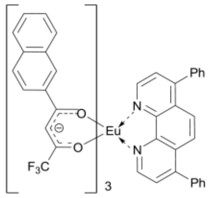
4	Tris(4,4,4-trifluoro-1-(2-naphthyl) butane-1,3-dionato-(1,10-phenanthroline) europium	**Eu(NTA)$_3$ (Phen)**	

Table 1. Structures and abbreviations of metal-organic phosphors used for HM's preparation.

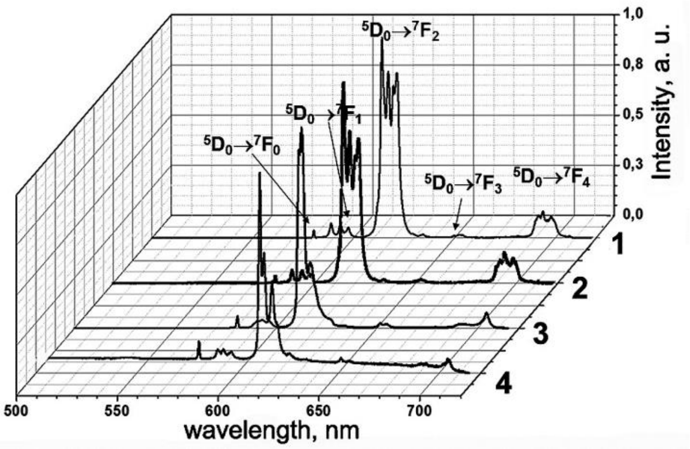

Figure 1. PL spectra of pure crystalline powder Eu(III) complexes (figures correspond to the sample numbers in Table 1).

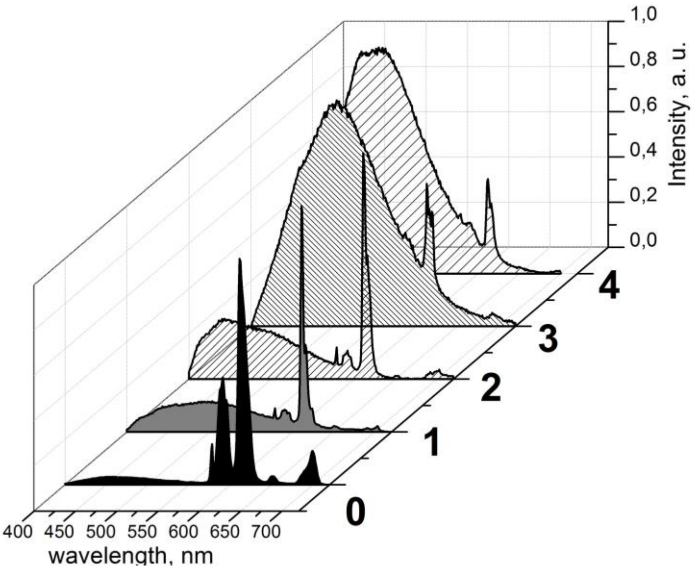

Figure 2. PL spectra of as-synthesized 79PbF$_2$-20B$_2$O$_3$-1EuF$_3$ glass (0) and HM's (1–4) (figures correspond to the sample numbers in Table 2).

N	Composition	Maximum peak wavelength, nm	Chromaticity coordinates (CIE)
0	79PbF$_2$-20B$_2$O$_3$-1EuF$_3$	612	X=0,5498 Y=0,3427
1	80PbF$_2$-20B$_2$O$_3$ + Eu(L^2)$_3$(Phen)	611	X=0,3476 Y=0,3272
2	80PbF$_2$-20B$_2$O$_3$ + Eu(L^1)$_3$(Phen)	611	X=0,2938 Y=0,2630
3	80PbF$_2$-20B$_2$O$_3$ + Eu(NTA)$_3$(Bath)	504	X=0,2592 Y=0,3749
4	80PbF$_2$-20B$_2$O$_3$ + Eu(NTA)$_3$(Phen)	480	X=0,2054 Y=0,2769

Table 2. Photo luminescent properties of the glass and hybrid materials.

The HM based on the Pb complex demonstrates more intense PL. The Pb complexes with similar ligands had been described in (Marandi et al., 2008, Marandi et al., 2010), but the spectral-luminescent properties of these compounds were not studied. The Pb-complex formation has been confirmed by PL peak's positions which cannot be attributed to transitions between the levels of the individual ligands (Eremina et al., 2008) or Eu^{2+} ion PL in a glass (Dorenbos, 2003).

A heat-treatment resulted to a partial crystallization of a glass matrix and changing of a PL spectrum (Fig.3). We observed the presence of a wide band and changing in the Eu^{3+} ion line position. The latter shifted from 611-612 nm ($^5D_0 \rightarrow {}^7F_2$) for the case of glass or organic ligands with non-centrosymmetric fields to 580 nm ($^5D_0 \rightarrow {}^7F_1$) for the case of cubic crystallites Pb$_{(1-x)}$Eu$_x$F$_{2+x}$ having a centrosymmetric crystalline field.

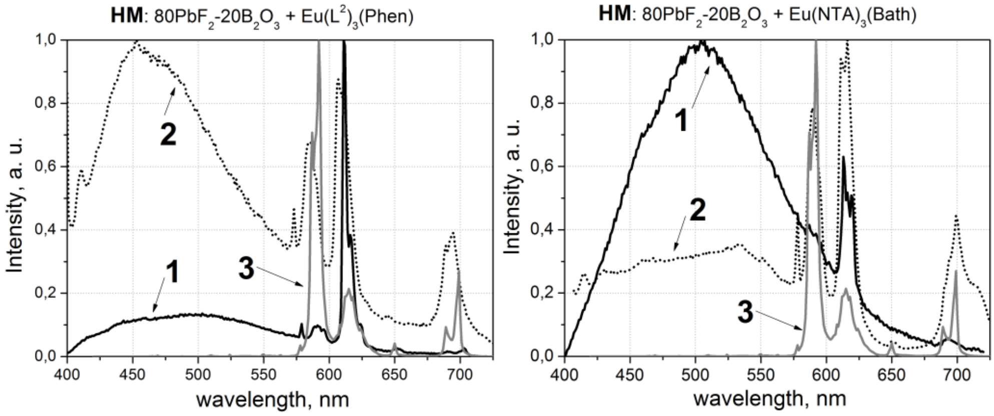

Figure 3. PL spectra of HM's: 1 – HM as-synthesized, 2 – HM after heat-treatment on 400°C, 2 hours, 3 – polycrystalline $Pb_{(1-x)}Eu_xF_{2+x}$.

Change the environment, and, accordingly, the symmetry of the Eu^{3+} ion can be detected by monitoring of the ratio of the PL intensities of hypersensitive $^5D_0 \rightarrow {}^7F_2$ and weakly sensitive $^5D_0 \rightarrow {}^7F_1$ transitions (Table. 3).

The luminescent material	PL intensities ratio $I(^5D_0 \rightarrow {}^7F_2) / I(^5D_0 \rightarrow {}^7F_1)$
Phosphor $Eu(NTA)_3(Bath)$	31,5
HM as-synthesized 80 PbF_2- 20 B_2O_3 +$Eu(NTA)_3(Bath)$	9,3
HM after heat-treatment 80 PbF_2- 20 B_2O_3 +$Eu(NTA)_3(Bath)$	1,6
Phosphor $Eu(C_6F_{13}Pyr)_3(Phen)$	20,1
HM as-synthesized 80 PbF_2- 20 B_2O_3 + $Eu(C_6F_{13}Pyr)_3(Phen)$	10,7
HM after heat-treatment 80 PbF_2- 20 B_2O_3 + $Eu(C_6F_{13}Pyr)_3(Phen)$	1,3
Glass 79 PbF_2 – 20 B_2O_3 – EuF_3	2,1
Glass after heat-treatment 79 PbF_2 – 20 B_2O_3 – EuF_3	1,6
Polycrystalline $Pb_{0.95}Eu_{0.05}F_{2.05}$	0,2

Table 3. PL intensities ratio for $^5D_0 \rightarrow {}^7F_2$ and $^5D_0 \rightarrow {}^7F_1$ transitions.

The Eu environment in the metal complex is non-centrosymmetrical. In the case of HM's symmetry increases and a still more increase is observed in the case of partially crystallized HM's. Most likely, this is due to an intrinsic crystallization of a fluoride cubic phase containing Eu. This trend confirms our hypothesis that the Eu ions are moving from the organic ligand's field into a glass matrix field and at a further heat treatment they are embedding into a crystalline phase. Ligands bind with glass components and stay in the glass.

Conclusions

We developed a synthesis technique for new luminescent materials by conducting a high-temperature exchange reaction between an inorganic glass matrix and organic complexes.

Acknowledgments

The research was financially supported by the Russian Science Foundation (grant N 14-13-01074).

References

Lebeaua, B., Innocenzi, P. Hybrid materials for optics and photonics. // Chem. Soc. Rev., (2011), V. 40, pp. 886–906

Avetisov, R., Petrova, O., Khomyakov, A., Mushkalo, O., Akkuzina, A., Cherednichenko, A., Avetissov, I. Organic luminophor metal complex in inorganic glass matrix—A new hybrid material // J. Cryst. Grow. (2014) V. 401, pp. 449-452.

Petrova, O.B., Avetisov, R.I., Khomyakov, A.V., Saifutyarov, R.R., Akkuzina, A.A., Mozhevitina, E.N., Zhukov, A.V., Avetissov, I.Ch. Prospective Electroluminescent Hybrid Materials // Eur. J. Inorg. Chem. (2015) V. 2015, №7, pp. 1269–1274.

Rao, R., Baskaran, G.S., Kumar, R.V. Influence of sesquioxides on fluorescence emission of Yb^3 ions in $PbO–PbF_2–B_2O_3$ glass system // J. Non-Cryst. Sol. (2013) V. 378, pp. 265-272.

Courrol, L.C., Kassab, L.R.P., Cacho, V.D.D., Tatumi, S.H., Wetter, N.U. Lead fluoroborate glasses doped with Nd^{3+} // J. Lumin. (2003), V. 102–103, pp. 101-105.

Taydakov, I.V., Krasnoselskiy, S.S. Modified method for the synthesis of isomeric N-substituted (1H-pyrazolyl)propane-1,3-diones // J. Het. Chem. (2011), V. 47, № 6, pp. 695-699.

Li, Y., Yan, B., Yang, H. Construction, Characterization, and Photoluminescence of Mesoporous Hybrids Containing Europium(III) Complexes Covalently Bonded to SBA-15 Directly Functionalized by Modified β-Diketone // J. Phys. Chem. C (2008), V. 112, № 10б pp. 3959- 3968..

Yu, J., Deng, R., Sun, L., Li, Z., Zhang, H. Photophysical properties of a series of high luminescent europium complexes with fluorinated ligands //J. Lum. (2011), V. 131, pp. 328-335.

Fernandes, J.A., Ferreira, R.A.S., Pillinger, M., Carlos, L.D., Jepsen, J., Hazel,l A., Ribeiro-Claro, P., Goncalves, I.S. Investigation of europium(III) and gadolinium(III) complexes with naphthoyltrifluoroacetone and bidentate heterocyclic amines //J. Lum. (2005), V. 113, № 1-2, pp. 50-63.

Weber, M. J. 1966. Relaxation processes for exited stated of Eu^{3+} in LaF_3. In: Crosswhite, H. M., Moose, H. W., Eds. 1967; Optical properties of ions in crystals. Interscience: New York, pp. 467-484.

Marandi, F., Asghari-Lalami, N., Ghorbanloo, M., Mcardle, P. Pb-II 4,4,4-trifluoro-1-naphthyl-1,3-butanedione complexes of 1,10- phenanthroline and 2,2 '-bipyridine ligands// J. Coord. Chem. (2008) V. 61, № 10, pp. 1545-1552.

Marandi, F., Rutvand, R., Rafiee, M., Goh, J.H., Fun, H.-K. Synthesis, properties and crystal structures of new binuclear lead(II) complexes based on phenyl, naphthyl-containing fluorine в-diketones and substituted 2,2’-bipyridines // Inorg. Chim. Acta. (2010) V. 363, pp. 4000–4007.

Eremina, N.S., Degtyarenko, K.M., Gadirov, R.M., Kopylova, T.N., Mayer, G.V., Samsonova, L.G., Meshkova, S.B., Topilova Z.M. Photo and electroluminescence of Eu(III) and Tb(III) coordination compounds in thin polyvinylcarbazole films // Rus. Phys. Jour. (2011) V. 53, № 12, pp. 1223-1228.

Dorenbos, P. Energy of the first $4f^7$-$4f^65^d$ transition of Eu^{2+} in inorganic compounds // J. Lum. (2003), V.104, pp. 239–260.

FABRICATION AND CHARACTERIZATION OF NANOCOMPOSITE Nb2O5/KBr

S. HALIMI, M. HEMARA, M.SEBAIS, Z. OUILI, O. HALIMI, B. BOUDINE. A. DJEBLI

S. HALIMI[1], M. HEMARA[2], M.SEBAIS[2], Z. OUILI[2], O. HALIMI[2], B. BOUDINE[2]. A. DJEBLI[2]
[1] Faculté des Sciences et de la Technologie, Mohamed Sadek Ben Yahia University, Jijel, Algeria
[2]Laboratory of crystallography, Department of physics, University Mentouri, Constantine, Algeria
msebais@yahoo.fr

Abstract

Nowadays, nanocomposites offer new technology opportunities for fabrication of materials with unique properties for all sectors of industry, in addition to being for the majority of them environmentally friendly. Combining the properties of the matrix and the filler, the resulting composite may develop exceptional mechanical, thermal, catalytic and optical properties. In this work we present the fabrication as well as the structural and optical characterization of nanocomposite Nb_2O_5/KBr. The nanocrystallites of the Nb_2O_5 semiconductor, with tetragonal structure and cell parameters a=b=20.44Å and c=3.83Å, were synthesized inside the KBr matrix using the Czochralski method. The pulling of samples of Nb_2O_5/KBr nanocomposite was done from melt of mixture of KBr and Nb powders. The samples thus prepared were cut into pellets for the purposes of the characterization. The characterization by X-ray diffraction showed that during the preparation of the samples which occurs at high temperatures (T>730°C), the doping particles of Nibium (Nb) have chemically reacted with the host matrix KBr and allowed the synthesis (in- situ) of Nb_2O_5 semiconductor crystallites whose average size was estimated a few nanometers. Also KBr matrix retains its crystalline nature, despite the insertion of Nb_2O_5 nanocrystallites. The size of Nb_2O_5 semiconductor crystallites may be modified by suitable thermal treatments. Analysis of samples by Raman and IR spectroscopy also confirmed the synthesis of Nb_2O_5 semiconductor by the highlighting of vibrational modes specific to the chemical bond Nb-O. The measurement of optical absorption revealed that the Nb_2O_5/KBr nanocomposite exhibits absorption bands in the visible range at 460, 580 and 626 nm and an absorption edge at 204 nm which is shifted towards higher energies compared to the Nb_2O_5 semiconductor gap. These bands are due to the presence of Nb_2O_5 crystallites in the KBr matrix which is optically transparent in this domain. The samples excited by a radiation of X-ray from tungsten source, exhibit a rather intense emission in the visible domain (400-740 nm). So the nanocomposite Nb_2O_5/KBr can be used to detect high energy radiations like X-ray.

Keywords: Nanocomposite Nb_2O_5/KBr, Czochralski method, X-ray diffraction, Raman and IR spectroscopy, UV-Visible absorption.

PHYTOCHEMICAL ANALYSIS , DIURETIC AND FREE RADICAL SCAVENGING ACIVITIES OF ORIGANUM GLANDULOSUM DESF. LEAVES EXTRACTS

AMEL BOUAZIZ, SEDDIK KHENNOUF, SALIHA DJIDEL, MUSSA ABU ZARGA, SHTAYWY ABDALLA, ABDERAHMANE BAGHIANI, SALIHA DAHAMNA, SMAIN AMIRA, LEKHMICI ARRAR

Abstract

The present study aimed to investigate the phytochemical analysis , the diuretic and the in vitro antioxidant activities of O.glandulosum (Lamiaceae) , an endemic spontaneous plant of North Africa (Algeria and Tunisia). In Algeria, this species is called " Zaatar" and is used for the treatment of cough, fever , bronchitis , colds rheumatism, hypertension, digestive disorders. The antioxidant potential of methanolic extract (ME)and its three fractions of Chloroform (CHE), ethyl acetate (EAE) and water (AqE) have been investigated using several assays, including the DPPH scavenging, ABTS scavenging, hydroxyl radical scavenging. Total phenolic and total flavonoid contents of the extracts were estimated using Folin- Chiocalteu reagent and $AlCl_3$, respectively. The diuretic activity of ME (100, 300 and 600 mg/kg) was assessed orally in rats using furosemide as a standard drug. Chemical analysis of EAE revealed to the isolation of two compounds, one flavanonol (katuranin), and one monoterpene (5-isopropyl-3-methylphenol) which was isolated for the first time from the genus Origanum. EAE extract showed the highest polyphenolic and flavonoids contents (514.81 ±4.26mg GAE/g of dry extract), whereas CHE contained the highest amount of flavonoids (22.62±0.79 QE/g of dry extract) respectively. Similarly , this extract possessed the highest scavenging activity for DPPH radical (IC 50 = 0.006 ± 0.00001 mg/ml) , ABTS radical (IC50 =0.001± 0.001 mg/ml) and hydroxyl radical(IC 50 = 0.285 ± 0.008 mg/ml).ME of O.glansulosum showed an interesting dose-dependent diuretic activity ; it produced an increase in urine output (76 %) and the urinary excretion of Sodium and potassium. In conclusion, The present study supported the significant potential to use O.glansulosum by-products as a source of natural antioxidants and diuretic agent, which provides scientific justification for its traditional uses as antihypertensive remedy.

ANTIOXIDANT ACTIVITY AND POLYPHENOLIC CONTENT OF ACETONE EXTRACT OF ALGERIAN PISTACIA LENTISCUS LEAVES

SENATOR ABDERRAHMANE, MORCHEDI WAHIBA, BOURICHE HAMAMA

Abstract

The aim of this study is to determine the antioxidant activities of the acetone extract of the Algerian Pistacia lentiscus leaves. This plant is largely used in traditional medicine in Mediterranean region. Polyphenols and flavonoids content evaluated by the Folin-Ciocalteu and aluminum trichloride methods were respectively 303,6 ± 8,1 µg GAE/mg and 13,4 ± 0,5 µg QE/mg of extract. The antioxidant activities were explored by the DPPH radical test, the metal chelating activity and the linoleic acid oxidation test. The results obtained show that the extract has a strong activity to scavenge the DPPH radical, with an IC50 = 1,8 ± 0,3 µg/ml however the IC50 of BHT used as standard is 18,27 ± 1,08 µg/ml 18. Moreover it has a relatively weak chelating activity of ferrous ions (IC50 = 556 ± 52,6 µg/ml). This extract exhibited a strong inhibition of the lipid peroxidation, evaluated by the total antioxidant activity test. According to these results we conclude that the acetone extract of the leaves of Pistacia lentiscus has a strong antioxidant activity which supports its use in folkloric medicine.

CHARGE-TRANSFER COMPLEX OF TETRACYANOETHYLENE WITH SULFAHYDANTOIN IN POLAR SOLVENT

SAIDA SERIDI, SONIA BADI, MALIKA BERREDJEM, MEKKI KADRI

SAIDA SERIDI* [1], SONIA BADI[1], MALIKA BERREDJEM [2], MEKKI KADRI
[1] Laboratoire de Chimie Physique, Université 08 Mai 45, BP401, Guelma 24000, Algeria.
[2] Laboratoire de Chimie Organique Appliquée, Groupe de Chimie Bioorganique. Université Badji-Mokhtar, Annaba, BP 12, Algeria.
seridisaida77@yahoo.fr

Keywords: Sulfahydantoins; Charge-transfer complex, TCNE, FTIR.

Abstract
The chemistry of charge transfer (CT) complexes is a center stage for chemists and biologists. Charge transfer complexes act as intermediates in a wide variety of reactions involving nucleophiles and electron deficient molecules and play an important role in biological systems like DNA binding, antibacterial, antifungal, insecticide, in ion transfer through lipophilic membranes [1] and in the study of drug receptor mechanism [2]. Charge transfer complexes are important as materials for superconductors, solar cells, optical devices and others [3,4]. Mulliken [5] described broadly the interactions between a number of donors and π acceptors. Charge transfer transitions involve the excitation of an electron on the donor to an empty orbital on the acceptor [6].

The properties of charge-transfer complexes formed in the reaction of electron acceptors with donors containing nitrogen, sulfur, oxygen atoms, have growing importance in recent years [7,8].

In connection with such studies and with our interest in studying charge transfer complexes, we investigated in this paper the formation of CT complex formed between one sulfahydantoins : 4-isopropyl-2-benzyl-1,2,5-thiadiazolidin-3-one1,1-dioxide (SF) and tetracyanoethylene (TCNE) as π-acceptor (fig.1) in chloroform at room temperature. The results indicated the formation of CT-complex with molar ratio1:1 between donor and acceptor at maximum CT-band (fig. 2). The data were analyzed in terms of their stability constant (K), molar extinction coefficient (ε_{CT}), thermodynamic standard reaction quantities (ΔG°, ΔH°, ΔS°), oscillator strength (ƒ), transition dipole moment (μ_{EN}) and ionization potential (I_D). The newly formed complex were isolated and characterized through FTIR.

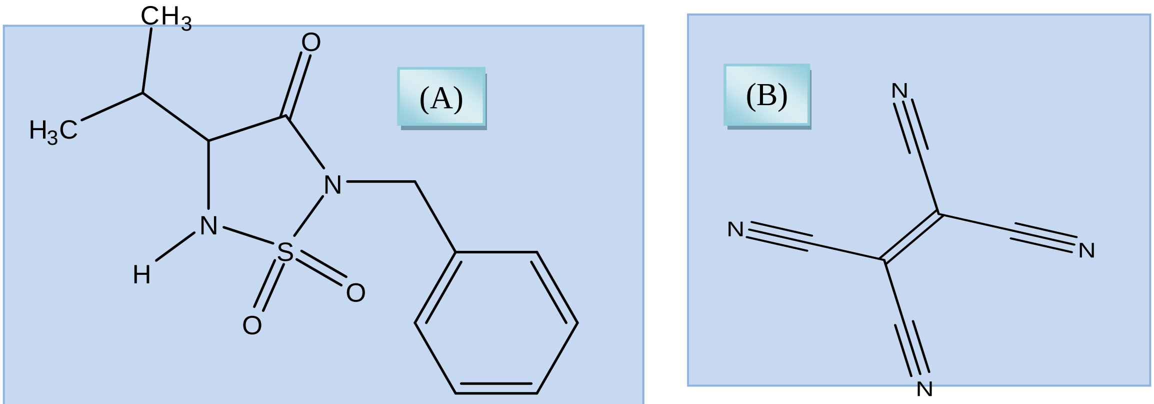

Fig.1 Structures of SF (A) and (TCNE) (B).

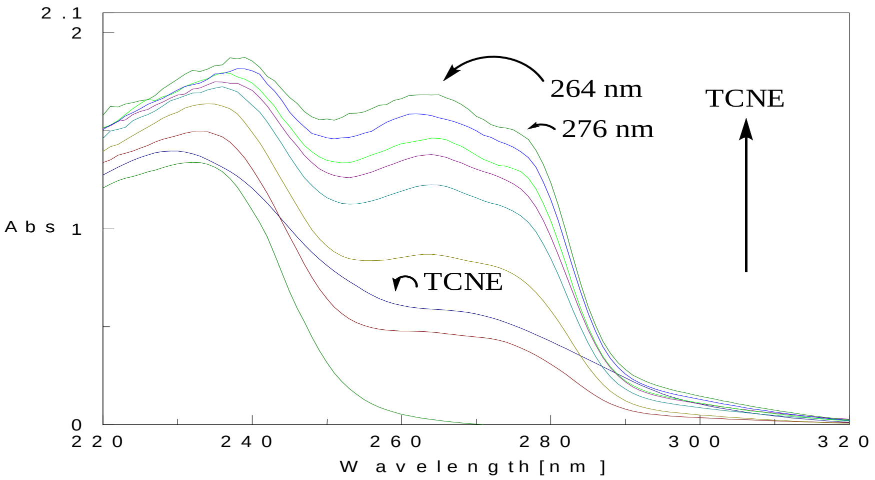

Fig. 2 Absorption spectra of SF (4×10^{-4} M) in chloroform containing various concentrations of TCNE.

References

[1] N. Singh, I. M. Khan ,A. Ahmad, S. Javed, J. Mol. Liquids 191 (2014) 142.
[2] J. Feng, H. Zhong, B.D. Xuebau, Zir. Kexu. 27 (1991) 691.
[3] A. Eychmuller, A.L. Rogach, Pure Appl. Chem. 72 (2000) 179.
[4] S.Y. AlQaradawi, H.S. Bazzi, A. Mostafa, E.M. Nour, Spectrochim. Acta A 71 (2008) 1594.
[5] R.S. Mulliken, J. Am. Chem. Soc. 74 (1952) 811.
[6] M.A. Zayed, S.M. Khalil, H.M. El-qudaby, Spectrochim. Acta A. 62 (2005) 461.
[7] M. Shukla, N. Srivastava, S. Saha, J. Mol. Struct. 1021 (2012) 153.
[8] M. Ting, N.J.S. Peters, J. Phys. Chem. A 113 (2009) 11316.

COMPARISON OF HYDROGEN SORPTION PROPERTIES OF ACTIVATED CARBONS PREPARED BY H3PO4 AND K2CO3 ACTIVATION OF CHERRY STONES

TANER ERDOGAN, FATMA OGUZ ERDOGAN

Taner Erdogan, Dr, Kocaeli University, Fatma Oguz Erdogan, Dr, Kocaeli University

Abstract

The adsorption of hydrogen on porous materials is widely studied for hydrogen storage applications. In recent years, several carbon based microporous materials such as activated carbon, single and multi-walled carbon nanotubes (SWCNT and MWCNT), nanofibers and metal organic frameworks (MOFs) have been proposed as promising adsorbents for hydrogen. Activated carbons have been extensively studied as hydrogen storage materials because of their high surface area, pore size distribution, low density, surface functional groups and chemical stability. In this study, cherry stone based activated carbons were prepared for hydrogen storage and the significance of microwave power on the properties of activated carbon was investigated. The activated carbon samples were characterized by scanning electron microscopy (SEM), Fourier Transform Infrared Spectroscopy (FTIR) and N_2 adsorption isotherms. The results showed that microwave power had the greatest impact on the surface area and micropore volume of activated carbon prepared with H_3PO_4 and K_2CO_3. The highest BET surface area was obtained as 1448 m^2/g at 300 W. Hydrogen storage capacity at 77.4 K was evaluated at atmospheric pressure. Hydrogen sorption characteristics of these activated carbon samples were investigated and the effects of activation time and chemical activation agent (H_3PO_4 and K_2CO_3) on hydrogen sorption characteristics were compared. The maximum hydrogen storage of 4.24 wt.% and 4.02 at 77 K was achieved by activation with K_2CO_3 and H_3PO_4, respectively. The study also showed that microwave-assisted activation is an effective and fast method converting cherry stones into activated carbon for hydrogen storage. The resulting samples (cherry stone based activated carbons) demonstrate both high surface area and large hydrogen storage capacity, implying their great potential as hydrogen storage materials.

Introduction

Hydrogen, the lightest element, is a clean, highly abundant and non toxic renewable fuel. When it burns, it releases only water vapour into the environment. However, the main problem in the use of hydrogen effectively is the lack of feasible hydrogen storage technologies. It is always desirable to develop a new storage vehicle with high capacity and light mass which may be applicable for portable electronics and moving vehicles. For this reason, the selection of the material as hydrogen storage medium becomes important as it is one of the key parameters affecting the efficiency of storage system (Yang, et al., 2012; Kustov, et al., 2014; Wróbel-Iwaniec, Díez and Gryglewicz, 2015; Park and Lee, 2010). The activated carbons are good candidates for hydrogen storage as they have promising hydrogen storage capacity due to their large surface area, high pore volume, small pore size and the catalytic effects of its surface; however, their storage capacities scatter over a range of magnitude. Activated carbons can be prepared by chemical or physical activations via conventional heating of many kinds of raw materials such as cherry stones, wood, agricultural products, lignite, peat and coal (Liu, et al., 2014; Wu, et al., 2015; Mahmoudi, et al., 2015; Xiao, et al., 2015; Zhao, et al., 2012; Erdogan, 2015; Erdogan and Erdogan, submitted; Erdogan and Erdogan, 2015). However, the biggest economic barrier to convert precursor to activated carbons is the high cost of activation, which usually requires extended activation time, high energy consumption and excessive activation agents. In terms of heating means, microwave heating has lots of advantages over conventional heating means, e.g. high heating efficiency, easy control of the heating process, rapid temperature rise at low energy consumption (Wu, et al., 2015). Recent studies showed that the hydrogen storage capacities of carbon materials are quite promising, further studies are still needed in this field. Jiménez et al. reported that the highest hydrogen storage value (2.02%) was obtained with activated carbon at 10 bar and 77 K (Jiménez, et al., 2010). Fierro, et al. (2010) prepared a kind of activated carbons which exhibited a high specific surface area up to 2772 m^2/g and demonstrated a large hydrogen uptake of 5.3 wt.% at 77 K and 4 MPa. Xie, et al. (2013)

prepared a kind of activated carbons which exhibited a süper-high specific surface area up to 3348 m^2/g and demonstrated a large hydrogen uptake of 5.65 wt.% and 4.98 wt.% when the adsorption temperatures were 0°C and 25°C, respectively, and the pressure was 9 MPa. Oguz Erdogan and Erdogan (2015) described a hydrogen storage capacity of 4.49 wt.% at 77 K of activated carbon with specific surface area up to 1380 m^2/g.

In our previous studies we have reported the preparation of activated carbon samples by microwave heating from cherry stones. In these studies we found the optimal parameters for activated carbon preparation with the highest surface area as follows: activating agent (KOH, NaOH, H_3PO_4 or H_2SO_4)/cherry stones mass ratio of 1/1 with a microwave power of 300 W at 300 °C (Erdogan, 2015; Erdogan and Erdogan, submitted; Erdogan and Erdogan, 2015). To the best of our knowledge, no study has been reported on the preparation of activated carbon from cherry stones via microwave activation with K_2CO_3. In this study, low-cost cherry stone based activated carbons were prepared by K_2CO_3 activation, the activated carbon samples are further treated by microwave to investigate the effect of microwave treatment on the surface area, pore structure parameters and on the surface properties. In addition, hydrogen sorption characteristics of these samples (activated carbons prepared in our laboratory with high porosity) were investigated and the effects of activation time and chemical activation agent (H_3PO_4 and K_2CO_3) on hydrogen sorption characteristics were compared.

Experimental

Preparation of activated carbon

The activated carbon samples were prepared according to the method reported by Oguz Erdogan (2015). Some adaptations have been carried out in the production method. Dried cherry stones were mixed with K_2CO_3 solution at 1g/g impregnation ratios (weight of K_2CO_3/ weight of cherry stones) at room temperature for 24 hours. The impregnated samples were next dried at 100 °C until complete dryness. The samples treated at 300 °C for different minutes (1, 3, 5 and 7 min) in microwave system (CEM Corporation, Discover SP) at 300 W. At the end of the activation period the samples were allowed to cool and the activated samples were washed with hot distilled water until pH 6-7 was attained. Microwave-treated activated carbons are termed as AC1, AC3, AC5 and AC7, here, the numbers refer to the radiation time of 1, 3, 5 and 7 min, respectively. After that, the samples were dried at 110°C for 24 hours and vacuum degassed at 200°C for 6 hours prior to gas sorption experiments.

Characterization of prepared activated carbons

Pore structure of the activated carbon sample was evaluated by measuring N_2 adsorption isotherm 77.4 K (Quantachrome Autosorb iQ). The specific surface area, S_{BET}, was calculated using the Brunauer-Emmett-Teller (BET) equation. The total pore volume (V_t) was calculated at relative pressure $P/P_0=0.995$. The micropore volume (V_{mi}) was determined by the t-method analysis. The pore size distribution was ascertained by Density Functional Theory (DFT) model. Fourier Transform Infrared Spectroscopy (FTIR) analyses were detected by a Jasco FTIR 480 Plus spectrophotometer. The spectra were obtained in the range of 400-4000 cm^{-1}. Due to high absorbance of activated carbon, very thin KBr pellets have been prepared. Surface morphology of the samples was viewed by using a scanning electron microscope (JEOL/JSM-6335F-INCA/EDS). The surface morphology was characterized by SEM (Jeol/Jsm-6335F-Inca/Eds).

Hydrogen storage capacities

Hydrogen storage capacity at 77.4 K was evaluated at atmospheric pressure. Measurements were carried out in a Autosorb iQ apparatus. Prior to these measurements, 0.1 g of each sample was outgassed overnight at 573 K. High purity hydrogen (99.99%) was used in order to remove the influence of other impurities and the volumetric measurement method was used to determine the hydrogen storage capacity.

Characterization

Activated carbons were prepared from cherry stones by microwave radiation and chemical activation with K_2CO_3. Adsorption behavior and pore structure of carbonaceous materials can be analyzed by using N_2 adsorption-desorption isotherms. General properties of carbonaceous materials can be explained by the shape of these isotherms. Fig. 1 shows the nitrogen adsorption-desorption isotherms at 77.4 K for the cherry stone based activated carbon samples produced by microwave radiation at different radiation times (1, 3, 5 and 7 min). The isotherms are a mixture of Type I and Type IV according to the IUPAC (International Union of Pure and Applied Chemistry) classification. This type of isotherm is usually exhibited by a combination of microporous and mesoporous structures.

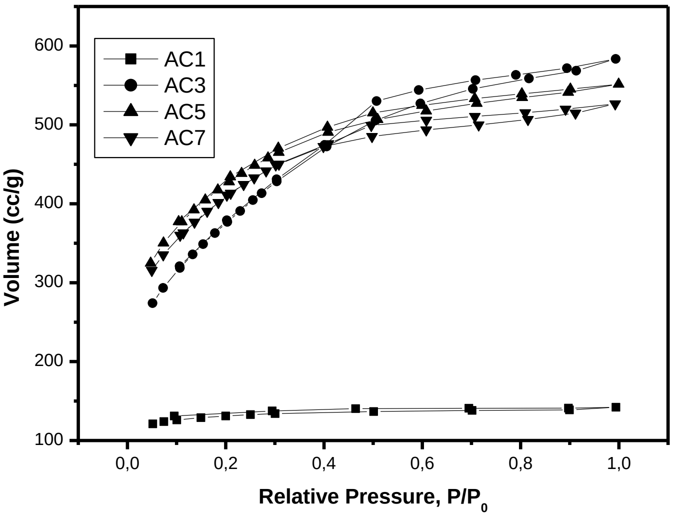

Fig. 1 Nitrogen adsorption-desorption isotherms at 77.4 K for the cherry stone based activated carbon produced by microwave radiation.

As shown in Fig. 1, by increasing the radiation time from 1 min to 5 min, the N_2 uptake increased. In this case, the greater amount of N_2 adsorption at low relative pressures indicates the creation of a large amount of new micropores. The development of larger micropores and the formation of mesopores is the cause of the increase in N_2 uptake at higher relative pressures (Hesas, et al., 2013). AC7 showed a gradual decrease in N_2 uptake by the micropores and mesopores compared with AC5. The reduction in N_2 adsorption can be attributed to the widening of the existing pores. AC3 showed a decrease in N_2 uptake at low relative pressures relative to AC5 and AC7. The nitrogen adsorption of AC3 is higher than the other samples at relative pressures greater than P/P_0=0.5, due to the destruction of existing microporous structure in favour of the new mesopores. A similar phenomenon was reported by Hesas, et al., (2013).

The textural parameters calculated from the isotherm data are collected in Table 1. AC1 showed the lowest S_{BET} and V_T. BET surface area of carbonaceous materials is important because, like other chemical and physical characteristics, it may strongly affect the reactivity behavior (Ioannidou and Zabaniotou, 2007). By increasing the radiatin time from 1 min to 5 min, the S_{BET}, S_L, V_t, V_m and microporosity % of the prepared activated carbons increased gradually to 1148 m^2/g, 2190 m^2/g, 0.7 cm^3/g, 0.672 cm^3/g and 96, respectively, and then decreased with further increases in the radiation time (AC7). The creation of micropores and mesopores leads to an increase in BET and Langmuir surface areas, whereas the widening and burning of the pores and the blocking pores by excessive irradiation on the surface of the activated carbon can lead to a reduction in the accesible area, thus resulting in a decrease in BET and Langmuir surface areas. As a comparison between the textural properties of the activated carbon samples, AC5 has an avarage pore size of 19.90 Å, which is approximately the same as the 19.66 and 19.80 Å for AC3 and AC7, respectively. AC1 showed the highest avarage pore size and the lowest microporosity%. In our previous study showed that the lowest microporosity was obtained at an activation time of one minute (Oguz Erdogan, 2015).

Samples	S_{BET} (m^2/g)	S_L (m^2/g)	V_t (cm^3/g)	V_m (cm^3/g)	L_0 (Å)	V_m/V_t %
AC1	404.9	597.5	0.208	0.153	20.55	73.6
AC3	1351	2067	0.6642	0.5785	19.66	87.1
AC5	1448	2190	0.700	0.672	19.90	96.0
AC7	1400	2120	0.695	0.650	19.80	93.5

S_{BET}: BET surface area
S_L: Langmuir surface area
S_m: micropore area
V_m: micropore volume
L_0: average pore size
V_t: total pore volume

Table 1. Textural characteristics of activated carbon samples determined by N2 adsorption at 77.4 K.

Fig. 2 shows the pore size distribution (from Density Functional Theory) of produced activated carbon samples. The structural heterogeneity and solid internal structure of activated carbon samples can be represented by characterization of the pore size distribution. It appeared from these figures and Table 1 that the radiation time has significant effects on the pore structure and surface area of the activated carbon prepared by microwave heating. A similar phenomenon was reported in our previous study (Oguz Erdogan, 2015).

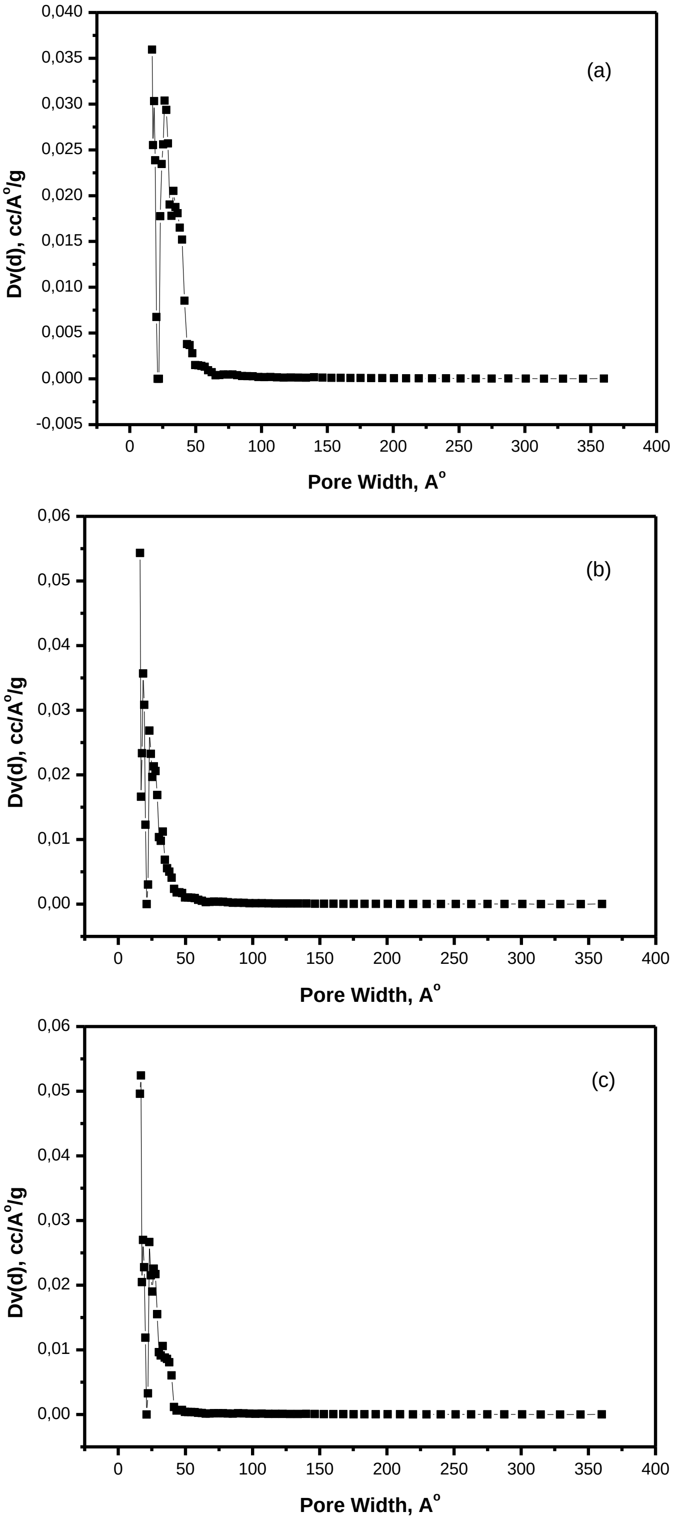

Figure 2: Pore size distribution of (a) AC3, (b) AC5 and (c) AC7.

Table 2 compares porosity structure of the samples prepared with K_2CO_3 from different carbonaceous materials. As listed in Table 2, the samples obtained with K_2CO_3 from cherry stones by microwave heating have higher BET surface area, total pore volume and micropore volume. A very important benefit of using cherry stone precursors is the low cost of carbon adsorbent production due to low temperatures and short microwave activation. Hence, the work reported here clearly demonstrates that the use of microwave heating in the preparation of cherry stones based activated carbon is more rapid, efficient and cheaper than in the use of a conventional furnace.

Heating methods	S_{BET} (m^2/g)	Pore Volume (cm^3/g)		Data sources
		V_t	V_m	
Microwave	621.47	0.380	0.110	[17]
Microwave	1165	0.780	0.330	[18]
Microwave	1411.55	0.836	-	[19]
Microwave	1104.45	0.615	0.247	[20]
Microwave	1098	0.611	0.334	[21]
Microwave	683.76	0.591	0.257	[22]
Conventional	1038	0.490	-	[23]
Conventional	1410	-	0.490	[24]
Microwave	1448	0.700	0.672	This work

Table 2: BET surface areas and pore volumes of activated carbons produced by K_2CO_3 activation from different carbonaceous materials selected from literature.

SEM was used to observe the surface physical morphology of the cherry stones and activated carbons prepared by microwave heating methods. SEM images of the AC3, AC5 and AC7 prepared with K_2CO_3 are shown in Fig. 3. SEM image of raw cherry stones was reported in our previous study (Oguz Erdogan, 2015). Significant differences of the surface topography between raw cherry stones and activated carbon samples were observed. The surface of cherry stones has very small pores. However, the activated carbons are full of cavities and pores with different sizes and shapes compared to cherry stones. This shows that K_2CO_3 was effective in creating well-developed pores on the surface of the cherry stones, hence leading to the activated carbons with large surface area and porous structure.

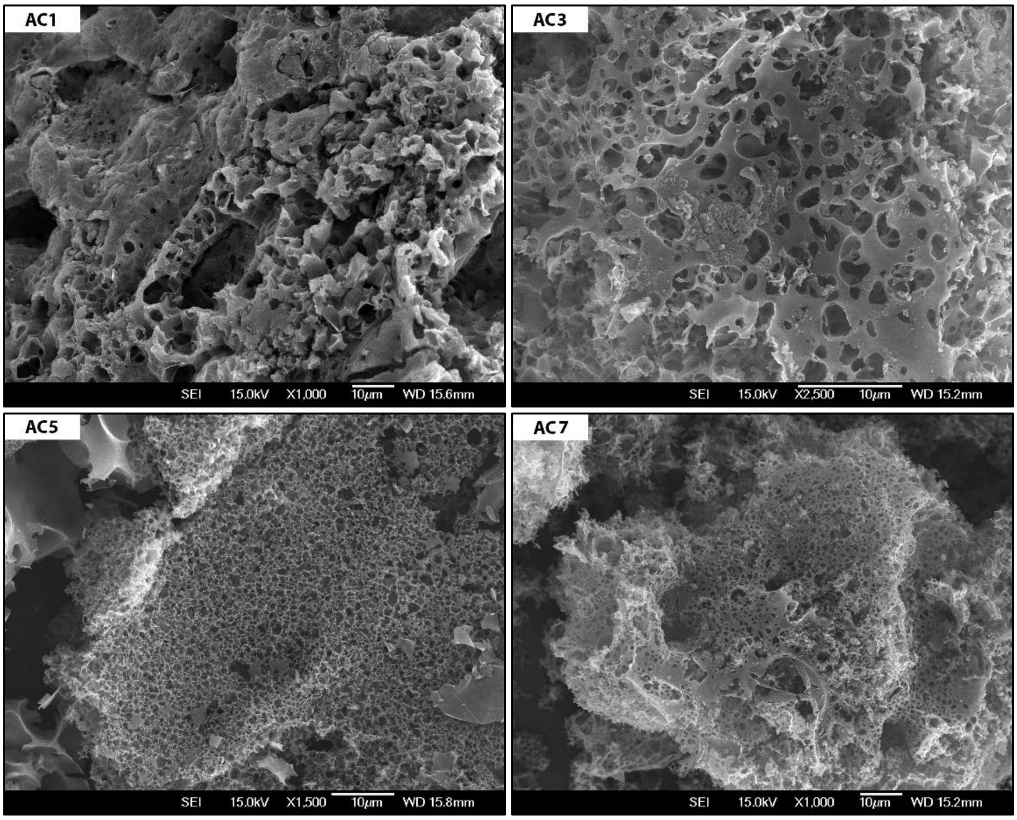

Figure 3: SEM images of activated carbons, AC1, AC3, AC5 and AC7.

The FTIR spectra of the AC5 are shown in Fig. 4. The broad bands observed in the spectra of K_2CO_3 activated carbons are expected for the surface functional groups, which exist in a wide range of different electronic environments. The FTIR spectrum of AC5 obtained revealed peaks between 3862, 3846 and 3759, 3402, 2917 and 2848, 1743 and 1694, 1568 and 1160, 881 and 615 cm^{-1}, corresponding to the presence of –OH (hydroxyl), C-H, C=O (stretching), C=C (stretching vibrations in the aromatic rings), -COOH (carboxylic acids), in-plane –OH, and C-O-C (esters, ether or phenol) functional groups (Erdogan, 2015; Erdogan and Erdogan, submitted; Erdogan and Erdogan, 2015; Mohamed, Khater and Mostafa, 2006; Evangelin, Gunasekaran and Dharmendirakumar,2014; Alslaibi, et al., 2013).

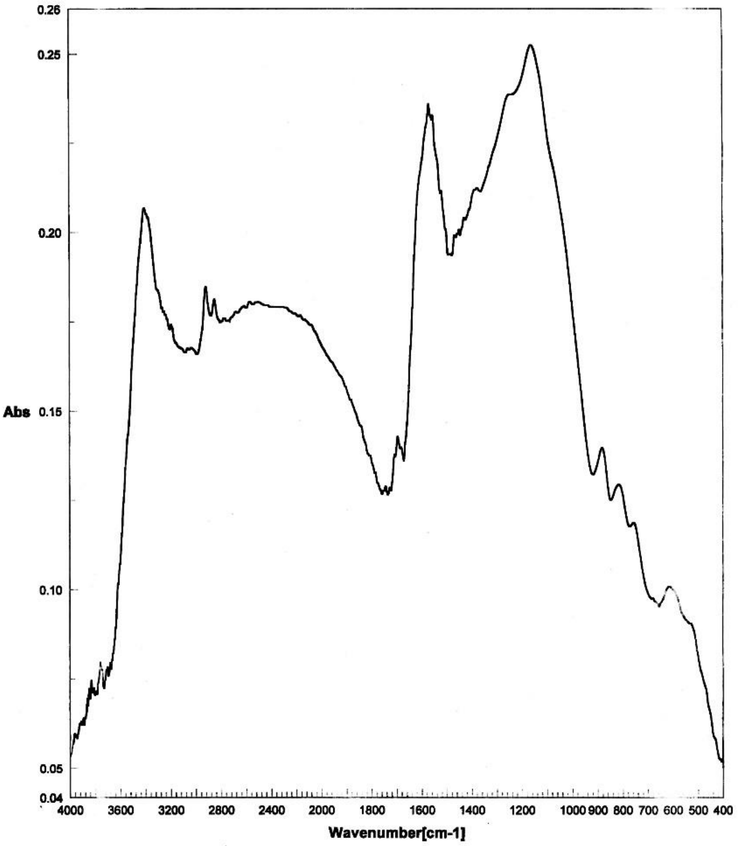

Figure 4: FTIR spectra of AC5.

Hydrogen adsorption

Hydrogen adsorption isotherms were obtained on K_2CO_3-activated carbons produced in the present work (AC1, AC3, AC5 and AC7) and H_3PO_4-activated carbons (HAC) produced in our previous study (Erdogan and Oguz Erdogan, 2015) in the atmospheric pressure at 77.4 K. The BET surface area, Langmuir surface area, total pore volume, micropore volume, average pore size and microporosity (%) of HAC were 1998 m^2/g, 2530 m^2/g, 1.40 cm^3/g, 0.83 cm^3/g, 28.52 Å and 59.3, respectively. SEM image of HAC was reported in our previous study (Erdogan and Oguz Erdogan, 2015). The amounts of adsorbed hydrogen were determined using the values of the adsorbed volumes at 0.99 P/P_0 and ideal gas equation. Fig 5 shows the hydrogen sorption capacity (wt%) collected at 77.4 K and P/P_0 from 0 to 1 for the K_2CO_3-activated carbons and H_3PO_4-activated carbons. The hydrogen adsorption capacities of these activated carbons are shown in Table 3.

Samples	Hydrogen adsorption capacity (%)
AC1	1.41
AC3	2.08
AC5	4.24
AC7	2.20
HAC	4.02

Table 3: Hydrogen adsorption capacities (%) of cherry stone based activated carbons at 77.4 K.

The highest hydrogen storage capacity of 4.24 wt% was achieved with AC5. The hydrogen storage capacities of the HAC, AC7, AC3 and AC1 were 4.02 wt%, 2.20 wt%, 2.08 wt% and 1.41 wt%, respectively. Certain K_2CO_3-activated carbon (AC5) showed higher hydrogen adsorption capacities than the H_3PO_4-activated carbons (HAC), depending on their activation conditions. The relationship between the hydrogen adsorption capacities and the BET surface area in activated carbons did not show a correlation. As shown in figure 1, the hydrogen adsorption capacities of activated carbon by alkaline activation agent process was significantly larger than that of activated carbon by acidic activation agent process. A similar phenomenon was reported in our previous study (Oguz Erdogan and Erdogan, submitted). In this previous work, NaOH-activated carbon and KOH-activated carbons showed higher hydrogen adsorption capacities than the H_2SO_4-activated carbons, depending on their activation conditions. The highest hydrogen storage capacity of 4.49 wt% was achieved with AC6 (KOH-activated carbon). Fig.5 shows hydrogen adsorption capacities of activated carbons.

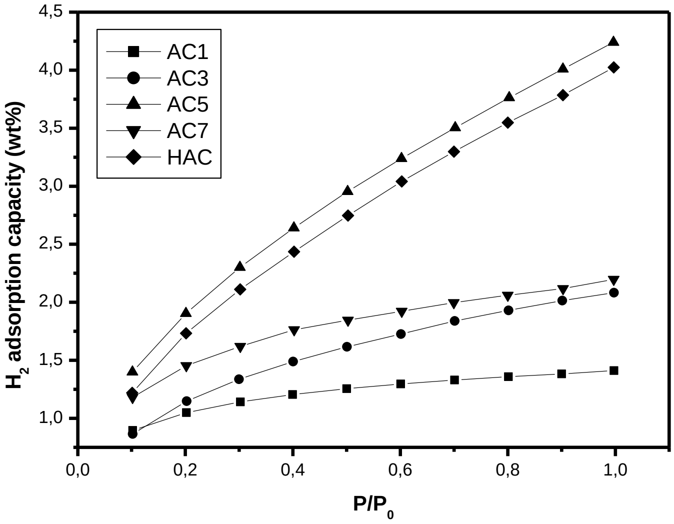

Figure 5: Hydrogen adsorption capacities of activated carbon samples.

As far as we know, no study has been reported on the hydrogen adsorption capacities on activated carbon prepared from cherry stones via microwave activation with K_2CO_3 and H_3PO_4. The maximum hydrogen storage of 4.24 wt.% and 4.02 at 77 K was achieved by activation with K_2CO_3 and H_3PO_4, respectively. As a result, the waste cherry stones based activated carbon are competitive with the most efficient adsorbents (such as nanotubes, commercial activated carbon and metal-organic frameworks) in relation to high specific surface area, large pore volumes, renewable resources and suitable for hydrogen storage.

Conclusions

We report a study of physisorption of hydrogen on activated carbon surfaces prepared with several activating agents such as K_2CO_3 and H_3PO_4. The surface area, pore size and pore volume of activated carbon samples depended on preparation parameters. The radiation time had the largest impact on the surface area, micropore volume and total pore volume. K_2CO_3 activation was employed to provide microporosity. AC5 provided a well-developed porous structure with a BET surface area of 1448 m^2/g, a total pore volume of 0.7 cm^3/g and a micropore volume of 0.672 cm^3/g. The maximum hydrogen storage of 4.24 wt.% and 4.02 at 77 K was achieved by activation with K_2CO_3 and H_3PO_4 at 300 °C and 300 W, respectively. The study also showed that microwave-assisted activation is an effective and fast method converting cherry stones into activated carbon for hydrogen storage.

Acknowledgements

The author acknowledge the financial support provided by Kocaeli University Scientific Research Projects Unit. (Project No:2011/062 and 2014/113 HDP).

References

Alslaibi, T.M., Abustan, I., Ahmad, M.A., Foul, A.A., 2013. Application of response surface methodology (RSM) for optimization of Cu^{2+}, Cd^{2+}, Ni^{2+}, Pb^{2+}, Fe^{2+} and Zn^{2+} removal from aqueous solution using microwaved olive stone activated carbon. J. Chem. Technol. Biotechnol., 88, pp. 2141-51.

Deng, H., Li, G., Yang, H., Tang, J., Tang, J., 2010. Preparation of activated carbons from cotton stalk by microwave assisted KOH and K_2CO_3 activation. Chemical Engineering Journal, 163, pp. 373-81.

Erdogan, F.O., Characterization of the activated carbon surface of cherry stones prepared by sodium and potassium hydroxide. Analytical Letters, DOI: 10.1080/00032719.2015.1065879.

Erdogan, F.O., Erdogan, T., Preparation and characterization of cherry stone based activated carbon for hydrogen storage: The effect of microwave heating. Progress in Natural Science: Materials International (submitted)

Erdogan, T., Erdogan, F.O., Characterization of the adsorption of Disperse Yellow 211 on activated carbon from cherry Stones following microwave-assisted phosphoric acid treatment. Analytical Letters, DOI:10.1080/00032719.2015.1086776.

Evangelin, C.D., Gunasekaran, S.G., Dharmendirakumar, M., 2014. Preparation and characterization of chemically modified silk cotton hull activated carbon and its effects on Cd(II) removal from aqueous solutions. Bioremediation Journal, 18, pp. 81-92.

Fierro, V., Zhao, W., Izquierdo, M.T., Aylon, E., Celzard, A., 2010. Adsorption and compression contributions to hydrogen storage in activated anthracites. Int. J. Hydrogen Energy, 35, pp. 9038-9045.

Foo, K.Y., Hameed, B.H., 2011. Preparation and characterization of activated carbon from sunflower seed oil residue via microwave assisted K_2CO_3 activation. Bioresource Technology, 102, pp. 9794-9.

Foo, K.Y., Hameed, B.H., 2011. Utilization of rice husks as a feedstock for preparation of activated carbon by microwave induced KOH and K_2CO_3 activation. Bioresource Technology, 102, pp. 9814-7.

Foo, K.Y., Hameed, B.H., 2012. Factors affecting the carbon yield and adsorption capability of the mangosteen peel activated carbon prepared by microwave assisted K_2CO_3 activation. Chemical Engineering Journal, 180, pp. 66-74.

Foo, K.Y., Hameed, B.H., 2012. Preparation, characterization and evaluation of adsorptive properties of orange peel based activated carbon via microwave induced K_2CO_3 activation. Bioresource Technology, 104, pp. 679-86.

Hesas, R.H., Arami-Niya, A., Daud, W.M.A.W., Sahu, J.N., 2013. Comparison of oil palm Shell-based activated carbons produced by microwave and conventional heating methods using zinc chloride activation. Journal of Analytical and Applied Pyrolysis, 104, pp. 176-84.

Ioannidou, O., Zabaniotou, A., 2007. Agricultural residues as precursors for activated carbon production-A review. Renewable and Sustainable Energy Reviews, 11, pp. 1966-2005.

Jiménez, V., Sánchez, P., Díaz, J.A., Valverde, J.L., Romero, A., 2010. Hydrogen storage capacity on different carbon materials. Chem. Phys. Lett., 485, pp. 152-155.

Kustov, L.M., Tarasov, A.L., Sung, J., Godovsky, D.Y., 2014. Hydrogen storage materials. Mendeleev communications, 24, pp. 1-8.

Liu, Z., Liu, Y., Chen, L., Zhang, H., 2014. Performance study of heavy metal ion adsorption onto microwave-activated banana peel. Desalination and Water Treatment, 52, pp. 7117-24.

Mahmoudi, K., Hosni, K., Hamdi, N., Srasra E., 2015. Kinetics and equilibrium studies on removal of methylene blue and methyl orange by adsorption onto activated carbon prepared from date pits-A comparative study. Korean J. Chem. Eng., 32, pp. 274-83.

Mestre, A.S., Bexiga, A.S., Proença, M., Andrade, M., Pinto, M.L., Matos, I., Fonseca, I.M., Carvalho, A.P., 2011. Activated carbons from sisal waste by chemical activation with K_2CO_3: Kinetics of paracetamol and ibuprofen removal from aqueous solution. Bioresource Technology, 102, pp. 8253-60.

Mohamed, F.S., Khater, W.A., Mostafa, M.R., 2006. Characterization and phenols sorptive properties of carbons activated by sulfuric acid. Chem. Eng. J., 116, pp. 47-52.

Park, S.J., Lee, S.Y., 2010. Hydrogen storage behaviors of platinum-supported multi-walled carbon nanotubes. Int. J. Hydrogen Energy, 35, pp. 13048-54.

Sun, Y., Wei, J., Wang, Y.S., Yang, G., Zhang, J.P., 2010. Production of activated carbon by K_2CO_3 activation treatment of cornstalk lignin and its performance in removing phenol and subsequent bioregeneration. Environmental Technology, 31, pp. 53-61.

Wróbel-Iwaniec, I., Díez, N., Gryglewicz, G., 2015. Chitosan-based highly activated carbons for hydrogen storage. Int. J. Hydrogen Energy, 40, pp. 5788-96.

Wu, M., Li, R., He, X., Zhang, H., Sui, W., Tan, M., 2015. Microwave-assisted preparation of peanut Shell-based activated carbons and their use in electrochemical capacitors, New Carbon Materials, 30, pp. 86-91.

Xiao, H., Peng, H., Deng, S., Yang, X., Zhang, Y., Li, Y., 2012. Preparation of activated carbon from edible fungi residue by microwave assisted K_2CO_3 activation-Application in relative black 5 adsorption from aqueous solution. Bioresource Technology, 111, pp. 127-33.
Xiao, X., Tian, F., Yan, Y., Wu, Z., Wu, Z., Cravotto, G., 2015. Adsorption behavior of phenanthrene onto coal-based activated carbon prepared by microwave activation. Korean J. Chem. Eng., 32, pp. 1129-36.
Xie, H., Shen, Y., Zhou, G., Chen, S., Song, Y., Ren, J., 2013. Effect of preparation conditions on the hydrogen storage capacity of activated carbon adsorbents with süper-high specific surface areas. Materials Chemistry and Physics, 141. pp. 203-7.
Yang, S.J., Jung, H., Kim, T., Park, C.R. 2012. Recent advances in hydrogen storage Technologies based on nanoporous carbon materials. Progress in Natural Science: Materials International, 22, pp. 631-8.
Zhao, W., Fierro, V., Fernández-Huerta, N., Izquierdo, M.T., Celzard, A., 2012. Impact of synthesis conditions of KOH activated carbons on their hydrogen storage capacities. Int. J. Hydrogen Energy, 37, pp. 14278-14284.

APPLICATIONS AT CLAY CHARACTERIZATION, WHICH SYNTHESIZED BY SUBJECTING WITH ACID, BASE, SALT, NEUTRAL MEDIA

TÜLAY ARASAN, ÇİĞDEM SARICI ÖZDEMİR

Tülay Arasan, Research Asistant, Tunceli University, Çiğdem SARICI-ÖZDEMİR, Associate Prof., İnönü University

Abstract

The purpose of this study the characterization is performed by subjecting the pretreated clay that used as natural adsorbent. The clay samples were synthesized by subjecting clay with acid, base, salt, neutral media. The structure and surface properties of clay were examined by FTIR, XRD, Boehm titration, and adsorption of methylene blue and iodine.

Introduction

Clay is the oldest industrial raw materials since the first people known to be used.[1] Clays and clay minerals, has been one of the common workspace art, in many disciplines. Today, clays plasticity, moisture retention and strength Besides organic or displacement with iodine all kinds of inorganic, high adsorption and other technological properties such as catalytic activity are used as industrial raw materials in the area of more than 100. Regarding the use of clay areas; from ceramics and cement production; paper, petrochemical and construction industries; vegetable oil, beer, wine and fruit juices of the bleached; radioactive waste and waste water to be cleaned; medicine, soap, detergent, diaphragm, electrodes, catalyst, rubber and plastic production can be listed a wide range of area [2-3]. Clay allowing them to use for different purposes in different areas, they have the common presence of clay minerals in nature are superior chemical and physical properties [4].Volcanic rocks, under the influence of strong drafts Clay minerals occur as a result of wear that minerals were stored or moved elsewhere in large beds with wind and water. Clay minerals that dispersible spontaneously under 2 µm are aluminum, magnesium and iron silicate. Pure clay mineral is seen rare in nature. Besides the type of clay minerals the sheer and lack of non-clay minerals increases the economic value of clays. A variety of methods have been developed to define clay from each other. However, it is difficult to decide about rocks by using only one of these methods. Therefore, clay and non- clay minerals contained in the rocks, can be determined by combining the results that obtained by applying several methods. Among these methods being applied meyhods are; chemical analysis (CA), X-ray diffraction (XRD), thermal analysis (DTA-TGA) may be listed on the form. For further studies scanning electron microscopy (SEM), infrared spectroscopy (IR), petrographic microscopy, dye adsorption and some other optical methods are used [5].

In this study the clay samples were synthesized by subjecting clay with acid, base, salt, neutral media. The structure and surface properties of clay were examined by XRF, FT-IR, XRD, SEM, TGA- DTA, Boehm titration, and adsorption of methylene blue and iodine.

Experimental work

In this study, a clay sample from Battalgazi / Malatya region selected as the material and after sample is broken with the aid of suitable breaker and grinding clay minerals were obtained under 200 by sieving with the help of molecular sieves. After the clay sample dried in the oven at 105 °C for 24 hours, subjected to various methods for the modification. These methods;

- Acid effect: In this method, the sample of clay stirred with 0.1 N HCl; 0.1 N HNO_3; 0.1 N H_3PO_4; 0.1 N H_2SO_4; 0.1 N CH_3COOH clay : acid ratio of 1: 3 to 600 rev / min speed for 6 h.
- Base effect: In this method, the sample of clay stirred with 0,1 M KOH; 0,1 M NaOH; 0,1 M NH_3 ,clay : base ratio of 1: 3 to 600 rev / min speed for 6 h.
- Solvent effect: In this method, the sample of clay stirred with 0,1 M $C_6H_5CH_3$; 0,1 M C_6H_6, clay : solvent ratio of 1: 3 to 600 rev / min speed for 6 h.
- Salt effect: In this method, the sample of clay stirred with 0,1 M NaCl , clay : salt ratio of 1: 3 to 600 rev / min speed for 6 h.

- Water effect: In this method, the sample of clay stirred with water, clay : water ratio of 1: 3 to 600 rev / min speed for 6 h.

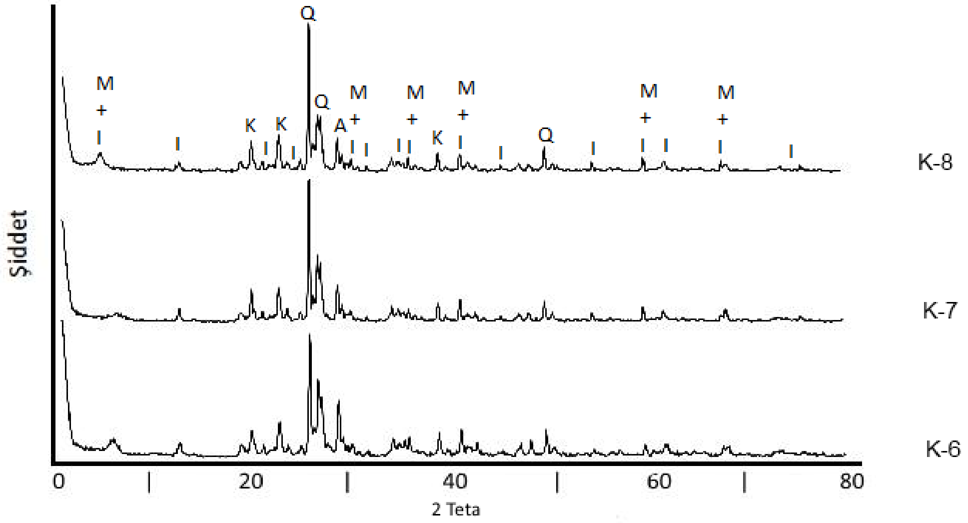

Figure 1. XRD spectrum of the clay treated with bases

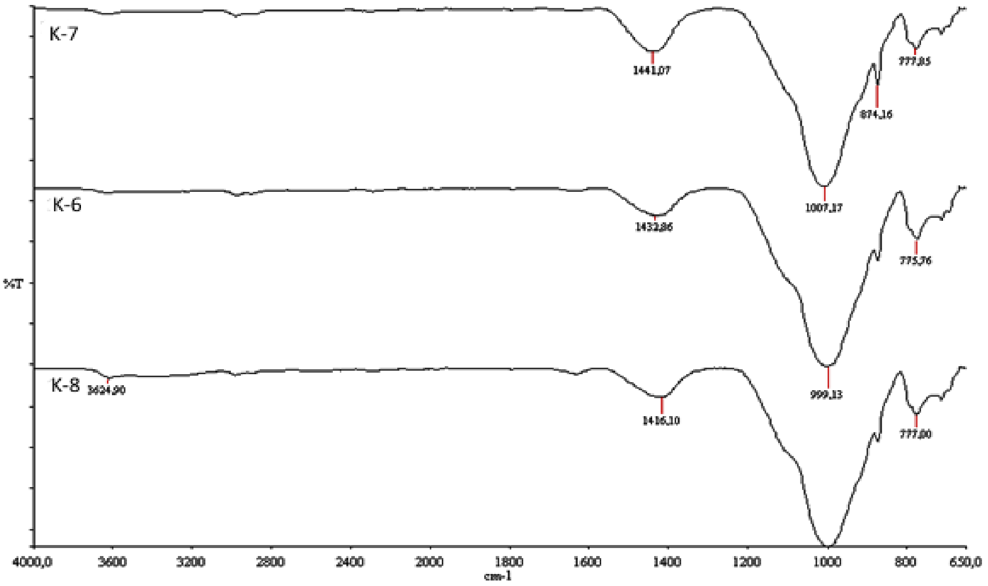

Figure 2. FT-IR spectrum of the clay treated with bases

Results and discussion

The structure and surface properties of obtained clays were examined by SEM, FT-IR, XRD, Boehm titration, and adsorption of methylene blue and iodine. One of the most commonly used method for the quantitative determination of organic structural functionality of carbonaceous materials is Boehm titrations. This method was applied to each of obtained clay samples. By Boehm titration of untreated clay sample, amount of the carboxylic 0,700; laktonic 1,250; and phenolic 0,200 was found. When all the samples analyzed, higher carboxylic and phenolic groups and various changes in lactonic goups was observed compared to untreated clay example. Adsorption of methylene blue and iodine was applied to each of obtained clay samples.the best result of adsorption of methylene blue was observed sample that treated with NaOH (58,39 mg/g) and the best result of iodine adsorption was taken observed sample that treated with H_2SO_4 (1209,32 mg/g). SEM, FT-IR, XRD methods applied each of caly samples and it is observed that structure of untreated clay is crystalline. By pretreatment some changes observed in this crystalline structure especially structure of the samples that treated with H3PO4 and NaOH are become away from crystalline structure and more amorphous structure was observed.

Combining the result of all methods information about the changes created in the structure by pre-treatment observed.

Resources

[1] Tahber, S. 2006. Adana Archeology Museum in Hellenistic and Roman periods, research and implementation of the construction techniques of terracotta figurines. Master Thesis, Cukurova University, Institute of Social Sciences, Ceramics Department, Adana.
[2] Sarikaya, the importance of Clay and properties. III. National Clay Symposium, 13-32 (eds. A.G. Türkmenoglu ve O. Akıman) METU Geological Engineering Department, Ankara.
[3] No, H. 2001. The development of the porous structure of the heat treatment and acid activation of bentonite. Master Thesis, Ankara University, Institute of Science and Technology, Ankara.
[4] Murray, H.H. 1999. Applied clay mineralogy today and tomorrow. Clay Minerals, 34, 39-49.
[5] Sailey, G.W. and Karichoff, S.W. 1973. “UV-VIS”., Spectroscopy in the characterization of clay mineral surfaces. Analytical Letters, 6(1), 43-49.

DESIGN OF IMPLEMENTATION OF RENEWABLE ENERGIES IN A SPANISH TRAINING SHIP

VÍCTOR ALFONSÍN, ROCÍO MACEIRAS, ANDRÉS SUÁREZ, MARTÍN SANJORGE

Víctor Alfonsín, Defense University Center, Rocío Maceiras, Defense University Center, Andrés Suárez, Defense University Center, Martín Sanjorge, Spanish Naval Academy

Abstract

The trend towards the use of renewable and alternative energy in the terrestrial has gained in the last decade by many factors. However, in the maritime scenario, the change is being slower. In this sense, some approaches to the use of alternative energy systems on ships mainly with photovoltaic energy have only tried. Recently, the shipping industry has begun to consider possible ways to reduce fossil fuel consumption and being environmentally friendly. The concepts of "Green Ship" or "Sustainable Shipping" are becoming important issues for the owners of shipping companies and ship owners worldwide. The main objective of this research is to design and simulate under Matlab®/ Simulink® environment a possible implementation of different systems of renewable energy (hydro generation, wind generation and solar generation) in the training ship for the Royal Spanish Navy “Juan Sebastián de Elcano”. The aim of this work was to design and verify the possible technical feasibility of a number of devices that use the energy that could be present in the sea in the form of wind (wind generation), sun (photovoltaic) and ocean currents (hydro generation) for generating electric power. With this attempt, it could be possible to provide energy to conventional auxiliary systems in emergencies. Finally, the feasibility of the installation of these renewable energies in Juan Sebastián de Elcano is shown in a friendly way, i.e., without dramatically altering the image of the ship.

Keywords: renewable energy, hybrid, batteries, ship

Introduction

The increase of energy prices and environmental catastrophes lead to a development of alternative and renewable energy systems (Balaguer et al., 2016). A high efficient electric engine with a variety of the source could replace the traditional internal combustion engine (ICE). A battery system with a renewable energy provider, like photovoltaic panels, affects promising results (Diouf, et al., 2015).

In the last few years, the implementation of renewable energy sources, for example photovoltaic and wind energy in Hybrid Renewable Energy Systems (HRES), is becoming more popular. Those systems are very depending on seasonal impacts and that is the main disadvantage (Iverson et al., 2013). Not only land vehicles can use HRES (Brown et al., 2008, Van Mierlo et al., 2004), but also boats can incorporate hybrid systems (McConnell, 2010). Electric energy production is performed with renewable energy provided by several photovoltaic panels and small eolic generators located in the own boat. Furthermore, this energy production can be increased during the sail navigation with one or more hydrogenerators.

For those types of systems, which mix many power sources, mathematical simulation has become an object of study for electric battery vehicles and all kind of hybrid configurations and even specific software has been developed (Wai et al., 2015). However, there is a lack of information about battery electric ship simulations and even less about renewable energy sources applied in these kinds of vehicles.

In this paper, an auxiliary power system with renewable energy is created, simulated and adapted for using in the training ship for the Royal Spanish Navy “Juan Sebastián de Elcano” (Figure 14). The energy provided with several renewable sources (eolic, solar and hydrodynamic) is stored with batteries. Subsequently independent modular models for each energy system will be development in Matlab®/Simulink® and embedded. All of these simulations are managed by a logic controller implemented in Matlab®.

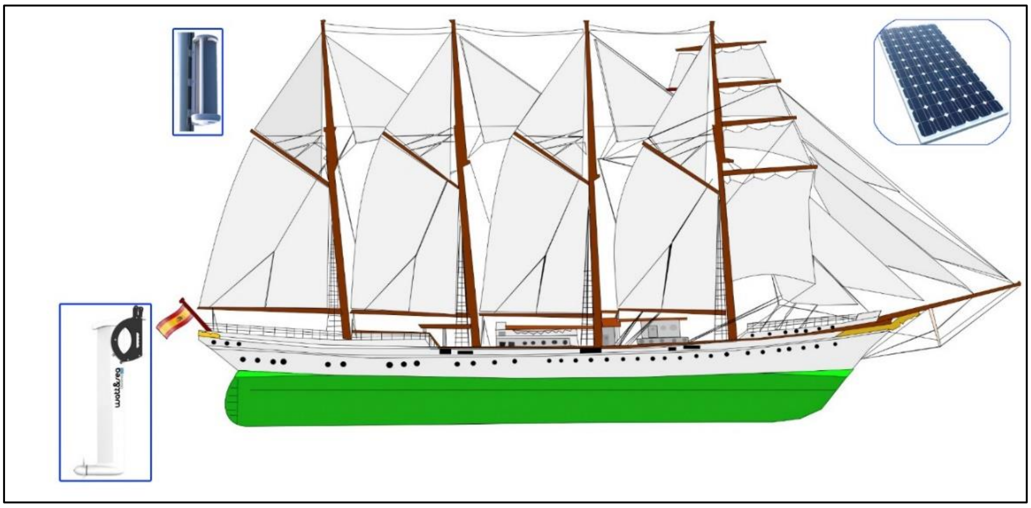

Figure 14. Royal Spanish Navy “Juan Sebastian de Elcano”

Photovoltaic generation system model

The base of a photovoltaic system is the operation of a photovoltaic panel. Those panels are photosensitive devices, which generate electricity by using the photovoltaic effect. This effect describes the transformation of solar radiation into electrical power.

The modelling of this system is used to give a forecast of the energy, generated by the integrated photovoltaic panels. The calculation requires an amount of variables, which are not public available, but the de Soto model only uses five inputs (De Soto, 2004), to find in every datasheet of a photovoltaic panel. Those data are: open circuit voltage (V_{oc}) short circuit current (I_{sc}), voltage (V_{mp}), current of maximum power (I_{mp}) and the temperature coefficients of V_{oc} and I_{sc}. They are to refer to the standard radiation of 1000 W/m^2 at 25°C cell temperature.

Moreover, this model has been modified by Hadj Arab, obtaining an expression which lets to evaluate the maximum power output (Hadj Arab et al., 2004):

$$\boldsymbol{P_{mp} = \frac{G}{G_{ref}} P_{mp,ref}\left[1 - \gamma\left(T - T_{ref}\right)\right]}$$

Where P is the power output, G is the incident irradiance, T is the temperature, m_p refers to maximum power, ref refers to standard conditions (G_{ref}=1000W m^{-2}, T_{ref}=25°C) and γ is the maximum power correction factor for temperature.

The selected panel was the Solbian FLEX-SP137 (Solbian Energie Alternative SRL , 2015). These panels are fully wheatherproof mono-cristraline solar modulles and they are designed for marine applicacions. In this ship, it is possible the emplacement of twenty panels. The mainly charecteristics are shown in **Hata! Başvuru kaynağı bulunamadı.**.

Peak power	137 W
Rated Voltage (V_{mp})	24 V
Rated current (I_{mp})	5.7 A
Open circuit voltage (V_{oc})	29.1 V
Short circuit current (I_{sc})	6 A
Temperature coefficient P_{max}	-0.38%/°C
Temperature coefficient V_{oc}	-0.27%/°C
Temperature coefficient I_{sc}	0.05%/°C
Temperature of reference	25ºC
Length	58.66”
Width	21.50”
Thickness	0.079”
Weight	4.4lbs
Number of cells	44

Table 4. Datasheet of photovoltaic panels

Eolic generation

The selected eolic generator was a vertical axis wind turbine. These aerogenerators are considered as the best solution since they can generate energy through wind low speed, allows their installation with other nearby wind turbines and finally do not disturb excessively the image of the training ship. A Savonius type (LE-V150) from Leading Edge was chosen. The technical specifications are shown in Table 5 (Leturbines, 2015):

Rotor diameter/Rotor height	270 mm/918 mm
Rotor Type:	Savonious
Blade Material:	Aluminium
Rated output	24 W at 8 m/s (17.8 mph)
Peak output	200 W
Cut-in speed	4 m/s (9 mph)
Weight	13 Kg
DC output voltage	12 V or 24 V

Table 5: LE-V150 Technical overview

The special shape of these generators allows their distribution and their emplacement in several zones of the ship. In our case, a possible emplacement of this type of devices could be on the top of the mast, one device in each mast. For the simulations a total number of 18 wind generators have been taking into consideration: two in the mizzen, two in each mainmast (stern and prow), two in the foremast, four in the wheelhouse, two in the castle, two in the poop deck and two in the access to the officers, with a maximum total power installed of 3.6 kW.

For modelling the wind generator, the characteristic curve with the representation of wind speed versus output power was parameterized using a polynomial adjustment. This characteristic curve was provided by the wind turbine manufacturer and it was adjusted with Matlab® adjustment tool (cftool), and the following equation that relates the eolic power (P_{eol}) with the wind speed (x) was obtained (Alfonsín et al., 2014):

$$\boldsymbol{P_{eol} = 0.003005x^3 + 0.1183x^2 + 2.2274x - 9.737}$$

Once implemented as Matlab® function, wind generator can be integrated with the other models in Simulink®. The simulated curve is shown in Figure 15.

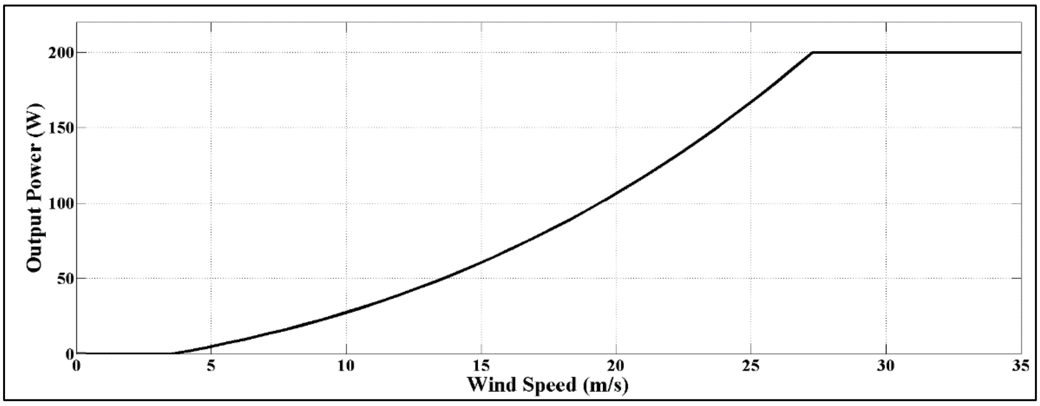

Figure 15. Wind generator characteristic curve under Matlab®/Simulink® environment

The wind speed values can be obtained with an anemometer placed on a boat or even via meteorological data of marine buoys. In the last case, it would be useful to subtract the forward speed of sailboat.

Hydrogeneration. Marine generation.

The marine generator or hydrogenerator is a device used only for sailing navigation (Queeney, 2012). This device generates electrical power from a propeller and a small generator. When the boat is running with electric motor, it is raised up to avoid the friction of propeller. But when boat is sailing without motor, it is submerged under water and the marine propeller generates the electrical power, in the same way as the wind turbine.

The procedure for the marine model is the same than eolic generator model. The polynomial adjustment is performed from manufacturer data and then implemented to Matlab-Simulink®.

The selected model was the Watt&sea cruising hydrogenerator with a maximum power of 500 W at 8 knots. Results of Watt&Sea hydrogenerator under Matlab®/Simulink® environmet are shown in Figure 16. The polynomial adjustment that relates the hydro power (P_{hyd}) with the sailboat speed (x) is the following (Alfonsin et al. , 2015):

$$P_{hyd} = 0.09208x^4 + 0.7897x^3 + 9.393x^2 - 29.02x + 2.896$$

Their emplacement was considered in three points of the ship: four devices on the starboard side, four on the port side and four in the astern. The total maximum power installed with hydrogeneration would be 6 kW.

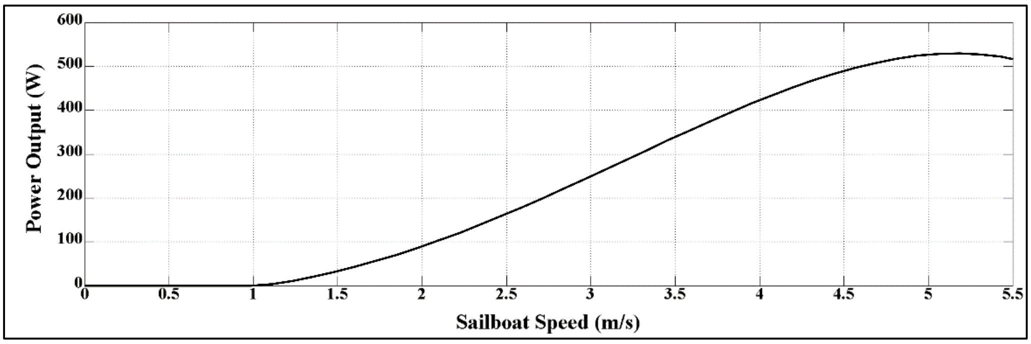

Figure 16. Hydro generator characteristic curve under Matlab®/Simulink® environment

Battery system

The battery dynamic behaviour was modelled through a simple battery equivalent circuit as a voltage source in series with a resistance. This circuit consists of a voltage source in series with a resistance. If the current (I) is flowing out of the battery, the equation to calculate the battery voltage (V) is the following (Larminie et al. 2003; Bird, 2007):

$$V = OCV - IR_{int}$$

Where OCV is the open circuit voltage and the internal resistance (R) is assumed with a constant value for the battery charge and other value for the discharge process. The open circuit voltage was implemented as Matlab®

Function which depends of battery state of charge (SoC). In order to considerer the effect of discharge power magnitude in the battery capacity the Peukert's equation is used. The Peukert's correction estimates the available capacity using the following equation (Peukert, 1897):

$$\boldsymbol{C_p = T_{disch} I_k^{disch}}$$

Where C_p is the theoretical capacity, I_{disch} is the discharge current, T_{disch} is the discharge time and k is the Peukert's coefficient.

The battery is used as an energy storage system. A battery system of the type $LiFePO_4$ was selected. The main advantages of this kind of batteries are: high theoretical capacity, moderate operating flat voltage, thermal stability, excellent reversibility, low cost and environmental benignity (Li et al., 2009). In this case, Solar power system lithium battery TB-48260F from TOPBAND was chosen for the simulation. Its properties are collected in Table 6 (Top Band Batteries, 2014):

Nominal Voltage	51.2 V
Nominal Capacity	260 Ah
Energy	13.3 kWh
Length	1430 mm
Width	455 mm
Height	358 mm
Weight	195 Kg
Battery life	2000 cycles

Table 6. Technical features (TB-48260F)

The battery system is sizing to supply energy to the distribution panel, whose maximum demanded power is 190 kW. Then, 36 batteries in series are necessary to provide this power.

Global model

The global model (Figure 17) collects all the individuals models simulated in this research. This model includes the renewable generation, its storage in batteries and the consumption of auxiliary devices. This model allows to simulate the renewable energies for a cruise of the ship.

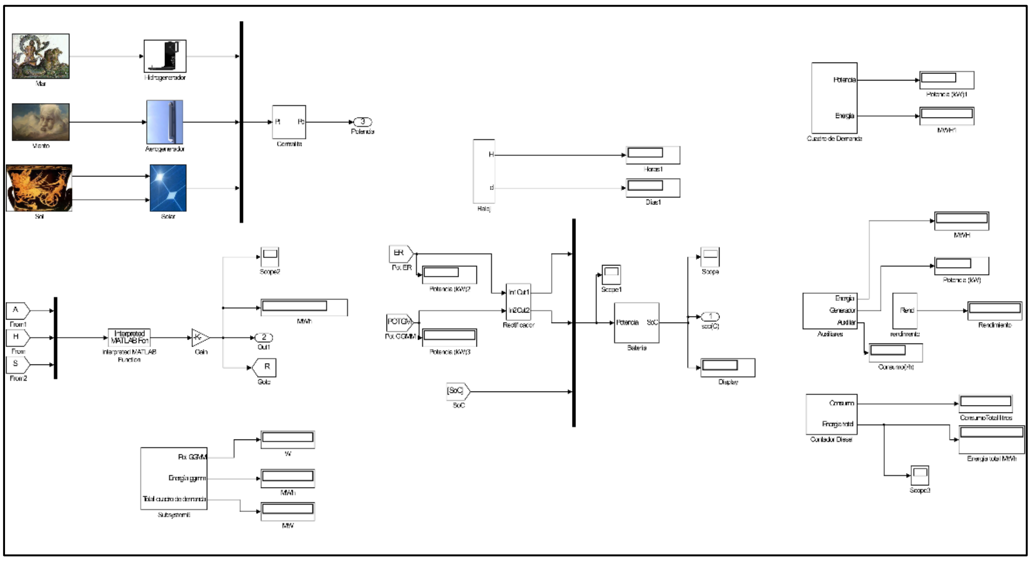

Figure 17. Renewable energy global model under Simulink®

Renewable energy production

In this research, it has been simulated the total renewable energy generated in a cruise of 90 days where the sailing would be of 90%. Figure 18 shows the total generation for the whole cruise. The renewable energy produced was 6820 kWh where: the 46% is hydro generated, the 35% is generated by the wind and the 19% comes from solar energy.

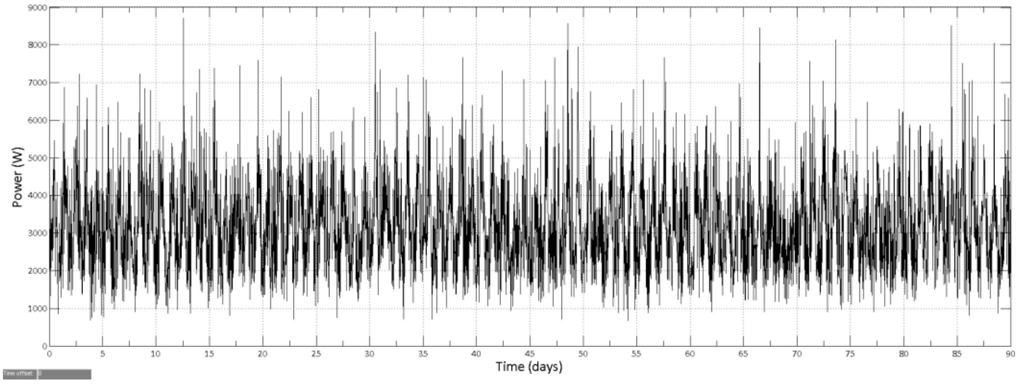

Figure 18. Renewable production

Auxiliary consumption

The main objective of the implementation of renewable systems is to supply energy to Midshipmen area in the ship. The most important section in this area is the cockpit and distribution panel. Then, the idea of this research is to provide energy to these systems in an emergency.

The distribution panel is divided in three different subpanels: vital consumption (116.88 kW), semivital consumption (7.18 kW) and no vital (29.54 kW). Once the simulations of charge batteries were carried out, it can be established that the battery system can be charged totally fourteen times. Considering that this result represents a high number of cycles and due to this system can only be used in emergencies, it would be interesting that its duration is the maximum. Then, the hypothesis of using this system twice during a cruise is assumed. Therefore, the batteries capacity can be increased seven times. For that, seven systems of batteries are connected in parallel. This allows that the autonomy can be increased seven times. Table 7 sums up the autonomy of battery system for the different scenarios.

	1 battery system		7 battery systems	
Autonomy Consumption	1 cycle	total (14 cycles)	7 cycles	total (2 cycles)
Vital	4.1 hours	57.4 hours	28.7 hours	57.4 hours
Vital + Semivital	3.8 hours	53.9 hours	26.6 hours	53.9 hours
Distribution panel	3.1 hours	14.3 hours	21.7 hours	14.3 hours

Table 7. Distribution of use of renewable energy for emergency systems

Conclusions

The obtained results in this research allows to conclude that the implementation of HRES (eolic, photovoltaic, hydro generated) is suitable in sailboats. In this case, this type of energy has been used to supply energy in emergencies, allowing the performance of distribution panel during almost one day (21 hours) and more than one day for vital and semivital consumptions (26-28 hours).

References

Alfonsin, V., Suarez, A., Urrejola, S., Miguez, J. and Sanchez, A., 2015. Integration of several renewable energies for internal combustion engine substitution in a commercial sailboat. International Journal of Hydrogen Energy, 40(20), pp. 6689-6701.

Alfonsín, V., Suarez, A., Cancela, A., Sanchez, A. and Maceiras, R., 2014. Modelization of hybrid systems with hydrogen and renewable energy oriented to electric propulsion in sailboats. International Journal of Hydrogen Energy, 39(22), pp. 11763-11773.

Balaguer, J. and Cantavella, M., 2016. Estimating the environmental Kuznets curve for Spain by considering fuel oil prices (1874–2011). Ecological Indicators, 60, pp. 853-859.

Bird, J., 2007. Electrical Circuit Theory and Technology. Oxford: Taylor & Francis.

Brown, D., Alexander, M., Brunner, D., Advani, S.G. and Prasad, A.K., 2008. Drive-train simulator for a fuel cell hybrid vehicle. Journal of Power Sources, 183(1), pp. 275-281.

De Soto, W., 2004. Improvement and validation of a model for photovoltaic array performance.

Diouf, B. and Pode, R., 2015. Potential of lithium-ion batteries in renewable energy. Renewable Energy, 76, pp. 375-380.

Hadj Arab, A., Chenlo, F. and Benghanem, M., 2004. Loss-of-load probability of photovoltaic water pumping systems. Solar Energy, 76(6), pp. 713-723.

Iverson, Z., Achuthan, A., Marzocca, P. and Aidun, D., 2013. Optimal design of hybrid renewable energy systems (HRES) using hydrogen storage technology for data center applications. Renewable Energy, 52(0), pp. 79-87.

Larminie, J. and Lowry, J., 2003. Electric Vehicle Technology Explained. Oxford: John Wiley & Sons.

Leturbines, 2015, 2015-last update, LE-V150 Technical overview. Available: http://www.leturbines.com/products/le-v150-wind-turbine/ [12/01, 2015].

Li, Z., Zhang, D. and Yang, F., 2009. Developments of lithium-ion batteries and challenges of LiFePO4 as one promising cathode material. Journal of Materials Science, 44(10), pp. 2435-2443.

McConnell, V.P., 2010. Now, voyager? The increasing marine use of fuel cells. Fuel Cells Bulletin, 2010(5), pp. 12-17.

Peukert, W., 1897. Über die Abhänigkeit der Kapazität von der Entladestromstärke bei. 27, pp. 287–288.

Queeney, T., 2012. Electricity from heavy water. Ocean Navigator, January/February, pp. 12.

Solbian Energie Alternative SRL, 2015-last update, Datasheet of Solbian FLEX-SP137. Available: http://www.solbian.eu/ [November, 2015].

Top Band Batteries, 2014-last update, Datasheet of TB-48260F. Available: www.topbandenergy.com [01/06, 2015].

Van Mierlo, J., Van Den Bossche, P. and Maggetto, G., 2004. Models of energy sources for EV and HEV: Fuel cells, batteries, ultracapacitors, flywheels and engine-generators. Journal of Power Sources, 128(1), pp. 76-89.

Wai, C.K., Rong, Y.Y. and Morris, S., 2015. Simulation of a distance estimator for battery electric vehicle. Alexandria Engineering Journal, 54(3), pp. 359-371.

CHEMICAL COMPOSITION AND BACTERICIDAL ACTIVITY OF AQUEOUS PROPOLIS EXTRACTS FROM BABOR ALGERIA

SOLTANI EL-KHAMSA, MEZAACHE-AICHOUR SAMIA, CHAREF NOUREDDINE AND ZERROUG MOHAMED MIHOUB

Abstract

Propolis is a plant resinous substance masticated with bee salivary enzymes and mixed with beeswax. This resinous hive product was used as a remedy for treatment of many diseases in folk medicine3. Progressive studies have shown that propolis has antimicrobial, anti-inflammatory, hepatoprotective, anti-oxidative effects and stimulates immune system along with many biological ways. The Algerian propolis raw samples were collected from Babor, Sétif region, east of Algeria, in 2011 scraping the sample off from the frames of beehives. Water extraction was carried out using. 25 g of air-dried propolis which were ground into a fine powder in a blender and mixed with 400 mL boiling water by magnetic stirrer 15 min until 1h then filtered and evaporated1. Propolis water extracts was chemically analysed by gas chromatography-mass spectrometry using Hewlett Packard Gas Chromatograph 6890 Series II Plus () linked to Hewlett Packard 6972 mass spectrometer system equipped with a 30 m long, 0.25 mm id, and 0.5 µm film thickness HP5-MS capillary column2. 49 compounds were identified including aromatic acids (Cinnamic acid, Ferulic acid), linear hydrocarbons and their acids, terpenes (Caryophyllene) and alcaloïdes (Cannabinol). Furthermore, the in vitro antibacterial activity of this aqueous extracts were evaluated against 11 bacterial strains. The obtained results showed that this extracts inhibit the growth of Pseudomonas aerugenosa, Staphylococcus aureus, Klebsiella pneumonia and Proteus vulgaris with inhibition zones of 10, 14, 13 and 11 mm respectively.

POLYPHENOL CONTENTS AND ANTIOXIDANT ACTIVITY OF AQUEOUS EXTRACT OF PROPOLIS FROM SÉTIF, ALGERIA

EL-KHAMSA SOLTANI, NOUREDDINE CHAREF, SAMIA MEZAACHE, MOHAMED MIHOUB ZERROUG

EL-KHAMSA SOLTANI[1], NOUREDDINE CHAREF[2], SAMIA MEZAACHE[3] , MOHAMED MIHOUB ZERROUG[3]
[1]Department of process engineering, University of Ferhat Abbas, Setif1, Algeria
[2]Laboratory of Applied Biochemistry, faculty of natural and Life sciences, University Ferhat Abbas Sétif 1 Algeria
[3]Laboratory of Applied Microbiology, faculty of natural and Life sciences, University Ferhat Abbas Sétif 1 Algeria
rina.saba@yahoo.fr charefnr@yahoo.fr, mezaic2002@yahoo.fr, med_zerroug@yahoo.fr

Abstract
The Propolis, an extremely complex resinous material, exhibits valuable pharmacological and biological properties attributed to the presence of polyphenols. In this study, we determined the antioxidant properties of aqueous extract of propolis (AEP) from Sétif of Algeria and correlated the values with total levels of polyphenolic compounds. In order to estimate the capacity of AEP to act as antioxidants, we studied its 1,1-diphenyl-2-picryl-hydrazyl radicals (DPPH$^\bullet$) scavenging activity. This study will bring an innovation for further studies with regard to the antioxidant properties of aqueous extract of propolis. Thus Setifian propolis, being a rich source of natural antioxidants, may be used in the prevention of various free radicals related diseases.

Keywords: Propolis; Polyphenol content; Antioxidant activity; radical scavenging.

INTRODUCTION

Propolis has been much popular as an agent in traditional medicine and food supplementary material for human health in the world [1.2]. It is a commercial resinous product and contains phenols and many other preventive agents. Propolis is produced by honeybees using collected extracts from leaves, buds and exudates of various plant floras. Propolis is used as a building material in order to strengthen the borders of combs and as a chemical weapon against the pathogen microorganisms [3]. It's antibacterial, antiviral, antitumor, anti-inflammatory, anticancer and immunomodulatory effects have been reported [4.5] .

Complexity and variety of the chemical composition of propolis has been reported in the literature. From different botanical and geographical origins of world, more than 300 compounds including volatile organic compounds, flavonoid aglycones, phenolic acids and their esters, phenolic aldehydes, alcohols and ketones, sesquiterpenes, quinones, coumarins, steroids, aminoacids were reported to have been isolated from propolis [2.6]. All of these compounds are responsible for its biological and pharmacological activities. Therefore, propolis has been used in traditional medicine, cosmetics and food industry from the Europe to East Asia [7].

The chemical composition of propolis is affected by climate conditions and the type of bee flora. As a result, various biological activities of propolis are directly influenced by botanical and chemical diversity [8].

In this study, we investigated the inhibition of reducing antioxidant power assay DPPH$^\bullet$ scavenging activities of AEP. This method is recommended to measure antioxidant properties of food or pharmacological materials that better reflect their potential protective effects. Furthermore, another significant goal of this study was to clarify the polyphenol contents of AEP.

MATERIALS AND METHODS

CHEMICALS

1,1-diphenyl-2-picrylhydrazyl (DPPH), gallic acid, quercetin from Sigma other reagents were of analytical grade.

Preparation of aqueous extract of propolis samples (AEP)

Propolis samples were collected from sétif (east of Algeria) and were then kept and dried in the dark until processing.

Extraction was carried out as described previously [9]. For water extraction, 25 g of air-dried propolis was ground into a fine powder and mixed with 400 mL boiling water by magnetic stirrer for 15 min. Then the aqueous extract was filtered over cheese-cloth and Whatman No. 1 paper, respectively. The filtrates were evaporated to near dryness on a rotary evaporator under reduced pressure at 40 °C and then freez-dried. The resulting powder was used for further studies.

Determination of total phenolic content

The total phenol contents of AEP were determined by using the method of Gülçin [10] based on the procedure described by Singleton[11]. The appropriate dilutions of propolis (0.1 ml) were oxidized with Folin–Ciocalteu's reagent (0.5 ml) in a volumetric flask. The reaction was neutralized with saturated sodium carbonate solution (0.4 ml). The contents in the tubes were thoroughly mixed and allowed to stand at ambient temperature for 2 h until the characteristic blue colour developed. Absorbance of the clear supernatants was measured at 765 nm using a spectrophotometer. The content of total phenolic in AEP was calculated based on a standard curve prepared using gallic acid and expressed as milligrams of gallic acid equivalent (GAE) per gram of sample. Standard calibration was made from 10 to 140 µg gallic acid (r^2: 0.9864).

$Absorbance\ (\lambda_{765}) = 0.0091\times [GAE] + 0.1005$

The content of total phenolic in AEP was calculated by employing a standard curve as above prepared using gallic acid and expressed as micrograms of gallic acid equivalents (GAE).

Determination of total flavonoids contents

The total flavonoid contents of AEP were determined using the aluminum chloride colorimetric method of Köksal [12] based on the method of Chang[13]. The appropriate dilution of extracts (1 ml) was mixed with 1ml of aluminum chloride (2%). After incubation at room temperature for 10 min, the absorbance of the reaction mixture was measured at 430 nm with a spectrophotometer. The flavonoid content was calculated using a standard calibration of quercetin solution and expressed as micrograms of quercetin equivalent (QE) per gram of sample.

$Absorbance\ (\lambda_{430}) = 0.0281\times [QE] + 0.0102$

The content of total flavonoids in AEP was calculated from the above standard curve prepared using quercetin and expressed as micrograms of quercetin equivalents (QE). Standard calibration was made from 1 to 40 µg quercetin (r^2: 0. 9982).

DPPH• scavenging activity

The DPPH• solution has a deep violet colour and radical scavenging activity of antioxidant compounds can be measured spectrophotometrically at 517 nm by the loss of absorbance as the pale yellow non-radical form (DPPH-H) is produced. The hydrogen atom or electron donation abilities of some pure compounds were measured by bleaching a purple-coloured methanol solution of the stable DPPH radical. The method of Blois [14], previously described by Gülçin [15], was used with slight modifications in order to assess the DPPH• free radical scavenging capacity of LAEP. The DPPH radical shows absorbance at 517 nm, but its absorption decreases upon reduction by an antioxidant or a radical. When a hydrogen atom or electron was transferred to the odd electron in DPPH•, the absorbance at 517 nm decreased proportionally to the increases in non-radical forms of DPPH [16]. Briefly, 0.04% solution of DPPH• was prepared in methanol and, 1.25 ml of this solution was added to 50 µl of AEP solution in ethanol at different concentrations (0.3–1 mg/ml). These solutions were vortexed thoroughly, and incubated in dark for 30 min. Thirty minutes later, the absorbance was measured at 517 nm against blank samples lacking scavenger. A standard curve was prepared using different concentrations of DPPH•. The DPPH• scavenging capacity was calculated from the calibration curve determined by linear regression (r^2: 0.9937):

$Absorbance\ (\lambda_{517}) = 51.725\times [DPPH\cdot] + 7.9125$

The capability to scavenge the DPPH• radical was calculated using the following equation:

$Scavenged\ DPPH^{\bullet}\ (\%) = (1 - \lambda_{517\text{-}S} / \lambda_{517\text{-}C}) \times 100$

Where $\lambda_{517\text{-}C}$ is the absorbance at 517 nm of the control reaction (containing all reagents except the test compound) and $\lambda_{517\text{-}S}$ is the absorbance at 517 nm containing the test compound. The concentration of AEP providing 50% inhibition (IC_{50}) was calculated from the graph plotted inhibition percentage against AEP concentration (mg/ml, DPPH significantly decreases upon exposure to radical scavengers) [14].

RESULTS AND DISCUSSION

Total polyphenol and flavonoid contents of aqueous extract of propolis samples (AEP)

The amounts of total polyphenol and flavonoid contents in Setifian propolis are 228.68 mg/g of AEP and 2.690 mg/g of AEP, respectively.

Phenolic compounds are commonly found in both edible and non-edible plants, and they have been reported to have multiple biological effects, including antioxidant activity [17]. Propolis contains a wide variety of phenolic compound, mainly flavonoids. Variation in the flavonoid content of propolis is mainly attributable to the difference in the preferred regional plants collected by honeybees. Contents of flavonoid and other phenolic substances have been suggested to play a preventive role in the development of cancer and heart disease [17].The Folin–Ciocalteu method and the $AlCl_3$ coloration are currently used to determine the total polyphenol and flavonoid contents, respectively [18]. In the present study, we applied these methods to determine the total polyphenol and flavonoid contents of Setifian propolis sample. These physicochemical methods are useful for evaluating various propolis samples because propolis contains many phenolics also evaluated propolis using these methods.

DPPH free radical-scavenging activity of various propolis samples

Because the free radical-scavenging activity of antioxidants is considered to be due to their hydrogen-donating ability, we used a method based on the reduction of DPPH, a stable free radical, to evaluate the antioxidant activity of AEP sample [19]. DPPH has been widely used to test the free radical-scavenging activity of various samples [20]. We evaluated the free radical-scavenging activity of AEP (Fig.1).the concentration of extract needed to scavenge the free radicals by 50% was calculated as 0.813 mg/ml.

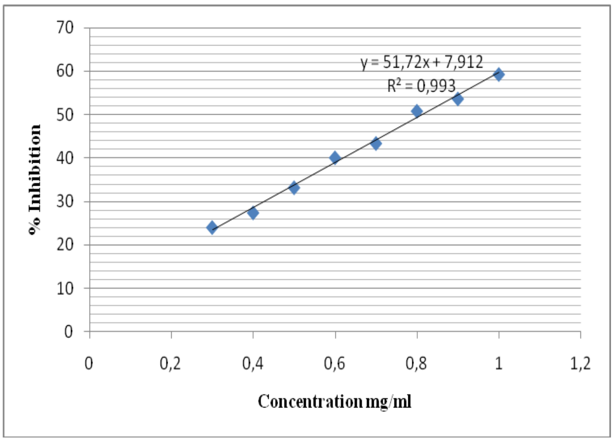

Figure 1. Variation of the inhibition of DPPH according to the concentration of EPA

On the other hand, there are few reports about water extract of propolis [21]. To date it is reported that water extract of propolis has good antioxidant activity, associated with high contents of phenolic compounds. This supports our present findings (quantity of phenolic compounds about 228.68 mg/g powder). It is suggested that water extract of propolis contains a mixture of natural substances, such as amino acids, phenolic acids, phenolic acid esters, flavonoids, cinnamic acid, and caffeic acid. The present studies reveal that water extract of propolis is a natural antioxidant and this explains the previously reported beneficial effects. At present, there are few reports about the components of water extract of propolis [22] ascribed the high hepatoprotective activity in water extract of propolis to four di-*O*-caffeoyl quinic acid derivatives: methyl 3,4-di-*O*-caffeoyl quinate, 3,4-di-*O*-caffeoyl quinic acid, methyl 4,5-di-*O*-caffeoyl quinate, and 3,5-di-*O*-caffeoyl quinic acid. It was not found whether these four compounds have an effect on the antioxidant activity in water extract of propolis. The water extract of propolis may have further potential value in patients with various diseases, such as cancer, cardiovascular disease, and diabetes. Research is underway to analyze the antioxidant compounds of propolis and to identify differences in chemical composition in relation to different climates and flora.

REFERENCES

[1] Pereira, A.D., Faloni de Andrade S., Swerts M.S.O., Maistro,E.L. 2008 First in vivo evaluation of the mutagenic effect of Brazilian green propolis by comet assay and micronucleus test. Food Chem. Toxicol., 46: 2580–2584

[2] Bankova,V.S,. De Castro, S.L., Marcucci, M.C. 2000. Propolis: recent advances in chemistry and plant origin Apidologie. 31: 3–15

[3] Wollenweber, E., Hausen,B.M., Greenaway,W. 1900. Phenolic constituents and sensitizing properties of propolis. poplar balsam and balsam of Peru Bull. Group Polyphenols, 15: 112–120

[4] Banskota,A.H., Tezuka, Y., Adnyana, I.K., Ishii, E., Midorikawa, K., Matsushige, K., Kadota S. 2001. Hepatoprotective and anti-*Helicobacter pylori* activities of constituents from Brazilian propolis. Phytomedicine, 8: 16–23

[5] Zhou, J., Xue, X., Li, Y., Zhang, J., Chen, F., Wu, L., Chen, L., Zhao, J. 2009. Multiresidue determination of tetracycline antibiotics in propolis by using HPLC–UV detection with ultrasonic-assisted extraction and two-step solid phase extraction. Food Chem., 115: 1074–1080

[6] Ahn, M.R., Kumazawa, S., Usui, Y., Nakamura, J., Matsuka, Zhu, M.F. *et al.* 2007. Antioxidant activity and constituents of propolis collected in various areas of China. Food Chem., 101: 1400–1409

[7] Chaillou, L., Nazareno M.A. 2009. Bioactivity of propolis from Santiago del Estero, Argentina, related to their chemical composition Food Sci. Technol., 42: 1422–1427

[8] Tosi, E.A., Ré, E., Ortega, M.E., Cazzoli A.F. 2007. Food preservative based on propolis: bacteriostatic activity of propolis polyphenols and flavonoids upon *Escherichia coli*. Food Chem., 104: 1025–1029

[9] Gülçin, I. 2008. Measurement of antioxidant ability of melatonin and serotonin by the DMPD and CUPRAC methods as trolox equivalent. J. Enzym. Inhib., Med. Chem., 23: 871–876

[10] Gülçin, I., Beydemir,Ş., Şat, İ.G., Küfrevioğlu, Ö.İ. 2005. Evaluation of antioxidant activity of cornelian cherry (*Cornus mas* L.). Acta Aliment. Hung., 34 (2005), pp. 193–202

[11] Singleton,V.L., Rossi, J.A. 1965. Colorimetry of total phenolics with phosphomolybdic phosphotungstic acid reagents. Am. J. Enol. Viticult., 16: 144–158

[12] Köksal, E., Gülçin, I. 2008. Antioxidant activity of cauliflower (*Brassica oleracea* L.). Turk. J. Agric. For., 32: 65–78

[13] Chang, C.C., Yang, M.H., Wen, H.M., Chern, J.C. 2002. Estimation of total flavonoid content in propolis by two complementary colorimetric methods. J. Food Drug Anal., 10: 178–182

[14] Blois , M.S. 1958. Antioxidant determinations by the use of a stable free radical. Nature, 26: 1199–1200

[15] Gülçin, I. 2006. Antioxidant and antiradical activities of l-Carnitine ,Life Sci., 78:. 803–811

[16] Ak, T., Gülçin, I. 2008 Antioxidant and radical scavenging properties of curcumin ,Chem. Biol. Interact., 174: 27–37

[17] Kahkonen, M.P., Hopia, A.I., Vuorela, H.J., Rauha, J.P., Pihlaja, K., Kujala, T.S. *et al.* 199. Antioxidant activity of plant extracts containing phenolic compounds. J. Agric. Food Chem., 47: 3954–3962

[18] Liu, M. Li, X.Q., Weber, C., Lee, C.Y., Brown, J., Liu, R.H. 2004. Antioxidant and antiproliferative activities of raspberries. J. Agric. Food Chem., 50: 2926–2930

[19] Tang, S.Z., Kerry, J.P., Sheehan, D., Buckley D.J. 2002. Antioxidative mechanisms of tea catechins in chicken meat systems. Food Chem., 76: 45–51

[20] Nagai, Sakai, T.M. Inoue, R., Inoue, H., Suzuki, N. 2001. Antioxidative activities of some commercial honeys, royal jelly, and propolis. Food Chem., 75: 237–240

[21] El-Ghazaly, M.A., Khayyal, M.T. 1995. The use of aqueous propolis extract against radiation-induced damage. Drugs under Experimental and Clinical Research, 21: 229–236

[22] Basnet, P., Matsushige, K.K., Hase, S. Kadota, T. Nanba, 1996. Four di-*O*-caffeoyl quinic acid derivatives from propolis. ”Potent hepatoprotective activity in experimental liver injury models Biol. Pharm. Bull., 19: 1479–1484

INVESTIGATING THE APPLICABILITY OF MECHANICAL RECYCLING IN KUWAIT BY STUDYING DEVELOPED STANDARDIZED FILM SAMPLES FROM VIRGIN/WASTE POLYMER RESINS SUBJECTED TO ACCELERATED WEATHERING

S.M. AL-SALEM, G. ABRAHAM, A.M. DASHTI, O.A. AL-QABANDI

S.M. Al-Salem[1*], G. Abraham[2], A.M. Dashti[2] and O.A. Al-Qabandi[3]
[1]Enviornment & Life Sciences Research Centre, Kuwait Institute for Scientific Research, P.O. Box: 24885, Safat 13109, Kuwait.
[2]Petroleum Research Centre, Kuwait Institute for Scientific Research, P.O. Box: 24885, Safat 13109, Kuwait.
[3]EQUATE Petrochemical Company, R&D Department, P.O. Box: 91717, Ahmadi 61008, Kuwait.

Abstract

Enigmatically, plastic solid waste (PSW) has been viewed in the region as a burden on the economy. On the other hand, plastics are nothing more than polymer(s) and additives, making them a crude oil derivative constituting high calorific value with a versatility for a number of applications. Once this view is established, PSW in context of municipal solid waste (MSW) could be considered as a resource.

In this work, plastic waste films generated in the state of Kuwait have been randomly sampled. A total of 150 samples were subjected to differential scanning calorimetry (DSC) to determine the melting point (T_m) of its constituting polymer(s). After which, the samples were milled in an industrial cutting mill (3x3 flakes) and fed to a single screw extruder (L/D ratio=30, DHT=175°C and P=40 bars) to produce the waste resin. Pelletized waste blends were compounded with virgin commercial linear low density polyethylene (LLDPE) resin in different weight ratios spanning over a wide spectrum of mixtures. The ratios extruded were (waste/virgin): 0/100, 5/95, 10.90, 25/75, 50/50, 75/25, 90/10 and 100/0. Standard moulds were used to cut and prepare films (20x1 cm) of the compounded material and were subjected to mechanical profile testing apparatus (Testometric - 2.5 kN load). Results were compared with commercial grade films in Kuwait and found to be comparable (if not superior) to commercial grade.

Accelerated weathering was performed and results of which shown in this communication for the waste and virgin blends, after exposure to a QUV accelerated weathering chamber, to investigate their outdoor application appropriateness and durability. It was concluded that waste films in Kuwait, which are used in a single cycle by consumers, constitute an excellent blend with virgin resins due to their lack of photo-oxidative and thermal degradability. In addition, waste acted as a deteriorating filler to the virgin resin as seen by the preliminary results of accelerated weathering, losing its mechanical integrity with hours of exposure.

Keywords: Plastic Solid Waste (PSW), Municipal Solid Waste (MSW), Polymer, Resin, Weathering, Engineering, Operating Pressure.

*Corresponding Author: Dr. Sultan Al-Salem, Kuwait Institute for Scientific Research, P.O. Box: 24885, Safat 13109, Kuwait. Tel:+965-2495-6877, Fax: +965-2398-7673, Email: ssalem@kisr.edu.kw.

Introduction

Polymers degrade via different paths, mainly due to photo-degradation (photo oxidation process), biodegradation (bio-agents additions to induce microbial degradation) and thermal degradation. These degressive routes lead to a number of deteriorating effects in the plastic article causing it to lose its integrity and properties. It is essential for plastic resin converters to keep commercial targets. This could be achieved by utilizing in-house process scrap and re-introduce it to the polymer heating cycle in conversion processes. This process is well established and commonly referred to as primary recycling (Al-Salem et al., 2010). However, to reduce conversion costs more effectively, plastic solid waste (PSW) could be utilized after collection and segregation in what is commonly referred to as mechanical recycling. The term originates from the use of mechanical means to process PSW. Blending takes place with virgin polymers, in order to, keep the integrity of products to acceptable standards for the market.

Polymer degradation is caused by a number of reactions on a molecular level. It initiates (in both photo and thermal degradation) chain scission and cross-linking, especially in polyolefins. This phenomena occurs whilst thermal processing takes place, i.e. conversion of plastic. It is also something that needs to be addressed when a product is being tested under certain weather for outdoor applications. Weathering also leads to degradation by irreversible molecular level reactions. These will ultimately change mechanical and physical properties of the polymer blend. Weathering degrades polyolefins by different mechanisms depending on type of polymer. It induces hydro-peroxide formation by chemical reactions, allowing oxygen to diffuse in the polymer matrix (i.e. photo-oxidation). And since natural weathering is an un controllable and unpredicted method of testing, accelerated weathering (AW) in laboratory conditions are normally applied to simulate weathering effects.

In the state of Kuwait, PSW is not handled optimally and ways of dealing with this ever growing fraction of municipal solid waste (MSW) can categorically improve. Landfilling is the standard practice of disposal in Kuwait with no means of energy recovery. However, waste scavengers do segregate PSW in landfill sites upon need of collection to recycle via private companies. The segregation is manual and very primitive, and is done to separate rigid products from film plastic only (Al-Salem et al., 2014). It is also worth noting that recent studies show Kuwait's PSW fraction in MSW has increased dramatically. Between the years of 2001 to 2012, a 35% increase has been estimated recently; and in 2013 PSW was estimated to be 200 ktons (KM, 2014; CSB, 2014; Al-Salem et al., 2014). Hence, it is imperative to implement mechanical recycling on a state level in efforts to reduce the carbon footprint of plastic products and give way to a more green practice in polymer conversion. Furthermore, it is important to start initiating research activities in implementing this waste fraction effectively, in order to start, a product development scheme for future utilization. It is also important to note that in mechanical recycling, it is paramount to study the polymeric blend intended for product development in knowing its history and applicability. It was deemed to be a misconception that polymer blends result in intermediate properties of each component in the mixture. Depending on the content of the waste, aged polymers or recyclate material, resultant properties could be counter-balance each other due to samples history. Governed by the content of the added material to the virgin resin; and thermal processing conditions, some polymers have been reported to act as a compatibleser or a deteriorant (Phillip et al., 2004). Polyolefin polymers, namely polyethylene (PE) has been widely used for various applications in packaging, agricultural and industrial applications. High and low density polyethylene (HDPE and LDPE, respectively) have been targeted in a number of past studies to study their post weathering properties (Basfar and Ali, 2006; Al-Salem, 2009; Mourad, 2010; Ojeda et al., 2011; Tuasikal et al., 2014). However, Linear low density polyethylene (LLDPE) is superior in tensile and tear strengths; and posses higher environmental stress cracking over HDPE and LDPE due to its branched structure making it less susceptible to UV irradiation (Basfar and Ali, 2006). It is produced by the co-polymerisation of ethylene and α-olefin. It contains short chain branches which gives it these characteristics. DuPont Canada is credited with operating the world's first commercial LLDPE line, built in Corunna, Ont., in 1960

In this work, PSW from Kuwait (plastic waste films) was blended with a virgin polymer (LLDPE) in order to study the effect of waste addition to virgin polymer. Mechanical and physical properties were compared before and after exposure to accelerated weathering in laboratory conditions. The polymer degradation was studied and results are compared with commercial products and international standards. This was carried out in to assess applicability of product development in the future.

Experimental

Materials and random sampling

Plastic waste films (200 kg comingled plastics) were secured from National Waste Management Company (Kuwait). The films supplied were exposed to different durations to sunlight up to 3 months at one time upon storage in the company's yard.

In order to investigate the polymer types present in the plastic film waste used from the MSW, melting point (T_m) of the samples was determined. The waste films were randomly sampled following ASTM D 1898-68, and 150 samples were tested using a TA instrument Q-series model differential scanning calorimeter (DSC). 150 samples were randomly selected from the different collections. A 9±0.1 mg sample was placed in the DSC crucible, equilibrated at 40^{o}C for 5 minutes, after which heated using a 10^{o}C min^{-1} ramp to 200^{o}C min^{-1}. The cooling cycle was achieved by same ramp to 40^{o}C.

Linear low density polyethylene (LLDPE) was graciously supplied by EQUATE Petrochemical Company (Kuwait) and used in this work as white and translucent pellets with a density of 0.918 g/cm^3 and MFI of 2 g/10 min. For the purpose of confidentiality the company did not provide details of additives in this commercial grade.

Samples compounding

The plastic waste films were milled using an industrial cutting mill machine (Tecnova model) reducing its size to 3x3 mm flakes. The milled films were then pelletized to a 3x3 mm brownish pellets using a Tecnova industrial single screw extruder (L/D = 30) at 40 bars operating pressure and 70 RPM. Cooling temperature of the extruded strands was maintained between 16-17^{o}C. The extruder's die head temperature (DHT) was set to 175^{o}C. Direct dry blending of the formulations intend for investigation was undertaken. The LLDPE and waste fractions, in weight, considered in this study follow the ratio of 100/0, 75/25, 50/50 and 75/25, respectively. The films studied (0.1 mm thickness) were extruded and blown using a single screw extruder (Tecnova, L/D=30, 45 bars and 85 RPM) and a film blowing machine (Kung Hsing monolayer, DHT = 175^{o}C) with water cooling temperature maintained between 16 to 17^{o}C. A Ray Ran cutting machine (model RR/PCP) was used to cut a standard 20x1 cm films of the prepared formulations for further characterization. The samples appeared consistent with no fractures or crazing and were comparable to each other by touch. All samples were stored in laboratory conditions at 23°C/50% relative humidity in the dark between sample formulation and testing.

Accelerated weathering

Films of the different formulations were submitted to the action of accelerated weathering in accordance with ASTM 4329-92 and ASTM 4329-05. Samples were mounted on the racks facing UV lamps with no empty spaces in the panels, in order to maintain repeatable test conditions. Cycle A procedure was used for general application, i.e. 8 hours of UV exposure at 60^{o}C followed by 4 hours of condensation at 50^{o}C. At the end of each weathering test, the chamber was cooled to room temperature and trays were set to rest on a flat surface for a minimum of 24 hours.

Mechanical properties

Mechanical properties evaluation was conducted at room temperature to determine the impact of weathering on the film samples following ASTM D882-95a. Experiments were conducted using a Testometric (UK) universal testing machine-model DBBMTCL-250 kg (M250-2.5 kN load) with a 500 mm min^{-1} speed. Measured properties included: Young's modulus (MPa), stress at rupture (MPa), strain at break (%) and force at break (N). The measurement values obtained came from the average of 5 replicate specimens stored directly from the machine's software.

Physical properties measurements

A MF709 (spherical) haze meter (model BS 2782) was used to measure the haze and transmission at mid point of the studied samples, in accordance with ASTM D1003. Standard colour parameters for light/dark(L_s^*), red/green (a_s^*) and yellow/blue (b_s^*) were measured using a Nippon Denshoku model NF333 colormeter following ASTM D2244. Parameters measured were then used to calculate the total change in colour between control samples and each weathered formulation thus (Al-Salem, 2009):

$$\Delta E = \sqrt{(\Delta L)^2 + (\Delta a)^2 + (\Delta b)^2} \tag{1}$$

where ΔL, Δa and Δb are the subtracted difference between control specimens measurements and those of each tested batch. Replicates of 5 films for each formulation were measured.

Results and discussion

Plastic film waste random sampling: Validation of constituting polymers

According to recent surveys in Kuwait (Al-Qabandi, 2015), 90% of carrier bags converters in Kuwait use a blend of HDPE and LLDPE (90/10 by weight%). The other 10% is reserved for high quality carrier bags in Kuwait, which converters use LLDPE with a trace of other polymers for. This is in order to produce high glossy quality bags. Hence, the random sampling in this work was essential to determine the type of polymers used in the country for plastic films in general. This was revealed after studying typical resins converted in the market and was determined to be blends of various polyolefins, i.e. LDPE, LLDPE, HDPE and polypropylene (PP), classed to six categories, all of which were blends of two polymers with the exception of one (type 3-LLDPE). Results are categorized (Fig.1) and revealed the following percentage of polymers: LLDPE (46%), LDPE (51%), HDPE (1%) and PP (2%).

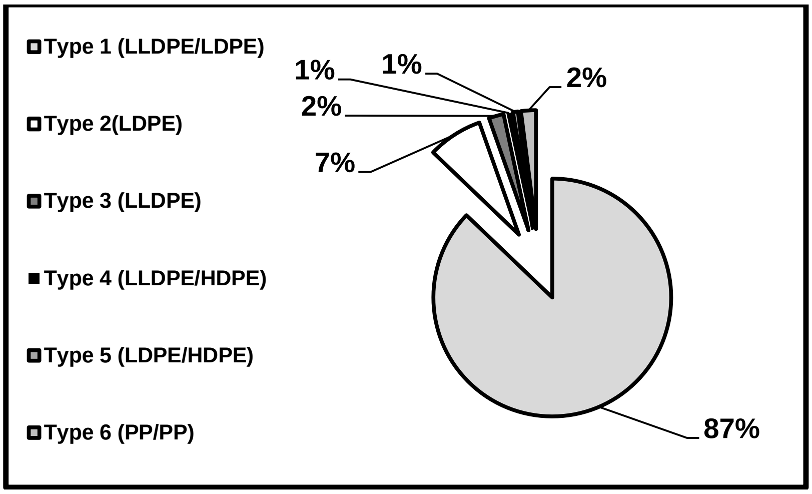

Fig.1. Random sampling analysis results conducted for plastic waste films.

Mechanical characterization

Mean values of mechanical properties were studied. The threshold limit of the virgin polymer (LLDPE) and the formulation of virgin/waste (75/25 wt.%/wt.%) was 360 hours of exposure to weathering with no deterioration or samples rupture. However, the other two formulations, with a waste content of 50 wt.% and 75 wt.%, respectively, had a 240 hours exposure threshold limit. Young's modulus showed an increasing trend in the studied materials with respect to exposure duration (Fig.2). This is attributed to the increase in **crystallinity** of the polyolefin matrix caused by the rearrangement of the molecules due to photo-oxidation. Photo-degradation induces cross-linking in polyolefins resulting in longer molecular chains, hence increasing the Young's modulus (Mendes et al., 2003; Lundin et al., 2004; Mourad, 2010). The addition of the waste fraction to the virgin polymer enhanced in the Young's modulus values proportionally. This could be due to the increasing content of LLDPE in the blend with the increase in the waste fraction added to the composition (Fig.2), indicating that waste in Kuwait does not reach degradation stage before export or commercial sales and could be utilized in mechanical recycling.

Stress (MPa) and strain at rupture (%) were studied independently and are represented with high regression using an exponential fit as shown in Figs.3-4. Virgin LLDPE showed a gradual increase by 3% up to 72 hours of exposure with a sharp drop as the polymer is exhibiting more **embrittlement**. This was witnessed in previous reports with virgin commercial grade polyethylenes (Al-Salem, 2009; Mendes et al., 2003, Basfar and Ali, 2006; Tuasikal et al., 2014). Adhesion exertion started to cause loss of property with the increase of the waste content. Molecular weight reduction has been reported in the past with increase of ageing time (Dehbi et al., 2010; Dehbi et al., 2011; Tuasikal et al., 2014). This phenomena causes the loss of stress making the polymer matrix less withstanding to applied stress.

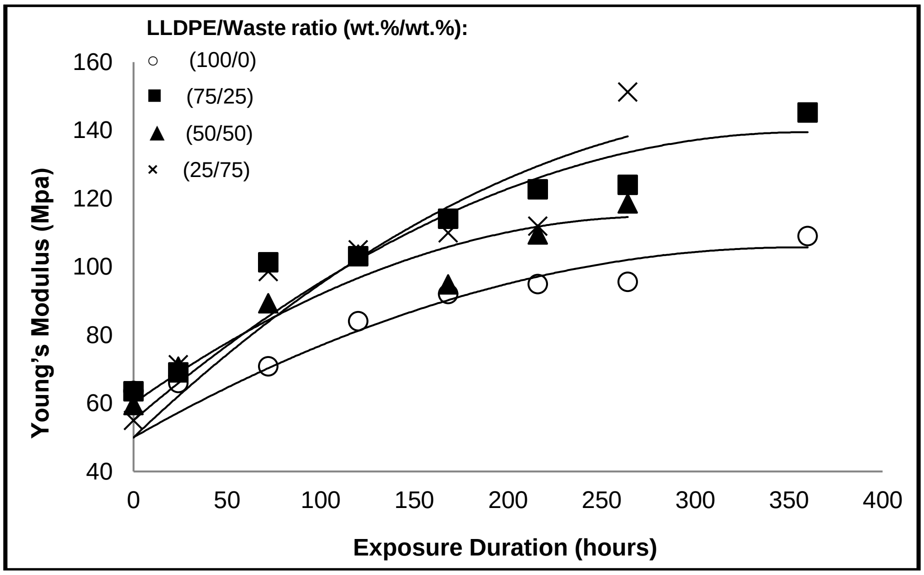

Fig.2. Young's modulus (Mpa) as a function of accelerated weathering duration (hours).

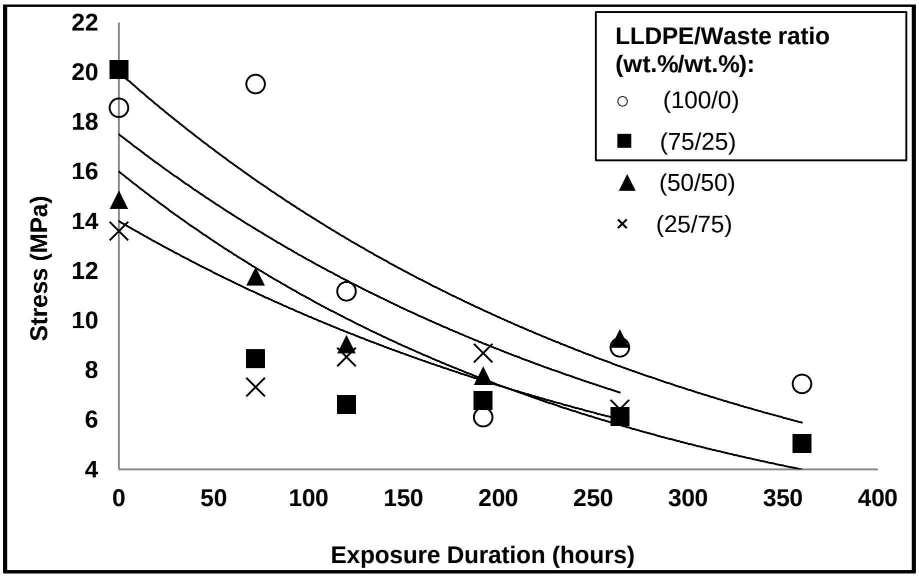

Fig.3. Stress at break (Mpa) as a function of accelerated weathering duration (hours).

Strain at rupture is typically monitored in polymer ageing studies as an indicator to mechanical integrity. The addition of waste to the studied formulations resulted in about 50% reduction in strain (%) measured after some 160 hours of exposure, after which values reduced to near zero. Strain in polymer depends on the changes occurring in the amorphous region (where chains are in disorder) in semi-crystalline polymers (Briassoulis et al., 2004). The cross linking occurring due to UV exposure in weathering disrupt the molecular chains and reduces the molecular weight as noted previously. In addition, the increase in waste content increases the PP fraction in the blend. PP posses extremely high frequency tertiary carbon atoms in its structure which makes it more susceptible to photo-degradation resulting in both molar mass reduction (consequently reduction molecular weight) and strain at rupture reduction (Ojeda et al., 2011). Changes in the materials due to weathering was also monitored by measuring the force at break (N) with respect to exposure time (Fig.5). Increase in applied mechanical forces required for rupture was proportional to virgin material content. However, intermediate values can not be deduced from the results with respect to waste material content (Fig.5).

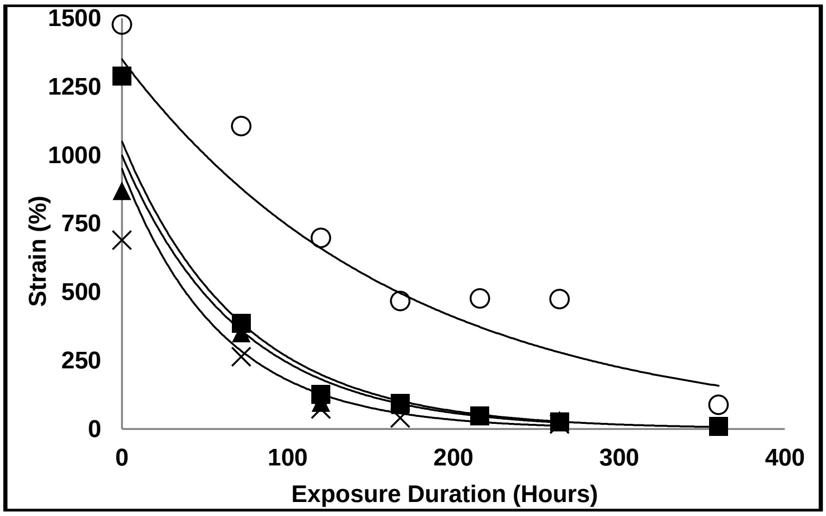

Fig.4. Strain at break (%) as a function of accelerated weathering duration (hours).

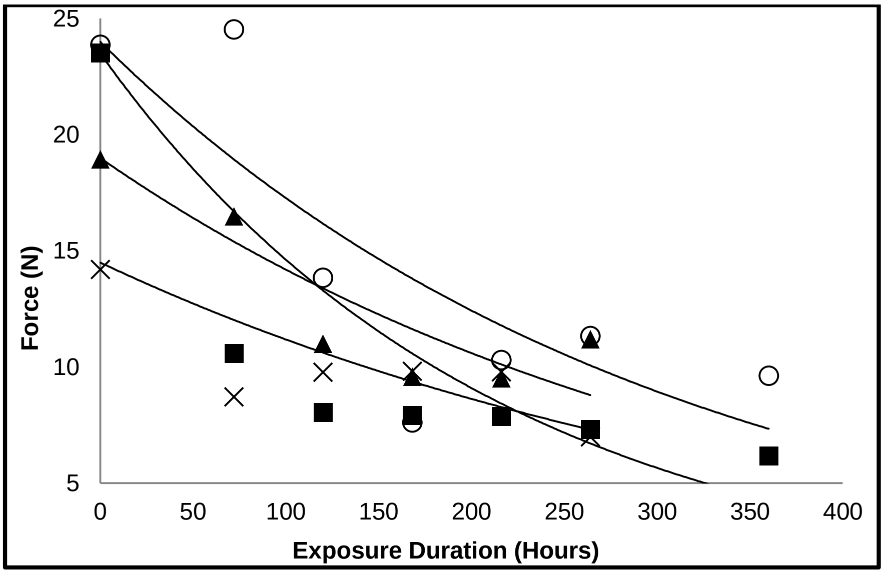

Fig.5. Force at break (N) as a function of accelerated weathering duration (hours).

It is also imperative to base decisions for product development on the acceptable standards of the market. This is especially true when trying to apply virgin/waste blends in the market for future product development as a replacement to certain polymeric products. To this end, and as initial starting point, mechanical properties results of two commercial carrier bags secured from co-ops in the state of Kuwait were examined (Table 1). A similar experimental procedure to the previously reported was followed for mechanical testing. By comparison, all formulations studied were comparable in terms of Young's modulus to the second tested batch (Co-Op 2). Camann et al. (2010), reported commercial grade mechanical properties in the UK which in terms of modulus were between 56 to 364 MPa). This range also fits the formulations tested in this work which ranged between 55 to 64 MPa. Stress and strain at rupture ranged between 14 to 20 MPa and 871 to 1478 %, respectively. Both properties are excellent indicators to the performance of the blend without any additional costs from additives.

Table 1: Commercial carrier (grocery bags) tested in Kuwait. Standard deviations (SD) are reported.

Specimens source	Thickness (mm)	Young's Modulus (MPa)	Stress at rupture (MPa)	Strain at rupture (%)	Force at rupture (N)
Co-op 1: Urban state area	0.03	134 ± 3	19 ± 7.9	582 ± 56	7.2 ± 3.2
Co-op 2: Urban/commercial area	0.03	10 ± 3	23 ± 7	711 ± 70	9.2 ± 2.8

This shows great potential in developing these formulations for commercial use as a standalone product. By doing so, carbon footprint of PSW in the State of Kuwait will be reduced drastically. In addition, converters could utilize the PSW in their commercial lines without the reliance on virgin resin consumption alone. This promotes a more green practice on a state level and can give way to reduction in PSW export as well, which is something practiced by waste management companies in Kuwait. It also shows that waste films in Kuwait do not reach total degradation, were waste fraction can not be utilized for dry mechanical blending. Parts of this work was previously published in Al-Salem et al. (2015).

Physical properties studied

In this work, haze (%), transmission (%) and total change in colour were studied for the considered materials. Colour parameters for control samples are shown in Table 2. The total change in colour (ΔE) for the materials studied did not show a clear trend with weathering time (Table 3). The change in the specimens colour was fluctuating and increasing until 7 days of exposure then reducing to recover its physical property. This was previously noted in past work (Al-Salem, 2009; Phillip et al., 2004; Youssef et al., 2008; Dehbi et al., 2010), and could be attributed to the following reasons:

- Change in specimens' colour is a continuous process resulting from surface degradation caused by irradiation. It is also associated with dye loss which was could be reasoned for these specimens, of which colours from the waste fractions were present.
- Colour change is also related to wash mechanisms either in UV chambers or rain in natural weathering, making samples collection time crucial.
- The surface structure of a polymer matrix is broken with UV exposure, hence it affects the gloss and colour parameters.

Table 2: Control samples (no exposure) colour parameters.

Materials (wt.%/wt.%)	L_s^*	a_s^*	b_s^*
LLDPE/Waste (100/0)	29.0	-0.4	-3.5
LLDPE/Waste (75/25)	25.2	-0.4	-4.8
LLDPE/Waste (50/50)	23.0	-0.6	-5.9
LLDPE/Waste (25/75)	20.1	-0.5	-5.6

Table 3: Colour parameters and total change in colour (ΔE) for studied formulations as a function of accelerated weathering exposure (hours).

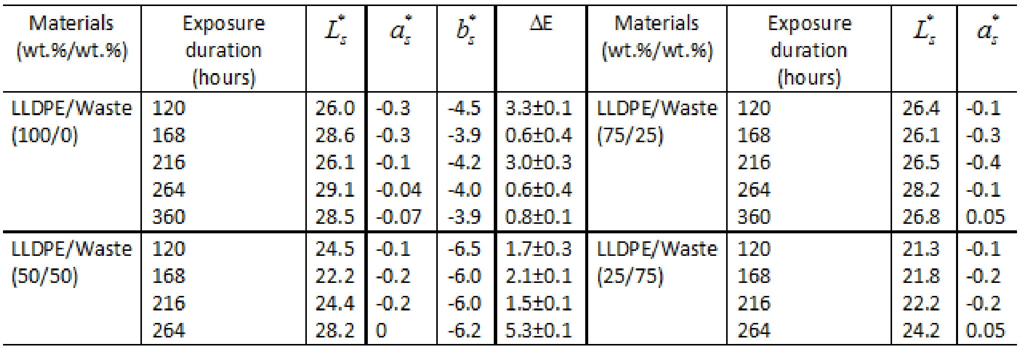

Materials (wt.%/wt.%)	Exposure duration (hours)	L_s^*	a_s^*	b_s^*	ΔE	Materials (wt.%/wt.%)	Exposure duration (hours)	L_s^*	a_s^*
LLDPE/Waste (100/0)	120	26.0	-0.3	-4.5	3.3±0.1	LLDPE/Waste (75/25)	120	26.4	-0.1
	168	28.6	-0.3	-3.9	0.6±0.4		168	26.1	-0.3
	216	26.1	-0.1	-4.2	3.0±0.3		216	26.5	-0.4
	264	29.1	-0.04	-4.0	0.6±0.4		264	28.2	-0.1
	360	28.5	-0.07	-3.9	0.8±0.1		360	26.8	0.05
LLDPE/Waste (50/50)	120	24.5	-0.1	-6.5	1.7±0.3	LLDPE/Waste (25/75)	120	21.3	-0.1
	168	22.2	-0.2	-6.0	2.1±0.1		168	21.8	-0.2
	216	24.4	-0.2	-6.0	1.5±0.1		216	22.2	-0.2
	264	28.2	0	-6.2	5.3±0.1		264	24.2	0.05

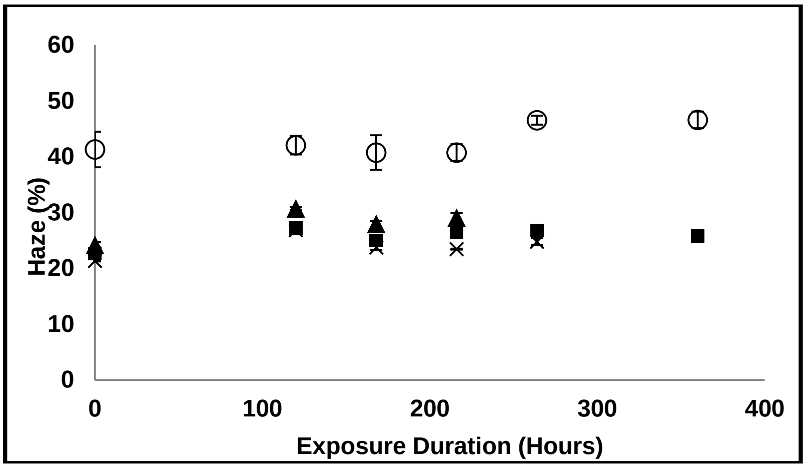

Fig.6. Haze (%) measured as a function of exposure time (hours). Symbols showing LLDPE/waste ratio in (wt.%/wt.%): ○ (100/0), ■ (75/25), ▲ (50/50) and × (25/75), respectively.

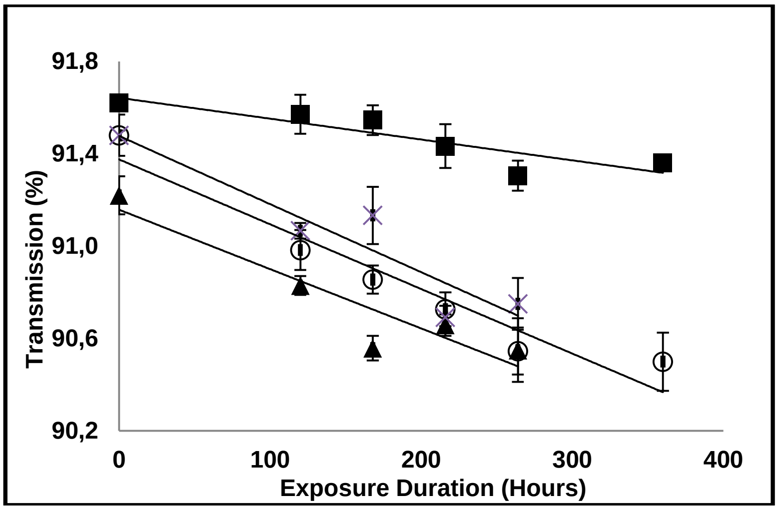

Fig.7. Transmission (%) measured as a function of exposure time (hours). Symbols showing LLDPE/waste ratio in (wt.%/wt.%): ○ (100/0), ■ (75/25), ▲ (50/50) and × (25/75), respectively.

Haze of polymeric films is caused from surface irregularities due to degradation effect (Sukhadia et al., 2001). Along with transmission, they are considered the key optical properties in polymer characterization (Espi et al., 2006). A general decrease in haze (%) was noticed in the studied materials (Fig.6). Virgin LLDPE proved to be more hazed than the blends, increasing with exposure to weathering. This could be explained by the loss of amorphous region in the LLDPE polymer. On the other hand, the same reasoning can be noted for the blends studied. However, haze (%) measured for the blends showed higher resistance and stability than the virgin polymer. This can be attributed to the action of stabilizers present in the waste films used, which is typically utilized in plastic film grades. This can explain the reduction in haze (%) with the increase in of waste content (Fig.6). transmission (%) in tested specimens showed a gradual decrease with exposure time (Fig.7). By comparison, the 50/50 (wt%./wt.%) formulation was clearly showing least transmission ability among tested materials. This indicates that a 1 to 1 blend ratio presents the superlative material for cover applications especially in sunny climates. Parts of this work was previously published in Al-Salem et al. (2015).

Conclusions

In this work, virgin LLDPE and plastic waste film blends were tested and the effect of accelerated weathering was studied on specimens formulated. Mechanical properties, namely the stress and strain at rupture showed a decreasing trend with weathering duration. However, Young's modulus (MPa) increased as the weathering time increased which is associated with the increase in samples crystallinity. Optical properties were adversely altered with weathering. However, the waste acted as a light stabilizer in the LLDPE matrix reducing haze due to amorphous region alteration. Commercial grades of two types of carrier bags in Kuwait were also tested and the blends obtained in this work were comparable. This shows that such products could be directly utilized for the market.

Acknowledgments

The authors wish to thank the Kuwait Institute for Scientific Research (KISR) and EQUATE Petrochemical Company for funding research project (PC017C). Mr. M. Mujaibel and A. Al-Marshad are gratefully acknowledged for their support in this work. Dr. A. Tuhl (NWM Co. Kuwait) is appreciated for his efforts at the start of this work. The Kuwait Foundation for the Advancement of Sciences (KFAS) are gratefully appreciated for funding the mission of Dr. Sultan Al-Salem to present this work.

References

Al-Qabandi, O., 2015. Personal communication ,EQUATE Petrochemical Company (Kuwait).

Al-Salem, S.M., Abraham, G., Al-Qabandi, O., Dashti, A.M., 2015. Investigating the effect of accelerated weathering on the mechanical and physical properties of high content plastic solid waste (PSW) blends with virgin linear low density polyethylene (LLDPE), Polym. Test. 46; 116-121.

Al-Salem, S., Mujaibel, M., Al-Banna, A., 2014. Standardized film samples preparation methodology of mixed polymers for mechanical recycling purposes in Kuwait. Technical Report, Project Code: PC005G, KISR no. 12484, December.

Al-Salem, S.M., 2009. Influence of natural and accelerated weathering on various formulations of linear low density polyethylene (LLDPE) films. Mat. Des. 30(5); 1729-1736.

Al-Salem, S.M., Lettieri, P., Baeyens, J., 2010. The valorization of plastic solid waste (PSW) by primary to quaternary routes: From re-use to energy and chemicals. Prog. Energy Combust. Sci. 36(1); 103-129.

ASTM D 1003-11, 2011. Standard test method for haze and luminous transmittance of transparent plastics. American Society for Testing and Materials, Philadelphia, Penn.

ASTM D 2244-11, 2011. Standard practice for Calculation of color tolerances and color differences from instrumentally measured color coordinates. American Society for Testing and Materials, Philadelphia, Penn.

ASTM D 4329-05, 2005. Standard practice for fluorescent UV exposure of plastics. American Society for Testing and Materials, Philadelphia, Penn.

ASTM D 4329-92, 1992. Standard practice for operating light and water apparatus (fluorescent UV and condensation type) for exposure of plastics. American Society for Testing and Materials, Philadelphia, Penn.

ASTM D 882-95a, 1995. Standard practice for fluorescent UV exposure of plastics. American Society for Testing and Materials, Philadelphia, Penn.

ASTM D1898-68, 1989. Standard practice for sampling of plastics. American Society for Testing and Materials, Philadelphia, Penn.

Basfar, A.A., Idriss Ali, K.M., 2006. Natural weathering test for films of various formulations of low density polyethylene (LDPE) and linear low density polyethylene (LLDPE). Polym. Deg. Stab. 91(3); 437-443.

Briassoulis, D.; Aristopoulou, A., Bonora, M., Verlodt, I., 2004. Degradation characterisation of agricultural low-density polyethylene films. Biosystm. Eng. 88(2); 131-143.

Camann, A., Dragsbaek, K., Krol, S., Sandgren, J., Song, D., 2010. Properties, recycling and alternatives to PE bags. An interactive qualifying project report. Worcester Polytechnic Institute.

CSB, 2014. Central statistics bureau of Kuwait. www.csb.gov.kw

Dehbi, A., Bouaza, A., Hamou, A., Youssef, B., Saiter, J.M., 2010. Artificial ageing of tri-layer polyethylene film used as greenhouse cover under the effect of the temperature and the UV-A simultaneously. Mater. Des. 31(2); 864-869.

Dehbi, A., Mourad, A.I., Bouaza, A., 2011. Ageing effect on the properties of tri-layer polyethylene film used as greenhouse roof. Proc. Eng. 10: 466-471.

Espi, E., Salmeron, A., Fontecha, A., Garcia, Y., Real, A.I., 2006. Plastic films for agricultural applications. J. Plast. Film Sheet. 22; 85-102.

KM, 2014. Kuwait Municipality (KM) landfill waste statistics, Environment Management Department.

Lundin, T., Cramer, S.M., Falk, R.H., Felton, C., 2004. Accelerated weathering of natural fiber-filled polyethylene composites. J. Mat. Civil Eng. 16(5): 547-555.

Mendes, L.C., Rufino, E.S., de Paula, F.O.C., Torres, A.C., 2003. Mechanical, thermal and microstructure evaluation of HDPE after weathering in Rio de Janerio city. Polym. Deg. Stab. 79(3): 371-383.

Mourad, A.I., 2010. Thermo-mechanical characteristics of thermally aged polyethylene/polypropylene blends. Mater. Des. 31(2); 918-929.

Ojeda, T., Freitas, A., Birck, K., Dalmolin, E., Jacques, R., Bento, F., Camargo, F., 2011. Degradability of linear polyolefins under natural weathering. Polym. Deg. Stab. 96(4); 703-707.

Philip, M., Attwood, J., Hulme, A., Williams, G., Shipton, P., 2004. Evaluation of weathering in mixed polyethylene and polypropylene products. The Waste & Resources Action Programme (UK), Report, ISBN: 1-84405-092-0, March.

Shukhadia, A.M., Wilkes, G.L., Rholfing, D.C., Johnson, M.B., 2001. Optical haze properties of polyethylene blown films-Part 2: The origin of various surface roughness. In proc: Society of Plastic Engineers (SPE) ANTEC conference, Dallas (Texas), USA, May 6-10.

Tuasikal, M.A., Alothman, O.Y., Luqman, M., Al-Zahrani, S.M., Jawaid, M., 2014. Influence of natural and accelerated weathering on the mechanical properties of low-density polyethylene films. Int. J. Polym. Anal. Charact. 19(3); 189-203.

Youssef, B., Dehbi, A., Hamou, A., Saiter, J.M., 2008. Natural ageing of tri-layer polyethylene film: Evolution of properties and lifetime in North Africa region. Mater. Des. 29(10); 2017-2022.